Durham University

Durham E-Theses

Overland flow resistance & flood generation in semi-arid environments: explaining the restrained draining of the rain in Spain

Mark William Smith

How to cite:

Smith, Mark William (2009) Overland flow resistance & flood generation in semi-arid environments: explaining the restrained draining of the rain in Spain. Doctoral thesis, Durham University.

Use policy

The full-text may be used and/or reproduced, and given to third parties in any format or medium, without prior permission or charge, for personal research or study, educational, or not-for-profit purposes provided that:

- a full bibliographic reference is made to the original source
- a https://etheses.durham.ac.uk/id/eprint/2919/ is made to the metadata record in Durham E-Theses
- the full-text is not changed in any way

The full-text must not be sold in any format or medium without the formal permission of the copyright holders.

Please consult the full Durham E-Theses policy for further details.

Academic Support Office, The Palatine Centre, Durham University, Stockton Road, Durham, DH1 3LE
e-mail: e-theses.admin@durham.ac.uk Tel: +44 0191 334 6107
https://etheses.durham.ac.uk

The copyright of this thesis rests with the author or the university to which it was submitted. No quotation from it, or information derived from it may be published without the prior written consent of the author or university, and any information derived from it should be acknowledged.

OVERLAND FLOW RESISTANCE & FLOOD GENERATION IN SEMI-ARID ENVIRONMENTS

EXPLAINING THE RESTRAINED DRAINING OF THE RAIN IN SPAIN

Mark William Smith

Department of Geography

Durham University

This thesis is submitted in accordance with the regulations for the degree of Doctor of Philosophy at Durham University, Department of Geography, 2008

24 JUN 2009

Everything is vague to a degree you do not realise
till you have tried to make it precise.

Bertrand Russell, 1918

DECLARATION

I confirm that no part of the material presented in this thesis has previously been submitted by me or any other person for a degree in this or any other university. In all cases, where it is relevant, material from the work of others has been acknowledged.

The copyright of this thesis rests with the author. No quotation from it should be published without prior written consent and information derived from it should be acknowledged.

Signed: 

Date: 08/06/09

ABSTRACT

OVERLAND FLOW RESISTANCE & FLOOD GENERATION IN SEMI-ARID ENVIRONMENTS

Resistance equations developed for pipe flows and open channel flows cannot be applied to model overland flows uncritically. The formulation of these equations employs several crucial assumptions that are specific to the conditions in which they were developed and cannot be universally applied. The hydraulic behaviour of overland flow is distinct from that of pipe and channel flows and can be characterised by a high degree of variability both over space and over time as roughness elements are progressively inundated with increasing depth. A novel methodology of measuring overland flows in the field at a high-resolution permits examination of the interaction between flow variables and surface roughness. Reconstructing the water surface from elevation data and flow extent provides an estimation of the distribution of flow depths and offers a complementary perspective to more conventional approaches.

Overland flows are observed to be highly variable both across and between hillslopes. The distribution of flow depths can be modelled using a two-parameter gamma distribution; both parameters show distinct variations with distance downslope and represent the progressive inundation of roughness elements with increasing depth. The flow interacts with soil surface form where it is capable of eroding its bed and the observed slope-independence of rill velocity can be explained by a feedback between flow state (as characterised by the Froude number) and surface roughness. While the existence of this

interaction is affected by soil-type, the soil is observed to have little influence on the relationship between surface roughness and overland flow.

Resistance is found to be spatially variable; some of this variability could be explained by the classification of areas of similar microtopography as identified in the field. This classification can be approximated by a thresholded index-based classification and provides a tool for up-scaling to the hillslope scale.

Relating roughness to resistance is not straightforward. Complex natural soil surfaces vary in innumerable ways. Traditional roughness measures fall short of providing an adequate description of the complex soil surfaces observed in the field. A variety of alternative measures are developed, each of which captures a different attribute of surface form. These measures are tested to examine their influence on overland flow resistance and a suite of roughness-resistance models is developed which includes the effect of hillslope position to different degrees. Modelled flow resistance can be separated into a constant term and a depth-dependent term and can be easily incorporated into models of hillslope hydrology. This resistance is observed to decline where a hydrological connection, once established, is then maintained.

Examination of the concept of hydrological connectivity in a semi-arid context suggests that the interaction between runoff generation and transfer determines not just flood peaks but also total flow amount. It is suggested that flow resistance and hence runoff transfer should be afforded the same detailed consideration as infiltration parameters, i.e. a spatially distributed and variable value (as a function of depth) that can be organised into discrete units akin to those developed for runoff generation. The parameterisation of both infiltration and resistance in this way provides a crucial interaction through the redistribution of soil moisture and runoff over hillslope surfaces. Through this mechanism, the observed complex and nonlinear runoff response to storm events may be explained as these attributes interact with rainfall characteristics and flow network development. Further understanding of this interaction could have practical implications for catchment management and affect the prioritisation of land management decisions.

ACKNOWLEDGEMENTS

I would like to thank my supervisors, Dr. Nick Cox and Dr. Louise Bracken, who have provided sources of funding, inspiration and guidance throughout my Ph.D. In addition, I would also like to thank Dr. Rich Hardy for commenting on several chapters and drafts, Dr. Nick Rosser both for his work on designing the camera boom and for his tireless attempts to send a replacement laser scanner out to Spain, and Dr. Sim Reaney for an overview of hydrological modelling. Professor Rob Ferguson also provided a variety of helpful suggestions and ideas that helped to shape this project as did Professor Mike Kirkby during our numerous trips to the field site.

The fieldwork stage of this project was especially challenging and suffered its fair share of setbacks. Thanks to Dave Milledge who worked ridiculous hours in the blistering sunshine during the first field campaign, and to John Thompson who bravely stepped in as an emergency field assistant when things were all going wrong. My dad, Gary Smith also showed amazing patience and endurance during our field trips: I wish the conditions could have been better for us, but thanks for sticking with it. Despite all the problems, I have some fantastic memories of my time in the field. It's funny how time does that.

I would also like to thank my fellow Ph.D. students and colleagues at the Department of Geography, my friends and many accumulated housemates for making my time in Durham so enjoyable. There are too many of you to start naming names, but you know who you are. Most of you are called Dave anyway. Additionally, Eddie Million and Merv Brown were instrumental in developing the various pieces of field equipment, and I would like to thank Derek Hudspeth, Neil Tunstall, Derek Coates and Frank Davies for their invaluable help over the last three years.

Finally, special thanks are reserved for my family who have provided continuous support over the years. This thesis could not have been written without their support and encouragement. I wish to dedicate this thesis to them.

CONTENTS

LIST OF FIGURES

LIST OF TABLES

NOTATION

Dimensions are given in terms of length L, mass M and time T.

A = area of flow [L^2]
A = steady drainage from soil moisture store [$L\ T^{-1}$]
A_{3D} = surface area [L^2]
A_P = projected frontal area of roughness element [L^2]
B = soil sorptivity [$L\ T^{-0.5}$] (Philip, 1957) or [$L^{-2}\ T^{-1}$] (Green and Ampt, 1911)
C = Chézy's factor of resistance [$L^{1/2}\ T^{-1}$]
C_D = coefficient of drag on roughness element [dimensionless]
d = pipe diameter or mean water depth [L]
d_{50} = median flow depth [L]
d_{sk} = depth skewness [dimensionless]
D_x = diameter of the x^{th} percentile of the particle-size distribution [L]
e = base of natural logarithm [dimensionless]
f = Darcy-Weisbach friction factor [dimensionless]
f_A = constant component of flow resistance [dimensionless]
f_B = depth-dependent component of flow resistance [dimensionless]
f_c = friction factor using corrected velocity [dimensionless]
f_i = infiltration rate [$L\ T^{-1}$]
F_D = drag force introduced by roughness element [$M\ L\ T^{-2}$]
F_P = frontal area per unit planar area [dimensionless]
Fr = Froude number [dimensionless]
F_T = frontal area per unit surface area [dimensionless]
g = gravitational acceleration [$L\ T^{-2}$]
h = runoff threshold [L]
h_f = head loss due to friction [L]
h_0 = suction at minidisk surface [L]
I = cumulative infiltration [L]
K = soil hydraulic conductivity [$L\ T^{-1}$]
L = characteristic length [L]
n = Manning's roughness parameter [dimensionless, or $L^{-1/3}\ T$ to balance equation]
n = number of observations [dimensionless]

n_i = soil van Genuchten parameter (Zhang, 1997) [dimensionless]
p = fluid pressure [M L^{-1} T^{-2}]
P = wetted perimeter [L]
P_d = mean pit density of transects parallel to flow direction [L^{-1}]
P_{dmin} = minimum pit density of transects parallel to flow direction [L^{-1}]
P_{dmx} = maximum pit density of transects parallel to flow direction [L^{-1}]
P_{dxc} = mean pit density of transects perpendicular to flow direction [L^{-1}]
P_r = proportion of the surface covered with roughness elements [dimensionless]
Q = discharge [L^3 T^{-1}]
r = pipe radius [L]
r = Pearson's correlation coefficient [dimensionless]
r_s = storm total rainfall depth [L]
r_0 = minidisk radius [L]
R = hydraulic radius (measured perpendicular to flow direction) [L]
Re = flow Reynolds number [dimensionless]
R_v = volumetric hydraulic radius [L]
S = slope [dimensionless]
S_f = energy gradient [dimensionless]
S_i = soil moisture storage [L]
t = time [T]
T_{3D} = surface tortuosity [dimensionless]
T_p = mean tortuosity of transects parallel to flow direction [dimensionless]
T_r = tortuosity ratio (T_p / T_{xc}) [dimensionless]
T_w = wet tortuosity of flow (= T_{xc}) [dimensionless]
T_{xc} = mean tortuosity of transects perpendicular to flow direction [dimensionless]
u = at-a-point velocity in a profile [L T^{-1}]
$u*$ = shear velocity [L T^{-1}]
V = average flow velocity [LT^{-1}]
V_l = flow volume [L^3]
w = width of flow [L]; unit weight of water [M L^{-2} T^2]
z = elevation; height above the bed in a velocity profile [L]
z_0 = roughness height in a velocity profile [L]
Z_d = mean surface elevation difference [L]
Z_{NN} = nearest neighbour [L]
α = shape parameter of depths (fitted to gamma distribution) [dimensionless]
α = mean velocity correction coefficient [dimensionless]
α_i = soil van Genuchten parameter (Zhang, 1997) [L]
β = scale parameter of (depths fitted to gamma distribution) [L]
ε = characteristic roughness height (Nikuradse equivalent sand roughness) [L]
θ = slope angle [dimensionless]
κ = von Kármán's constant in a turbulent velocity profile [dimensionless]

Λ = inundation ratio [dimensionless]
Λ_σ = inundation ratio STDEV [dimensionless]
Λ_{Zd} = detrended inundation ratio [dimensionless]
μ = absolute fluid viscosity [$M\ L^{-1}\ T^{-3}$]
μ = location parameter of distributions fitted to flow depths [L]
ν = kinematic fluid viscosity [$L^2\ T^{-1}$]
ρ_w = fluid density [$M\ L^{-3}$]
σ_Z = surface standard deviation [L]
σ_{Zxc} = mean standard deviation of transects perpendicular to flow direction [L]
τ = shear stress [$M\ L^{-1}\ T^{-2}$]

Abbreviations

DEM = Digital Elevation Model
EU = European Union
HYSS = Hydrologically Similar Surface
LD = Limiting Distance (Linden and Van Doren, 1986)
LS = Limiting Slope (Linden and Van Doren, 1986)
MDS = Maximum Depressional Storage
MIF = Microrelief Index and Peak Frequency (Römkens and Wang, 1986)
MRZ = Morphological Runoff Zone
MUD = Mean Upslope Difference (Hansen *et al.*, 1999)
RMS = Root Mean Square
RR = Random Roughness (Allamaras *et al.*, 1966)
TLS = Terrestrial Laser Scanner
VSA = Variable Source Area

CHAPTER 1

INTRODUCTION: STATEMENT OF AIMS

1.1 Context

Given the flashy and torrential nature of flood events in semi-arid environments, the increased probability of such events occurring (predicted by Poesen and Hooke, 1997), and increasing occupation and vulnerability of flood-risk areas, an ability to predict the arrival time of flood waves and flood peaks is of great importance. There is a need to develop our understanding of flood routing both through ephemeral channels and over hillslope surfaces. Though recent advances have been made modelling the former (e.g. Shannon *et al.*, 2002), methodological and conceptual advances are required to provide a clearer perspective of overland flow generation and resistance over natural hillslope surfaces.

Drylands represent nearly 50% of the terrestrial Earth (Figure 1.1), supporting nearly 20% of its population on land which is marginal for many economic activities and is considered to be highly sensitive to the effects of hypothesised climatic changes related to global warming (UNEP, 1992; Nanson *et al.*, 2002; Yair and Kossovsky, 2002). Unlike more humid environments, the permanent (or seasonal) soil moisture deficit means that many dryland rivers are ephemeral and overland flows are intermittent and rare, occurring only briefly during and after large rainstorms (Bull *et al.*, 1999; Hooke and Mant, 2000; Bull and Kirkby, 2002). Overland flows are attenuated by high infiltration rates, particularly in channel beds, and so flow rarely reaches the catchment outlet (Shannon *et al.*, 2002). When

flood events do occur, more than 95% of the floodwater is generated on hillslopes and transported into streams as overland flow (Kirkby, 1988), emphasising the relative importance of hillslope processes (Scoging, 1982).

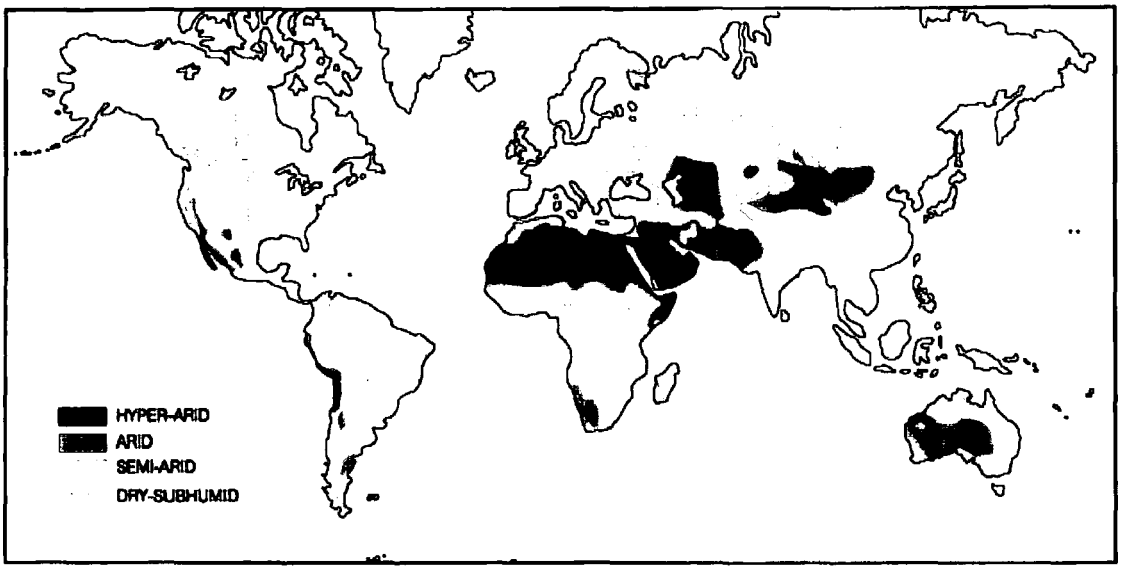

Figure 1.1. World distribution of warm drylands. The term 'drylands' encompasses hyper-arid, arid, semi-arid and dry sub-humid areas. Of these, semi-arid areas are the most extensive, covering 18% of the world's land surface. Source: Tooth (2000: p.68) after UNEP (1992).

Runoff generation is spatially non-uniform; the propagation of flood-waves downstream integrates climatic factors with properties of the Earth's surface as runoff travel-distance is determined by the interaction between rainfall characteristics, infiltration and the hydraulics of the overland flow (Yair and Raz-Yassif, 2004). Often only isolated areas of semi-arid surfaces generate overland flow; these areas enlarge with increasing storm rainfall not because of expanding saturated area (as observed in humid climates) but from a decrease of the surface infiltration rate below rainfall intensity (the Hortonian 'infiltration excess' mechanism). Such expansion of the contributing area has many parallels with the 'variable source area' theory of humid environments (Hewlett and Hibbert, 1967). However, in semi-arid systems, this expansion of the contributing area is nonlinear and can rapidly increase as a result of developing overland flow connections between runoff generating areas and the channel network. As a rainstorm progresses, decreasing surface infiltration rates allow

surface runoff to travel further before infiltrating, encouraging the development of continuous flowpaths.

The velocity at which overland flow is routed will determine the rainfall characteristics necessary for production of connected flow, yet overland flow resistance is afforded relatively little attention in the development of models of hillslope hydrology (and is frequently represented as a constant parameter lumped over entire hillslopes). Soil microtopography has been observed to demonstrate systematic variations over hillslope surfaces (Bracken and Kirkby, 2005), which will influence the efficiency with which runoff is routed. This study provides a detailed investigation of surface factors influencing transfer of runoff at the hillslope and small catchment scale, which provides a crucial interaction with runoff generation to determine hillslope outflow. This is especially relevant in semi-arid environments where, as a result of the large annual water deficit, water redistribution and horizontal fluxes (affecting erosion, nutrient depletion and pollution; Brazier *et al.*, 2007) are dominated by overland flows with subsurface flows providing a negligible contribution to outflows.

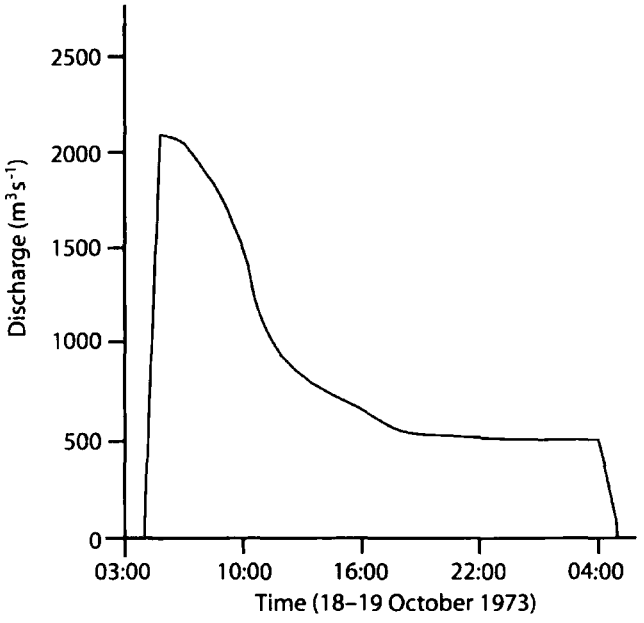

Figure 1.2. Flood hydrograph of the Nogalte ephemeral channel during a flood event of October 1973 demonstrating a typically sharp rising limb and short base duration. Source: López-Bermúdez *et al.* (2002: p.338).

Hillslope runoff generation drives the flashy and often torrential flood events experienced in semi-arid catchments. Figure 1.2 presents a typical high-magnitude flash flood event recorded in the Rambla Nogalte (a field site investigated in this study) in October 1973 which resulted in a flood peak of 2100 $m^3 s^{-1}$ at Puerto Lumbreras (López-Bermúdez *et al.*, 2002). The hydrograph shows a single peak with a very sharp rising limb and a base duration of less than two days. Such high-magnitude events represent a higher proportion of runoff totals than in more temperate environments (events with a return period of over 10 years are responsible for more than 40% of total sediment transport; Richards, 1982). However, the long interval between such events means that inundated areas are often occupied (Figure 1.3) and have been subject to recent development (e.g. use of channels as roads, wells in the channel bed, urban development, increase in human settlement and agriculture; Figure 1.4).

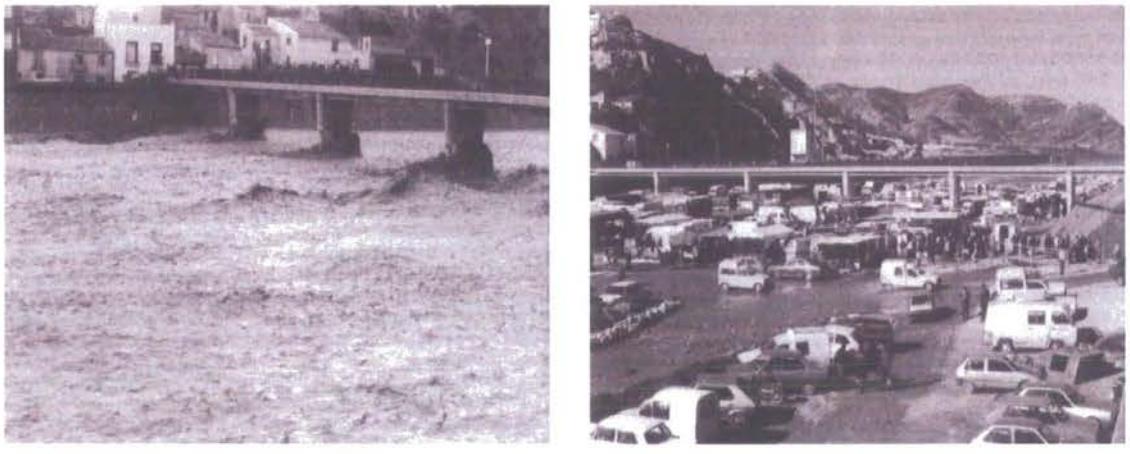

Figure 1.3. The Rambla Nogalte through Puerto Lumbreras (see map in Figure 4.28); (a) during a torrential flood event of 7th September 1989; (b) human activity in the dry channel (26th January 1990). Source: López-Bermúdez *et al.* (2002: p.334).

The inter-annual rainfall variability of semi-arid areas is particularly high (Corte-Real *et al.*, 1998). The magnitude and frequency of recent flood events condition the policy adopted by a country towards alleviating the flood risk. However, high-magnitude flood events will inevitably exceed the capacity of some flood relief structures (López-Bermúdez *et al.*, 2002). In this situation, flood relief structures can offer a false sense of security to an area

that is becoming increasingly vulnerable to flood events; their failure can even make the flood worse. Targeting preventative measures at areas where the floodwaters have yet to develop significant erosive capacity may be more effective: that is, at the hillslope and headwater areas that contribute the majority of the floodwaters.

Figure 1.4. The Rambla Nogalte beyond Puerto Lumbreras (flow is from left to right). Note the encroachment of agriculture and infrastructure on the flood plain below the town. The bridge in Figure 1.3 crosses the channel at the town centre. Source: Google Earth.

Hillslope runoff generation and transfer remains a poorly understood process. While much research has been undertaken at the plot scale (e.g. Bergkamp *et al.*, 1996; Lasanta *et al.*, 2000; Parsons *et al.*, 1996a, 1997), attempts to up-scale our understanding to larger scales where management decisions can be made are hampered by our limited conceptualisation of emergent processes (Tetzlaff *et al.*, 2008; Sidle, 2006; Cammeraat, 2004). At the hillslope scale, spatial heterogeneity and connectivity of runoff generating areas is of fundamental importance; yet McDonnell *et al.* (2007) note the need to look beyond such variability to establish organising principles. The relationship between catchment form, the morphological influence of water flows and the resultant self-organising structure of

catchments and hillslopes may provide such unifying properties (Wagener *et al.*, 2007; Sivapalan, 2005). Recently, integration of experimental work with hydrological modelling experiments has facilitated progress in the area of hillslope runoff response (Tetzlaff *et al.*, 2008; Seibert and McDonnell, 2002).

Despite the importance of understanding routing velocities, flow resistance parameters are afforded minimal consideration, even in distributed, physically-based hydrological models. The routing of overland flows over hillslope surfaces relies heavily on theoretical and experimental insights developed from pipe and open channel flows. Yet the hydraulics of a thin layer of water moving over a rough and complex soil surface may be distinct from these more idealised flows. In particular, the traditional formulation of concepts such as roughness and resistance requires re-evaluating for overland flows where even small-scale microtopography can exert a large influence on the resultant flows (Morvan *et al.*, 2008). Recent technological advances open a window through which the processes in which microtopography (or roughness) influences flow hydraulics can be examined; however, given the conceptual difficulties discussed above, the challenge remains to incorporate this understanding into a hillslope-scale hydrological model. This represents the main goal of this thesis.

1.2 Aims and Objectives

The overall aim of this project was to provide a detailed examination of overland flow hydraulics, focusing on the influence of surface roughness and infiltration on flow resistance and hillslope-scale flood generation in semi-arid environments.

The following specific objectives were identified:

(1) To develop a methodology that allows the variables of overland flow to be precisely defined and measured in the field.

(2) To examine the variation of overland flows across and between hillslopes.

(3) To identify which particular attributes of surface roughness or flow characteristics can be usefully parameterised for modelling the hydraulics of overland flow.

(4) To examine how hillslope location, soil type and land-use influence these roughness-resistance relationships.

(5) To establish the effect of infiltration rate on the hydraulics of flow on hillslopes.

(6) To integrate this information within the framework of hydrological connectivity to develop an improved understanding of the role of topography, infiltration and the temporal structure of rainstorms for flood generation in semi-arid environments.

1.3 Thesis Structure

Chapter 2 discusses the history of flow resistance equations, focusing on the assumptions made during the development of these equations and the limitations encountered when applying them to overland flows. Part of this discussion has been previously published in Smith *et al.* (2007). **Chapter 3** explains the motivation for increasing our understanding of overland flow hydraulics by placing the discussion in the context of flood generation in semi-arid environments. The connectivity framework is introduced and used to review the conceptual model of flood generation applied in this thesis, highlighting several key research questions that must be addressed to satisfy the aims and objectives presented above. This chapter provides a basis for the interpretation of the data generated in this thesis. **Chapter 4** briefly reviews measurement techniques applied to overland flows before presenting a detailed description of the innovative high-resolution methodology developed in this study. This chapter also describes the locations in south-east Spain where the data collection took place.

The main body of data generated in this study is presented in Chapters 5–7. **Chapter 5** focuses on the variation of the measured characteristics of overland flows both across a hillslope and between different soil types. This chapter also demonstrates the potential of this new methodology to advance the study of overland flows, using the high-resolution dataset to test existing theories of overland flow hydraulics (including those discussed in Chapter 2). **Chapter 6** then examines the most appropriate method of representing flow resistance in overland flows, evaluates the traditional approaches described in Chapter 2

and develops a suite of empirically-developed equations to model flow resistance using various measures of surface roughness. **Chapter 7** places the results within the framework of hydrological connectivity, examining the development of flowpaths on hillslopes during rainstorms and the influence of infiltration rates on flow resistance and flood generation.

Chapter 8 then synthesises the results from the previous three chapters in an attempt to explain runoff response in semi-arid catchments. The discussion highlights research priorities for the development of a thoroughly quantitative approach to hydrological connectivity. The results of the previous three chapters are combined with a basic analysis of rainfall patterns to inform a conceptual model of semi-arid hillslope hydrology that can be easily assimilated into existing hydrological models of hillslope runoff. The implications of this development for conceptualising hydrological connectivity and predicting flood generation are discussed. Suggested improvements to the methodology implemented in this thesis and future research opportunities are described at the end of this chapter.

Finally, **Chapter 9** presents the main conclusions of this thesis and the consequences for hillslope and flood risk management.

CHAPTER 2

HYDRAULICS OF OVERLAND FLOW: BACKGROUND

2.1 Introduction

Accurate predictions of streamflow require calculation of flow velocities within stream channels and over hillslopes. Such calculations cannot be made without accounting for the hydraulic resistance experienced by flow over different morphologies. Hydrological and erosion models use the water depth to estimate the routing velocity and resultant erosion at each spatial element and are typically very sensitive to the hydraulic resistance parameters employed in these estimations (Jetten *et al.*, 1998; Takken *et al.*, 2005). Two-dimensional runoff models capable of representing cross-sectional variability of velocity and depth continue to treat the issue of flow resistance using relations developed from one-dimensional flow descriptions (Bates *et al.*, 1992). The Darcy-Weisbach, Chézy and Manning equations are the most widely used empirical equations for the calculation of flow velocity in these models.

The purpose of this chapter is to state explicitly and discuss critically the assumptions upon which the study of overland flow hydraulics currently rests. Some of the following discussion was published in Smith *et al.* (2007). In providing background information for users of flow resistance equations, a brief history of the discipline of hydraulics is presented. Table 2.1 gives a summary of major contributions discussed in this paper; for a

more complete history of hydraulics, see Rouse and Ince (1957); for a more concise survey see Mikhailov (1994). This thesis aims to discourage blind acceptance of conventional methods and to encourage developments in the field of overland flow hydraulics by suggesting a way forward which reduces the restrictions of these assumptions (Chapter 4), permits high-resolution measurement of overland flows on natural surfaces (Chapters 5 and 7) and allows the development of a new approach to overland flow resistance (Chapters 6 and 8).

Fluvial hydraulics takes much theory from its parent subject of fluid mechanics; therefore this chapter begins by briefly examining the basic concepts of this discipline (section 2.2). Section 2.3 then charts the historical development of flow equations developed for ideal pipe flows. The term 'hydraulics' first appeared in the early Renaissance and is based on the Greek words for water and pipe (Mikhailov, 1994). Many analyses (including the Darcy-Weisbach equation) were first developed from experiments with water flow in pipes (Figure 2.1a), and then generalised and applied to both natural and artificial open channel flows (for which the Chézy and Manning equations were developed; Figure 2.1b). The same principles have since broken free of channels and pipes and been used to inform the study of overland flow hydraulics (Figure 2.1c).

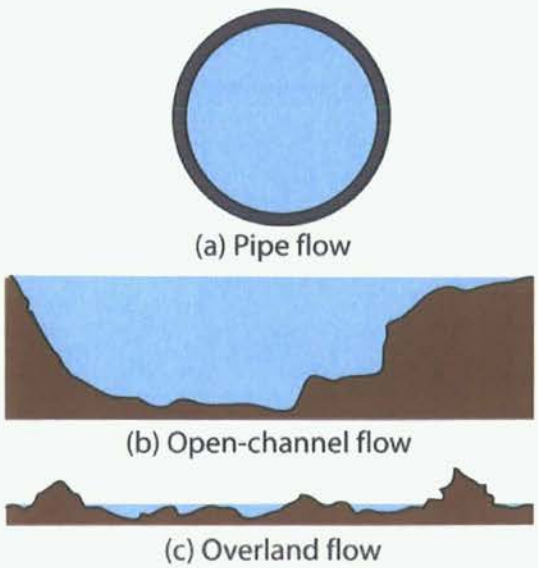

Figure 2.1. Cross-sections of typical: (a) pipe flow, (b) open-channel flow, (c) overland flow.

Isaac Newton	1643-1727		First developed a quantitative physical and mathematical treatment of fluid flows in Book II of *Principia Mathematica*.	1687	Britain
Daniel Bernoulli	1700-1782		Proposed the Bernoulli equation for frictionless flows in *Hydrodynamica*. This states that the total of all forms of energy is constant along an enclosed path.	1738	Switzerland
Antoine Chézy	1718-1798		Developed the Chézy equation relating uniform flow velocity of a stream to the hydraulic radius and bed slope.	1776	France
Gaspard Riche de Prony	1755-1839		Student of Chézy. First developed an equation predicting head loss due to friction from velocity and pipe dimensions which was the starting point for the Darcy-Weisbach equation.	1804	France
Julius Weisbach	1806-1871		First proposed the Darcy-Weisbach equation in the form now in use.	1845	Germany
Henry Darcy	1803-1858		Proposed new relations for Prony coefficients and introduced the concept of relative roughness.	1857	France
William Froude	1810-1879		Characterised flow speed relative to speed of surface waves with the ratio of inertial to gravitational forces. Froude number is used to distinguish different flow states.	1871	Britain
Osborne Reynolds	1842-1912		Developed the Reynolds number describing transition from laminar to turbulent flow using the ratio of viscous and inertial stresses in pipe flows.	1883	Britain
Robert Manning	1816-1897	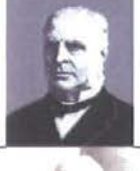	Proposed that Chézy's C increases approximately with the sixth-root of channel size to develop Manning's n.	1891	Ireland
Ludwig Prandtl	1875-1953		Introduced the boundary layer concept: that viscous effects dominate in a small region at the edges of a fluid in contact with a stationary solid.	1904	Germany

Table 2.1. Key figures in the early development of hydraulics mentioned in the text.

The shortcomings of applying these principles to flow in artificial and natural channels (section 2.4) and finally overland flow (section 2.5) are addressed. What is crucial, although quite often overlooked in the literature or in practice, is that each analysis depends on assumptions about the nature of the flow. As in any area of physical science, some assumptions are unavoidable and they may even be totally unproblematic, as when it is asserted, usually tacitly, that quantum or relativity effects may be neglected in environmental science problems. However, overland flow is markedly different from pipe flow, and these empirical relations should be used only with due caution outside the conditions for which they were developed.

It is important that researchers consider how far the various assumptions apply to their field or laboratory situation. The following assumptions will be brought into question:

- flow can be described as uniform,
- flow is parallel to the surface,
- flow is of a constant width and the boundary to the flow is longitudinally uniform,
- grain roughness is homogeneous over the wetted perimeter and can be considered as random,
- form roughness and other sources of flow resistance can be ignored,
- resistance is independent of flow depth, and
- resistance can be modelled as a function of the Reynolds number.

2.2 Fundamental Concepts of Fluid Dynamics

Gravity exerts a force which acts to propel water downslope. If a water body moves downslope at a uniform speed, the component of the gravitational force acting in the downslope direction must be balanced by an equal and opposite friction force (Leopold *et al.*, 1964). This force corresponds to a shear stress and arises from the resistance of the boundary to flow. Resistance is a function of the surface area in contact with the flow, and so flow becomes more efficient when the ratio of the flow cross-sectional area A to the wetted perimeter P is high (defining the hydraulic radius R). The velocity of water will

therefore depend on this hydraulic radius, the boundary roughness and the energy gradient of the flow. Attempts to quantify these relationships have resulted in numerous flow resistance equations.

Unlike an elastic solid, a fluid body is unable to withstand a static shear stress and instead responds with an irrecoverable flow. Shear forces in a fluid are possible only while relative movements take place between layers (Massey and Ward-Smith, 2001). Therefore, a fluid will continuously move and deform while the shear stress is applied. The resistance to this shear stress can be measured by the fluid viscosity, which determines the strain generated by any shear stress. This 'viscous stress' can be explained by inter-molecular forces and the interchange of molecules between two layers moving relative to each other (and the resultant momentum exchange). Newton (1687) proposed that the absolute fluid viscosity μ is defined as the ratio of the stress at a point to the velocity gradient of straight parallel flow.

Viscous stresses act to stabilise and organise flow, whereas inertial forces (arising as a resistance to acceleration) disrupt organised flow and encourage chaotic and turbulent motion. Hagen (1839) first noticed that the nature of flow through a pipe changes once a certain velocity is exceeded. Reynolds (1883) suggested that this was a consequence of the relative significance of both viscous and inertial stresses in fluid flow and proposed a dimensionless grouping to describe this (see Strahler (1958) for a geomorphological discussion of dimensional analysis). Viscous forces are reflected in μ while inertia forces are reflected in fluid density ρ_w and characteristic length and velocity measures L and V. Kinematic fluid viscosity ν is defined as the ratio μ/ρ_w. The Reynolds number can thus be defined as

$$\mathrm{Re} = \frac{VL}{\nu}. \tag{2.1}$$

At large Reynolds numbers, viscous forces are not important to the flow dynamics as viscosity cannot dissipate the smallest scales of fluid motion, which remain undamped (White, 2003). Flow in this case is described as turbulent and produces random eddies, vortices and other flow fluctuations. Conversely, at low Reynolds numbers, viscosity

damps out the smaller scales of motion, and only the larger scales remain. At Reynolds numbers below 2300 (in circular pipes) the flow is characterised by smooth constant fluid motion and is described as laminar. Above a Reynolds number of 4000 the flow is considered to be fully turbulent. An ill-defined region between these two limits is known as the transitional zone.

The characteristic length and velocity terms provide a means of comparing different observations. The pipe-flow experiments of Reynolds (1883) used pipe diameter (twice the radius, $2r$, in a circular pipe) and mean fluid velocity. Massey and Ward-Smith (2001: p.43) warn that the use of this characteristic length requires that the "essential condition of geometric similarity" applies. The critical Reynolds number transition to turbulent flow depends on the exact flow configuration and should be determined experimentally: it can be altered by smoothing pipes or changing their shape. Therefore, the value for the onset of turbulence observed in a smooth circular pipe cannot be directly used to predict turbulence in a pipe of a different shape or in a channel.

Turbulent flow is neither steady nor uniform. Steady flow moves at a constant rate; uniform flow moves at the same velocity throughout its cross-section. However, turbulent flow may be described as being steady or uniform or both: this describes the mean movement of the fluid over some 'reasonable' time interval. The following discussion of pipe flow experiments is limited to uniform flow conditions. However, as Graf (1998: p.71) notes with reference to open channel flow, although uniform flow occurs rarely, "this type of flow is usually taken as the standard (reference) flow for any theoretical and experimental study of other types of flow, but notably for the understanding of the flow resistance".

2.3 Flows in Pipes and Ducts

Friction forces in pipes can be assumed to comprise both the loss of mechanical energy used to overcome the viscous forces that arise from velocity being zero at the walls and higher at the centre and energy losses from the grain resistance of the pipe material (Tritton, 1988). Daniel Bernoulli's (1738) principle of constant energy may be extended to quantify this fluid friction (or 'head loss due to friction', h_f) between two points in a straight pipe.

Assuming uniform and incompressible flow, the flow velocity can be cancelled and the steady flow energy equation becomes

$$h_f = \left(\frac{p_1}{\rho_w g} + z_1\right) - \left(\frac{p_2}{\rho_w g} + z_2\right) = \Delta z + \frac{\Delta p}{\rho_w g}, \tag{2.2}$$

where g is the acceleration due to gravity, p is the fluid pressure (the force per unit area arising from molecular 'collisions' with the adjoining fluid or solid boundary), ρ_w is the fluid density and z is elevation. To predict head loss using this equation, the pressures would need to be measured at a specific flow rate. An equation to predict h_f from a property of the fluid, velocity, and pipe diameter and internal roughness would be much more useful.

de Prony (1804) made the first advances towards such an equation, suggesting that

$$h_f = \frac{L}{d}(aV + bV^2), \tag{2.3}$$

where L and d are the length and diameter of the pipe, and a and b are empirical constants in a friction term (Newton had previously used equations of this form for analytical calculations in *Principia*). From this starting point the Darcy-Weisbach equation was developed. Darcy (1857) used a larger number of experiments to propose new relations for the Prony coefficients (Brown, 2002) and thereby introduced the concept of pipe roughness scaled by the diameter (commonly known as the 'relative roughness'). Darcy proposed that

$$h_f = \frac{L}{d}\left[\left(c + \frac{e}{d^2}\right)V + \left(c' + \frac{e'}{d}\right)V^2\right], \tag{2.4}$$

where c, c', e and e' are empirical coefficients for a given type of pipe (Brown, 2002).

However, Weisbach (1845) earlier proposed the version of the equation now used. Weisbach suggested that as h_f is proportional to both L/d (from equations 2.3 and 2.4) and V^2 (from the experiments of Hagen, 1839), this can be combined to give

$$h_f = f\frac{L}{d}\frac{V^2}{2g}. \tag{2.5}$$

The dimensionless term f is now known as the Darcy-Weisbach friction factor. Since the diameter of a circular pipe is equal to four times the hydraulic radius R and the energy gradient $S_f = h_f/L$ we may solve for the friction factor as

$$f = \frac{8gRS_f}{V^2}. \tag{2.6}$$

In pipe flow, f depends on the Reynolds number (although not in turbulent flows), the pipe shape, and (except in laminar flows) the relative roughness of the pipe ε/d, where ε is the 'characteristic roughness length scale' (also known as the Nikuradse equivalent grain roughness).

In laminar flow, the pipe friction factor decreases inversely with the Reynolds number:

$$f = \frac{64}{\mathrm{Re}}, \tag{2.7}$$

as plotted on the left-hand side of Figure 2.2 (Blasius, 1913).

Beyond a Reynolds number of approximately 2300 (i.e. for turbulent flow) the flow also depends on the relative roughness ε/d of the pipe, and different curves are obtained for different values of relative roughness. Nikuradse (1933) simulated roughness by gluing uniform grains of sand on to the inner walls of pipes and then measured pressure drops and flow rates to correlate f and Re. For very turbulent pipe-flow, f becomes independent of Re; this represents the region of horizontal lines on the right-hand side of Figure 2.2 (plotted for several values of ε/d). von Kármán (1930) suggested this region could be explained by the interaction of pipe roughness with the fluid boundary layer.

The boundary layer theory was first proposed by Prandtl (1905). It suggests that viscous shear dominates in a small layer close to the fluid boundary (the viscous wall layer). Prandtl (1926) later proposed the "law-of-the-wall" to describe the velocity profiles within this layer (which he suggested is independent of its thickness). Beyond the viscous wall layer exists an outer layer where the velocity profile is independent of viscosity. In the outer layer the difference between velocity and the local mean velocity is determined by the

boundary layer thickness and friction velocity u_* (the "velocity-defect law"; von Kármán, 1930). The friction velocity is related to shear stress τ by

$$u_* = \sqrt{\frac{\tau}{\rho_w}} = \sqrt{gds}\ .$$

(2.8)

Between these two regions exists an overlap layer where both viscous and turbulent shear are important. Millikan (1938) matched the velocity profiles of the law of the wall and the velocity-defect law and suggested that in the overlap layer the at-a-point velocity u must vary logarithmically with distance from a surface z such that

$$\frac{u_*}{u} = \frac{1}{\kappa}\ln\left(\frac{z}{z_0}\right),$$

(2.9)

where $\kappa \approx 0.41$ is von Kármán's constant (Connelly *et al.*, 2006). z_0 is the 'roughness length' or projected height above the bed at which the velocity is zero: experiments have calculated that z_0 is approximately equal to $\varepsilon/30.1$ (Robert, 2003). This equation is often referred to as the law of the wall. The right-hand side can be integrated between $z = z_0$ and $z = d$ to give the average velocity of the profile V, yielding an estimated flow resistance (with the ratio V/u_*):

$$\frac{V}{u_*} = 2.5\ln\left(\frac{d}{\varepsilon}\right) + 6.0\,.$$

(2.10)

This is known as the Keulegan equation. The resultant profile provides a theoretical basis for estimating flow resistance, yet it is no more than a "shrewd correlation of velocity profiles" (White, 2003: p.360). Substituting equations 2.6 and 2.8 gives a way of predicting f from d and ε for turbulent flow through rough pipes (plotted on the right side of Figure 2.2):

$$\frac{1}{\sqrt{f}} = 2\log\left(\frac{3.7d}{\varepsilon}\right).$$

(2.11)

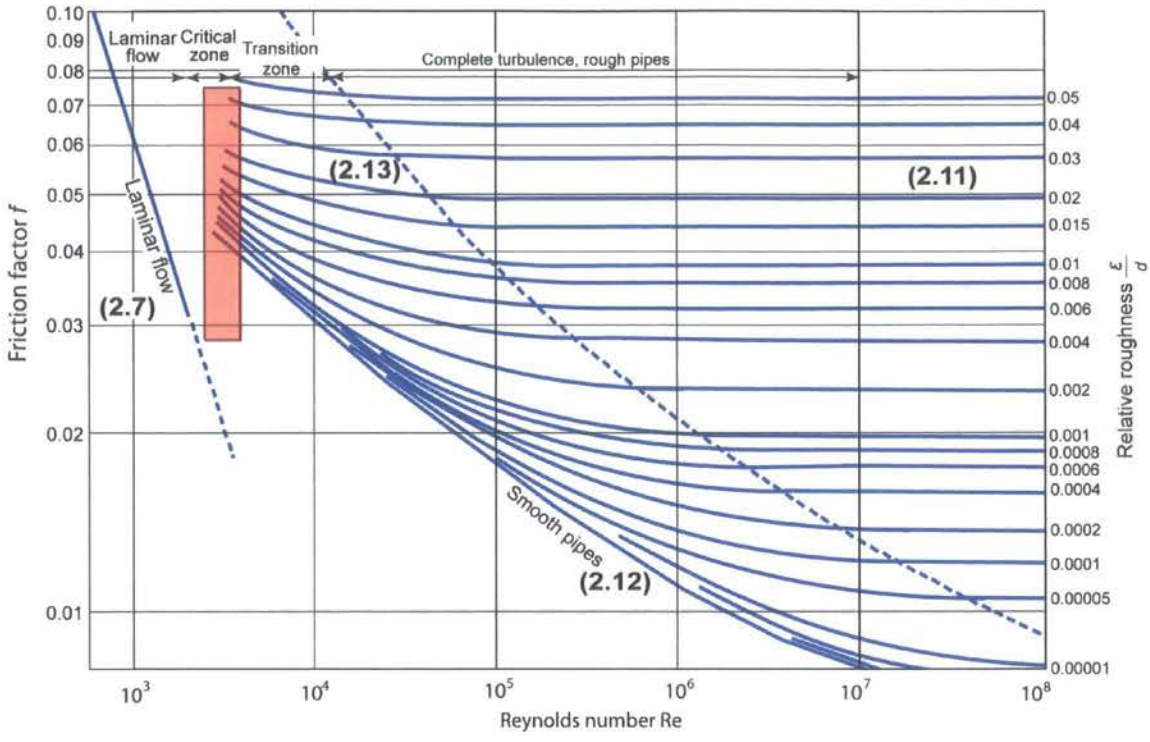

Figure 2.2. Moody chart for pipe friction with smooth and rough walls (Moody, 1944). Redrawn from White (2003: p.349). Numbers in brackets relate to the regions represented by the equations in this chapter.

von Kármán (1930) and Prandtl (1935) further applied the logarithmic law relation to develop an analytical prediction of f for smooth pipes over the turbulent flow range, with the relationship

$$\frac{1}{\sqrt{f}} = 2\log\left(\mathrm{Re}\sqrt{f}\right) - 0.08 \tag{2.12}$$

to be solved iteratively for f. This equation approximates the line labelled 'smooth pipes' in Figure 2.2.

Colebrook and White (1937) suggested that rough pipes in the 'transition zone' would display a different relation from that of equation 2.12. Colebrook (1939) then showed that the transition zone can be described by the empirical relation

$$\frac{1}{\sqrt{f}} = -2\log\left(\frac{\varepsilon}{3.7d} + \frac{2.51}{\mathrm{Re}\sqrt{f}}\right), \tag{2.13}$$

also to be solved iteratively for f. This equation is plotted in the 'transition zone' of Figure 2.2 for several values of ε/d. The development of Figure 2.2 by Rouse (1943) and Moody (1944), the 'Moody diagram', accelerated the adoption of the Darcy-Weisbach equation as it eased the calculation of f.

The lightly shaded area in Figure 2.2 indicates the critical transition range from laminar to turbulent flow. There are no reliable friction factors which cover the range $2000 < \mathrm{Re} < 4000$. Each relation illustrated is based on assumptions about the velocity profile in pipes (all formulas are based on an average velocity and pipe-flow is considered to be one-dimensional). White (2003) notes that the Moody diagram is only accurate to ± 15 % for design calculations over the range shown, while Brown (2002) voices surprise that the diagram has not been supplanted over the last 60 years. Despite these concerns, the Moody diagram remains in use for both circular and non-circular pipe flows, and the resistance modelling concepts contained therein are even applied to open-channel flows (Webber, 1965).

2.4 Open-Channel Flows

The behaviour of open-channel flow, like that of pipe flow, is governed basically by the effects of viscosity and gravity relative to the inertial forces of the flow (Graf, 1998). Despite this initial similarity, it is much more difficult to solve problems of flow in open-channels than in pressured pipes. Open-channel flow must have a free surface subject to atmospheric pressure; the position of this free surface is likely to change with respect to time and space. The treatment of open-channel flows is more empirical than that of pipe-flow, yet this empirical method, when cautiously applied, can yield results of practical value (Chow, 1959).

2.4.1 The Chézy Equation

In the eighteenth century, Antoine Chézy designed a canal on the river Yvette near Paris. From experiments on the Courpalet canal and the Seine, Chézy (1775) developed what is now known as the Chézy formula for comparing uniform flows in open channels (see Herschel, 1897). The formula is based on the proportionality $V^2P \propto AS$ and is commonly expressed as

$$V = C\sqrt{RS}\,, \tag{2.14}$$

where P is the wetted perimeter, A is the area of flow, S is the channel slope and R is the hydraulic radius. The constant of proportionality C is a factor of resistance, called Chézy's C.

The functional relationship between the mean velocity and the mean depth of a free water surface is determined by the total resistance to flow (Lawrence, 2000). This resistance is parameterised by C using two assumptions: the flow is uniform (i.e. a local equilibrium exists where the flow resistance balances the flow), and the force resisting flow (per unit area) is proportional to the square of the velocity.

For this equation to be of practical use there needs to be an acceptable description of the roughness coefficient. Many attempts have been made to determine the value of C. Ganguillet and Kutter (1869) calculated C from the hydraulic radius, slope and an estimation of Kutter's n (a coefficient of roughness). Bazin (1897) used the hydraulic radius in combination with an alternative roughness coefficient (Bazin's m) (see Chow, 1959).

2.4.2 The Keulegan Equation

Graf (1998) notes that it is extremely useful to express the friction coefficient of channel-flow with the Darcy-Weisbach equation (equation 2.6). Henderson (1966) suggests that the behaviour of C can be inferred directly from that of f. From equation 2.6 it can be established that

$$V = \left(\frac{8g}{f}\right)^{1/2} R^{1/2} S^{1/2}. \tag{2.15}$$

For a given channel shape and roughness, $(8g/f)^{1/2}$ is constant and equal to Chézy's C. Note an important difference between f and C: f describes flow resistance (which increases with surface roughness), whereas C describes flow conveyance or conductance (and decreases with roughness). White (2003: p.698) suggests that equation 2.15, with f estimated from the Moody diagram, is "the most fundamentally sound approach to the Chézy formula".

Keulegan (1938) applied the Prandtl-von Kármán equation for flow in open channels, which is very similar to the pipe-flow equivalent (equation 2.12). However, evaluation of the Darcy-Weisbach friction factor in rivers is a complex matter. f varies with fluid viscosity, flow depth, grain size, bedform configuration, and vegetation. Chow (1959: p.9) warns that "owing to the free surface and to the interdependence of the hydraulic radius, discharge and slope, the f-Re relationship in open-channel flow does not follow *exactly* the simple concepts that hold for pipe flow". The cross-sectional shape of the channel and differences in bed and bank roughness have a substantial effect on flow resistance (Hey, 1979). The Colebrook equation (2.13) was modified to take this into account, but this breaks down where the relative roughness is greater than 0.3 (Hey and Thorne, 1984).

Much experimental data have been collected to determine the open-channel f-Re relationship in smooth flows (e.g. Straub, 1939). However, there are major limitations to this: the channels should ideally be of circular cross-section and bed roughness should approximate the uniform grains used in the experiments of Nikuradse (1933). Some modifications are necessary. The cross-section may be accounted for by a multiplicative factor (0.95 for rectangular channels, 0.80 for trapezoidal channels, 1.25 for triangular channels, etc.). Channel shape is more of an influencing factor for laminar than turbulent flow in smooth channels; the data in the laminar region can be defined by a generalisation of equation 2.7, where the numerator is replaced with a factor dependent upon channel shape. The critical transitional range is even more poorly defined than for pipe flow, as flow in large, wide channels is nearly always in the turbulent regime (and independent of Re). Wolman (1955) found resistance to turbulent flows in Brandywine Creek,

Pennsylvania to be a function of relative roughness, deriving an equation similar to equation 2.11.

Equation 2.11 was derived from the law-of-the-wall and the Keulegan equation. Robert (2003) suggests that the logarithmic law can be applied to the bottom 20% of relatively deep rivers (where $d/\varepsilon >>10$); deviation from the log-law beyond is a result of secondary circulation caused by stream curvature or steps. Experimental results not only confirm the assumption of logarithmic velocity profiles in rivers, but even suggest that it can be used to approximate nearly the entire velocity profile for steady uniform flows in wide straight channels with roughness dominated by uniform grains on the bed (e.g. Ferro and Baiamonte, 1994; Tominaga and Nezu, 1992). Least-squares regression is often used to fit velocity and depth to a linear form of equation 2.10 from which empirical estimates of shear stress and roughness height can be made (e.g. Ferguson and Ashworth, 1992).

Various equations relate ε to a measurable bed grain size. Keulegan (1938) suggested that ε equates to the mean particle size for flow in rough, circular pipes. In artificial channels, the equivalent roughness established for industrial pipes may be taken; in granular channels with heterogeneous bed material, more complex relations must be sought. Wilcock (1996) suggests taking z_0 to equal $0.1D_{84}$ ($\varepsilon \approx 3D_{84}$) and then estimating shear stress as above. Many studies empirically fit field measurements to the Keulegan equation and obtain values of ε as high as $6–7D_{50}$ or $3.5D_{84}$ (e.g. Hey, 1979; Bray, 1982; Robert, 1990; Clifford *et al.*, 1992). The practice of applying multiples of grain-size percentiles to represent roughness values is counter-intuitive; such estimates of ε are questionable as they no longer represent a directly measurable quality of the bed and may be considerably greater than the largest particle diameter observed in the stream reach. Other authors report that flow resistance cannot be predicted from particle size (Gessler, 1990; Dingman and Sharma, 1997; Smart, 1999). In situations where particles are arranged into complex bedforms (providing considerable 'form resistance'), the standard deviation of bed surface elevations represents a more appealing measure of bed roughness (Smart *et al.*, 2002). Recently, Cooper *et al.* (2006) proposed a novel approach to measuring resistance in gravel-bed rivers using an acoustic remote sensing technique to estimate hydraulic resistance from the dynamics of the water surface.

Empirical estimates of roughness length can be highly variable (Wilcock *et al.*, 1996) and controlled by local bed conditions. Recent investigations into the logarithmic law have suggested that the vertical velocity profiles of gravel-bed rivers are segmented into two component parts. Robert (1990) notes that this separation represents different scales of resistance. The flume experiments of Nowell and Church (1979) revealed that an inner layer reflects grain resistance, and higher up the water column a separate outer log-linear layer reflects total resistance (including form resistance). Wiburg and Smith (1991) found that this inner layer was non-logarithmic for relatively rough flows but can be approximated as logarithmic by inflating ε beyond D_{50}. Lawless and Robert (2001) first attempted to isolate the effects of individual roughness scales on the shape of these profiles downstream. Their flume experiments found that the vertical extent of the profile deviation as the new boundary layer extends its height is directly related to the scale of roughness found on the bed and may be independent of flow depth.

2.4.3 The Manning Equation

A further assumption is added in the equation of Manning (1891) which, despite the advantages of equation 2.15, many engineers and geomorphologists use frequently. Manning (1891) suggested that Chézy's C increased approximately with the sixth-root of the hydraulic radius, or

$$C = \left(\frac{8g}{f}\right)^{1/2} \approx \frac{R^{1/6}}{n}. \tag{2.16}$$

Here n is a roughness parameter (Henderson (1966) suggests that this conclusion was independently arrived at by both Gauckler (1868) and Hagen (1881) and wrongly attributed to Manning). The Manning equation for uniform flow velocity (in SI units) is

$$V \approx \frac{R^{2/3} S^{1/2}}{n}. \tag{2.17}$$

To balance the dimensions of equation 2.17, the $1/n$ term must have units of $m^{1/3}\ s^{-1}$. However, the usual preference is to leave n dimensionless and attach all the remaining units to an implicit coefficient, with value 1 $m^{1/3}\ s^{-1}$. The equivalence between C, f and n is thus

$$C \equiv \sqrt{\frac{8g}{f}} \equiv \frac{R^{1/6}}{n}. \tag{2.18}$$

The application of the Manning equation also requires that a measure of resistance is known or can be accurately estimated. Manning's n is usually approximated from tables, or by comparison with photographs illustrating channels of known roughness (as found in Chow, 1959; Barnes, 1967). Gordon *et al.* (2004) suggest that n can be thought of as a calibration factor which integrates the effects of flow resistance caused by bed roughness, the presence (and flexibility) of vegetation, the volume of sediment or debris transported, and many other factors. Strickler (1923) attempted to relate n to a measurable property of a river channel so that for gravel bed streams with median grain size D_{50}

$$n = sD_{50}^{1/6} \tag{2.19}$$

where s is approximately 0.013 (Henderson, 1966).

The Manning equation has several benefits. It is simple and provides quite accurate results (in some situations). Because of its long and extensive application, there exists a wealth of publicly available values of n for a very wide range of channels. However, Manning later rejected it in favour of a dimensionally homogeneous improvement (Fischenich, 2000). It was King (1918) who championed the earlier, now commonly used form of the equation (equation 2.17).

The use of the Manning equation is further complicated when considering the nonlinear variation of n with the height of the free water surface. n will generally decrease with increasing flow depth up to bankfull discharge. Beyond this point, the flow spreads out over a larger area and n will increase. The exact form of this relationship will depend upon the channel topography. Limerinos (1970) includes relative roughness in an equation for estimating Manning's n. Variable water depths represent the main difficulty of applying any one-dimensional flow resistance coefficient to open channel flows, especially in

shallow flows: resistance increases dramatically as d/ε falls below ~10. Chow (1959) suggests that Manning's equation ceases to be applicable where d/ε falls below 3. Despite this variation, published values of n are based on channel form alone and are assumed independent of flow parameters. Manning (1891) noted that equation 2.17 is entirely empirical. The sixth-root approximation is not exact, and Manning found the exponent on R in equation 2.17 varied from 0.6499 to 0.8395. Figure 2.3 demonstrates the limits of the sixth-root size approximation of Manning (assuming a wide, rectangular channel where water depth can be substituted for the hydraulic radius).

The range of d/ε (called the inundation ratio Λ, the inverse of relative roughness) over which the Manning equation is valid is apparent in Figure 2.3. It is only in reasonable agreement with field measurement for $100 < d/\varepsilon < 10000$. The poor agreement where flow depth is less than 100 times greater than grain roughness becomes particularly relevant in mountain streams and overland flows where $d/\varepsilon < 1$ may be recorded. Moreover, in this situation, estimation of f from the Moody diagram is impossible as only very small relative roughness values have been used in pipe flow experiments.

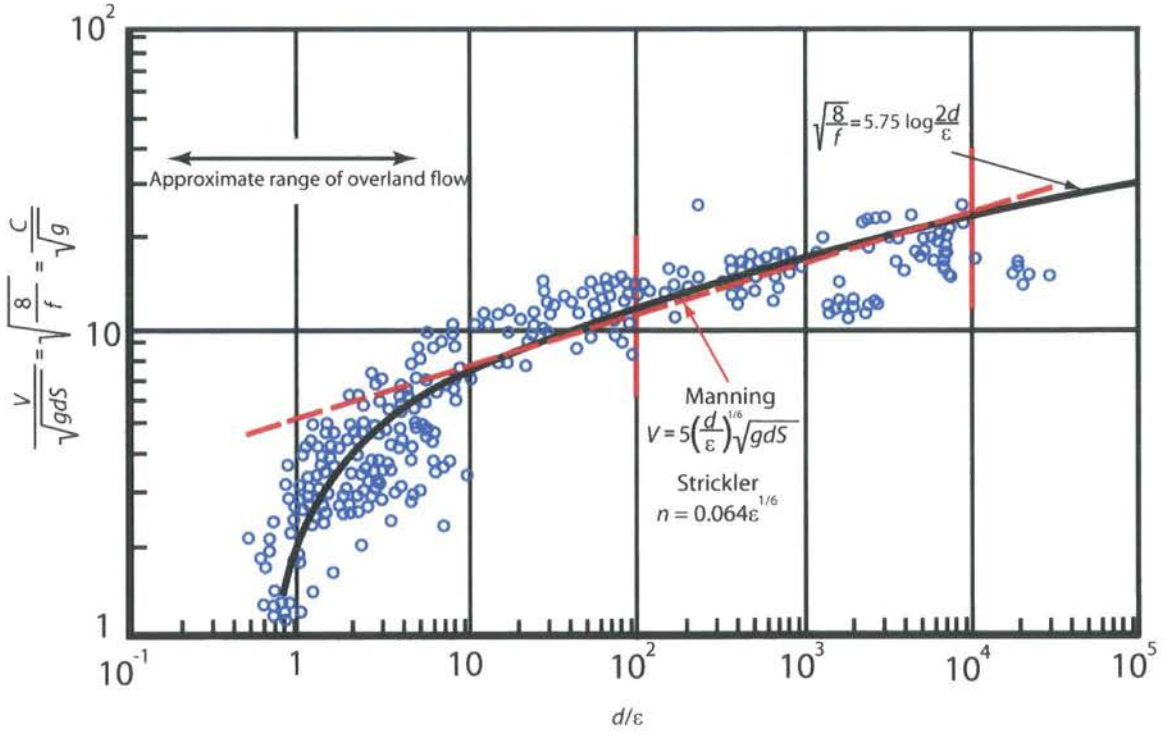

Figure 2.3. Resistance to flow for hydraulically rough rivers displaying the predictions of the Keulegan and Manning equations. Adapted from Julien (2002: p.93).

2.4.4 Limitations of Flow Equations in Open Channels

The selection of friction coefficients is subject to greater uncertainty for open channels than for pipes. A single friction coefficient is valid only as long as the entire wetted perimeter has the same roughness: i.e. the wetted section is homogeneous. Yet the geomorphic and hydraulic properties of natural channels are generally rather irregular; the wetted surface may comprise rough, irregular river beds and total channel roughness varies with the position of the free surface. Many theories have been developed for prismatic channels where cross-section, longitudinal slope and roughness remain constant. The application of such hydraulic theories yields only approximate results because numerous assumptions must be made.

Uniform flow equations are inapplicable to many upland streams with pool-step structures. Adjustments must be made for conditions which deviate substantially from uniform flow to account for head losses (Henderson, 1966). Localised flow separation creates an area of high pressure upstream from bedforms and an area of low pressure in the wake of the object. This increases viscous energy losses and is commonly known as form resistance. Wahl (1994) suggests that the hydraulic equations developed for low gradient channels may not properly represent upland stream conditions because the steep gradient and large grain and form roughness promote complicated velocity profiles and three-dimensional flow. Marcus *et al.* (1992) evaluated methods for calculating an effective value of n in upland streams (e.g. Jarrett, 1984). They found that most methods underestimated it by inadequately addressing the effect of large sediment sizes on flow resistance. A well tested, consistently accurate equation for calculating the resistance coefficients of upland streams has yet to be developed (Wohl, 2000) (see Ferguson, 2007).

While non-uniformity can be allowed for by using a gradually-varied flow equation, Gordon *et al.* (2004) emphasise that the equations of Darcy-Weisbach, Chézy, and Manning can be safely used only within the range over which they were developed (pipes, or trapezoidal channels with uniform flow and clear water). They suggest that the equations will perform best where flow is through a straight stream of fairly constant cross-section

where mean velocity and bed roughness can be considered uniform. The accuracy of flow resistance estimation in channels which deviate from this idealised model suffers from the limited quantitative understanding of the real-world processes contributing to this resistance (Bathurst, 1993).

2.5 Hydraulics of Overland Flow

As with open-channel flow, the three most widely used equations to predict overland flow velocity are the Darcy-Weisbach, Chézy and Manning equations. Again, each requires the value of a friction factor or roughness coefficient. The correct specification of the equation of motion of overland flows is particularly important in semi-arid environments, where interrill flows are an important contributor to streamflow (Abrahams *et al.*, 1986a). Engman (1986) summarises a number of studies on friction factors and displays published values of n for surfaces that are qualitatively described in terms of type of tillage, degree of crusting, presence of vegetation, etc. However, the problems of applying the hydraulic equations to upland streams are magnified when considering overland flow hydraulics.

The hydrodynamics of overland flows are very different from those found in pipe flows; if upland streams lie at the extreme end of the spectrum for which conventional hydraulic formulas can be applied, then such equations may be inappropriate for describing overland flows. The empirical velocity profile method described for open channels is unsuited to overland flows, as many accurate velocity measurements are needed in the bottom 20% of the flow (Biron *et al.*, 1998). The small depth ranges mean that obtaining even a single velocity estimate becomes a delicate operation. Acoustic Doppler Velocimeters and electromagnetic current meters used to take velocity profiles of channel flows (Lawless and Robert, 2001; Lamarre and Roy, 2005) require a minimum water depth to function and must be positioned several centimetres from the soil surface (see section 4.2.1). In any case, the non-logarithmic velocity profiles observed near the bed of rivers with large bedforms (e.g. Wiberg and Smith, 1991) suggest that it is unlikely that logarithmic velocity profiles will be observed in overland flows. Robert (1990) notes that flow acceleration and deceleration in channels distort vertical velocity profiles; this effect would be especially pronounced in overland flows. Therefore, as Bathurst (1993) suggests, understanding of

flow resistance decreases moving upstream through the channel network. Further research would be most beneficially directed towards developing an improved understanding of overland flow resistance.

Contrary to field studies (which commonly use f to model resistance), most hydrological and soil erosion models apply Manning's n to model overland flows (Hessel *et al.*, 2003). This is surprising given the range of the relationships presented in Figure 2.3 and may reflect the large number of estimates of n in the literature and the long-lasting convention of applying n to streamflows. Some models assume an aggregated value of hydraulic resistance for the whole soil surface (e.g. LISEM: De Roo, 1996), whereas other models separately route water through the non-permanent channel network by calculating either n (EUROSEM: Morgan *et al.*, 1998) or f (WEPP: Gilley and Weltz, 1995) individually for rill and interrill areas. Morgan *et al.* (1998) treat hydraulic and form resistance independently: the former is modelled with n and used to route flows through catchments, while the latter is modelled with a measure of cross-sectional tortuosity (T_{xc}, the ratio between the distance between two points measured over microtopographic irregularities and their straight-line separation; see Boiffin, 1984) and used only as part of an empirical relationship to predict depression storage.

Each of these models presents an extremely simplistic vision of resistance to overland flows. Many experimental workers have begun to query the continued application of these friction coefficients in such models. The challenge is to develop a more sophisticated yet simple representation of roughness that can be efficiently incorporated into such large-scale runoff and erosion models. The following section questions the dependence of the Darcy-Weisbach friction factor on the Reynolds number and suggests that the relationship does not hold for overland flows which can be very turbulent (section 2.5.1). Alternative methods for conceptualising hydraulic resistance are then discussed in section 2.5.2, before the applicability of the uniform flow assumption is examined (section 2.5.3).

2.5.1 *f*-Re Relationships for Overland Flow

Emmett (1970) shows that resistance to overland flow varies with the rate of flow. Since the rate of flow is highly variable in space, so too is *f*. Resistance will also vary with time due to continuously changing flow conditions. In an analogy to pipe-flow, this dependence is often expressed using relationships between the Darcy-Weisbach *f* and Reynolds number (Abrahams *et al.*, 1992). Similarly, Dunne and Dietrich (1980) assumed this dependence, suggesting that variation in the coefficient could be attributed to surface roughness. Therefore, *f*-Re relations similar to those displayed in Figure 2.2 are employed in many models of hillslope runoff. Most assume a power-law relation with the exponent dependent upon the state of flow (e.g. Blasius, 1913), yet this relationship applies only for plane beds where the resistance to flow is entirely grain resistance. Lawrence (1997) suggests that the Reynolds number at which the roughness ratio becomes the dominant dimensionless group should be much smaller for overland flows in the presence of macroscale roughness elements than for classical pipe flows.

Although interrill flows are usually modelled as a broad, shallow sheet-flow, few natural surfaces are planar and free of subtle undulations or prominences. Rill incision, scour, deposition and tillage all increase the roughness of soil surfaces. In contrast to the grain roughness of the empirical pipe-flow studies which generally applied a relative roughness of 0.04 or less (Figure 2.2) roughness elements in overland flows may be greater than the flow depth. Where sheet-flow is assumed, the entire surface is considered to be fully submerged and flow width is constant. However, substantial protrusions of the soil surface mean that flow width may actually increase with increasing discharge. Such lateral extension will change the hydraulic resistance as parts of the surface become progressively submerged (Takken and Govers, 2000).

Roels (1984) and Abrahams *et al.* (1992) present field data suggesting that the standard plane-bed *f*-Re relation is not ubiquitous. They present a suite of at-a-point *f*-Re relations: a combination of positively and negatively sloping power-law relations and convex-upward relations. Such non-monotonic variation of frictional resistance is entirely different from the functional dependence demonstrated by flow through pipes and later applied in

hydrological models. Abrahams *et al.* (1992) suggest that these variable relationships can be attributed to the progressive inundation of roughness elements. This is essentially the same problem presented by applying single values of f or n to channels with a variable flow stage. Resistance will increase with flow rate as the wetted projected area increases; as elements gradually become submerged, f will then begin to decrease with Re. When this is the case, the f-Re relation is no longer a function of the state of flow, but becomes instead a reflection of surface form configuration. As such, given their empirical nature, f-Re relations are of little value as models predicting flow resistance at locations other than those where they were developed (Govers *et al.*, 2000). Flow concentrates in the downslope direction altering the surface form, so that no single f-Re relation can describe the hydraulics of an entire slope (Moore and Foster, 1990). Despite this, most field and experimental studies continue to report frictional resistance as a function of Reynolds number when presenting data on overland flow hydraulics (Lawrence, 1997).

The conventional f-Re relations of pipe-flow experiments are not obtained in overland flow studies because grain roughness and viscous stress no longer represent the only sources of resistance to flow. 'Form resistance' may also be influential. Yen (1965) defines form resistance as that imparted by soil particles, stones and vegetation that protrude into the flow more than 10 times the thickness of the viscous sublayer and give rise to spatially varying cross-sections or three-dimensional flow. As interrill flow on hillslopes rarely submerges the soil surface entirely, water will concentrate on lower parts of the surface and flow lines differ from the simple parallel flow observed in the pipe flow experiments. The inherently three-dimensional character of flow over rough surfaces introduces substantial inertial stress which becomes the dominant source of frictional resistance. It is important to note the difficult distinction between topography and form roughness; the scale of enquiry will dictate the amount of topography that must be dealt with implicitly, as roughness (Lane, 2005). Large-scale runoff models will represent much hillslope variation with a roughness value.

Wave resistance also represents an additional and significant source of energy loss that is absent in pipe-flow experiments which Abrahams *et al.* (1992) suggest makes a substantial contribution to total resistance to overland flows. This added resistance is due to the

hydrostatic pressure imbalance generated by the superelevation and subelevation of the free surface around individual roughness elements (Lawrence, 2000) and so is a consequence of the free water surface. A sudden reduction of velocity (e.g. as water flows into a depression) creates violent local vorticity which may result in a volume adjustment (Leopold *et al.*, 1960). The resultant energy loss depends on the velocity of the water relative to the value of $\sqrt{gd}$ (with no loss of energy where $V < \sqrt{gd}$; Leopold *et al.*, 1960). Wave resistance is thus dependent upon the Froude number, defined as

$$\mathrm{Fr} = \left(\frac{V^2}{gd}\right)^{1/2}. \tag{2.20}$$

The Froude number characterises the flow speed relative to the speed of surface waves and is important wherever a flow possesses a free surface (Lawrence, 1997). Where roughness elements protrude through the water surface, this wave resistance will be highly variable as the flow is diverted (Bunte and Poesen, 1994).

Finally, rain resistance may be significant in overland flows; this is the resistance due to velocity retardation as flow momentum is transferred to accelerate a raindrop mass to the velocity of the flow. Savat (1977) conducted rainfall simulation experiments on a laboratory flume and found that, for gentle slopes experiencing laminar flow, rain resistance may contribute up to 20% of total resistance. However, overland flow on natural slopes is more turbulent: Dunne and Dietrich (1980) found that rain resistance was several orders of magnitude smaller than total resistance on such slopes. Parsons *et al.* (1994) suggest that due to the lower flow depths and velocities, rain resistance may provide a substantial source of resistance at locations close to a drainage divide.

2.5.2 Alternative Methods of Conceptualising Resistance

The preceding discussion points towards the need to reconceptualise the resistance experienced by overland flows. Abrahams *et al.* (1992) and Gilley *et al.* (1992) suggest that if f is largely determined by surface form, it may be predicted by measures such as percentage gravel cover rather than by Re. Gilley *et al.* (1992) and Hirsch (1996) develop

regression equations for estimating f over a range of surfaces by breaking it down into components and assuming the different contributions can be linearly combined (see Chapter 6). Gilley and Finkner (1991) used experimental data to derive regression relationships predicting f and n from the Reynolds number and the 'random roughness index' of Allmaras *et al.* (1966) (defined as the standard deviation of the surface elevation once the general plot slope has been removed). They found that the largest hydraulic roughness coefficients usually occurred on those plots with the greatest random roughness. However, different factors will control hydraulic roughness on different surfaces so that, considering the distinctly empirical nature of such equations, extrapolation to surfaces other than those for which they were developed is questionable (Takken and Govers, 2000).

Lawrence (2000) notes that the scaled boundary roughness has been neglected as a parameter determining overland flow resistance. Nevertheless, studies of pipe-flow and open-channel flow previously described recognise ε/d as a principal dimensionless group governing flow behaviour (e.g. Nikuradse, 1933; Colebrook, 1939; Keulegan, 1938). Lawrence (1997) advocates the use of the inundation ratio Λ defined as the reciprocal of the relative roughness, such that

$$\Lambda = \frac{d}{\varepsilon}. \tag{2.21}$$

Here ε represents a roughness height. As most natural surfaces consist of a range of particle sizes exposed on the surface, uniquely specifying ε is clearly problematic. Lawrence (1997) uses $0.5D_{50}$, suggesting that the median particle size offers a practical advantage since it is frequently reported. However, this measure of grain size cannot be usefully transferred to a surface where form roughness is dominated by aggregates or flow concentrations (e.g. a tilled or incised surface). Takken and Govers (2000) approximate Lawrence's ε on such surfaces using the median cross-sectional elevation; Smart *et al.* (2002) use the standard deviation of elevations.

Lawrence (1997) defines three distinct flow regimes using Λ (Figure 2.4). Each represents a varying contribution of boundary roughness and demonstrates a distinct method of conceptualising resistance in flows with high relative roughness. This is because the

physical sources of resistance are different in each of these regimes (Ferguson, 2007). Well-inundated flows (where $\Lambda \geq 10$) are treated as analogous to pipe and open-channel flows with roughness decreasing with increases in Λ (presented in equation 2.11 above). Flow is considered parallel to the surface and conventional hydraulic analysis is applied to establish a relationship between flow resistance and surface roughness as earlier (see Figure 2.3):

$$\frac{1}{\sqrt{f}} = 1.64 + 0.803 \ln\left(\frac{d}{\varepsilon}\right). \tag{2.22}$$

A similar approach is described in Smart *et al.* (2002). This theory, developed for turbulent flows, will not fully describe transitional flows which will demonstrate some dependence on the Reynolds number. Indeed, Lawrence (1997) found that frictional resistance was underpredicted by the inundation ratio wherever Re < 1,000. Therefore, it remains unclear whether the inundation ratio is a key parameter for laminar flows (Myers, 2002).

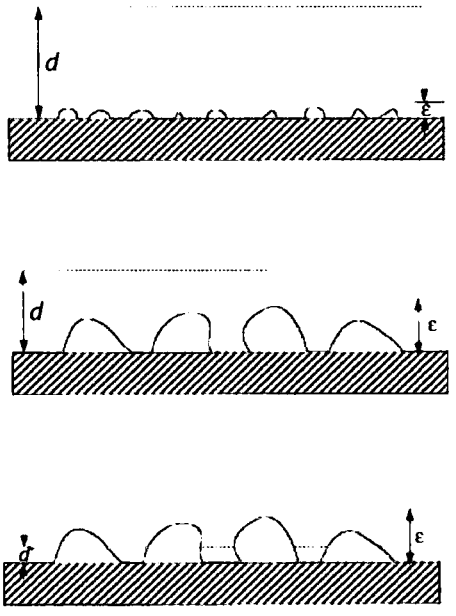

Figure 2.4. Well-inundated (top), marginally inundated (middle) and partially inundated (bottom) regimes. From Lawrence (1997: p. 370).

In marginally-inundated flows (where $2 < \Lambda < 10$), roughness affects the entire velocity profile and the flow is of a multi-dimensional nature. Lawrence (1997) used a simple mixing model suggesting that the disturbance introduced into the flow field by a roughness element will scale roughly with its height and will effectively mix the flow over a similar length scale (agreeing with the findings of Lawless and Robert, 2001). This approach suggests that frictional resistance will decrease very rapidly with flow depth such that

$$f \approx 10\left(\frac{d}{\varepsilon}\right)^{-2}. \tag{2.23}$$

Thus, for these marginally-inundated flows, C will increase linearly with d/ε (Ferguson, 2007). As the flow becomes increasingly shallow ($\Lambda \leq 2$) the water depth eventually becomes less than the height of roughness elements which act to block the flow. Changes in flow depth then not only are associated with simple variations in resistance to flow, but also produce changes in the hydraulic radius, which in this regime is not simply equal to d (Abrahams and Parsons, 1990). Flow resistance becomes positively related to both inundation ratio and the percentage of the surface covered with roughness elements P_r (which may prove difficult to define in the field). In this situation, the flow resistance can be approximated through consideration of the drag introduced by individual elements.

In an ideal situation all the water encountering the projected frontal area A_P of a roughness element would come to a complete stop. Considering the resultant change of momentum, the drag force F_D can be calculated as

$$F_D = \frac{1}{2} C_D \rho V^2 A_P, \tag{2.24}$$

where C_D is the coefficient of drag, the ratio of the drag for the real object to that of the ideal situation described. This relationship between force and velocity is identical to that assumed in the Chézy equation. Assuming that a surface is composed of randomly packed hemispherical particles with a bimodal size distribution, Lawrence (1997) shows that

$$f = \frac{8}{\pi} P_r C_D \min\left[\frac{\pi}{4}, \frac{d}{\varepsilon}\right] \tag{2.25}$$

where min[a,b] denotes the smaller of a and b. Lawrence (2000) notes that this assumes that the resistance of individual particles is additive, which may cause it to overestimate total resistance by ignoring wake interaction effects (the 'skimming' or 'wake interaction' flow described by Nowell and Church, 1979).

Equations 2.22, 2.23 and 2.25 can be combined to approximate the functional dependence of f on the inundation ratio (Figure 2.5). This model performs well on the granular surfaces on which it was developed. However, Takken and Govers (2000) found that it performed less well on tilled soil surfaces where the implicit assumption that individual hemispherical roughness elements relatively uniform in size are randomly distributed on a flat surface becomes less appropriate. The use of a single measure (in this case, Λ) to characterise flow conditions is sufficient only where this assumption holds true. Natural surfaces contain roughness of a wide size range which is spatially structured. Where wave resistance is substantial, C_D will also depend on the Froude and Reynolds numbers; therefore, Smart *et al.* (2002) suggest that a drag model may be inappropriate wherever flow geometry is complex and flow is constricted by roughness elements.

Takken and Govers (2000) tested the partial inundation model of Lawrence (1997) on a rough soil surface (using a P_r of 100%) and concluded that the flow behaviour could not be characterised by a single measure of submergence. They suggest that any model predicting hydraulic resistance as a function of discharge needs to account for the spatial distribution of the flow over the surface in addition to the roughness within the flow.

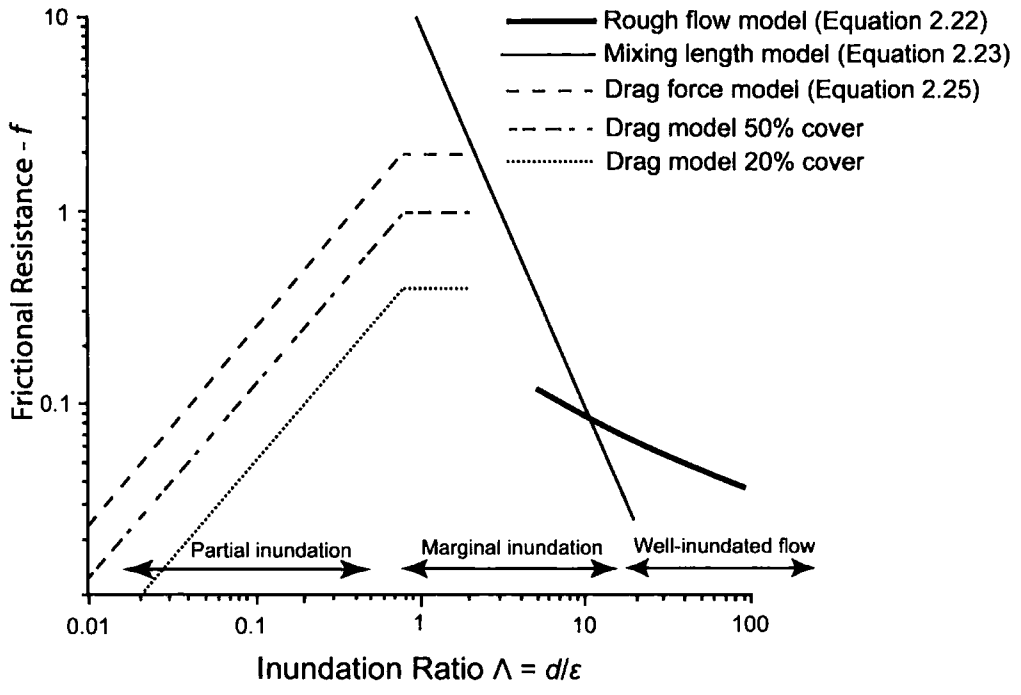

Figure 2.5. The approximate functional dependence of frictional resistance, f, on the inundation ratio $\Lambda = d/\varepsilon$ for the three flow regimes described. From Lawrence (1997: p.373).

Takken and Govers (2000) developed an alternative model whereby detailed cross-sections were used to divide the surface into fully submerged threads to which the model of Savat (1980) was then applied. Flume data were used to compute the optimum value of equivalent roughness for several runs at different discharges. They found that this value could be accurately predicted from a single flow-dependent measure of surface roughness, the 'wet tortuosity' T_w (see Boiffin, 1984):

$$T_w = \frac{P}{w} - 1 = \frac{P - w}{w} \tag{2.26}$$

where w is the flow width. (Apart from subtracting 1, this measure is that used for measuring channel sinuosity in fluvial geomorphology.) This relationship has yet to be properly validated and does not account for roughness in the flow direction.

2.5.3 Questioning the Assumption of Uniform Flow

Each of the studies described above proceeded on the simplifying assumption that surface runoff can be treated as though it was hydraulically uniform, namely, it exhibits a constant depth and speed that are mutually adjusted. Emmett (1970) notes that overland flow is neither steady nor uniform since it is supplied by rain and depleted by infiltration, neither of which is necessarily constant with respect to time or location. Interrill flow generally occurs as a shallow sheet with narrow threads of relatively deep and fast flow moving within broader, shallower, slower-moving regions (Hessel *et al.*, 2003). Dunkerley (2004) conducted runoff-plot experiments on arid soils in New South Wales and found that even on subtle microtopography, average thread velocities were commonly 2.5 times greater than the flow-field mean, and locally 6–7 times greater. This suggests that the tortuosity and connectedness of such flow threads are parameters with great potential significance for the hydrologic and erosional responses on plot to hillslope scales. While two-dimensional runoff models are able to represent such cross-sectional velocity variations, the resolution at which they are applied means that they are incapable of explicitly representing this variability.

Flow threads have been frequently reported for several decades, yet even where they have been thoroughly detailed, the uniform flow equations of Darcy-Weisbach, Chézy or Manning are still applied (e.g. Emmett, 1970). These equations implicitly assume that depth and speed are linked by a single equilibrium relationship. As Dunkerley (2004) points out, this denies the possibility, frequently observed in practice, that the flow contains both relatively deep but slow-moving areas where increased resistance increases the depth needed to support a given runoff rate (e.g. water backed up by an overflowing depression; Horton, 1945) and deep but fast-moving areas following thalwegs across the soil surface. Where deeper flow threads have been identified within a shallow, slower-moving flow, fixed values of f, C or n cannot be applied over the entire surface (although effective values may be estimated as representing the surface as a whole). As overland flow depth and velocity are highly variable in space, the uniform flow assumption must be restricted to a small and strictly confined locality.

Overland flow may be laminar, turbulent, or transitional, or consist of patches of any of these flow states (Abrahams *et al.*, 1992). Horton (1945) suggested that overland flow is likely to be laminar near drainage divides and become more turbulent with increasing distance downslope. Surface runoff discharge is low towards the divide (due to the low contributing area), allowing the diffusive effects of rainsplash to stabilise the soil surface against the advective processes of wash which tend to incise the soil surface (Smith and Bretherton, 1972). Moving downslope from the drainage divide (increasing the contributing area) towards Horton's (1945: p.320) "critical distance", the microtopography of the soil surface demonstrates systematic changes as runoff gathers into depressions. These depressions increase in size downslope and as the depressions deepen they capture more flow through the cross-grading of the hillslope surface (Dunne *et al.*, 1995). Surface runoff deepens as a result of this 'micropiracy', eventually resulting in the initiation of incision of the soil surface.

Few studies have examined the variable relationship between flow characteristics and frictional resistance in the field. Abrahams *et al.* (1986a, 1994) and Abrahams and Parsons (1991) provide notable exceptions. Many experimental field- and laboratory-based studies focus on interrill flow and most models partition interrill and rill flows and treat them as separate processes (Foster and Meyer, 1975). However, this rill-interrill dichotomy underestimates the role of concentrated flow threads in the interrill zone (Baird *et al.*, 1992). A continuum exists between micro-rills and rills, especially noticeable at the hillslope scale.

These changing surface configurations with runoff volume suggest that there will be downslope changes in the variables that influence resistance to flow. This echoes the ideas of Prestegaard (1983) and Bathurst (1993) who make a similar suggestion for the channel network as a whole. Prestegaard (1983) suggests that while individual grains are most important at headwaters, bedforms dominate middle reaches, and channel beds become increasingly important at lower gradients. This idea could be recast in the context of hillslope runoff and has already been suggested through the use of different modelling approaches for different inundation regimes. For example, Govers (1992), Nearing *et al.* (1997, 1999) and Takken *et al.* (1998) have each shown that once flow reaches a defined,

free-adjusting channel, flow velocity becomes independent of slope gradient and can be predicted from discharge only.

2.6 Conclusions

The Darcy-Weisbach equation (2.6) represents the head loss due to friction h_f with the energy gradient S_f. This is approximated as the soil surface slope in studies of overland flow as, for uniform flows, the velocity terms of Bernoulli's (1738) principle of constant energy will cancel. Overland flows on natural surfaces are permanently accelerating or decelerating in response to the complex topography they encounter. This is ignored in calculations of flow resistance. One possible solution is to apply the uniform flow assumption over a very small area for which velocity measurements are available both before and after a water body passes through the topography. Then h_f can be approximated (assuming pressure changes to be negligible) in an alternative formulation of equation 2.2 more suited to overland flows:

$$h_f = \left(\frac{V_1^2}{2g} + z_1\right) - \left(\frac{V_2^2}{2g} + z_2\right) = \Delta z + \frac{\Delta V^2}{2g}. \tag{2.28}$$

This would allow individual flow threads to be treated separately. Greater understanding of the connectedness of flow threads would represent an important advance in hillslope hydrology. To meet these data requirements, a full visualisation of overland flows would be necessary alongside considerable advances in the measurement of overland flows (e.g. Figure 2.6). Further adaptations of the Darcy-Weisbach equation (2.6) for overland flows are explained in section 6.3.

An over-reliance on laboratory-based studies has also bred an ignorance of the changing soil surface configurations with distance downslope and the need to account for the resultant changes in the variables that influence resistance to flow. The study of overland flow hydraulics can overcome measurement issues by embracing new technologies available to assist the acquirement of accurate measurements of flow depth and velocity (demonstrated in Figure 2.6). The development of an innovative methodology for

measuring overland flows in the field is described in Chapter 4. In particular, the use of a terrestrial laser scanner allows rapid generation of accurate, densely spaced measurements of surface elevation. These are used in Chapter 6 to test and develop measures of surface roughness helpful in predicting hydraulic resistance (e.g. standard deviation of heights σ_Z; the depth distribution of overland flows; the total projected frontal area A_P).

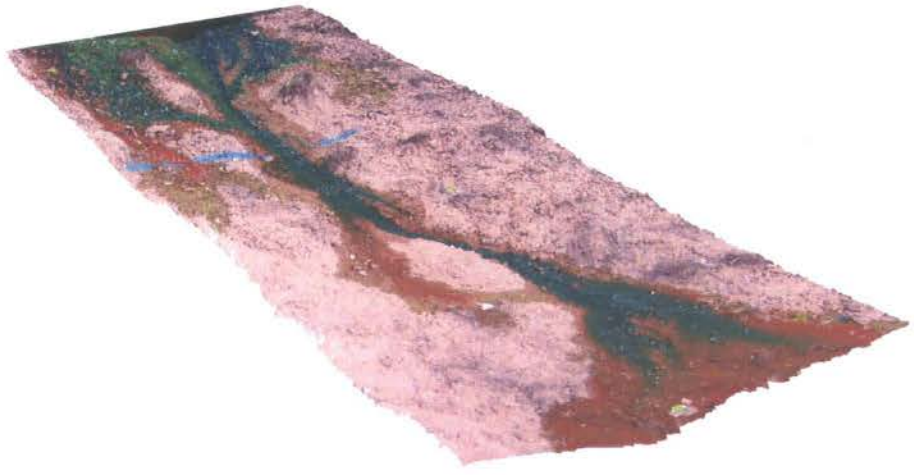

Figure 2.6. Artificially generated overland flow on a natural, semi-arid surface. The production of this image is discussed in Chapter 4.

Describing resistance to overland flows in terms of f is advantageous considering its sound theoretical basis and its widespread use in hydrological models. Techniques allowing depth, width, velocity and roughness data to be extracted from raw data after an experiment has been completed permit the use of f to describe resistance to overland flows over reduced spatial and temporal scales, thereby reducing the limitations of the assumptions described in this chapter. As measurement is transferred from field to desk, visualisation of overland flows will advance our understanding of the real-world processes that affect them. Such developments may lead the way to substantially improved roughness descriptions and evaluations of flow hydraulics, particularly resistance to flow.

The level of understanding of overland flow hydraulics that is needed for physically-based modelling of runoff and soil erosion has not been achieved to the extent that might be

expected in light of the long history of work in this area (Lawrence, 2000). This is an inevitable consequence of the focus on modifying and adapting existing pipe-flow and open-channel flow principles to overland flows, rather than developing an individual theory of overland flow hydraulics consistent with the observations of the field-workers in the discipline. As the Darcy-Weisbach, Chézy and Manning equations are transferred to overland flows, their numerous implicit assumptions are transferred with them. In most situations, and despite the best attempts of a great deal of researchers to untangle the two, this renders conventional descriptions of channel flow unsuitable as models of overland flow hydraulics. While some progress has been made in reconceptualising overland flow resistance, many widely-used runoff and soil erosion models have lagged behind these developments and have yet to incorporate them into their predictions.

Predicting catchment responses to rain events requires an understanding of resistance to flow both within stream channels and over hillslopes. Therefore, any study investigating new ways of modelling overland flow resistance will eventually develop our understanding of flooding events. This is particularly relevant in semi-arid environments where intense rainfall events generate extreme floods, mostly via infiltration-excess overland flows. This study is framed within the context of predicting the response of semi-arid catchments to these rainfall events. Chapter 3 now explains this rationale in greater detail.

CHAPTER 3

FLOOD PROPAGATION IN SEMI-ARID ENVIRONMENTS: RATIONALE

3.1 Introduction

Runoff generation is determined by complex interactions between spatial and temporal patterns of rainstorms and catchment surface characteristics (Michaelides and Wainwright, 2002). Both factors are highly variable in semi-arid environments. The conceptual model for flood generation applied in this chapter is shown in Figure 3.1. Examples from south-east Spain are introduced throughout the discussion to ensure that this theory is appropriate to the field sites visited in this study (to be described in section 4.5). The chapter begins with an examination of the spatial and temporal structure of semi-arid rainfall events (section 3.2). The temporal structure of rainstorms is shown to be especially important for flood generation at the hillslope scale. Section 3.3 briefly considers the vertical water exchanges that influence runoff production focusing on the nonlinear abstractions from total rainfall amounts by both depression storage and infiltration into the soil. Such abstractions vary greatly throughout a rainfall event. This temporal variability combines with catchment morphology and the spatial configuration of runoff-producing characteristics introduced in section 3.3 to develop flowpaths across hillslopes and catchments.

Section 3.4 considers this conveyance of runoff, examining the concept of hydrological connectivity. The spatial continuity and connectivity of runoff-producing areas, the distribution of flowpath lengths and their integration influence the development of connected hydrological pathways. The velocity of overland flows (as determined by overland flow resistance) also interacts with the configuration of the hydrological pathways and structure of rainstorms to determine the arrival time of rainwater at any point in the catchment (discussed in section 3.5). Finally, section 3.6 concludes by summarising key research questions that must be addressed to increase our understanding of flood generation in such environments where overland flows provide a substantial contribution to floodwaters.

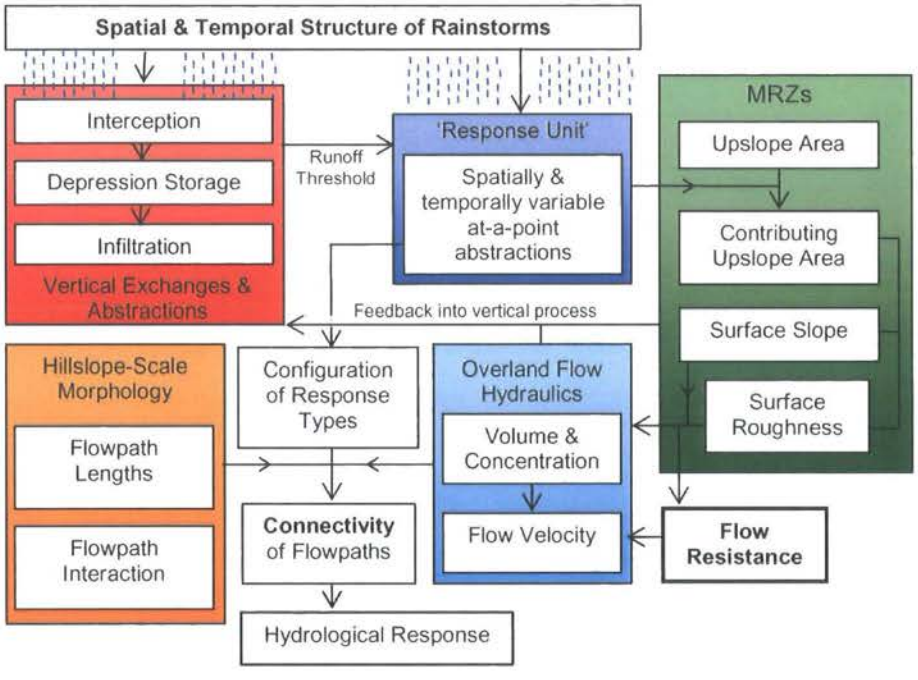

Figure 3.1. The conceptual model for flood generation applied in this thesis illustrating the links between the various concepts influencing catchment hydrological response. Morphological Runoff Zones (MRZs) classify hillslope surfaces by observed surface morphological features and are discussed in section 4.5.3.

3.2 Rainfall Characteristics

Convectional precipitation, dominant in many semi-arid areas, produces rainfall amounts and intensities that are highly variable in space and time (Wolman and Gerson, 1978). This

pattern is distinct from frontal precipitation caused by the large-scale uplift of air associated with tropospheric circulation. Such precipitation dominates many cool temperate climates.

Most semi-arid areas receive variable proportions of both convectional and frontal precipitation. Areas of high relief may also receive precipitation from orographic effects. For example, the rainfall episodes of south-east Spain are dominated by two types of event: storms resulting from Mediterranean thermodynamics, and frontal depressions from the Atlantic. The semi-enclosed Mediterranean receives high insolation during the summer season and the restricted outflow over the sill of Gibraltar promotes the development of high sea surface temperatures over these months (Bethoux *et al.*, 1999). Latent heat fluxes increase towards the autumn season when the Mediterranean airmass exhibits convective instability (Ramis, 1995; Romero *et al.*, 1997). Convective rainfall events over south-eastern Spain arise from this cyclogenesis. They are often associated with an easterly wind (Alonso-Sarría *et al.*, 2002) and have a relatively low frequency of occurrence. Convective events are often torrential, exhibiting high intensity over a small area which can result in localised flash-flooding.

South-east Spain also receives frontal depressions from the Atlantic related to westerly air flows. These storms are of greater areal extent and slower-moving, generating rain of an amount and intensity similar to storms experienced in more temperate climates. The western Mediterranean region lies in the transition zone between mid-latitude low pressure systems and subtropical highs (Romero *et al.*, 1999). This leads to a noticeable seasonal contrast in pluviometric conditions. A major element of the Köppen definition of a Mediterranean climate is that winter rainfall is more than three times summer rainfall (Köppen, 1936). The acute seasonality of rainfall is echoed by a pronounced seasonal cycle in other climatic variables (Palutikof *et al.*, 1996) and influences runoff production in semi-arid environments through soil moisture and the 'wetting up' of catchments after the dry summer season.

High-magnitude rainfall events in semi-arid environments are often characterised by a few relatively short-lived, high-intensity bursts of rainfall with restricted spatial coverage. Precipitation is commonly the result of vertically unstable atmospheric conditions leading

to convection and the release of latent heat. Rainstorms often contain several short 'pulses', brief periods of high-intensity rainfall. Bracken *et al.* (2008) note that our understanding of the influence of the fine structure of rainfall events on flood generation in semi-arid environments is hindered by a paucity of available data. Many authors argue that rainfall intensity is important in the production of runoff (e.g. Costa, 1987; Schick, 1988; Cammeraat, 2004) whereas others emphasise the intensity-duration relationship of storms (Yair and Raz-Yassif, 2004) or total storm rainfall (Bracken *et al.*, 2008). The temporal variation of rainfall intensity, including the location of intense 'pulses' within the rainfall time series of a storm event, is crucial when considering the development of hydrological connections (van de Giesen *et al.*, 2000; Wainwright and Parsons, 2002), and so soil moisture conditions and total storm rainfall are also influential factors. Reaney *et al.* (2007) used a distributed dynamic hydrology model (the Connectivity of Runoff Model, CRUM) to examine the effect of storm characteristics on a model hillslope. Travel distances of overland flow were strongly influenced by the relationship between rainfall intensity and vertical abstractions and the fragmentation of periods of high-intensity rainfall (whenever pulses are shorter than the travel time of overland flow, the runoff may infiltrate further downslope). However, it is difficult to reduce the relevant properties to only a few measurable quantities (see Chapter 8).

3.3 Runoff Generation

Overland flow will only occur at a point once ponding takes place. Bull *et al.* (2003) suggest that the hydrological response of a soil surface can be divided into an 'at-a-point' local response (vertical exchanges or abstractions from the water available for runoff) and a topographic response (the routing of the remaining runoff through the catchment). The horizontal transfer of runoff eventually feeds back into the vertical process domain to determine the total catchment runoff response (Becker and Braun, 1999). This section briefly considers the vertical exchanges and extractions from received rainfall. Horizontal transfers and the topographic response are discussed in the following section.

Kirkby *et al.* (2002) emphasise the importance of the one-dimensional (vertical) water balance for runoff-generation in semi-arid environments (lateral subsurface flow is usually

considered to be negligible: Bull and Kirkby, 2002). Precipitation that passes through any vegetation layer and reaches the soil surface may be immediately infiltrated, may immediately become overland flow, or alternatively may be temporarily stored in a surface depression before taking one of the above pathways. Compared with rainfall totals, interception and transpiration of rainfall by the sparse vegetation cover and evaporation from bare soil surfaces during rainfall events are thought to be negligible in semi-arid regions (Sharma *et al.*, 1996). While this study is limited to bare soil surfaces (thereby ignoring the effect of interception), depression storage and infiltration complicate matters as they introduce threshold nonlinearities into the hydrological system (where a unit increase in rainfall does not produce an equivalent increase in observed runoff). Once local interception, depressional storage and infiltration have been satisfied at a particular point on the surface, any additional rainfall will be directly transferred into runoff; before this, abstractions will be made from the received rainfall. The magnitude of these abstractions at any time before the stores are filled is nonlinearly dependent on the 'wetness' of that particular point (i.e. the local soil moisture content or storage depth) (Nicolau *et al.*, 1996). Consolidating all the vertical abstractions over the course of a rainfall event reveals the simple concept of a local runoff threshold, the threshold depth of rainfall necessary h before runoff begins. Given storm total depth r_s and runoff total depth d, then

$$d = r_s - h . \tag{3.1}$$

3.3.1 Surface Depression Storage

Roughness as measured in the downslope direction represents the element of surface topography that impedes surface runoff, temporarily holding water in surface depressions (Kirkby, 2001; Smith, 2005). Depression storage is highly dependent on the recent history of the soil surface (Moore and Larson, 1979) and is influenced by rainfall, flow concentrations, land-use, slope, and random surface variations due to the nature of the soil. Smith (2005) notes that various attempts have been made to relate measures of surface roughness to depression storage. Surface detention of water is particularly important where the infiltration rate is slightly lower than rainfall intensity (Kamphorst *et al.*, 2000) and plays a regulatory role in the generation of surface runoff. This situation of 'precipitation

excess' is often found in semi-arid environments where high-intensity storms fall upon soils which may exhibit a relatively low infiltration capacity. The depth of depression storage to be satisfied will affect the duration of high-intensity rainfall necessary before runoff is generated at a point. However, Hansen (2000) notes that runoff begins before maximum depressional storage is completely satisfied; therefore during the filling of surface depressions precipitation excess is partitioned between surface storage and runoff.

3.3.2 Infiltration

In a landscape of uniform soils, surface topography would dominate the development of hydrological pathways through its influence on lateral water transfers and the resulting spatial distribution of soil moisture (Puigdefábregas *et al.*, 1998). In humid environments the spatial variability of infiltration is mainly attributed to such spatial differences in soil moisture and the gradual expansion of saturated areas (e.g. Beven and Kirkby, 1979). However, in more arid areas this variability is less predictable and runoff generation is primarily controlled by a patchwork of soil surface physical and chemical properties (Martínez-Mena *et al.*, 1998).

In most semi-arid areas runoff is generated primarily through the infiltration-excess or Hortonian mechanism (Bryan and Yair, 1982; Puigdefábregas *et al.*, 1998) where rainfall intensity exceeds infiltration capacity. The infiltration capacity will therefore determine the rainfall intensity necessary for runoff to begin. The decrease of infiltration capacity observed during storm events reflects a decline in the effective capillary pressure gradient (Beven, 2001). Vertical abstractions by infiltration become proportionally less as the storm event continues. This places emphasis on the initial soil surface moisture before rainfall commences. However, due to the large evaporation potential of semi-arid environments, water stored in the soil is rapidly lost to the atmosphere by evaporation or transpiration (Bracken *et al.*, 2008).

Philip (1957) modelled this decline of infiltration rate f_i [L T^{-1}] as a function of the square root of time t [T],

$$f_i = A + \frac{B}{2} t^{-0.5},$$

(3.2)

where the empirically derived constant A represents the steady rate of drainage from the soil moisture store (the steady 'leak' of the 'bucket' [L T^{-1}]) and B [L $T^{-0.5}$] represents the declining suction component or sorptivity of the soil (a measure of the ability to absorb water by capillarity).

Kirkby (1975, 1985) developed an infiltration equation to predict infiltration rate from soil moisture storage S_i [L] (which contributes to the tension gradient) rather than time. This simplified version of the Green and Ampt (1911) equation

$$f_i = A + \frac{B}{S_i}$$

(3.3)

has numerous advantages despite not having a strong basis in soil physics (note that here the constant B is of dimension [L^{-2} T^{-1}]). The use of a storage term allows the equation to be applied to a detailed rainfall time-series of varying rainfall intensity (Beven, 2001; Kirkby *et al.*, 2005; Reaney, 2008).

3.3.3 Hydrologically Similar Surfaces (HYSS)

Bull *et al.* (2003) aggregated areas of similar runoff thresholds in the Rambla Nogalte catchment of south-east Spain (a field-site of this study) into 'Hydrologically Similar Surfaces' (HYSS). These exist independently of topography and have been identified at a variety of scales. HYSS can be used for scaling-up plot and field measures of vertical exchanges while preserving catchment heterogeneity for model inputs (Bull *et al.*, 2003). GIS techniques were used to map HYSS in the Rambla Nogalte based on the macroscopic characteristics of geology, land use and slope (Figure 3.2). The field sites investigated in this study were selected to reflect the full range of HYSS categories observed.

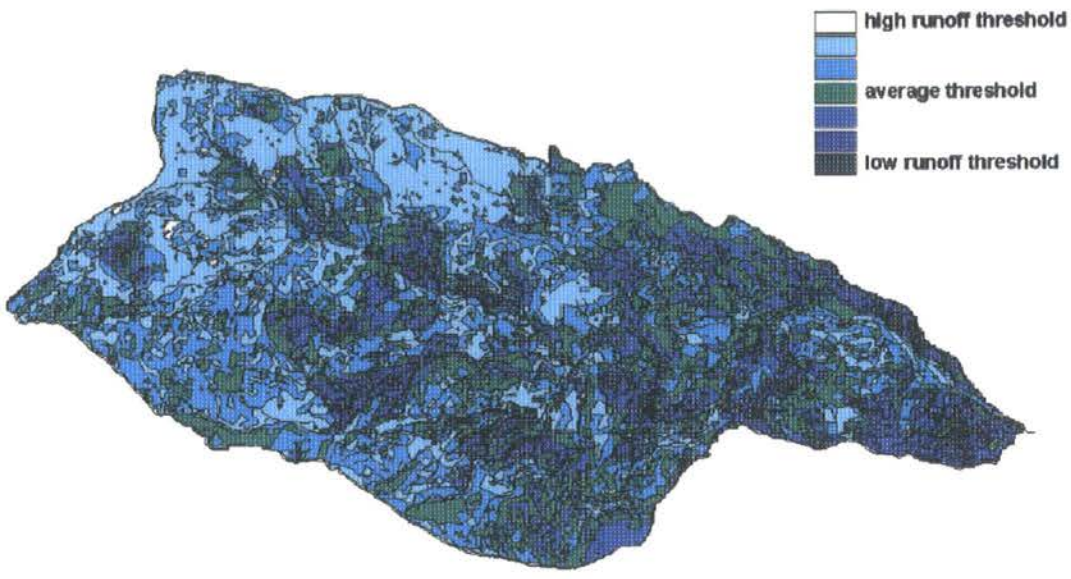

Figure 3.2. Predicted HYSS for the Rambla Nogalte (from Bull *et al.*, 2003: p.16). Total catchment area is 171 km^2.

This notion (labelled 'atomistic' by Cox, 1978) that the essentially continuous landscape can be divided into a mosaic of discrete units has inspired geomorphological subdivision of landscapes at many different scales; the HYSS classification has numerous predecessors (e.g. Flügel, 1995). Any attempt to partition the landscape into units is inevitably compelled to make contentious decisions, none more fundamental than how and where to delimit boundaries. One advantage of the HYSS scheme is the macroscopic criteria of classification. These permit rapid survey and can be resolved from aerial photographs. However, the HYSS divisions integrate over much finer-scale landscape complexity. For example, section 4.5.3 presents a further subdivision of the HYSS scheme at the hillslope scale, the aggregation of areas demonstrating similar morphological evidence of runoff intensity ('Morphological Runoff Zones', MRZs).

A patchy spatial mosaic of HYSS classes is produced when geology, land-use and slope were mapped in the Rambla Nogalte (Figure 3.2). Low runoff thresholds were associated with steep slopes and areas of carbonates, marls and greywackes. However, Bull *et al.* (2003) found that land-use was most strongly related to runoff production. Tillage operations remove vegetation; on matorral surfaces, vegetation cover and litter may

influence infiltration rates and protect the soil surface from crust formation (Bochet, 1998). However, areas of matorral scrub often have smooth, stony, compacted surfaces and demonstrate low runoff thresholds, whereas in agricultural areas, tillage produces substantial increases in surface roughness and subsequent depression storage, with significant implications for soil and water conservation (Onstad, 1984). As a result of increased depression storage and the development of surface crusts, the response of ploughed areas to rainfall is especially nonlinear.

Moore and Larson (1979) found that surface depression storage was increased 3.5 times by ploughing, although this effect was soon lost through breakdown of the soil surface by raindrop impact (Onstad, 1984). Abandoned agricultural land soon loses its characteristic surface roughness at a rate dependent upon aggregate stability (Zobeck and Onstad, 1987). Bull *et al.* (2003) suggest that it takes approximately 1–2 years to erode the roughness derived from ploughing. After this time preferential flow pathways begin to emerge as channelisation takes place and gullies potentially form, increasing surface roughness by channelling overland flow.

Lasanta *et al.* (2000) showed that abandoned agricultural land demonstrates a particularly rapid runoff response to rainfall with high peak flows and low runoff thresholds. This is especially relevant to semi-arid environments, many of which have experienced large-scale land abandonment in the twentieth century, with migration to urban centres. In particular, the agrarian policy of the EU has encouraged the set-aside of cultivated lands in Spain and elsewhere (Lasanta *et al.*, 2000).

3.4 Connectivity and the Conveyance of Runoff

The spatially and temporally variable vertical exchanges discussed in the previous section determine the proportion of received rainfall that becomes the rainfall excess (or 'effective rainfall') available for runoff. This water is then routed from its source, into channels and eventually towards the catchment or hillslope outlet. Topography and surface roughness are required for the calculation of overland flow velocities and travel times; this is an essential component of all process-based hydrological models (Takken *et al.*, 2005) as it is needed

for the prediction of the timing and peaks of outflow hydrographs. Understanding overland flow velocities is particularly crucial in semi-arid environments where active overland flow generating areas may be initially disconnected from the drainage network (Figure 3.3b) and travel distances to channels or flow concentrations may be greater. Under such conditions, the distinction proposed by Ambroise (2004) between 'variable active' (runoff generating but disconnected) and 'variable contributing' areas (runoff generating and connected) is especially relevant.

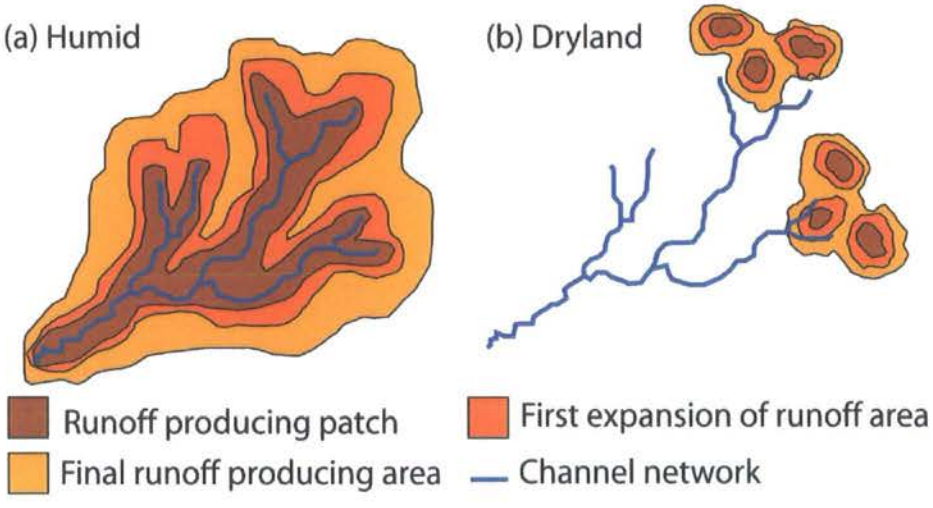

Figure 3.3. Saturated areas expanding in humid-temperate environments (a) and mosaic patches of runoff that connect to produce flooding in dryland areas (b). Adapted from Bracken and Croke (2007: p.1753).

Observations of such patchiness of runoff generating areas support the need to update the Variable Source Area (VSA) concept developed 40 years ago (Hewlett and Hibbert, 1967). Indeed the VSA concept does not apply in areas dominated by Hortonian overland flow as this runoff-producing mechanism invalidates the assumption of a saturated wedge expanding outwards from the channel network and gradually increasing the contributing area (Figure 3.3a) (McDonnell, 2003). Where such saturation-excess flow takes place, hillslope processes will increasingly affect hydrograph characteristics as saturation increases. However, the mosaic pattern of Hortonian runoff generating areas means that the routing of overland flows over hillslopes is important for all runoff events (D'Odorico and

Rigon, 2003). Semi-arid hillslope outflow is inherently nonlinear and subject to threshold behaviour as 'active' areas connect to the drainage network to become 'contributing' areas. Bracken and Croke (2007) argue that the framework of connectivity is of fundamental importance in post-VSA conceptualisations of rainfall-runoff relationships.

As there are many possible flowpaths to a catchment outlet, the hydrological connectivity of a (sub-)catchment can be placed at any point on a continuum between the extremes of totally isolated and totally connected (Fitzjohn *et al.*, 1998). No consistent definition of connectivity has emerged from the literature. The recent review of Bracken and Croke (2007) made steps towards the standardisation of the connectivity framework as applied in hydrology, proposing that further advances in the field must be supported by a measurable quantitative variable (e.g. 'volume to breakthrough'; Bracken and Croke, 2007). Here hydrological connectivity is defined as the ease of transfer of water from one part of a landscape to another.

Connectivity can be understood in terms of patterns in the landscape (static or *structural* connectivity) (Turnbull *et al.*, 2008). While infiltration rate and the friction factor are the most important characteristics for runoff generation at the plot scale, their spatial variation is more important at the hillslope and catchment scales. In a recent modelling experiment, Mueller *et al.* (2007) investigated different parameter scaling tools for representing the variability of the Darcy-Weisbach friction factor and saturated hydraulic conductivity in a kinematic-wave overland flow model over small semi-arid catchments. They found that while an appreciation of spatial variability is necessary, retaining the spatial pattern of connectivity is of crucial importance.

The position of a storm cell and the temporal structure of the rainfall determine which flowpaths become activated and when. Connectivity is therefore a dynamic property that describes the interconnection of areas by a process (*functional* connectivity; Turnbull *et al.*, 2008). Much research has been conducted in more temperate environments examining the heterogeneity and connectivity of subsurface flow pathways as a possible explanation for threshold behaviour observed in hillslope drainage (e.g. Western *et al.*, 2001; Sidle *et al.*, 2001; Lehmann *et al.*, 2007). Tromp-van Meerveld and McDonnell (2006) suggest that the

spatial pattern of active flow pathways is the key to conceptualising the nonlinear process of subsurface stormflows.

Structural and functional connectivity interact to determine the dynamic and nonlinear behaviour of a hydrological system (*dynamic* connectivity; Bracken and Croke, 2007). Our understanding of this interaction is extremely limited at present. In a semi-arid context, Fitzjohn *et al.* (1998) suggest that the spatial arrangement of areas with high and low vertical abstraction potentials (structural connectivity) ceases to affect development of continuous hydrological pathways (functional connectivity) once a threshold surface soil moisture level has been reached (Figure 3.4b). Below this threshold the spatial configuration of responsive (low abstraction potential) and unresponsive areas (high abstraction potential) determines hydrological connectivity (Figure 3.4a).

The distribution of flowpath lengths will affect the connectivity of a (sub-)catchment as rainfall that travels further will encounter more potential abstractions. Yair and Kossovsky (2002) report that typical flow distances over semi-arid hillslopes may be exceptionally short. Where abstractions are large and flowpaths are longer, an area will be hydrologically disconnected throughout most storm events. Goodrich *et al.* (1997) suggest that this explains the increasing nonlinearity of runoff response with catchment area: larger areas imply longer flowpaths through ephemeral channels with large potential abstractions (high storage capacity). This also relates to the concept of a 'travel opportunity time' discussed by Aryal *et al.* (2003) which they suggest influences the 'effective length' of temperate hillslopes (beyond which the flow becomes disconnected).

Conversely, rain close to the catchment or hillslope outlet will have a shorter flowpath, be less affected by potential abstractions and be more effective in delivering storm runoff. Thus, the distribution of area within a (sub-)catchment is important: a distal distribution produces longer flowpaths (Figure 3.5a), whereas a proximal distribution has a higher proportion of shorter flowpaths (Figure 3.5b) which have a greater chance of generating connected flow (Kirkby *et al.*, 2005). This effect becomes less important as the magnitude of the rain event increases (Michaelides and Wainwright, 2002).

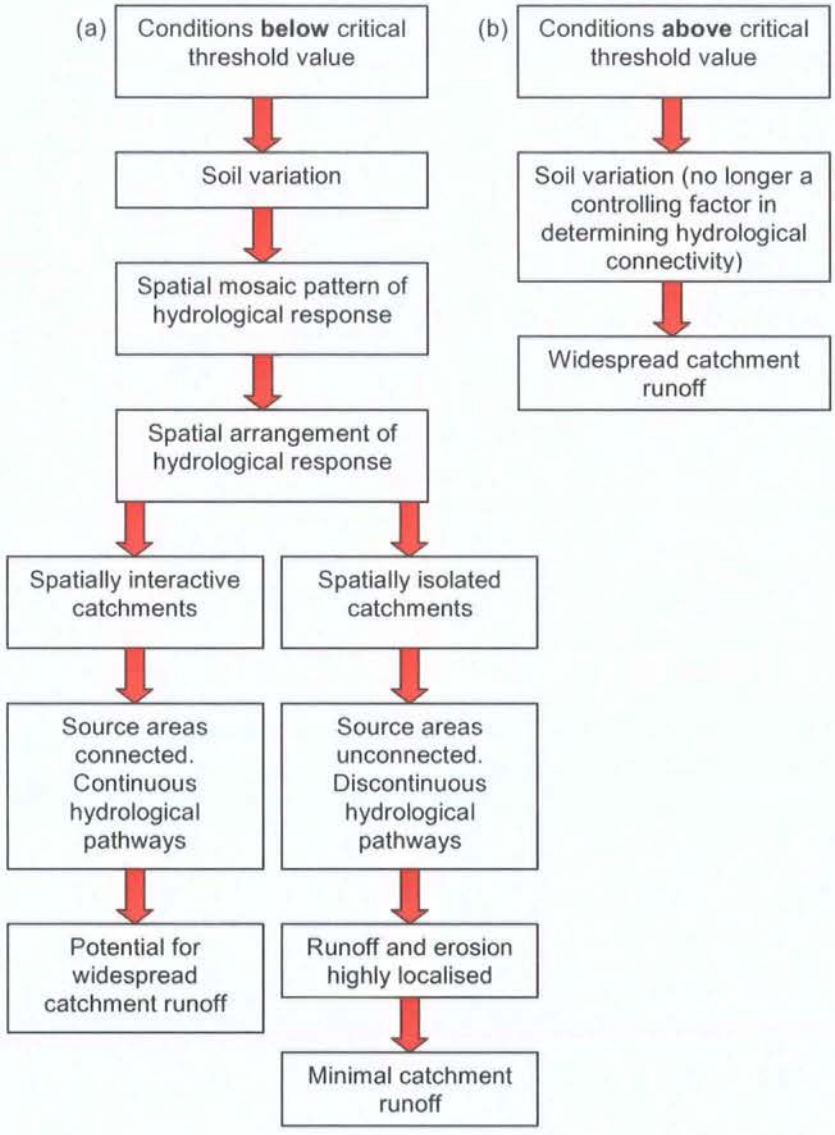

Figure 3.4. Relationships between soil variation, the spatial arrangement of hydrological response units, critical thresholds and the occurrence of widespread runoff and erosion. From Fitzjohn *et al.* (1998: p.66).

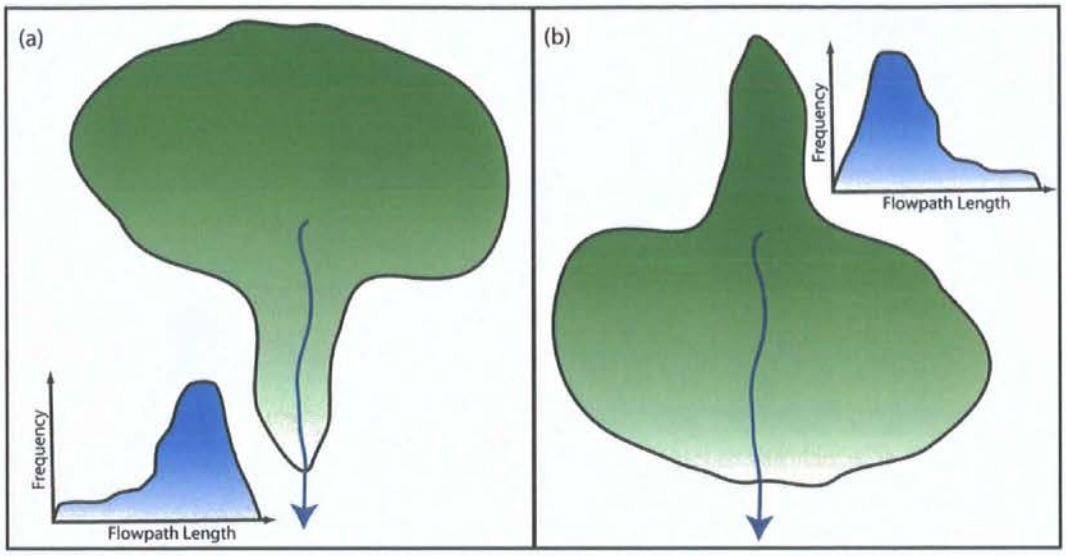

Figure 3.5. Plan view of catchments with biases towards (a) longer flowpaths from a distal area distribution, (b) shorter flowpaths to outlet from a proximal area distribution.

When one water parcel travelling down a flowpath is abstracted (infiltrated or stored in a depression), there is less chance of the following parcel being abstracted at the same spot (as moisture stores gradually become satisfied), and so it may travel slightly further before infiltrating. The probability of a parcel of water travelling along a flowpath to the drainage network is determined by the magnitude of vertical abstractions. This probability will increase with previous flow though this increase will vary with the threshold factors discussed in section 3.3. Therefore, with increasing total storm rainfall, the proportion that overcomes these abstractions will increase. Through this mechanism, the routing of overland flow, particularly the integration of flowpaths, determines the storm characteristics necessary for runoff to contribute to the outflow hydrograph. For example, Yair and Raz-Yassif (2004) discuss the duration of intense rainfall (or 'concentration time') necessary for continuous flow to develop over a hillslope.

Flowpath integration occurs at all scales from the plot up to the catchment, reflecting both fine-scale development of flow concentrations around roughness elements and larger-scale integration of rill systems and ephemeral channels. This will partially determine the efficiency of overland flow. Kuhn and Yair (2004) stress that the form of rill systems is

crucial in the generation of runoff; parallel rills show little integration of flowpaths and so experience high total transmission losses and frictional resistance (Figure 3.6a), but integrated rill networks encourage continuous flow as runoff is concentrated into more efficient flows (Figure 3.6b). When two water parcels arrive at the same point synchronously, they become superimposed and are more likely to propagate downstream as a consequence of the hydraulics of the overland flow previously discussed. The increasing flow depth with distance down such a network enhances the strength of the 'delivery pathway', thereby improving hillslope connectivity (Bracken and Croke, 2007) and reducing the effective rainfall necessary for the development of continuous flow.

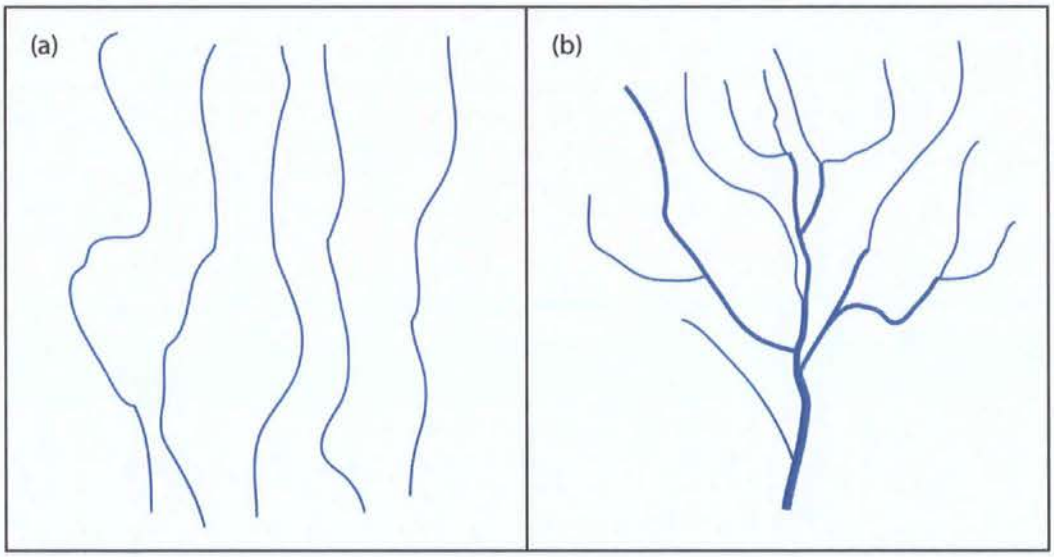

Figure 3.6. Plan view of (a) a parallel, isolated drainage network; (b) an integrated drainage network.

Figure 3.6 displays continuous flowpaths. However, as discussed in section 3.2, rainfall intensity may only exceed infiltration rate for a small period of time and flow may be intermittent. The (a-)synchronous arrival of overland flow bursts generated from high-intensity rainfall pulses at a flowpath junction will influence the subsequent propagation of the flow towards the hillslope outlet. The routing velocity of overland flow is therefore an important consideration.

3.5 Velocity of Overland Flow

The preceding discussion of hydrological connectivity has emphasised the importance of timing. Specifically, at any flowpath junction the relative arrival times of overland flow generated in active areas will influence the hydrological connectivity of a hillslope during a particular storm event and in turn affect the magnitude of flood events and flood peaks. This is highly dependent upon the friction factor used to route the overland flow over the hillslope surface. Singh (1996) notes that the friction factor is one of the most influential factors in runoff generation, affecting the shape of the hydrograph, time to peak runoff and also the total runoff amount. The sensitivity of hydrological models to hydraulic resistance parameters was mentioned in Chapter 2 (also Jetten *et al.*, 1998; Wainwright and Parsons, 2002; Takken *et al.*, 2005).

The routing velocity of flow will also determine the time available for infiltration (or 'infiltration opportunity time'; van de Giesen *et al.*, 2000). Rainfall pulses must be long enough for the routing velocity of overland flow to connect active runoff producing areas to the point where the delivery pathway is strong enough to overcome vertical abstractions (transmission losses). Reaney (2008) suggests that this condition is met where the pulse is of a greater duration than the travel time to the nearest flow concentration (similar to the 'concentration time' of Yair and Raz-Yassif (2004)). However, this is a simplification as transmission losses in flow concentrations and ephemeral channels can have a marked effect on hydrograph propagation in semi-arid regions (Shannon *et al.*, 2002). Routing velocities are commonly considered as uniform across a hillslope, but as flow begins to concentrate and incision occurs, the runoff efficiency increases and the delivery pathway strengthens with a concurrent increase in routing velocity. An understanding of the variation of velocity with distance downslope is crucial for modelling runoff response.

3.6 Conclusions and Research Gaps

Catchment connectivity shapes the operation of geomorphic processes over a range of scales (Brierley *et al.*, 2006) and is a key consideration in environmental management. A connectivity framework is especially relevant for the management of semi-arid catchments where large runoff-generating areas may remain disconnected from the channel network for all but the largest of rainfall events. The establishment of a connection between source and channel leads to nonlinear threshold behaviour in hydrograph response and can contribute to the flash floods experienced in such areas (Leopold and Miller, 1956; Peebles *et al.*, 1981). The high variability of rainfall in semi-arid environments (Bracken *et al.*, 2008; Wainwright and Parsons, 2002) means that each flood event is unique with a large variety of hydrological responses to storms of a similar size (e.g. Huckleberry, 1994).

Section 3.3 examined the mechanisms through which soil surfaces can prevent or delay connections from developing by storing rainfall. The infiltration capacity of the surface will determine the necessary rainfall intensity that must be maintained before runoff can be generated, while surface depression storage determines the duration for which this intensity must be maintained before outflow occurs. This simplification may be valid at the plot scale. However, up-scaling techniques must also capture the spatial pattern and connection of runoff generating areas (structural connectivity). From a consideration of orders of magnitude, Kirkby *et al.* (2002) suggest that the effects of local patchiness are dominant at areas of ~100 m^2. At the hillslope scale (~10,000 m^2) they suggest that storm intensity variations are the dominant influence (though patchiness of response remains an important consideration). For larger areas (~1 km^2) the spatial variability of rainfall (storm size and path, etc.) is also important. The results presented in this thesis are limited to the plot and hillslope scales and so spatial rainfall variations may be considered negligible.

Section 3.4 noted the importance of the distribution of travel times and the arrival of water parcels at key points in the flow network. Several factors that influence delivery times at the hillslope scale were identified. These can be summarised as:

- the temporal structure of the rainfall event;
- the spatial structure of active runoff-generating areas;

- the distribution of flowpath lengths;
- the integration of flowpaths (drainage structure);
- the velocity of overland flows.

This suggests that for any specific hillslope, there is a particular combination of rainfall characteristics that will maximise hydrological connectivity and hillslope outflow. From the combination and interaction of these five relatively simple spatial and temporal patterns a great variety of extremely complex hydrological responses emerge, providing an explanation for the observed scale dependency of runoff (Goodrich *et al.*, 1997; Wainwright and Parsons, 2002). Developing our understanding of these interactions is the key to understanding semi-arid hillslope hydrology; the connectivity framework provides us with the necessary perspective to manage this. Such an approach should be grounded on insights and observations made in the field (Brierley *et al.*, 2006).

There is a lack of measured data on the spatial distribution of runoff in semi-arid environments (Mueller *et al.*, 2007). This is no doubt a consequence of the infrequent and heterogeneous nature of such overland flows. Recent experimental work on temperate hillslopes has developed our understanding of connectivity development of subsurface flows and produced some useful theoretical insights into the application of the connectivity framework in hydrology with practical implications for the management of diffuse pollution issues (e.g. modelling hydrological connections using percolation theory; Lehmann *et al.*, 2007). The study of Hortonian overland flow patterns in this manner could contribute a great deal to this research frontier, as the processes operating on the soil surface are more readily observed.

Section 3.4 described the variety of recent studies that have begun to examine the importance of spatial patterns and connectivity of runoff generating patches on semi-arid hillslopes. The majority of these studies have focused on the spatial variation of infiltration rates as an explanation for the scale-dependency of runoff (e.g. Sharma *et al.*, 1980; Wilcox *et al.*, 1997). This has enhanced our appreciation of how the distribution of active (and non-active) areas within a hillslope and the morphology of the hillslope itself affect the intensity-duration relationship of a rainstorm that is necessary for connected flow to

develop. However, the flow resistance of the soil surface also has an important influence upon the necessary duration of high-intensity rainfall. This flow resistance may vary with distance downslope and as the delivery pathway becomes stronger as a rainstorm progresses. To the author's knowledge, no previous study has examined the effect of variations in flow resistance produced by the systematic downslope transitions of microtopography observed on semi-arid hillslopes (discussed in section 2.5.3 and 4.5.3; Bracken and Kirkby, 2005) on the development of connected flowpaths and hillslope hydrological response. This represents a central focus of this thesis. The variable hydraulic resistance to overland flows on natural soil surfaces is examined in Chapter 6; the resultant impact on hydrological connectivity development is then considered in Chapters 7 and 8.

CHAPTER 4

MEASURING OVERLAND FLOWS: METHODOLOGY & FIELD SITES

4.1 Introduction

The non-uniform nature of overland flow complicates any attempt to define relevant flow variables precisely (Emmett, 1970). Measurement of flow depth and velocity on rough surfaces is especially difficult and relatively large measurement errors can be expected (Govers *et al.*, 2000). This chapter reviews measurement techniques presently applied to overland flows (section 4.2) and provides a detailed description of an alternative and novel methodology (section 4.3). This new method is currently at the prototype stage: while it represents an exciting development and provides an innovative solution to the problems of measuring overland flow, it remains subject to limitations. The methodology presented here estimates the characteristics of overland flows at an unprecedented spatial and temporal resolution. A side-effect is that current definitions of overland flow variables are insufficiently precise to describe the nature of these flows. This inadequacy presents an urgent need for a more precise standardisation of flow variables (section 4.3.7).

Infiltration measurements conducted are described in section 4.4. This methodology was applied to three hillslopes in south-east Spain. The fieldwork locations are described in section 4.5. The measurements presented are limited to the plot-scale; section 4.5.3 explains the techniques employed to upscale these results to the hillslope scale. Finally, section 4.6

summarises the potential for this methodology to advance understanding of the nature of overland flows.

4.2 Review of Current Methodologies

4.2.1 Velocity Measurement

A thorough understanding of overland flow velocities is necessary for studies of soil erosion. A variety of techniques have been developed to measure this. However, the shallow and variable nature of these flows presents considerable challenges and places limitations on the applicability of each of these measurements.

Many studies of fluvial hydraulics use Acoustic Doppler Velocimeters to obtain high-resolution velocity data; this approach has rarely been applied to overland flows (e.g. Giménez *et al.*, 2004) as they require flows over 15 mm in depth. Instead, dye tracing techniques are commonly applied to studies of overland flows. A dye is injected into the flow (often food colouring, fluorescein or rhodamine) and the arrival of the leading edge of the dye front is manually timed. Local variability of velocity cannot be detected; flow paths of several metres are necessary as human reaction time limits the reliability of rapid measurements (Dunkerley, 2003).

It is commonly assumed that the leading edge of a dye streak provides a measure of surface velocity. This is corrected for mean velocity using a coefficient, α. Horton *et al.* (1934) theoretically derived $\alpha = 0.67$ for laminar flow on a smooth bed. However, this correction factor has since been reported to vary with the Reynolds number (e.g. Emmett, 1970), gradient (e.g. Li and Abrahams, 1997) sediment load (e.g. Li *et al.*, 1996) and surface roughness (e.g. Phelps, 1975; Dunkerley, 2001). Planchon *et al.* (2005) report that such findings have increased the range to at least $0.2 < \alpha < 0.8$, highlighting considerable uncertainty in this method of estimating mean flow velocity (Dunkerley, 2001). Each reported coefficient is based on an assumption about the velocity profile which may not hold for shallow flow over rough surfaces. Eddy mixing in turbulent flow reduces the difference between the mean and surface speeds. Moreover, non-uniform flow brings the use of a single coefficient into question; dye tracing techniques are biased towards the

deeper, smoother flow threads because dye dominantly follows the faster flow (Dunkerley, 2001, 2004).

The correction for mean velocity can be avoided by directly timing the arrival of the centroid of a tracer plume. This is made possible when dye arrival is recorded using an automatic logging fluorometer (e.g. Gilley *et al.*, 1990; Holden *et al.*, 2008). A similar procedure is applied when measuring velocity using salt tracers, where dye is replaced with an injection of saline solution, the passage of which is recorded by an electrical conductivity probe or ion-selective electrodes (e.g. Li and Abrahams, 1997). Such studies often require the concentration of the flow at the end of a flume (Li *et al.*, 1996) and may measure a slower mean velocity as the dense saline solution travels towards the bottom of the flow where speeds are lower.

Planchon *et al.* (2005) report an improvement on the salt tracer method, where conductivity of the salt plume is recorded at two locations and the mean velocity is calculated by modelling the propagation of the salt plume between these points. They report a high measurement accuracy of their 'Salt Velocity Gauge' ($\pm$ 15 mm s^{-1}) over a wide range of flow depths and velocities. Tatard *et al.* (2008) used miniaturised Salt Velocity Gauges to provide high resolution overland flow velocity measurements (averaged over 100 mm long by 10 mm wide sections). However, this requires the path of the salt plume to be predicted when locating conductivity probes, may disturb the flow around the probes and can be relatively time-consuming when obtaining these measurements over a large surface area.

The 'optical tachometer' method of Dunkerley (2003) also requires prediction of flow paths. Here, buoyant reflectors made of aluminium foil are carried on the surface tension film of overland flows and pass between reflective sensors mounted above the flow. Particle Tracking Velocimetry can be used to track the velocity vectors of buoyant particles using rapid-fire photography (e.g. Adrian, 1991; Holland *et al.*, 2001). While these methods reduce travel time restrictions caused by operator reaction times, they provide a measure of surface velocity and are therefore subject to the problem of applying a correction factor. The floating particles may also become snagged on rough surfaces.

The difficulty of measuring mean flow velocity in overland flows means that it is often estimated using the continuity equation. Flow width w and discharge Q (supplied by either rainfall or trickle-flow at the upper end of the plot) are constrained experimentally and velocity is then calculated from flow depth d such that

$$V = \frac{Q}{wd}. \tag{4.1}$$

d is directly measured, often estimated as the mean of several point measurements (e.g. Emmett, 1970, 1978). On rough surfaces, Dunkerley (2004) found that the use of such flow-field average depths to estimate friction coefficients produces an areal bias toward the shallower, high roughness part of the flow as these areas are overweighted. Therefore, flow velocities calculated from depth measurements are often lower than the velocities measured by tracing methods.

The different and poorly-defined experimental errors and sensitivities for these methods of mean velocity estimation suggest that comparison of published values requires caution. Dunkerley (2004) notes that the errors in calculated friction coefficients associated with the application of these methods to non-uniform flows are not readily quantified and appear not to have been addressed properly. The approximations and scalings used in estimating f, C or n (discussed in Chapter 2) mean that a single average depth and velocity are required. Yet, the use of flow-field mean depths and velocities conceals the existence of regions where the flow may differ from this mean. The non-uniform nature of such overland flow raises a sampling issue unless the proportions of dye paths and depth measurements that are in thread and non-thread flow states can be estimated (Dunkerley, 2004).

4.2.2 Depth Measurement

Supplying equation 4.1 with a measure of flow depth is, however, not as simple as may first appear. While some studies neglect even to mention the method of depth measurement (e.g. Li *et al.*, 1996) it is often measured with a point gauge or millimetre scale (e.g. Abrahams *et al.*, 1986b; Parsons *et al.*, 1996a) and the resultant measurements are averaged to provide a mean flow depth. Dunkerley (2001, 2004) used a computer-controlled gantry and a

stepper motor-controlled electronic needle gauge, quoting the precision of depth to 25 μm. This system was applied in the field with 49 point measurements taken over a 2 m^2 plot. This is a considerably higher resolution of depth measurements than is achieved in most field-studies: Emmett (1970) reports a grid of 9 point measurements per m^2; Holden *et al.* (2008) collected just 10 randomly chosen points over plots of 3 m^2. Parsons *et al.* (1990) and Parsons *et al.* (1996b) installed miniature flumes into the flow at several cross-sections and measured the average water depth inside the flumes.

Accurately measuring flow depth on rough, partially-inundated surfaces presents an awkward challenge. Emmett (1970) calculates depth using the mean elevation of the top of the roughness elements, thereby ignoring inter-particle voids. Using mean bed level or maximum bed height as a reference level results in negative depths for some partially inundated flows. Abrahams and Parsons (1990) observe that many authors (e.g. Emmett, 1970, 1978; Dunne and Dietrich, 1980) include point measurements of zero depth in their estimations of mean depth (i.e. where a surface protrudes from the flow) and that this acts to underestimate mean depth, and in turn, Re and f.

Abrahams *et al.* (1996) calculate flow cross-sectional area in rills by measuring depth at a point and assuming a horizontal water surface over a measured cross-section. Smart *et al.* (2002) also present an interesting approach to measuring the hydraulic radius of complex rough surfaces by defining a volumetric hydraulic radius R_v. This represents the volume of overlying water per unit plan area of the bed and avoids the problem of defining an ambiguous reference water level. Where all the roughness elements are fully inundated, this approximates the mean flow depth. This term provides the necessary information to account for the upward volumetric displacement of the water surface by submerged roughness elements, which, Dunkerley (2002) suggests, greatly influences total resistance to flow.

In summary, due to the complex nature of overland flows, their measurement poses a technical challenge. A multitude of techniques are presently applied, though each is limited by issues of accuracy, precision and resolution. The following section presents a new high-resolution methodology of measuring shallow flows over complex, partially inundated bare

soil surfaces. Much like the techniques discussed above, it too is subject to limitations; however, the high resolution available provides an alternative perspective that may enhance understanding of such flows.

4.3 A New Method of Measuring Overland Flows

The methodology developed in this study is now described in detail. This method represents a combination of different techniques, integrating terrestrial laser scanning with overhead imagery. Each is discussed in turn before describing how they were combined to provide a novel measurement of overland flows. A camera-boom system was rigged up above each plot surface (section 4.3.1) from which rapid-fire digital photographs were taken. Overland flows were supplied by two troughs situated at the top end of each plot (section 4.3.2). A high-resolution DEM was provided by a terrestrial laser scanner (4.3.3) onto which each image could be accurately georeferenced (4.3.4). The resultant dataset allows velocity and depth data to be extracted (section 4.3.5) together with information of soil surface roughness and microtopography (4.3.6). This offers the potential to synthesise the different strands of data, providing a complete picture of the nature of overland flows on natural surfaces (section 4.3.7). Finally, section 4.3.8 suggests further refinements to the methodology which would substantially speed-up processing time.

4.3.1 Camera Boom System

An 8 m camera boom was designed to elevate a wirelessly-operated digital camera above a plot surface (Figure 4.1). The boom system was made from inexpensive materials which could be transported across hillslopes by one person and assembled in 15 minutes. It requires only one operator and once in place can be left unsupervised. The long neck of the boom was assembled in the field from 2 m long segments of lightweight, hollow, aluminium poles fastened together with basic pipe-fittings. This allowed the length of the neck to vary between 2 m and 8 m, chosen depending on the size of the plot under investigation. It was found that a length of 6 m was sufficient to provide a vantage point over an area of 2 m by 3 m. Any further height gain poses a trade-off between area covered and image resolution.

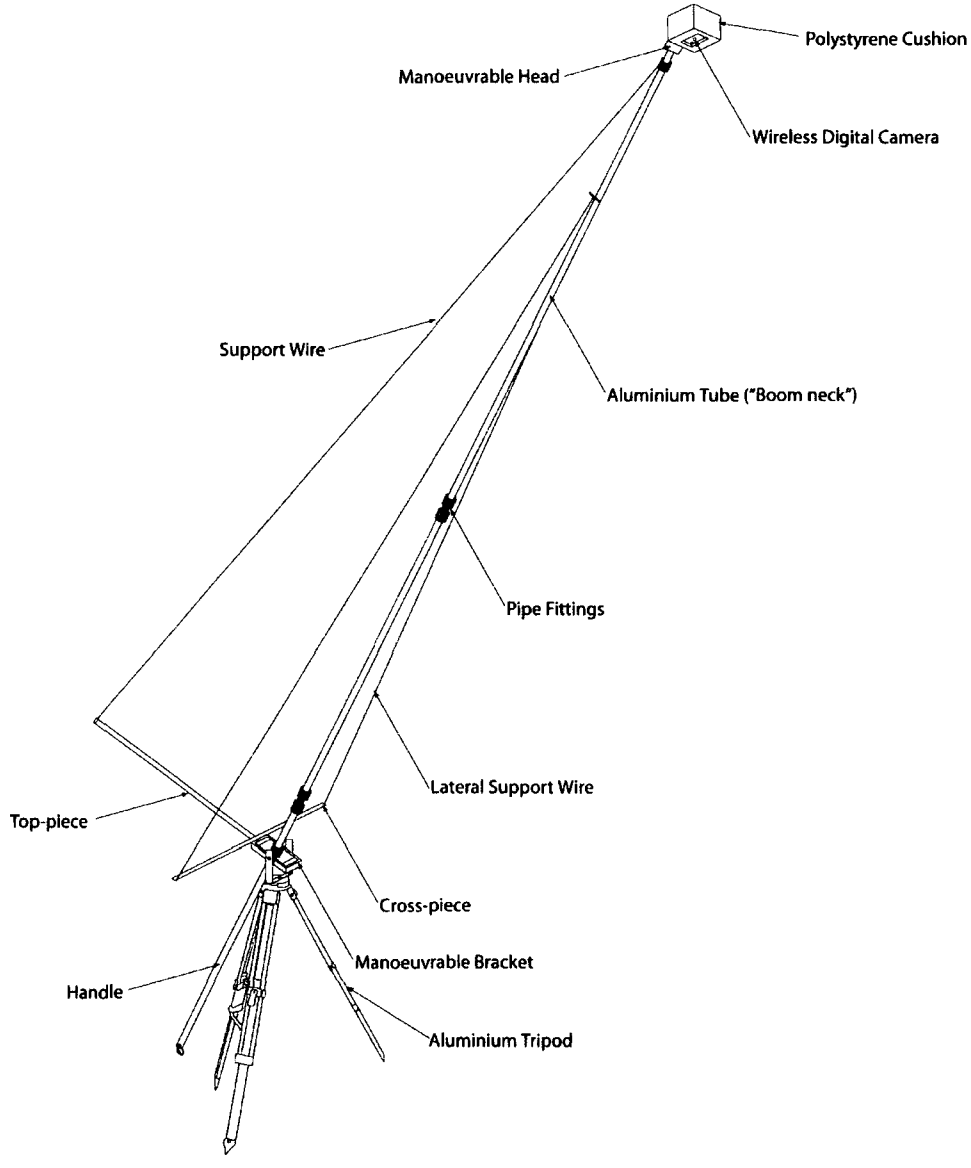

Figure 4.1. Sketch of the camera boom developed for this study.

At the top of the boom, the boom head component housed the 5 megapixel digital camera (Canon IXUS-WIRELESS) which had a zoomed-out maximum aperture of f/2.8. This camera wirelessly transmitted a video stream to a laptop computer located on the ground. Though this video stream was not recorded, high-resolution images were remotely captured using the laptop. The boom head could be manually manipulated in 2-axes (adapted from a

typical mop-head fixing) and cushioned the digital camera within a protective polystyrene casing.

The base of the boom was an adapted aluminium tripod – a bracket was fastened on to the tripod made of a metal-framed wooden block through which a circular hole allowed the lower neck of the boom to be inserted. The bracket was hinged to raise and lower the boom and could be loosened to allow horizontal rotation of the boom away from the plot under investigation. The lower neck inserted through the bracket could be used as a handle to control the boom. The combination of tripod bracket and boom head hinges permitted the camera to be manipulated to face any plot surface. Once the video stream from the camera confirmed that the boom was in place, the system was fixed by fastening the end of this handle to a secure object using a large carabiner hooked on the end.

The georeferencing method described below (section 4.3.4.) prevented minor camera wobbles from affecting flow measurements. However, in windy conditions, major movements of the boom head could cause the camera to point away from the plot. This was avoided by supporting the boom head with a system of metal wires. A top-piece screwed on to the boom bracket was fastened to the boom head with metal wires. This provided the tension necessary to prevent the boom from sagging. Additionally, a cross-piece fastened beneath the bracket and attached to a middle pole joint prevented any sideways movement.

Images such as that of Figure 4.2 were taken at approximately 1 s intervals, recording the advancing flow wave. The exact interval between images is necessary to calculate flow velocity: this was especially important as the interval was found to vary between experiments (with a range of 0.91−1.32 s), possibly as a function of lighting conditions. To avoid such variations propagating error into velocity calculation, two timing systems were established to provide the exact interval between images. A large stop-watch was placed on the edge of the plot, facing the camera, alongside a laptop computer running a stopwatch timing program (Figure 4.2). While the interval was found to vary slightly between experiments, it remained constant during each flume run.

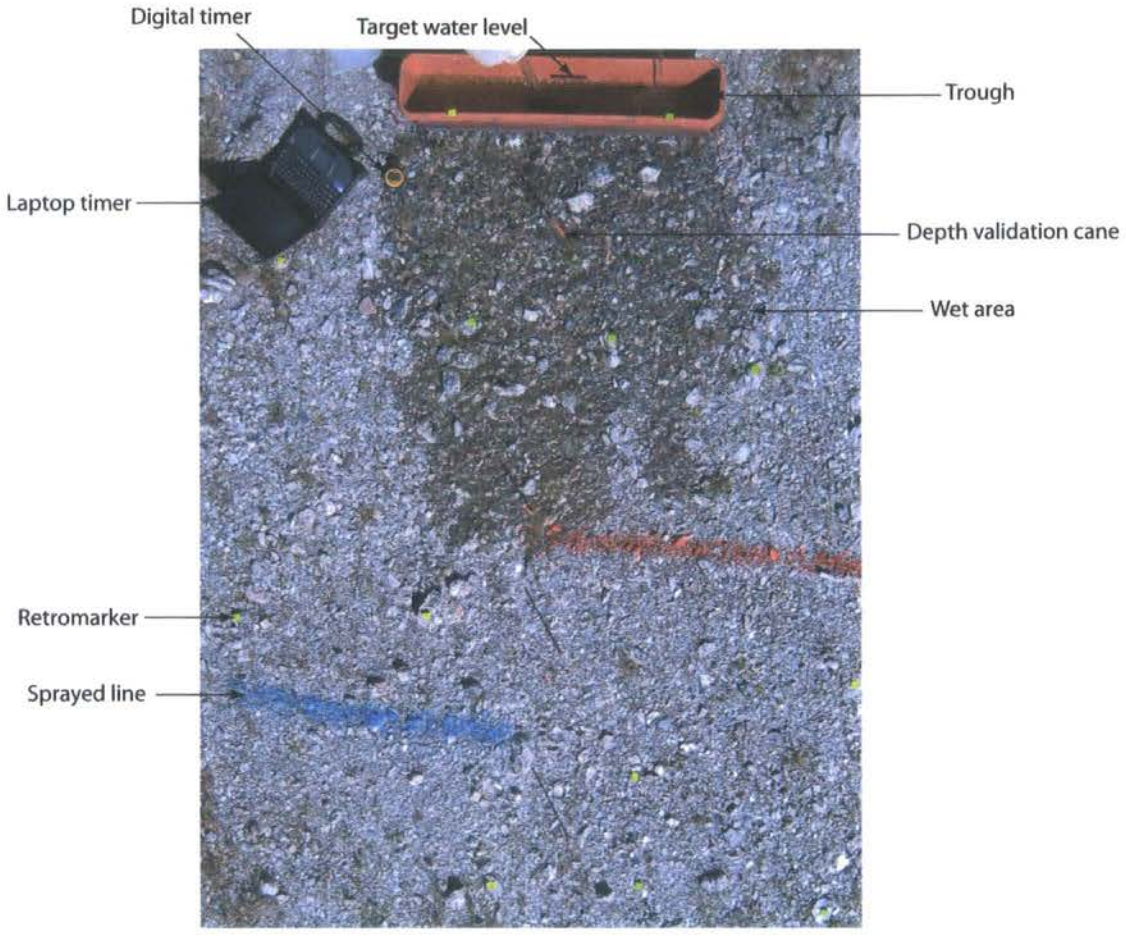

Figure 4.2. Example of overhead images captured during flow experiments.

4.3.2 Artificial Generation of Overland Flow

The flows described in this study were generated from a trough located at the upslope plot boundary. The effects of raindrop impact were not investigated in this study, despite the findings of Parsons *et al.* (1994) that natural, rain-induced flows have f values nearly an order of magnitude greater than the types of flows simulated here. The experimental design demanded two features of the flow:

1. the flow should be as wide as possible to allow a large surface to be examined;
2. the discharge should be variable to simulate a range of runoff conditions.

These two requirements both demand a large water supply. Such a supply was neither readily available in the remote areas in which fieldwork was conducted, nor was it particularly amenable to experiments taking place near the crest of hillslopes. Rather than compromise on these requirements, two separate water supply systems were designed. The first (most frequently used in this study) was 0.81 m wide and provided a constant discharge (0.52 l s^{-1} per metre width) evenly spread across the top of the plot. The second inundated a much narrower surface but could provide a variable discharge. The experiments were conducted separately, on the same plot surfaces and water temperatures were recorded before each run.

4.3.2.1 Wide Trough

The first trough was adapted from a 1 metre long planter (Figure 4.2). A thin slot 0.81 m wide was made near the bottom and a metal fixture was attached along the length of the planter and above the slot to prevent the strong plastic from bowing under water pressure. A thin metal strip covers the slot at the centre of the planter. Although this provides a small localised disturbance to the flow, it was unavoidable, as it provides support for the planter and prevents the plastic from sagging and narrowing the centre of the slot.

The slot is submerged by water in the planter which is maintained at a constant level (indicated by several markers around the inside rim of the trough) by continuous water replacement during the flume test. This permits a steady and known discharge to be added to the top of the plot over a relatively large flow width. The discharge was estimated by maintaining the water level with a known amount of water (4 litres) and recording the time lapsed before the water ran out. This experiment was repeated 5 times (Figure 4.3).

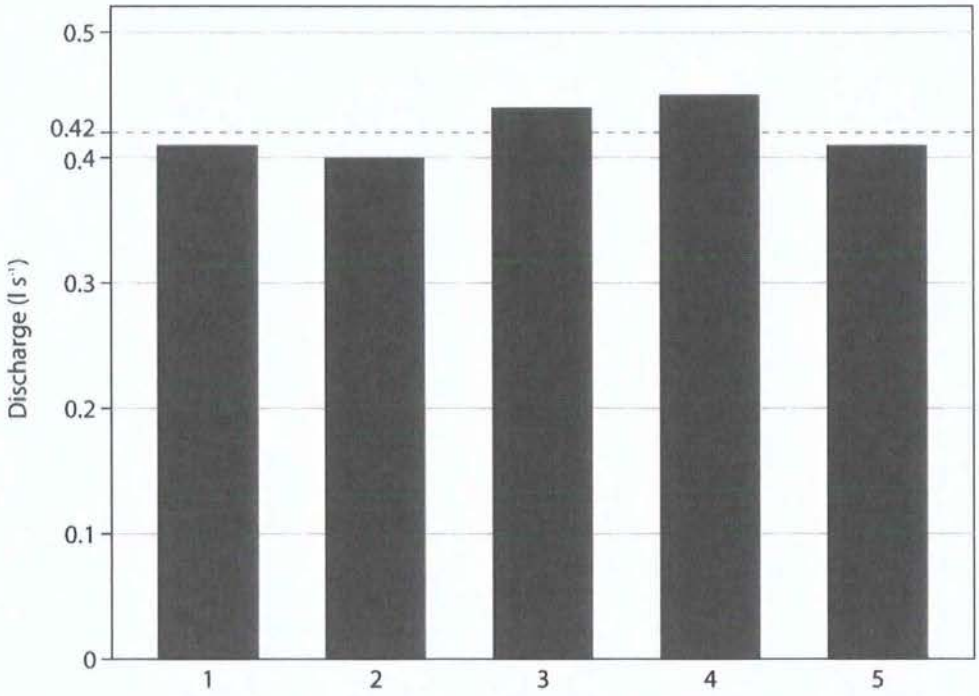

Figure 4.3. Discharge (in litres per second) from the wide trough over 5 different experimental runs. Points are tightly clustered around the mean value of 0.42 l s^{-1}.

Figure 4.3 shows that the discharge was reasonably constant (draining at a rate of between 0.40 and 0.45 l s^{-1}). This gives a mean discharge of 0.42 l s^{-1}, representing 0.52 l s^{-1} per metre width. The low variability about the mean demonstrates the reproducibility of this discharge.

It is also necessary for the water to flow out of the trough evenly across the plot width. Before each experiment, the trough was carefully levelled to ensure this was achieved. The distribution of flow across the submerged slit was assessed by placing six beakers below the trough slit (Figure 4.4). A small amount of water was held in the trough by covering the slot with masking tape. This was rapidly ripped off from both ends allowing the water to drain into the collecting beakers. Figure 4.5 displays the volumes of water collected in each beaker over four runs of this experiment. No systematic bias in water discharge was observed and almost uniform flow was produced across the slot width.

Figure 4.4. An experiment to assess the spread of discharge supplied to the top of the plot. Beakers numbered from left to right (1–6).

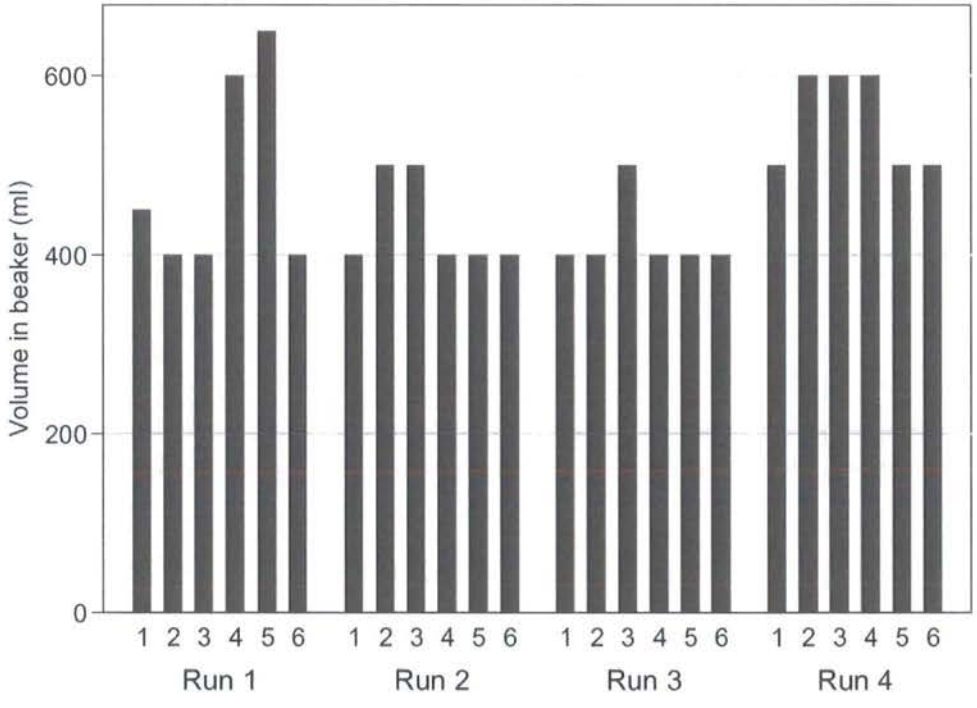

Figure 4.5. Water collected in each beaker (1–6) over 4 different runs (50 ml resolution). The volume of water added in each run was slightly different; therefore absolute values are not comparable between runs.

4.3.2.2 Variable Discharge Trough

The second trough was used to examine overland flows of variable discharges. This trough, made from perspex, was 0.20 m wide and had 5 discharge settings provided by slits of varying thickness (Figure 4.6). These slits were each cut into a 'gate' which was then tightly slotted into a holder located towards the front end of the trough to provide a seal. Water was poured into a 'tank' located at the upslope end and was free to trickle through each gate and out on to the plot. As the slits were of a varying thickness, the discharge was limited by the thinnest slot. To increase the discharge provided to the plot, the gate with the thinnest slit was removed.

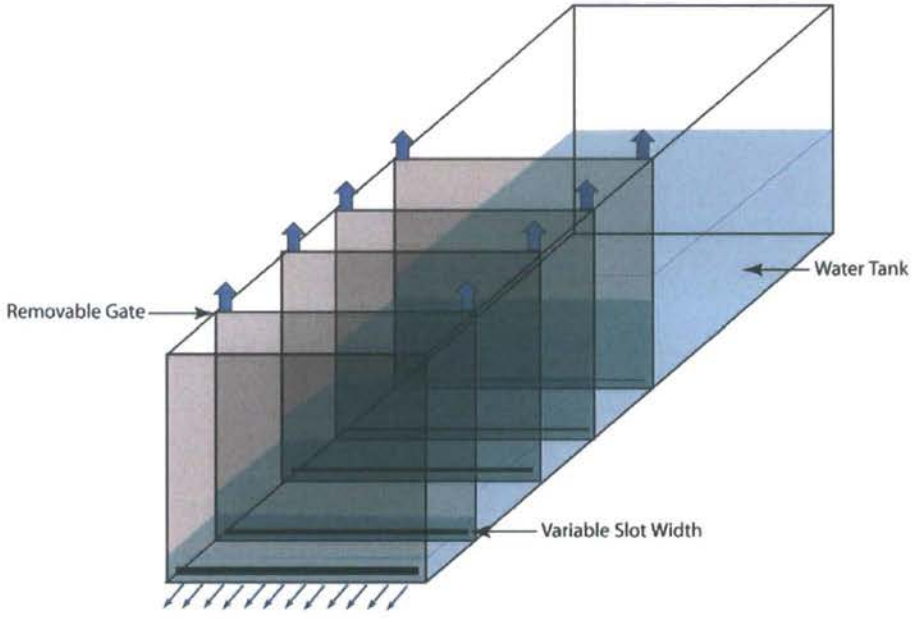

Figure 4.6. Sketch of the variable discharge trough.

While the design permitted both increasing and decreasing flows to be simulated (the gates could be removed and replaced in any sequence), the experiments undertaken in this study were limited to increasing flows. The trough was designed to operate on a slope of approximately 10 degrees; this was incorporated into the design to save time completely levelling each surface by digging back into the hillslope. For each experiment the tank was filled with water and continually topped up to maintain designated marked levels. The

discharges provided by the trough were approximately 0.4, 0.8, 1.2, 1.6 and 2.0 l s^{-1} over the 0.20 m flow width.

4.3.2.3 Comparison with Observed Flow Depths

Simulated overland flows are a gross simplification of naturally generated flows. Natural overland flow is supplied by rainfall and depleted by infiltration. These processes are neither uniform nor constant (Emmett, 1970). The aim of the experiment is to supply a depth of overland flow that each surface could potentially receive during a high-magnitude flood event. In the case of constant discharge, the systematic downslope sampling of plot surfaces applied in this study presents a problem: plots near the hill crest will normally receive less run-on overland flow than those towards the bottom.

Between 2002 and 2007, several mini crest-stage recorders were placed over the hillslopes examined in this study (Figure 4.7.). These recorded maximum flow depth at a single point and were monitored every six months. They were constructed from a 35 cm length of 32 mm square wooden poles sharpened at one end and forced into the ground (Bracken and Kirkby, 2005) until approximately 30 cm remained above ground. The pole was then painted with a mixture of food dye and salt and left to dry. It was also covered with a length of drainpipe with a cap on one end and a hole near the top to let the air escape as the pole becomes inundated (Bracken and Kirkby, 2005). This is a cheap and accurate method which uses materials readily available in the field area. However, it only records maximum flow depth and may present accuracy problems if the dye and salt are removed diagonally (as seen on steep slopes).

One such mini-crest stage recorder located within a plot used for overland flow simulation allows direct comparison of flow depths. It can be seen in Table 4.1 that the flow depths simulated by the wide trough are below the maximum depths generated from relatively large natural rainfall events. The recorded 24 hour maximum rainfall for each storm event can be used to compare the data with a nearby 30-year record (described by Bull *et al.*, (1999) and Bracken *et al.* (2008)). This suggests that the largest storm event has a recurrence interval of approximately 5 years.

Figure 4.7. Flow depth measurement using the mini-crest stage gauge discussed here. Note that the cover has been removed for measurement.

Date	Type of Event	Point Flow Depth Recorded (mm)	24 hour maximum rainfall (mm)
1st July 2002	Natural rainstorm	100	63.8
15th April 2004	Natural rainstorm	75	45.4
27th May 2006	Simulated overland flow	55	-
27th Jan 2007	Natural rainstorm	60	87.4
29th March 2007	Simulated overland flow	40	-
22nd August 2007	Natural rainstorm	60	36.2

Table 4.1. Recorded depth measurements near the foot of the Del Prado hillslope.

The same discharge was applied across each hillslope. Therefore it is suggested that this represents a slight overestimate of what could be reasonably expected from a high-magnitude storm event near the hill crests, and an underestimate of what would be expected

near the foot of the hillslopes. The discharges applied here are similar to those applied in other overland flow simulations. Rainfall simulation experiments at Walnut Gulch by Parsons *et al.* (1996b) produced discharges up to 0.4 l s^{-1} for each metre of flow width during a simulated 60 year event, a discharge similar to that recorded in section 4.3.2.1.

There is a further limitation to the runoff simulations described here. Parsons *et al.* (1994) note that rainfall simulation should be used in studies of overland flows. The hydraulic resistance values calculated from rainfall simulations were found to be an order of magnitude larger than those calculated by Abrahams *et al.* (1994) using runoff generated at the top of a similar plot. While runoff experiments can still be used to identify controls on resistance to overland flow, they cannot provide values suitable for physically-based hydrological and soil erosion models. However, in reality, at any point on a hillslope, flow is provided by a combination of upslope run-on and rainfall. With distance downslope, proportionately more flow is provided by this run-on overland flow. The value of hydraulic resistance of a surface represents a combination of these two types of flow, a combination which varies with hillslope position. Therefore, the hydraulic resistance observed in this study will be appreciably less than that of flows generated by a natural rainstorm.

4.3.3 Terrestrial Laser Scanning

The collection of high-resolution elevation data is problematic. Many methods involve laborious field techniques which provide low resolution data. A variety of microrelief meters have been used, ranging from hand-held rulers and pin meters to remote sensors, laser scanning techniques and digital photogrammetry (see Table 4.2). While early techniques involved instruments (rows of pins or chains) that were lowered on the surface itself (Saleh, 1993), techniques not based on contact are preferable in the measurement of the surface elevations to avoid disturbance of the roughness elements.

Roughness Measure	Measurement Method	Plot Type	Plot Area	Number of Surfaces	Measurement Spacing	Subject	Study
Random Roughness (mm)	Mechanical pin meter	Tilled field plots	1 m × 1 m	16	5 cm × 5 cm	Effect on rainfall on roughness and runoff	Moore & Larson (1979)
Random Roughness (mm)	Pin meter	Tilled field plots	0.9 m × 1.5 m	1060	15 cm × 1.3 cm	Predicting MDS from surface roughness measures	Onstad (1984)
Random Roughness (mm)	Mechanical pin meter	Tilled field plots	1 m × 1 m	2	6.4 mm × 50 mm	Relationship between RR and hydraulic roughness	Gilley & Finkner (1991)
Random Roughness (mm)	Laser scanner	Flume (seedbed)	0.65 m × 0.65 m	4	2 mm × 2 mm	Relationship between RR and hydraulic roughness	Takken & Govers (2000)
RR (mm) & Tortuosity	Laser scanner	Flume (tilled)	2 m × 4 m	6	1.5 mm × 1.5 mm	Effect of roughness on runoff distribution and soil erosion	Gómez & Nearing (2005)
LD (mm) & LS	Pin meter	Tilled field plots	2 m × 2 m and 0.9 m × 0.9 m	159	2 cm × 2 cm or 5 cm × 5 cm	Predicting MDS from surface roughness measures	Linden & Van Doren (1986)
MUD (mm)	Automated pin meter	Ploughed/ drilled field plots	2.6 m × 1.3 m	32	6 cm × 3 cm	Predicting MDS from surface roughness measures	Hansen *et al.* (1999)
MIF	Automated non-contact surface profile meter	Tilled field plots	1.5 m × 1.8 m	33	5 mm × 20 mm	Effect of tillage on roughness	Römkens & Wang (1986)
MIF	Automated non-contact surface profile meter	Tilled field plots	1.5 m × 1.8 m	3	5 mm × 20 mm	Effect of rainfall on roughness	Römkens & Wang (1987)
Tortuosity	Stereo-photogrammetry	Lab plots (seedbed)	0.4 m × 0.5 m	5	2 mm × 2 mm	Predicting MDS from surface roughness measures	Morgan *et al.* (1998)
Surface Tortuosity	Laser microrelief meter	Flume (seedbed)	0.6 m × 3.7 m	9	3 mm × 3 mm	Effect of roughness on runoff distribution and soil erosion	Helming *et al.* (1998)
Various	Terrestrial laser scanner	Natural and ploughed surfaces	2 m × 4 m	15	~ 2 mm × 2 mm	The influence of surface roughness on resistance to overland flows	This study

Table 4.2. Methods used to generate surface roughness measures.

Terrestrial laser scanning (TLS) has been used in the field of surveying since the late 1990s. It offers the potential of directly capturing the three-dimensional geometry of complex objects extremely rapidly. TLS is now frequently used in civil engineering. The comprehensiveness of data capture has resulted in the application of laser scanners to document items of cultural significance (e.g. Lichti and Gordon, 2004). More recently, TLS techniques are being employed for measuring and monitoring in geomorphology (e.g. Nagihara *et al.*, 2004; Rosser *et al.*, 2005; Rumsby *et al.*, 2008).

Laser scanners can rapidly make many elevation and position measurements from which high-density point clouds can be produced. This removes the need to conduct laborious measurements of elevation data and so reduces the restrictions that this poses. Such time-consuming measurements may disturb the soil surface and are commonly of a lower resolution than data obtained using scanning equipment. Terrestrial laser scanners are appropriate for data collection in the natural environment as they are portable (in contrast to laser scanners mounted on a rail system: Huang and Bradford, 1990), are water and dust resistant, can run off car batteries, and are relatively simple to set up in the field.

Jester and Klik (2005) review many techniques to measure soil roughness, concluding that laser scanner measurements offer a higher resolution and precision than photogrammetry

and are more suitable for measuring fine-scale surface roughness (although this will depend on the specifics of the laser-scanning equipment used). Considerable potential exists for the integration of the qualitative information derived from the overhead photography techniques described in section 4.3.1 with the high resolution elevation data provided by terrestrial laser scanning (see, for example, Lim *et al.*, 2005).

This study uses a Trimble GS200 terrestrial laser scanner to obtain elevation data (Figure 4.8). The GS200 uses a Class 2 pulsed 532 nm green laser and operates under the assumption that the speed of this laser pulse remains constant. Using this time-of-flight principle, the delay recorded as the backscattered portion of the signal is returned can be used to calculate the distance to the surface from which the beam was reflected. The scanner then records the three-dimensional coordinates of any solid surfaces from which the laser rays are returned. The standard maximum range of the scanner is reported as 200 m, while the minimum operating range is 1 m. Lim *et al.* (2005) note that as coordinates are collected directly, many uncertainties associated with data processing and digital elevation model (DEM) generation are by-passed. While some laser scanners have a small maximum scan area (often limited to less than 10 m^2; Darboux *et al.*, 2001), this scanner manipulates the laser emitter using motorised rotating mirrors enabling the scanner to pan around 360° and tilt through a 60° angle collecting up to 5000 points per second (Trimble, 2005).

4.3.3.1 TLS Accuracy and Precision

Establishing measurement errors of laser scanners is a difficult process as the measuring procedure is influenced by a variety of factors. The angular and range accuracy of each laser scanner depends on the applied calibration routine and the care taken in handling the machine since calibration (Boehler and Marbs, 2005). Moreover, reported specifications are insufficient to calculate accuracy, precision and maximum resolution over the possible measurement ranges.

Figure 4.8. Trimble GS200 laser scanner.

Range accuracy and precision of laser scanners have been examined in a number of studies. Reshetyuk (2006) discusses the sources of range error in detail. Kersten *et al.* (2004) tested the range accuracy of the Trimble GS200 using a 3D test field where 53 reference points were established. Absolute average errors of the order of 2 mm were found over distances of 27 m. Reshetyuk (2006) suggests that this systematic error may be caused by a discrepancy between electrical and mechanical zero positions of the scanner (termed 'zero error'). Such a systematic error is more problematic when using a terrestrial laser scanner to survey objects in reference to an established co-ordinate system.

The absence of a calibrated target provides a further source of measurement error. As the emitted radiation reflects off the ground surface itself, numerous variables are introduced, so that the time taken for the pulse to return is not exclusively a function of distance. Lichti and Harvey (2002) and Kersten *et al.* (2005) observe that surface properties such as

roughness, wetness, colour, reflectance and angle of incidence may influence the strength of the return signal.

Trimble (2005) report a measurement precision of 1.4 mm from a range of 5 m. Hanke *et al.* (2006) tested the influence of surface colour and reflectivity on the range precision of the GS200 and found a systematic error of several millimetres. However, Boehler and Marbs (2005) conducted a similar test and found that, unlike some other laser scanners available, no correction was needed for the GS200. This systematic error is only problematic if a range of different materials is scanned and is unlikely to be a major source of error when scanning soil surfaces.

Boehler and Marbs (2005) assess the relative merits of several terrestrial laser scanners currently available. The main advantage of the Trimble GS200 is that it can achieve high resolution point-spacing with a large maximum range. The minimum angular resolution reported by Trimble (2005) is 32 μrad (equivalent to 3 mm point spacing from 100 m range, or 0.1 mm point spacing from 3 m range). This angular resolution describes the minimum angular separation of two successive points that can be resolved separately by the laser. Lichti and Jamtsho (2006) observe that while this is commonly reported in scanner specifications as simply the sampling interval, it is also a function of the laser beam-width. Laser beams experience divergence with distance from the laser transmitter (Trimble (2005) report the beam divergence as 3 mm at 50 m range; equivalent to 0.1 mm at 3 m range). The GS200 also has an 'auto-focus' capability, which allows the laser beam to focus depending on the range. Therefore, the laser spot size for any surface is kept to a minimum. Lichti and Jamtsho (2006) demonstrated that the fine angular resolution and small spot size of the GS200 meant that it outperformed many similar laser scanners when the achievable angular spatial resolution was compared using a variety of measures. The beam width at a 2.5 m range was measured during the test described in section 4.3.3.3 and was found to be 0.76 mm in width.

Finally, all laser scanning systems are subject to 'edge effects' where 'phantom' points are often produced in the vicinity of sharp edges. These points arise when the laser spot glances off the edge of an object. Only part of the laser beam is reflected from there; the remainder

may be reflected from a surface behind the object. Such 'mixed pixels' produce a trail of points behind the edge (from the viewpoint of the scanner). The resultant range error is difficult to estimate and can vary from sub-millimetre to several centimetres. While this is unavoidable, it can be minimised by reducing the laser spot size with an optimally-focused beam.

In conclusion, the application of terrestrial laser scanners to the study of soil roughness at the plot scale demands high-resolution, close-range scans towards the limits for which these techniques were intended. However, previous tests have shown that the Trimble GS200 is suitable for such a task, offering a high angular resolution, acceptable accuracy and precision, with minimised edge effects from the onboard auto-focus function. The angular resolution applied in this study was greater than the beam-width of the laser, thereby avoiding resolution issues as discussed by Lichti and Jamtsho (2006). The complex nature of the soil surfaces meant that any edge effects were difficult to quantify. However, these relatively flat surfaces viewed from above contained few sharp edges such as might be encountered when scanning the built environment and therefore should be less problematic than for civil engineering applications.

4.3.3.2 Experimental Setup

The terrestrial laser scanner was set up 3 m from the plot surface. Scanning took place before each overland flow simulation to examine the initial contact between flow and topography. Where the dye pulses are examined, it is assumed that the surfaces did not erode during the experiment. A comparison of scans conducted before and after flow simulation at a plot experiencing high velocity flow suggests that little sediment transport occurred. Each plot was scanned from multiple directions to minimise any occlusion effects. The scans were later merged in the Realworks software package. The registration operation was automated by surveying a minimum of five control targets for each scan. These control points (Figure 4.9) were automatically recognised by the scanner and permitted point clouds to be accurately merged. Residual errors were reported in each case and consistently were below 2 mm (exceeding this value only twice, with reported errors of 2.27 and 2.39 mm).

Figure 4.9. Target used to merge plot scans

This provided a digital elevation model (DEM) of the plot surface (~2 m wide by 3 m long) to the designated resolution of 2 × 2 mm (using the average of four shots). In practice, the complexity of the soil surfaces meant that the actual resolution varied over the surfaces; 2 mm was chosen, as once the different scans had been combined, most areas were covered to this resolution. The scanner recorded both metric (XYZ) and visual (intensity, RGB) data. An onboard camera supplied the RGB data and provided a tool for framing the area of interest. Small retroflective markers were placed in the plot alongside spray-painted patterns enabling images taken from the camera boom to be easily and accurately georeferenced over the DEMs (section 4.3.4). Examination of these spayed lines after the experiments confirmed that erosion and sediment transport was minimal and can be assumed to be negligible compared with the flow volume and roughness height.

4.3.3.3 TLS Precision Test

The difficulty of obtaining reliable estimates of error over a full distribution of measurement ranges means that it is necessary to evaluate the limitations of a laser scanner for individual applications. This study is primarily concerned with obtaining a high-resolution (2 mm × 2 mm) Digital Elevation Model (DEM) at the plot-scale, so the relevant measurement range to consider is 2–3 m. As already discussed, this resolution is achievable

with the Trimble GS200. The main limitation for this study is the attainable measurement precision. Measurement noise limits the capability of the laser scanner to extract roughness data from plot DEMs. An experiment was designed to test the ability of the GS200 to distinguish roughness elements of a known size on a plane.

The experimental design replicated the field set-up (Figure 4.10). The laser scanner was situated at a range of 2.5 m from a flat table. The table-top was levelled using adjustable screws of the base of each leg. The resultant extreme occluded angle represents the 'worst-case' plot scenario encountered in a field situation. The table surface was scanned to a designated resolution of 2 mm × 2 mm (taking the average of four shots to reproduce the field method).

Figure 4.10. Experimental setup to establish the absolute precision of the GS200 laser scanner at the plot scale.

Roughness elements of various heights were then added to the plane to determine the minimum roughness height that can be distinguished by the scanner. It was thus necessary to have detailed measurements of the roughness elements to compare with those obtained by the scanner. Standard playing cards (57 mm × 87 mm) stacked to various heights were used to simulate roughness elements (these were in pristine condition to minimise any

shape irregularities). The card thickness (or 'roughness height') was the dimension under scrutiny; repeated measures (to a precision 0.01 mm) were taken using a pair of digital callipers. Five measurements of thickness were taken for each of 15 card stacks (ranging between 1 and 52 cards) and the average card thickness in these stacks was then calculated, yielding a total of 75 measurements. Figure 4.11 shows that measured card thickness varied between 0.30 and 0.325 mm (with mean of 0.310 mm) and that calculated thicknesses increased with stack size. It is thought that this increase of measured thickness with stack size is due to minor non-uniformities of the cards generating air pockets between cards. This was reduced to some extent by the squeezing effect of the digital callipers. It should be noted that this effect was not replicated during the laser scanning process and so the resultant height measurements may be slightly greater.

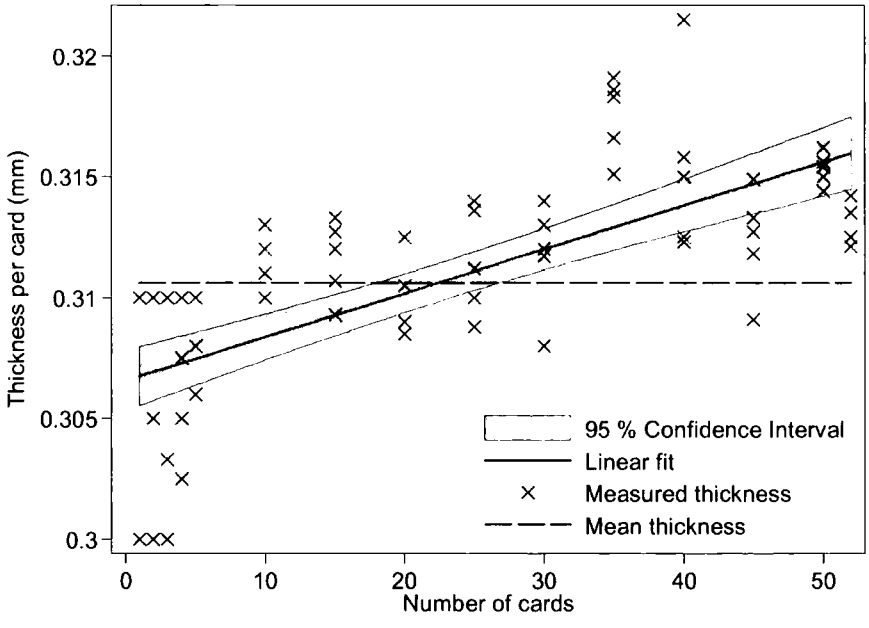

Figure 4.11. Thickness of an individual playing card measured by a pair of digital callipers.

Playing cards were placed on the level tabletop in the arrangement displayed in Figure 4.12. Stacks ranging from one card to six were taped to the tabletop (to reduce the gaps between cards). Additionally, piles of ten and twenty cards were placed on the second row (along with a further two individual cards). This 'rough' surface was rescanned as before. To establish the minimum roughness height that the scanner is able to resolve, a DEM of each scan was created and a 'difference' DEM calculated (Figure 4.13).

Figure 4.12. Card arrangement used to investigate scanner precision (from the viewpoint of the laser scanner). The card value represents the number in each stack on the front row. On the back row (from left to right) are card stacks of 1, 10, 20 and 1.

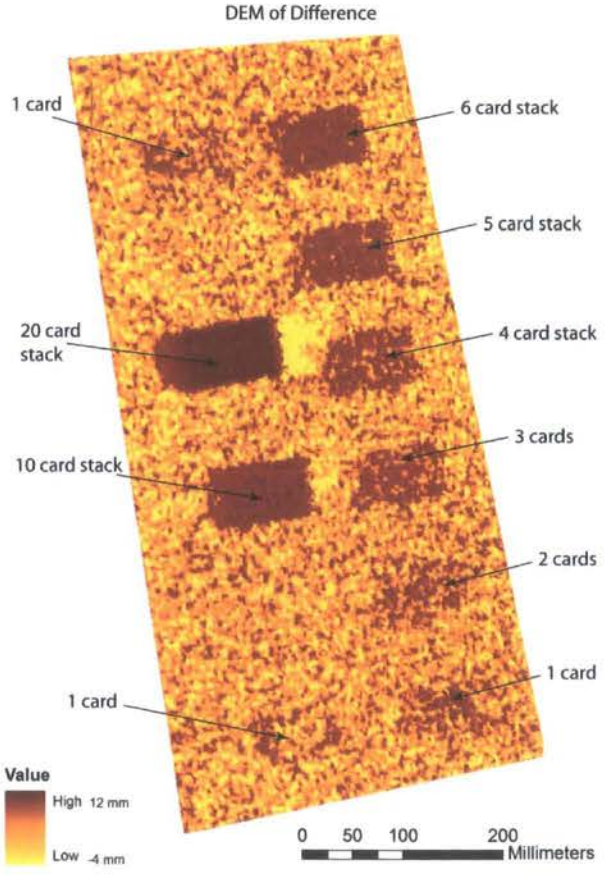

Figure 4.13. DEM of differences ('rough scan' – 'table scan') for the scanner precision experiment.

The DEM of differences shows that most of the card stacks were clearly differentiated from the table, even down to a stack of 3 cards (<1 mm in height). Traces of the 1 and 2 card stacks can also be seen, although these appear to lie within the scatter of elevations created by the smooth table. This suggests that despite the reported precision of the laser scanner, the achievable density of points means that it is able to distinguish sub-millimetre variations in topography.

To provide a quantitative assessment, points contained within a window of 30 × 30 mm were examined from each of the card stacks (228 points). These were sampled from both the bare 'table scan' and the 'card scan'. To provide a control, two such samples were also taken from two areas of the surface which experienced no change. The distribution of elevations found within each sample is displayed in Figure 4.14. Diagnostic plots suggest that each of these distributions approximates a normal distribution; however, there is some deviation at the tails. Testing the skewness and kurtosis of each distribution (following D'Agostino *et al.*, 1990) suggested that this deviation from the normal was significant. A Wilcoxon rank-sum test (Wilcoxon, 1945; Mann and Whitney, 1947) was thus applied (rather than a *t*-test). This found that each card sample was statistically different from the respective table sample; however, this was also the case for the two control (bare table) samples (albeit with a smaller probability that a random selection of the 'card' elevations would be larger than a random selection of 'table' elevations). A noticeable feature of Figure 4.14 is that while the laser scanner is able to detect very small, sub-millimetre mean changes in elevation, the spread of elevations recorded (the precision) within each sample is of the order of several millimetres. This scatter can be seen clearly on the transect of the 'card DEM' shown in Figure 4.15 (note that the general trend observed is a result of the table surface being slightly off-level).

Finally, the difference between the median elevations of the two scans displayed in Figure 4.13 was used to estimate the thickness of a single card for each stack. As expected, these estimates are substantially larger than those measured by the digital callipers (Figure 4.16). This may arise from the different reflectance properties of playing card and table top. However, the thickness estimates decrease to more reasonable levels once the stack of cards reaches 1.2 mm in height (as measured by the digital callipers). Hence, the results of this

experiment suggest that the precision of the laser scanner at the range used in this study is approximately 1–2 mm.

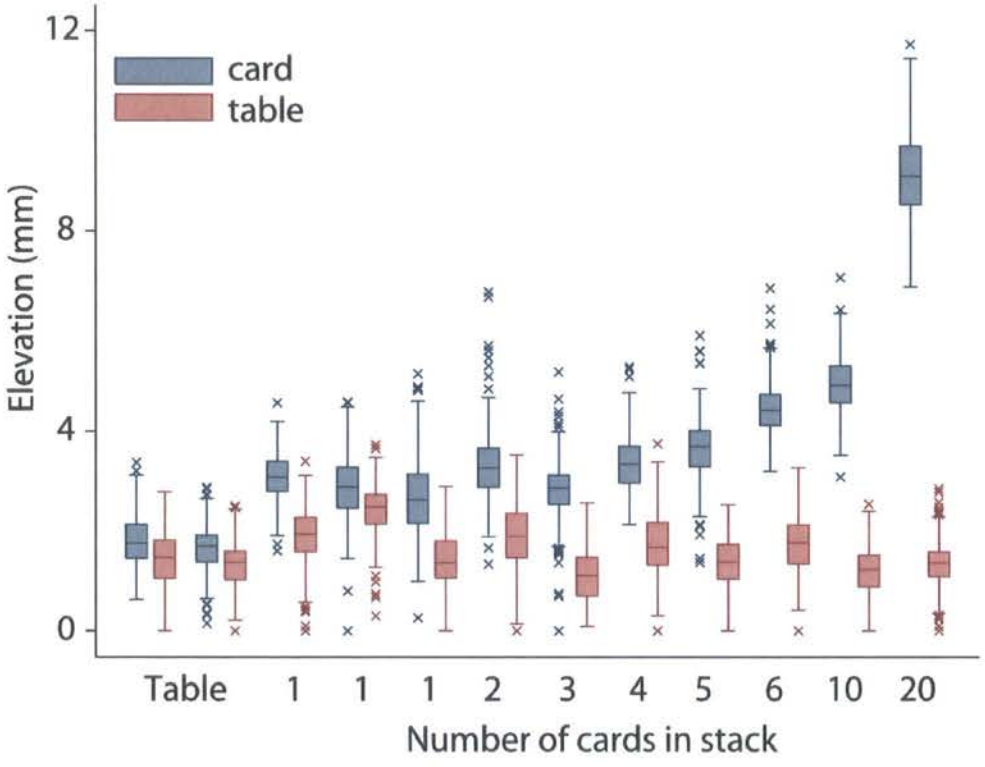

Figure 4.14. The spread of elevations found within a 30 × 30 mm sample of the scanner precision experiment. These are compared between the two scans for each stack (three stacks contained only a single card). For an explanation of the box plot see Figure 5.2.

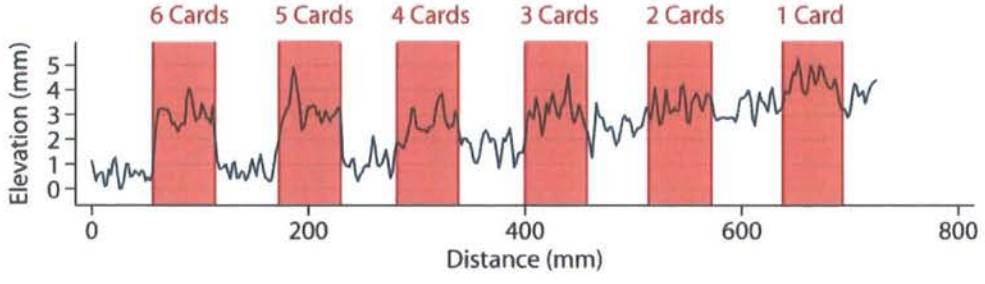

Figure 4.15. Transect taken over the 'card DEM' crossing the six cards stacks of the front row. The surface noise appears to be over a range of approximately 2 mm. This also reveals that the table (or the laser scanner) was not perfectly level, being 4 mm higher at one end.

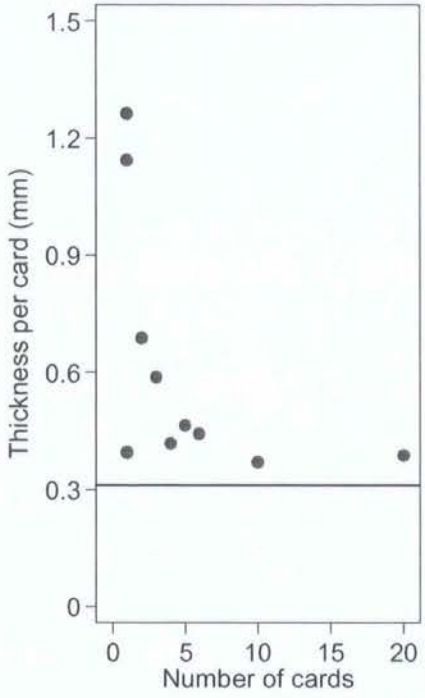

Figure 4.16. Thickness of an individual playing card as measured by the Trimble GS200 laser scanner at a range of 2.5 m. The horizontal line at 0.31 mm represents the mean measurement using the digital callipers.

4.3.4 Georeferencing Overhead Images

Previous versions of this methodology encountered problems of accurately georeferencing camera boom images over the plot DEM. The plot surfaces were of a variable slope, while the 'look-angle' of the camera was not necessarily perpendicular to the surface. The varying relative positions of camera and plot meant that numerous reference points between DEM and image were required for accurate georeferencing. A third-order polynomial transformation requires a minimum of 10 common points, although in practice many more are required.

Twelve high-visibility retroflective markers were placed in each plot in a 3 × 4 grid. These can be easily spotted by the boom camera but also provided a strong intensity return signal to the laser scanner (Figure 4.17).

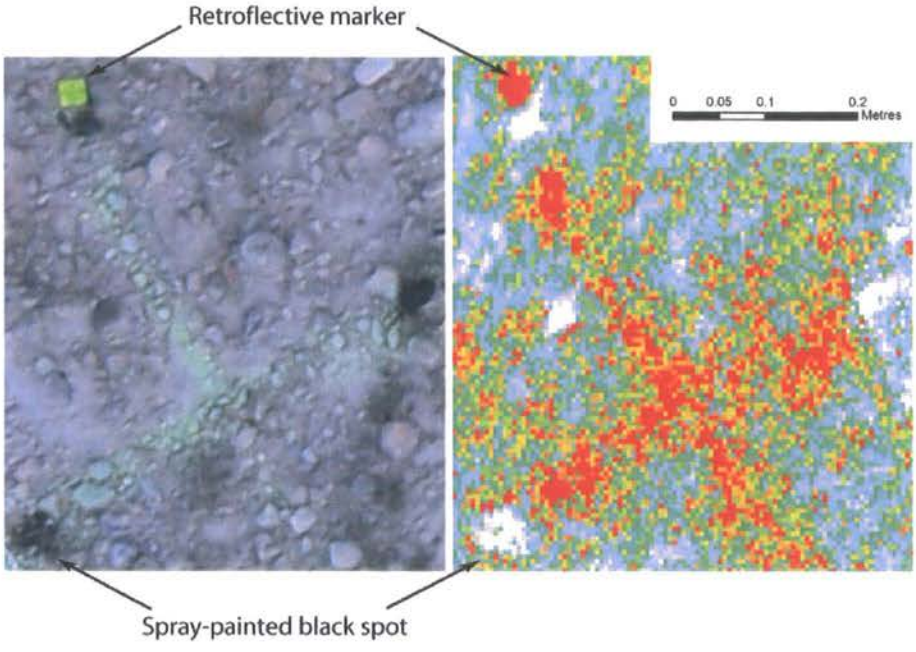

Figure 4.17. Example of intensity signal returned by the laser scanner demonstrating the potential for georeferencing images to DEM.

Although these retroflective markers provided sufficient data to georeference the images, subtle undulations of the plot surface meant that the image transformation was not reliable over the whole plot surface. This problem was solved by using the RGB data that the MENSI GS200 (along with other more recent terrestrial laser scanners) attaches to each point. This development provided many more common points between image and DEM needed for georeferencing. The DEM can be viewed as an image in itself (Figure 4.18) on to which the boom photographs could be overlaid. Any mismatch between DEM and image could be easily recognised and corrected through the addition of further reference points.

Each image was georeferenced over the plot DEMs using a grid of a minimum of 15 common points. The georeferencing software reported any errors (common points which were not perfectly matched after the transformation was applied). The RMS errors reported from this procedure were between 2 and 12 mm with a median RMS error of 5.7 mm. The georeferencing error is therefore greater than the DEM resolution and may affect the depth calculations discussed in section 4.3.5.2. In practice, this degree of error will have a negligible effect on depth calculations, except where very sharp changes in slope are found

(as seen where gully erosion is present). Multiple control points must be positioned where such sharp changes of slope occur to transform the images properly over the DEM.

Figure 4.18. Example overhead photograph georeferenced over a DEM using the colour pixels exported from the laser scanner.

4.3.5 Estimation of Hydraulic Variables

Images taken at a known time-interval georeferenced over a DEM provide sufficient information to extract estimates of hydraulic variables of overland flows. Flow width can be measured directly from the images. However, the estimation of velocity and depth is more complicated and subject to limitations discussed in detail below.

4.3.5.1 Velocity Calculation

At each timestep the wet area (or dyed area for later pulses) was digitised. This was calculated as the entire wet outline with any protruding dry areas subtracted (Figure 4.19a–b) thereby following Abrahams and Parsons (1990) by including only the submerged area in investigations of overland flows on rough surfaces. A sequence of these areas was thus produced (Figure 4.19c).

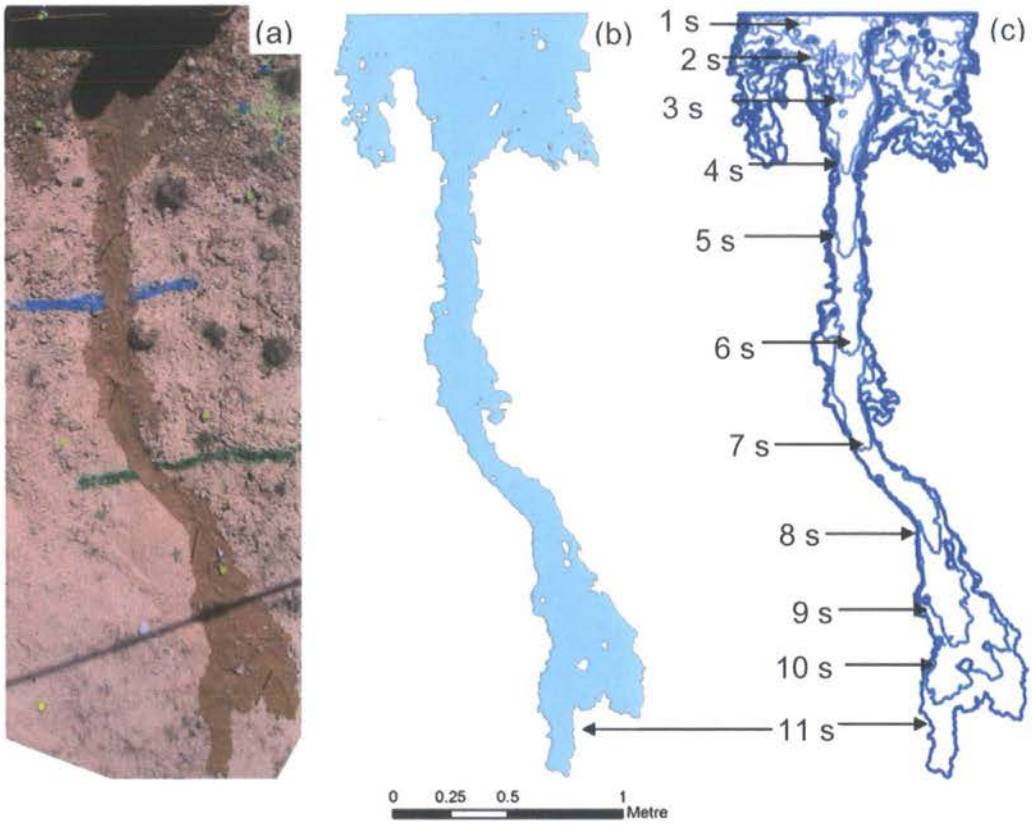

Figure 4.19. Example of (a) overhead plot photograph; (b) digitised wet area; (c) sequence of wet areas over 11 timesteps.

To calculate the distance travelled between each image, the outline of the wet area was converted into points at 2 mm intervals (matching the resolution of the underlying DEM) (Figure 4.20). A simple calculation determined the distance from each point to the nearest part of the previous wetted outline. Therefore, the assumption made here is that the flow has travelled in a straight line from the nearest point of the wetted extent of the previous timestep. This calculates the minimum possible flow distance and will therefore slightly underestimate the actual distance travelled. The flow velocity is then calculated by dividing this distance travelled by the time interval between images. Therefore, the spatial resolution of velocity measurements is limited by the interval between images and the speed of flow.

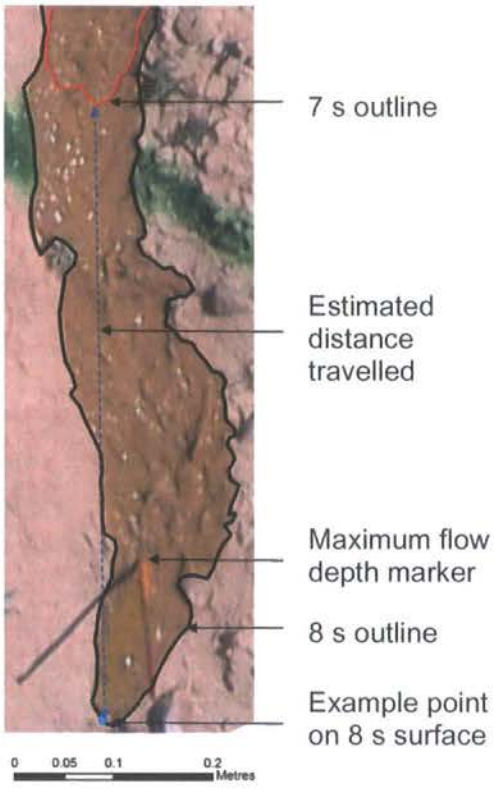

Figure 4.20. Example of velocity calculation. For each point on the black line (2 mm intervals) the minimum possible distance travelled is calculated (dashed blue line).

Each overland flow simulation begins by measuring the advancing flow over the soil surface. Measurement of this initial flow over the soil surface forms the basis for the majority of the results examined in Chapters 5 and 6. Once this was completed, three pulses of dye (one pulse of fluorescein dye followed by two pulses of food colouring) were added to the flow. These results are examined in section 7.4. Fluorescein dye was added directly into the trough and emerged out of the slit with the water. The pulses of food dye were added in a strip directly below the trough opening. The velocity of the dye pulses could be measured in the same manner as the advancing water front; however, this provides a measure of surface velocity and will be subject to errors when selecting a suitable correction factor, as discussed in section 4.2.1. An advantage of this method is that the advance of the dye pulse can be visualised across the entire flow width. This produces the fine-resolution velocity measurements provided by the use of automatic fluorometers

without the need to estimate or pre-select flow pathways. It also permits velocity measurements to be taken simultaneously across the flow width.

In total, each simulation with the wide trough (section 4.3.2.1) lasted just 60–90 seconds; it is not suggested that flow equilibration was achieved during this time. Most overland flow events in semi-arid environments are of a short duration; Parsons *et al.* (1990) suggest that few last long enough for equilibrium to be achieved. Yet most studies of overland flows examine flows in equilibrium, so caution must be applied when comparing the results of this study with those conducted under equilibrium conditions.

4.3.5.2 Depth Calculation

Each sequence of advancing wet areas was divided into several 'threads' (Figure 4.20 above shows a single flow thread). These were defined as distinct areas demonstrating an advance of water between timesteps and the terminology is not limited to those areas experiencing fast water flow as used in Dunkerley (2004). The flow area of each thread is assumed to be experiencing uniform flow conditions within each timestep and so the rationale behind dividing the surfaces in this way was to reduce the error introduced by this assumption. All studies of overland flow necessarily aggregate a volume of flow and assume uniform flow conditions within that volume. This study is no exception, but the dimensions to which the uniformity assumption is applied are much smaller than those reported elsewhere (this study typically aggregates over time periods of 1 s and spatial dimensions of < 0.2 m).

For each timestep, the newly wetted area within each thread could be identified. This was used as a mask to crop the underlying DEM. It is from this cropped DEM that water depth can be estimated.

The approach described here allows the spatial distribution of flow depths to be estimated at a resolution of 2×2 mm. This is an unprecedented resolution for such measurements, particularly for a field method. However, for such estimates to be obtained, numerous assumptions about the water surface must be made. These are now discussed in detail.

The direction perpendicular to flow was identified for each 'thread DEM' and the DEM was thus divided into cross-sections (at 2 mm intervals). An algorithm was developed to estimate the water surface at each point on these cross-sections. Several rules were employed to make this estimation.

1. The water surface elevation will equal the soil surface elevation at the end-points of each cross-section.
2. The water surface can then be estimated by linearly interpolating between these two endpoints.
3. Where a dry area protrudes from the centre of a cross-section, the water surface is also forced through these points, as they also represent the extent of flow.

These rules were sufficient for most cross-sections (such as that displayed in Figure 4.21a.). Water depth is then calculated as the difference between the water surface elevation and the soil surface elevation at each point (of 2 mm spacing).

These are simple and sensible rules. However, they do not adequately describe some cross-sections. In particular, for some cross-sections the submerged soil surface protrudes above the water depth estimated from rules 1–3. This situation arises from the dynamic nature of the water surface. Water flow can build up behind, and move over, obstacles at the small-scales investigated here so the water surface is not necessarily horizontal in cross-section. Such superelevation of the water surface could be observed in the field. In this situation the water surface elevation cannot be accurately estimated. However, additional rules can be employed:

4. Where soil surface peaks protrude from the water surface estimated by rules 1–3, the water surface elevation is then linearly interpolated between such peaks. The new water elevation is then estimated as the greater of this interpolation and the level estimated from rules 1–3.

5. The water surface cannot be below the soil surface level. This avoids minor problems caused by concavities in the soil cross-section as a result of rule 4.

These rules assume the minimum superelevation necessary to inundate each part of the surface that was observed to be submerged. As such, in the situation where rule 4 is applied, it may underestimate the water depth. The result of applying rule 4 to a soil surface can be seen in Figure 4.21b.

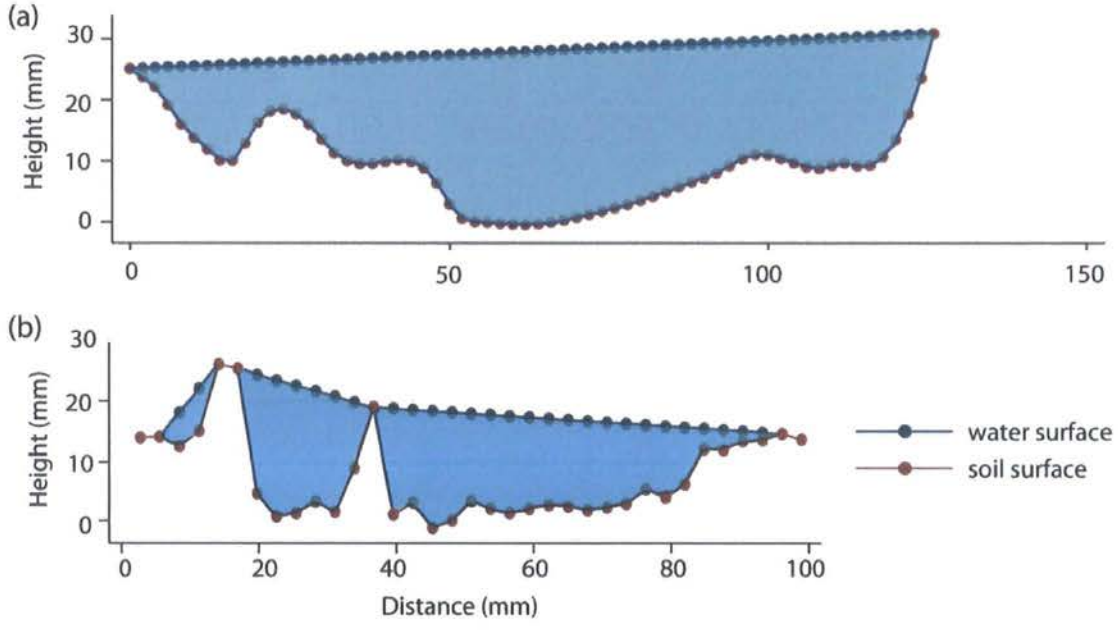

Figure 4.21. Example cross-sections used for depth estimation.

This algorithm provides a reasonable estimate of water depths in many situations encountered in the field. However, it should be noted that it may provide erroneous calculations when vertical surfaces are bounding the advancing flow. Fortunately, this situation was not encountered in the experiments described here. Moreover, surface tension effects at the edge of the water flow are not included in the calculations of depth.

4.3.5.3 Depth Validation

A dataset of measured flow depths was assembled to provide a method of validating the estimated depths. Small canes painted with orange food colouring and salt were placed into the flow (Figure 4.22). During the experiment, the colouring and salt washed off, providing a measurement of maximum flow over an area 6 mm in diameter. The 45 stick depths (measured in the field with a ruler) are considered to be accurate to ±2.5 mm, although splash effects may cause them to overestimate maximum depth. These measurements were used to test the depth predictions made using rules 1–5 (the average depth of the ~10 cells making up the area of the cane was used in this test). This test assumes that the maximum water depth occurred at the end of the flume run (when infiltration was lowest) and therefore must calculate water depths over a wide flow (sometimes >1 m in width). This will add a further degree of error into the calculations which was not experienced when measuring the depths of advancing flow threads.

Figure 4.22. Maximum flow depth measured with painted canes placed in the flow.

Figure 4.23 shows that there is much scatter present within the dataset. This is to be expected as the calculated depth varies considerably within a small area. However, a linear regression of the dataset (forced through the origin) yields a coefficient of 1.017 (or 1.092 when regressing stick measured depth on calculated depth), suggesting a strong degree of concordance between the two methods of depth measurement. Following Lin (1989, 2000)

and Cox (2006), the concordance correlation is 0.820, only a little below the Pearson correlation (0.834). This measure of concordance considers both the tightness of the data around its reduced major axis (a summary of the centre of the data) and the nearness of this reduced major axis to the line of perfect concordance.

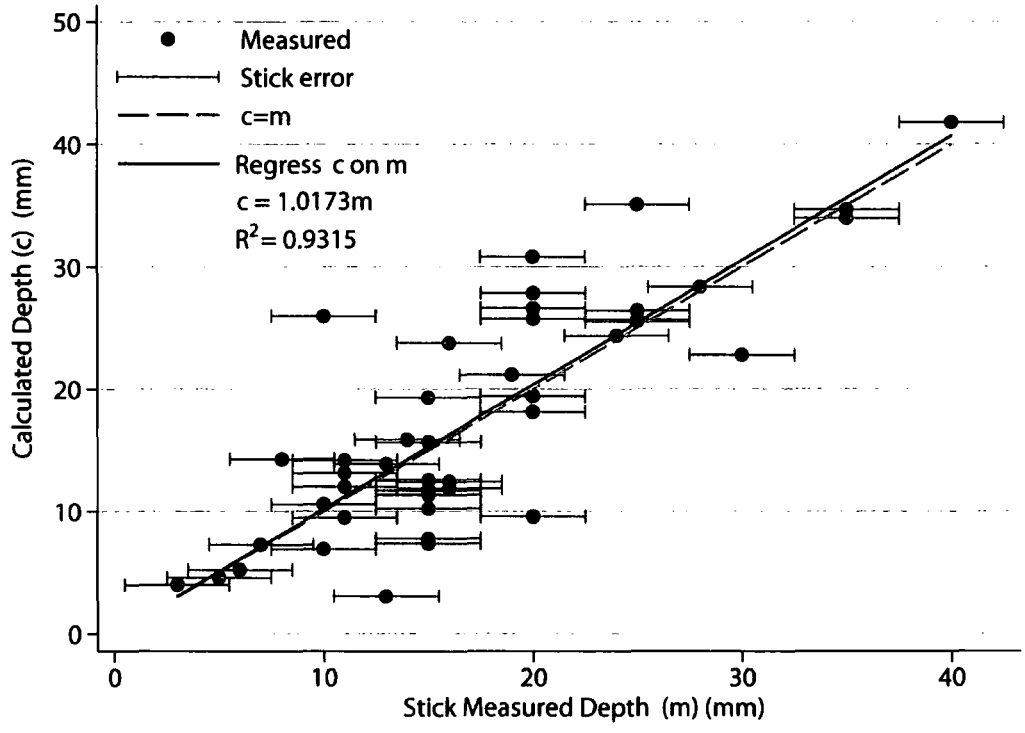

Figure 4.23. A comparison of depths calculated using the methodology described (c) and depths measured in the field (m). The error bars are estimated for the stick measurements. The line of perfect concordance (c=m) and regression of calculated depth from stick measured depth are also displayed.

Figure 4.24 plots paired differences against pair-wise means. The DEM calculation has the tendency to underestimate shallow depths slightly and overestimate larger ones. It is also apparent that most of the differences lie within the supposed error range of the stick measurements and that average difference (0.378 mm) is very close to the line of perfect agreement and well within the 95 % limits of agreement (Bland and Altman, 1986).

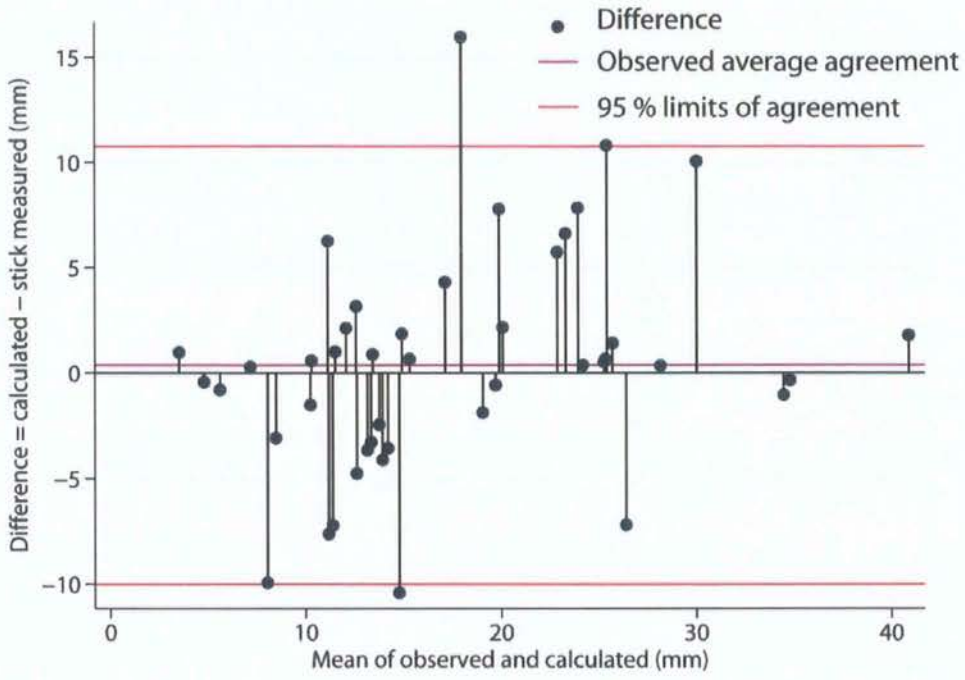

Figure 4.24. Differences versus means for stick measured depths and DEM calculated depths. The horizontal line difference = 0 represents perfect agreement.

4.3.6 Extracting Surface Roughness Measures

The DEM underlying the images can be cropped to any extent identified from the overhead images. For example, Figure 4.25 shows a three-dimensional image of the wet area of a plot. This has numerous advantages. Of particular relevance here is that the roughness of any area can be selected and examined. Each plot divided the flow into numerous finger-like threads moving over the plot with a wide range of velocities. Images such as that of Figure 4.19 can be used to isolate areas of interest and examine their roughness in greater detail.

Various roughness measurements can be calculated from the elevation data. As 'roughness' is an imprecise term, it can be defined in many ways (see section 6.4). Table 4.3 lists the measurements of roughness examined in this study (for a complete definition of each, see Appendix 1).

Symbol	Measure	Units
d	Mean flow depth	[L]
d_{50}	Median flow depth	[L]
d_{sk}	Depth skewness	[Dimensionless]
F_P	Frontal area per unit planar area 1−20	[Dimensionless]
F_T	Frontal area per unit surface area 1−20	[Dimensionless]
P_d	Parallel pit density	$[L^{-1}]$
P_{dmin}	Minimum parallel pit density	$[L^{-1}]$
P_{dmx}	Maximum parallel pit density	$[L^{-1}]$
P_{dxc}	Perpendicular pit density	$[L^{-1}]$
R	Perpendicular hydraulic radius	[L]
R_v	Volumetric hydraulic radius	[L]
S	Slope	[Dimensionless]
T_{3D}	3d tortuosity 1−20	[Dimensionless]
T_p	Parallel tortuosity	[Dimensionless]
T_r	Tortuosity ratio	[Dimensionless]
T_{xc}	Perpendicular tortuosity	[Dimensionless]
Z_d	Mean surface elevation difference	[L]
Z_{NN}	Nearest neighbour	[L]
α	Gamma alpha (of depth distribution)	[Dimensionless]
β	Gamma beta (of depth distribution)	[L]
ε	Mean roughness height	[L]
Λ	Inundation ratio (d / ε)	[Dimensionless]
Λ_σ	Inundation ratio s.d. (d / σ_Z)	[Dimensionless]
Λ_{Zd}	Detrended inundation ratio (d / Z_d)	[Dimensionless]
σ_Z	3d standard deviation	[L]
σ_{Zxc}	Perpendicular standard deviation	[L]

Table 4.3. Roughness measurements employed in this study (with scaling flow measures). Dimensions are given in the right column (all in terms of length L). For full definitions, see Appendix 1. The fitting of a two-parameter gamma distribution to flow depths is described in section 5.4.

Figure 4.25. Example of a DEM cropped to the observed wetted area.

4.3.7 Data Synthesis & Terminology Requirements

Once the patterns of advancing flow have been mapped over the DEMs, the flow field can be divided up into areas within which uniform flow is assumed to exist. The division of the flow into these areas or 'threads' is similar to the division of flow into 'multiple partial sections' discussed by Abrahams *et al.* (1986b) (see section 4.3.5.2.). Figure 4.26 demonstrates a synthesis of the hydraulic data available for a single flow thread. Three cross-sections are displayed. Cascades of such DEMs for a sequence of timesteps allow flow resistance to be calculated. Measurements of roughness can be examined to attempt to relate roughness to resistance (this is described in Chapter 6 and was calculated only once the flow had moved at least 0.5 m from the trough and the initial velocity increase had slowed; see Figure 7.17). The result is a detailed description of overland flows over natural surfaces to an unprecedented resolution.

The enhanced resolution of hydraulic variables afforded by this method creates some issues for studies of these flows. The notion of a uniform depth becomes invalid and the idea of a single velocity needs further clarification. Indeed, the nomenclature surrounding overland flow hydraulics is imprecise: it requires updating and standardising.

When considering an isolated flow thread (as pictured in Figure 4.26) the attribution of a single velocity or depth measurement requires a further degree of definition. The methodology described above produces a distribution of velocities. A number of summary values are possible; however, many measurements at the smaller end of the distribution are irrelevant (the edges of the flow showing little or no advance). The maximum recorded velocity appears to be the most relevant measurement. Smart *et al.* (2002) discuss similar ambiguities surrounding flow depth measurements wherever bed roughness is large relative to the mean depth of flow (section 4.2.2).

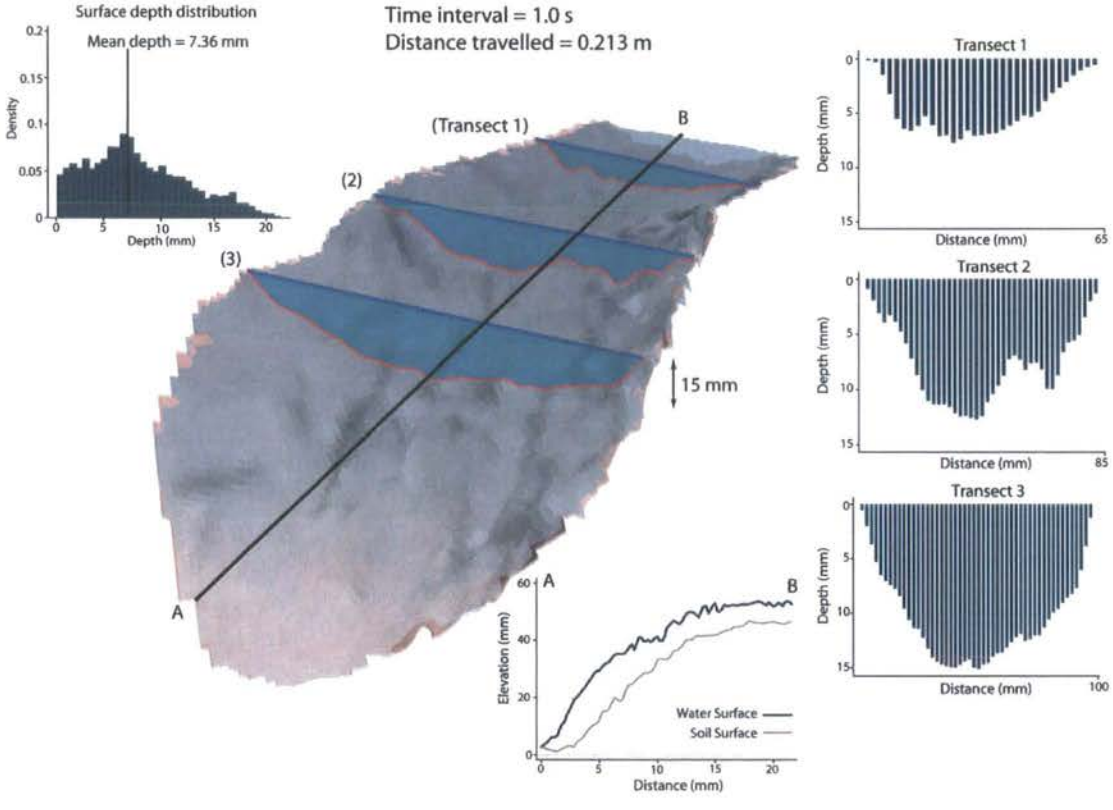

Figure 4.26. Example flow thread. The DEM has been cropped to just the surface over which water flowed during an interval of 1 s. The Figure shows a soil surface with the calculated water surface overlain and depths on three example transects. The distribution of calculated depths for the surface as a whole is shown on the top-left, and longitudinal profiles of soil and water surface elevation are found at the bottom of the image.

4.3.8 Future Methodology Development

Unfortunately, the many large datasets produced by this methodology mean that, although fieldwork time is short, data processing time is much longer. Each image takes about one hour to process. However, opportunities exist to automate and speed-up data processing. Images may be automatically georeferenced to each other using a module contained within the Leica Photogrammetry Suite. Also, image correlation software is increasingly available. This could automate the identification of the expanded wet area by recognising any pixels demonstrating a different RGB value from the previous timestep. Such developments would greatly reduce the resources required to apply this methodology whilst potentially yielding an increase in measurement accuracy. This is discussed further in section 8.5.

4.4 Infiltration Measurements

To assess the influence of surface roughness on infiltration properties it is necessary to make infiltration measurements *in situ* with minimum disturbance of the soil surface. Additionally, the small-scale of some roughness features means that point measurements of infiltration are preferable. Zhang (1997) suggests that hydraulic conductivity is the single most important hydraulic property affecting water flow in soils. However, its measurement can be difficult and time-consuming.

The minidisk infiltrometer (Figure 4.27) is well suited to this task. The minidisk infiltrometer is an acrylic tube with a semi-permeable plastic disk as a base. A small tube installed just above the disk regulates the suction rate. It takes a reading over an area of just 20 mm in diameter, and so can measure the variability of infiltration rates at a scale appropriate for this investigation. While the minidisk infiltrometer does not disturb the soil surface, a thin layer of wet sand (~3 mm) placed on the soil surface is necessary for a good contact (Figure 4.27). The infiltrometer is filled with water and a rubber stopper is inserted in the top. It is then placed on the sand layer and the volume change is recorded over a period of five minutes.

The method is quick and easy, requires no large equipment (such as a rainfall simulator) and very little experimental set-up, and uses very little water (~100 ml) per test, which is advantageous in a semi-arid environment where supplies of water are limited. It provides comparative data, and can be repeated several times at each site. Li *et al.* (2005) report that steady infiltration rate measured by a minidisk infiltrometer at a tension of 0.5 cm produces results consistent with studies using rainfall simulators. However, a minidisk infiltrometer does not simulate raindrop impact, as would allow an analysis of changes in runoff and roughness with aggregate breakdown and surface sealing.

Figure 4.27. The minidisk infiltrometer (left) and the small layer of wet sand needed to ensure a good contact with the soil surface (right).

Using this method, infiltration measurements were taken on transects through the site of each plot scan, ensuring that the different elements of surface roughness were all represented at each plot. Soil hydraulic conductivity could then be calculated using the method proposed by Zhang (1997) where the measured cumulative infiltration I is fitted as a function of time t

$$I = At + B\sqrt{t}\,, \tag{4.2}$$

where A and B are fitted parameters. This is equivalent to the Philip (1957) equation (equation 3.2); the parameters may be converted into those of the Green and Ampt (1911) equation (equation 3.3) following Kirkby *et al.* (2005). The soil hydraulic conductivity K may be estimated from the minidisk radius r_0, the suction at the disk surface h_0 and the van Genuchten parameters for the soil n_i and α_i (Zhang, 1997):

$$K = \frac{A(\alpha_i r_0)^{0.91}}{11.65(n_i^{0.1} - 1)\exp[2.92(n_i - 1.9)\alpha_i h_0]} \quad (n_i \geq 1.9) \tag{4.3}$$

or

$$K = \frac{A(\alpha_i r_0)^{0.91}}{11.65(n_i^{0.1} - 1)\exp[7.5(n_i - 1.9)\alpha_i h_0]}\,. \quad (n_i < 1.9) \tag{4.4}$$

The van Genuchten parameters are empirical parameters with no direct physical interpretation. The minidisk infiltrometer used in this study has a radius of 1.59 cm and infiltrates water at a suction of 2 cm. The van Genuchten parameters for the 12 texture classes of soil were obtained from Carsel and Parrish (1988).

4.5 Fieldwork Location

The methodology described above is most suited to the study of overland flows in semi-arid environments. The low annual rainfall supports limited vegetation cover, leading to large areas of exposed soil. This is necessary as any vegetation would obscure the advancing flow and lead to serious errors when calculating depths from DEMs. Moreover, flood events in semi-arid areas are often dominated by 'new water', mostly infiltration-excess overland flows. Therefore, not only is this methodology most suited to semi-arid environments, it is also most effectively applied there, contributing towards prediction of the timing and magnitude of flood events in semi-arid catchments.

4.5.1 Catchment Characteristics

The Guadalentín River of south-east Spain is one of the most torrential rivers in the country (Benito *et al.*, 2002). This investigation considers two typical Mediterranean semi-arid catchments situated within that basin: the Rambla Nogalte catchment, which is on the border of the provinces of Murcia and Almeria, and the Rambla de Torrealvilla catchment, nearby in Murcia (Figure 4.28). This area of Spain is the driest part of the western Mediterranean; Bull *et al.* (2003) report that the catchments receive approximately 300 mm of rain annually. Therefore, Hooke and Mant (2000) suggest that these conditions provide a valuable exemplar of an environment that may become more widespread should global warming predictions prove accurate. These catchments were also chosen because much research has previously been conducted; several Casella 0.2 mm tipping bucket rain gauges with integral loggers have already been installed (Figure 4.28). The two rivers also offer contrasting catchment characteristics, as seen in their different responses to an extreme storm event in September 1997 (Bull *et al.*, 1999). A Metrolog logging system with Druk pressure transducers (PTX 530-1521) also measures flow stage on the Del Prado tributary in the Rambla de Torrealvilla. These gauges were established in 1997 and have been recording rainfall and stage data intermittently over the past 10 years. Additionally, two crest stage gauges (described in section 4.3.2.3 and shown in Figure 4.7) were placed on and below the Del Prado hillslope. These gauges provide a basic record of the hydrological response of the Del Prado hillslope and surrounding area to rainfall events.

The Rambla Nogalte is a broad gravel bed river draining an area of 171 km^2 which is dominated by schist and other metamorphic rocks. Most of the soils are developed on thick brownish-red mica schist, but localised outcrops of thin, flaky, blue mica schist are also present (which supports only sparse or no matorral vegetation cover) (Bull *et al.*, 1999). Figure 4.29 shows that natural matorral (mainly anthyllis, grasses, rosemary and thyme) remains on only about a third of the surfaces, as 64.1 % of the convex hillslopes of the Nogalte catchment are used for almond and olive tree cropping (Bull *et al.*, 1999). These ploughed surfaces provide large areas of bare soil between the almond or olive trees, and therefore provide a much less continuous vegetation cover than the matorral.

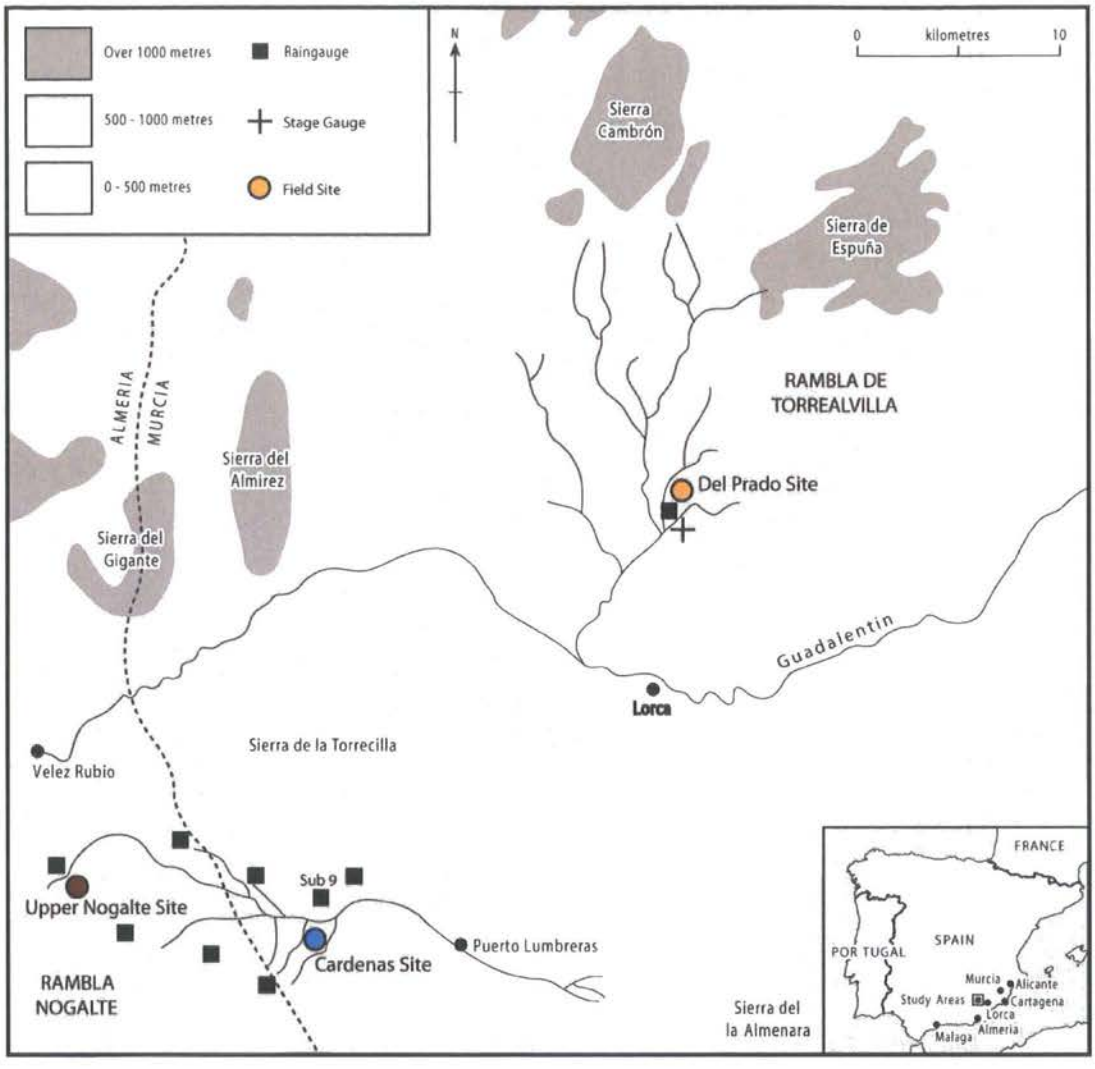

Figure 4.28. The study area in south-east Spain indicating the locations of the Rambla Nogalte and Rambla de Torrealvilla, field sites, rain and stage gauges. Adapted from Bracken and Kirkby (2005: p.185).

The Rambla de Torrealvilla catchment drains an area of 200 km^2 which is dominated by marls. Intensive farming of wheat, water melons and lettuces takes place on the flat pediment surfaces (which are dissected by box-shaped channels). Areas not used for arable farming are left as matorral. Bull *et al.* (1999) report that this catchment generally produces much higher flood peaks from rainfall events than the Rambla Nogalte catchment.

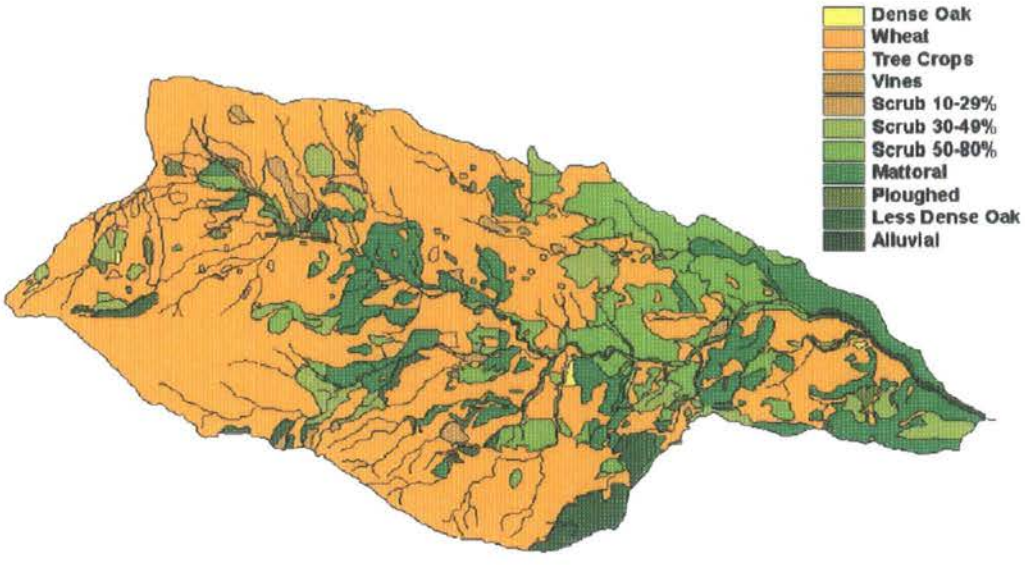

Figure 4.29. Land use within the Rambla Nogalte catchment (from Bull *et al.*, 2003: p.6).

4.5.2 Experimental Locations

Experimental locations were selected on the basis of the size of the hillslopes, their gradient, soil-type, land-use (following the mapping of HYSS categories by Bull *et al.*, 2003; section 3.3.3) and the availability of suitable vantage points for laser scanning. Additionally, hillslopes with little vegetation cover were selected to maximise soil surface exposure for scanning. The three sites selected represent the entire range of hydrological characteristics found on hillslopes within the catchments, allowing this investigation to be as representative as possible.

The Upper Nogalte hillslope (Figure 4.30) is located in an area of red schist in the Nogalte catchment. This soil is low in clay minerals and high in quartz and feldspar, has a high infiltration capacity and exhibits weak crust development. The vegetation cover consists of thin grasses, thistles and thyme bushes; however, an area of the hillslope has been recently ploughed. This area of the Nogalte catchment has a relatively high runoff threshold and is thought to be particularly unresponsive to rainfall (Bracken and Kirkby, 2005).

Figure 4.30. Upper Nogalte hillslope located in an area of red schist in the Rambla Nogalte.

Figure 4.31. Cardenas hillslope, situated in an area of blue schist in the Rambla Nogalte. The SE side of the slope (left) supports almond trees whereas the NW side (right) remains untouched.

The Cardenas site (Figure 4.31) is situated in the Cardenas sub-catchment, an area of blue schist which is one of the key runoff-producing areas in the Nogalte catchment (Bull *et al.*, 1999, 2003). Soil in this area is high in clay minerals and slaty fragments, susceptible to strong crust development, and considered to have a low runoff threshold (Bracken and Kirkby, 2005). The vegetation cover is made up of small bushes of thyme and anthyllis

separated by extensive bare areas. The Cardenas sub-catchment is characterised by steep gorge-like topography which generates large volumes of runoff compared with the rest of the Nogalte catchment. Land-use of the hillslope is divided: half is used for almond cropping, and the rest has been left to matorral.

Finally, the Del Prado site (Figure 4.32) is situated on a bare area of marl in the Rambla de Torrealvilla which is also suspected of producing large amounts of runoff. Bull *et al.* (1999) suggest that runoff thresholds are much lower on the marls of the Torrealvilla than on the schists of the Nogalte. The surface is composed mainly of fines, with evidence of both a structural crust and a lichen crust, and is mostly devoid of vegetation (with occasional grasses and thyme bushes visible) (Bracken and Kirkby, 2005).

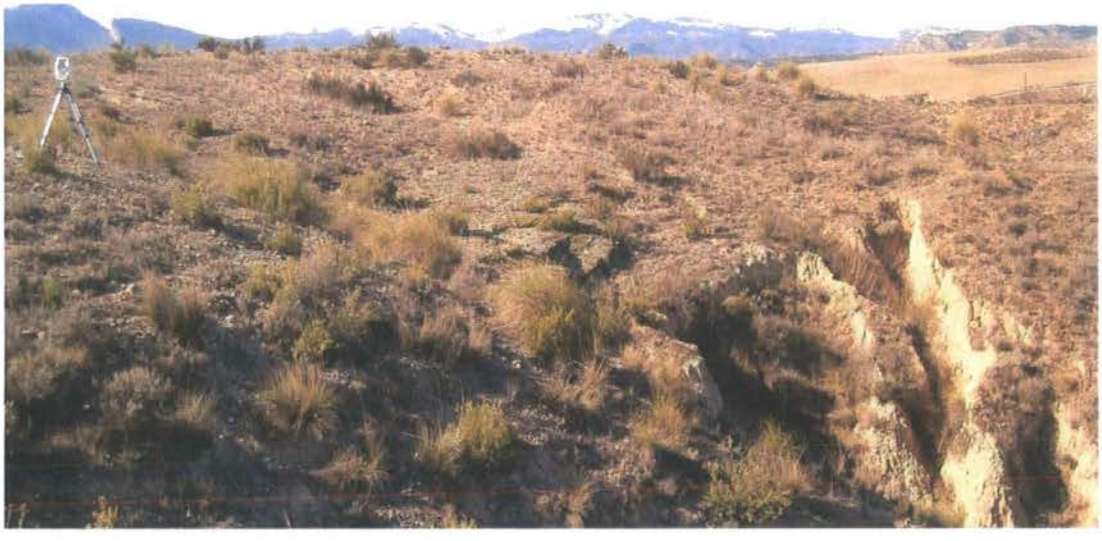

Figure 4.32. Del Prado site, situated on a bare area of marl in the Rambla de Torrealvilla.

4.5.3 Morphological Runoff Zones

Upscaling the runoff plot approach of measuring the overland flow variables (described in section 4.3) to the hillslope scale requires the variation of such variables and the presence of emergent features to be accounted for. Moreover, the important consideration of hillslope connectivity (discussed in Chapter 3) necessitates an appreciation of the spatial configuration of any such variability. Therefore, the hillslope surfaces were aggregated into

five 'Morphological Runoff Zones'. This classification is nested within the HYSS scheme chosen to select the three hillslopes (section 3.3.3) and offers an appropriate method of systematically sampling hillslope-scale variations of soil surface microtopography.

Bracken and Kirkby (2005) mapped variations in morphological evidence of runoff intensity and established Morphological Runoff Zones (MRZs) based on the observed surface features outlined in Table 4.4. Small-scale morphological evidence of splash erosion indicates level 1; in level 2 areas of wash deposits may also be observed (indicating small amounts of runoff); level 3 is reached when minor headcuts are also found (suggesting that flow is able to erode the soil surface and is locally concentrated); in level 4 flow is concentrated further and rills are also found. Gullies are formed in level 5. These qualitatively-defined zones indicate different combinations of processes operating on the soil surface and thus may be used to suggest varying sediment transport rates. Such systematic downslope changes in roughness will influence depressional storage, resistance to overland flow and will ultimately determine the connectivity of flowpaths.

These qualitative morphological descriptors were employed to map the extent of each MRZ; each zone is easily distinguished in the field. Any ploughed areas of the hillslopes were also aggregated into a single zone. A hand-held GPS device (GS20) was used to outline the extent of each zone across the hillslopes. At the Upper Nogalte hillslope, substantial land-use changes took place during the period of study; a large, previously unploughed area was converted into an expanded ploughed field. The MRZ configuration was mapped both before and after this land-use change.

Level of hillslope erosion	Types of evidence noted in the field	Example
1	Surface crusting **Armouring** **Splash pedestals** Small areas of wash deposits	
2	**Depositional steps** (<10 cm^2) (often behind vegetation) Larger areas of **wash deposits** (<50 cm^2)	
3	Some concentrated flow Erosional steps/**small headcuts**	
4	**Concentrated rills** (~0.1 m^2)	
5	**Gullies** (>1 m deep) with own side slopes	

Table 4.4. Morphological Runoff Zones (adapted from Bracken and Kirkby, 2005). Example photographs from the Upper Nogalte field site.

The spatial configuration of Morphological Runoff Zones was then overlaid onto a DEM of the entire hillslope. Each hillslope-scale DEM was generated using the Trimble GS200 laser scanner. The survey method employed at the hillslope scale was very similar to that described for the plot scale (section 4.3.3) but over distances an order of magnitude larger. There was greater variation around the target resolution of 50 mm due to the variation of hillslope form. However, between 3 and 5 hillslope scans were merged to reduce these effects and to avoid occlusion issues presented by almond trees. Such obstacles were directly removed from the resultant point clouds, as demonstrated in Figure 4.33. The point

clouds were rotated to the perspective where the features could easily be distinguished from the soil surface (Figure 4.33a). The points representing the vegetation elements could then be highlighted (Figure 4.33b) and deleted from the point cloud (Figure 4.33c) cleanly and efficiently.

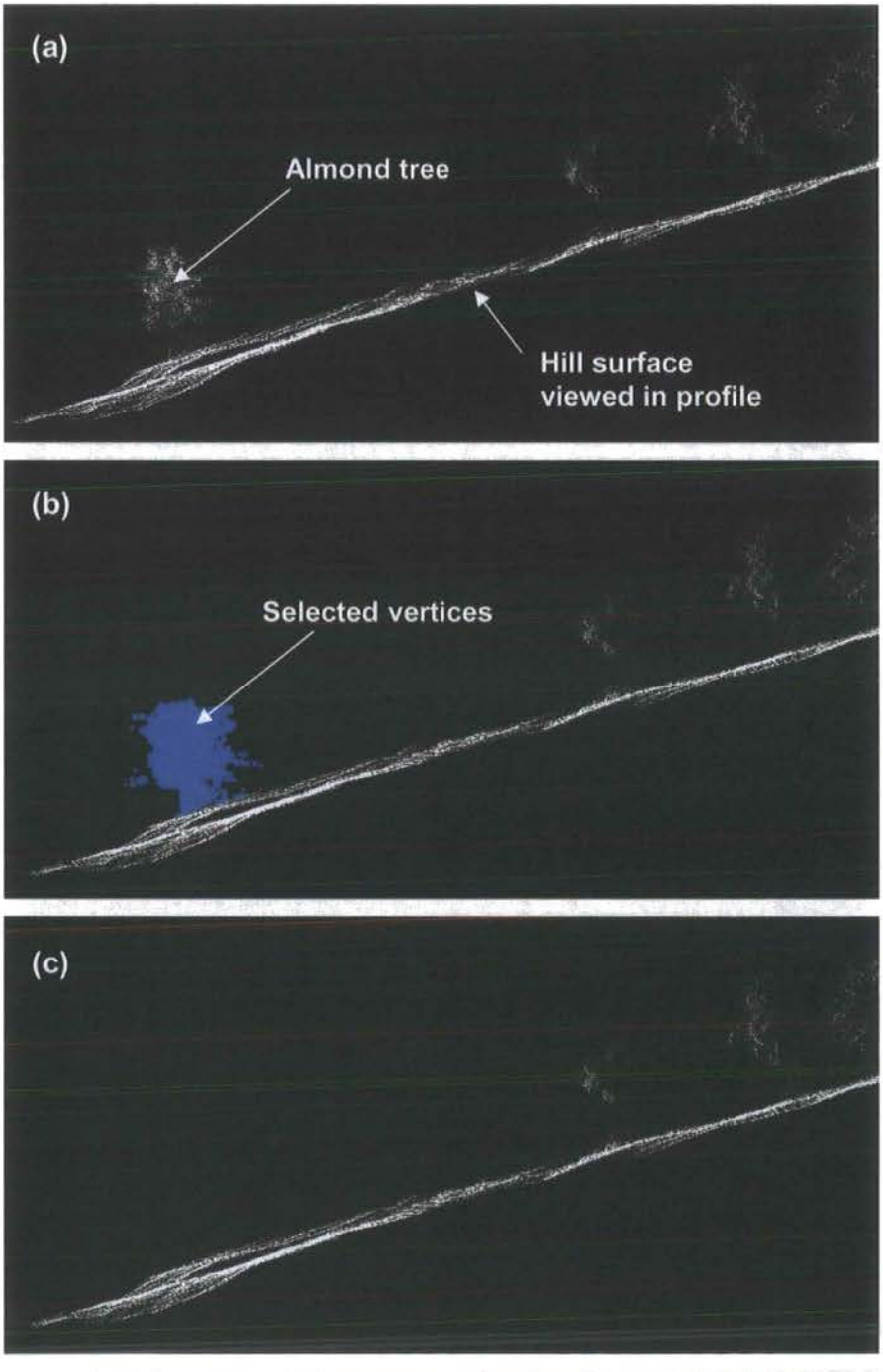

Figure 4.33. Method for removal of trees: (a) point cloud is rotated to an angle where trees protrude from the soil surface; (b) tree is highlighted; (c) tree is removed from point cloud.

However, several areas of the hillslopes (particularly the matorral area of the Cardenas hillslope) were covered with low-lying shrubs so that a thick density of foliage was present near the soil surface. These could not be easily removed from the point clouds. Being so close to the surface, they are likely to affect the processes acting on the surface. Therefore, such low-lying features remained in the coarser resolution hillslope scans as they would only have a limited influence on the resultant surface topography.

An overland flow simulation was conducted on each of the MRZs identified at each hillslope during May 2007 (summarised in Table 4.5). These were repeated as two further simulations using only the wide trough (described in section 4.3.2.1) also took place on each of these plots during May 2006 and March 2007. While problems and inaccuracies with the Terrestrial Laser Scanner mean that high-resolution DEMs are unavailable for these earlier simulations, the data are sufficient to provide velocity estimates and flow patterns. This provides a useful examination of the influence of antecedent conditions as the field campaign of March 2007 was conducted either during or just after a light rainstorm.

Hillslope	MRZ 1	MRZ 2	MRZ 3	MRZ 4	MRZ 5	PLOUGHED
Upper Nogalte	✓	✓	✓	✓	×	✓
Cardenas	✓	✓	✓	✓	×	✓
Del Prado	✓	✓	✓	✓	✓	×

Table 4.5. Locations of overland flow simulations.

4.6 Summary

This study develops a new method for measuring the hydraulics of overland flows on natural soil surfaces and presents a framework for upscaling these measurements to the hillslope scale. Conventional methods (directly measuring flow depths at-a-point with a point gauge or similar device) provide arguably more accurate measurements; however, these offer only a limited spatial resolution. The methodology described here is not

intended to replace such traditional techniques. It is proposed as an alternative perspective, and can be used in conjunction with existing methods. Ultimately, the new method sacrifices a degree of accuracy (through estimating depth indirectly by applying various assumptions about the nature of the water surface) as a trade-off for an enhanced appreciation of the spatial distribution of water depths and many other hydraulic variables. Such data can potentially fill an important gap in our knowledge of overland flows. Several recent studies of overland flows have concluded that their theories can only be thoroughly tested with the provision of new data. In the majority of these cases, we can now provide this (section 5.2).

There are further advantages which arise as important by-products of the method. First, it can reduce the time-pressures of data collection in the field. The method quickly provides the user with the raw data necessary to make many future calculations. These can be made from the relative comfort of a desk, where the user is able to deliberate on the measurements necessary and return to the problem at a later date.

Moreover, the method offers an enhanced level of visualisation. The rapid-fire overhead photography captures much of the processes occurring in the field and can be reviewed in real-time at any point in the future. Should researchers seek explanation or confirmation of some anomalous measurement, they can return to an advantageous viewpoint for the moment of interest. Many new remote sensing techniques or items of field equipment increasingly detach the researcher from the measurement process, through automating a previously complicated and time-consuming method. This is an understandable and ultimately desirable trade-off. However, the level of interaction between researcher and subject is reduced. In this case, the visualisation offered by this technique (albeit at the expense of data storage requirements) offers the best of both worlds.

CHAPTER 5

OVERLAND FLOWS ON NATURAL SLOPES

5.1. Introduction

The aim of this chapter is to provide an introduction to the results presented in this thesis by describing the observed variations of overland flows across and between the three hillslopes examined. Section 5.2 begins with a summary of the variation of basic measurements, (median depth, velocity, and Reynolds number) recorded between plots and sites. Hydraulic geometry relationships at each plot are examined; however, these measurements were taken under conditions of constant discharge. Section 5.3 examines the effect of increasing discharge on 'at-a-section' flow hydraulics. Attempts to explain the patterns presented in section 5.2 and 5.3 suggest that two aspects of the flow require more detailed attention: the distribution of estimated depths (examined in section 5.4) and interactions between the flow regime (characterised by the Froude number) and the nature of the soil surface (discussed in section 5.5). Section 5.6 then summarises the results presented.

5.2. Variation of Flow Hydraulics

Figure 5.1 provides a basic overview of the flow patterns observed in the field. The most striking difference between each plot is the degree of flow concentration. Flow appears to increasingly concentrate with distance downslope, with the Upper Nogalte hillslope

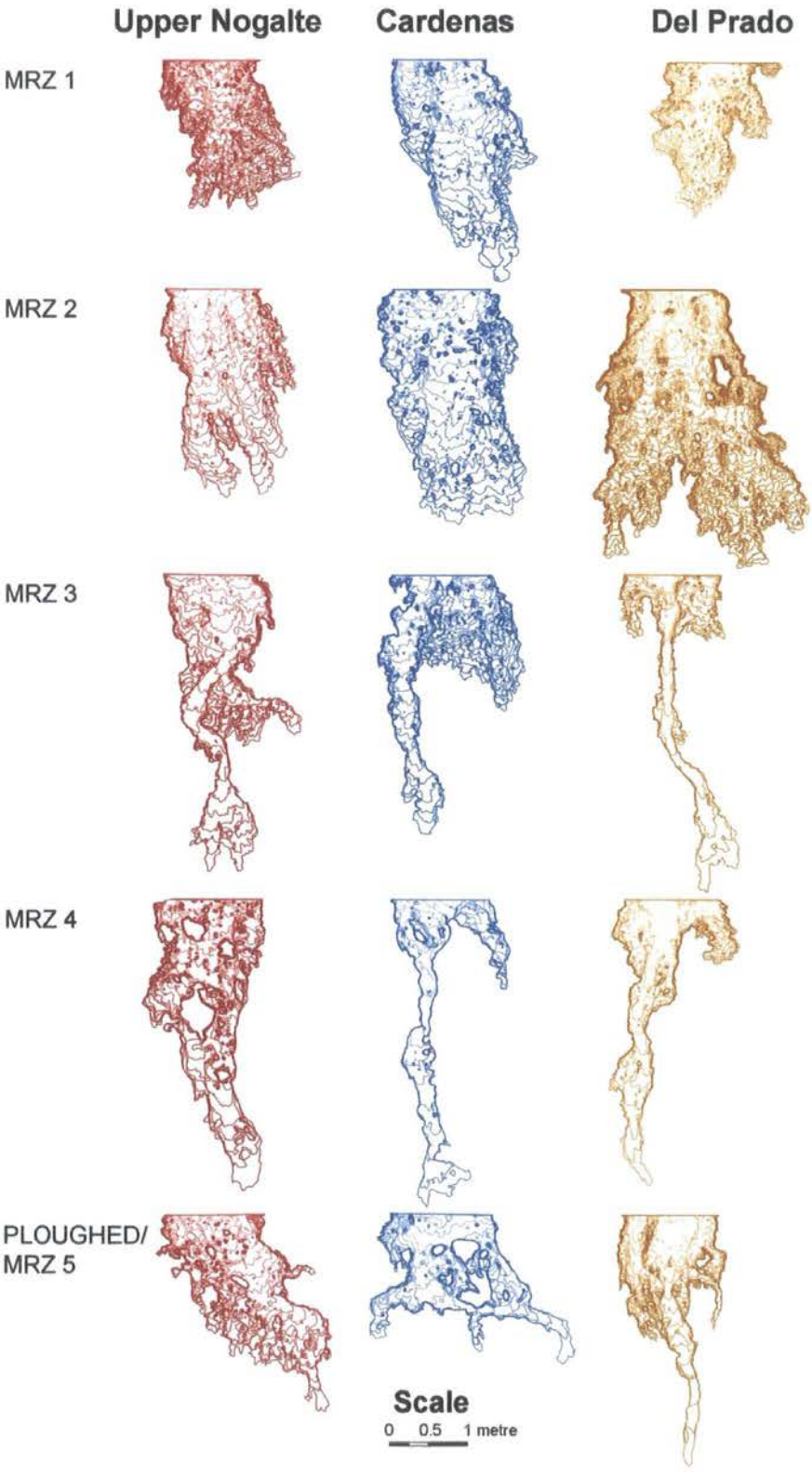

Figure 5.1. Flow patterns recorded at each plot. The interval between flow outlines varied between 0.91 and 1.32 s but was consistent for each plot.

generally displaying less concentrated flow than the other two hillslopes. Similarities can be observed in the general flow patterns within each Morphological Runoff Zone (MRZ), despite being located on different soil types. Such similarities are determined by similarities in microtopography which act to distinguish each MRZ. Chapter 7 examines these flow patterns in a more quantitative way and observes the relative degrees of flow concentration exhibited by each plot. This section now examines the resulting differences of flow depth, velocity, Reynolds number (Table 5.1) and hydraulic geometry (Table 5.2) between and across the three hillslopes examined in this study.

		Depth (mm)					
Hillslope	**Plot**	**25th Percentile**	**Median**	**75th Percentile**	**IQR**	**Velocity ($m\ s^{-1}$)**	**Reynolds Number**
Upper Nogalte	MRZ 1	1.192	1.656	1.997	0.805	0.060	352
	MRZ 2	1.617	1.999	2.393	0.776	0.118	878
	MRZ 3	4.918	6.486	8.239	3.321	0.139	3462
	MRZ 4	2.400	5.307	5.999	3.599	0.104	2336
	Ploughed	1.874	3.192	3.952	2.079	0.080	1115
Cardenas	MRZ 1	1.779	2.481	3.084	1.306	0.079	865
	MRZ 2	4.315	5.077	5.828	1.513	0.103	2301
	MRZ 3	2.597	5.234	7.908	5.311	0.090	2327
	MRZ 4	4.738	9.500	12.68	7.941	0.127	5246
	Ploughed	2.510	4.893	5.959	3.449	0.092	1783
Del Prado	MRZ 1	1.568	2.083	2.449	0.881	0.089	905
	MRZ 2	4.820	5.584	6.432	1.612	0.093	2059
	MRZ 3	2.921	4.213	5.349	2.428	0.212	5097
	MRZ 4	3.786	5.883	7.094	3.308	0.171	4792
	MRZ 5	2.860	7.068	6.370	3.510	0.158	5561

Table 5.1. Values of basic flow variables examined in this section for each plot.

5.2.1 Flow Depth

Estimates of flow depth were made over the inundated area at a resolution of 2 × 2 mm. This typically resulted in over 3,000 depth measurements per thread. As the depths were not normally distributed, the median depth of each thread is used here as a summary statistic to compare flows between plots. Section 5.4 analyses the distribution of these measurements in detail. The variation of median flow depth between plots and hillslopes is shown in Figure 5.2 and in more detail in Figure 5.3.

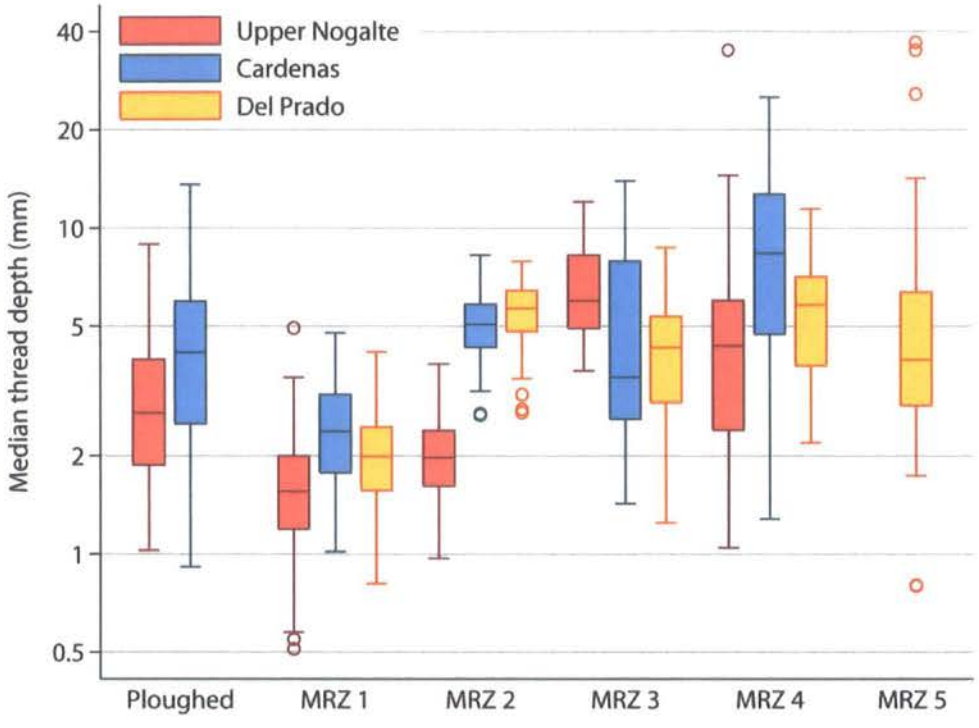

Figure 5.2. The variation of median water depth (mm) (log scale) between each plot and hillslope. The box plot (repeated throughout this thesis following Crowe (1933) and Tukey (1977)) allows comparison of distributions. The limits of the coloured boxes represent the 25th and 75th quartiles and the central line is the median value. The whiskers represent the limits of the dataset unless any values are greater than 1.5 times the interquartile range from the nearest quartile (plotted separately as rings).

Median flow depth increases moving downslope from the hillcrest. A constant discharge was supplied; therefore an increase in median depth reflects either flow concentration (a decrease in width) or a decrease in velocity. Median depth stabilises by MRZ 2 (or MRZ 3 for the Upper Nogalte hillslope) where any further flow concentration is balanced by an increase in velocity. The ploughed plots maintain median flow depths similar to those found where the flow begins to concentrate. With increasing flow concentration, the range of median thread depths observed increases, as each surface exhibits a wider range of features. With the exception of MRZ 3, the Cardenas hillslope has the deepest flow, Upper Nogalte the shallowest, with the Del Prado hillslope displaying an intermediate median depth. This order is reversed at the MRZ 3 plot.

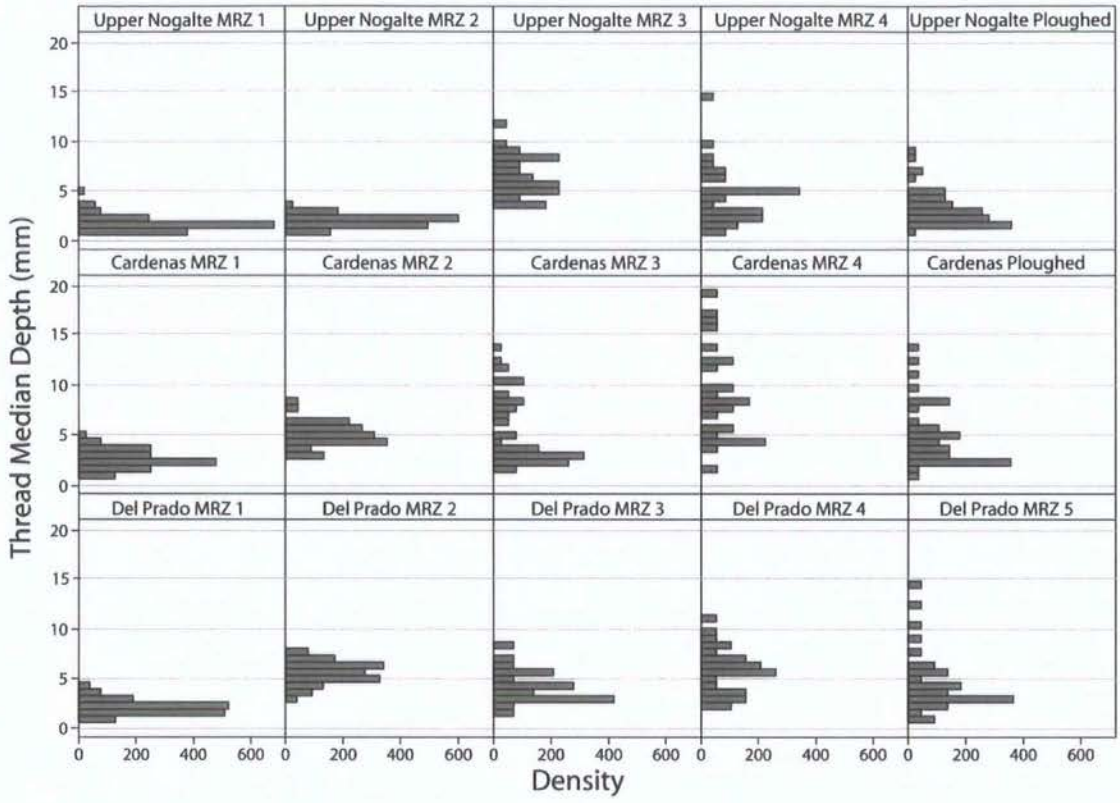

Figure 5.3. Vertical histograms showing the distribution of median thread depths (mm) for each plot and hillslope. Note that the 5 measurements > 20 mm (shown in Figure 5.2 above) have been excluded here for clarity.

5.2.2. Flow Velocity

The distribution of measured velocities between each plot and hillslope is displayed in Figure 5.4. In general, the Del Prado hillslope displays the fastest flow and Upper Nogalte the slowest; however, there is no definite systematic pattern. The order of the hillslopes completely reverses between MRZ 1 and MRZ 2. There appears to be a pattern of gradually increasing velocity with distance downslope, and (as seen with median depths) and increasing range. The two ploughed plots have very similar velocities despite being located on different soil types.

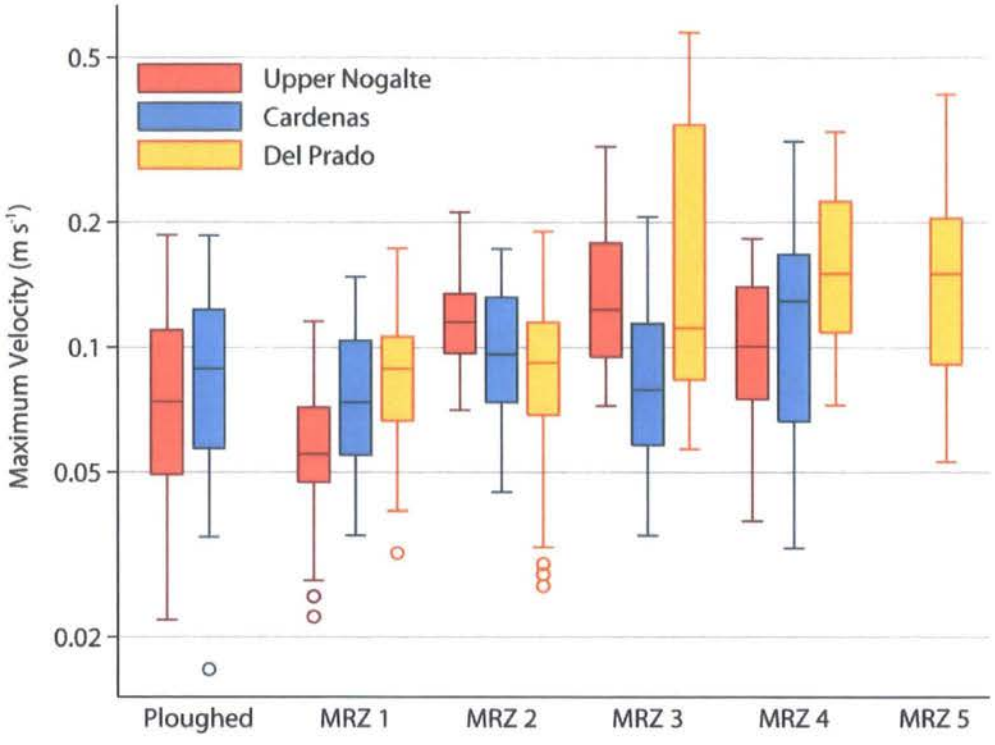

Figure 5.4. Variation of velocity (m s^{-1}) (log scale) between each plot and hillslope.

5.2.3 Reynolds Number

The flow depth and velocity combine with the kinematic fluid viscosity (which is temperature dependent) to determine the dimensionless Reynolds number (equation 2.1). The flow simulated in locations near the hill crest is in the laminar regime (Figure 5.5). Moving downslope, the Reynolds number increases. This downslope increase levels-off once transitional/turbulent flows develop; by MRZ 3 for the Cardenas hillslope, by MRZ 4 at the Upper Nogalte hillslope and by MRZ 5 at the Del Prado hillslope. Beyond this point, a slight increase further downslope is seen. Most flows found in concentrations are either turbulent or in the ill-defined 'transitional zone'. The location of the boundaries between laminar and turbulent flow may be subject to considerable uncertainty as the condition of geometric similarity (with pipe-flows) is not met. Field observation suggests that the flow was more turbulent than suggested by Figure 5.5.

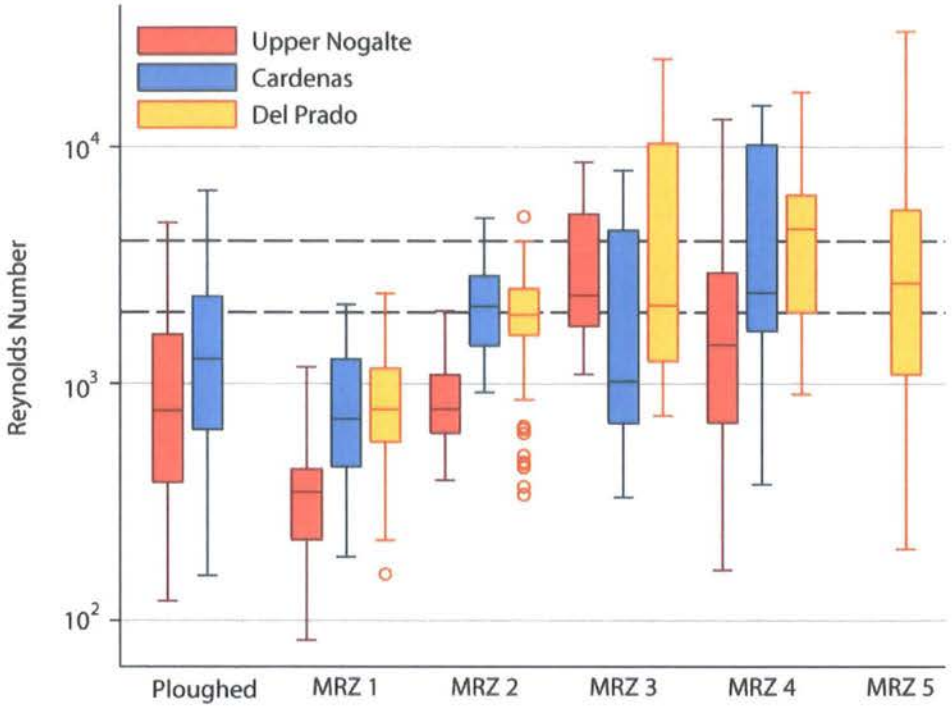

Figure 5.5. Variation of the Reynolds number (log scale) between each plot and hillslope. Dashed horizontal reference lines represent the conditions Re = 2300 (approximately the upper bound of laminar regime) and Re = 4000 (lower bound of turbulent regime).

5.2.3. Downstream Hydraulic Geometry

The mutual adjustment of flow depths and velocity is examined here through the hydraulic geometry approach. From the continuity equation (equation 4.1) relationships between discharge, velocity, width and depth can be established. These are represented empirically in the form of the power relations

$$w \propto Q^b \tag{5.1a}$$

$$d \propto Q^f \tag{5.1b}$$

$$v \propto Q^m. \tag{5.1c}$$

This section examines the variation of these relationships, particularly exponents b, f and m, between each plot and hillslope. The relations presented here are not at-a-section variations as only a single data point is presented per section in this constant discharge experiment. The observed spread of discharges reflects the differential concentration of the imposed flow within each plot. The results presented here characterise the overall variability of hydraulics, and as such the dataset can be divided in several different ways. Table 5.2 presents the variation of the exponents between hillslopes, plots and between interrill and concentrated flows. At-a-section hydraulic geometry is then presented in section 5.3 for the variable discharge experiments (described in section 4.3.2.2). These two datasets provide complementary approaches to examining the hydraulic geometry of the hillslopes.

Figure 5.6 shows little difference in the hydraulic geometry relationships when dividing the dataset by hillslope. The large number of data points makes any differences difficult to detect. In an attempt to summarise the data, polar smooths have been superimposed over the scatter; this gives a graphical depiction of the central part (approximately half) of each dataset and is created by transforming the coordinates of the data into polar coordinates, smoothing on a periodic scale and transforming back. For further explanation of this process see Cleveland and McGill (1984) and Cox (2005).

There is much overlap between the three hillslopes. However, from Figure 5.6 it appears that the Cardenas hillslope generally displays wider flow with a flow width that increases more steeply at higher discharges. The Del Prado hillslope holds the water in the narrowest flow width. The relationship between flow depth and discharge also shows minimal variation between hillslopes. The Cardenas hillslope maintains deeper flows on the whole, and also displays the most rapid increase of depth with discharge; this is at the expense of velocity which increases slower than at the other hillslopes. The Del Prado hillslope demonstrates the fastest flow per unit discharge with a larger velocity exponent m (Table 5.2). From Figure 5.6 it also appears that there is a break in this relation; at larger discharges velocity increases more rapidly.

	Exponent		
By Hillslope	Width (*b*)	Depth (*f*)	Velocity (*m*)
Upper Nogalte	0.331	0.360	0.307
Cardenas	0.301	0.412	0.294
Del Prado	0.249	0.403	0.339
By Plot			
MRZ 1	0.375	0.295	0.329
MRZ 2	0.430	0.290	0.289
MRZ 3	0.247	0.387	0.367
MRZ 4	0.235	0.436	0.323
MRZ 5	0.279	0.461	0.268
Ploughed	0.358	0.316	0.329
By Flow Concentration			
Interrill Flow	0.332	0.374	0.295
Concentrated Flow	0.338	0.415	0.260

Table 5.2. Variation of exponents *b*, *f* and *m* of equation 5.1a–c between hillslopes, plots and degree of flow concentration. Exponents represent averaged values, hence their sum may not exactly equal 1.

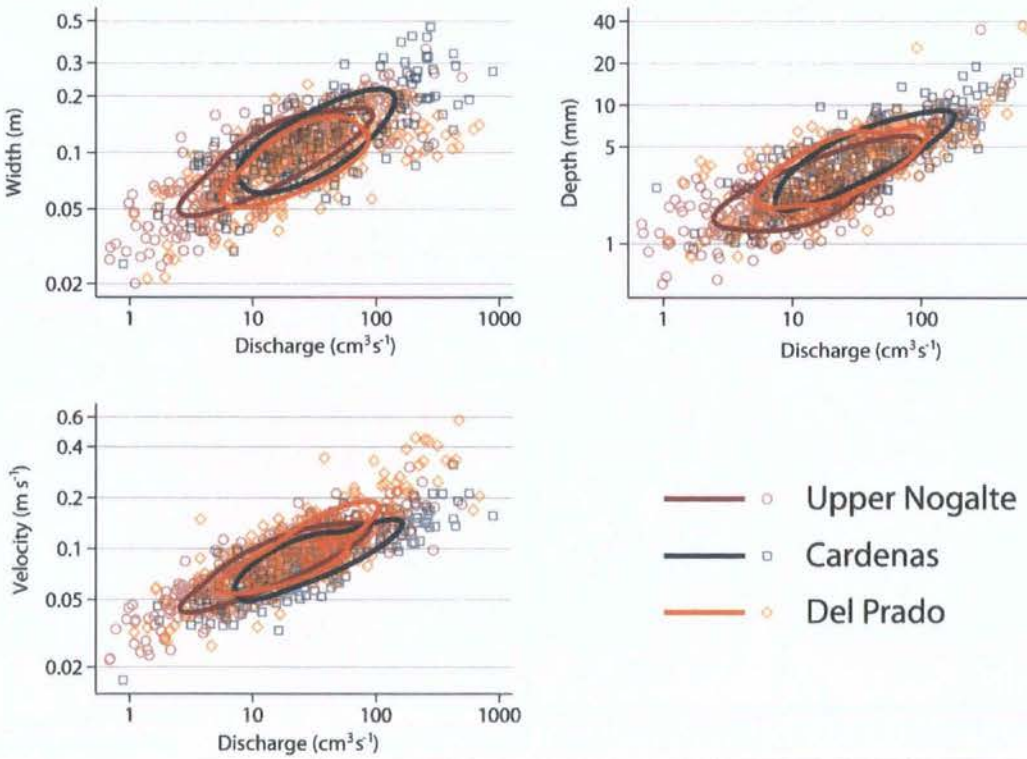

Figure 5.6. Hydraulic geometry relations separated by hillslope (summarised with polar smooths).

Greater differences can be distinguished when considering each plot type separately (Figure 5.7) suggesting that variation of hydraulic geometry across these hillslopes is potentially more important than variation between hillslopes. Flow is wider further upslope and width increases faster with discharge. Width per unit discharge decreases systematically with distance downslope; the variation of the b exponent of equation 5.1a is more complicated (Table 5.2), but there is a noticeable difference between the large exponents of the two upslope plots (MRZ 1–2) and the remainder of the dataset. The MRZ 4 plot shows the lowest increase of width with discharge.

The reverse trend is observed when examining the f exponent of the depth-discharge power relation. The depth exponent increases systematically with distance downslope; both MRZ 4 and MRZ 5 appear to show a steepening of this relationship at greater discharges. From the exponents in Table 5.2, the ploughed plots display behaviour most similar to that of the upslope plots MRZ 1.

The minor flow concentrations of the MRZ 3 plots display the greatest increase of velocity with discharge (m = 0.37); velocity appears to increase even more at the highest discharges. The most upslope plots (MRZ 1) also have a high value of m (0.33), with MRZ 2 then displaying the lowest (m = 0.29). The scatter about the observed velocity-discharge relations noticeably increases at higher discharges.

Figure 5.7 demonstrates distinct behaviour of hydraulic geometry between the areas of the hillslope that act to concentrate flow and areas of interrill flow that diffuse it. To examine this pattern further, Figure 5.8 divides the dataset into these two subsets. The constant discharge supplied means that areas of concentrated flow will necessarily exhibit larger discharges at each thread than the interrill areas as they capture a larger proportion of the upslope flow width.

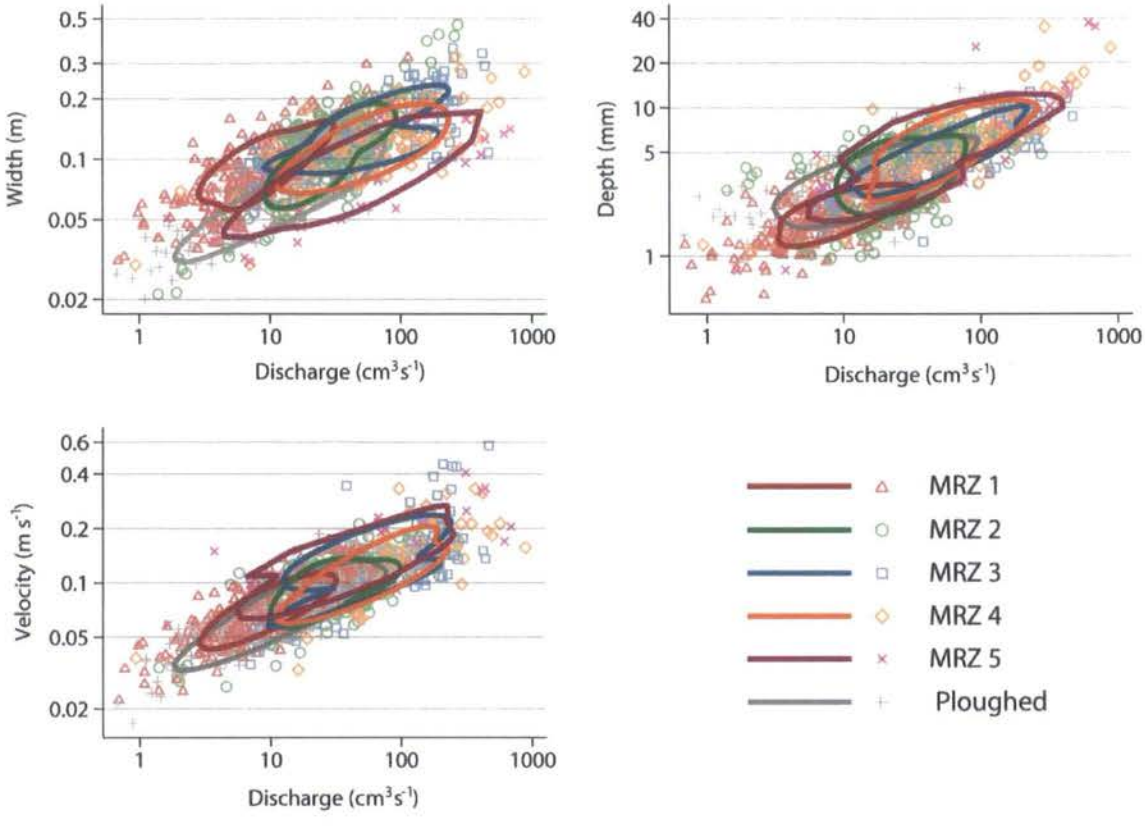

Figure 5.7. Hydraulic geometry relations separated by plot type (summarised with polar smooths).

In concentrations, the flow is narrower (although width does increase slightly faster with discharge). Concentrated flows are also deeper with a more rapidly increasing depth with discharge. The *m* exponent of the velocity-discharge relationship is greater for the interrill flows than concentrated flows. However, the scatter observed in Figure 5.8 suggests that this generalises a more complex relationship. Concentrated flow velocity at high discharges splits into two velocity-discharge relationships. Analysis of the dataset suggests that flow in the upper limb is mostly in the supercritical regime (Fr > 1), whereas that in the lower limb is subcritical. Thus the relationship between velocity and discharge has two states determined by the flow regime, which is particularly noticeable in concentrated flows.

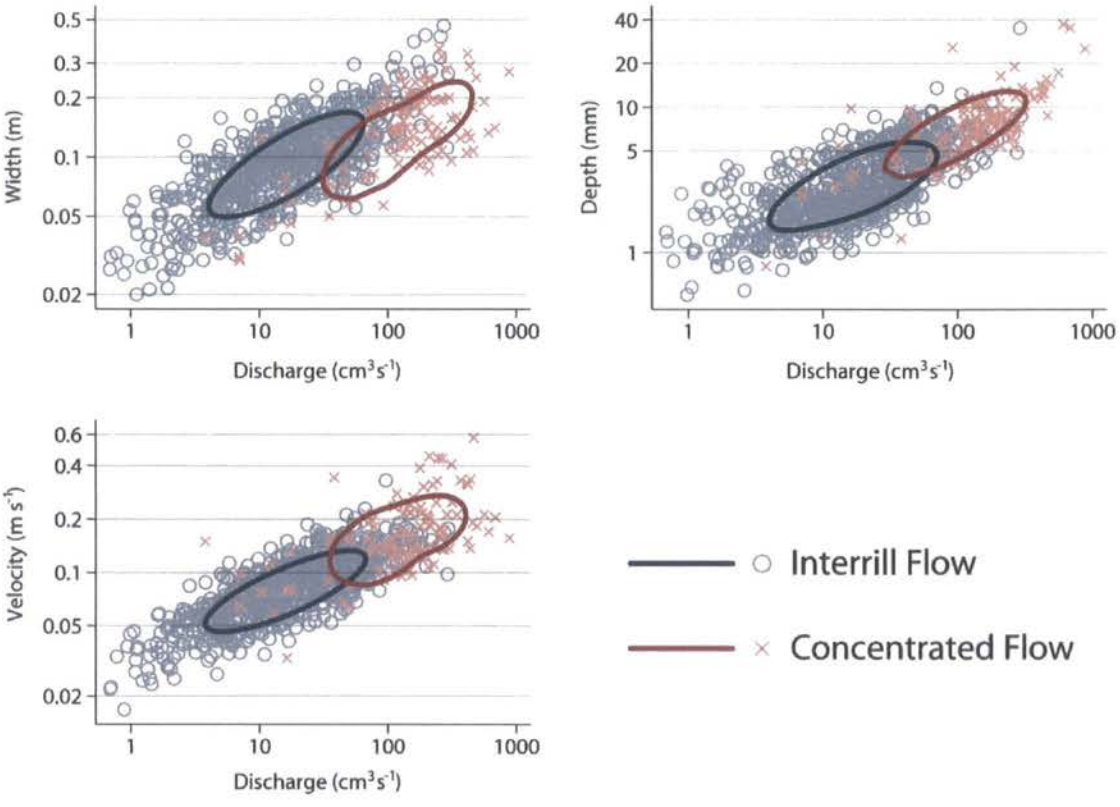

Figure 5.8. Hydraulic geometry relations with interrill and concentrated flows (as identified in the field) considered separately (summarised with polar smooths).

The exact nature of this process is difficult to detect from this dataset as each point represents a different area of the hillslopes. However, the experiments were repeated using a trough capable of simulating several different discharges at a single location (Figure 4.6). This permits a closer examination of the processes operating to determine the hydraulic geometry relationships seen in this section. The results of these experiments are described below.

5.3 At-a-Section Flow Hydraulics

The variation of flow hydraulics with discharge deserves attention: this provides a clearer picture of the relationships between overland flow and the soil surface and the influence of the changing nature of the flow as a storm progresses and roughness elements become progressively inundated. For this purpose, a variable discharge trough (described in section

4.3.2.2) was developed. The trough allowed 5 discharges to be provided to the top of the plot; these were approximately 0.4, 0.8, 1.2, 1.6 and 2.0 l s^{-1} over a 0.20 m width. The flow concentrated or dispersed to a different degree at each plot, so the actual discharges examined are not identical for each section. This reflects the distribution of hillslope runoff during a natural rainstorm.

The flow was examined at two sections in each plot; each section represents the average of three closely-spaced transects. Due to practical limitations, no data of at-a-section hydraulics are available from either the Cardenas MRZ 2 or Upper Nogalte ploughed plots.

Figures 5.9–5.11 display the relationships between f and Re for each plot. This type of analysis follows Emmett (1970) and is instructive in that it provides direct comparison with both the theoretical relationships discussed in Chapter 2 and a number of other studies of overland flows (for example, Abrahams *et al.* 1992). Such comparisons are also made in Chapter 6, but these are limited to the case of the steady discharge trough. The Reynolds number is substituted for discharge as it corrects for water temperature effects on viscosity. The median flow depth was used to calculate both variables. However, as Parsons *et al.* (1996b) note, this convention eliminates any consideration of flow width from the analysis. Results presented later in this section demonstrate that flow width effects need to be included in this type of analysis due to the progressive inundation of soil surfaces with increasing discharge.

Abrahams *et al.* (1992) examine f-Re relationships on irregular, gravel-covered semi-arid hillslopes. They suggest that the conventional form of the relationship developed for flow over a plane bed (the Blasius relationship of equation 2.7) does not apply to flows over such rough surfaces where roughness elements are progressively inundated with increasing discharge. This conventional form of the f-Re relation used in many models of hillslope runoff proposes a power law relationship with an exponent of −1.0 for laminar flows (equation 2.7) and −0.25 where flow is turbulent. Such power-law relationships are displayed in Figures 5.9–5.11 with fitted lines.

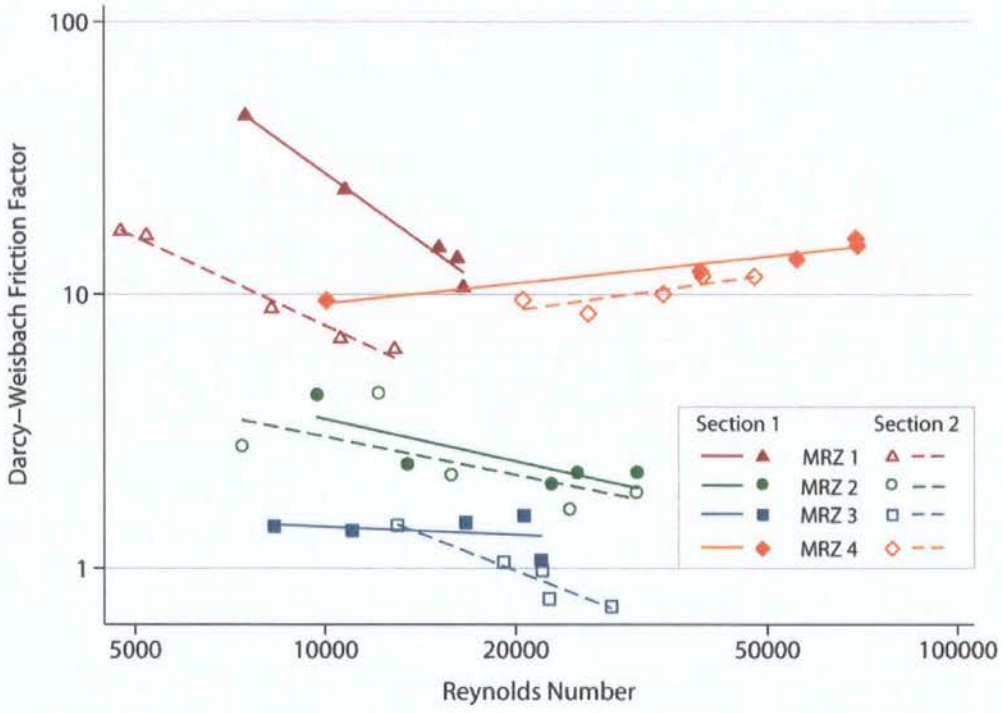

Figure 5.9. *f*-Re relationships for each plot at the Upper Nogalte hillslope.

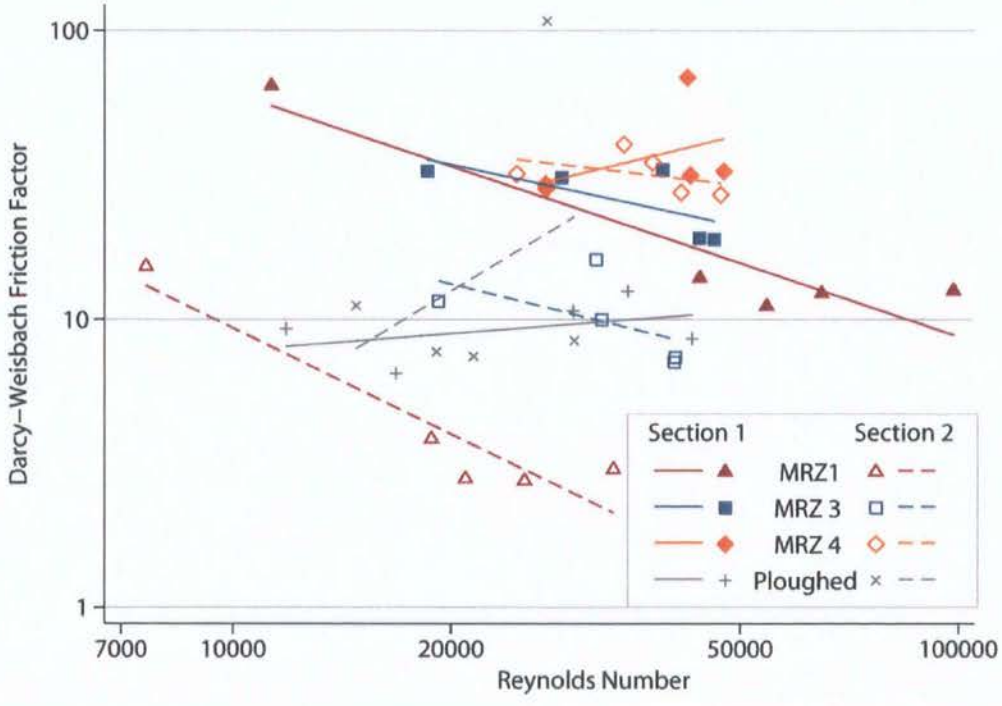

Figure 5.10. *f*-Re relationships for each plot at the Cardenas hillslope.

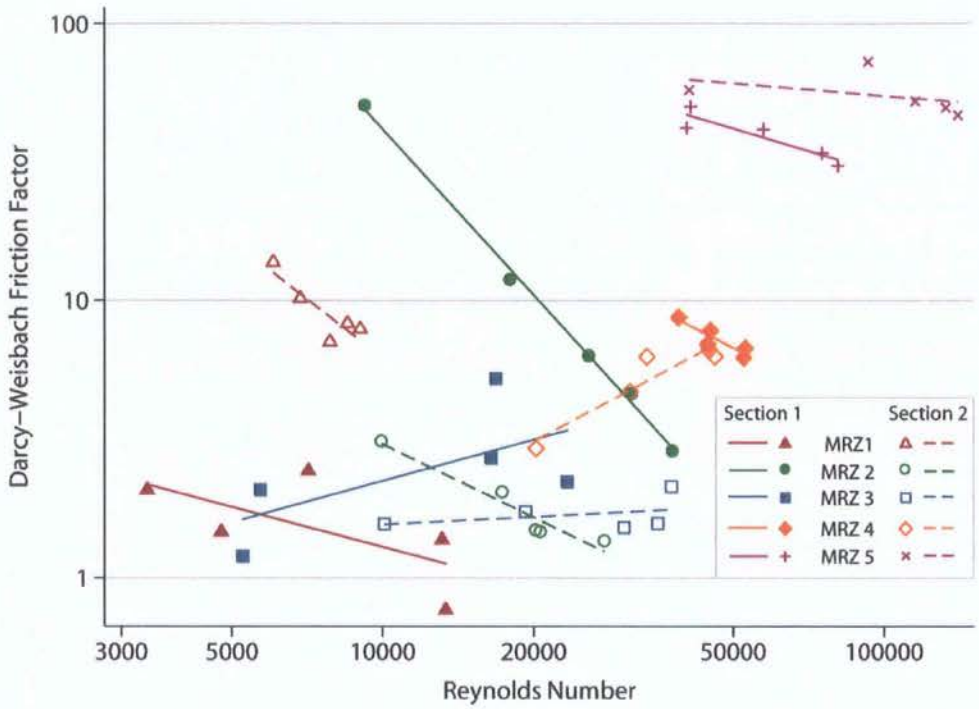

Figure 5.11. *f*-Re relationships for each plot at the Del Prado hillslope.

The results here suggest that most relationships approximate a power-law relationship (the data-points are scattered around straight lines in Figures 5.9–5.11). No convex-upward relationships of the type reported by Abrahams *et al.* (1992) have been observed. Emmett (1970) notes that the slope of the relationship is determined by the hydraulic geometry of the flows in that it is equal to $f-2m$ (where f and m are the exponents of the depth-discharge and velocity-discharge power relations of equations 5.1b and 5.1c).

There is a consistent pattern with distance downslope. Towards the crest of the hillslopes (MRZ 1–2) the *f*-Re relationship is strongly negatively sloping: the friction factor decreases more rapidly with increasing discharge and closely approximates the Blasius equation (equation 2.7) for laminar flows, with exponents around −1.0 (however, the flows recorded in this section were all in the turbulent regime). Conversely, the plots towards the foot of the hillslopes demonstrate a less obvious decrease in the friction factor (with exponents closer to that of the turbulent Blasius equation). In some cases (often the rilled MRZ 4 plots) there is an increase in the friction factor with discharge. In such flow concentrations,

the median flow depth is increasing more rapidly than further upslope without a concomitant increase in velocity, thereby preventing a sharp decrease in f.

Figures 5.12–5.14 show graphs of width, depth and velocity against discharge for each section examined. The ability of the flow width to vary appears to have a large effect on the hydraulic geometry relationships. The rapidly increasing flow width (with increasing discharge Q) found at the upslope plots occurs at the expense of the flow depth, which shows relatively little increase with Q. Depth increases more rapidly with Q at the downslope plots. However, at the Upper Nogalte and Del Prado hillslopes, velocity increases faster with discharge at the upslope plots than further downslope in flow concentrations. A similar effect is seen at the Cardenas hillslope, though it is less obvious.

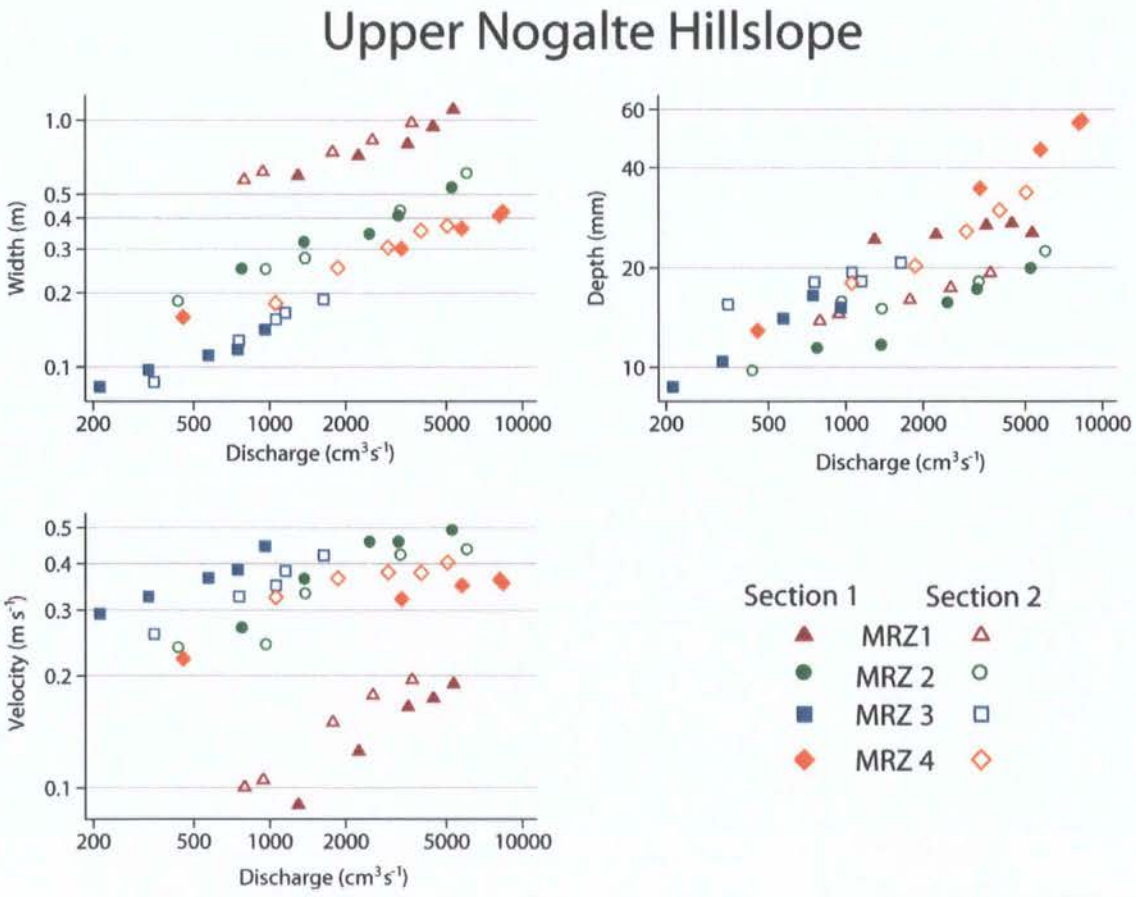

Figure 5.12. Hydraulic geometry relationships for the Upper Nogalte hillslope.

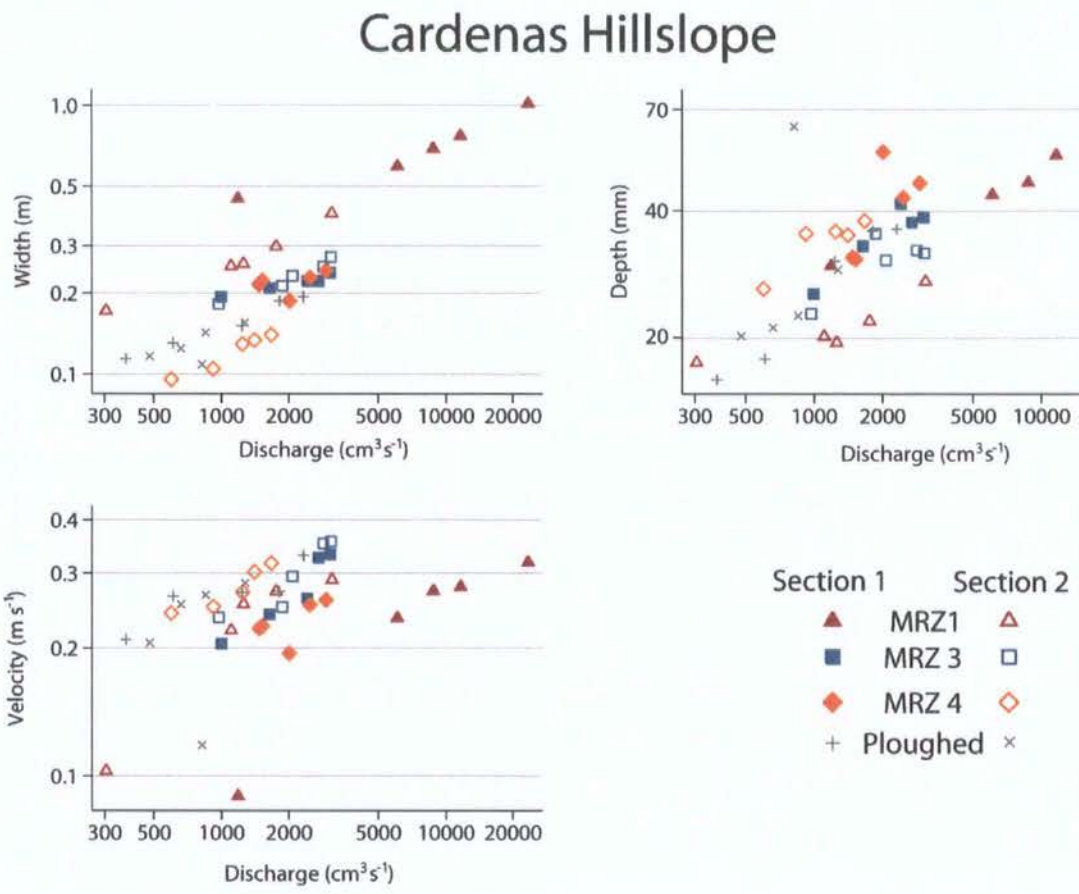

Figure 5.13. Hydraulic geometry relationships for the Cardenas hillslope.

An increase in Q appears to have less effect on flow velocity in the flow concentrations found towards the bottom of each hillslope than it does in the sheet-type flow found further upslope. This is despite the more rapidly increasing flow width further upslope (such width increases are magnified here due to the finite width of supplied flow). One hypothesis to explain this difference is that the velocity-discharge relationship is affected by progressive inundation of roughness elements at the downslope plots. Even at the lowest discharges supplied in these experiments, most roughness elements at the upslope locations (MRZ 1 and MRZ 2) are already mostly submerged. Any increase in Q causes the flow to spread out; velocity increases with depth and is not modified by the additional flow resistance encountered by an increased wetted perimeter.

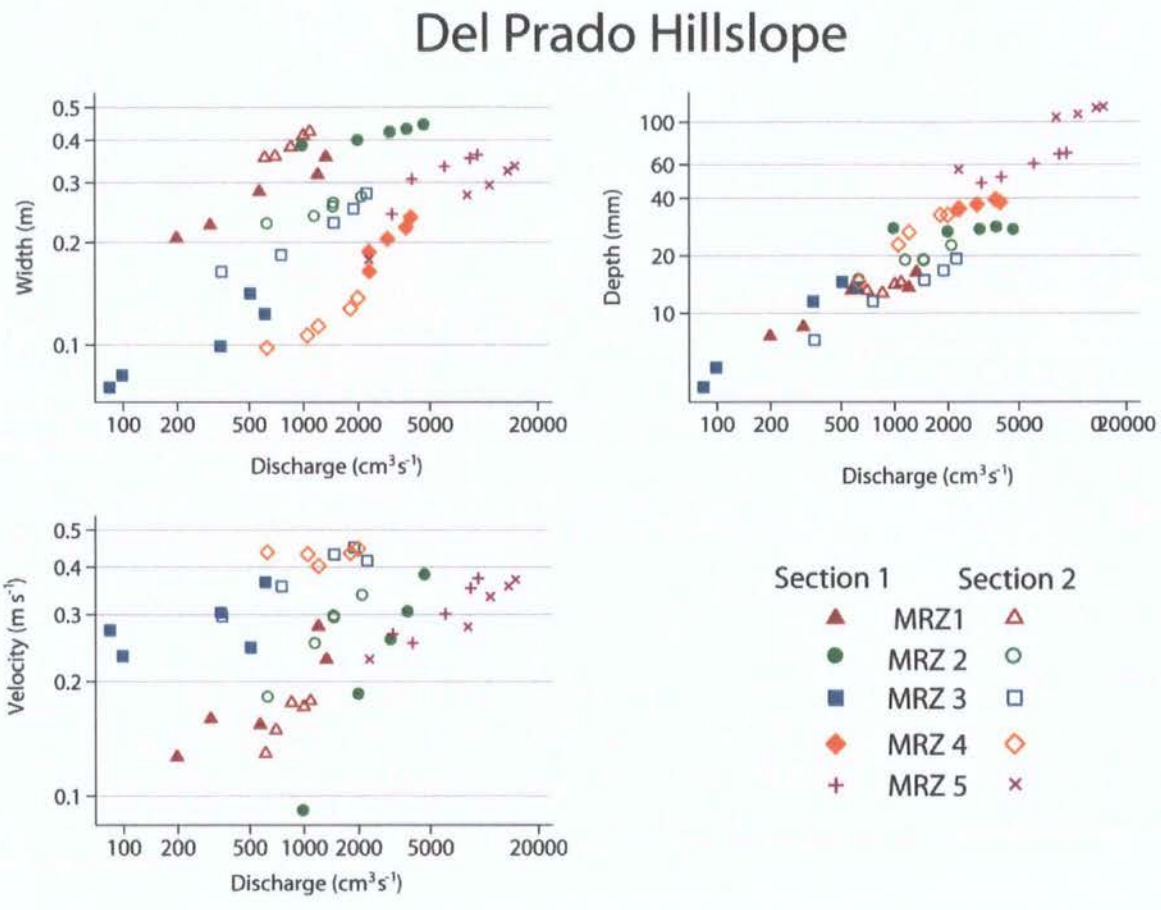

Figure 5.14. Hydraulic geometry relationships for the Del Prado hillslope.

Further downslope, the soil surface configuration is such that an increase in Q progressively submerges additional roughness elements which contribute additional flow resistance and restrict concomitant increases in velocity. The differences in soil surface configuration can be observed in the transects displayed in Figure 5.15 (note the different scales between transects). Near the hill crest, the additional discharge produces an increase in flow width, but there are few roughness elements that become submerged. Further downslope at the MRZ 3 plot where flow concentrations are beginning to develop, the additional discharge increases flow depth more than flow width. Roughness elements are progressively submerged; the resultant increase in resistance appears to offset the enhanced hydraulic efficiency of deeper flow.

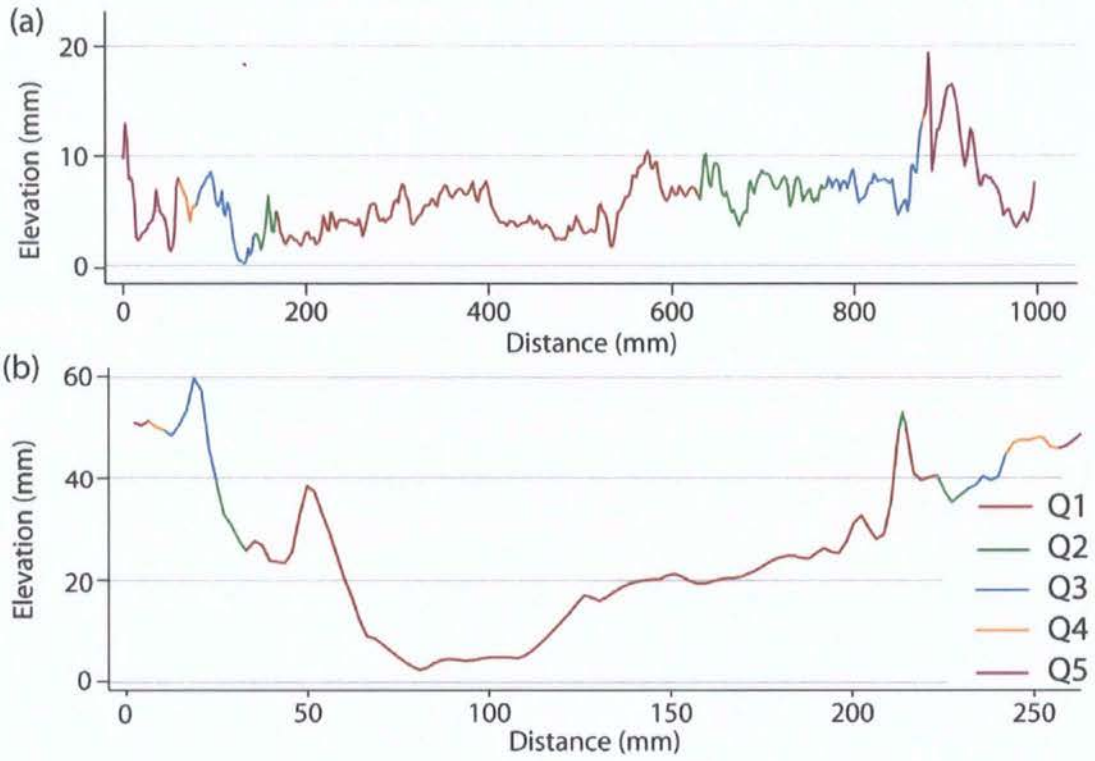

Figure 5.15. Progressive inundation over a surface (a) near the crest of the Cardenas hillslope (MRZ 1) and (b) in a flow concentration at the Cardenas MRZ 3 plot (different scale). The discharge increases from Q1–Q5 (exaggerated vertical scales).

To investigate the relationship between depth, width and velocity for increasing discharges at-a-section, Figures 5.16–5.18 illustrate the variation of depth with width (a) alongside the variation of depth with velocity (b). In both graphs, the data points are connected in the order of the progressive increase in discharge, thereby permitting the step-wise changes to be observed side-by-side. Both flow width and velocity increase more rapidly with depth at the upslope plots; this effect is most pronounced at the Del Prado hillslope. In every case the flow width only increases with discharge; however, velocity and median flow depth display both increases and decreases. Depth is represented by the median flow depth and so may decrease where a small increase in water surface level spreads the flow over a thinly inundated area. Whether such breaching of flow concentrations increases or decreases the median flow depth will ultimately depend on the details of the distribution of observed flow depths.

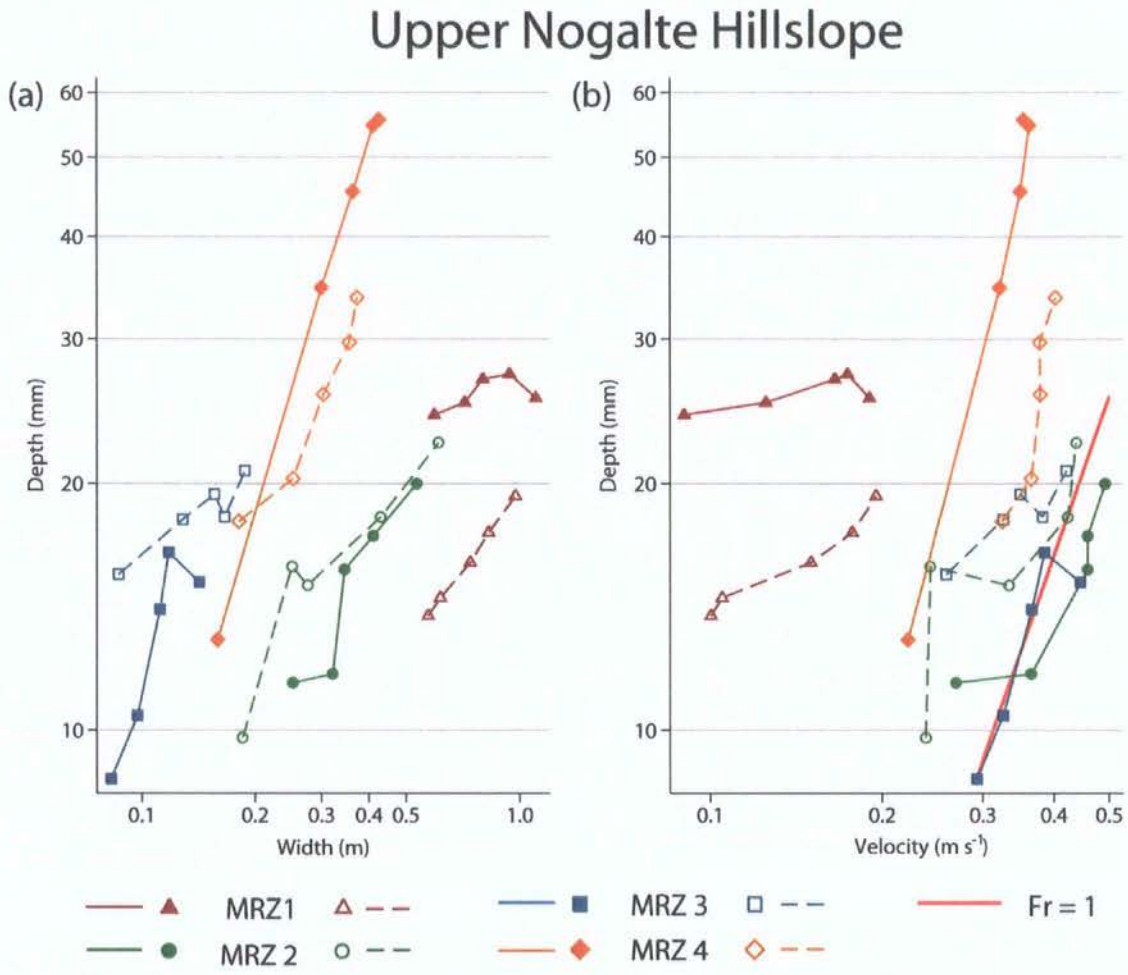

Figure 5.16. Variation of depth (mm) with (a) width (m) and (b) velocity (m s^{-1}) for the Upper Nogalte hillslope. The red line represents the relationship between depth and velocity where Fr = 1.

Many of the MRZ 3 and MRZ 4 sections observe this pattern; a point can be identified in Figures 5.16(a)–18(a) where flow width increases, but median flow depth either decreases or remains steady. As an example, Figure 5.15b displays the inundated surface for section 2 of the Cardenas MRZ 3 plot (dashed blue line in Figure 5.17a). The two decreases in median depth represent lateral spreading into marginally inundated areas. However, inspection of Figures 5.16–5.18, suggests that such progressive inundation is not responsible for every decrease in median depth, as in most cases the reduction in median depth occurs simultaneously with an increase in velocity.

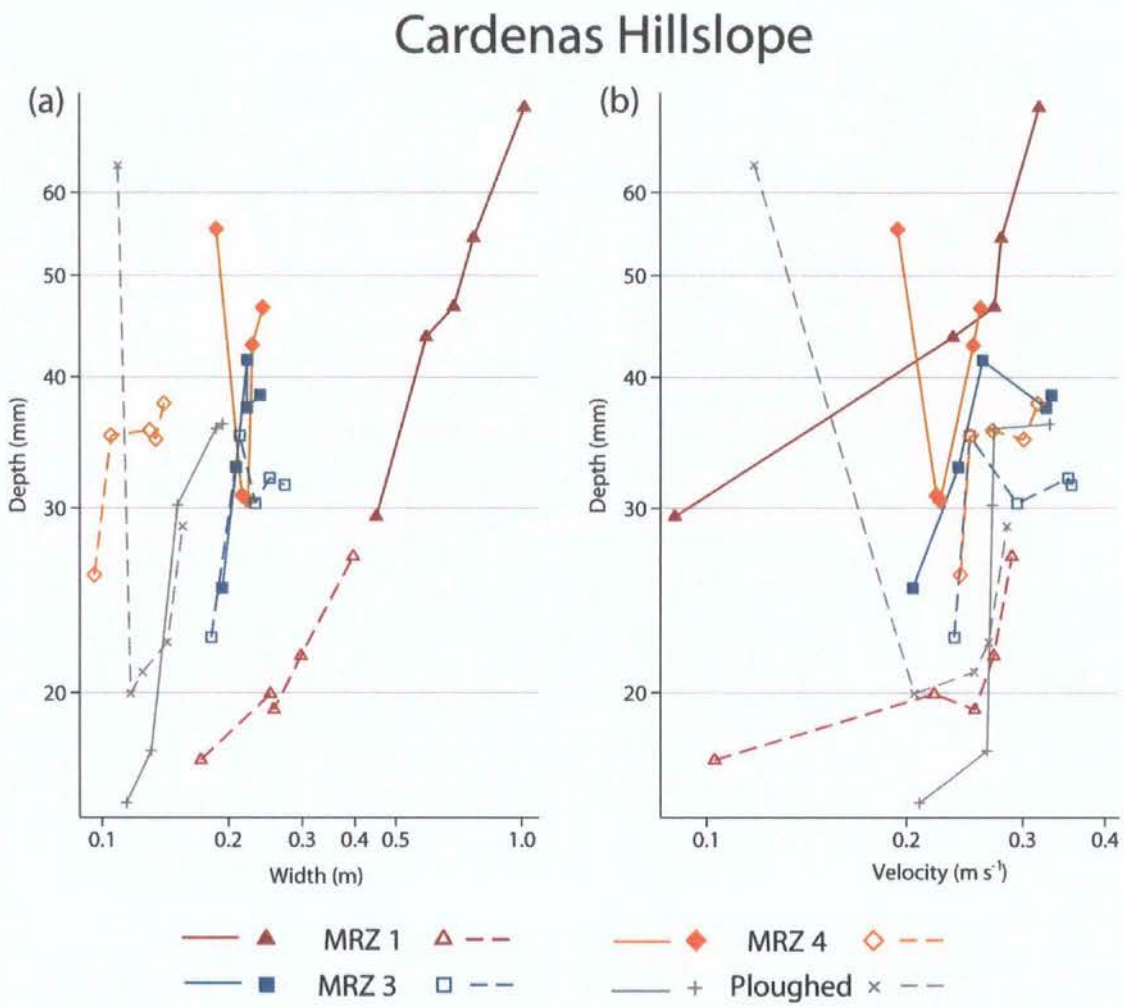

Figure 5.17. Variation of depth (mm) with (a) width (m) and (b) velocity (m s^{-1}) for the Cardenas hillslope. The relationship between depth and velocity where Fr = 1 plots to the right of the x-axis displayed in (b).

The minor velocity decreases observed at the MRZ 4 and 5 plots of the Del Prado hillslope (Figure 5.18) occur alongside negligible increases of depth. The observed decreases of median depth with discharge, due to the interaction between progressive submergence and generally deepening flow, suggest that the summary measure of median depth insufficiently describes the nature of flow over partially inundated, complex topographies. This is examined further in section 5.4.

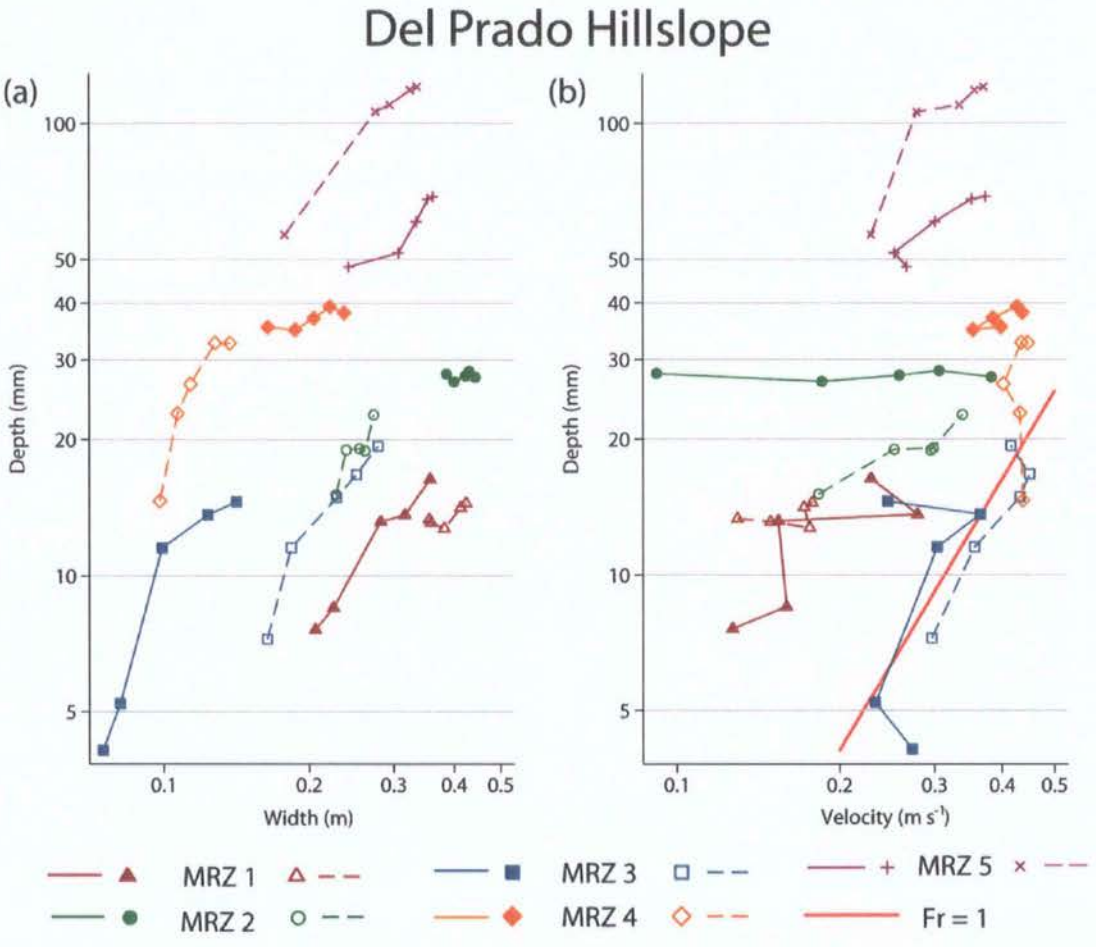

Figure 5.18. Variation of depth (mm) with (a) width (m) and (b) velocity (m s^{-1}) for the Del Prado hillslope. The red line represents the relationship between depth and velocity where Fr = 1.

The results plotted in Figures 5.16 and 5.18 identify an alternative trigger for the observed decreases in velocity. In many cases, velocity decreases where the flow regime shifts from supercritical to subcritical and a hydraulic jump occurs. A decrease in velocity occurs alongside an increase in flow depth during a hydraulic jump; this represents the flow switching from the upper limb of the velocity-depth relationship (identified in Figure 5.8) to the lower sub-critical relationship. Therefore, flow regime appears to have a strong influence on the relationship between velocity and discharge in flow concentrations.

This examination of flow hydraulics at-a-section reduces the confounding factor of variable surface roughness between sections. Examining the relationship between roughness and overland flows represents a crucial element of this thesis; however, this section has identified several important facets of the nature of surface-flow interactions worthy of further investigation.

Progressive inundation of roughness elements alters the depth-discharge relationship in a complex manner. As noted by Parsons *et al.* (1996b), this is manifest in the distribution of depths in the overland flow. The simplification of this distribution by using only a single measure of depth (often the mean, or median as used here) has an important effect when examining hydraulic geometry relationships. While such customary measures may be relevant for studying some processes, the distribution of values and occurrence of extreme values may be more crucial for overland flow hydraulics (see Leopold, 1951; Cox, 1992). Therefore, the distribution of depths of overland flows is examined in detail in the next section.

Furthermore, results presented here suggest that the shift between supercritical and subcritical flow can lead to a decrease in velocity with increasing discharge. Such hydraulic jumps have been identified here at-a-section and are possibly a consequence of the changing hydraulic resistance encountered as increasing discharge gradually inundates roughness elements and pushes the velocity-depth relationship over a threshold. Section 5.5 takes this suggestion further by investigating the variation of the Froude number with surface roughness as water flows downslope and by examining the precise nature of the roughness that is able to tip the velocity-discharge relationship over this threshold.

5.4 Depth Distributions

Estimates of flow depth were made over the inundated area at each flow thread and timestep at a spatial resolution of 2 × 2 mm. The results of section 5.3 suggest that to provide a better understanding of the variable relationships between flow depth, discharge and velocity found across the hillslope, a more sophisticated representation of depth may be

required than simply the median depth. Therefore, this section analyses the depth distributions observed in the field.

Before the results are described, a brief technical note is required. The method of depth estimation described in section 4.3.5.2 interpolated a water surface between endpoints and any protruding surface peaks (Figure 4.21b). One consequence of this is that although these points were observed to be submerged and are located within the wetted area, the estimated depths equal zero. These estimations have been retained for the calculation of all other flow variables, but they are excluded from analysis in this section because of the effect of a large number of zero depths on the overall depth distributions. In any case, the methodology of depth estimation means that the depths located around these protrusions are the least reliable of all the estimated depths. Abrahams *et al.* (1989) discuss the idea of assigning all non-inundated areas a depth of zero; as this convention makes little physical sense, it will not be followed in this analysis.

The spatial variability of flow depth over a soil surface influences the distribution of shear stress imparted on that surface. This places great importance on modelling flow depth distributions and has prompted numerous studies fitting observed flow depths to various statistical distributions. Interrill overland flow is often simplified as a shallow sheet of water displaying a uniform flow depth, although Emmett (1970, 1978) long since observed anastomosing threads of more concentrated, deeper and faster flow within interrill flow.

Abrahams *et al.* (1989) observed an exponential distribution of flow depths at cross-sections measured on a semi-arid hillslope. Such a distribution is described by a single location parameter (the mean; Table 5.3). However, Abrahams *et al.* (1995) and Parsons *et al.* (1996a) found that the mean flow depth was not linked to rill formation: a comparison of two hillslopes revealed that while mean flow depth increased downslope on one hillslope, it was the other that displayed rill initiation.

Recently, this led Parsons and Wainwright (2006) to suggest a (two-parameter) Gumbel distribution for maxima as an appropriate model for the depths of interrill overland flow (defined by both scale and location parameters) (Gumbel, 1958). Their decision to use this

distribution was theoretically driven, but is based on the assumptions that the soil surface is completely inundated and that surface roughness is normally distributed. While Currence and Lovely (1970) and Moore and Larson (1979) (among others) suggest a normal distribution of surface roughness, Smith (2005) found that this was not the case due to the underrepresentation of extreme values (as high peaks are eroded and deep pits filled). In areas where structural roughness elements dominate microtopography, the distribution of surface roughness and hence flow depths will be affected by the finer details of the structure of the soil surface.

The high-resolution flow depth data obtained in this study present an opportunity to examine the best distribution for overland flow depths and how this changes both between and across natural semi-arid hillslopes. While the results here represent the flow depths estimated over a surface, each surface was divided into adjacent cross-sections for depth estimation. Hence the results should be comparable with those obtained in other studies. Although the water surface was only estimated, a comparison with direct measurements suggested that this technique provided a sufficient representation of flow depth (section 4.3.5.3). It is assumed that variation of the water surface elevation (across slope) is minor compared with microtopographic variations, thus ensuring an accurate depth distribution. It should be noted that this assumption may be invalid where the flow is in the supercritical regime (where superelevation of the water surface is more common); this represents a limitation of this approach.

Each of the distributions discussed above was examined as a candidate for describing overland flow depths across the hillslopes. Normal, lognormal and gamma distributions were also fitted to the observed flow depths using maximum likelihood, as these distributions have frequently been applied to describe patterns observed in hydrology and geomorphology (Markovic, 1965). A summary of the main properties of each distribution can be seen in Table 5.3.

Distribution	Parameters	Probability Density Function	Comments	Examples
Normal	Location μ Scale σ	$\frac{e^{-(x-\mu)^2/(2\sigma^2)}}{\sigma\sqrt{2\pi}}$	Symmetrical, invariable shape	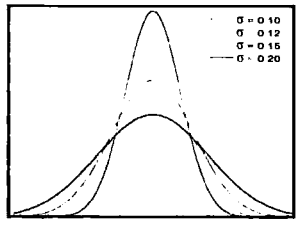
Log-normal	Scale β Shape α	$\frac{e^{-0.5\alpha^{-2}(\log(x)-\beta)^2}}{x\alpha\sqrt{2\pi}}$	Variable shape	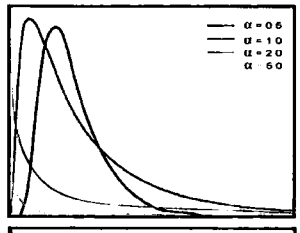
Gamma	Scale β Shape α	$\frac{x^{\alpha-1}e^{-x/\beta}}{\beta^{\alpha}\Gamma(\alpha)}$	Variable shape	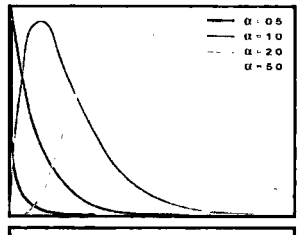
Exponential	Location β	$\frac{1}{\beta}e^{-x/\beta}$	Invariable shape (special case of gamma $\alpha = 1$)	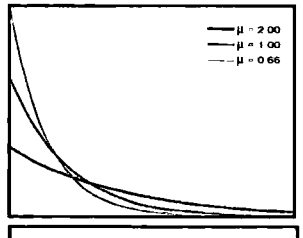
Gumbel (maxima)	Location μ Scale β	$\frac{1}{\beta}e^{-\frac{x-\mu}{\beta}}e^{-e^{-\frac{x-\mu}{\beta}}}$	Invariable shape	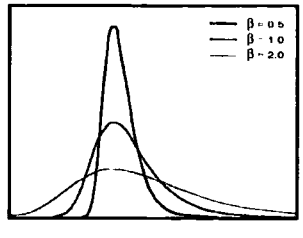

Table 5.3. Summary of distributions fitted to observed flow depths. Note the gamma function $\Gamma(\alpha) = \int_0^{\infty} t^{\alpha-1}\exp(-t)dt$. For a discussion of alternative parameterisations of the gamma distribution see Cox (1992).

Figures 5.19a–c compare the maximum log-likelihoods of the five distributions fitted to the depths of each inundated surface (n = 782). Maximum log-likelihoods between each surface are not directly comparable as they are influenced by the number of depths recorded

(which varies with surface area). To visualise the performance of each distribution across the range of surfaces examined in this study, the maximum log-likelihoods were rescaled for each surface. The scale used for Figure 5.19a–c plots the relative maximum log-likelihoods by surface; the distribution with the best fit is assigned a value of 1, the worst 0, and the intermediate fits are scaled between these two extremes. A summary of these values is reported in Table 5.5. Table 5.3 shows that the shape parameters α of the gamma and lognormal distributions offer a greater degree of flexibility to match the observed distribution of depths. The performance of each distribution can be compared directly as each has two parameters with the exception of the exponential, which is fitted to the depths with only a location parameter.

In almost every case, the gamma distribution outperforms the other distributions. This distribution has previously been used in hydrology to characterise stream link lengths (Abrahams, 1984; Stark, 1991) and precipitation data (Cox, 1992) and has various uses in geomorphology (e.g. to examine particle travel distances; Hassan *et al.*, 1991). As the exponential distribution represents a special case of the gamma, their relative performance is not surprising (and explains the 47 occasions where the exponential fit almost matches that of the gamma). The Gumbel distribution outperforms the gamma for only 12 surfaces. Table 5.4 shows that the most common rank order of maximum likelihoods places the gamma distribution as the best fit, followed by the exponential, Gumbel, log-normal and finally the normal distribution. The Gumbel and log-normal distributions often return similar maximum likelihoods. However, Figure 5.19a–c shows that for several observations, the lognormal provides a much poorer fit.

Rank	**1**	**2**	**3**	**4**	**5**
Normal	26	11	44	67	634
Log-Normal	12	9	274	340	147
Exponential	0	589	117	75	1
Gamma	732	23	27	0	0
Gumbel	12	150	320	300	0

Table 5.4. Frequency table of ranks of depth distribution fits. Note: the exponential distribution nearly tied with the gamma distribution for 47 observations where the two distributions were almost identical.

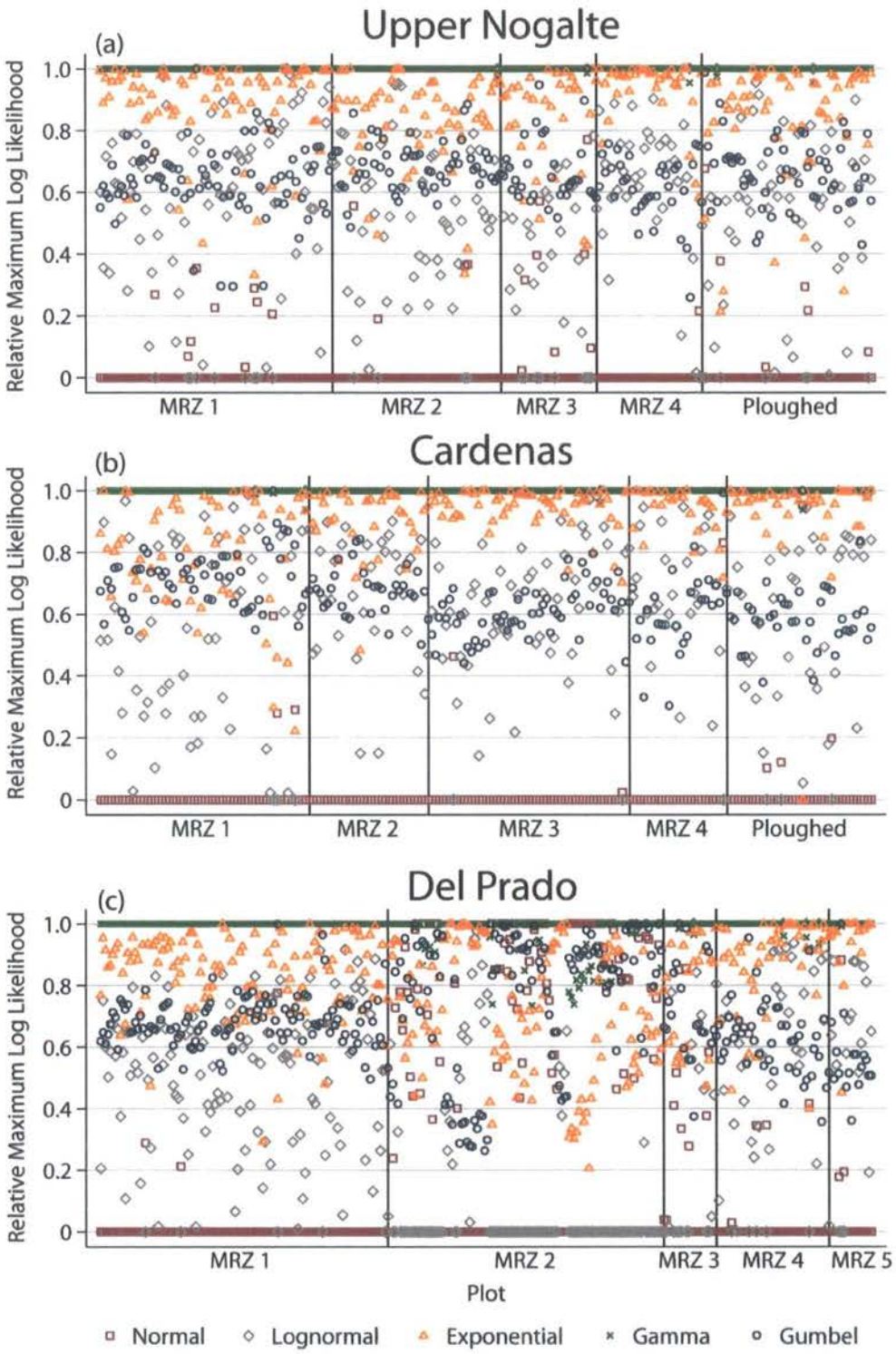

Figure 5.19. Comparison of fits of five statistical distributions to depths observed at each surface on the (a) Upper Nogalte (b) Cardenas (c) Del Prado hillslopes (1 represents the best fit distribution and 0 the worst).

Table 5.5 shows that the relative fits of the distributions are mostly unrelated to plot type and hillslope. The only observable patterns are a decreasing fit to the Gumbel distribution downslope and a progressively better fit to the exponential distribution. This can be seen most clearly at the Del Prado hillslope (Figure 5.19c). Further analysis of Figure 5.19c shows that while the order of distributions at the MRZ 1 plot resembles other surfaces, the depth distributions at the MRZ 2 plot are clearly different. They most closely approximate a normal distribution.

	Normal	Log-Normal	Exponential	Gamma	Gumbel
Total	0.119	0.475	0.848	0.994	0.670
By Plot					
MRZ 1	0.022	0.515	0.842	1.000	0.676
MRZ 2	0.364	0.317	0.782	0.980	0.728
MRZ 3	0.068	0.476	0.879	0.999	0.651
MRZ 4	0.027	0.590	0.909	0.999	0.625
MRZ 5	0.048	0.624	0.928	0.997	0.575
Ploughed	0.031	0.534	0.879	0.999	0.634
By Hillslope					
Upper Nogalte	0.031	0.518	0.864	0.999	0.655
Cardenas	0.018	0.595	0.894	0.999	0.646
Del Prado	0.262	0.355	0.803	0.986	0.699

Table 5.5. Variation of relative maximum log-likelihoods of depth distribution fits with plot type and hillslope.

These results suggest that a gamma distribution consistently provides the best fit to the dataset of flow depths. As seen in Table 5.3 this distribution is fitted using two parameters, the scale parameter and the shape parameter. The product of the two parameters gives the mean depth (which is consistently below the median depth used previously). However, they vary in markedly different ways. The effect of changing just the shape parameter is demonstrated in Figure 5.20a. A smaller value of α creates a more steeply-declining distribution (more similar to an exponential decline) whereas a larger value produces a distribution where the mode is further from the minimum value and more resembles a log-

normal or Gumbel distribution. Figure 5.20a plots the probability density function obtained using the mean value of the shape parameter for each plot. Though a large range is found at each plot, there is a noticeable decrease in the mean gamma shape factor with distance downslope (no such pattern could be observed for the shape parameter of the lognormal distribution). The pattern of this decrease is shown in Figure 5.21a. The effect on the distribution is to produce a distribution more similar to an exponential decline than a Gumbel-type distribution with distance downslope (and explains the pattern observed in Table 5.5).

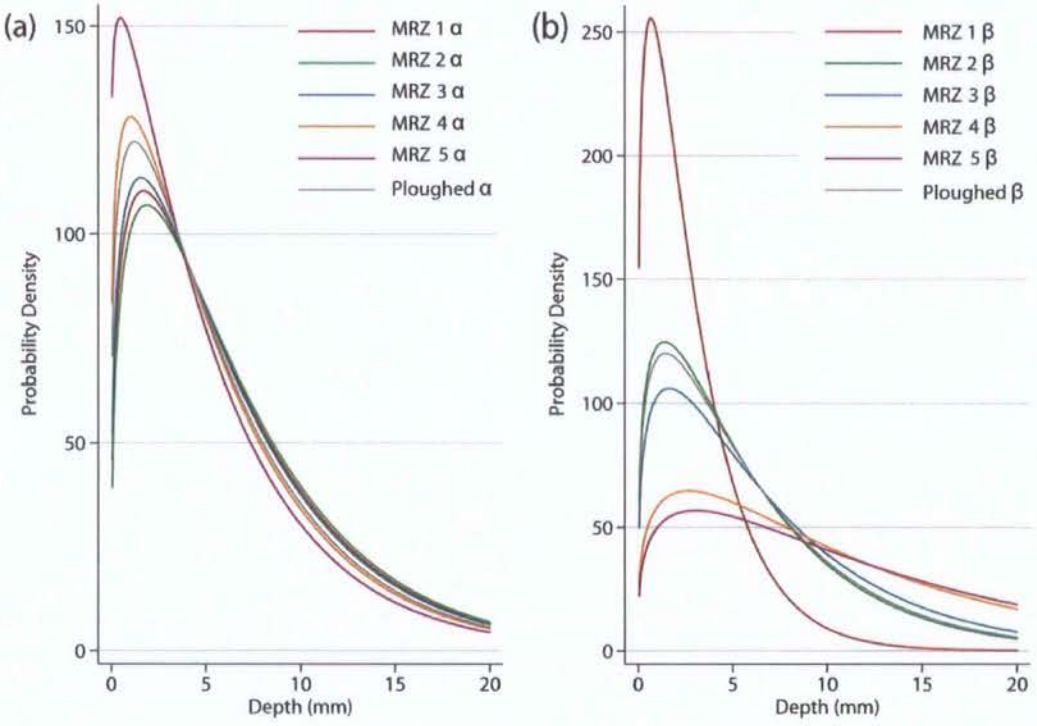

Figure 5.20. Gamma probability density functions for the mean (a) shape parameter α and (b) scale parameter β, for each plot type. For each graph the overall mean value of the other parameter is used.

Increasing the scale parameter stretches the distribution across greater depths (Figure 5.20b). The gamma scale parameter increases with distance downslope (Figure 5.21b) in a manner that resembles the observed variation of median depth (Figure 5.2). As flow concentrates, deeper flows are encountered (and individual flow threads receive higher

discharges); the gamma scale parameter appears to respond to this. The scale or location parameters of the other distributions also reflect this increase in depths.

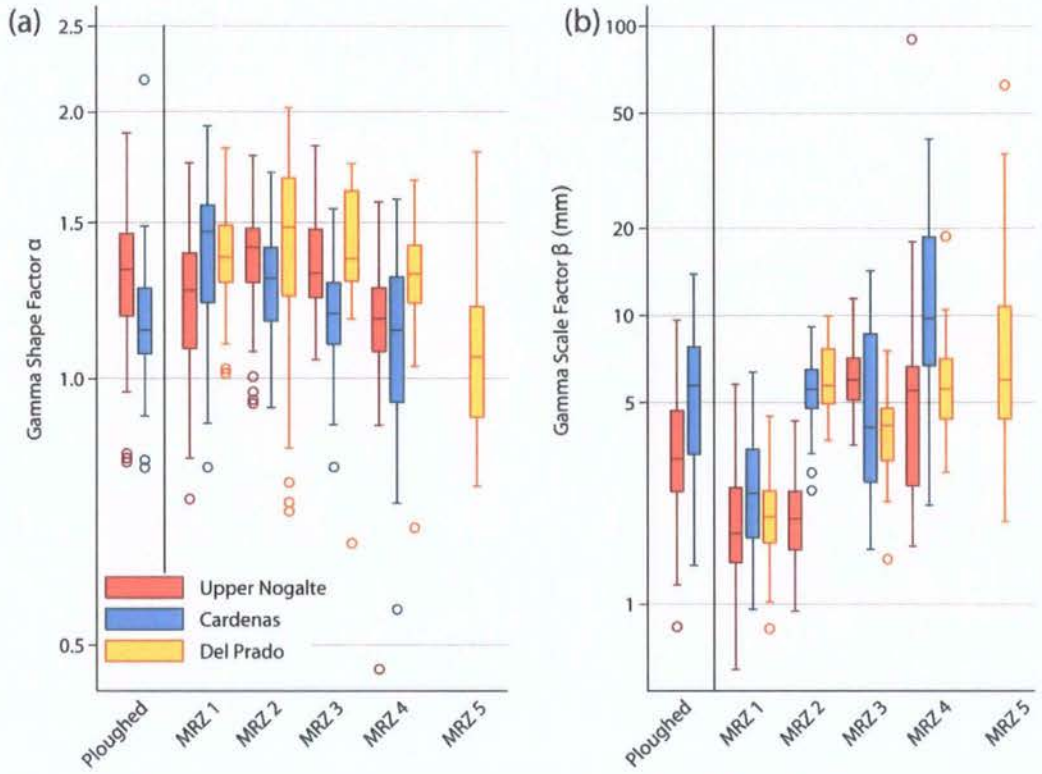

Figure 5.21. Variation of the (a) gamma shape parameter α and (b) gamma scale parameter β, between each hillslope and plot-type.

Figure 5.22 shows the statistically significant positive relationship observed between the gamma scale parameter and discharge (significance level of Pearson correlation $P<0.0001$). The scale parameter picks up the same patterns as the median depth and increases more rapidly with discharge at downslope plots; in this way it resembles the variation of the median depth-discharge power-relation but with a more systematic increase in the exponent with distance downslope (compare Figure 5.7).

While the relationship of the scale parameter β to discharge for each plot resembles the depth-discharge relationship, the shape parameter α appears to affect the exponent of this relationship. The average value of the shape parameter at each plot demonstrated a

statistically significant negative correlation (P=0.0073) with the exponent of the depth-discharge power relation (equation 5.1d). Substituting β for median depth raises the significance level to P=0.0018. The parameters of each of the other distributions were also examined for relationships with each of the hydraulic geometry exponents discussed in the previous sections, with only the shape parameter of the lognormal distribution (P=0.0245) demonstrating a similar (weaker) relationship with the depth-discharge exponent.

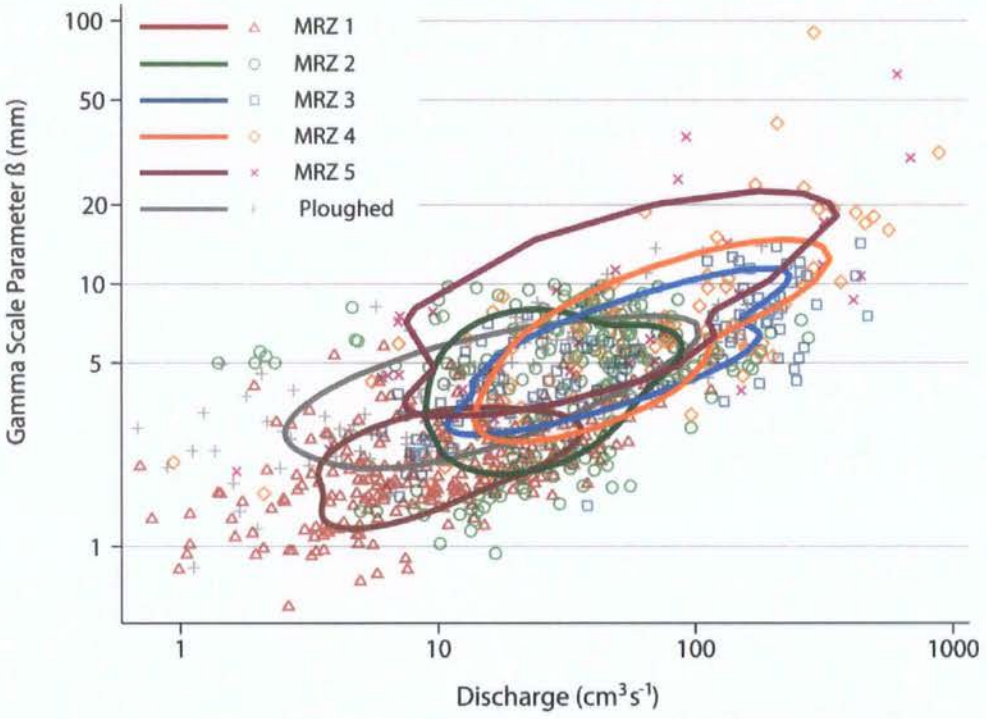

Figure 5.22. Relationship between the gamma scale parameter β, and discharge separated for plot type.

As flow incises the soil surface, a smaller number of larger depths are added to the depth distribution. This stretches the distribution in the manner exemplified in Figure 5.20b but also causes the overall shape of the distribution to decline more steeply with increasing depth (Figure 5.20a) with a steep drop in the probability density function and a long tail of larger extreme values. Surfaces where this type of distribution can be fitted to the depth measurements appear to demonstrate a more rapid increase of median depth (and β) with discharge (as they are often flow concentrations). Where the shape factor is very low, the

few extreme deep flows are found alongside a large number of shallower flows; this may represent the condition identified in section 5.3 where progressive inundation has spread the flow out of the concentration and explains the increase in distributions of this type with distance downslope. Hypothetically, this would increase flow resistance and lead to a more rapidly increasing flow depth with discharge. Such (exponential-type) gamma distributions would not be found for interrill flows as the absence of flow incision features makes small areas of deeper flows unlikely. Simulating an increased water surface level in areas of flow concentrations produces a spike in the β:α ratio (where α decreases with increasing β) at the point where flow spills out of the concentration.

This theory suggests a relationship between the gamma shape parameter and the exponent of the velocity-discharge relationship (a more exponential-type relationship would mean velocity increases more slowly with discharge as more roughness elements become submerged). While such a correlation was observed, it was only significant to P=0.1142.

Figure 5.23 shows the combined effect of the decreasing gamma shape parameter and increasing gamma scale parameter with distance downslope for each hillslope; their values are presented in Table 5.6. The changing depth distributions of the Upper Nogalte and Del Prado hillslopes are very similar; moving downslope the mode shifts closer to the minimum depth and the distribution spreads over a wider range of depths. Cardenas hillslope has the lowest gamma shape factor (Figure 5.21), with the most asymmetric depth distribution of the three hillslopes. As flow concentrations and rills incise, the depth distributions at each hillslope spread over a much wider range of depths, as depth increases more rapidly with discharge (Figure 5.22). From the relationships presented above, it can be suggested that the overland flows on the Cardenas hillslope progressively inundate more roughness elements with increasing discharge. This causes depth to increase more rapidly with discharge, and limits the increase of velocity with discharge (and agrees with observed roughness values presented in Chapter 6).

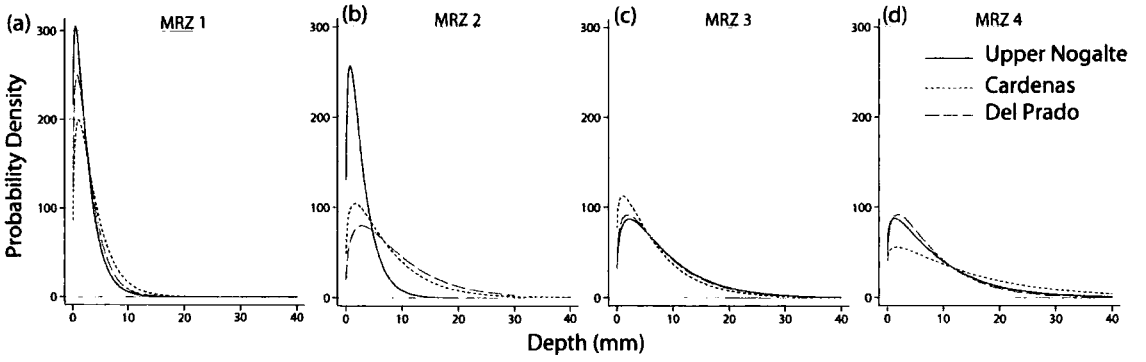

Figure 5.23. Variation of gamma distributions of overland flow depths down the three hillslopes investigated.

	Upper Nogalte		Cardenas		Del Prado	
	Shape α	Scale β (mm)	Shape α	Scale β (mm)	Shape α	Scale β (mm)
MRZ 1	1.245	2.00	1.400	2.63	1.384	2.12
MRZ 2	1.374	2.09	1.300	5.52	1.456	6.27
MRZ 3	1.356	6.27	1.181	5.89	1.403	4.12
MRZ 4	1.176	7.66	1.132	12.82	1.311	6.20
MRZ 5	-	-	-	-	1.097	10.13
Ploughed	1.322	3.66	1.168	5.96	-	-

Table 5.6. Variation of the gamma shape and scale parameters between each plot.

In conclusion, the gamma distribution consistently provides a better fit to the distribution of depths than the Gumbel, normal and lognormal distributions over the entire hillslopes examined here (both interrill and rill flows). It provides the best fit for 94% of the surfaces tested. The exponential distribution also performed well considering that it requires only one parameter. A further advantage of the gamma distribution is that examination of the two parameters is potentially useful as they appear to capture and isolate different aspects of the changing nature of overland flow with distance downslope. Much like the scale (and location) parameters of other statistical distributions, the gamma scale parameter responds to the overall increase in flow depths observed with increasing flow concentration (and discharge) downslope. The shape parameter appears to represent effectively the characteristics of the soil surface that determine the increase in depth with discharge.

Where depth increases rapidly with discharge (at the expense of an increase in velocity) the shape factor is small and the modal depth is closer to the minimum depth.

This relationship is potentially useful. Although the product of the two parameters defines the mean depth, both parameters vary systematically with distance downslope in different ways. The decreasing gamma shape parameter represents the incision of small areas of deeper flow with distance downslope. Such relationships were not observed for the parameters of the other distributions. Providing a quantitative assessment of the flow hydraulics at a point and different variations downslope will impact upon the routing of the flow down hillslopes. The Cardenas hillslope consistently demonstrated a lower gamma shape parameter, which may provide an influence on the more rapidly increasing depth with discharge as it suggests that increases in depth progressively inundate additional roughness elements. This increase in depth over velocity will influence the regime of the overland flow, which (as noted in previous sections) may play a key role in determining velocity-discharge relationships.

The gamma shape parameter of depths is determined by the interaction between surface roughness and overland flows. The following section will examine associations between surface form and flow regime and question whether process-form interactions play a key role in moderating the influence of roughness on the form of the velocity-discharge relationship.

5.5 Surface-Flow Interactions

Govers (1992) proposed that the flow velocity of eroding rills was independent of slope and soil type. From an analysis of several datasets collected in different studies, he suggested that flow velocity V (m s^{-1}) could be estimated using only discharge Q (m^3 s^{-1}) from the hydraulic geometry relation

$$V = 3.52Q^{0.294}. \tag{5.2}$$

This is a simple regression equation; the coefficient and exponent have no physical basis. Many studies have since confirmed the insensitivity of velocity to slope in rills in different soil conditions (e.g. Nearing *et al.*, 1997, 1999). This relationship potentially offers a simple method of routing runoff through rills, avoiding the need for estimating a resistance coefficient as required by the traditional approaches to modelling flow resistance discussed in Chapter 2 (namely, the Darcy-Weisbach, Chézy and Manning equations), which may not apply in these situations.

Recently, hypotheses have been proposed to explain this phenomenon; these focus on the relationship between the soil surface and the nature of the flow itself. In particular, the influence of the flow regime on the ability of flow to erode its bed and the resulting bed roughness have been proposed as moderating influences, reducing the dependency of velocity on slope. Previous sections have described how such bed roughness may affect the velocity-discharge relationship through altering the distribution of flow depths; it is possible that this roughness is in turn influenced by the nature of the flow itself. Testing such hypotheses requires an appreciation of the fine scale variation of rill flows; such information has become available only recently (see Giménez *et al.*, 2004 for an example). The dataset presented in this thesis is now used to test equation (5.2) (section 5.5.1) and to examine the nature of interactions between rill flow and bed roughness (section 5.5.2).

5.5.1 Slope Independence of Rill Flow

The discharges measured in this study span the same range as Govers (1992), yet recorded velocities are generally less than those predicted by equation 5.2 (Figure 5.24). There are several possible reasons for this. Equilibrium conditions were not established in the rills in this study. The flows examined are travelling over previously exposed soil surfaces and so suction forces may act to slow the advancing water. Also, the studies examined in Govers (1992) examined flow over silty loamy soils. The soils at all three hillslopes can be defined as sandy loams containing a coarser grain size distribution. A final difference of note is that the flow in this study is divided into small sections of just several centimetres in length and the slope of that section is calculated. This localised calculation of slope results in much

higher gradients in Figure 5.24a than those larger-scale gradients examined by Govers (1992).

From Figure 5.24a it is clear that, at this scale, greater slopes do not result in faster flows in rills. This agrees with the findings of Govers (1992). However, examination of the data suggests that the opposite may be true: faster flows are found on shallower slopes. When this calculation is repeated for the general plot slope, slope independence is evident.

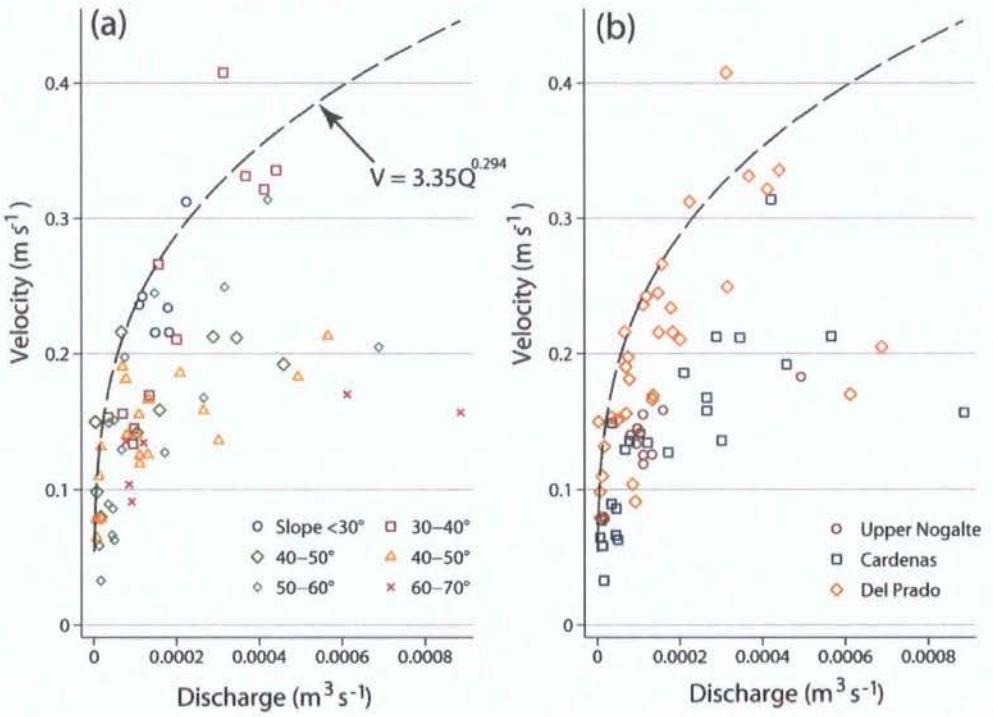

Figure 5.24. Measured rill flow velocities plotted against discharge for (a) different slope categories and (b) different hillslopes. The equation displayed is that of Govers (1992).

The pattern observed in Figure 5.24a may be a consequence of the distribution of slopes between the three hillslopes studied. Figure 5.24b shows the same relationship, but with the data points categorised by hillslope. A clear division can be seen. The Del Prado hillslope closely obeys equation 5.2. The measured velocities of the other two hillslopes plot below this line. The Del Prado hillslope has the finest grain-size distribution and lowest infiltration which more closely resembles the conditions for which the equation was

developed, while the Cardenas and Upper Nogalte hillslopes have an increasingly coarsening grain size distribution (with a thicker crust observed at the Cardenas hillslope). While Govers (1992) observed no systematic effects of soil characteristics, there was a suggestion that equation 5.2 should be tested over different soil types.

Abrahams *et al.* (1996) found that rill flow velocities on semi-arid hillslopes plotted below that of Govers (1992). The data of Abrahams *et al.* (1996) are comparable to that plotted in Figure 5.24. However, the minimum discharge recorded was 5×10^{-4} m^3 s^{-1} and so the two datasets do not completely overlap. The rill velocities recorded by Nearing *et al.* (1999) and Takken *et al.* (1998) also plot below those predicted by equation 5.2. However, the authors conclude that their data just fell within the envelope of Govers (1992), either corroborating equation 5.2 or at least demonstrating a relationship of a similar form. Previously, Nearing *et al.* (1997) reported that the velocity-discharge relationship was independent of soil type only in laminar flows; there was a detectable influence of soil type in the turbulent regime. This finding agrees with the data presented below: most rill flows are in the turbulent regime (the 17 data points representing laminar flows are located at the lowest discharges).

Figure 5.25a shows several relationships between velocity and discharge. Again, the equation of Govers (1992) overpredicts velocity. Four other regression equations are also shown, developed from the rill-flow (MRZ 4) dataset of this study. A 'general equation' was developed, relating velocity and discharge for the dataset as a whole

$$V = 1.77Q^{0.266}; \tag{5.3}$$

a further three empirical equations show separate relationships for each hillslope.

$$\text{Upper Nogalte} \quad V = 1.44Q^{0.259} \tag{5.4a}$$

$$\text{Cardenas} \quad V = 2.38Q^{0.324} \tag{5.4b}$$

$$\text{Del Prado} \quad V = 1.47Q^{0.221} \tag{5.4c}$$

The exponents differ from those in Table 5.2 because only rill flows are considered here. As already noted, the Govers (1992) equation was produced from flow measurements under

different conditions from those examined here; therefore the observation that the concordance correlation (a summary of the tightness of fit of data around its reduced major axis and the nearness of that axis to the line of perfect concordance; see Lin, 1989, 2000 and Cox, 2006) between the velocity prediction of equation 5.3 and the measured velocities (0.586) is greater than that of the Govers (1992) equation (0.425) is not surprising. The division of the dataset into different hillslopes (and therefore soil types), however, provides a greater increase still (with a concordance correlation of 0.768). The Pearson correlation coefficient demonstrates a more pronounced increase.

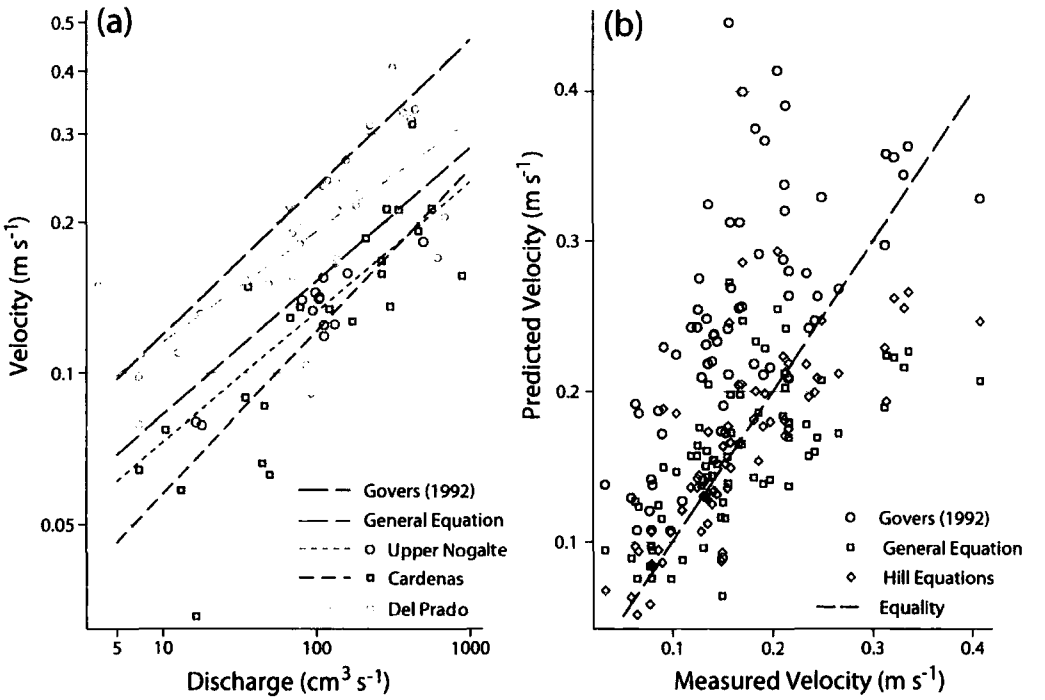

Figure 5.25. (a) Relationships between discharge and velocity developed in this study and Govers (1992) (log scale), (b) Comparison of velocity predictions using equation 5.2, a general equation developed from this dataset (5.3), and hill equations (considering each hillslope separately, 5.4a–c).

This suggests that soil type has a significant influence on the relationship between velocity and discharge in rills. In more resistant materials, the walls of a rill will be more stable: narrower rills can be maintained, thus making flow more efficient hydraulically. The rills of the Cardenas hillslope have a larger hydraulic radius than those of the other hillslopes

(measured simply from median depth and width of rill, thereby ignoring roughness effects). This suggests that the Cardenas rills should have the fastest flow for any given discharge, yet the opposite is true.

A compensating effect must be retarding the flow. Govers (1992) proposes such an effect (represented schematically in Figure 5.26). A more resistant soil will be able to maintain greater roughness in the rill bottom which acts to resist the flow. Indeed, Abrahams *et al.* (1996) found that bed roughness had a greater effect on flow velocity than slope. The question of measuring roughness and its relationship with flow resistance is raised in Chapter 6. However, note that, in general, the rills of the Cardenas hillslope maintain a rougher bed than those of other hillslopes. This effect appears to over-compensate the increased hydraulic radius in resistant soils (and is manifested as a lower gamma shape parameter of depth distributions).

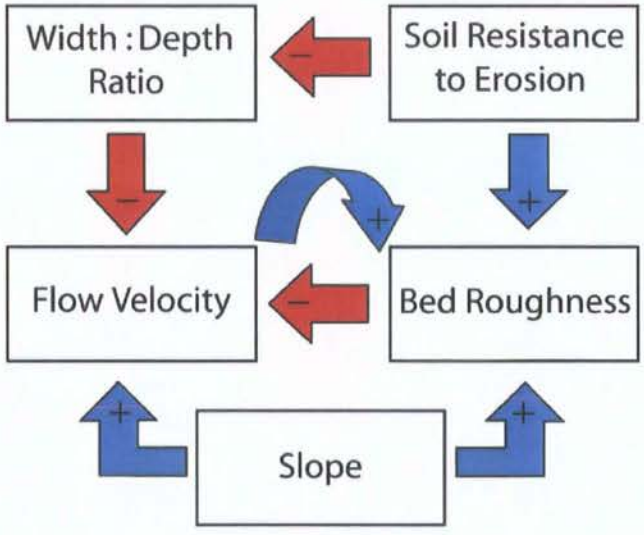

Figure 5.26. Flow diagram summarising Govers' (1992) conceptual model of the factors influencing flow velocity in rills (for a constant discharge) with the addition of a feedback between velocity and roughness. Pluses indicate a positive relationship; minuses indicate negative relationship. Adapted from Giménez and Govers (2001: p.792) and Abrahams *et al.*, (1996: p.37).

This relationship is found only where the rill flow is capable of eroding its own bed. Takken *et al.* (1998) noted that the velocity-discharge relationship of equation 5.2 did not apply in areas where soil was strongly consolidated. Studies using fixed-beds (Rauws, 1988; Foster *et al.*, 1984) observed increasing velocities with increasing slope. Where flow is capable of eroding the soil, hydraulic resistance will depend on the relationship between the soil surface and flow characteristics. There must be a feedback mechanism in operation linking characteristics of the flow to the nature of the bed (this feedback has been added to the hypothesis of Govers (1992) in Figure 5.26). How does flow velocity alter bed roughness to moderate itself?

5.5.2 Linking Rill Flow to Bed Roughness

Recent studies suggest that the Froude number and hydraulic jumps provide the mechanism linking velocity to roughness. As mentioned in Chapter 2, the Froude number is a dimensionless number of fluid mechanics which characterises the flow speed relative to the speed of surface waves (equation 2.20). The Froude number appears in a key classification of flows into two regimes: where Fr < 1 the flow can be described as subcritical (a disturbance in the flow can travel upstream), but when the velocity becomes too high for flow disturbances to propagate upstream (Fr > 1), the flow becomes supercritical. Flow switches from supercritical to subcritical when the wave is stationary relative to the bed; at this critical condition there is an abrupt increase in depth, known as a hydraulic jump. The effect of such jumps of velocity-depth relationships was mentioned briefly in section 5.3.

Massey and Ward-Smith (2001) note that hydraulic jumps are an effective way to dissipate mechanical energy in flows as they induce eddy formation and turbulence. The loss of mechanical energy is a function of the difference in depths before and after the jump. On an erodible soil surface, the resultant downward flux of momentum can cause intense bed scour and erode the soil surface. Grant (1997) examined the physical mechanisms behind the transition between flow regimes, presenting a cyclical model of surface wave and bedform deformation where accelerating flow deforms an initially plane bed, which in turn initiates surface waves eventually leading to a hydraulic jump and bed scour. Grant (1997)

hypothesised that such interactions between flow hydraulics and bed configuration maintain a constant average Froude number in high-gradient alluvial channels.

Giménez and Govers (2001) argued that such interactions between soil microtopography and flow characteristics can be applied to eroding rills. Minor variations in surface roughness (such as those produced as flow progressively inundates roughness elements; Figure 5.18b) can initiate a hydraulic jump, similar to the development of hydraulic jumps in flow over a broad-crested weir. Giménez *et al.* (2004) showed that the resultant energy dissipation leads to the formation of pools and steps along a rill bottom. It is possible therefore that transitions between supercritical and subcritical flows are a precondition for rill erosion to provide a mechanism for regulating flow velocity on steeper slopes. Giménez *et al.* (2004) emphasise the need for further experimental research on different soil types and detailed data on longitudinal variations of flow velocities in rills.

Figure 5.27 displays the distributions of observed Froude numbers (across the entire hillslopes) separated for each hillslope. Each distribution has a median around 0.44 (Cardenas) or 0.54 (Upper Nogalte and Del Prado) with a long tail of upper values. All values are below 2.0 with the single exception of one outlier at the Del Prado plot. The Del Prado hillslope showed the most evidence of supercritical flow, while the Cardenas hillslope displayed the least (only 2 observations).

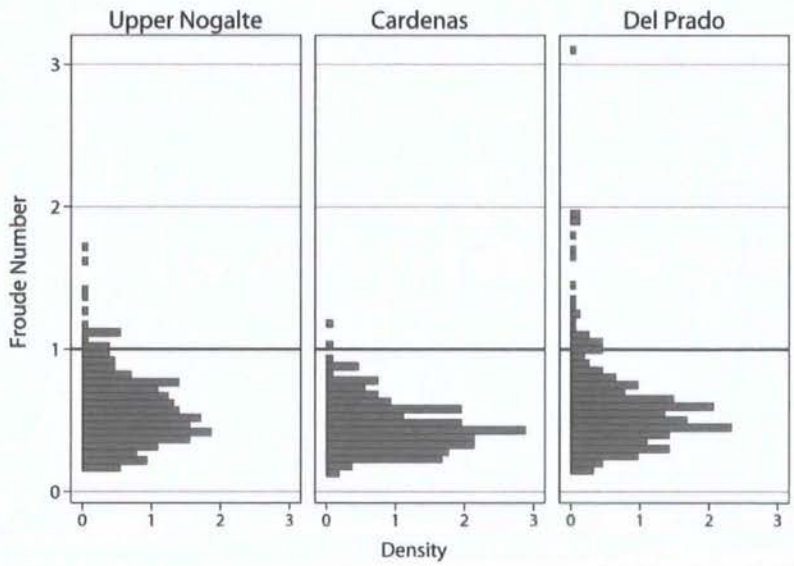

Figure 5.27. Vertical histograms demonstrating the distribution of observed Froude numbers for each hillslope.

Figure 5.28 shows that the areas of supercritical flow are predominantly (though not exclusively) located in flow concentrations. 6% of all measurements showed supercritical flow (this increases to 20% considering only areas of observed flow concentration).

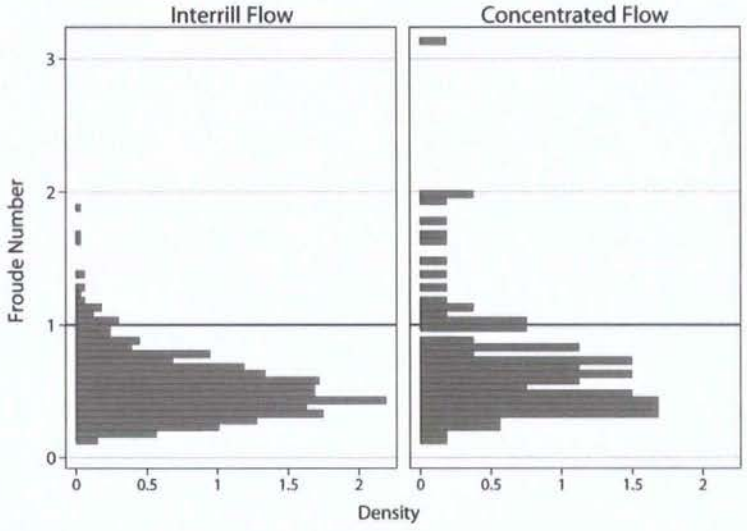

Figure 5.28. Vertical histograms demonstrating the distribution of observed Froude numbers for both interrill flow and concentrated flow.

The spatial distributions of areas experiencing supercritical flow can be mapped for each plot. This is displayed for the Del Prado hillslope in Figure 5.29. Flow concentration begins at MRZ 3; rills start to form at MRZ 4. Considering the MRZ 3 plot, the area where $Fr > 1$ exactly corresponds to where flow concentration was identified in the field. Few areas of supercritical flow exist upslope of this point (note that MRZ 2 is missing from Figure 5.29 as it exhibits no supercritical flow). For the MRZ 4 plot, the rill becomes fully incised just upslope of the middle patch of supercritical flow. This is also found on the MRZ 3 plot of the Upper Nogalte hillslope (Figure 5.30).

The Upper Nogalte hillslope demonstrates fewer areas of supercritical flow. Interestingly, most were located on the MRZ 2 plot; this was the steepest plot surface containing fast flow yet no evidence of rill formation. The imposed discharge may be larger than previously experienced on this particular plot surface; the pattern seen in Figure 5.30 might be an example of this fast flow beginning to erode a rill. While erosion and sediment transport

was negligible during these experiments, this MRZ 2 plot was the only surface where some sediment transport was observed (where small clasts from sprayed lines had travelled downslope). However, it is envisioned that this process-form feedback mechanism operates on longer timescales than could be observed during these flow experiments.

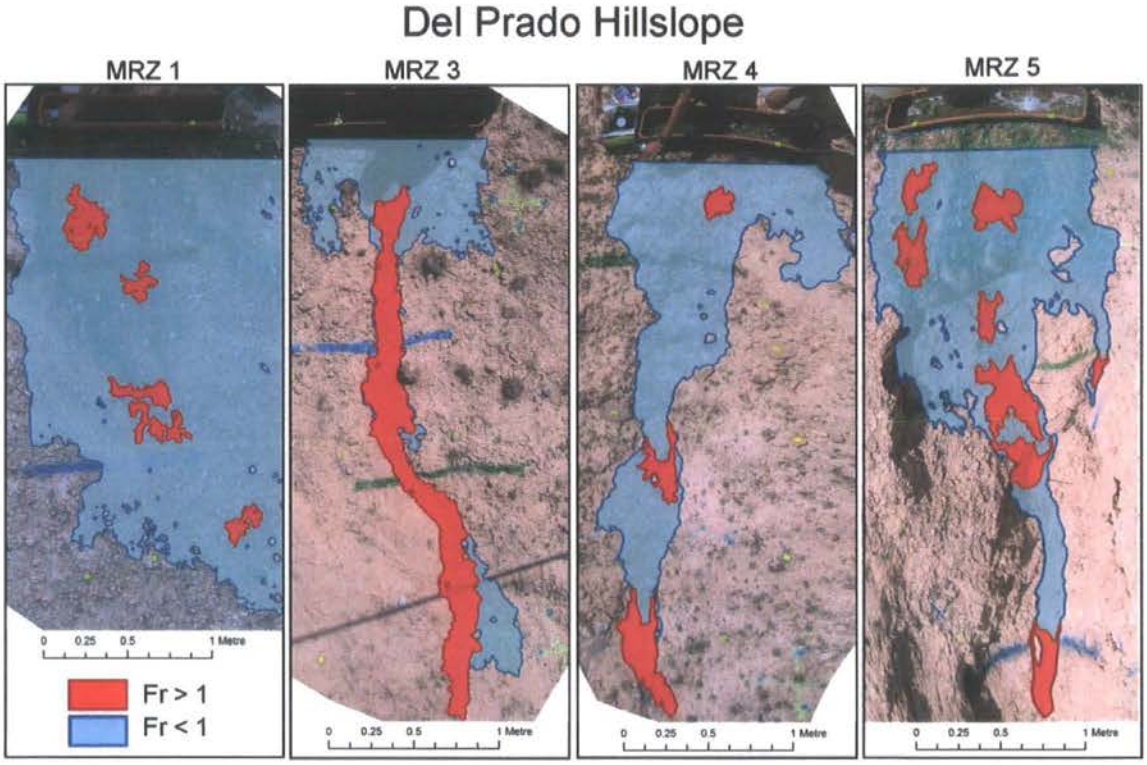

Figure 5.29. Areas of supercritical (Fr > 1) and subcritical (Fr < 1) flow observed on the Del Prado hillslope. The MRZ 2 plot showed no areas of subcritical flow.

Only two occurrences of supercritical flow were observed at the Cardenas hillslope; none were located in rills. Nevertheless, no correlation was observed between slope and the Froude number. Placing this in the context of the Grant (1997) hypothesis and the results previously discussed, it appears that the Cardenas hillslope has the most resistant soil, and the narrowest rills. This resistant bed maintains a higher roughness, reduces the flow velocity and prevents hydraulic jumps from eroding the surface further thereby causing roughness effects on velocity to dominate over slope effects (removing the feedback between velocity and roughness in Figure 5.26). This feedback mechanism may have been interrupted by the development of the strong crust that was observed on this hillslope.

Thus, a large rainfall event with high rill discharges would be required for the system to return to the equilibrium Froude numbers of the Grant (1997) hypothesis. Conversely, the Del Prado hillslope has the most erodible soil, which erodes wider, smoother rills. The faster flow produces supercritical flow and more hydraulic jumps which may eventually increase the roughness and maintain the balance between slope and roughness proposed by Govers (1992). Thus the feedback mechanism proposed in Figure 5.26 is in place.

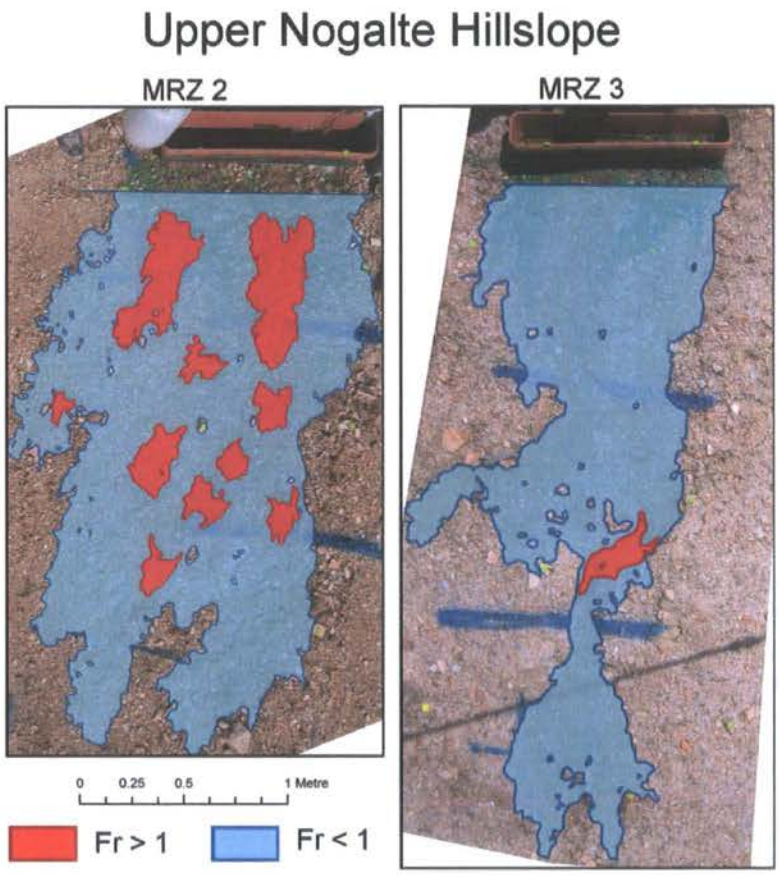

Figure 5.30. Areas of supercritical (Fr > 1) and subcritical (Fr < 1) flow observed on the Upper Nogalte hillslope.

In total, 27 hydraulic jumps were recorded over the three hillslopes. The question remains: are these jumps triggered by a specific property of the soil surface (just as supercritical flow is induced over a broad-crested weir)? Giménez *et al.* (2004) examined interactions between flow velocity and bed morphology, suggesting that hydraulic jumps took place as flow decelerated after steps in the rill bottom profile. The data presented here have the

potential to be more specific than this; perhaps some measurable property of the bed roughness can be isolated as a likely candidate for inducing hydraulic jumps. While Chapter 6 examines the relationship between flow and roughness in greater detail, a brief investigation of the relationship between roughness and hydraulic jumps is presented here.

To test whether surface roughness influences hydraulic jumps, *t*-tests were performed on a variety of roughness measures (described in Table 4.3 and Appendix 1). The flow was divided into patches where supercritical flow was maintained and those patches where a hydraulic jump was observed. Table 5.7 displays the two-sided *P*-values for each roughness measure demonstrating a significant difference between groups (i.e. $P < 0.05$).

Roughness Measure	*t*-test two-sided *P*-value ($\Pr(\|T\| > \|t\|)$)	
Complete Dataset (*n* = 76)		
Slope	0.0038	
Protruding Frontal Area (per m^2)	0.0221	
3d Tortuosity (~35 mm scale)	0.0285	
Rills only (*n* = 16)		
3d Tortuosity	0.0021*	(0.0050)
Protruding Frontal Area (per m^2)	0.0077*	(0.0095)
Thread Nearest Neighbour	0.0098	
Perpendicular Tortuosity	0.0132	
Parallel Tortuosity	0.0385	

* Standard deviations of two groups tested were unequal. Numbers in brackets indicate results from a Wilcoxon rank-sum test.

Table 5.7. Two-group mean comparison tests (between areas maintaining supercritical flow and those triggering a hydraulic jump) for roughness measurements with *P*-values $P < 0.05$. Roughness measures are defined in Table 4.3 and Appendix 1.

Slope had an influence on the complete dataset but was not significant when considering just rill flows. The most significant difference between the groups was displayed by surface (3d) tortuosity (Figure 5.31a). In general, roughness measurements which examine the ratio

between measured area (or length) and that of the equivalent plane (or straight line) appeared to influence flow regime more than other measures of roughness. This influence was more pronounced when just rill flow is considered (Figure 5.31b).

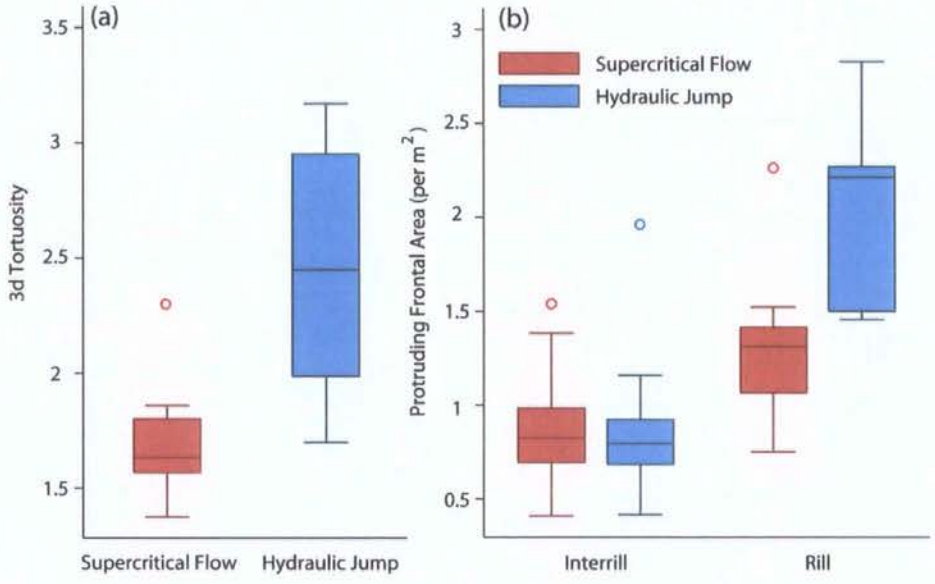

Figure 5.31. Comparison of the distributions of roughness measures found in areas of supercritical flow and where hydraulic jumps take place. (a) 3d tortuosity T_{3D}; (b) frontal area protruding into the flow F_T (per m^2) separated for interrill and rill flows.

Figure 5.31 suggests that supercritical flow can only be maintained where these roughness measures are below some limit. In areas where the surface becomes rougher (as defined by these specific measures) a hydraulic jump is triggered. This hypothesis is examined in greater detail in Figures 5.32–5.34.

For the rill flow in the Del Prado MRZ 4 plot (Figure 5.32), supercritical flow is initiated immediately downstream from a point where each measure identified a reduction in roughness. As the bed becomes rougher, a hydraulic jump occurs. This alternating pattern can be seen several times in the gully flow at the Del Prado MRZ 5 plot.

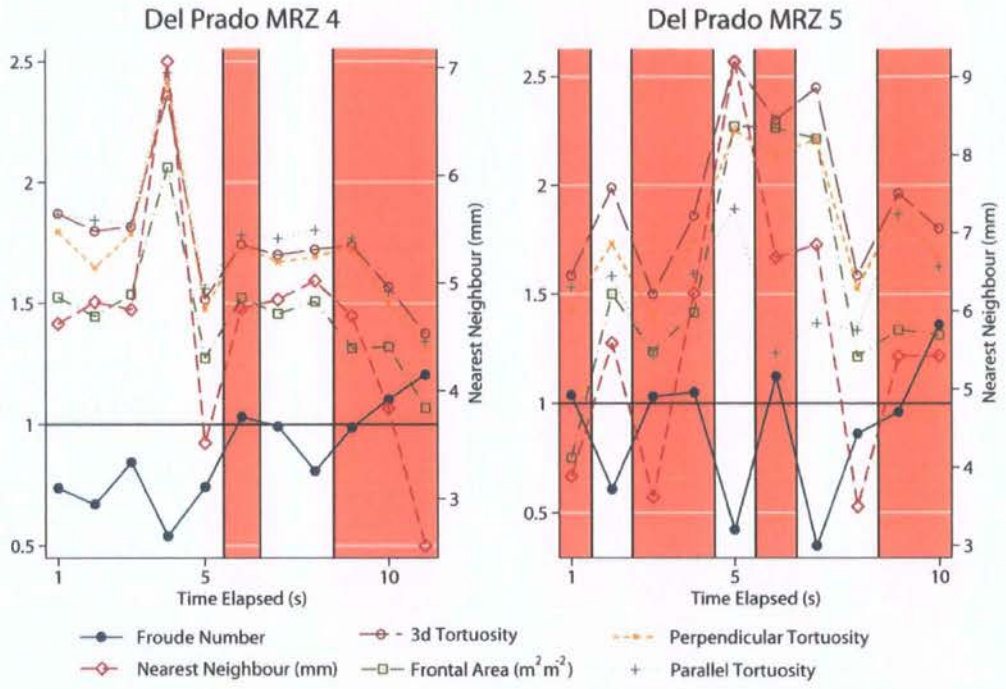

Figure 5.32. Variation of Froude number and selected roughness measures (y-axis) down a rill (MRZ 4) and gully (MRZ 5) at the Del Prado hillslope (as shown in Figure 5.29). The flow was tracked downslope; therefore time elapsed also represents movement downslope. The red shaded areas represent conditions where Fr > 1; the Nearest Neighbour measure is plotted on a separate scale.

Further upslope, before any rill has been incised, the Froude number in a flow concentration remained above 1 (Figure 5.33). Here the roughness measurements were generally lower than further downslope, perhaps below the threshold necessary to initiate a hydraulic jump (which for the discharge imposed in these experiments appears to be between 1.5 and 2.0 for the three tortuosity measures, around 1.5 for the protruding frontal area (per m^2), and 5–6 mm for the Nearest Neighbour measure). An increase in roughness towards the end of the flow concentration appears to result in a decline of the Froude number. It is likely that lower discharges would trigger a hydraulic jump and increase the roughness of the bed through localised scour (potentially initiating rill erosion). Indeed, such hydraulic jumps were observed at this plot during the variable discharge experiments (Figure 5.18b). The rill at the Cardenas hillslope which showed no supercritical flow also displayed a rougher bed, with values generally above the proposed thresholds.

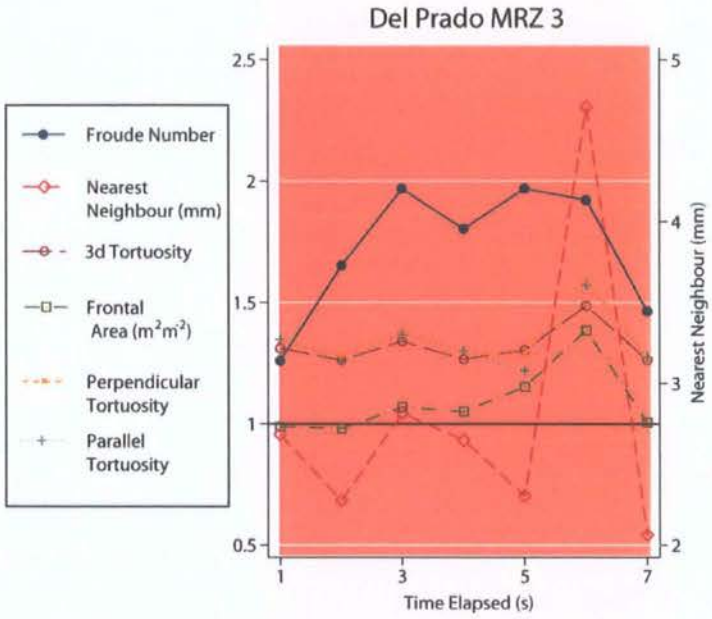

Figure 5.33. Variation of Froude number and selected roughness measures (y-axis) down a flow concentration (MRZ 3) at the Del Prado hillslope (as shown in Figure 5.29). The flow was tracked downslope; therefore time elapsed also represents movement downslope. The red shaded area represents conditions where Fr > 1; the Nearest Neighbour measure is plotted on a separate scale.

The strongest interactions between these roughness measures and the flow regime have been discovered in rill flows. Figure 5.33 shows that this relationship potentially holds for minor flow concentrations, but as no hydraulic jumps were recorded here, the data remains inconclusive. Figure 5.34 displays roughness measures and the Froude number for both a flow concentration (MRZ 3) and further upslope in an area of wash deposits (MRZ 2). A much smaller variation of roughness is found over the MRZ 2 wash deposits (note the exaggerated scale for the Nearest Neighbour measure). The locations of hydraulic jumps appear unrelated to the roughness variations at this hillslope location. The concentrated flow, however, appears to behave more like rill flow, responding to a decrease and subsequent increase in roughness with supercritical flow and a hydraulic jump respectively.

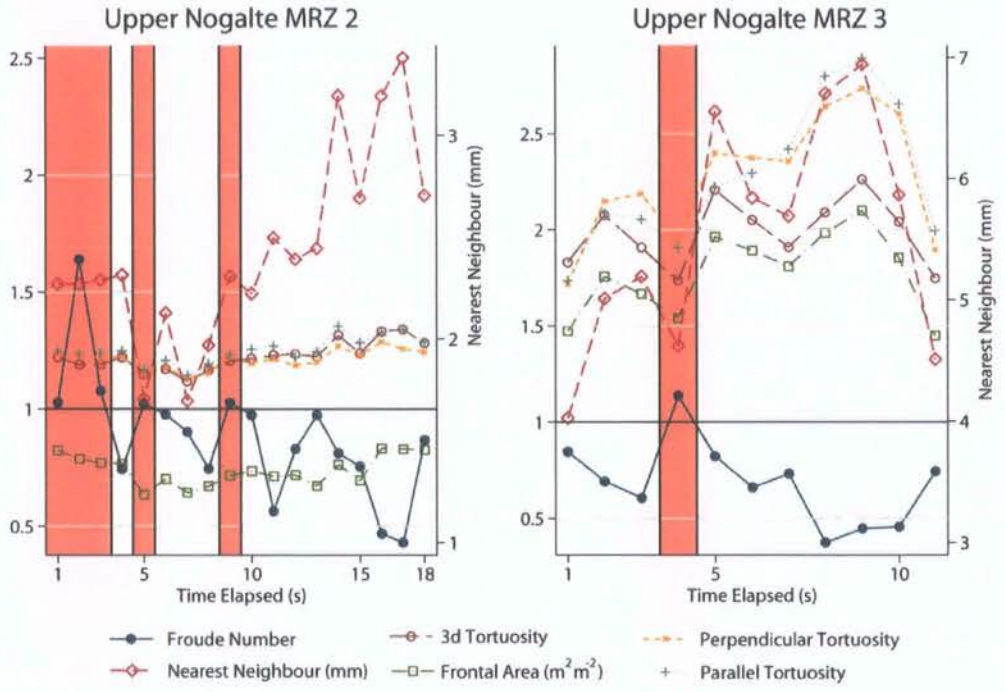

Figure 5.34. Variation of Froude number and selected roughness measures (y-axis) moving downslope over an area of wash deposits (MRZ 2) and down a flow concentration (MRZ 3) at the Upper Nogalte hillslope (as shown in Figure 5.30). The flow was tracked downslope; therefore time elapsed also represents movement downslope. The red shaded areas represent conditions where Fr > 1; the Nearest Neighbour measure is plotted on a separate scale.

In conclusion, the rill flows examined in this study display lower velocities than those predicted by Govers (1992) (equation 5.2). This is in agreement with many other studies. The results support the conceptual model of Govers (1992) with further emphasis on the influence of soil resistance. This is unsurprising as this study considered three hillslopes which were selected because they cover the range of soil types found in the study catchments. The hypothesis presented here details a feedback loop between flow velocity and bed roughness (added into Figure 5.26), which provides a mechanism through which the properties of the flow influence soil surface form. This feedback is primed by the soil type, particularly its resistance to erosion. The data agree with the suggestions of Giménez and Govers (2001) and Giménez *et al.* (2004) that the dissipation of energy as a consequence of a hydraulic jump erodes a rill bed, creates a rougher surface, thereby

slowing the flow. It is likely that this is a dynamic process, which will depend on rain magnitude and intensity and can be affected by the development of a surface crust (as seen at the Cardenas hillslope). While Giménez *et al.* (2004) suggested that this feedback loop between flow and bed roughness is necessary for rill erosion, the results here suggested that this can occur with even minor flow concentrations. Finally, the measurement of bed roughness was examined more precisely and several key parameters extracted. The results appeared to emphasise the importance of 'tortuosity' (on both surfaces and transects), protruding frontal area and nearest neighbour measurements as the components of roughness responsible for this feedback.

5.6 Summary

This chapter describes the range of overland flows simulated on three natural semi-arid hillslopes before proposing explanations for these observed variations. Systematic changes in flow variables were observed over the range of hillslopes examined in this study. These patterns found across each hillslope are more notable than differences between hillslopes of different soil type. As flow begins to concentrate, both median depth and velocity increase and flows become more turbulent. Further downslope, depth increases more rapidly with discharge; velocity increases less rapidly. Where flow concentrations have formed, an increase in discharge will inundate roughness elements that were previously protruding from the flow, which acts to moderate any increase in velocity. This places emphasis on the importance of characterising the changing nature of surface form with increasing discharge, particularly the distribution of depths. Depth distributions have been shown to fit most closely to a two-parameter gamma distribution, with each parameter apparently isolating a different aspect of the changing nature of the soil with distance downslope. The scale parameter appears to represent the general increase of depths with discharge as flows concentrate; the shape parameter is more related to the form of the soil surface and potentially provides a control on the rate of depth (and velocity) increase with discharge.

The flow regime also appears to influence the velocity-discharge relationship. Figure 5.8 shows a bifurcation in this relationship at high discharges (with a high-velocity super-critical limb and a lower velocity sub-critical limb). A hydraulic jump has been shown to

produce a decrease of velocity with increasing discharges (as flow moves from the supercritical limb to the subcritical limb). Such jumps appear to be triggered by an increase in certain roughness parameters (particularly those representing a tortuosity measurement) and provide a mechanism for the observed slope-independence of velocity in concentrated flows with erodible beds (through process-form interactions). Where the soil is less erodible, overland flow cannot modify the soil surface, a higher roughness is maintained which leads to a more rapid increase in median depth with discharge (at the expense of velocity, which follows the sub-critical limb) and the progressive inundation of roughness elements with increasing discharge produces an exponential-type depth distribution (low gamma shape parameter). This link between depth distribution and roughness provides an explanation for the observed increase in the exponent of the depth-discharge relationship with decreasing shape parameter (and the opposite relationship for the velocity-discharge power relation).

This chapter has begun to examine the influence of surface roughness upon overland flows through its relationship with flow depth distribution and its effect on flow regime. Chapter 6 now focuses on this interaction between form and process, questioning whether flows over such complex surfaces can be characterised using the conventional approaches outlined in Chapter 2, or whether an approach based on quantifying the observed form-process interactions may better represent the process of overland flows over natural slopes.

CHAPTER 6

PREDICTING FLOW RESISTANCE FROM SURFACE ROUGHNESS

6.1. Introduction

The review presented in Chapter 2 emphasised the difficulties of developing resistance equations for both steep mountain streams and overland flows where the assumptions underlining more conventional approaches limit their range of applicability. This chapter tests the ability of the conventional (and some more recent) approaches, discussed in Chapter 2, to predict the flow resistance observed in this study (section 6.2). Reasons for any shortcomings are also suggested. Section 6.3 briefly summarises improvements to the representation of resistance to overland flows made possible by the high-resolution dataset available in this analysis. To conform to the best practice suggested in Chapter 2, this section includes a brief outline of how this approach of representing flow resistance (essentially a modified Darcy-Weisbach friction factor) can be derived from the principles of fluid mechanics and explicitly identifies the assumptions made in doing so.

Section 6.4 discusses the different roughness measures used in this thesis. The calculation of each roughness measure represents an implicit hypothesis that the method of expressing complex surface form is related to flow resistance. Section 6.5 then develops empirical relationships between the observed flow resistance and these roughness measures. The observed relationships vary across hillslopes and the best method of incorporating this variation is investigated. The resulting equations may be used to replace standard resistance

equations, predicting overland flow velocity across semi-arid hillslopes. Although the regression equations are purely empirical, section 6.5.3 attempts to infer process from these equations. Finally, section 6.6 summarises the results presented in this chapter and places them in the context of the remaining chapters.

6.2 Conventional Methods of Determining Resistance

This section revisits the methods of conceptualising flow resistance discussed in Chapter 2 and tests them against the overland flow data obtained in this study. A common method of representing flow resistance is the Darcy-Weisbach friction factor f (defined in equation 2.6). Figure 6.1 displays the recorded variation of f across and between hillslopes. The pattern between hillslopes appears to partly reflect the variation of slope angles (indicating the importance of the slope term in the calculation of f). The Cardenas hillslope shows the greatest resistance and most pronounced increase of f downslope; this pattern is less obvious at the other two sites. The Del Prado plots demonstrate the lowest resistance and widest range of f values. Table 6.1 displays the median values of f observed at each plot.

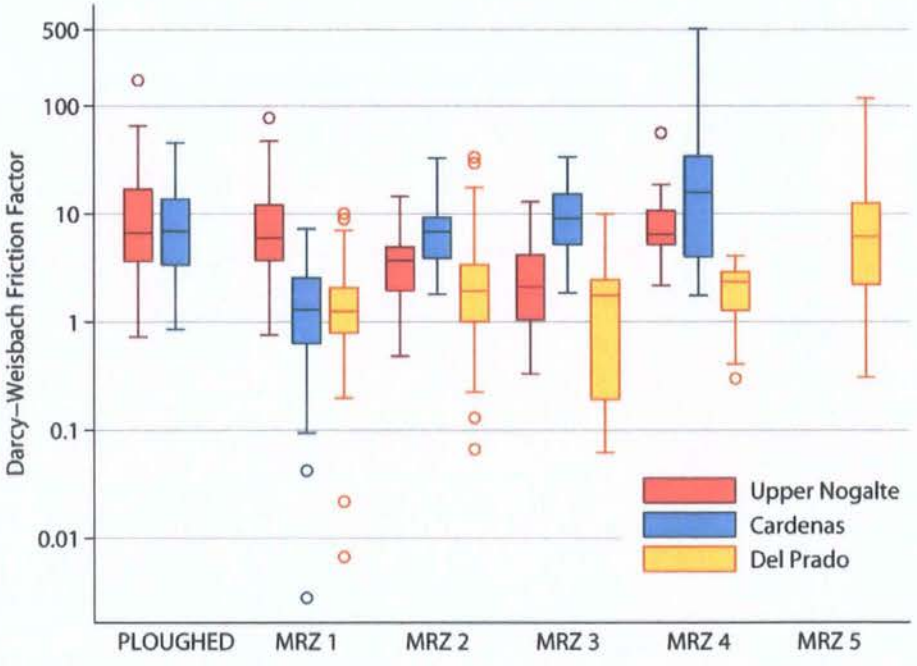

Figure 6.1. Variation of the Darcy-Weisbach friction factor (calculated with equation 6.6) between each plot and site. MRZs (Morphological Runoff Zones) relate to hillslope position (moving downslope 1–5) and are described in Table 4.4.

Hillslope	Plot	f (Equation 2.6)	f (Equation 6.6)	Reynolds Number	Inundation Ratio
Upper Nogalte	MRZ 1	5.86	10.64	348	0.407
	MRZ 2	3.46	5.30	780	0.336
	MRZ 3	2.09	1.79	2358	0.489
	MRZ 4	6.32	6.64	1453	0.320
	Ploughed	6.26	10.64	770	0.424
Cardenas	MRZ 1	1.09	1.71	708	0.336
	MRZ 2	6.25	8.53	2117	0.492
	MRZ 3	8.73	8.65	1021	0.560
	MRZ 4	14.36	12.00	2422	0.516
	Ploughed	6.15	9.24	1272	0.468
Del Prado	MRZ 1	1.10	1.96	779	0.469
	MRZ 2	1.67	1.90	1954	0.569
	MRZ 3	1.74	2.57	2135	0.434
	MRZ 4	2.27	3.23	4487	0.528
	MRZ 5	4.32	7.77	2656	0.276

Table 6.1. Variation of median Darcy-Weisbach friction factor, Reynolds number (equation 2.1 using median depth as the characteristic length term, multiplied by a factor of 4 for conversion from pipe flows) and inundation ratio (equation 2.21) between plots. f has been calculated using the conventional form (equation 2.6) and that developed in section 6.3 (equation 6.6).

These f values were calculated using S (in equation 2.6) as the energy slope S_f. Due to the relatively low velocities recorded, this term is dominated by the surface slope. The high resolution of this dataset presented an issue in the calculation of this general slope: where the general slope was low, the dominance of roughness in the overall topography very occasionally led to the calculation of an increasing elevation in the downslope direction (only negligibly different from zero). This resulted in a negative f on such slopes (mostly the Cardenas MRZ 1 and Del Prado MRZ 1 and 2 plots). This is clearly physically impossible and demonstrates the impracticality of calculating a single slope value for a rough surface. Therefore, such negative values were discounted from this analysis but it should be noted that the few very low values of f (< 0.1) may also be influenced by this inaccuracy. The length scale used to measure S was determined by the ~1 second interval of flow measurements. Increasing this length scale would reduce the range of resistance measurements recorded.

Blasius (1913) proposes that the Darcy-Weisbach friction factor varies inversely with the Reynolds number in laminar flows. The distribution of Reynolds numbers between hillslopes was discussed in section 5.2.3. Figure 6.2 plots the variation of f with Re for the whole dataset. The dashed black line represents the equation developed for laminar flow in smooth pipes (equation 2.7). As such, it provides a minimum value of f for flows in the laminar regime and plots below the data presented here. The solid black line represents the best fit of the inverse f–Re relationship over the laminar range; while it describes the general shape of the observed pattern, there is considerable scatter over more than two orders of magnitude. A similar scatter exists about the relationship expected for turbulent flows (with an exponent of −0.4) when fitted to the dataset.

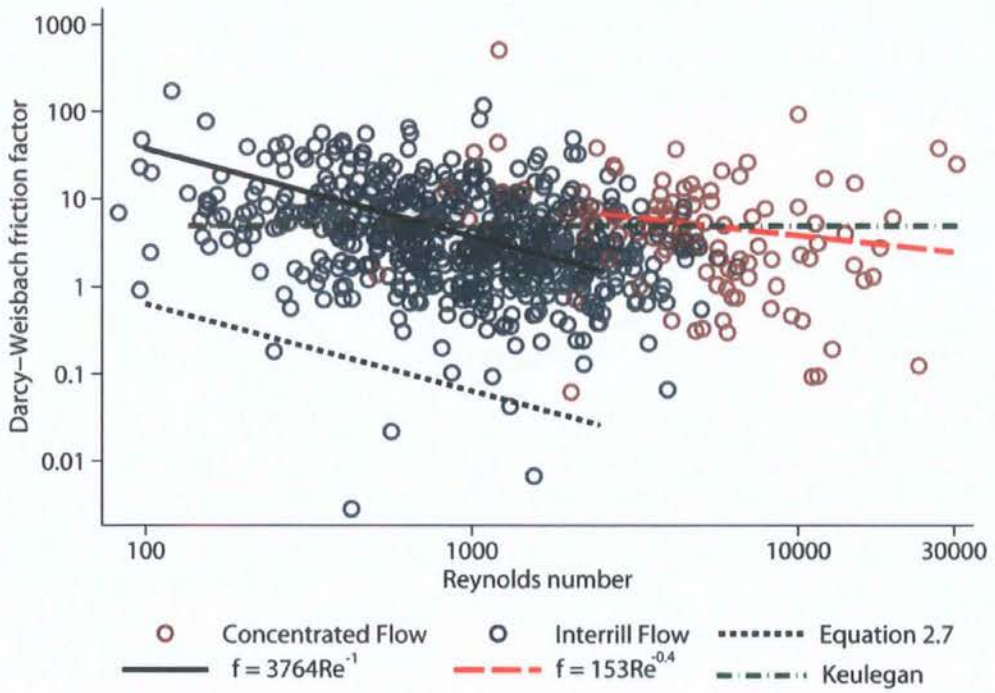

Figure 6.2. Darcy-Weisbach friction factor (as calculated in equation 2.6) as a function of Reynolds number. The dashed black line represents the laminar relationship developed for smooth pipes. This is also fitted to the dataset (solid black line). The dashed red line shows the expected relationship for turbulent flow fitted to the dataset.

Much like the Moody diagram of Figure 2.2, this approach provides no explanation for the discontinuity in predicted values around the transition zone. However, the pattern seen in

Figure 6.2 suggests that the separation of laminar and turbulent flows is unnecessary as no such discontinuity is observed in the measured values. An almost identical pattern is produced by replacing the hydraulic radius with median flow depth in the calculation of f. Section 6.5.2 examines the variability of the f–Re relationship with distance downslope.

Approaches such as the Keulegan equation (equations 2.10 and 2.11) require the specification of a roughness height ε. Studies of open channels may calculate ε from velocity profiles or approximate the roughness height from a multiple of a representative grain size (see section 2.5.2). However, the geometric structure of roughness elements on these soil surfaces cannot be adequately described by such a multiple of grain size (see also Aberle and Smart, 2003). The surface roughness of bare hillslope surfaces is dominated by the clumping together of soil particles into clods and the development of surface morphological features. The use of a 'representative' grain size does not provide a comparable roughness height in this situation. Following Takken and Govers (2000), the representative roughness height was calculated as the median height of each cross-section (with the point of lowest elevation established as the zero level). The median roughness height ε for each inundated surface was then calculated. While Takken and Govers (2000) set ε as half this value, there is no rational basis for doing so (their reasoning was to provide a comparison with Lawrence (1997) who modelled roughness elements as hemispheres of a height half the sphere diameter).

Only the inundated area is considered in this analysis, thereby avoiding the situation described by Abrahams (1998) where the height of protruding roughness elements (which have no contact with the flow itself) is incorporated into estimates of hydraulic resistance. The representation of ε in this way encompasses both the resistance of roughness elements and that of the form of the soil surface (or channel).

The Keulegan equation (2.11) relates flow resistance to the ratio of flow depth to this roughness height (defined as the dimensionless 'inundation ratio' Λ in equation 2.21) and provides a theoretical basis for estimating resistance to turbulent flows in rough pipes. The observed distribution of this inundation ratio is shown in Figure 6.3. The method of calculating the roughness height described above produces low values of Λ, especially

where large roughness elements (such as gullies) are present. Few surfaces recorded an inundation ratio greater than 1; the median Λ is 0.454. In this situation the median height of the soil surface above a zero datum was over twice the median flow depth; as all the surface was actually submerged, this measure is now more representative of the degree of submergence compared with the roughness of the soil surface, or the roughness height distribution.

Figure 6.4 shows the variation of the inundation ratio between each plot and hillslope. A wide range of Λ values are found at each plot. Initially, the inundation ratio increases with the increasing depths observed with distance downslope. Where flow concentrations develop, Λ decreases with distance downslope (see Table 6.1 for a summary). This reflects the influence of the high rill walls and so use of this version of the inundation ratio may be inappropriate under such conditions. No consistent pattern can be observed between the three hillslopes. The Del Prado hillslope generally displays a higher Λ than the other hillslopes.

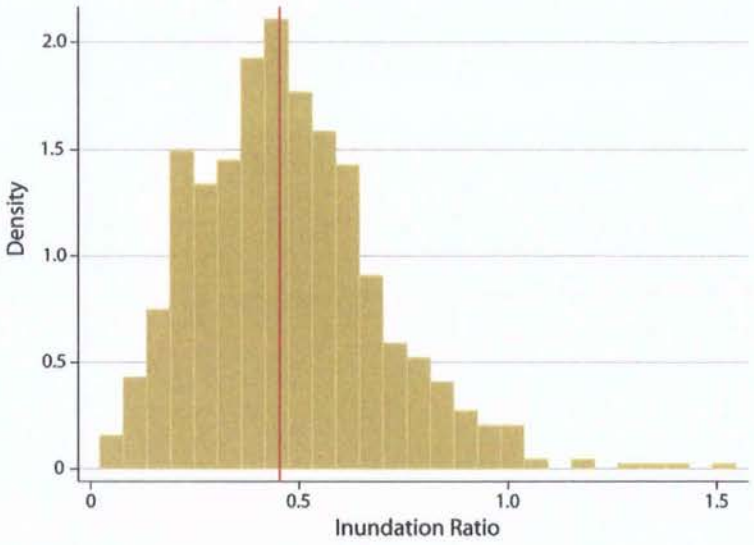

Figure 6.3. Observed distribution of the inundation ratio Λ (as defined in equation 2.21) of flows over three semi-arid hillslopes. The median value is indicated by a red line.

Substituting the median inundation ratio found in this study (0.454) into the version of the Keulegan equation above predicts a value of f (4.923) that is independent of the Reynolds number and can be plotted for turbulent flows (the dashed green line of Figure 6.2). This

performs surprisingly well (the median observed f was 3.42) as the Keulegan equation should only be applied to flows where the depth is greater than the average roughness height (plotted on the right side of Figure 2.2).

While this approach appears valid, there is a fundamental problem in applying the Keulegan equation to shallow overland flows which lie outside the range of its intended use. Figure 6.5 shows that the equation to predict f tends to infinity within the range of the inundation ratio observed in this study. This is a mathematical consequence of the empirical development of the Keulegan equation within a restricted range of flows (overland flows are outside this range). This effect makes no physical sense and effectively prohibits use of equation 2.11 to predict resistance to overland flows without substantial reformulation.

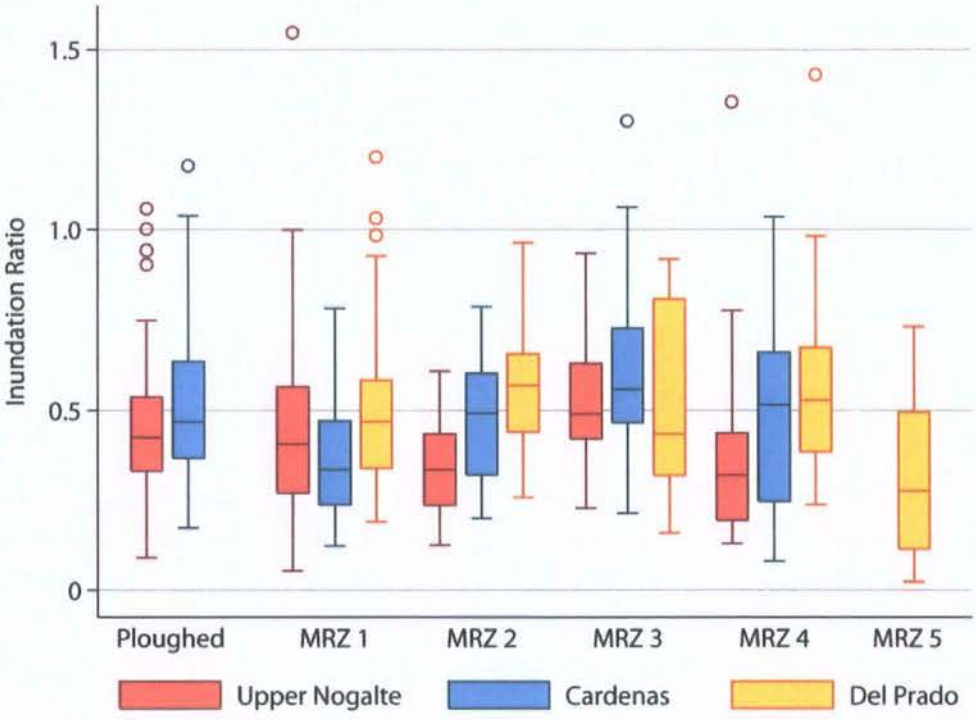

Figure 6.4. Observed distributions of the inundation ratio Λ for each plot and hillslope.

The Manning-Strickler approach (combining equations 2.17 and 2.19) calculates resistance as a function of this inundation ratio with the sixth-root approximation. Figure 2.3 plots the Manning-Strickler and a form of the Keulegan equation over a range of inundation ratios typically observed in gravel-bed rivers. Figure 6.6 merges a dataset from hydraulically rough rivers (from Julien (2002: p.93)) with the overland flow data presented here.

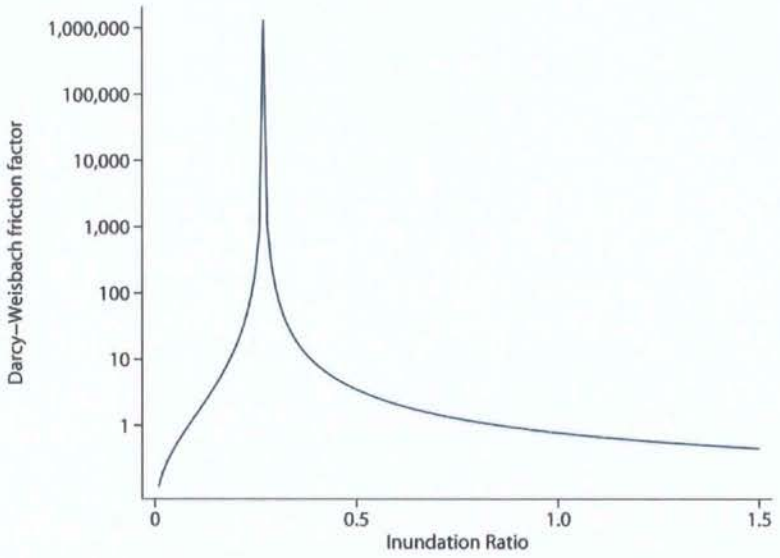

Figure 6.5. Variation of predicted f using the Keulegan equation (equation 2.11) within the range of the inundation ratio observed in this study.

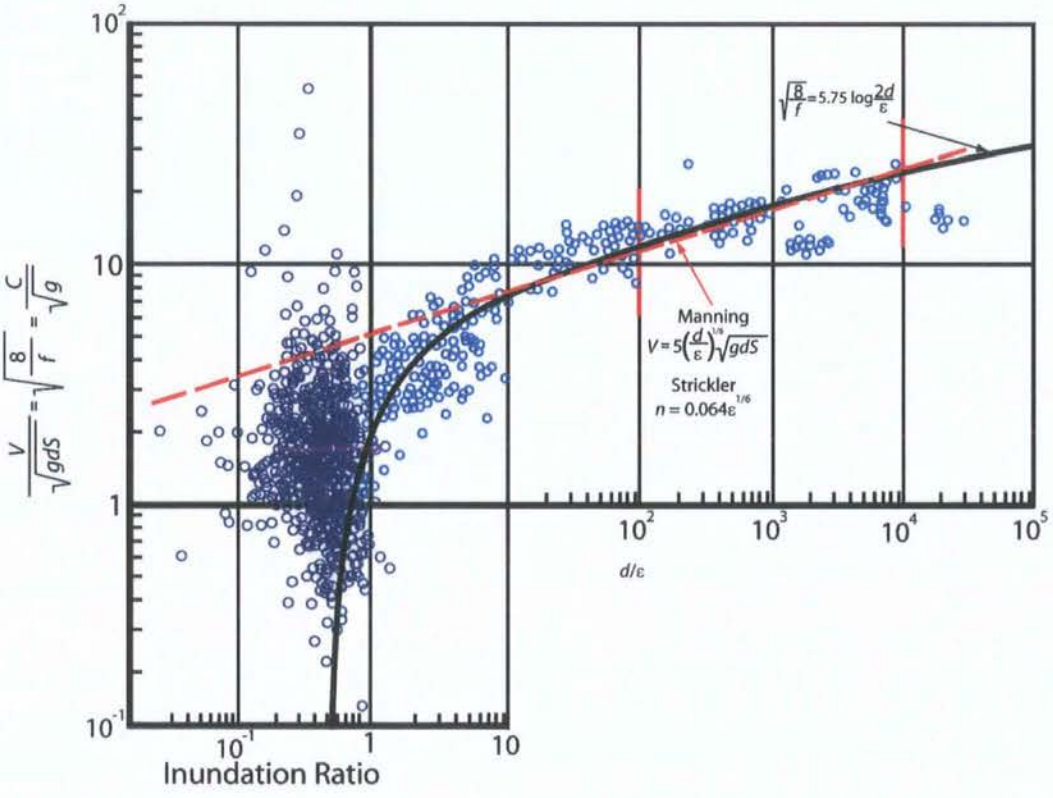

Figure 6.6. Resistance to flow as a function of the inundation ratio (y-axis is conveyance). This figure synthesises data collected in this study (in dark blue) with that of Julien (2002: p.93). Compare Figure 2.3. Overland flow values above 8.9 correspond to observations where $f < 0.1$ and should be treated with caution.

The combination of these two datasets shows that while the Manning-Strickler equation and the Keulegan equation provide a reasonably adequate description of channel flow resistance, they diverge below an inundation ratio of 10. The limit of the sixth-root assumption of the Manning equation (discussed in section 2.3.3) and the asymptotic behaviour of the Keulegan equation are both noticeable. The two equations approximate a wide envelope within which the overland flow data can be found; the Manning equation describes the minimum observed resistance at each inundation ratio and the Keulegan equation describes the maximum resistance (where $\Lambda > 0.6$). However, the data points are scattered over two orders of magnitude with no general trend detectable, suggesting that the inundation ratio does not adequately determine the observed flow resistance. No pattern can be found separating the different hillslopes. Although Ferguson (2007) showed that flow resistance can be modelled with a variable power-law on the inundation ratio in gravel- and boulder-bed rivers over a wide range of relative submergences, this general and flexible approach cannot explain the observed variation in overland flows.

Specifying a resistance length scale such as the roughness height ε is problematic for flows over complex geometries (see Lee and Ferguson (2002) for a similar discussion of resistance in step-pool channels). Replacing ε with the standard deviation of heights σ_Z (suggested by Aberle and Smart, 2003) does not decrease the scatter observed in Figure 6.6 (demonstrating an even weaker relationship). A similar degree of scatter is also found when ε is replaced with the average elevation difference of neighbouring cells Z_d (following Ergenzinger, 1992).

Section 2.5.2 describes the attempt of Lawrence (1997) to determine overland flow resistance using the inundation ratio. The flows are divided into three different regimes according to their inundation ratios (well-, marginally- and partially-inundated) and a separate model is applied to each. Figure 6.7 shows the performance of these models when applied to overland flows measured on natural hillslope surfaces. The ranges of the equations have been extended beyond those specified by Lawrence (1997) for illustrative purposes. The flow is separated into laminar and turbulent regimes to test the hypothesis of

Lawrence (1997) that laminar flows are less accurately described by these equations; no systematic differences can be detected among the observed scatter.

The black line plots the version of the Keulegan equation used by Lawrence (1997) to model well-inundated flows where $\Lambda > 10$ (equation 2.22) and has been extended to the range of flows observed here. The mixing model of equation 2.23 was developed for marginally inundated flows (where $2 < \Lambda < 10$) and is shown as a red line in Figure 6.7. The drag model for partially inundated flows approximates the highest resistance observed at each inundation ratio (purple line, equation 2.25 using a 20% cover of roughness elements); this was developed for the range of flows observed in this study. This equation assumes hemispheric roughness elements distributed over the soil surface and can be reformulated to describe flow resistance as a function of measured frontal area (green line, uses median value for dataset). The use of the protruding frontal area to determine resistance to flow is tested further in section 6.4.

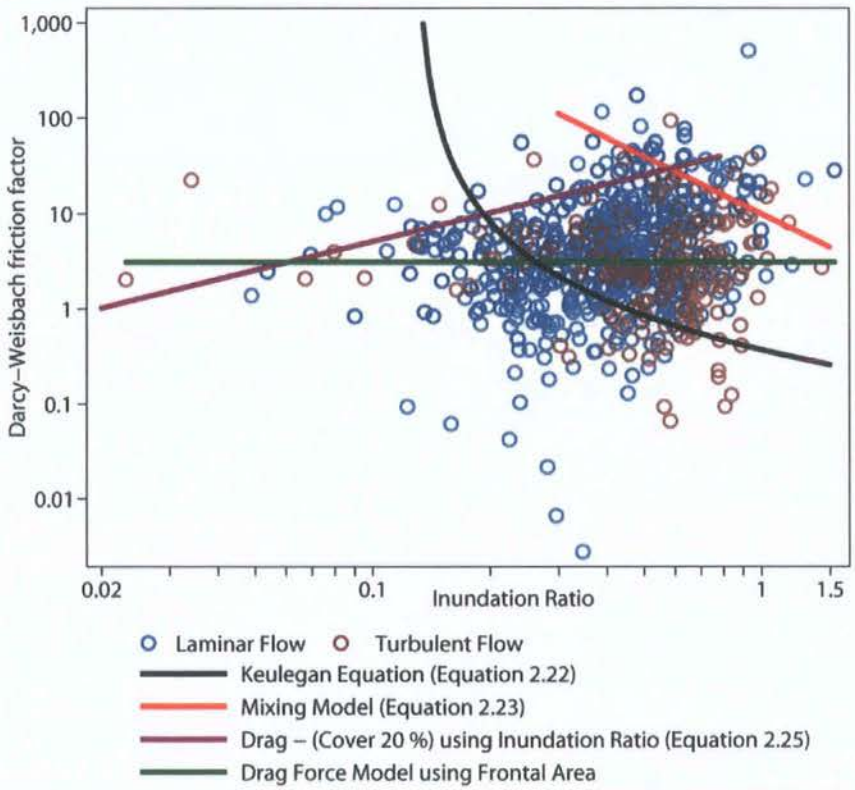

Figure 6.7. The dependence of resistance on the inundation ratio: a comparison with the relationships of Lawrence (1997). Compare Figure 2.5.

These equations appear to either bound or bisect the spread of f with Λ observed in this study. The fundamental problem remains that f and Λ do not appear to vary in a systematic manner over the range of conditions examined. This limits the ability of any single resistance model based on just the inundation ratio to describe the observed variation of resistance.

Hirsch (1996) developed a mathematical model to partition overland flow resistance into grain, form and wave resistance (described in Abrahams *et al.*, 1992). This model was developed using cylindrical roughness elements on a flume surface. Grain resistance was assumed to be a power function of the Reynolds number (derived experimentally from flows over a plane bed). The final empirical model predicts f from the Reynolds number, flow volume V_l, surface area A_{3D} (it is unclear whether surface or planar area was used in the model) and roughness concentration P_r (proportion of the planar area covered with roughness elements; assumed to be 1 over a natural, rough surface)

$$\log f = \log\left(3.19\,\mathrm{Re}^{-0.45} + \frac{4.8V_l}{A_{3D}}\right) + 2.80P_r . \tag{6.1}$$

Figure 6.8 plots measured f against f estimated using equation 6.1. The model only predicts 7% of the observed variation of f; the observed scatter is likely to be a result of more complex variations in topography found on natural surfaces.

No clear relationship between the 'wet-tortuosity' measure suggested by Takken and Govers (2000) (equation 2.26) and flow resistance was found, either for the dataset as a whole, or separated for each hillslope position (MRZ). Other approaches described in section 2.5 are not tested further. For example, Abrahams *et al.* (1992) and Gilley *et al.* (1992) incorporate surface rock cover and other such measures of surface form into equations estimating flow resistance. A single value of surface rock fragment cover may take any of a wide variety of topographical forms. Therefore, these equations, although valuable, do not conform to the objective of this thesis: the estimation of flow resistance

from precisely and logically defined roughness measures derived from high-resolution topographic data. Resistance equations developed using the 'random roughness' measure of Allmaras *et al.* (1966) are also not examined here (e.g. Gilley and Finker, 1991) as the calculation of 'random roughness' in the manner directly specified by Allmaras *et al.* (1966) makes little physical sense (for example, the upper and lower 10% of values are arbitrarily removed). Smith (2005) provides a more detailed discussion. The 'random roughness' term may be adequately (and more practically) described by the standard deviation of elevations; this is examined in section 6.4.

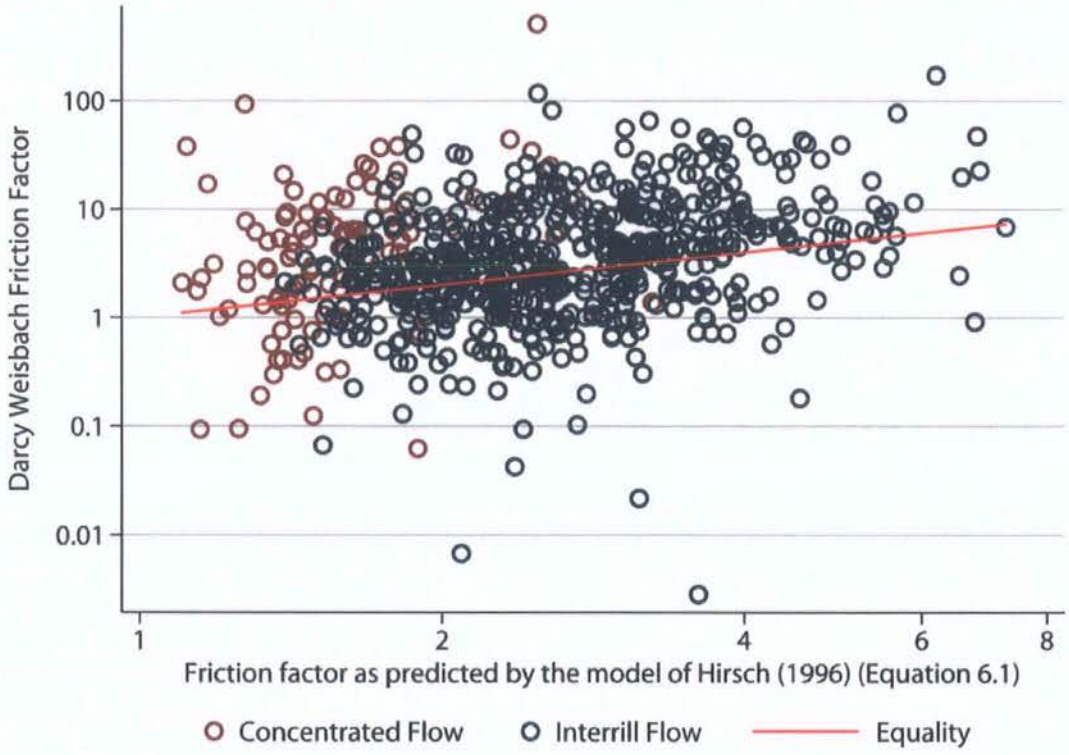

Figure 6.8. Comparison of observed f against that predicted by the model of Hirsch (1996) (equation 6.1).

Figures 6.2, 6.6 and 6.7 show that substantial scatter is produced when attempting to model flow resistance over complex topographies using conventional approaches. Difficulties encountered when specifying a representative roughness height (or resistance length scale) to describe the average surface inundation introduce additional uncertainties. Alternative roughness measures (such as protruding frontal area) may provide a more sensible substitute over such complex surfaces. The development of new methods of representing

roughness in resistance equations is described in section 6.5. While their measurement requires high-resolution topographic data (and may also be scale dependent), the consistent (and predictable; section 7.2) variations in soil surface microtopography (the Morphological Runoff Zones described in Table 4.4) that emerge on natural semi-arid hillslopes indicate that these roughness measures may demonstrate systematic and predictable changes in the downslope direction as flow incision increases. Using the dependency of flow resistance to such roughness measures and their downslope variation provides a framework for determining flow resistance over semi-arid hillslopes.

6.3 Representing Flow Resistance over Complex Topographies

Before examining the relationship between flow resistance and surface roughness, it is necessary to investigate the most appropriate method of representing the resistance to flow. In this section, an attempt is made to reformulate the resistance equations introduced in Chapter 2 to develop a velocity-resistance relationship that is suitable for overland flows. Lawrence (1998) notes that approximations and scalings used in estimating the Darcy-Weisbach friction factor mean that including additional detail of surface geometry in predicting f is inappropriate. This section examines the possibility of amending current resistance measures to better suit situations where high resolution topography and flow data are available. Chapter 2 suggested that the assumptions inherent in commonly used resistance equations should be explicitly stated. In this spirit, the resistance measure employed in the following sections is now described in detail and related to the principles of fluid mechanics.

The high resolution data available permit the limitations introduced by the application of several assumptions to be minimised through minor alterations to more conventional flow resistance equations. This analysis uses the Chézy resistance equation as a starting point. The derivation of the Chézy equation requires several assumptions. First, Chézy proposed that the force resisting the flow per unit bed area is proportional to the square of the velocity. This is an experimentally verified relationship (although with some exceptions; Shapiro, 1961). As Chow (1959) notes, this resisting force can be explained by the principles of fluid dynamics; the drag or resisting force can be described by the drag

equation (equation 2.24). This is only strictly valid for values of Re greater than the range where Stokes' Law of drag can be applied (Stokes, 1851), but in practice this is only where Re is very small.

The methodology outlined in Chapter 4 divides the flow-field into small areas of a finite volume within which resistance to flow is assumed to be uniform. The Chézy equation then calculates the contact surface area as the product of the wetted perimeter P and stream length L. This is inaccurate when dealing with complex topographies. The choice of a reference area in the drag equation depends on which component of drag is under examination (skin friction drag, form drag, etc.). Form drag is related to the area of projection of the bed on a plane perpendicular to the direction of motion (the frontal area), whereas skin friction drag is related to the total surface area. As overland flows are not necessarily parallel to the surface, the total bed surface area is applied here and the discrepancy between the drag force produced and that of an idealised situation (where all water encountering the projected area comes to a complete stop) is described by the coefficient of drag C_D.

This estimates the total force resisting the flow as KV^2A_{3D} where K is a constant of proportionality and A_{3D} is the bed surface area in contact with the flow. From equation 2.24 it can be shown that $K = \rho_w C_D/2$.

The basic principle of uniform flow (Brahms, 1754) states that the effective (downslope) component of the gravity force causing the flow must equal the total force of resistance. This downslope component is the product of the total weight of the water and sin θ (where θ is the slope angle in radians). The Chézy equation calculates the total weight of water as ALw where w is the unit weight of water. For flow over complex topographies this can be restated more precisely as $g\rho_w V_l$ where V_l is the water volume. Although θ here is the soil surface slope angle (assuming uniform flows within each section), this offers an opportunity to introduce an appreciation of the non-uniformity of the flow between each measurement area by replacing θ with the energy slope (using the water surface slope and correcting for the different velocity heads at each end of the section). Where the energy slope is steeper than the bed slope, this effectively increases the resistance force. In this

formulation, the sine of the energy slope sin $\theta = S_f$ (for the relatively steep slopes encountered it is imprecise to apply the conventional approximation that $\theta = \sin\theta$).

Balancing the resistance and gravity forces leaves

$$0.5\rho_w C_D V^2 A_{3D} = g\rho_w V_l S_f. \tag{6.2}$$

The ratio of the water volume to the bed surface area is similar to the volumetric hydraulic radius R_v proposed by Smart *et al.* (2002). The volumetric hydraulic radius represents a practical measure for overland flows, avoiding the problem of defining a datum from which to measure flow depth. It subtly differs from that used by Smart *et al.* (2002) as it scales the flow volume by bed surface area rather than planar area. The use of bed surface area makes R_v equivalent to the more conventional hydraulic radius and provides a better estimate of a reference area in the drag equation (2.24). Cancelling for the water density ρ_w and rearranging gives

$$V^2 = \frac{2gR_v S_f}{C_D}. \tag{6.3}$$

Where flow is in a uniform channel and R_v approaches the hydraulic radius, C_D relates to Chézy's C and the Darcy-Weisbach friction factor f:

$$C \equiv \sqrt{\frac{2g}{C_D}} \equiv \sqrt{\frac{8g}{f}}; \tag{6.4}$$

hence

$$C_D \equiv \frac{f}{4} \tag{6.5}$$

and

$$f = \frac{8gR_v S_f}{V^2}. \tag{6.6}$$

The denominator of equation 6.5 arises from the multiplication of the hydraulic radius by 4 to equal the diameter of a circular pipe in the derivation of the Darcy-Weisbach equation (see section 2.3). Equation 6.6 has been developed directly from principles of fluid mechanics; any further assumptions have been explicitly stated in the hope of encouraging such best practice. It is suggested that this approach provides a more suitable theoretical framework for studying resistance of shallow flows over complex surfaces. The resulting velocity-resistance relationship is only subtly different from the traditional Darcy-Weisbach and Chézy equations, but has been recast in a form more appropriate to the type of overland flow measurements available in this study. In such complex flows, C_D is not a simple parameter for quantifying skin friction drag, but because of the multiple sources of drag it depends on the Froude number, Reynolds number, element shape and relative depth (Smart *et al.*, 2002). As with any application of the drag equation, the coefficient of drag contains all such complex dependencies and needs to be determined experimentally. To aid comparison with other studies of overland flows, flow resistance will be calculated as f (as defined in equation 6.6) for the remainder of this thesis. Section 6.5 uses this formulation of f to develop equations predicting resistance from roughness measures. First, section 6.4 discusses the concept of surface roughness and the different ways in which it can be characterised.

6.4 Measuring Surface Roughness

Geomorphology is essentially the study of rough surfaces, yet roughness remains an enigmatic concept, which geomorphologists have yet to tackle effectively. There is no single property that can be uniquely defined as roughness; it can be characterised in a variety of ways (e.g. as elevation standard deviation, tortuosity, semi-variance, etc; Kuipers, 1957; Boiffin, 1984; Linden and Van Doren, 1986). Roughness measures emphasise either the deviation of elevations from a smooth plane (with dimensions of length) or the spatial arrangement of such elevation variations (typically resulting in dimensionless measures). Moreover, the distinction between roughness and topography remains problematic and entirely scale-dependent. For example, which components of surface elevation variation within a plot can be considered part of the general slope, and which represent the sub-grid scale irregularities commonly considered to be roughness?

This will depend on the resolution of available measurements and, perhaps more importantly, the scale of the problem. This study examines plot-scale variability and attempts to upscale the observed relationships to the hillslope using the Morphological Runoff Zones framework. Despite the increased availability of high-resolution topographic data made possible through advances in terrestrial laser scanners, it remains impractical to survey the microtopography of an entire hillslope. Therefore, the variability observed at the plot-scale that is not captured in the hillslope-scale Digital Elevation Model is considered to be roughness.

As Lane (2005) suggests, such conceptual issues warrant further contemplation, as all processes operating at the Earth's surface interact with surface roughness (at whatever scale) in a multitude of ways. These processes often exhibit a complex relationship with roughness, and so any attempt to represent roughness must be sensitive to and informed by such behaviour. This interaction is particularly apparent in the situation of overland flows on hillslopes where a thin layer of flowing water can be influenced by even the finest of microtopographic irregularities.

Before proceeding, further clarification of what is meant by surface roughness and resistance is necessary, as the two terms are interrelated and often confused. While the 'effective roughness height' of fluvial hydraulics is technically a property of the flow itself (that theoretically can be related to a grain size measure), here surface roughness is used to describe the form of the soil surface that exists regardless of whether water flows over this topography (although such a roughness term may be scaled to water depth). Similarly, the Darcy-Weisbach friction factor f, Chézy's C and Manning's n are sometimes referred to as roughness calibration factors (e.g. Lane, 2005). Here, these are described as measures of flow resistance which, unlike surface roughness, is considered to be a property of the flow itself (directly and indirectly influenced by surface roughness).

Surface roughness is a vague concept, and as such, it can be made precise in many ways. No single value of surface roughness can be given to entirely describe a surface; instead a large variety of measures have been developed. Each offers a particular representation of a single perspective of surface roughness, rather than encapsulating the entire concept. The

different approaches to surface roughness can be summarised in several ways. A roughness measure may be classified as: direct or indirect (a measurable quality of the surface itself or simply the remaining residuals that must be accounted for after the general 'topography' has been removed); dimensionless or dimensional (a ratio of measurements or a 'roughness height'); spatial or aspatial (the order of elevation points is important or a random reordering yields an identical roughness value); for profiles or for surfaces (roughness is divided into perpendicular directional components and analysed on profiles or the roughness value describes the surface as a whole).

A wide range of surface roughness measures have been applied in the literature. Many have been excluded from this analysis for a variety of reasons. As discussed above with reference to the 'random roughness' measure of Allamaras *et al.* (1966), those measures that appear to include arbitrary decisions and calculations (e.g. the Mean Upslope Depression measure of Hansen *et al.*, 1999) have been replaced with more general and justifiable measures (such as downslope pit density). Many studies characterise soil roughness using a geostatistical approach (e.g. Linden and Van Doren, 1986). However, the non-random component of natural soil surfaces alters the form of semi-variograms such that standard assumptions do not apply (see Oliver and Webster (1986) and Smith (2005) for a more detailed analysis of this problem).

Table 4.3 briefly defines the wide variety of roughness measures employed in this study. For a more thorough definition, see Appendix 1. This selection of roughness measures represents a variety of different features present on a complex, rough surface. The calculation of any measure in this thesis effectively represents an implicit hypothesis that the characterisation of roughness in that precise way will influence resistance to overland flows (at least in part). It is possible that resistance to flow is most effectively influenced by a specific feature of a complex surface; this thesis attempts to precisely define any such features. Roughness measures may be very specific (e.g. pit density measured in a downslope direction) or very general (e.g. standard deviation of elevations). Some roughness measures incorporate a flow measurement in their calculation (e.g. the inundation ratio) and so account for the variation of resistance with flow properties. Characteristics of the depth distributions examined in section 5.4 are therefore equally valid

as predictors of resistance (given an understanding of their variation with flow stage). The range of surfaces over which such relationships can be found remains unclear. Some may be valid only until flow incision is initiated yet others only after such concentrations are found. The wide range of surfaces examined here allows the effect of hillslope position to be examined and enables the empirical relationships developed in this chapter to be applied to the widest possible range of bare semi-arid surfaces.

This study uses high resolution topographic data to relate roughness to flow resistance. It is recognised that such data are not always available, but it is suggested that the systematic variations in microtopography observed with distance downslope on semi-arid hillslopes, as encapsulated in the Morphological Runoff Zone concept, may lead to systematic changes in roughness measures and flow resistance over such hillslopes. For example, though a simple roughness height ε may be sufficient to model interrill flow resistance, once substantial concentrations have developed, the organised surface structure of the rill walls may over-inflate such a measure, making the mean elevation difference Z_d between each cell and its neighbours a more suitable measure (as it is less affected by the presence of such structures). Similarly, the formation of concentrated flows represented by the density of pits in transects perpendicular to the flow direction (P_{dxc}) may influence flow resistance at upslope locations, but where these pits are within a larger flow concentration that has developed, this relationship may be less important. For a detailed description of all roughness measures see Appendix 1. The next section attempts to relate surface roughness to flow resistance both across the entire range of surfaces (section 6.5.1) and within each plot-type (section 6.5.2).

The three hillslopes examined in this study were chosen to represent the entire range of hydrological characteristics found on bare hillslopes within the Nogalte and Torrealvilla catchments. It is not expected that surface roughness will vary identically between these hillslopes. Indeed the variable flow resistance recorded both within and between hillslopes (Figure 6.1) suggests that this is not the case. Variations in properties such as soil structure, crusting, clay content, etc., will alter the exact form of the surface (an examination of the influence of these factors on roughness deserves further investigation).

6.5 Relating Resistance to Roughness

While many studies relate the Darcy-Weisbach friction factor to the Reynolds number, Scoging (1992) notes that the direction of causality should be from f (determined by surface roughness) and depth (from inflow and rainfall excess) to velocity as described by the Darcy-Weisbach equation. A similar objection could be made to predicting wave resistance as a function of the Froude number (as in Hu and Abrahams, 2006) as for any slope angle, f is necessarily proportional to Fr^{-2}. Scoging (1992) suggested that resistance could be partitioned into that representing a grain size or roughness height and that which is some (inverse) function of flow depth. While the inundation ratio has previously been used to scale resistance to depth, the complexity of natural surfaces and potential for progressive inundation of roughness elements suggests that a more complicated relationship may exist, although this will vary with the exact form of the soil surface.

This section examines different methods of predicting flow resistance, using conventional predictors (the Reynolds number and inundation ratio) and more novel alternatives which require no previous knowledge (or iteration) of either Q or V. Those measures which vary with flow depth may require an understanding of how the wetted area changes with increased inundation (this is discussed in Chapter 8).

Section 6.2 predicted flow resistance from conventional theories. Modifications to existing approaches were informed theoretical and practical insights into the nature of overland flows (e.g. replacing roughness height ε with mean elevation difference between neighbouring cells Z_d to remove the effect of rill structure). Section 6.4 describes a variety of representations of surface roughness (see Table 4.3 and Appendix 1) which may relate to resistance in different ways. In contrast to the previous sections, the approach described below includes roughness measures in regression models on the merit of their statistical association with resistance, attempting to infer process from these relationships.

6.5.1 General Equation for Predicting Resistance

This section describes a regression model developed to predict flow resistance from surface roughness and flow rate over the entire range of surfaces examined in this study. This

covers a wide range of process domains. Multiple linear regression was performed to identify the most relevant variables to include in the model. Stepwise regression procedures (both forwards and backwards) predicted flow resistance from an unattractively large number of roughness measures. Instead, the predictor with the most significant Pearson's correlation coefficient was added into the regression model. This process was then repeated using the residuals of that relationship and the remaining roughness measures until no further significant relationships ($P<0.05$) could be found.

General linear models are subject to a number of assumptions; their application to the physical sciences should both recognise and minimise their effects. The regression technique assumes that variables can be linearly combined, that the observations are independent and that errors are both homoscedastic and normally distributed (Berk, 2004; Weisberg, 2005). Lehmann (2008) charts the origin of these assumptions to the use of the method to model astronomical data where the distribution of (observational) error was well established and the functional form of the equations was known from Newtonian mechanics (Freedman, 2005). The complex sources of variation observed in environmental science necessitates caution when applying regression methodology. The model diagnostics displayed and discussed for equation 6.7 below were repeated for each model developed in this section. Unless specified, each equation was considered to represent a suitable description of the relationships identified without unduly violating the assumptions implicit in the development of a regression model.

Transformation of both predictor and response variables was performed to ensure linearity. The resultant model predicts flow resistance (as defined in equation 6.6, retaining the title 'Darcy-Weisbach friction factor' f) from soil surface slope S (measured at the length scale over which the flow travelled during a single timestep), Reynolds number Re and the inundation ratio Λ:

$$\ln f = 4.26S - 0.578 \ln \mathrm{Re} + 1.98\Lambda + 2.16, \tag{6.7a}$$

or

$$f = \frac{e^{4.26S+1.98\Lambda}}{0.12\,\mathrm{Re}^{0.58}} \cdot \tag{6.7b}$$

Multiple linear regression assumes a linear relationship between predictors and response variables. Both f and Re were log-transformed to ensure that the assumption of linearity was not violated. No transformations were necessary for S or Λ. Figure 6.9a shows the linearity of the relationships included in model 6.7. Running line smooths of the Darcy-Weisbach friction factor (log-scale) on all predictors (with each smooth adjusted for the others; see Royston and Cox, 2005) show an approximately linear relationship between predictors and response (note that the Reynolds number has also been log-transformed).

The model of equation 6.7b explains 61% of the variation in the natural log of the Darcy-Weisbach friction factor; however, several outliers were identified from the model of equation 6.7b. The influence of these outliers was examined using Studentised residuals (a measure of the residual (measured−estimated) from the fitted relationship), a measure of leverage (the influence each point has on the fitted relationship) (Helsel and Hirsch, 1992; Chen *et al.*, 2003), Cook's d (Cook, 1977) and DFITS (both composite measures of residual and leverage). Table 6.2 shows that model 6.7 considerably overestimates flow resistance in 9 observations (where Studentised residual < -3) and that the 8 most extreme cases were at an MRZ 1 plot. These points also recorded the highest Cook's d and most negative DFITS values, but were relatively less influential according to the leverage measure. The f values given in Table 6.2 show that these residuals represent the low values of f calculated over nearly horizontally-sloping rough surfaces (discussed previously) and arguably represent the most inaccurate measures (removal of these points increased R^2 to 0.64 and altered the regression coefficients only slightly due to their low leverage).

Another assumption in regression modelling is that the errors are homoscedastic and normally distributed. Figure 6.9b shows a residual-versus-fitted plot which highlights the extreme residuals and demonstrates over-prediction of several observations. Aside from these observations, no pattern can be detected and the errors are taken to be roughly homoscedastic. The model predicts resistance equally well for each hillslope as no bias can be seen when the dataset is separated by hillslope. The inset of Figure 6.9b plots the

quantiles of the residuals against those expected from a normal distribution. Aside from the influence of the outliers already discussed, the distribution of residuals very closely approximates a normal distribution. Excluding the 9 observations where the Studentised residual < −3, the residuals are found to be normal by both the Shapiro-Wilk and skewness-kurtosis tests for normality (Shapiro and Wilk, 1965; D'Agostino *et al.*, 1990).

Hillslope	Plot	Measured f	Studentised Residual	Cook's d	DFITS	Leverage
DP	MRZ 5	7.67	2.88	0.03	0.33	0.01
DP	MRZ 5	32.49	2.75	0.04	0.40	0.02
UN	PLOUGHED	12.03	2.57	0.01	0.14	0.00
DP	MRZ 5	49.56	2.30	0.02	0.27	0.01
DP	MRZ 5	19.28	2.22	0.01	0.14	0.00
DP	MRZ 5	17.45	2.15	0.03	0.32	0.02
CARD	MRZ 4	251.06	2.08	0.02	0.25	0.01
UN	MRZ 1	71.34	2.02	0.00	0.14	0.00
DP	MRZ 2	0.56	−2.00	0.00	−0.11	0.00
DP	MRZ 2	1.90	−2.00	0.00	−0.13	0.00
CARD	MRZ 1	1.93	−2.12	0.00	−0.13	0.00
CARD	MRZ 1	0.38	−2.17	0.00	−0.12	0.00
CARD	MRZ 1	0.33	−2.45	0.01	−0.15	0.00
CARD	MRZ 1	0.61	−2.48	0.00	−0.11	0.00
DP	MRZ 2	0.08	−2.71	0.01	−0.24	0.01
DP	MRZ 4	4.03	−2.79	0.07	−0.52	0.03
DP	MRZ 2	0.16	−2.86	0.01	−0.16	0.00
DP	MRZ 5	0.54	−3.02	0.01	−0.17	0.00
UN	MRZ 1	1.27	−3.44	0.04	−0.39	0.01
CARD	MRZ 1	0.14	−3.89	0.02	−0.29	0.01
CARD	MRZ 1	0.33	−3.99	0.02	−0.29	0.01
DP	MRZ 1	0.03	−4.12	0.04	−0.43	0.01
CARD	MRZ 1	0.16	−4.48	0.02	−0.26	0.00
CARD	MRZ 1	0.07	−4.62	0.02	−0.28	0.00
DP	MRZ 1	0.01	−6.18	0.05	−0.47	0.01
CARD	MRZ 1	0.00	−7.85	0.09	−0.62	0.01

Table 6.2. Measures of influence of the largest residuals on model 6.7 Hillslope key: UN = Upper Nogalte, CARD = Cardenas and DP = Del Prado

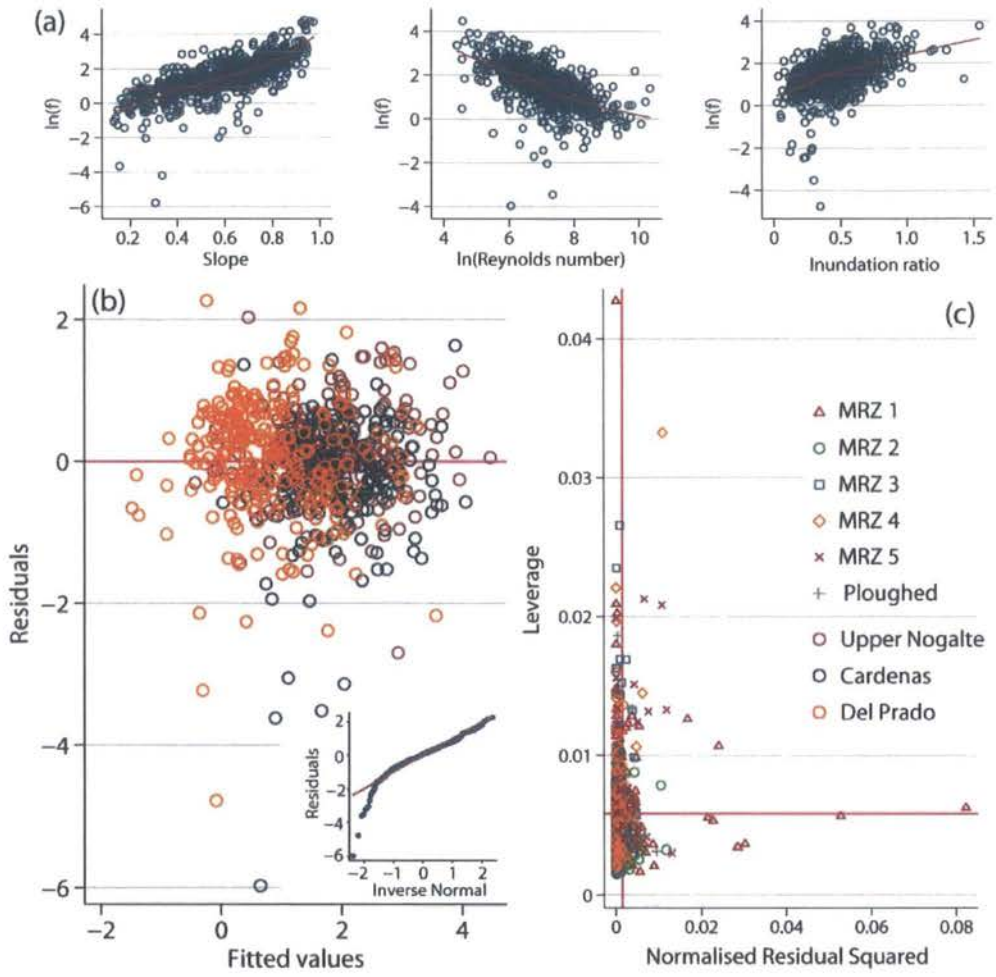

Figure 6.9. Diagnostics for model 6.7. (a) Running line smooths of ln(Darcy-Weisbach friction factor) on all predictors in model 6.7 with each smooth adjusted for the others (demonstrates linearity between predictors and response); (b) residual-versus-fitted plot (observations separated by hillslope) with quantiles of residuals plotted against those of a normal distribution (inset); (c) leverage versus normalised squared residual plot with data separated by plot-type (reference lines indicate mean values).

Figure 6.9c displays a plot of the leverage against the squared residuals, separating the dataset by hillslope location (MRZ). Observations with high leverage plot at the right of the plot space while extreme residuals plot towards the top. Therefore, any point with a large influence on the model would be located in the upper-right corner of the plot space. No such point exists in Figure 6.9c. The several large residuals can be seen (each from the

MRZ 1 plots), yet none of these have a large degree of leverage on the model (suggesting that these data points do not substantially alter the regression results).

Finally, the assumption of independence of observations has received comparatively little attention. Spurious dependence may be caused by the presence of a common factor (Lehmann, 2008). Such dependence can take many forms and is thus difficult to either demonstrate or account for. The models developed in this study are not exempt from this limitation and thus, the results of this section should be analysed with this in mind.

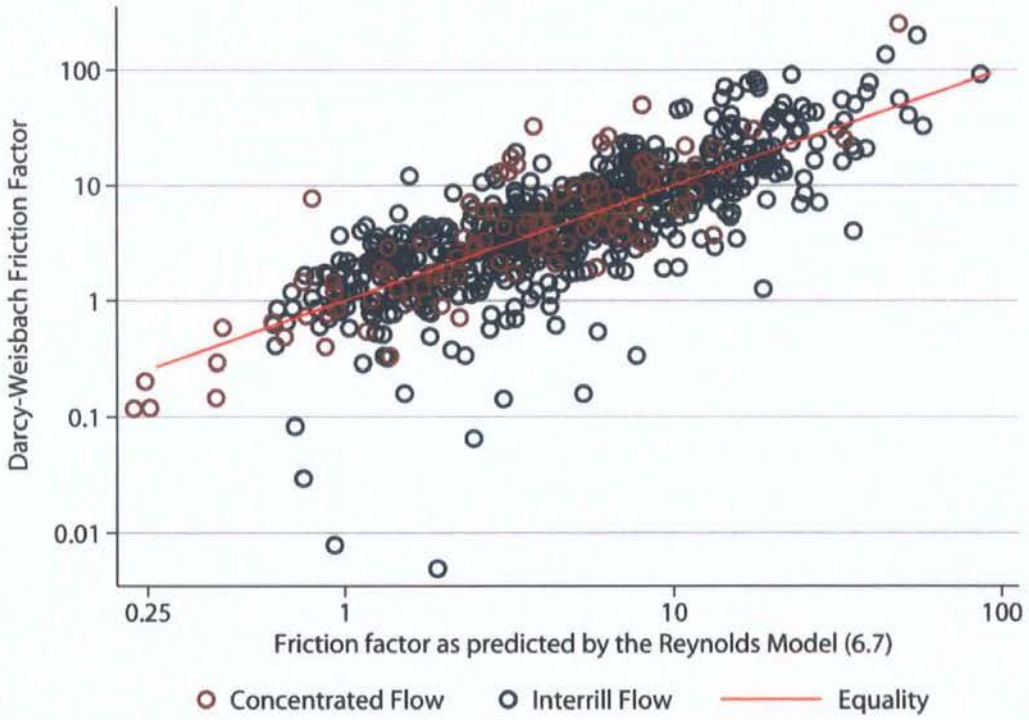

Figure 6.10. Comparison of observed f (as calculated in section 6.3) against that predicted by model 6.7.

Analysis of the influence of the residuals suggested that the very few extreme values had little effect on the model and so were retained in the development of model 6.7. Figure 6.10 plots the observed f against the predicted value. A reasonable fit can be seen especially given the range of surfaces over which the observations were taken. Repeating this procedure for each hillslope separately showed little variation in the coefficients of

equation 6.7, suggesting that the model is valid across the entire range of non-vegetated hillslope surfaces in the Nogalte and Torrealvilla catchments, even for ploughed surfaces.

As previously mentioned, predicting resistance from the Reynolds number in models of hillslope hydrology is problematic as values of both velocity and depth are not always available (their calculation may require iteration as there is circularity with velocity in Re and the final velocity prediction). The following regression equation relates flow resistance to more specific measurements of the soil surface. The same regression methodology was performed (excluding the Reynolds number from the list of possible predictors). The results suggest that flow resistance can be predicted from the slope S, the inundation ratio Λ, the pit-density measured perpendicular to the flow direction P_{dxc}, the standard deviation of elevations σ_Z and the proportion of surface area directly opposing the flow direction F_P (measured at 20 mm resolution):

$$\ln f = 4.9S + 1.2\Lambda - 1.34F_P - 0.77\ln(\sigma_Z P_{dxc}) - 1.45 \tag{6.8a}$$

or

$$f = \frac{e^{4.9S+1.2\Lambda-1.34F_P}}{4(\sigma_Z P_{dxc})^{0.77}}. \tag{6.8b}$$

Equation 6.8 explains 59% of the variation of the data. The pattern of residuals is similar to that described above for model 6.7 (shown in Figure 6.10). Each predictor shows a linear relationship with the response. The friction factor increases with S and Λ but decreases with each of the other roughness measures. The precise nature of these relationships is now examined.

Including the plot slope S in this relationship partly reflects the results discussed in section 5.5, that rill flow velocity is independent of slope (similarly, Hessel *et al.* (2003) found flow resistance to increase with slope angle on steep slopes). This places energy slope on the numerator and bed slope on the denominator of velocity calculations which will cancel out to some extent. Nevertheless, following the definition of f established in this chapter,

and to provide comparison with previous studies, both slope terms will be used for velocity calculation in this thesis.

The dimensionless product of the standard deviation of elevations and cross-sectional pit density $\sigma_Z P_{dxc}$ increases when a surface displays greater deviation from a plane and when this is represented as more pits identified in a cross-slope direction. In this context, more pits on a profile perpendicular to the flow direction (P_{dxc}) produces more flow concentrations and preferential flow paths with less resistance to flow, while the σ_Z term measures the magnitude of variations.

Resistance increases with an increase in the inundation ratio Λ, suggesting that over the entire hillslope, progressive inundation of roughness is more important than the overtopping of roughness with increasing depth, further emphasising this important difference between overland flow and channel hydraulics (compare Figure 2.3). This analysis only considers submerged flows as the size of non-inundated roughness elements has no bearing on resistance to flows (this is discussed in section 6.2). As most surfaces were not completely inundated, the variation of Λ with water level is more complex than in fluvial systems (representing a measure of surface elevation relative to water level). The observed positive relationship between f and Λ may partly be a consequence of the limited width of the flume experiments and the absence of rainfall simulation (allowing space into which the supplied water flow can expand). However, this effect would be important where overtopping flow concentrations route water from contributing areas through an area that is not actively generating runoff.

Finally, the proportion of surface area directly opposing the flow F_P increases when much of the roughness is represented as a surface area directly protruding into the flow. It measures the absolute protruding area scaled by total surface area. The reason for the decline in resistance with an increase in this roughness measure is unclear. It may represent wake interaction effects and skimming flow or the channelling of the flow into one dominant flowpath. Alternatively, as water is continuously supplied to the surface, a barrier may encourage a build-up of momentum until the obstacle is over-topped. This measure does show a negative correlation with microtopographic slope (possibly as such protrusions

would be eroded down at higher slopes) and so the inclusion of this variable could be a consequence of this covariance (yet measures of collinearity show that both terms should be included in the model).

Figure 6.11 plots the observed f against the predicted value. Again a reasonable fit can be observed, with only slightly more scatter than Figure 6.10. This equation does not use flow rate to predict resistance; the resistance is scaled to the flow using only the median depth term in the calculation of the inundation ratio.

Figure 6.9 shows that no obvious differences exist between the three hillslopes investigated. However, it is possible that the scatter observed in Figures 6.10 and 6.11 is due to the variation of soil surfaces within each hillslope. Specifically, as the processes operating on the surface change (as reflected by variations in surface morphology e.g. incision of flow concentrations) it was hypothesised in Chapter 1 that the relationship between roughness and resistance will change. As observed in section 5.5.2, the relationship between the Froude number and measures of surface roughness could only be identified in areas of flow incision. Therefore, the following section examines the effect of plot-type (MRZ) on relationships between roughness and resistance.

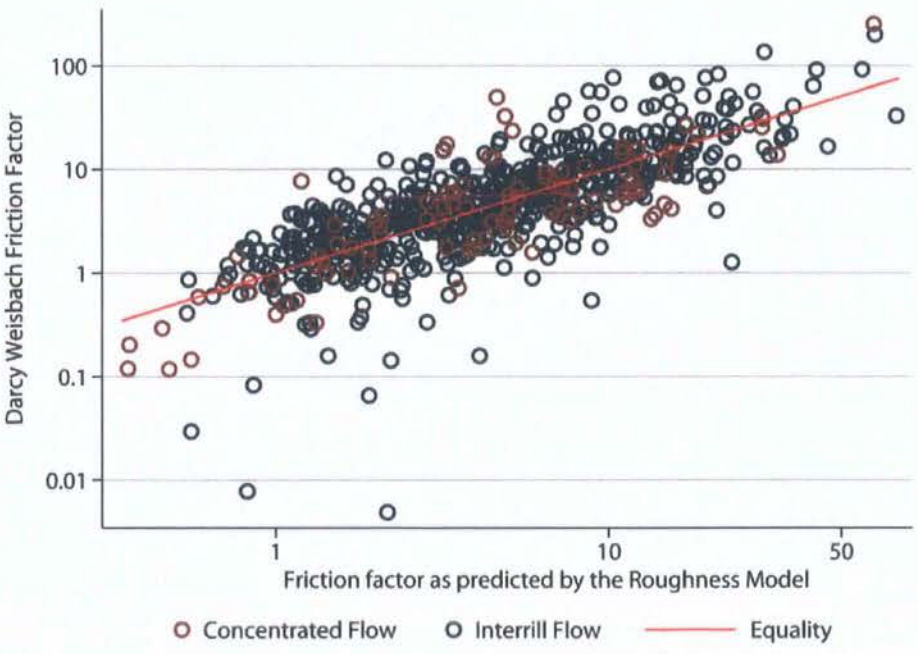

Figure 6.11. Comparison of observed f (as calculated in section 6.3) against that predicted by model 6.8.

6.5.2 Predicting Resistance by Hillslope Location

Flow resistance can be seen to vary with flow rate over most hillslope surfaces. This is usually represented by the dimensionless Reynolds number. As discussed above, knowledge of flow depth and velocity required for the calculation of Re is not always available (or must be calculated iteratively). Indeed, it is with the aim of predicting flow velocity that a resistance equation is required in the first place. Despite this, many authors report flow resistance as a function of Re (e.g. Abrahams *et al.* 1992; Gilley *et al.*, 1992). When f is predicted using only the Reynolds number, the exponent b of $f \propto \mathrm{Re}^b$ demonstrates a systematic increase with distance downslope (Figure 6.12), from −1 at MRZ 1 (as theoretically predicted for laminar flows) to −0.91 (MRZ 2), −0.84 (MRZ 3) and −0.42 at MRZ 4. The exponent is negligibly different from zero at the gullied locations. The reported R^2 values also decreased where rills incise the surface (although the unequal number of observations n makes direct comparison difficult). This finding agrees with the theory that the Reynolds number is related to flow resistance for more laminar interrill-type flows and this relationship becomes less important further downslope as the overland flow generally becomes more turbulent (as seen in Figure 5.5).

This finding suggests caution is required when applying a general relationship using Re to predict f and provides a demonstration of the variability of flows over hillslope surfaces, thereby justifying the decision to partition the surfaces according to the processes observed to be operating. While interrill areas may dominate the spatial coverage of the hillslopes, the discussion of the connectivity framework emphasises the role of the flow concentrations as runoff must be transferred through these areas before contributing to hillslope outflow. It is recognised that the use of Morphological Runoff Zones (defined in section 4.5) to categorise the soil surfaces by hillslope position is one of many possible categorisations. The models developed in this section could equally be transferred to other systems of dividing hillslope surfaces.

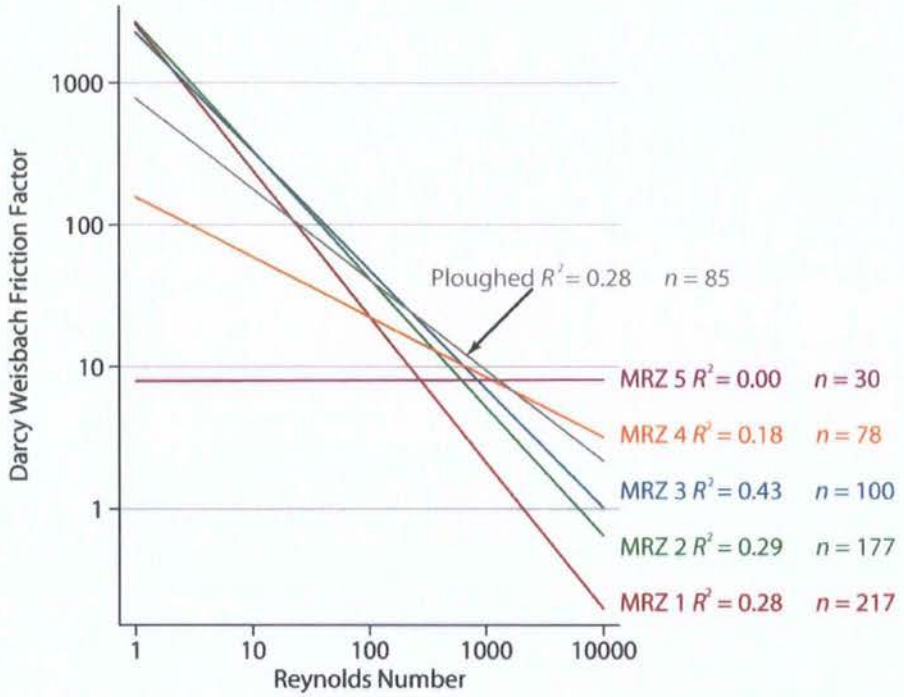

Figure 6.12. Modelled relationships between the Darcy-Weisbach friction factor *f* and Reynolds number categorised by Morphological Runoff Zone.

A range of options are available to account for hillslope position in the development of a model predicting *f* from measures of surface roughness. The previous section described an end member (a) of this spectrum which can be summarised as follows:

(a) predictions with no MRZ term (model 6.8);

(b) predictions where intercept of the relationship can vary with hillslope location (MRZ term is incorporated as a dummy variable);

(c) predictions made separately by hillslope location (coefficient of each predictor and intercept can vary with each MRZ);

(d) independent regression equation developed for each hillslope location (separate models with different predictors for each MRZ).

Each of these models adds an increasing degree of complexity and flexibility in incorporating hillslope position. This may be necessary where roughness measures are affected by the systematic shifts in microtopographic structure (for example the incision of

flow concentrations inflating ε) and is analogous to the limitations encountered when applying fluvial hydraulics to overland flows.

Incorporating hillslope location as a dummy variable gives an additive term for each MRZ (using MRZ 1 as a reference). The variable is, in a sense, artificial such that it takes the value unity wherever the property it represents occurs (in this case, the hillslope position as categorised by Morphological Runoff Zones), and zero otherwise (Kennedy, 1998). The coefficient on each dummy variable determines the additive term for each hillslope position. MRZ 3 has the only negative offset (−0.18) followed by the reference case MRZ 1 (0), MRZ 2 (+0.13), MRZ 4 (+0.28), ploughed plots (+0.40) with MRZ 5 plots demonstrating the largest y-intercept (+0.95). This prediction of f produces a slightly larger R^2 (0.62) than when no reference to hillslope location is made ($R^2 = 0.59$).

Figure 6.13 shows the variation of the coefficients of each predictor in model 6.8 with Morphological Runoff Zone (type (c) in the list above). Slope is most important at MRZs 2 and 5, becoming gradually less important as flow concentrations incise. The inundation ratio Λ becomes a less important predictor with distance downslope until rills develop at MRZ 4 where $P > 0.01$. However, Λ is a significant predictor of $\ln f$ at the MRZ 5 plots. The coefficient of $\sigma_Z P_{dxc}$ (product of the standard deviation of elevations and cross-sectional pit density) becomes increasingly negative moving downslope from MRZ 1 to MRZ 3; beyond this point the trend is reversed and the predictor becomes insignificant at MRZ 5. The frontal area F_P coefficient becomes less negative with distance downslope (though this pattern is reversed at MRZ 4). The ploughed plots show intermediate values of all coefficients, although F_P is not a significant predictor of $\ln f$ at these plots. When the coefficients of each term are allowed to vary with MRZ (alongside the y-intercept) the R^2 of model 6.8 increases to 0.66.

The following section subdivides the dataset into the five Morphological Runoff Zones described in section 4.5.3 (while also grouping ploughed surfaces together) to develop separate resistance equations (the other end-member (d) of the spectrum identified above). Equations to predict resistance using the Reynolds number were also developed at each plot, although these are not presented. At MRZ 1–3 they demonstrated a similar (or slightly

higher) R^2 to the roughness models and much less at MRZ 4. Further downslope Re was no longer a significant predictor of resistance ($P<0.05$). Model diagnostics are not presented for each equation but were employed to ensure that no limiting assumptions were unduly violated.

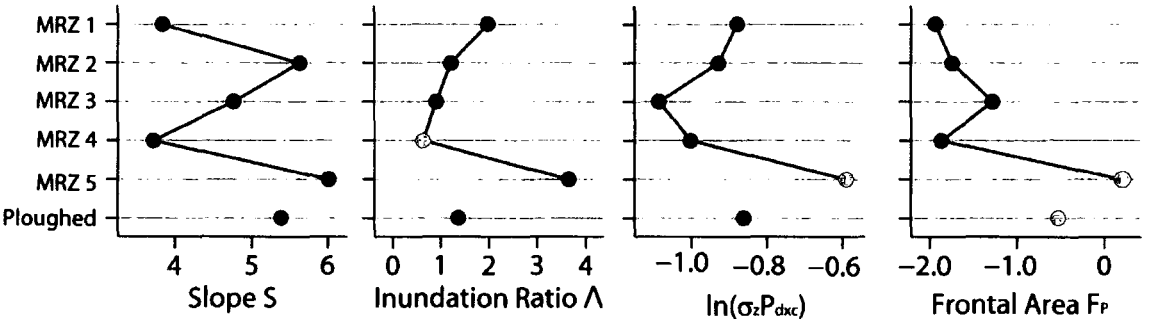

Figure 6.13. Variation of the coefficients of each roughness measure included in model 6.8 with Morphological Runoff Zone. Red points indicate the condition where $P > 0.01$. Note that zero is located at the right side of the two graphs displaying negative coefficients and that the observations are not equally distributed between each MRZ.

6.5.2.1 MRZ 1

At the most upslope location (MRZ 1), resistance to overland flows was found to be related to the slope S, the surface standard deviation of elevations σ_Z, the cross-sectional pit-density P_{dxc}, the proportion of surface area directly opposing the flow direction F_P (measured at a 20 mm resolution) and the inundation ratio Λ. The resulting regression equation

$$f = e^{4S+2\Lambda-1.8F_P-1.5(\sigma_Z P_{dxc})} \tag{6.9}$$

explains 56% of the observed variance in $\ln f$ at the MRZ 1 plots. Figure 6.14a plots the observed f against the predicted value (showing the MRZ 1 data only). Residuals showed the same pattern as for the entire dataset (as the main outliers in model 6.8 were from MRZ 1 plots - removing those points where $f < 0.1$ increases R^2 to 0.63). This equation uses the same roughness measures as the general equation developed in the previous section (model 6.8).

The change in resistance with flow rate is represented through the inundation ratio (in this range resistance increases with Λ as roughness elements are progressively submerged and flow rate increases). The soil surfaces at this location show little autocorrelation; it could be suggested therefore that the inundation ratio provides an adequate measure of roughness in this case (where incision occurs, the structure of soil surface elevations will influence the calculation of a roughness height and other measures may be more appropriate).

Again the slope term is strongly positively related to flow resistance (suggesting an inefficiency of steep microtopographic forms in transferring gravitational potential energy into kinetic energy) and F_P is negatively related. Finally, the dimensionless product of the standard deviation of elevations σ_Z and cross-sectional pit density P_{dxc} was also found to be negatively related to flow resistance. This suggests that the more roughness that is represented as pits in the cross-slope direction (potential flow concentrations), the lower the observed resistance to flow.

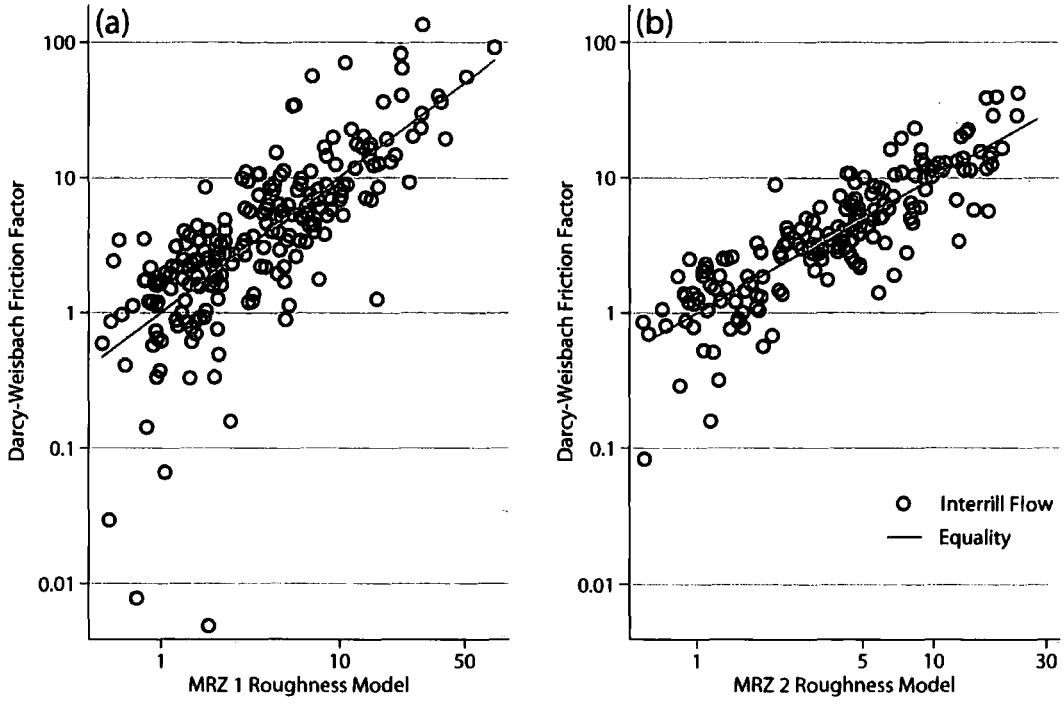

Figure 6.14. Comparison of observed f with that predicted by (a) model 6.9 (MRZ 1 Roughness Model) at MRZ 1 and (b) model 6.10 (MRZ 2 Roughness Model) at MRZ 2.

6.5.2.2 MRZ 2

Moving downslope, evidence of previously-formed wash deposits becomes noticeable as the upslope contributing area increases. The relationships developed between resistance and roughness are similar to those developed for the MRZ 1 plots though the negative relationship between resistance and the proportion of surface area directly opposing the flow direction is no longer found. It seems that the effect of increasing discharge is no longer simply represented by the inundation ratio. While the Λ term remains significant (and again positively related, $P<0.0005$) the median depth d_{50} also becomes a relevant predictor. Resistance increases less rapidly with Λ at MRZ 2; this effect is also counteracted by the negative relationship between resistance and median depth (mm). Again σ_Z and P_{dxc} were negatively related to resistance. This yields the predictive model

$$f = \frac{e^{6S+1.44\Lambda-190d_{50}}}{7(\sigma_Z P_{dxc})^{0.63}}, \tag{6.10}$$

explaining 73% of the observed variation of $\ln f$ for the MRZ 2 plots (Figure 6.14b).

6.5.2.3 MRZ 3

Further downslope still, the soil surface becomes incised where preferential flowpaths develop. Again, flow resistance can be predicted using the plot slope and the inundation ratio (both increasing with resistance). The product of the standard deviation of elevations σ_Z and the cross-sectional pit-density P_{dxc} was again negatively related to resistance. At this point of the hillslope, cross-sectional pits represent a greater degree of flow concentration. Although the pit-density measure provides no indication of the size of these pits, this effect is partially captured by the σ_Z term. The resultant regression model

$$f = \frac{e^{5.7S}\Lambda^{0.5}}{7(\sigma_Z P_{dxc})^{1.36}} \tag{6.11}$$

explains 78% of the variability of the dataset for the MRZ 3 surfaces. These plots include flows within the observed concentrations, and adjacent interrill flows. Therefore, Figure 6.15a shows the relationship between observed and predicted f categorised by flow concentration (as identified in the field). The flows with the lowest resistance were located in concentrations; in a few cases this resistance is slightly overestimated by the roughness model. Restricting analysis to just the flow concentrations yields a relationship of a similar form, though the skewness of the depth distributions D_{sk} also becomes a significant predictor (P<0.0005).

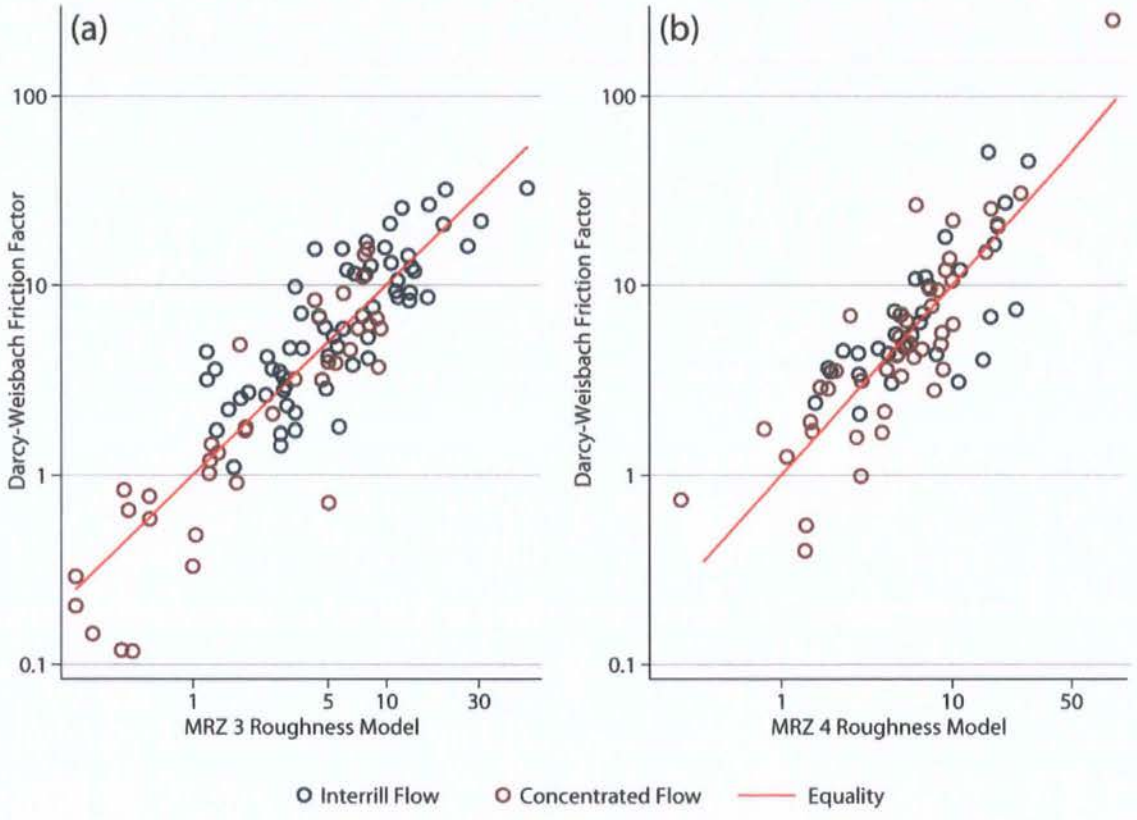

Figure 6.15. Comparison of observed f with that predicted by (a) model 6.11 (MRZ 3 Roughness Model) at MRZ 3 and (b) model 6.12 (MRZ 4 Roughness Model) at MRZ 4.

6.5.2.4 MRZ 4

Where rills begin to incise the soil surface, some flow will be concentrated into a rill while interrill flow still occurs either side of the main flow channel. Thus far, the MRZ 4 flows

have been lumped together; as such they represent a wide range of conditions. This section begins by examining all flows at the MRZ 4 plots together before then considering the rill-flows separately.

Flow resistance was found to be related to slope S, skewness of depths D_{sk} and the product of the standard deviation of elevations σ_Z and the downslope pit-density P_{dd} such that

$$f = \frac{e^{6.2S}}{4D_{sk}^{0.89}(\sigma_Z P_{dd})^{0.95}}. \tag{6.12}$$

This model explains 67% of the variability of flow resistance at the MRZ 4 plots (Figure 6.15b) and is similar to the relationship identified for the MRZ 3 flows, but with the inundation ratio replaced with depth skewness and the cross-sectional pit density replaced with the downslope pit-density. The absence of the inundation ratio suggests that soil structure in the form of the rill itself affects the calculation of a roughness height ε. This hillslope location corresponds to the point where Λ was observed to decrease with distance downslope (Figure 6.4). Where the Reynolds number is included as a predictor, the inundation ratio of Smart *et al.* (2002) is also included in the model (where ε is replaced with σ_z to give Λ_σ; see Appendix 1).

A negative relationship between P_{dd} and flow resistance was consistently observed for each hillslope; this result is counter-intuitive and could possibly represent a limitation of dividing surfaces into transects for the calculation of roughness measures (as the neighbouring cells in the perpendicular direction may be lower).

From Figure 6.15b it appears as if model 6.12 overestimates the resistance of rill flows experiencing low resistance and underestimates areas of high resistance in rills. To avoid such a systematic pattern of residuals, the analysis was repeated for just those flows within the rills as identified in the field. This raises a broader question of the process domains acting within each Morphological Runoff Zone; this issue is revisited in section 7.2.

Repeating the analysis for just the rill flows produces a similar model to 6.12:

$$f = \frac{e^{6.6S}}{5D_{sk}^{0.65}\sigma_Z P_{dd}}. \quad (6.13)$$

R^2 increases slightly to 0.73 and the residuals were normally and homoscedastically distributed.

6.5.2.5 MRZ 5

The development of a predictive model for resistance at the gullied plots was less reliable as only 35 observations were available from a single gullied plot. Most flow was located within the gully itself though there was a short area of interrill flow upslope of the headcut. The empirical relation

$$f = \frac{e^{6S+3.6\Lambda}}{23(\sigma_Z P_{dxc})^{0.6}} \quad (6.14)$$

explained 72% of the variance at the MRZ 5 plot (Figure 6.16a). This model is similar to that observed at the MRZ 3 plot. There is no detectable pattern in the residuals, although an extreme outlier (f measured as less than 1) was removed from the analysis. Developing a model for just gully flows showed little difference as very few interrill measurements were taken at this site.

6.5.2.6 Ploughed Surfaces

In the Nogalte catchment, large areas of natural hillslopes have been converted into ploughed fields for almond crops. To understand the effect of this land-use change on storm hydrographs, these ploughed surfaces were considered as a separate category from the MRZ division described above as their surface form is relatively independent of hillslope position. The flow resistance at these plots was found to be unrelated to the Reynolds number. The following model was developed, relating resistance to slope, the skewness of the depth distribution and the standard deviation of elevations, such that

$$f = \frac{e^{6.4S}}{1100 D_{sk}^{0.92} \sigma_Z^{1.2}}. \tag{6.15}$$

This model explained 69% of the variability of the measured flow resistance at the ploughed plots (Figure 6.16b).

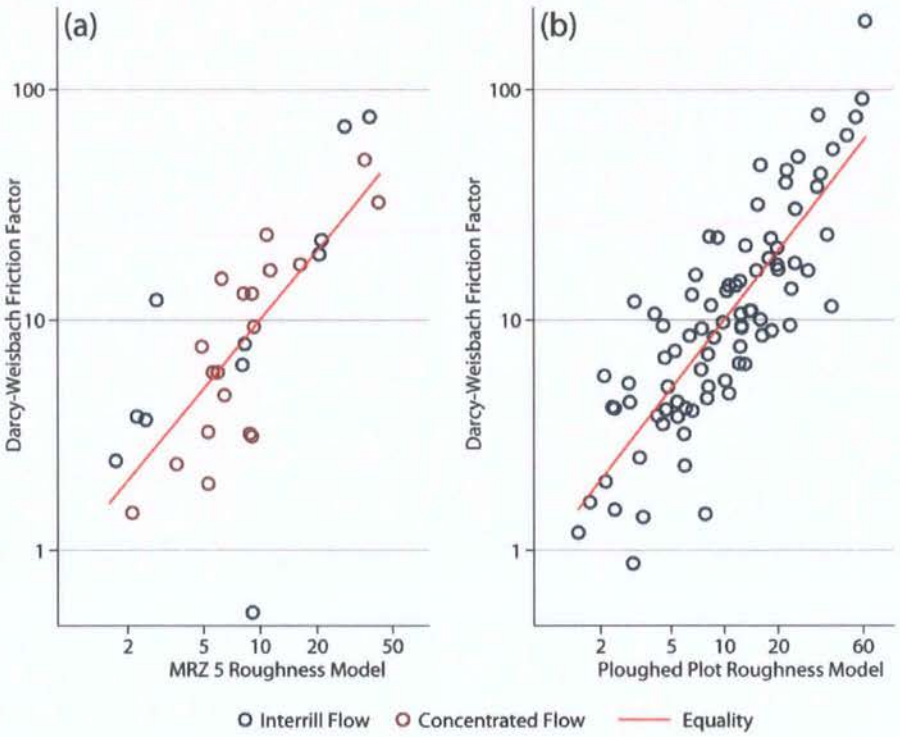

Figure 6.16. Comparison of observed f with that predicted by (a) model 6.14 (MRZ 5 Roughness Model) at MRZ 5 and (b) model 6.15 (Ploughed Surface Roughness Model) at the ploughed plots.

6.5.3 Integrating Plot Equations: Interpreting Process

The regression equations outlined in the previous section predict flow resistance from a variety of roughness measures. The relationships are summarised in Table 6.3. Figure 6.17 shows the measured resistance plotted against that predicted applying the derived roughness equations to each plot-type separately. Despite subdividing the surfaces by plot and calculating resistance for each, the R^2 is still only 0.67, which is a slight improvement on that reported for the general hillslope roughness equation (equation 6.8) and the

intermediate models (b) and (c) where hillslope location was incorporated into predictions with dummy variables and variable coefficients.

Table 6.3 indicates that the parameterisation of surface roughness explaining flow resistance varies with distance downslope, although some measures remain important over the entire hillslopes. This section briefly attempts to link these empirically derived equations to explanations of process, although this is speculative and must be treated with caution.

Plot	Roughness Equation	Predictors			R^2
GENERAL	$f = \frac{e^{4.9S+1.2\Lambda-1.34F_P}}{4(\sigma_Z P_{dxc})^{0.77}}$	S	+	Slope	0.59
		Λ	+	Inundation Ratio	
		F_P	−	Frontal Area (per m^2)	
		P_{dxc}	−	Pit density (perp)	
		σ_Z	−	Elevation STDEV	
MRZ 1	$f = e^{4S+2\Lambda-1.8F_P-1.5(\sigma_Z P_{dxc})}$	S	+	Slope	0.56
		Λ	+	Inundation Ratio	
		F_P	−	Frontal Area (per m^2)	
		P_{dxc}	−	Pit density (perp)	
		σ_Z	−	Elevation STDEV	
MRZ 2	$f = \frac{e^{6S+1.44\Lambda-190d_{50}}}{7(\sigma_Z P_{dxc})^{0.63}}$	S	+	Slope	0.73
		Λ	+	Inundation Ratio	
		d_{50}	−	Median depth	
		σ_Z	−	Elevation STDEV	
		P_{dxc}	−	Pit density (perp)	
MRZ 3	$f = \frac{e^{5.7S}\Lambda^{0.5}}{7(\sigma_Z P_{dxc})^{1.36}}$	S	+	Slope	0.78
		Λ	+	Inundation Ratio	
		σ_Z	−	Elevation STDEV	
		P_{dxc}	−	Pit density (perp)	
MRZ 4	$f = \frac{e^{6.2S}}{4D_{sk}^{0.89}(\sigma_Z P_{dd})^{0.95}}$	S	+	Slope	0.73
		D_{sk}	−	Depth skewness	
		σ_Z	−	Elevation STDEV	
		P_{dd}	−	Pit density (parallel)	
MRZ 5	$f = \frac{e^{6S+3.6\Lambda}}{23(\sigma_Z P_{dxc})^{0.6}}$	S	+	Slope	0.72
		Λ	+	Inundation Ratio	
		σ_Z	−	Elevation STDEV	
		P_{dxc}	−	Pit density (perp)	
PLOUGHED	$f = \frac{e^{6.4S}}{1100D_{sk}^{0.92}\sigma_Z^{1.2}}$	S	+	Slope	0.69
		D_{sk}	−	Depth skewness	
		σ_Z	−	Elevation STDEV	

Table 6.3. Summary of roughness-resistance relationships developed. + and − indicate the direction of the relationship with resistance (measured by f).

Figure 6.18 shows that increasing model complexity yields a more accurate model fit to observed values. Yet the application of a general model to a location where several predictors have been shown to be unrelated to resistance (Figure 6.13) and even related to some other roughness measure (Table 6.3) could produce some spurious results. The independent resistance equation for the MRZ 1 plot was very similar to the general hillslope equation. Indeed the number of observations (shown in Figure 6.12) was much larger for this plot-type, reflecting the spatial dominance of this MRZ over the hillslope surfaces (see section 7.2 for a more detailed discussion). Despite the limited areal extent of the more downslope morphological zones, these flow concentrations play an important role in flood generation as all runoff generated in upslope areas must be routed through these features before it reaches a channel (discussed in the explanation of the connectivity framework given in Chapter 3). Therefore, the influence of the MRZ 1 dataset over the general roughness equation (model 6.8) hides the variability seen in Table 6.3.

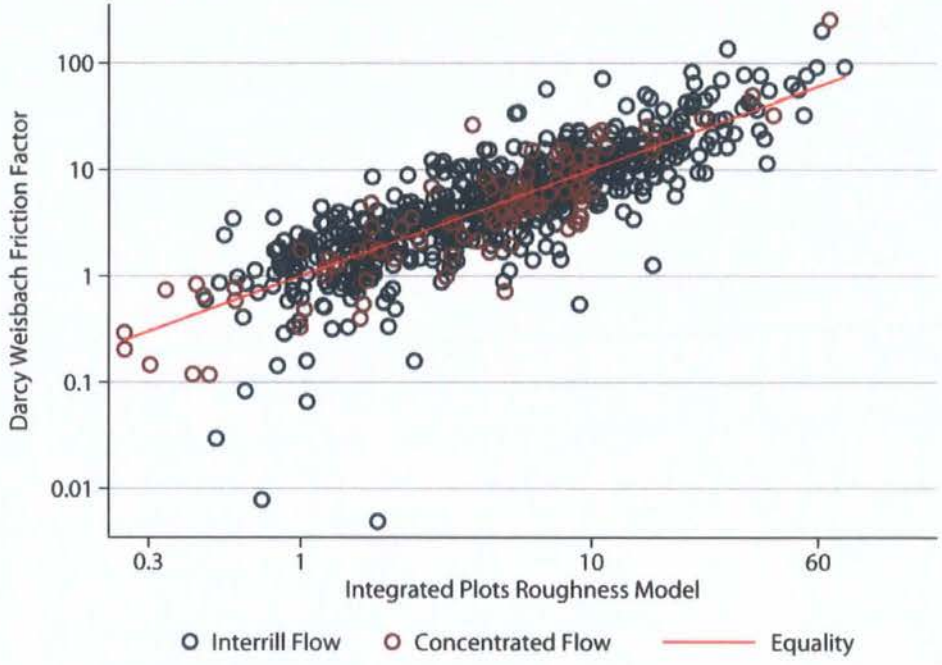

Figure 6.17. Comparison of observed *f* with that predicted using the individual plot roughness equations outlined in section 6.5.2.

The variable relationship of roughness and resistance with hillslope position seen in Table 6.3 is a demonstration that the subdivision of hillslopes by MRZ for resistance calculation is necessary if we are to predict *f* from roughness for the right reasons. The dependency of flow resistance on the Reynolds number, for instance, was not found at every hillslope position. This suggests that predicting resistance from Re (as in equation 6.7) will inadequately describe flows further downslope.

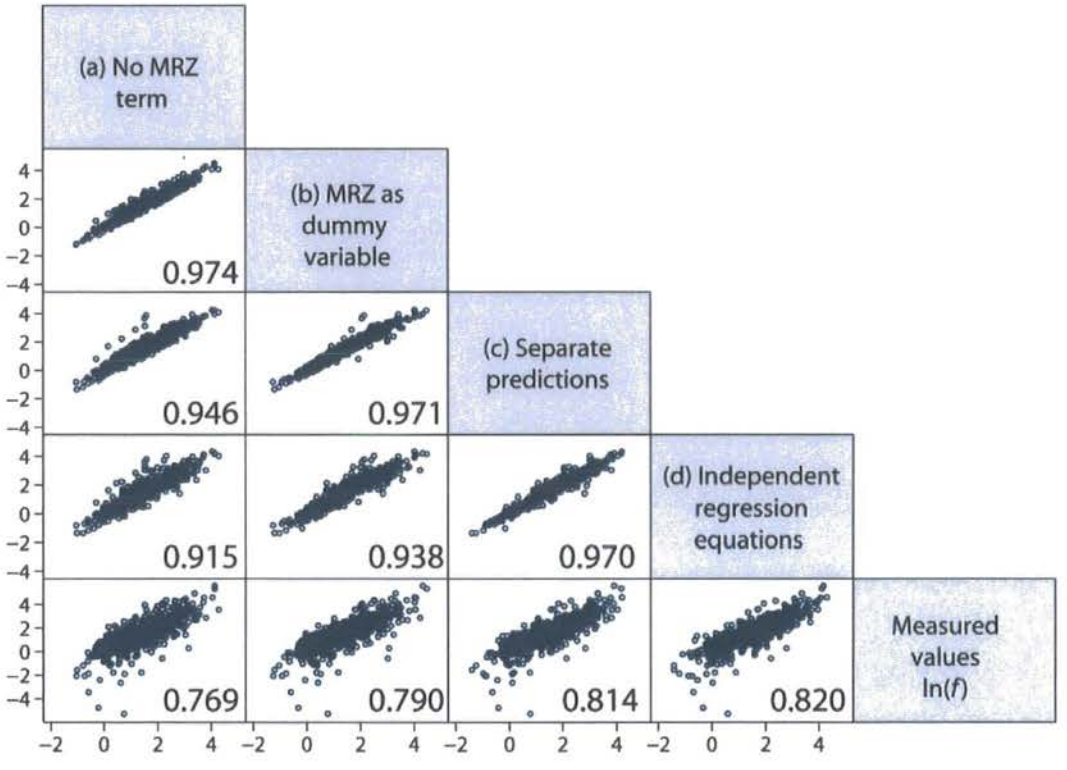

Figure 6.18. Scatter matrix demonstrating relationships between different methods of incorporating hillslope position into predictions of resistance to overland flows and the measured values (log scale). Pearson's correlation coefficient is displayed in the lower right corner of each plot region.

Analysis of Table 6.3 shows that despite checking 36 possible roughness measurements (including some dimensionless combinations), the same 8 appear each time (to different degrees) and explain the variability of resistance within each plot-type. Using these equations to inform a more general model would avoid the exclusion of predictors that are relevant at some hillslope locations. Including each roughness measure found in the models

in Table 6.3 into a general model (model 6.16) and allowing the coefficients to vary between plot types (to reflect the dominant process at each hillslope location) offers an interesting two-step approach.

Representing hillslope position as a dummy variable or additive term in the new regression model (using MRZ 1 as a reference) produced smaller between-plot differences than previously (model 6.17). Again the MRZ 3 observations had the only negative offset at just −0.08 (insignificant at the P=0.05 level). The MRZ 2 offset was also insignificant at this level (+0.03). Further downslope, the offsets for MRZ 4 (+0.35), MRZ 5 (+0.96) and ploughed plots (+0.39) were similar to those described in the previous model.

Table 6.4 and Figure 6.19 show the variation of the coefficient of each roughness measure when the prediction is made separately for each plot. This analysis shows that the coefficient on the slope term increases with distance downslope (with a spike at MRZ 2). Table 6.3 shows that flow resistance measured by f always increases with soil surface slope; this is unsurprising as this term dominated the energy slope term used to calculate f. However, this slope term should be compensated for by the relationship between velocity and depth. The results presented here suggest that increased slope (measured at a scale that incorporates microtopographic variation) makes the flow less efficient at converting potential energy into kinetic energy, and therefore, slope measured at the sub-grid scale is positively correlated with resistance.

Each equation of Table 6.3 contains at least one roughness term that incorporates some dependency on flow depth. This took the form of the inundation ratio (at the upslope locations), skewness of depth distribution or median depth. The inundation ratio was positively related to resistance, suggesting that progressive inundation is an important consideration. The inundation ratio is no longer a significant predictor (P>0.01) at MRZ 4 and 5. The median depth term is included because of its presence in the MRZ 2 equation (model 6.10), yet with this combination of measures, the resultant coefficient is not significant at the 0.01 level at any MRZ. However, this term affects the overall model performance. Depth skewness has the most influence at MRZ 1 and MRZ 4. The non-monotonic variation of each of these depth-dependent terms with increasing height of the

water surface can be used to calculate flow resistance at any water depth. This approach is discussed further in Chapter 8.

GENERAL	$\ln(f) =$	5.068	$S +$	1.141	$\Lambda +$	−0.617	$\ln(\sigma_Z P_{dxc}) +$	−1.171	$F_P +$
MRZ 1		4.113		1.384		−0.884		−1.868	
MRZ 2		5.693		1.374		−0.782		−1.213	
MRZ 3		4.779		1.063		−0.850		−1.546	
MRZ 4		4.962		1.113		−0.882		−1.293	
MRZ 5		5.282		2.117		−0.728		−0.156	
Ploughed		5.711		1.577		−0.510		−0.135	

GENERAL	−0.149	$\ln(d_{50}) +$	−0.245	$D_{sk} +$	−3.100	$\ln(P_d) +$	12.492
MRZ 1	0.131		−0.355		−3.604		17.239
MRZ 2	−0.268		−0.030		−0.497		−1.193
MRZ 3	−0.090		−0.249		−7.024		31.496
MRZ 4	−0.469		−0.422		0.579		−5.799
MRZ 5	0.397		−0.104		−1.980		9.544
Ploughed	−0.438		−0.543		−1.594		3.431

Table 6.4. Variation of the coefficients of each roughness measure related to flow resistance for the dataset as a whole (model 6.16) and at each Morphological Runoff Zone (MRZ) (model 6.18).

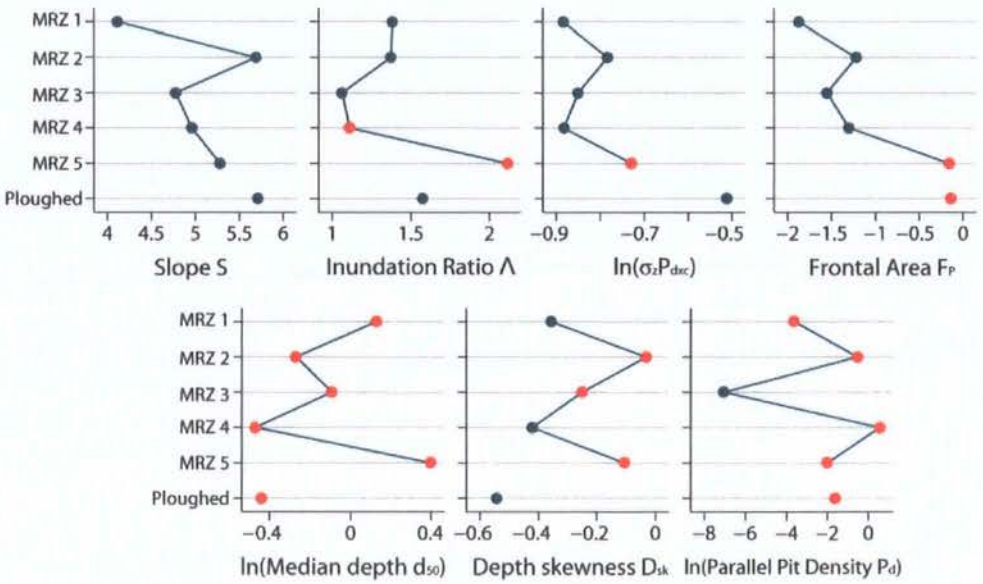

Figure 6.19. Variation of the coefficients of each roughness measure included in Table 6.3 with Morphological Runoff Zone. Red points indicate the condition where $P > 0.01$. Note that zero is located at the right side of the graphs displaying negative coefficients and that the observations are not equally distributed between each MRZ.

The dimensionless product $\sigma_Z P_{dxc}$ (the standard deviation of surface elevations and the pit density measured in a cross-slope direction) combined a general roughness measure (σ_Z) with a more specific measure (P_{dxc}). The hypothesis behind the inclusion of this variable was that increased roughness (defined generally with σ_Z) that manifested itself as flow concentrations (specifically, pits in the cross-slope direction) would increase the conveyance of flow (thereby decreasing resistance). This was found to be significant at a range of plots (although not at the MRZ 5 plots). In contrast, the pit density measured parallel to the flow direction is significant only at MRZ 3.

The F_P measure is also insignificant at the MRZ 5 plot. Elsewhere, the negative coefficient shows that resistance decreases with increasing frontal area (scaled by total surface area). This relationship is most significant at the upslope locations. It could be suggested that the minor obstacles to flow encountered on these surfaces (often small clasts with no flow features visible) encourage minor concentration of flow. Such a relationship was not found in the rougher flow concentrations further downslope where the flow was already concentrated and protruding frontal areas present an obstacle to concentrated flow.

Figure 6.20 repeats the analysis shown in Figure 6.18 using this new model (model 6.16 in Table 6.4). Predictions of measured resistance have generally improved (note that (d) remains the same and the variable coefficients seen in Table 6.4 represent (c)). A notable difference is that the separate predictions (using the variable coefficients but same roughness measures) predict $\ln f$ better ($R^2 = 0.70$) than when different roughness measures are selected for each model ($R^2 = 0.67$). This shows the value of this two-step approach and examining the relationships at each hillslope location before generating a model to predict resistance from roughness over a wide range of soil surfaces.

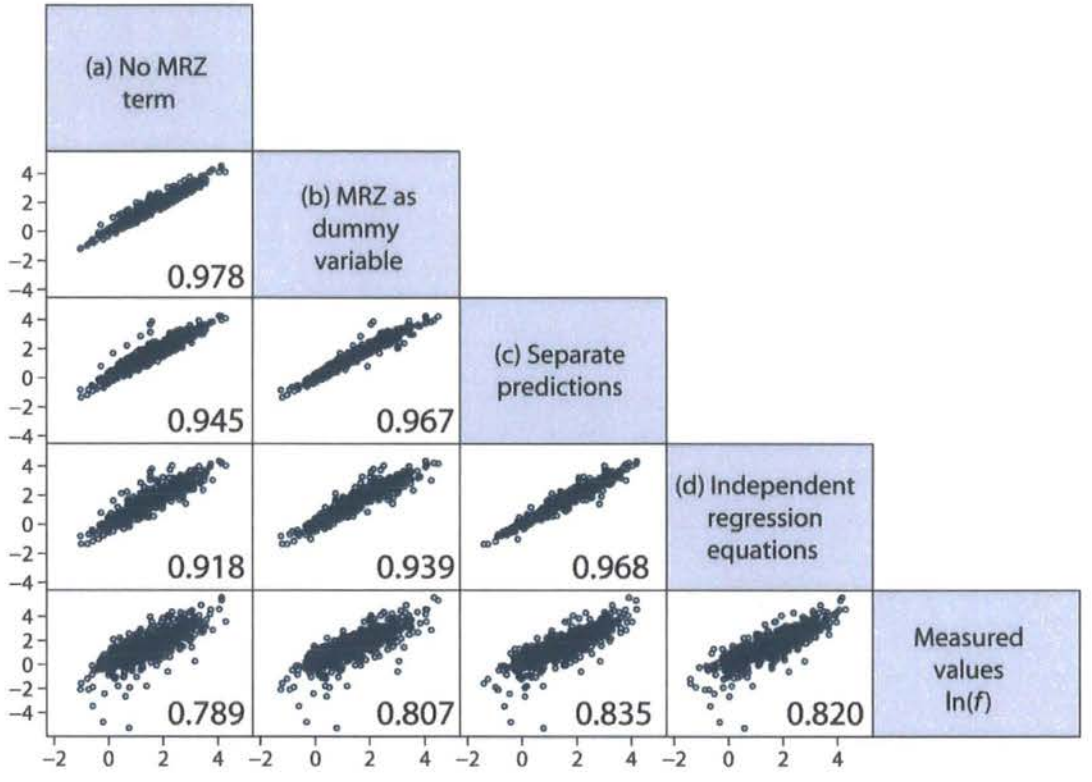

Figure 6.20. Scatter matrix demonstrating relationships between different methods of incorporating hillslope position into predictions of resistance to overland flows and the measured values (log scale). All roughness measures in Table 6.3 have been included in each prediction in a two-step approach. Pearson's correlation coefficient is displayed in the lower right corner of each plot region.

Although these separate equations require artificial boundaries to be drawn within each hillslope and make no attempt to provide any generalised predictive equation for flow resistance over a wide range of conditions, this approach develops an increased understanding of the variable relationship between resistance and roughness and provides an indication of the different processes operating at a small scale. While the details of these separate relationships may be specific to the dataset examined in this study, the general patterns observed may be of some wider importance. The range of surfaces for which these empirical relationships have been developed is sufficiently wide to suggest that they may be appropriate for most bare semi-arid surfaces.

6.6 Summary

This chapter has attempted to relate overland flow resistance to measures of surface roughness and has produced a suite of equations that require an extensive knowledge of soil surface microtopography. Many studies of hillslope hydrology assume knowledge of Re (or flow rate) with which to predict resistance. This approach has the advantage of requiring less information about the overland flow itself to model resistance. Assuming knowledge of flow depth (as might be given by abstracting infiltration rates from rainfall totals) and the variation of submerged microtopography with flow stage, the changing resistance with discharge can be accounted for. The inclusion of a depth-dependent term in each model suggests that f varies with increasing flow depth. Chapter 8 discusses how that incorporation of this dependency in models of hillslope hydrology affects the conceptualisation of the hydrological connectivity framework of semi-arid flood generation described in Chapter 3.

The relationships identified in section 6.5 are complex and empirical. They cannot be applied to conditions outside those in which they were developed. In semi-arid environments, this may not be as much of a limitation as it first appears. The present study conducted a high-resolution topographical survey of three contrasting hillslopes previously thought (e.g. Bull *et al.*, 1999; Bull *et al.*, 2003; Bracken and Kirkby, 2005) to be end-members of the range of hydrological responses observed at the Rambla Nogalte and Rambla de Torrealvilla catchments of south-east Spain. Relationships found to be valid across all three hillslopes are assumed to be true for all intermediate hillslopes in these catchments.

Relating roughness to resistance is not straightforward. Complex natural soil surfaces vary in innumerable ways. Capturing those particular aspects of topographic variation that combine to resist flows may prove to be an impossible task. This chapter has made some initial advances towards this aim. It shows that morphological representations of overland flows relate to resistance differently as the general form changes. While the specific details of the equations may not be universally applicable, general points can be drawn which may be of wider significance and help develop our understanding of hillslope hydrology.

Moreover, section 6.2 demonstrated that the resistance equations developed from theoretical analysis of pipe-flows and open-channel flows present an overly simplistic picture of the relationship between flow resistance and roughness. It is not surprising that the models developed from this dataset out-performed those more traditional (and often substantially simpler) approaches of predicting resistance; but Figure 6.11 shows that even where high-resolution topographic detail is available, it remains difficult to make predictions of resistance over the wide range of flow conditions typically experienced on semi-arid hillslopes.

Several methods of incorporating the variable microtopography with distance downslope (the MRZ transition discussed in section 4.5.3) were investigated. The most effective approach was to examine the individual relationships between resistance and surface roughness at each Morphological Runoff Zone and then to incorporate each relevant roughness measure into a general model, allowing the coefficients of each predictor to vary with plot-type. This two-step approach ensured that the relevant relationships at each MRZ are included in the overall model.

Chapter 7 attempts to extend the conditions analysed beyond the range encountered thus far by examining the changing nature of the flows as the soil surfaces become increasingly saturated and infiltration rate declines. Until this point it has been implicitly assumed that variable infiltration rates do not affect flow resistance (examining solely the effect of topographic variability), but the initial development of connected flowpaths over hillslopes will be greatly affected by infiltration rates. This next chapter attempts to distinguish any signal of infiltration from the topographic influence. Additionally, it examines the influence of topography and infiltration rates on the development of connected flowpaths across the three hillslopes investigated. The definition of Morphological Runoff Zones is also analysed by relating the results of the qualitative field survey to a more robust and reproducible method of calculation.

Chapter 8 will then bring the results together, suggesting how these results can be implemented in models of hillslope hydrology and used to investigate connectivity development and the potential for flash-flooding in semi-arid catchments.

CHAPTER 7

FLOW CONCENTRATION & CONNECTIVITY OF HILLSLOPES

7.1 Introduction

This chapter integrates the plot measurements discussed in previous chapters into a hillslope-scale assessment of hydrological connectivity. The first step is to examine the Morphological Runoff Zones (MRZs) used to aggregate the hillslope surfaces into five categories, each representing a plot examined in the preceding chapters. Section 7.2 presents the mapped distribution of MRZs over each of the hillslopes in this study and formalises their definition for a more robust method of classifying hillslope surfaces from a Digital Elevation Model.

Chapter 3 introduced the connectivity framework and the importance of connectivity development for flood generation in semi-arid catchments. Connectivity depends on both runoff production and transfer; at the hillslope scale it is strongly associated with flowpath development. Reaney (2008) suggests that travel time over interrill surfaces to flow concentrations is an important property of connectivity in semi-arid environments. While the connectivity of ephemeral channels is also a fundamental issue, it is beyond the scope of this study; see Shannon (2003). Section 7.3 examines the transfer of runoff during the field flume experiments described in Chapter 4. The velocity and concentration of flow is described in detail in section 7.3.1. These tests were repeated several times under different conditions; section 7.3.2 explores the effect of a 'wetting-up' event on simulated flow

velocities and concentration. Section 7.3.3 then up-scales these results to a basic analysis of hillslope travel-times.

Section 7.4 investigates infiltration in more detail, attempting to separate the resistance caused by soil roughness from that generated by the infiltration of overland flow into the soil and storage in surface depressions. The roughness-resistance relationships identified in Chapter 6 were found for runoff flowing over a dry soil surface. As the experiment continued and the soil became more saturated and depression stores filled, further dye pulses were added into the flow. Section 7.4 attempts to separate the resistance caused by roughness from that generated by the depression storage and infiltration and argues that this distinction may be difficult to determine for natural overland flows. The suite of equations presented in Chapter 6 is applied to the dye-pulse dataset (section 7.4.1) and infiltration (7.4.2) and depression storage (7.4.3) are examined as potential candidates to explain the differences between measured and modelled resistance. Section 7.4.4 develops a new suite of resistance equations more applicable to established flow connections. Section 7.5 summarises these results and places them in the context of the synthesis presented in Chapter 8.

7.2 Distribution of Morphological Runoff Zones

The purpose of dividing the hillslopes into Morphological Runoff Zones is to provide an approximate categorisation of surfaces with similar microtopography. The methodology originally proposed by Bracken and Kirkby (2005) has been modified. The boundaries between zones were identified by eye in the field. While this adds a degree of subjectivity into the methodology, in practice, it provides a quick and efficient survey method. Bracken and Kirkby (2005) paced down hillslope profiles noting where the first evidence of flow features occurs and interpolating between profiles across-slope. Here, the boundaries were marked by attempting to follow the limit of flow features in a cross-slope direction, recording a track of data-points using a handheld GPS device (GS20). There will be considerable imprecision in this technique. However, it represents a convenient first estimate of the extent of each Morphological Runoff Zone (Table 7.1; Figures 7.4–7.6a). This dataset is used as a training set to develop a more robust estimate of MRZ thresholds.

MRZ AREA (m^2)	**Upper Nogalte March 2007**	**Upper Nogalte May 2007**	**Cardenas**	**Del Prado**
MRZ 1	123	123	267	573
MRZ 2	507	506	925	731
MRZ 3	762	342	1007	687
MRZ 4	395	201	783	470
MRZ 5	122	122	–	225
PLOUGHED	878	1493	3747	–
TOTAL	2787	2787	6729	2686

Table 7.1. Areas of each Morphological Runoff Zone observed at each hillslope (m^2).

The GPS tracks were draped over 50 mm resolution hillslope Digital Elevation Models captured using the Trimble GS200 terrestrial laser scanner described in section 4.3.3. The field survey method described in section 4.5.3 permitted such a high-resolution DEM to be obtained directly for an entire hillslope, avoiding any problems of disaggregating lower-resolution DEMs (Mueller *et al.*, 2007). Recent developments in terrestrial laser scanning have created an opportunity to undertake an analysis of hillslope-scale processes: Chapter 3 emphasised the role of such processes contributing to flood generation in semi-arid environments (e.g. D'Odorico and Rigon, 2003).

Kirkby *et al.* (2005) suggest that MRZs are consistently related to the overland flow length-slope product within the same lithology and land-use. Differences in the value of the length-slope product reflect differences in runoff response (Bracken and Kirkby, 2005). To examine this topographic index further, the slope and the upslope contributing area were calculated for each cell of the hillslope DEM. This used a deterministic 8 (d8) flow routing algorithm (where all flow is routed through the lowest of eight neighbouring cells in a grid). This was chosen because it performs reasonably well over the relatively rough hillslope surfaces and allows individual flow pathways to be tracked. To provide a measure of the same dimensions as the slope-length product, the square-root of the upslope contributing area was calculated. The measurements of slope and $\sqrt{\text{area}}$ recorded at the base of each MRZ are displayed in Figure 7.1.

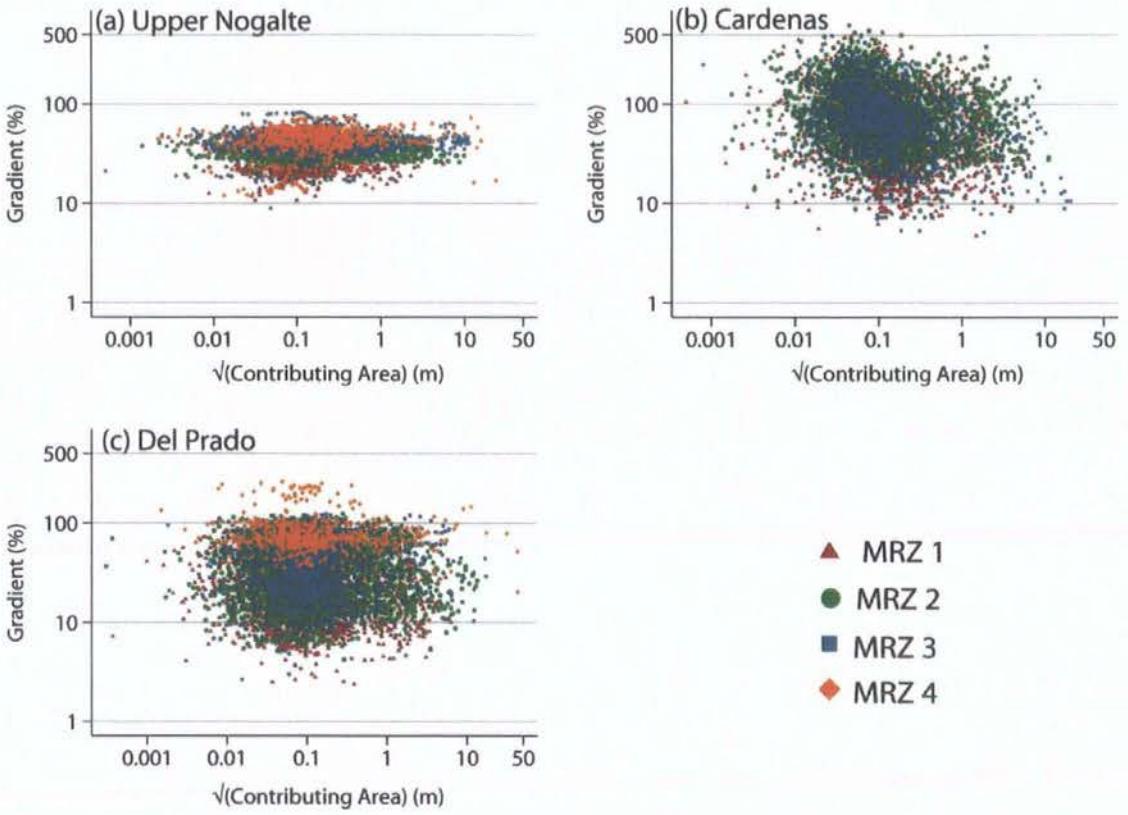

Figure 7.1. Values of $\sqrt{area}$ and gradient recorded at the base of each Morphological Runoff Zone found at each hillslope. As flow was routed off the Upper Nogalte and Del Prado hillslope in gullies, there is no base recorded for the MRZ 5 areas. Similarly, no base can be identified for the MRZ 4 areas at the Cardenas hillslope as no gully erosion was observed.

There is considerable overlap between each MRZ; this is a consequence of the field mapping aggregating areas with negligible upslope area with flow concentrations. A range of slope angles is also seen within each MRZ. The Upper Nogalte has the lowest range of slopes and the Del Prado hillslope shows the most pronounced increase in slope with distance downslope. The steepest slopes are found at the Cardenas hillslope. The most interesting feature of Figure 7.1a–c is the upper-right corner of each plot region where thresholds of the slope-area product can be examined. To make this analysis clearer, those data-points with the highest slope-$\sqrt{area}$ product within each MRZ are plotted in Figure 7.2a–c.

There appears to be a relatively consistent relationship between the lower boundaries of each MRZ and the slope-$\sqrt{\text{area}}$ product (as suggested by Kirkby *et al.*, 2005). Beyond certain thresholds, wash deposits (below the downslope limit of MRZ 1), flow concentrations (below MRZ 2), rills (below MRZ 3) and gullies (below MRZ 4) will inevitably form. The nature of these thresholds varies slightly between each hillslope, reflecting differences in either soil erodibility or runoff response.

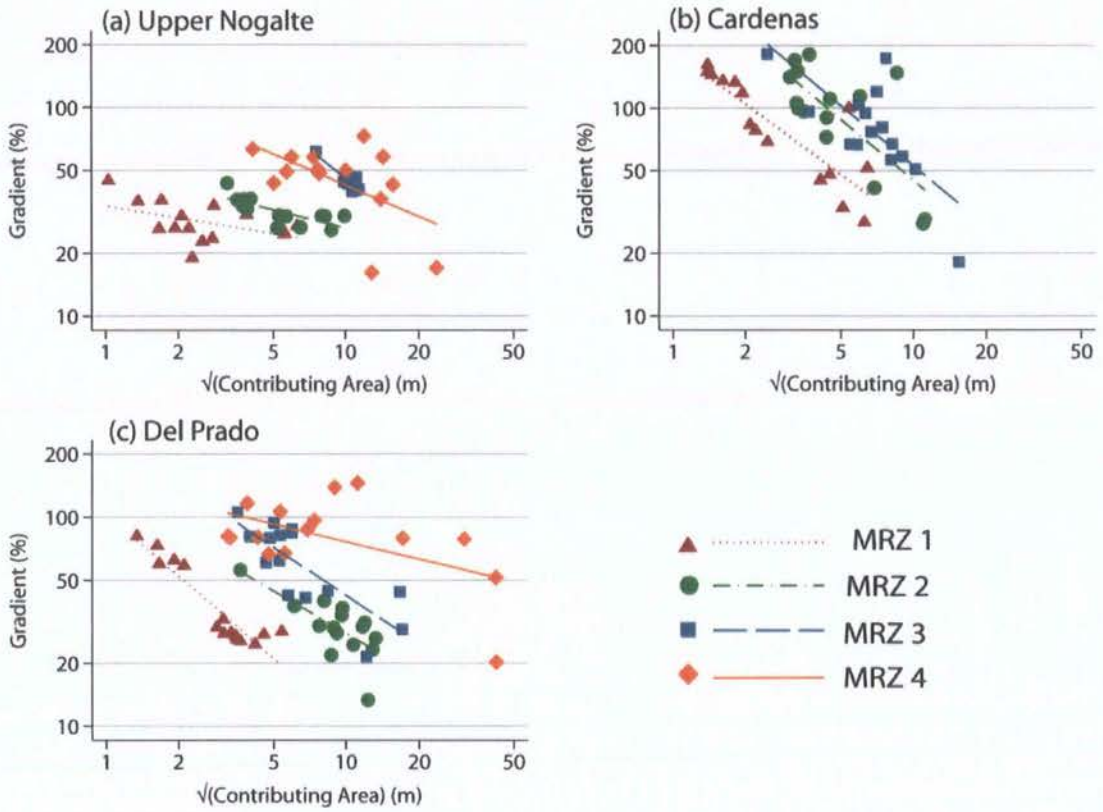

Figure 7.2. The relationship between $\sqrt{\text{upslope area}}$ and gradient for different Morphological Runoff Zones at each hillslope.

The Cardenas hillslope appears to have the highest threshold for the downslope limit of each MRZ. The narrow window between the bases of MRZ 2 and MRZ 3 suggests that once flow concentrations form, they rapidly develop into rills. This is compatible with the observation of a relatively thick soil crust at this hillslope, shifting erosional features further downslope. Once the crust has been eroded away (in flow concentrations) further erosion

would be relatively rapid, possibly explaining the narrow window of flow concentrations before rill initiation.

A steeper threshold slope-$\sqrt{area}$ relationship (in Figure 7.2a–c) suggests that incision occurs at lower contributing areas (at any given slope angle). This indicates the dominance of the upslope area measure in determining the erosional threshold (possibly a consequence of a high runoff-response). The Cardenas hillslope demonstrates the steepest threshold lines (with the soil crust promoting a high runoff response) followed by the Del Prado and Upper Nogalte hillslopes. The MRZ 4 lower thresholds are generally shallower with a dominance of slope gradient determining the onset of gully erosion. The crossover between the downslope boundaries of MRZ 3 and MRZ 4 at the Upper Nogalte hillslope (Figure 7.2a) possibly represents the combining of the flow concentrations into much fewer rills and the absence of a lower MRZ 4 boundary over parts of the hillslope (Figure 7.4a). Consequently, fewer points of a high contributing area are available at the downslope boundary of MRZ 4.

The maximum of the root of the upslope area found in each MRZ was multiplied by the mean slope angle of the mapped area. This measure provided a threshold for each MRZ which could be derived from the DEM alone (Figure 7.3). These thresholds were then applied to each hillslope DEM to give a prediction of the locations of each MRZ (Figure 7.4c, 7.5b and 7.6b). This avoids the problematic lumping of areas of low contributing area surrounding the rills and flow concentrations into the MRZ 3/4/5 categories (a consequence of the field mapping; e.g. Figures 7.4a–7.6a) that was responsible for the overlap found in Figure 7.1.

The Cardenas hillslope demonstrates the largest value of the slope-$\sqrt{area}$ product before each level of morphological features is observed; this may support the previous suggestion that the soils of this hillslope are the least erodible. Del Prado requires a much lower slope-$\sqrt{area}$ product for erosion to initiate, although there is a slight kink in the relationship as flow concentrations occur more readily than expected.

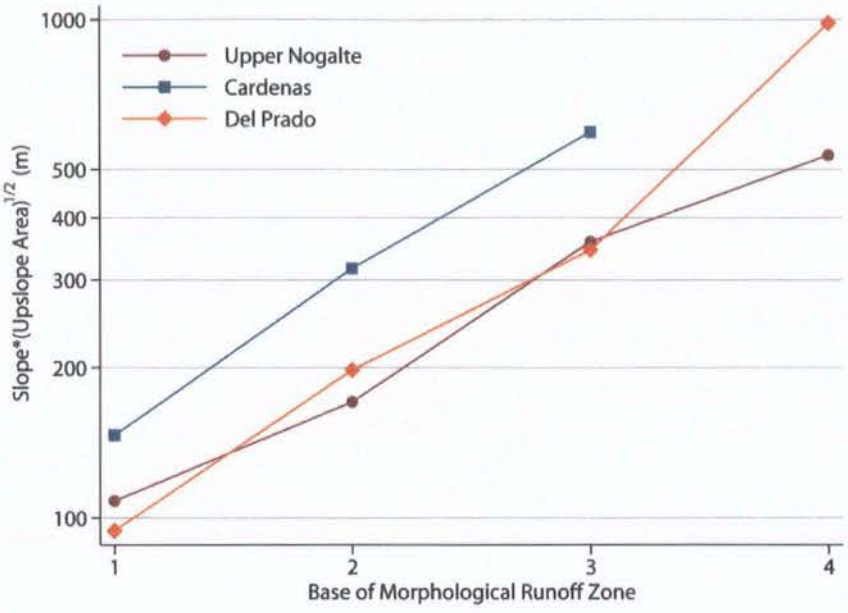

Figure 7.3. Calculated slope-$\sqrt{\text{area}}$ product of the lower bounds of Morphological Runoff Zones 1–4 for each hillslope.

The predicted threshold values of the Upper Nogalte hillslope are difficult to interpret because the natural grading of the Morphological Runoff Zones is interrupted by the presence of a ploughed band. The base of the MRZ 2 plot is artificial (as this was a result of the ploughed band – Figure 7.4a), explaining the low value of the slope-$\sqrt{\text{area}}$ product at the base of Morphological Runoff Zone 2. However, the base of MRZ 4 is also relatively low. The ploughed band should have the opposite effect by trapping more runoff in surface depressions (section 7.4.3) and decreasing the effective contributing area. Previous research (e.g. Bull *et al.*, 2003) indicated that the red schist of the Upper Nogalte hillslope has the lowest runoff response (confirmed by infiltration measurements presented in section 7.4.2). It was expected that this hillslope should have the highest threshold of the three hillslopes. While Figure 7.3 shows this not to be the case; the shallow slope-$\sqrt{\text{area}}$ relationship in Figure 7.2a suggests that slope angle is a more influential factor of erosion thresholds than upslope area.

Maps of Morphological Runoff Zone locations calculated from the erosion thresholds in Figure 7.3 are very different from the field-sketches. As mentioned in Chapter 6, the field

sketches mix areas of flow concentrations and interrill flows into a single unit. This new method provides a more robust index-based method of identifying MRZs and limits the designated MRZ 3–5 areas just to those specific areas where concentrated flows are found. Although this reduces their spatial coverage, these incisional flowpaths remain crucial for hydrological connectivity and flood generation, as much of the hillslope runoff must be routed through them before reaching the outlet (e.g. Croke and Mockler, 2001).

The mapped distribution of MRZs on the Upper Nogalte hillslope (Figure 7.4a–c) is interrupted by a band of ploughed surface stretching across most of the hillslope. This had not been ploughed for approximately a year before March 2007. Between March 2007 and May 2007 additional ploughing took place (Figure 7.4b). Unfortunately, this destroyed several of the previously established plots on this hillslope. However, it provides an interesting comparison between Figure 7.4a and 7.4b. The ploughed area expanded to cover much of the MRZ 3 and MRZ 4 areas upslope of the gully erosion. While this land is left fallow and has been used for goat herding over the past 4 years, the farmer targeted the areas that route overland flow into the gullies; this was presumably to prevent further backward expansion of the gully heads. The expansion of the ploughed land into this area will affect the travel times of runoff reaching the river channels; this is explored further in section 7.3.3. This hillslope displays evidence of a complex interaction between agricultural and topographical features that produces temporary hydrological structures (see Ludwig *et al.*, 1995).

Figure 7.4c shows that the Upper Nogalte hillslope is dominated by parallel drainage lines, merging only at the foot of the hillslope as flow is routed towards the outlet. The pattern of MRZs along a drainage line includes transitions in and out of each state, showing the influence of slope angle on the calculated MRZ threshold. Calculating MRZs in this manner integrates the effect of high drainage density on steeper slopes (Kirkby *et al.*, 2005). The calculations show flow concentrations (MRZ 3) and rill incision (MRZ 4) in approximately the correct places, although it slightly under-predicts the occurrence of gully erosion.

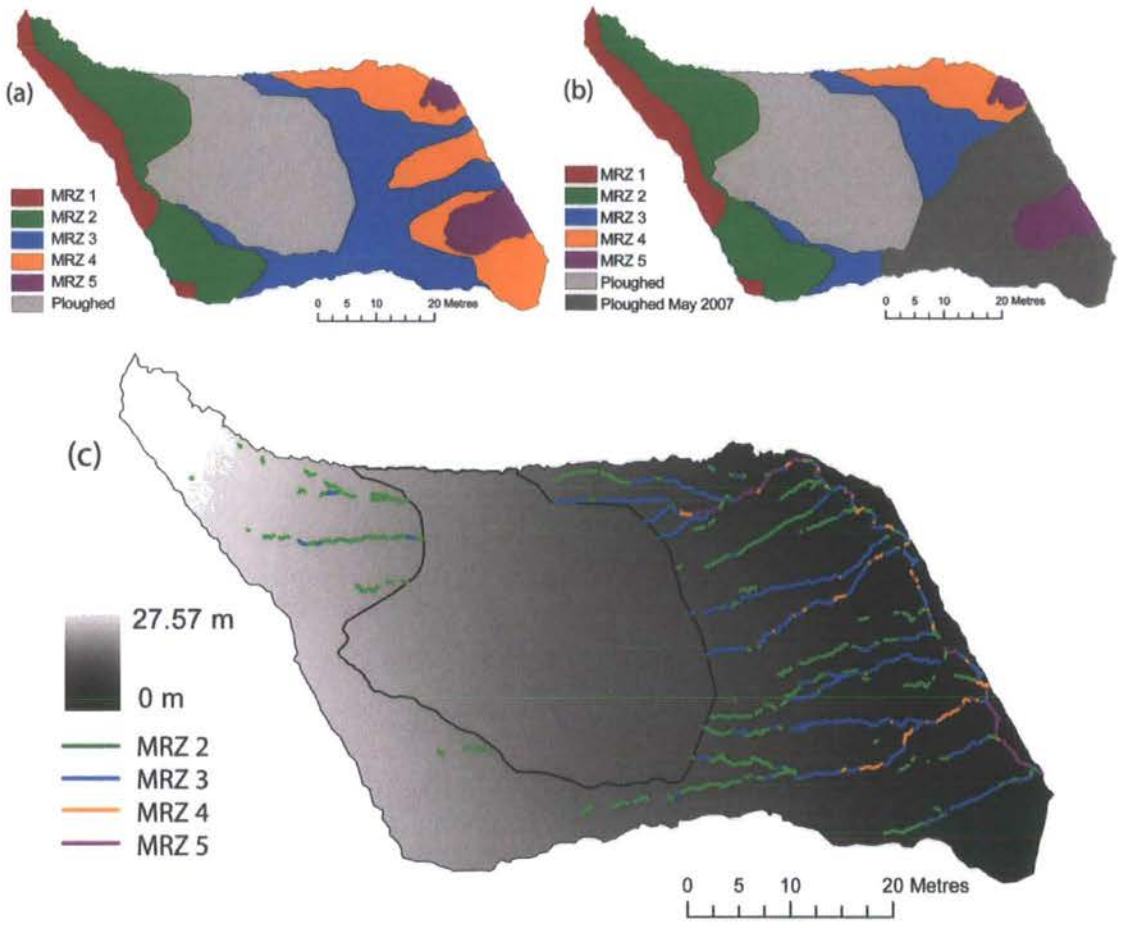

Figure 7.4. Distribution of Morphological Runoff Zones over the Upper Nogalte hillslope (a) March 2007; (b) after additional ploughing in May 2007; (c) calculated distribution of flowpaths over each threshold (for March 2007).

The Cardenas hillslope (Figure 7.5a–b) is more circular in planform with a radial distribution of flowpaths. Half of the hillslope has been ploughed to support almond trees (Figure 4.30) while the other half shows a gradual downslope transition between MRZs. The calculations appear to over-predict the threshold for rill erosion. The limited area calculated as MRZ 3 is a consequence of the similar calculated thresholds seen in Figure 7.2b, although patches are observed across most of the area mapped as MRZ 3.

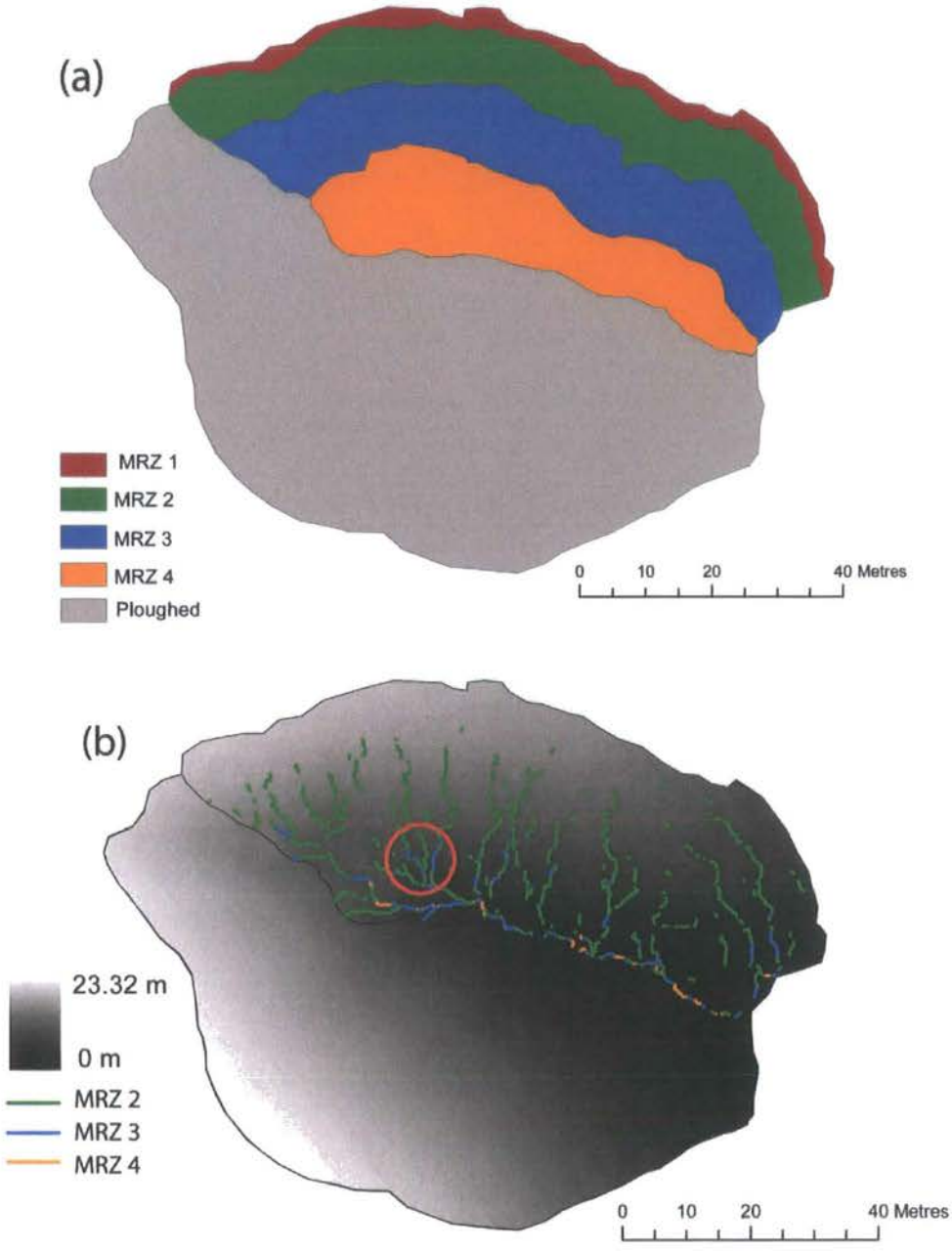

Figure 7.5. (a) Distribution of Morphological Runoff Zones over the Cardenas hillslope; (b) calculated distribution of flowpaths over each threshold. The red circle indicates an area where rills were observed in the field, but not predicted using this technique.

The Del Prado hillslope is again quite circular in planform, routing runoff from a large upslope area through a narrow constriction where evidence of rill and gully erosion is found. The calculated locations of MRZs agree well with the field mapping. This approach

was able to simulate discontinuities in the MRZ network, thus giving a more accurate interpretation of the location of flow concentrations than the mapped extents. Over a small area of the Del Prado hillslope, a small discontinuity in the rill network was observed, most probably as a consequence of the gentle slope at that patch of the hillslope. Mapping such features in the field would be time-consuming and relatively subjective. Through its dependence on slope angle, the erosion threshold applied to the hillslope DEM was able to reproduce this feature (Figure 7.6b). While such a discontinuity over a small area may seem relatively unimportant, the review of Chapter 3 emphasises the hydrological significance of even the smallest discontinuities in the flow network when viewed through the framework of hydrological connectivity (e.g. Fitzjohn *et al.*, 1998). Similar reversals of the normal downslope MRZ transitions are predicted at each of the hillslopes studied.

This approach to identifying areas of similar flow features ignores the different infiltration rates observed across the hillslopes. Some patches may absorb more rainfall and therefore remain disconnected from the hillslope outlet, altering the effective contributing area (e.g. Van de Giesen *et al.* 2000; Yair and Kossovsky, 2002). The distribution of infiltration rates over the hillslopes is examined in section 7.4.2. While these point measurements were distributed between MRZs, no attempt was made to examine their variation across the hillslope. This has been the focus of much recent research (e.g. Solé-Benet *et al.*, 1997; Cantón *et al.* 2002, 2004). However, as suggested in Chapter 3, it is the spatial configuration of runoff producing areas and areas of high infiltration alongside areas of high and low flow resistance that is the key to understanding hillslope hydrological responses. The technique described in this section provides a basic understanding of such spatial relationships.

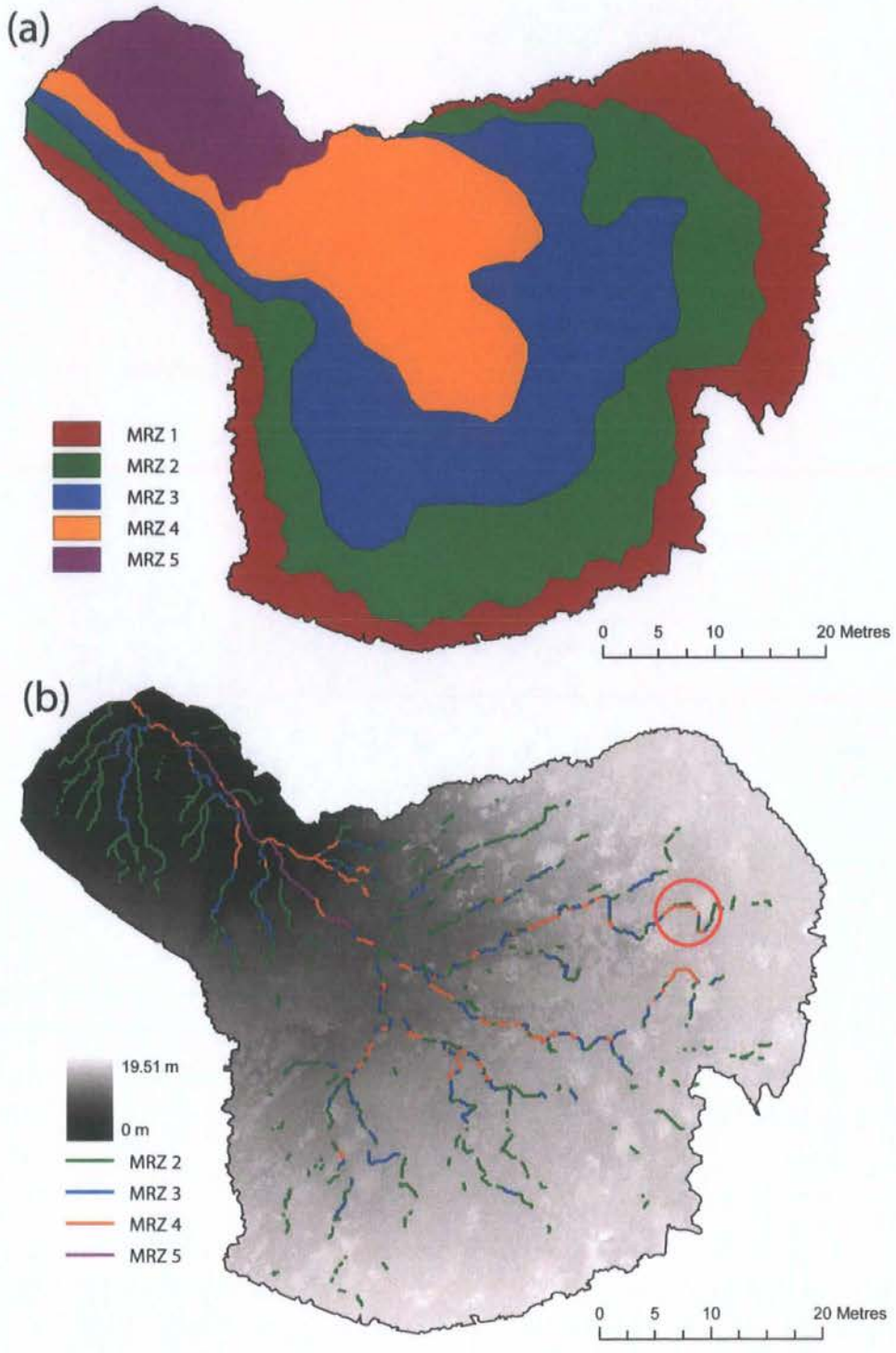

Figure 7.6. (a) Distribution of Morphological Runoff Zones over the Del Prado hillslope; (b) calculated distribution of flowpaths over each threshold. The red circle indicates an area where rills are predicted by this technique yet not observed in the field.

Assuming that the spatial variation of rainfall and soil erodibility is relatively unimportant at this scale, any disparities between the predicted extent of rill erosion (for example) and that observed in the field may be explained by the presence of an area with a high (or low) infiltration capacity. As the range of thresholds observed in the field has been integrated into a single hillslope average value and used to predict the exact MRZ locations, areas where the threshold was above this value may be downslope of an area with a high runoff threshold. At the Del Prado hillslope, rills are predicted at a small area where they were not found in the field (circled in Figure 7.6b) suggesting that the upslope area can absorb a greater amount of runoff relative to the hillslope average (supported by observations presented in section 7.4.2). Conversely, areas where the threshold was below this value are potentially important runoff source areas. For example, the rill network of the Cardenas hillslope was observed to extend further up the hillside, particularly in the area marked with a circle in Figure 7.5b. As no rill erosion was predicted to take place here, this may indicate an important runoff source area upslope of this point. Such differences can be examined at each MRZ boundary, permitting a reasonable estimate of the hillslope-scale variation of runoff-absorbing potential. This represents minor errors in the MRZ calculation technique providing a crude evaluation of areas of high runoff potential relative to the rest of the hillslope and should only be used to develop a broad appreciation of the patterns observed to help target further research.

7.3 Transfer & Routing of Runoff at the Hillslope Scale

This section examines field observations of flow velocity and the expanding area of flow moving downslope over the experimental plots (section 7.3.1). The experiments were repeated up to three times on each plot. The experiments of March 2007 took place subsequent to a small 'wetting-up' rainstorm (see Figure 7.12) and provide an interesting comparison with the May 2006/7 experiments (section 7.3.2). The influence of 'wetting-up' on flow velocity changes the travel times to the hillslope outlet; this may have a major effect on the duration of high-intensity rainfall necessary for hillslope outflow, thereby highlighting the importance of storm structure and the location of high-intensity pulses within the rainfall time series (section 3.2; Costa, 1987; Reaney *et al.*, 2007). This analysis

is limited at the Upper Nogalte hillslope as several of the original plots were destroyed during recent ploughing. Additionally, a gullied plot was investigated at this hillslope; although the DEM was of an insufficient resolution at the gully bottom for the soil roughness to be investigated, the MRZ 5 plot results are available for this analysis of flow velocity and concentration.

The measurements of flow discussed here were taken from a constant imposed discharge, which provides a useful comparison between locations, even though it limits the conditions under which these results represent real-world conditions. Section 7.3.3 scales up these velocity measurements to examine the distribution of travel times observed at each hillslope. This analysis is a precursor to the discussion of Chapter 8, using measured velocities rather than applying flow resistance equations calculated in Chapter 6. It does, however, show the influence of the configuration of MRZs and hillslope morphology on runoff transmission.

7.3.1 Flow Velocity & Concentration

The travel time to a flow concentration is a key factor determining the hydrological connectivity of a hillslope (Kuhn and Yair, 2004; Reaney, 2008). This distinction between interrill and concentrated flows is somewhat artificial; the Morphological Runoff Zone concept demonstrates the spectrum of surface types which concentrate flows to different degrees. Figure 7.7 displays the degree of flow diffusion (the inverse of concentration, defined as the ratio of the total flow area to distance travelled from source) observed at each plot. Flow concentration (lower diffusion) occurs abruptly at MRZ 3; the maximum degree of concentration was observed at the Del Prado MRZ 3, Cardenas MRZ 4 and Upper Nogalte MRZ 5 plots. Flow concentration increased as rills incised the soil for the Upper Nogalte and Cardenas hillslopes. At Del Prado, the flow became gradually less concentrated with distance downslope from MRZ 3, as the rill and gully bottoms became gradually wider. This situation is specific to the discharges simulated in these flow experiments.

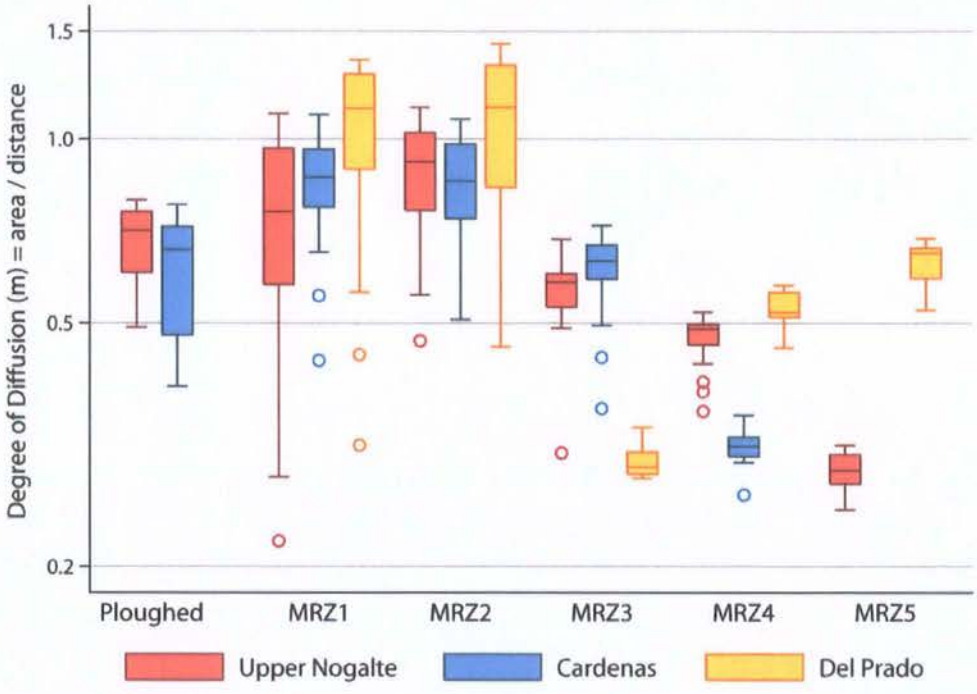

Figure 7.7. Flow diffusion (m) at each plot and hillslope (the inverse of concentration).

Figure 7.7 shows that a range of flow concentrations were found at each plot. The variation of these with time (and therefore with distance travelled) shows some interesting patterns (Figure 7.8a–c). All the flows exit the supply trough equally concentrated and travel approximately 1 metre before differences become noticeable. A defining property of MRZs 1–2 is the diffuse flow they produce. The upslope plots at the Del Prado hillslope disperse flow over a wide surface area; this is least noticeable at the Cardenas hillslope. Flow at the Cardenas MRZ 3 plot is much less concentrated than the equivalent flows at the other hillslopes. The concentrations were either relatively wide or the flows overtopped the minor incision and spilled out over the interrill area. For each hillslope, the between-plot patterns are very similar, although the MRZ 3 plot is the most concentrated at the Del Prado hillslope (the MRZ 4/5 plots are more concentrated at the other two hillslopes). The gully bottom at the Upper Nogalte hillslope was much narrower than at Del Prado; this is reflected in the degree of flow concentration observed. Flow velocity was generally observed to increase with degree of concentration, although this effect was most pronounced at the MRZ 3 and MRZ 4 plots. At each degree of concentration the Del Prado hillslope recorded the most rapid velocities and Upper Nogalte recorded the slowest.

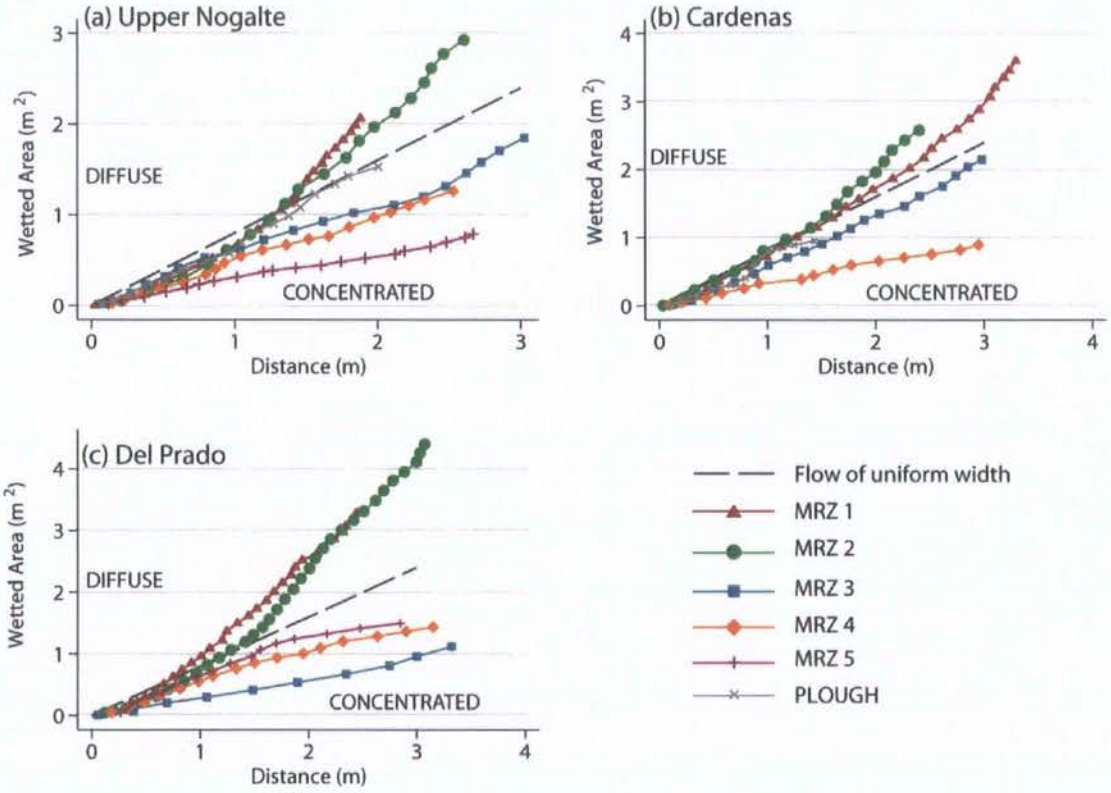

Figure 7.8. Increase of wetted area with distance travelled for each plot and hillslope.

Figures 7.9–7.11 display (a) the maximum distance travelled from the source, (b) the maximum velocity, and (c) the expansion of the wetted area against time (a function of both velocity (increases area) and flow concentration (decreases area)) for each plot and hillslope. The most upslope plot (MRZ 1) of the Upper Nogalte hillslope (Figure 7.9) consistently showed the slowest flow, demonstrating little variation through the experiment. The MRZ 2 plot initially demonstrated faster flow than expected; this can be explained by the steep plot slope. This flow velocity decreased during the course of the experiment. As little flow concentration occurred, the rate of expansion of the wetted area was the most rapid of all the plots. The decrease in velocity coincided with a spreading out of the flow (Figure 7.8a). The MRZ 3 plot also showed rapid flow expansion, increasing throughout the experiment. This plot concentrated the supplied flow more and so travelled furthest from the source, recording the fastest velocity at this hillslope (0.30 m s^{-1}). The velocity of this MRZ 3 plot was the most variable. A comparison between Figure 7.8a and 7.9b demonstrates the relationship between velocity and degree of concentration. The

ploughed plot showed a highly variable flow velocity as the water advanced over ridges and furrows. A similarly variable pattern was observed at the MRZ 5 plot as the flow advanced over obstacles in the gully bottom.

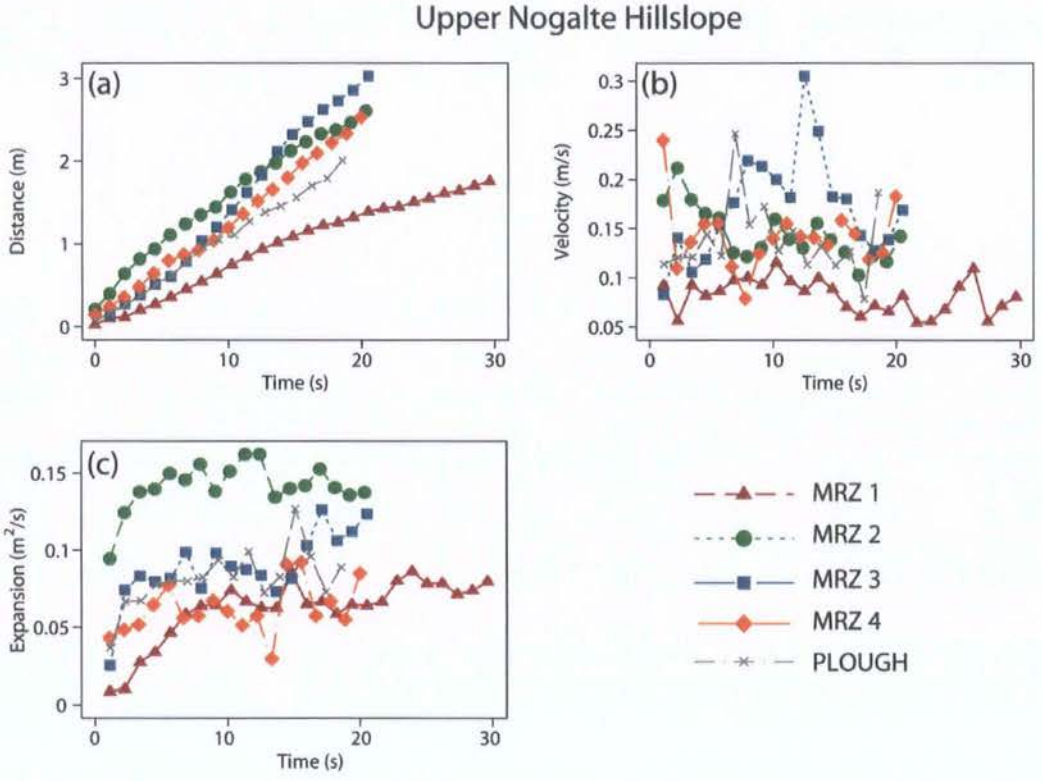

Figure 7.9. (a) The maximum distance travelled from the source, (b) the maximum velocity, and (c) the expansion of the wetted area against time for each plot at the Upper Nogalte hillslope.

At the Cardenas hillslope (Figure 7.10) the rilled plot (MRZ 4) showed the fastest velocity (0.31 m s^{-1}). However, this was only maintained for one second with the remainder of the flow only reaching 0.2 m s^{-1}. The high degree of flow concentration carried the flow the furthest distance in the downslope direction while also recording the smallest expansion of the wetted area. The two upslope plots recorded very similar flow characteristics throughout the experiment, with the MRZ 3 plot intermediate between the upslope plots and MRZ 4. The downslope plots again showed the greatest variation in velocity. The ploughed plot recorded similar velocities to the upslope plots. However, the flowpaths deviated from a downslope direction as the flow encountered furrows (shown in Figure 5.1), so that it travelled the shortest distance from the water source.

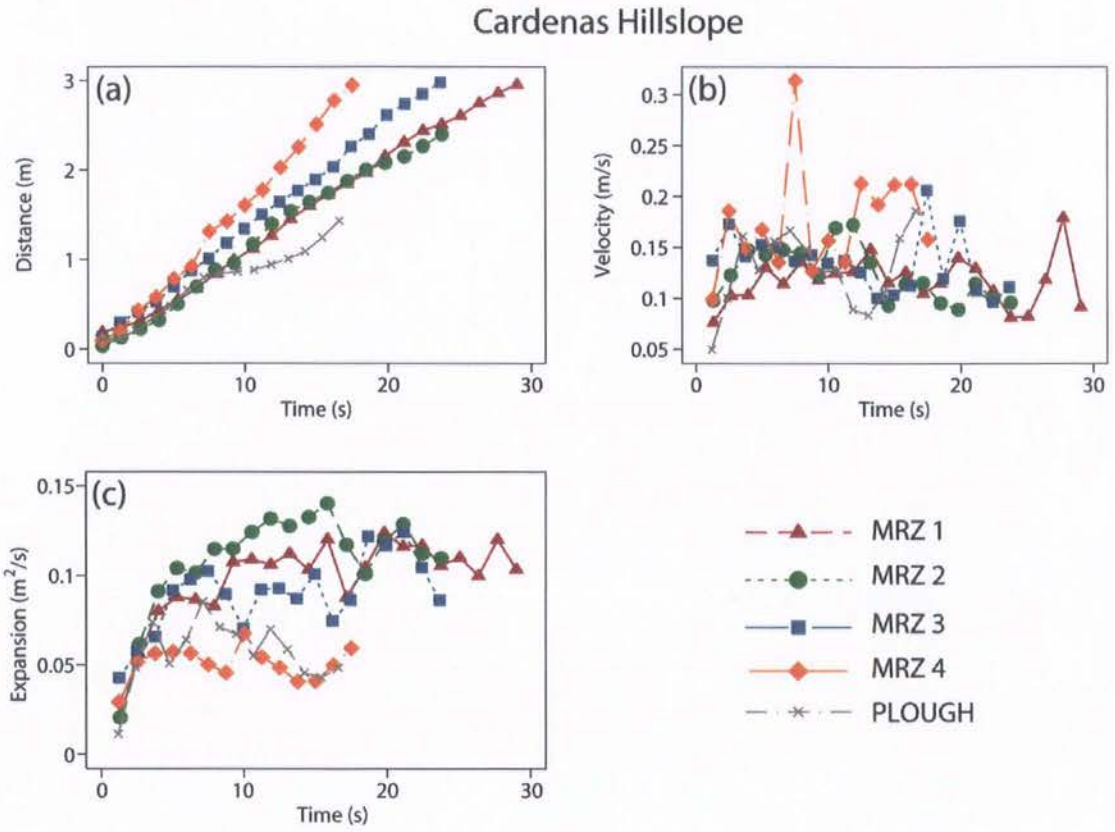

Figure 7.10. (a) The maximum distance travelled from the source, (b) the maximum velocity, and (c) the expansion of the wetted area against time for each plot at the Cardenas hillslope.

An even more distinct divide between flow concentrations and interrill flows can be seen at the Del Prado hillslope (Figure 7.11). The MRZ 3–5 plots showed much faster velocities than were recorded on the other hillslopes. The MRZ 3 plot was by far the most efficient at routing runoff down the hillslope, travelling 3 m in just under 9 s and reaching a maximum flow velocity of 0.58 m s^{-1}. Where the MRZ 4 and 5 plots become more concentrated, the expansion of the wetted area per second decreases and the velocity demonstrates a noticeable increase.

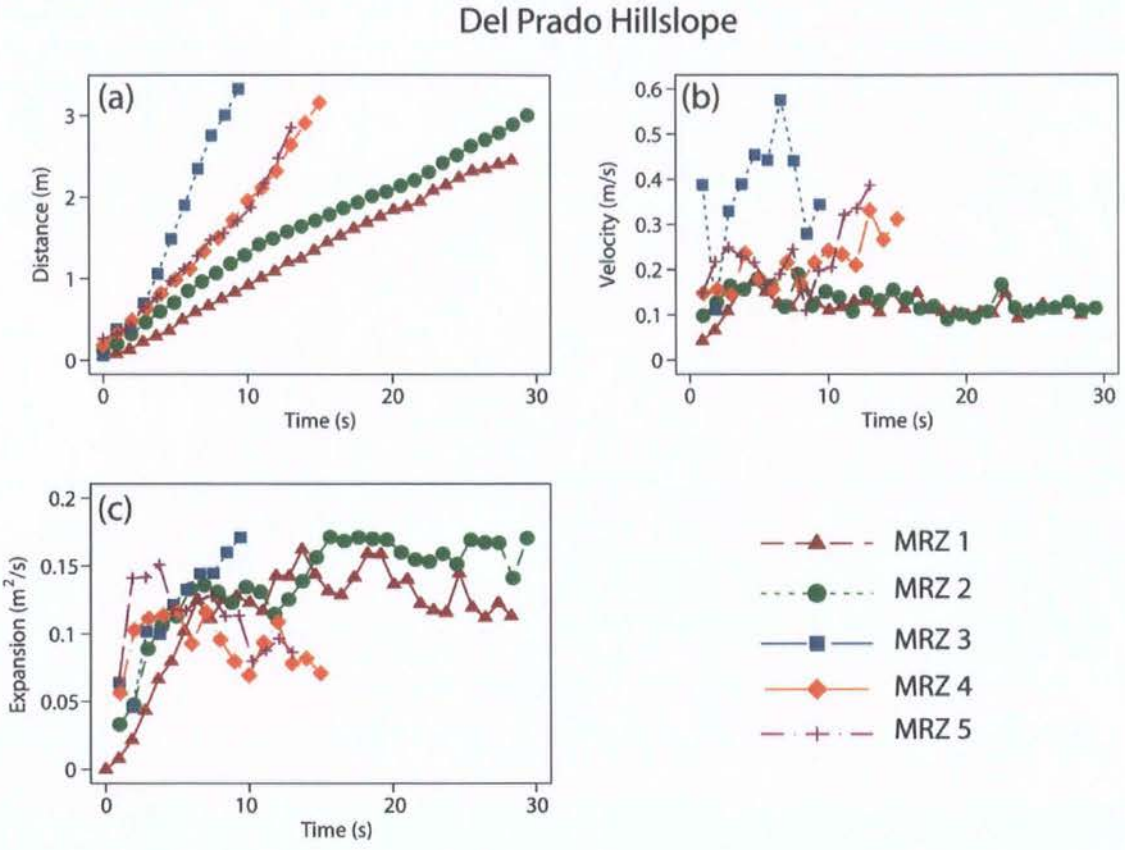

Figure 7.11. (a) The maximum distance travelled from the source, (b) the maximum velocity, and (c) the expansion of the wetted area against time for each plot at the Del Prado hillslope.

The general pattern observed between plots is very similar for each hillslope, suggesting that this categorisation of hillslope surfaces for establishing the routing velocity of overland flow is particularly relevant at the hillslope scale. At each hillslope the flow velocity showed most variation in rills and other flow concentrations. The distinction between the upslope and downslope plots was least evident at the Upper Nogalte hillslope and most obvious at Del Prado. The hydraulic behaviour of such efficient mechanisms of routing runoff through rill networks will greatly affect the hydrological response of a hillslope as most of the generated runoff will be routed through these concentrations (e.g. Figure 7.6b).

7.3.2 Antecedent Moisture Conditions & Runoff Transmission

The results in section 7.3.1 are from field experiments recording the first wave of flow moving over an initially dry soil surface. During a rainstorm, the soil surface gradually absorbs more moisture, thereby reducing the infiltration rate (as described with equation 3.3; Green and Ampt, 1911; Kirkby 1975). Section 7.4 examines the influence of infiltration rate on flow resistance. First, this section examines the impact of soil moisture on flow velocity and concentration. The field flume experiments were repeated in March 2007 after a rainstorm event. Figure 7.12a–c shows the structure of this rainstorm (recorded at three rain gauges shown in Figure 4.28) which was too small to produce runoff and could be described as a 'wetting up event'. Reaney *et al.* (2007) suggest that the sequence of intense bursts of rainfall and such wetting-up events is a key factor for runoff and flood generation in semi-arid catchments through its impact on hillslope travel times and effective hillslope lengths (runoff travelling at a higher velocity requires high-intensity rainfall for a shorter duration of time). See also Van de Giesen *et al.* (2000), Aryal *et al.* (2003) and Yair and Raz-Yassif (2004). The rain gauges used in Figure 7.12 were selected to represent (a) the Upper Nogalte hillslope, (b) the Cardenas hillslope and (c) the Del Prado hillslope. The rainstorm of 27th March 2007 produced just 12.4, 13.6 and 13.4 mm of rainfall, shown in Figures 7.12a–c respectively, reaching a maximum intensity of 12 mm hr^{-1} at the Upper Nogalte (03:00) and Cardenas sites (09:00) and 24.0 mm hr^{-1} at the Del Prado gauge (at approximately 11:00).

Figure 7.12 shows that although the total rainfall amount changed only slightly as the storm moved across the catchment (from 7.12a to 7.12c), the fine structure of the rainstorm is highly variable. Only a single high-intensity pulse was recorded at the Del Prado hillslope; the pulses of rain recorded after 18:00 in Figures 7.12a and 7.12b were not found in the Del Prado record. Given the importance of the sequence and structure of such pulses for runoff generation (e.g. Wainwright and Parsons, 2002), this variability greatly complicates the task of predicting flood events in semi-arid catchments.

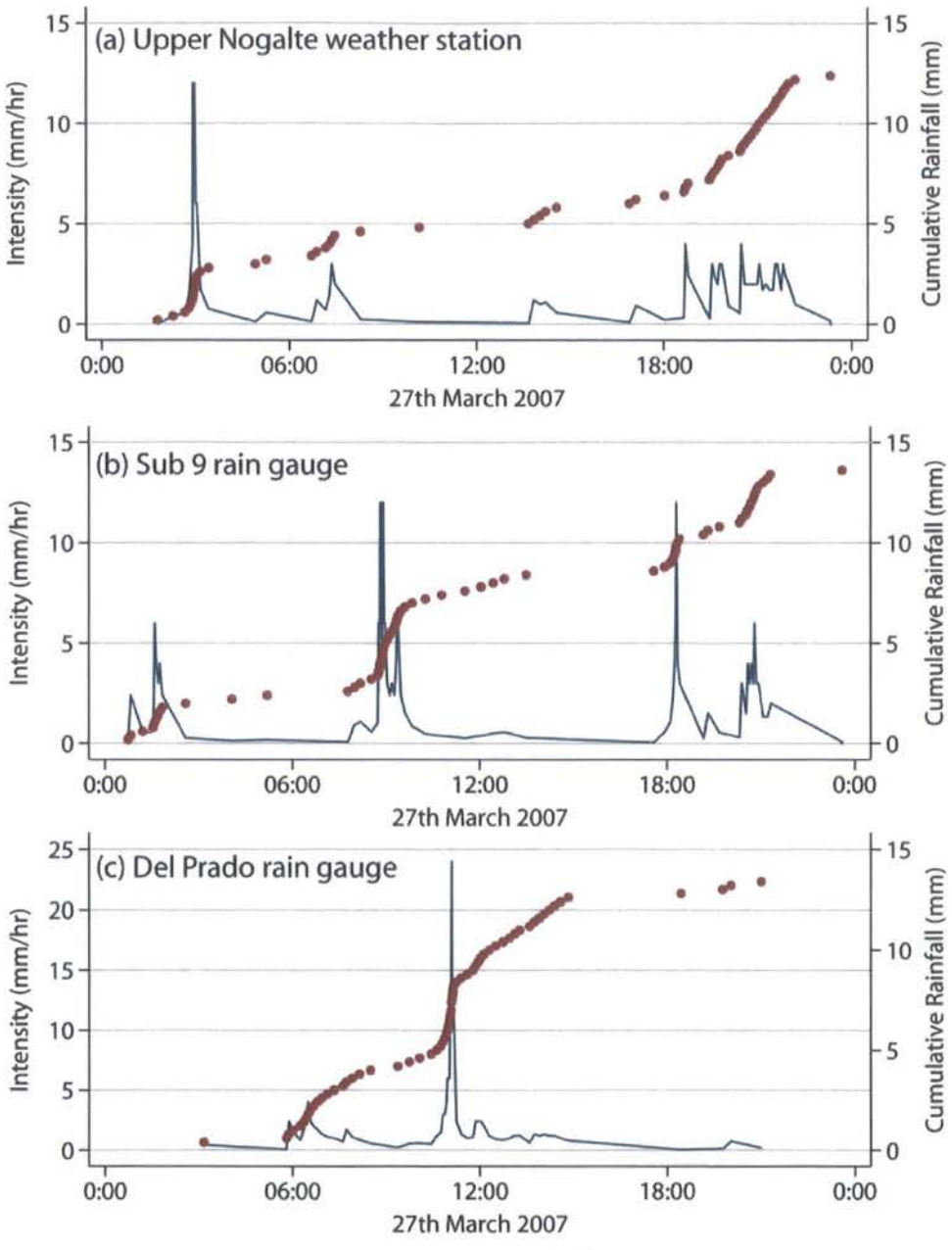

Figure 7.12. Structure of the 'wetting up' event of 27th March 2007 recorded at three rain gauges in the Nogalte and Torrealvilla catchments (locations shown in Figure 4.28).

The total amount of rainfall was very similar at each location and was followed by several days of light drizzle and 100% cloud cover. The experiments under these conditions took place over several days and so the moisture conditions for each plot surface were not identical. While much of the soil moisture may have evaporated or infiltrated in the interim, Figure 7.13 demonstrates that even on the final day of the March 2007 'wet' experiments

(when the Del Prado MRZ 3 flume run took place; Figure 7.13b) there is a noticeable difference between the soil conditions and those of the dry runs (Figure 7.13a). Figures 7.14–7.21 summarise the differences observed at each plot.

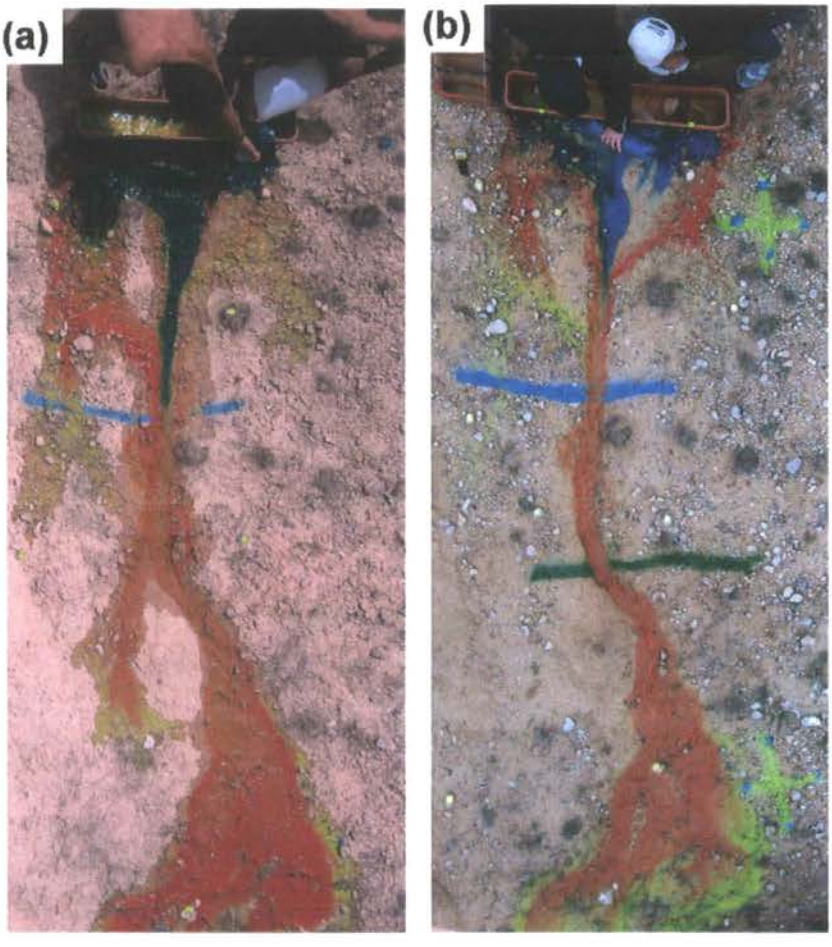

Figure 7.13. Example images taken from the camera boom during (a) dry conditions of May 2006, (b) wet conditions of March 2007. Note: these images are for illustration only and do not represent synchronous moments between the two experiments.

The ploughing between March and May 2007 destroyed many of the original plots established at the Upper Nogalte hillslope. As a result, the dry and wet runs can only be compared at the MRZ 1 and MRZ 5 plots. Figure 7.14 shows the expansion of the wetted area with distance downslope. The MRZ 1 plot showed faster flow during the 'wet' run of

March 2007. Examining the expansion of the wetted area at each timestep shows that both runs followed the same general pattern with the wet run moving consistently faster.

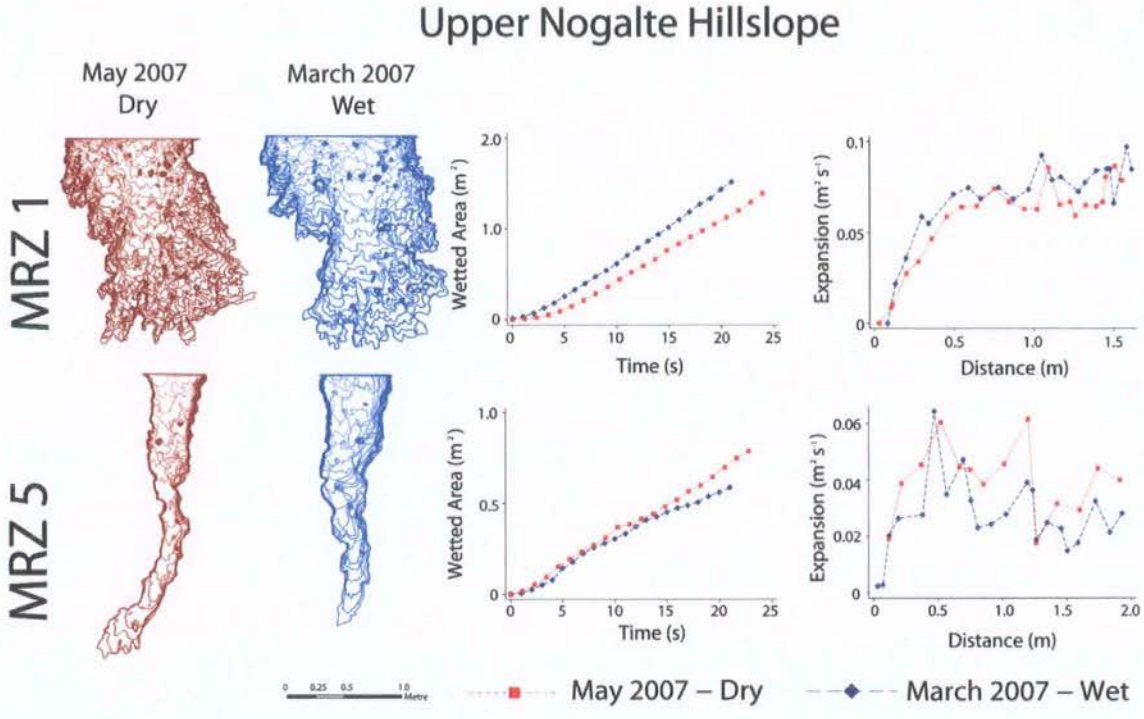

Figure 7.14. Flow outlines depicting water advance at the Upper Nogalte hillslope. Each line represents the edge of the floodwave at a different timestep. Red and blue lines represent the dry- and wet-soil experiments respectively. For each plot the growth of the wetted area with time and its expansion ($m^2 s^{-1}$) with distance travelled from the source is displayed.

Figure 7.15 shows the concentration of flow during each experiment while Figure 7.16 displays the median velocities recorded. These figures show that the difference of expanding area at the Upper Nogalte hillslope was not due to more diffuse flow; rather the flow was travelling downslope faster. This may be a consequence of the reduced infiltration rate influencing the experiment. This was not observed at the MRZ 5 plot, where the dry run expanded faster than the wet run, despite being slightly more concentrated (Figure 7.15). The median velocity of the dry run of May 2007 was faster than during wet conditions (Figure 7.16). A comparison between plots shows that (as previously discussed) the upslope plot demonstrates more diffuse flow. The differences of flow concentration

between the two Upper Nogalte plots are much greater than the negligible differences between the wet and dry runs. At upslope locations, the flow spreads over a greater area and so the infiltration rate will have a greater influence on the transmission of runoff over the surface. This effect would be most noticeable at the MRZ 1 plot as the results presented in section 7.4.2 show that this plot demonstrates the highest infiltration rates measured in this study.

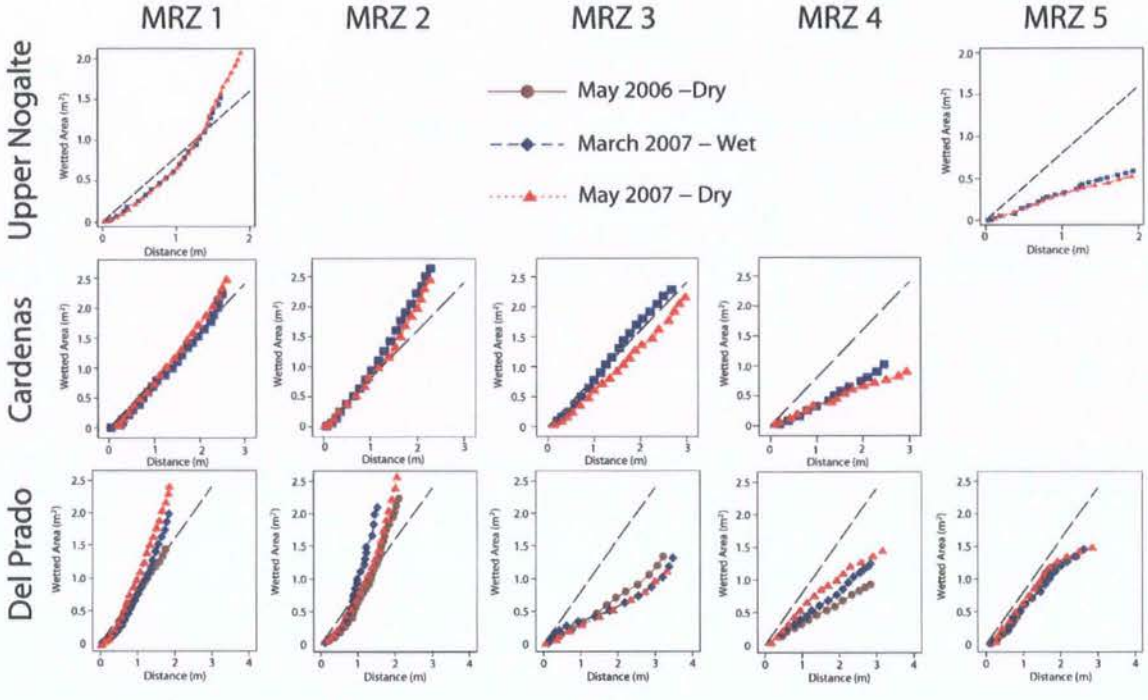

Figure 7.15. Increase of wetted area (m^2) with distance travelled (m) for dry and wet runs at each plot and hillslope.

At the Cardenas hillslope, only minor differences in overall flow pattern can be observed between the two runs (Figure 7.17). With distance downslope, the area of the 'wet' experiments increased more rapidly than that of the 'dry' run. In contrast to the Upper Nogalte hillslope, dry run area actually increased faster than the wet run at the MRZ 1 plot. This is shown in more detail on the far right on the plot of expansion of the wetted area (per second) against distance travelled downslope. A similar pattern can be identified between the two runs as they respond to the topography in a similar way, with the dry run consistently expanding more rapidly than the wet run. By MRZ 2 the dry and wet

experiments have switched places, and with distance further downslope, the wet run expands increasingly faster than the dry run. The flow outlines show that the differences are not caused by any dramatic shift in flow patterns; this can be seen quantitatively in Figure 7.15 where the differences in flow concentration observed for each run are minor compared with those differences seen between each plot.

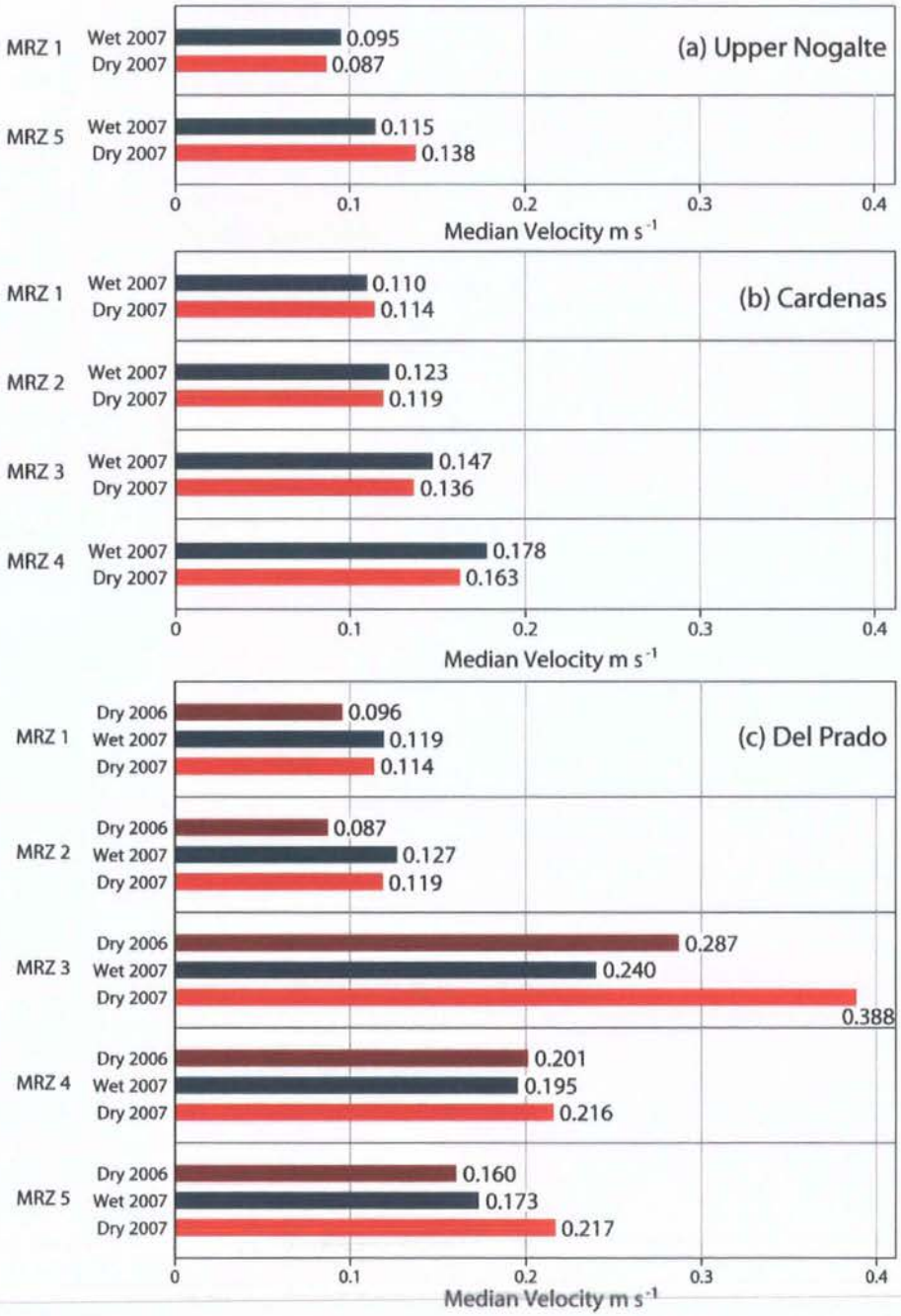

Figure 7.16. Median flow velocities under different soil moisture conditions.

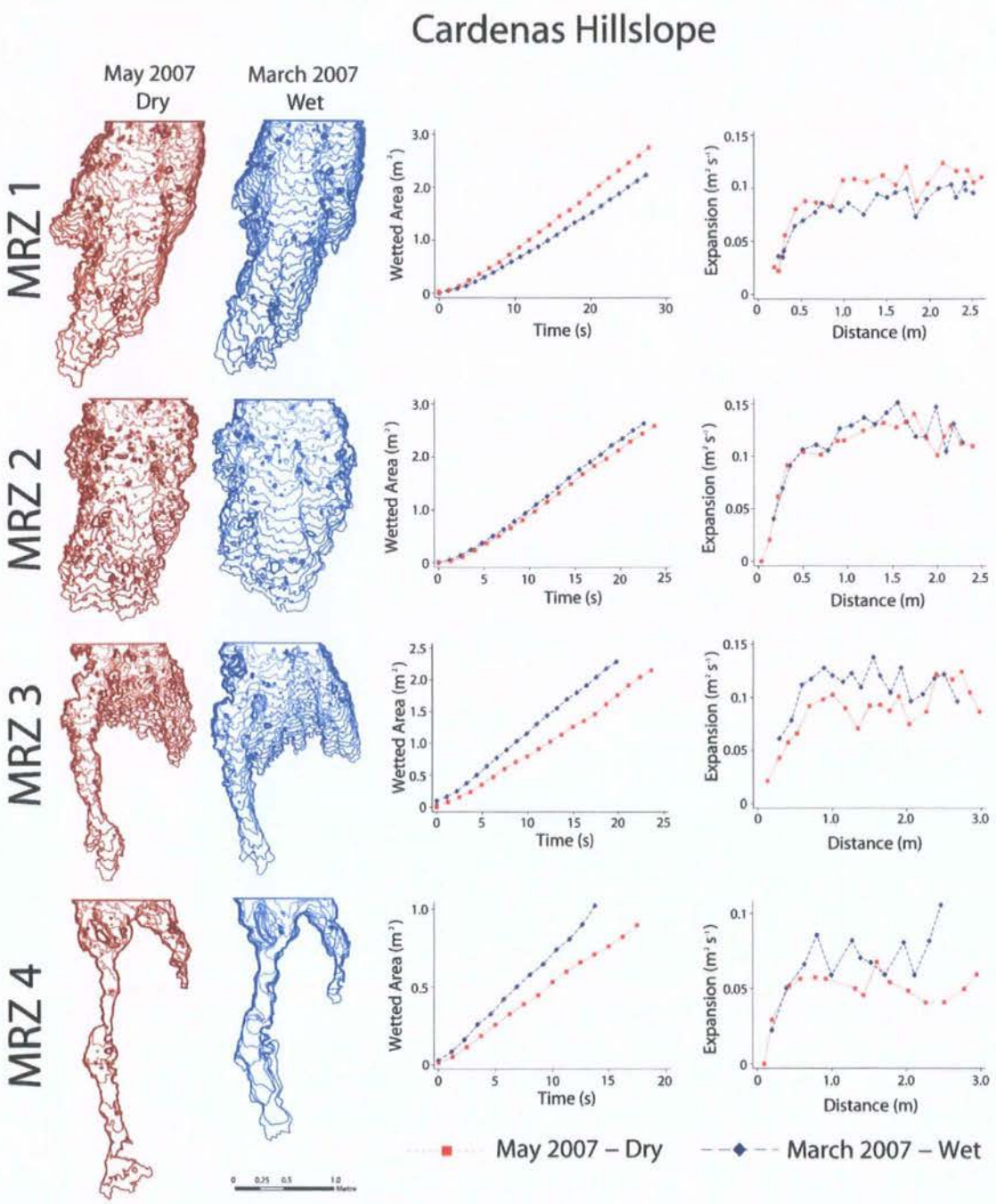

Figure 7.17. Flow outlines depicting water advance at the Cardenas hillslope. Each line represents the edge of the floodwave at a different timestep. Red and blue lines represent the dry- and wet-soil experiments respectively. For each plot the growth of the wetted area with time and its expansion (m^2 s^{-1}) with distance travelled from the source is displayed.

The minor differences in flow concentration follow the same pattern as the increasing area (Figure 7.15): at the top of the hillslope the wet run is relatively more concentrated, the positions reverse by MRZ 2 with increasingly exaggerated differences by MRZ 3 (where the wet run diffuses the flow and the dry run concentrates it slightly). The relative differences are smaller by MRZ 4 as the flow is mostly contained within a deeply incised rill. The decreased concentration of the wet run may explain the more rapid expansion of the wetted area with time.

Figure 7.16b summarises the velocities recorded at each plot of the Cardenas hillslope. Again, these follow the same pattern with only minor differences between the two runs on each plot. Therefore, with distance downslope the wetted area increased more rapidly on moist soils than on dry soils. This increased area was a result of both less concentrated flows and faster flows, although the overall differences are very small compared with the differences observed between plots.

At the Del Prado hillslope, an extra experiment was conducted on dry soils in May 2006. Figure 7.18 shows that the expansion of the wetted area of the 'wet run' occurred at a rate between the two dry experiments. This suggests that any observed differences may be caused by other factors. At MRZ 1 the 2007 dry and wet runs are virtually indistinguishable, with the area of the May 2006 dry run increasing more slowly with time. At MRZ 2 the wet run lies between the two dry runs. This pattern is repeated at MRZ 4 and 5. At MRZ 3 the area of both the dry runs increases slightly faster than the wet run. The rate of expansion is similar for each run at each plot, although differences in the fine structure are more noticeable than at the Upper Nogalte or Cardenas hillslopes.

Figure 7.15 shows the differing degrees of concentration during each of the runs on the Del Prado hillslope. The May 2007 dry run generally shows more diffuse flow than the others (this at least partially explains its rapid increase in area). Only at MRZ 2 is the wet run most diffuse.

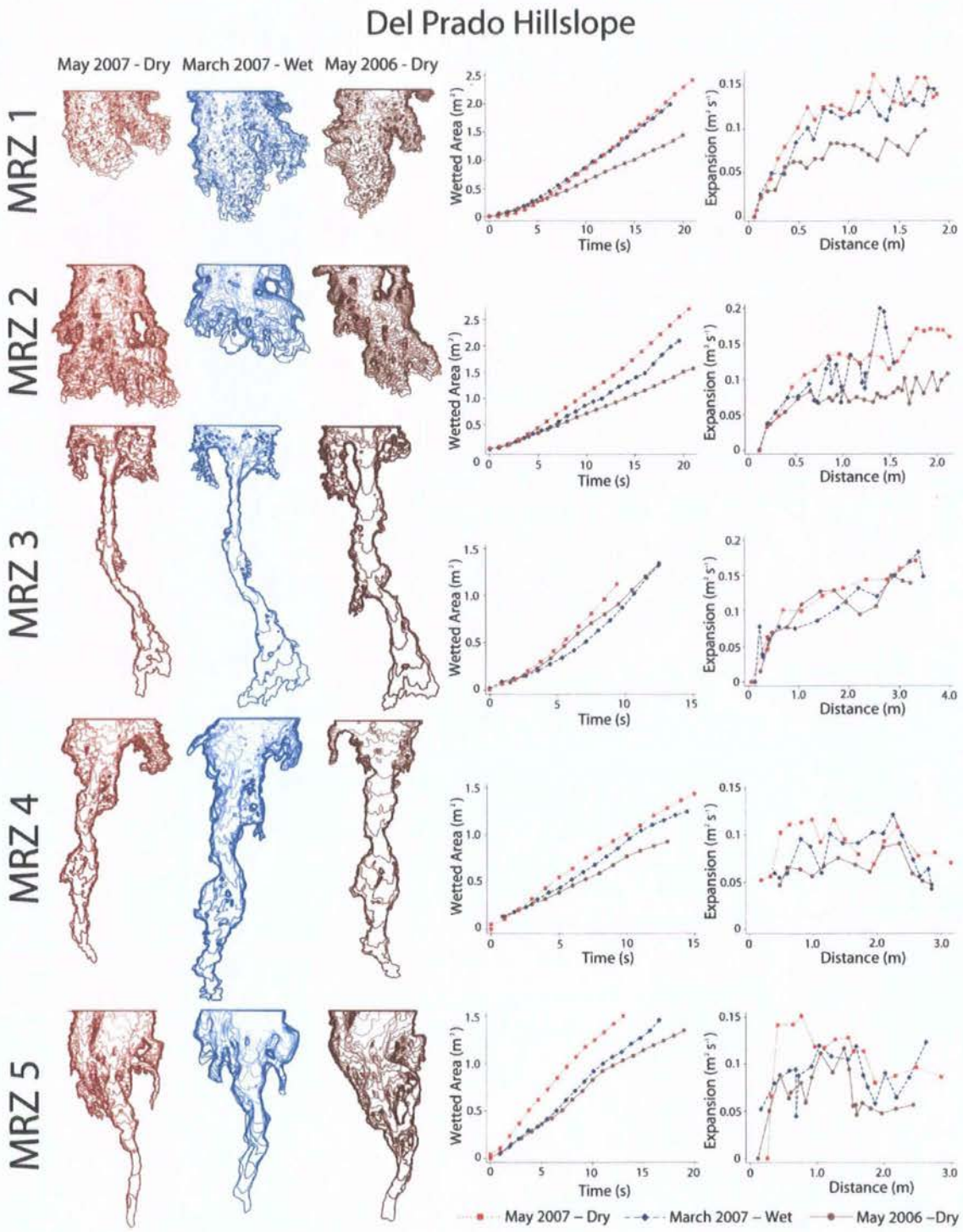

Figure 7.18. Flow outlines depicting water advance at the Del Prado hillslope. Red and blue lines represent the dry- and wet-soil experiments respectively. For each plot the growth of the wetted area with time and its expansion ($m^2\ s^{-1}$) with distance travelled is displayed.

Figure 7.16c summarises the velocities recorded at each plot for the three experimental runs. The MRZ 3 plot recorded the fastest velocity in each run. The wet run was slightly faster than both the dry runs at the upslope plots, although the difference between May 2007 and the wet run of March 2007 was less than that between both 2007 runs and the dry run of May 2006. Further downslope, the dry runs were both considerably faster than the wet run in flow concentrations; this effect is less pronounced in the rill flows. At the MRZ 5 plot, the wet run was faster than May 2006, but not faster than May 2007.

These results suggest that antecedent conditions are relatively more important at upslope locations. Where the flow is concentrated, less of the runoff is in contact with the soil itself and so antecedent conditions are less influential. In general, antecedent conditions appear to make very little difference to the rate of flow transfer. Any observed differences are possibly a result of variability between the experiments as no consistent changes were observed. These results suggest that the influence of antecedent conditions is limited to the generation of runoff at the source areas. However, this investigation has thus far been limited to the plot scale. The following section investigates the influence of antecedent conditions on hillslope outflow.

7.3.3 Hillslope Travel Times

This section attempts to transfer the results of sections 7.3.1 and 7.3.2 from the plot scale to the hillslope scale using the Morphological Runoff Zone framework examined in section 7.2. The discussion of Chapter 3 emphasised the importance of the distribution of flow travel times. This is partly determined by hillslope morphology and flow routing velocity. This section briefly explores the influence of these factors. The median velocities of water at each MRZ (for both wet and dry runs) are extrapolated to represent the routing velocity of the water over any cell classified into that zone using the calculated MRZ extents of section 7.2. This permits a crude first estimate of hillslope travel times for the discharge applied in these experiments. Although a range of velocities was recorded at each plot, the median velocity is used in this analysis as a representative velocity and is much less affected by the initial low velocities than the mean value. A more sophisticated methodology is demonstrated in Chapter 8 but this offers a useful comparison between

antecedent conditions. The result is a hillslope-scale Instantaneous Unit Hydrograph (IUH) approach (e.g. Sherman, 1932; Nash, 1957; Dooge, 1959; Rodríguez-Iturbe and Valdès, 1979) directly informed by field measurements of flow velocity distributed by Morphological Runoff Zone.

Figure 7.19 shows the increasing area connected to the hillslope outlet with time for the Upper Nogalte hillslope. Three different simulations are shown; these represent the two MRZ arrangements shown in Figure 7.4a–b (before and after the ploughing of May 2007) and a prediction of the travel times if no ploughing occurred. This final simulation is subject to considerable error as the ploughed bands interrupted the natural hillslope MRZ sequence which was used to inform the MRZ thresholds. Hence the influence of ploughing will affect the travel times. The destruction of plots mentioned previously means that the influence of antecedent conditions on travel times cannot be considered at this hillslope.

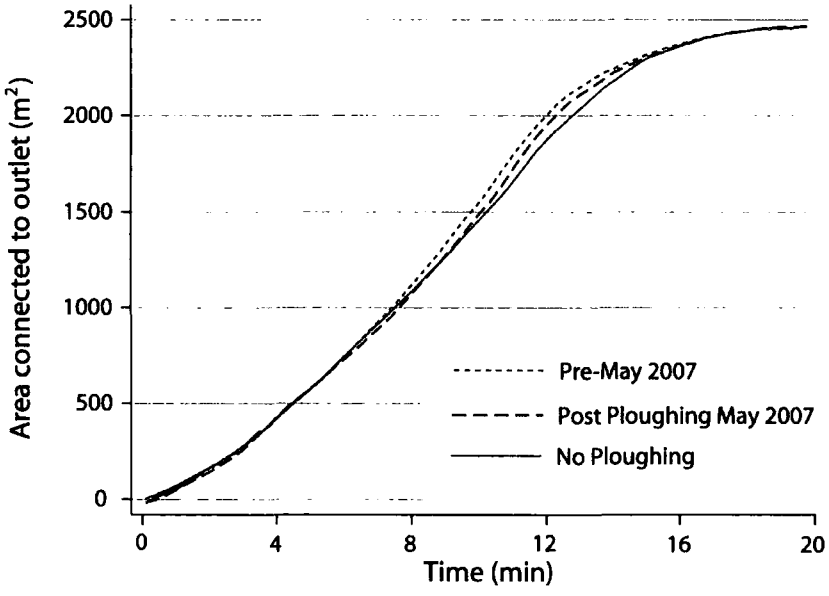

Figure 7.19. Increasing area connected to the hillslope outlet with time for the Upper Nogalte hillslope.

The three simulations connect the whole hillslope virtually simultaneously, although divergence occurs around the 10 minute point. This can be seen more clearly in Figure 7.20d. The distribution of travel times gradually reaches a single peak at around 10 minutes in each case. The 'no ploughed surfaces' simulation shows a more lagged response than the

other runs (as the ploughed area was mostly categorised as MRZ 1, which displayed a lower velocity). The original ploughed band was located towards the crest of the hillslope where runoff would otherwise be flowing at a restrained rate.

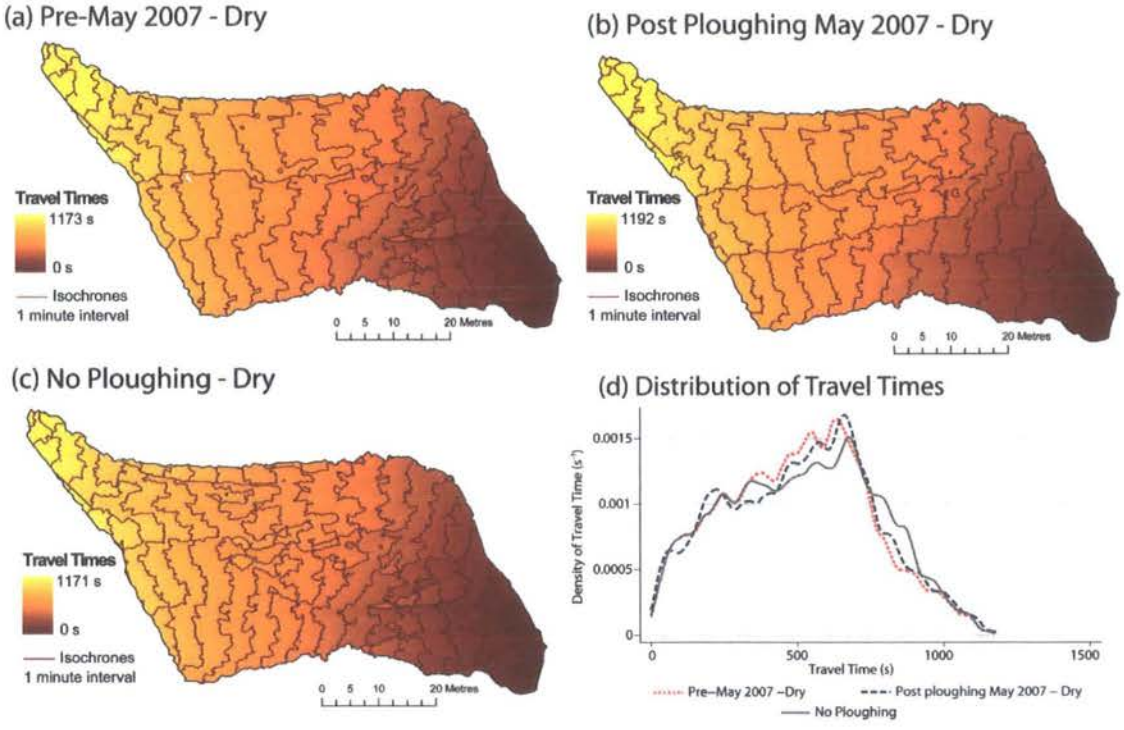

Figure 7.20. Travel Times calculated for the Upper Nogalte hillslope using velocity data from the May 2007 experiments (dry conditions) (a) using the MRZ arrangement of Figure 7.4a, (b) using the MRZ arrangement of Figure 7.4b (additional ploughing), (c) using an MRZ arrangement where no ploughed surfaces are present, (d) kernel density estimate showing the distribution of travel times (using the Epanechnikov kernel with a half-width of ~10 s; Cox, 2007a).

Comparison of the isochrones in Figures 7.20a–c demonstrates the slower transfer of runoff over the mid- to upper section of the hillslope under the 'no ploughing' conditions (dense isochrones). The pre-May 2007 surface recorded the fastest time to peak; the extra ploughing in May 2007 acted to slow the runoff (as the newly ploughed areas were towards the foot of the hillslope where runoff would otherwise be flowing more rapidly). Therefore, hillslope position appears to influence the effect of ploughing as the more recent ploughing of this hillslope was more effective at restraining runoff from the hillslope than the earlier

ploughed band. It should, however, be noted that ridges and furrows degrade with time (Bull *et al.*, 2003) and as a result their influence is very variable.

Figure 7.21 shows the increasing area connected to the hillslope outlet with time at the Cardenas hillslope. Three different calculations were performed. Velocities measured during dry and wet runs were applied to route the water. No velocities for wet conditions at the ploughed plot were available at this hillslope; the applied velocity was not changed from the dry run. However, as the ploughed area is mostly isolated from the flowpaths of the other side of the hillslope (Figure 7.5) this should not greatly affect the matorral slope travel times. Additionally, the effect of ploughing the hillslope was simulated by treating the ploughed surface as a natural hillslope and estimating the distribution of MRZs using the method of section 7.2. The 'dry' velocities were then applied to these cells. Figure 7.21 shows that, as with the Upper Nogalte hillslope, very few differences between the three runs can be observed. This will be partly down to the identical flowpaths over the ploughed half of the slope during the wet simulation, and on the matorral during the 'no ploughing' simulation. This is examined more closely in Figure 7.22.

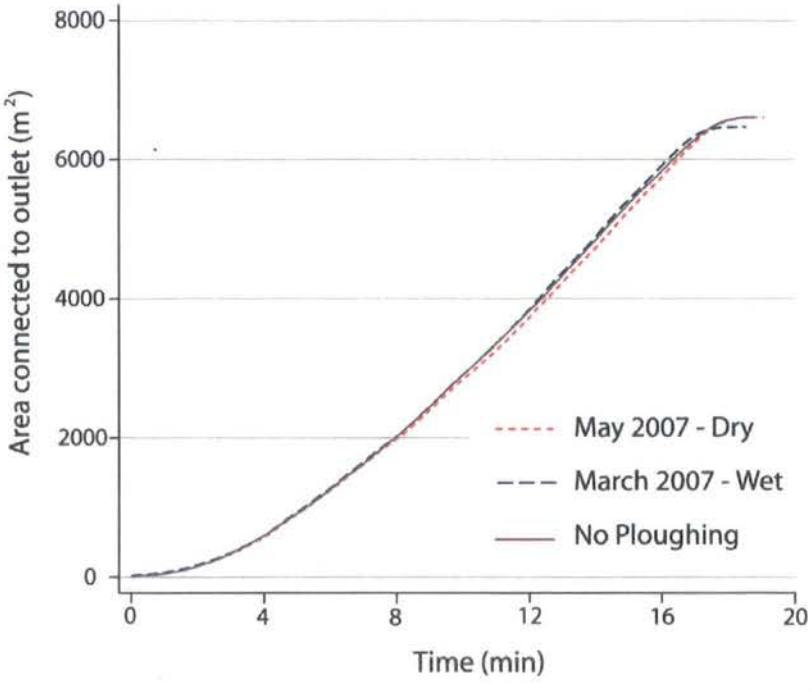

Figure 7.21. Increasing area connected to the hillslope outlet with time for the Cardenas hillslope.

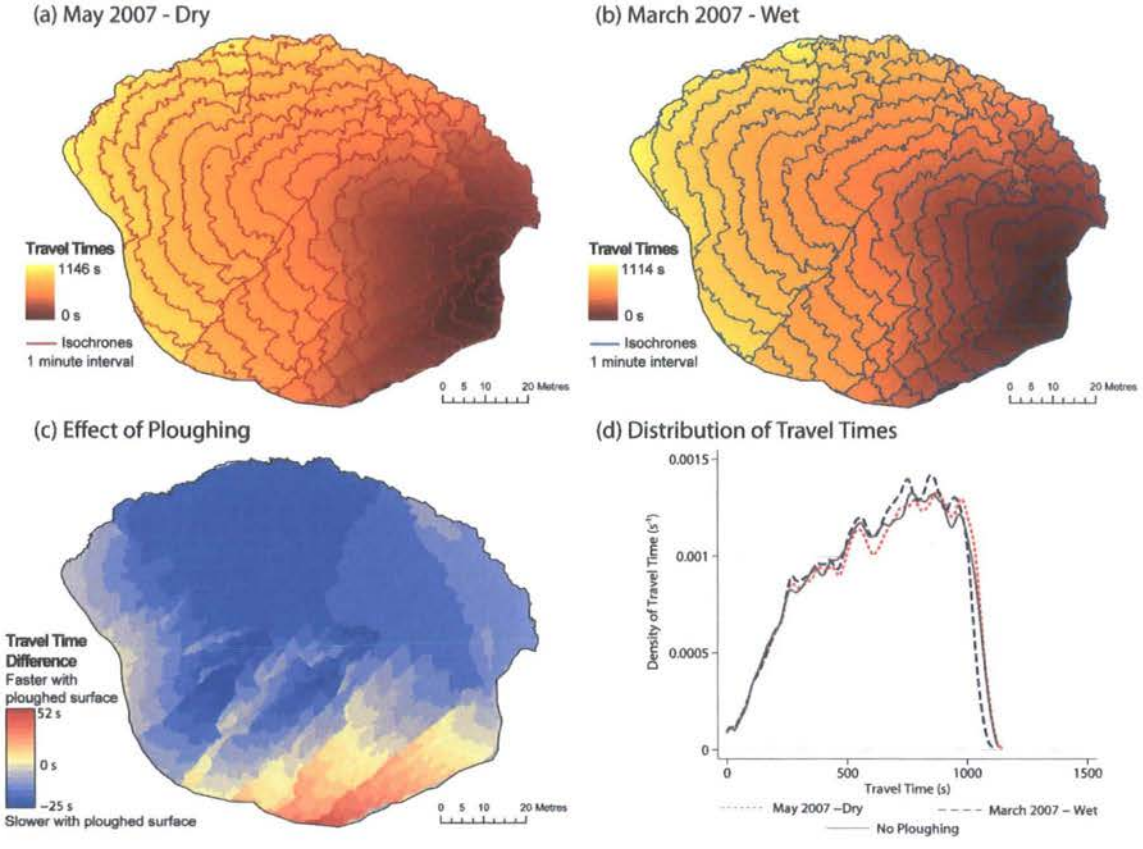

Figure 7.22. Travel Times calculated for the Cardenas hillslope (a) using data from the May 2007 experiments, (b) March 2007, (c) effect of ploughing on dry travel times, (d) kernel density estimate showing the distribution of travel times (using the Epanechnikov kernel with a half-width of ~10 s; Cox, 2007a).

The isochrones of Figures 7.22a and b extend outwards from the outlet in a radial pattern. Each of Figures 7.22a–c shows a sharp divide on the bottom-left of the hillslope. This is a ridge on the hillslope; water draining either side of this ridge follows different routes down to the hillslope outlet. As discussed in Chapter 3, the distribution of runoff travel times is important for flood generation in semi-arid environments. A more peaked distribution means that at the maximum flow, less transmission loss is likely. Few differences are seen between the wet and dry runs. As shown by Figure 7.16, only minor differences in flow velocity were observed (the constant velocity used for the ploughed plot increases the degree of similarity). The three simulations show a gradual rise to a peak after about 14

minutes (with some fluctuations). Figure 7.22c shows the effect of removing the ploughed area from the hillslope. The ploughing slows much of the runoff (the effect is seen over the entire hillslope as even the runoff from the matorral crosses a small ploughed area in the central basin of the hillslope). Only a small (previously ploughed) area experiences faster flow under ploughed conditions; no flow concentrations were predicted in this area and the ploughed plot showed a faster median velocity than either MRZ 1 or MRZ 2 plots. This analysis is limited to the effect of velocity as the hillslope DEM was captured over the ploughed surface. Although the velocities have been altered to simulate a natural hillslope, the flow routing remains the same. The flow pathways of the natural side of the hillslope are less tortuous than those of the ploughed plots. The overall decrease in travel times with the removal of the ploughed surface is therefore a minimum estimate.

Both the Upper Nogalte and Cardenas hillslopes show a negligible influence of antecedent conditions on flow velocity. Figure 7.23 shows the increasing connected area to the hillslope with time at the Del Prado hillslope. A much greater difference is observed between runs. The entire hillslope is connected first on the May 2007 dry run (fully connecting after approximately 11 minutes), followed by the wet run (12 minutes) and finally the May 2006 dry run (14 minutes).

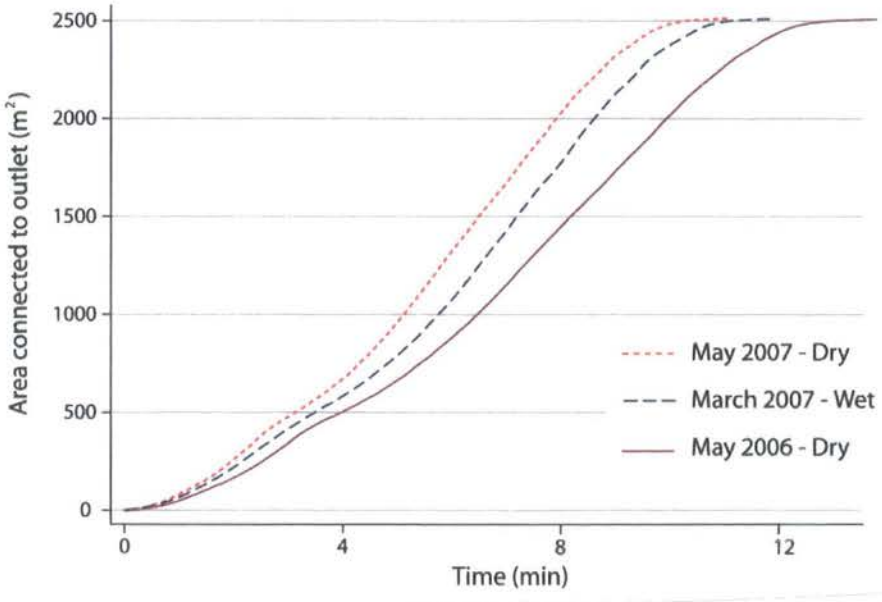

Figure 7.23. Increasing area connected to the hillslope outlet with time for the Del Prado hillslope.

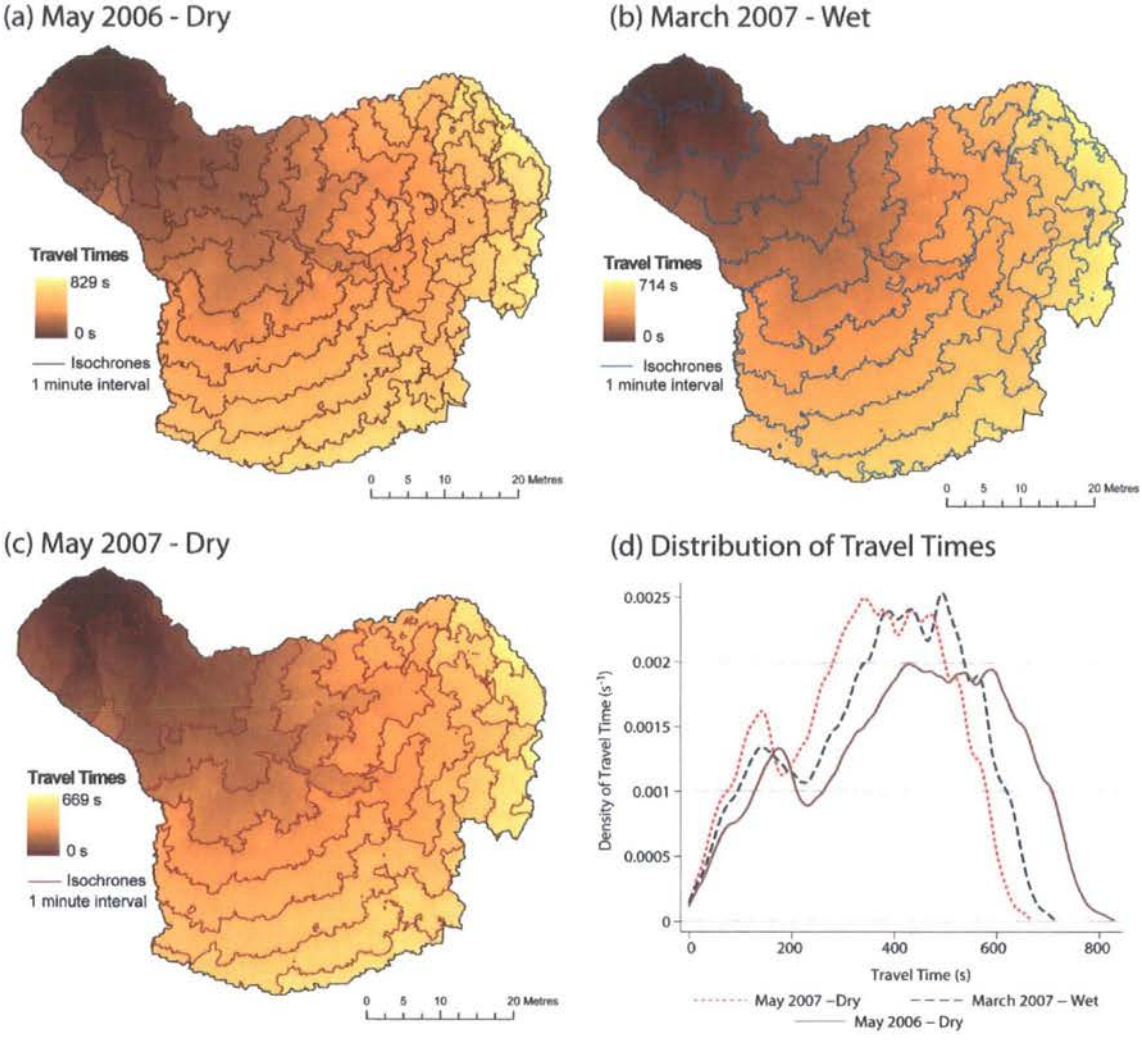

Figure 7.24. Travel Times calculated for the Del Prado hillslope (a) using data from the May 2006 experiments, (b) March 2007, (c) May 2007, (d) kernel density estimate showing the distribution of travel times (using the Epanechnikov kernel with a half-width of ~10 s; Cox, 2007a).

Two distinct peaks in the travel time distributions can be observed at the Del Prado hillslope (Figure 7.24d). The smaller, sharper first peak arrives after approximately 3 minutes and was observed for all three simulations. This peak is a product of the efficient routing of runoff through the gully and rill system at the foot of the hillslope. The larger second peak arrives after 6 minutes. This appears to reflect the shape of the hillslope and represents the hydrological connection of the large area at the top of the hillslope to the outlet (seen by an increase in gradient in Figure 7.23).

The differences in the travel time distributions between runs are more defined at this hillslope. Both dry runs have a flatter peak travel time distribution; the run on wet soil had the highest and most defined peak. The peak of May 2006 lags behind the other two runs. A comparison of travel times for each cell (between May and March 2007) shows that most times became shorter on the drier plot, but some areas routed water faster on the wet March 2007 run. Either these flowpaths avoided flow concentrations (found near the catchment outlet), or they were at the extreme top end of the catchment and so a greater proportion of their flow was as non-concentrated interrill flow.

Overall, antecedent moisture conditions appear to have only a small effect on routing velocities. The overall morphology of the hillslope seemed to dominate the travel time distributions. The largest effect was seen at the Del Prado hillslope, although the comparison between the two dry runs and one wet run showed no systematic difference. The thin soil crust and soil cracks seen at this marl hillslope may present the complicated situation of an increasing infiltration rate under 'wet' conditions.

While antecedent moisture conditions do not appear to influence overland flow velocity, two other factors are now investigated. The surface depression storage and variable infiltration rates may influence flow resistance on dry soils. While the influence of these factors on overland flows is not normally conceptualised as 'flow resistance', they nevertheless restrain the advance of runoff over a soil surface in a manner that is encompassed within flow resistance measurements. This effect may have been influential in determining the resistance equations of Chapter 6. Once a connected flowpath has been established during a high-magnitude storm event, their influence will be greatly reduced. The final section of this chapter explores this idea further.

7.4 Infiltration, Depression Storage and Flow Resistance

The above analysis presents a very simplified picture of the connection of the hillslopes to the outlet. The velocities were obtained experimentally for a single discharge, and no appreciation of infiltration is built into the simulations. Differences have been observed

between experiments conducted on previously wetted soils and those on dry soils. Thus far, this has not been related to measured infiltration rates or depression storage. The following section attempts to explain these patterns from measurements of infiltration. It is well established that infiltration rates are of fundamental importance in determining the production of runoff (e.g. Berndtsson and Larson, 1987; Wilcox *et al.*, 1990; Cantón *et al.*, 2002); section 7.4.1 examines the effect of infiltration on the transfer function of runoff by testing flow measurements taken after saturation occurred against the models developed in Chapter 6. Variations of infiltration parameters (section 7.4.2) and depression storage (section 7.4.3) are presented and investigated as explanatory factors for observed differences. Section 7.4.4 presents a further suite of resistance equations (developed in the same manner described in Chapter 6) that were created from data of flows over saturated soils and examines the differences between the two sets of equations.

7.4.1 Roughness–Resistance Relationships over Established Flowpaths

Section 7.3 examined the influence of a 'wetting up' rainfall event on flow velocity, suggesting that while it may have an effect on abstractions of surface water by infiltration, it had only a limited effect on the velocity of generated overland flow. Under these conditions, the depression store must still be satisfied and this volume will be abstracted from the flow. The turbulence induced from this process may have a large effect on the resultant momentum transfer which would decrease with time where the hydrological connection remains and depression storage is filled. Therefore, there is reason to suggest that once a flowpath has developed and become connected to the hillslope outflow point, the resulting overland flow will experience different conditions from those at the initiation of connected flow. This section examines the difference in flow resistance experienced once a flow connection has been established.

As described in section 4.3.5.1, once the simulated overland flow had travelled over the plot area, three additional pulses of dye (green, red and blue) were added to the flow (Figure 7.13). These were tracked across the plot in the same manner as the initial water wave. Given time limitations this analysis was only performed at the Del Prado hillslope, chosen because it already provides the most complete record of experiments. Section 4.2.1

discusses the difficulties of calibrating a measure of surface velocity to mean velocity, suggesting that the choice of a coefficient depends on a variety of factors. Dunkerley (2001) examines this variability and suggests that a coefficient α of 0.56 be applied. However, in the calculation of the Darcy-Weisbach friction factor, the velocity gradient of overland flows is relatively unimportant compared with the surface gradient. Where the velocity gradient is negligible, the calibrated friction factor f_c will be related to f by

$$f_c = \frac{f}{\alpha^2}. \tag{7.1}$$

Figure 7.25 shows the variability of f_c around the relationship predicted using equation 7.1 and the correction factor α of 0.56 for the resistance values calculated from these dye pulses. There is very little variability around the predicted values. To provide an easier comparison with the first wave of advancing water, measurements of flow velocity in this thesis remain uncorrected. This avoids the difficulties of selecting a coefficient α (discussed in section 4.2.1 and Dunkerley, 2001). All resistance equations developed in this thesis are purely empirical and are designed to provide greater insight into the process of overland flow over complex surfaces. They can be easily converted to a mean velocity using equation 7.1.

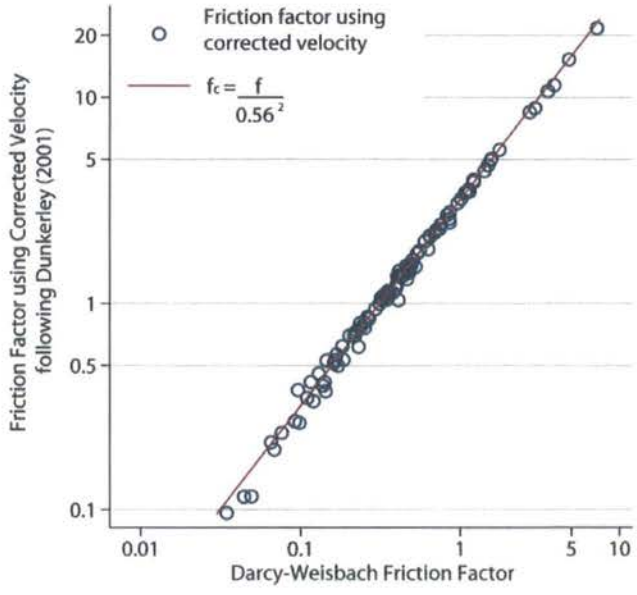

Figure 7.25. The effect of using a single surface velocity correction coefficient on the calculation of f. The red line indicates the predicted value, neglecting the effect of the velocity gradient on the energy slope ($R^2 = 0.999$).

Figure 7.26 shows the decrease of f observed at each plot between the first water wave and the arrival of dye pulses (values decreased by 82% at MRZ 1, by 81% at MRZ 2, 96% at MRZ 3, 81% at MRZ 4 and 95% at MRZ 5). This decrease is exaggerated by the use of an uncorrected friction factor. Applying equation 7.1 and the correction factor of Dunkerley (2001) would increase the measured resistance by a factor of three. There is less variability of the Darcy-Weisbach friction factor for the pulse dataset, although this partly reflects the lower number of data points. The measured f of this dataset does not exceed a value of 10.

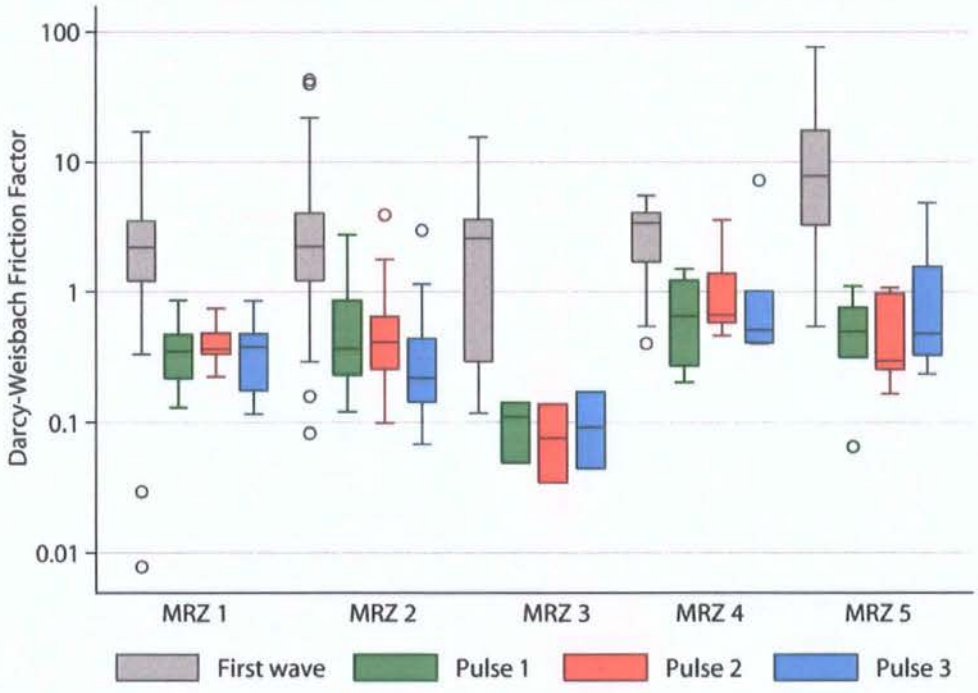

Figure 7.26. Variation of f between pulses at each plot of the Del Prado hillslope.

Figure 7.27 applies the resistance equations developed in Chapter 6 to this new dataset. The points are coloured to represent the dye colour (applied in the order of green, red, blue). The original dataset is also displayed (grey crosses). As expected, the resistance equations of Chapter 6 over-predict the resistance of the later dye pulses. The later pulse measurements show the highest correlation with the predictions of the most general model discussed in Chapter 6 (Figure 7.27a). This correlation decreases as model complexity increases. There is no obvious pattern between the three dye pulses; any causal mechanism

for the difference between the later pulses and the initial flood wave must operate within the first few seconds of saturation. The equations of Chapter 6 fit the measurements of the later pulses slightly better than the earlier pulses, though the correlation coefficients are considerably less than the first wave dataset.

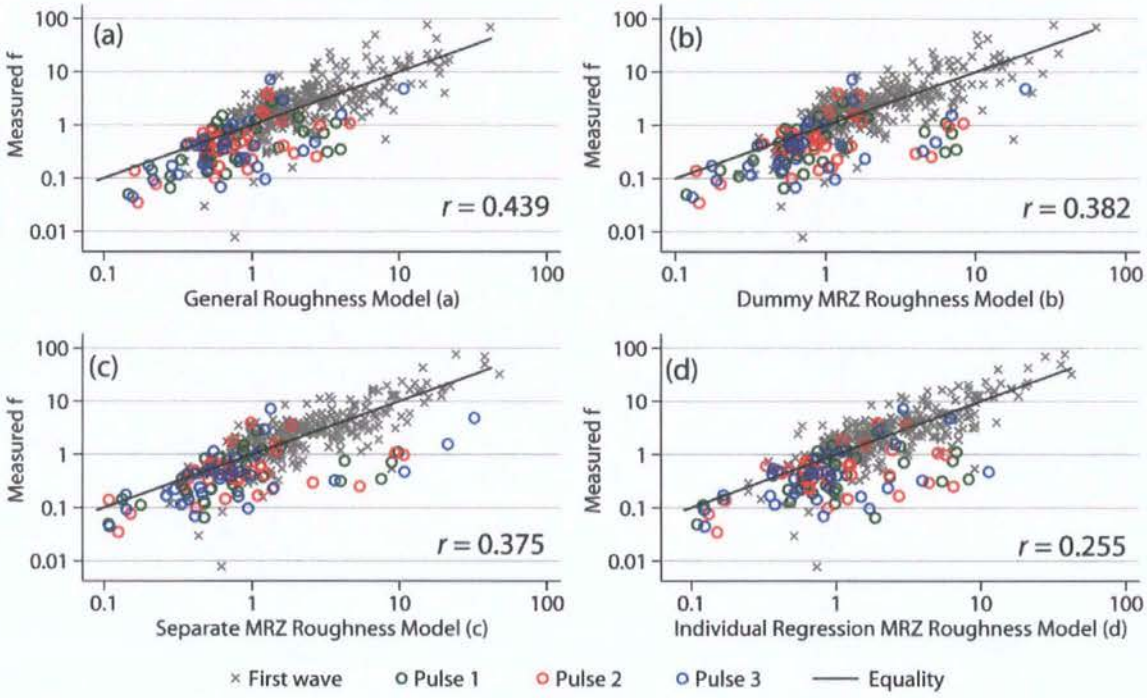

Figure 7.27. Roughness-resistance equations developed in Chapter 6 applied at the Del Prado hillslope. Grey crosses represent the dataset with which these equations were developed. Models (a)–(d) indicate the different representations of hillslope position in the model (as discussed on p.196). The Pearson correlation coefficient r shows the relationship between the predictions and the measured values for the dye-pulse dataset.

Figure 7.28a–e separates this dataset by hillslope position (MRZ) for model (d) of the individual regressions shown in Table 6.3. Table 7.2 summarises the main differences between those patterns observed in Figure 7.28 and the other regression models. At every plot of the Del Prado hillslope the equations of Table 6.3 over-predict the resistance of the later dye pulses, although this occurs to a different degree.

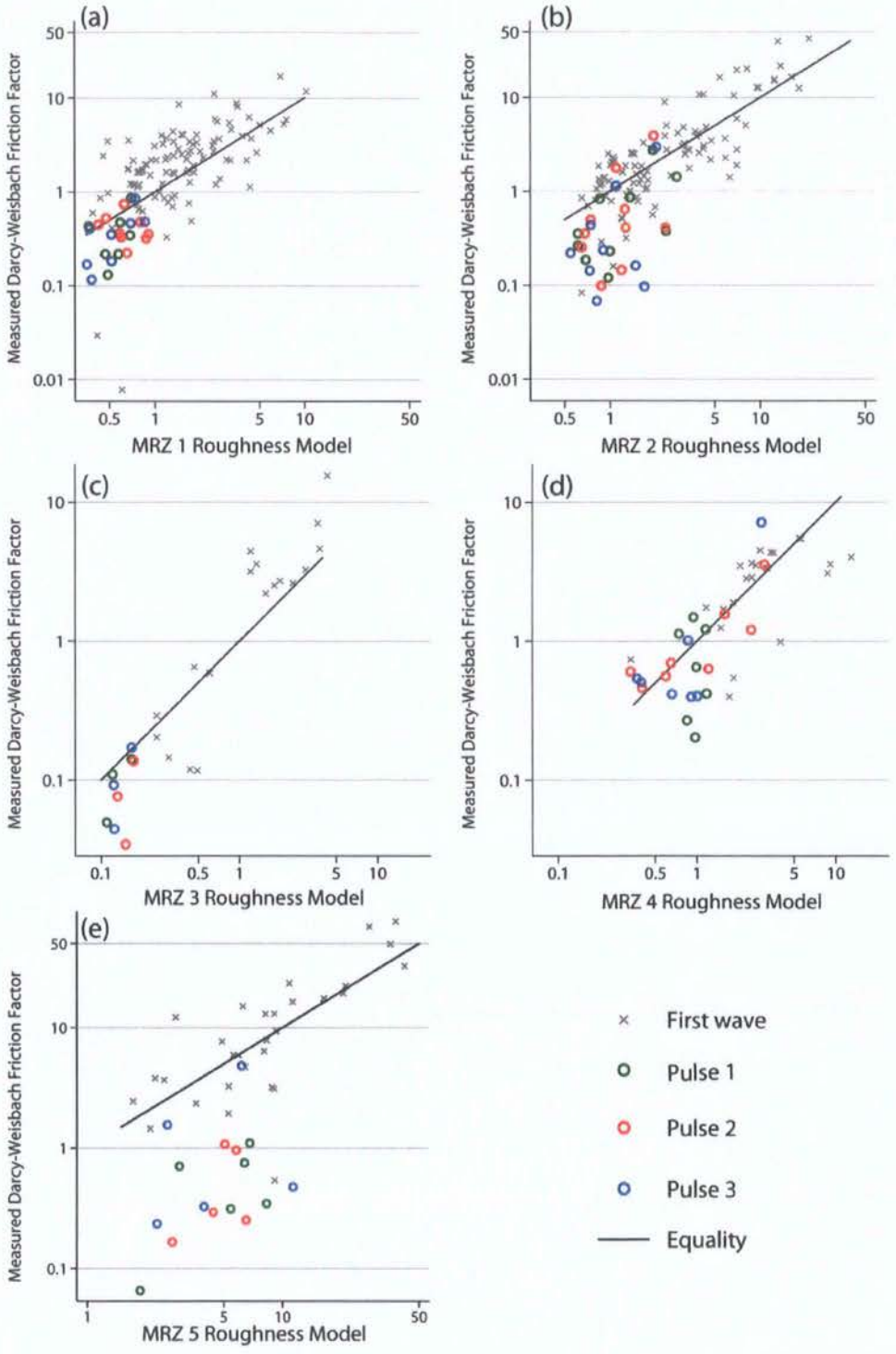

Figure 7.28. Roughness-resistance equations displayed in Table 6.3 applied at the Del Prado hillslope separated by Morphological Runoff Zone.

The resistance of the pulses is most closely predicted at the MRZ 4 plot which displays scatter around the line of equality (although with a bias towards over-prediction). No systematic differences can be observed between the successive dye pulses, although at the MRZ 5 plot the measured resistance gives a better approximation of the modelled value during the later dye pulses. This appears to be an artefact of the small dataset available to examine these patterns. Indeed, the small number of measurements is a limiting factor in this examination of dye pulses (especially at the MRZ 3 plot). In summary, Figure 7.28 shows minor over-prediction at MRZ 1–4 while the measured resistance at the MRZ 5 plot was much lower than that predicted by equation 6.18.

Model	(a)		(b)		(c)		(d)	
	r	Residual	r	Residual	r	Residual	r	Residual
Combined	0.439	−0.218	0.382	−0.247	0.375	−0.201	0.255	−0.332
MRZ 1	0.233	−0.192	0.159	−0.213	0.158	−0.238	0.359	−0.238
MRZ 2	0.483	−0.322	0.483	−0.315	0.480	−0.129	0.440	−0.547
MRZ 3	0.363	−0.113	0.396	−0.085	0.290	−0.058	0.666	−0.034
MRZ 4	0.582	−0.016	0.585	−0.110	0.587	−0.081	0.777	−0.005
MRZ 5	0.928	−2.310	0.934	−5.115	0.922	−6.180	0.121	−4.046

Table 7.2. Pearson's correlation coefficient r and median residuals (measured − predicted) for the later dye pulses for each regression model developed in Chapter 6 (for the dataset as a whole and separated by hillslope position).

The median residuals in Table 7.2 show that this pattern of overprediction with hillslope location is mostly consistent between models. However, the predictions of individual regression models (shown in Figure 7.27d) are more strongly correlated with observed measurements at the MRZ 3 and MRZ 4 plots and much less correlated at the MRZ 5 plot.

Such differences between plots offer an opportunity for a brief examination of the factors responsible for the decreasing resistance with increased duration of a flow connection and increasing strength of delivery pathway (as would develop through a storm event once a hydrological connection is established; Bracken and Croke, 2007). While there is considerable scatter within all the datasets examined in this study (expected from flows over such complex natural surfaces) the results of Figure 7.28 suggest a systematic shift for

the dye pulse data. Several hypotheses can be identified to explain this shift. From the discussion of Chapter 3 it could be suggested that this decreased resistance may be due to one or more of:

(a) decreased infiltration losses and associated suction forces;
(b) filling of the depression store and less induced turbulence;
(c) reduced energy loss from three-dimensional flow vectors;
(d) alteration of roughness measures between first wave and dye pulses;
(e) natural variability between measurements.

The systematic differences observed suggest that (e) alone is insufficient to explain the observed variability. Sections 7.4.2 and 7.4.3 now briefly examine the variation of infiltration rates and depression storage over the plots described in this study and question whether these factors can be used to understand the differences observed in Figure 7.28a–e. Finally, section 7.4.4 develops an alternative suite of resistance equations to examine the influential roughness measurements for these later pulses and examines any differences.

7.4.2 Minidisk Measurements

Point measurements of infiltration rates were taken over each of the hillslopes using minidisk infiltrometers (section 4.4). Ten measurements were taken on each plot; these were distributed between roughness elements. Figures 7.29 and 7.30 show that a large range of infiltration rates were observed at each plot (Table 7.3). The differences observed between each plot are less obvious than the differences between hillslopes. This would be expected as the hillslopes were chosen to represent the end-members of the soil types over the two catchments. Therefore, the spatial variation of infiltration is determined more by soil type, whereas the variation of flow resistance is better described by surface morphological variations (as described by MRZs).

The Del Prado hillslope consistently demonstrates the lowest unsaturated hydraulic conductivity and total depth infiltrated (during a 5 minute test) for each plot. The red schist of the Upper Nogalte hillslope consistently infiltrated the most water and showed a greater range of values. This agrees with the assessment of Bull *et al.* (2003). At the MRZ 3 plots

the blue schist of the Cardenas hillslope showed a slightly greater unsaturated hydraulic conductivity, but for each of the other plots it demonstrated an intermediate value.

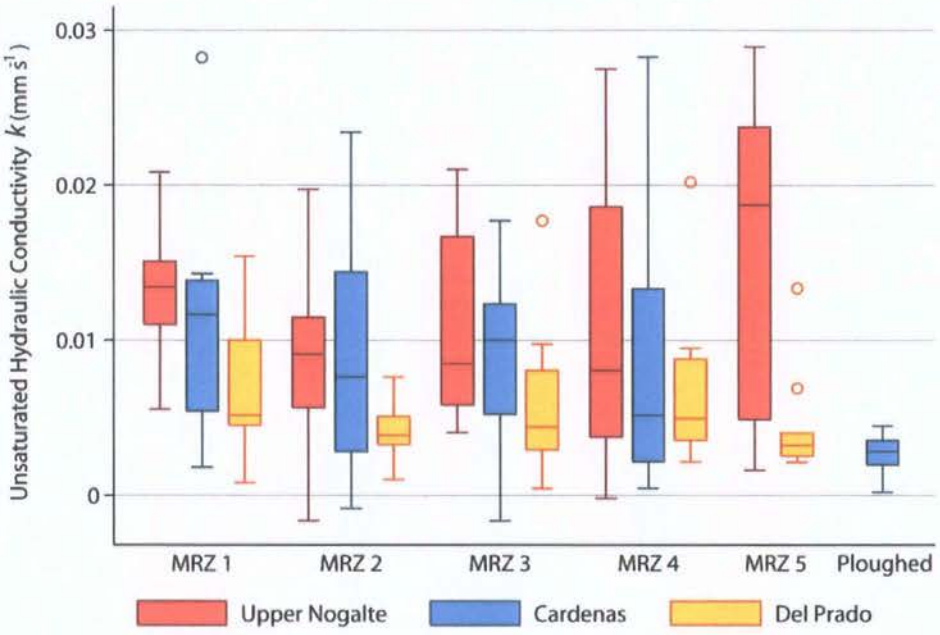

Figure 7.29. Variation of unsaturated hydraulic conductivity k (mm s^{-1}) between each plot and hillslope.

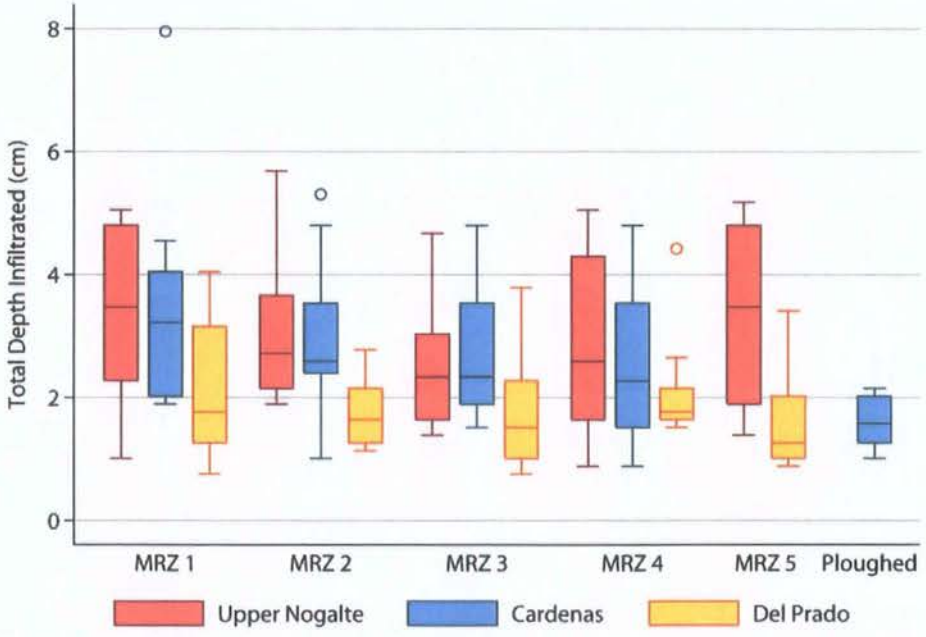

Figure 7.30. Variation of total depth infiltrated (cm) during a five minute experiment between each plot and hillslope.

Hillslope	Plot	k (mm s^{-1})	Total Depth Infiltrated (mm)	Maximum Depressional Storage (mm)
Upper Nogalte	MRZ 1	0.01327	34.47	0.000666
	MRZ 2	0.00907	31.94	0.000715
	MRZ 3	0.01062	25.63	0.025436
	MRZ 4	0.01111	28.66	0.007719
	MRZ 5	0.01534	33.96	0.045350
Cardenas	MRZ 1	0.01131	34.85	0.030423
	MRZ 2	0.00951	29.29	0.019737
	MRZ 3	0.00927	27.65	0.005740
	MRZ 4	0.00840	25.63	0.013055
	Ploughed	0.00262	15.91	0.288797
Del Prado	MRZ 1	0.00678	21.34	0.020932
	MRZ 2	0.00408	17.42	0.042142
	MRZ 3	0.00586	17.42	0.043431
	MRZ 4	0.00696	21.21	0.050590
	MRZ 5	0.00444	16.04	0.175805

Table 7.3. Variation of unsaturated hydraulic conductivity k (mm s^{-1}), total depth infiltrated during a five minute experiment (mm) and maximum depressional storage (mm) for each plot.

There is a slight trend towards decreasing values of k or infiltration rates with distance downslope. However, this is minor compared with the large range of values found at each plot. Figure 7.31 examines the variation of k within the MRZ 3 and MRZ 4 plots. The measurements were divided between those in the bottom of flow concentrations or rills and those measurements taken in interrill areas. In every case the unsaturated hydraulic conductivity was higher in flow concentrations than elsewhere. This effect was more noticeable on those hillslopes with a higher overall infiltration rate and was least noticeable at the Del Prado hillslope. This difference will have an important effect on the initial generation of connected flow over a hillslope, but will become less important with time as more water becomes routed through these concentrations and transmission losses decrease.

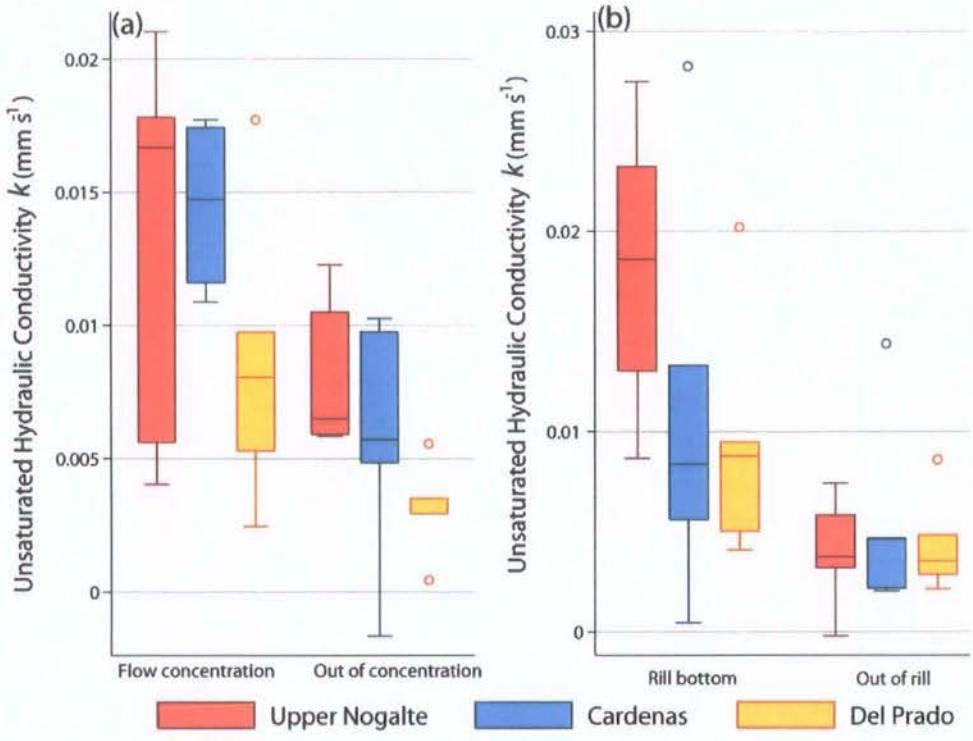

Figure 7.31. Variation of unsaturated hydraulic conductivity (mm s^{-1}) with flow concentration at the MRZ 3 and 4 plots of each hillslope.

No systematic relationship can be found between the observed variation of infiltration over the plots and the effect of antecedent conditions investigated in section 7.3.2. At the Upper Nogalte hillslope, the MRZ 5 plot shows a wide range of unsaturated hydraulic conductivity. The median value is higher than at the MRZ 1 plot, but the MRZ 5 plot showed faster flow under dry conditions. The high infiltration rate at the Upper Nogalte may reflect the importance of wetted area determining differences between wet and dry runs. At the Cardenas hillslope, MRZ 1 demonstrates the highest infiltration rate despite this plot showing faster flow over the dry surface than after the 'wetting-up' event. However, at the Del Prado hillslope, the higher infiltration rate of MRZ 1 appears to be reflected in the increased velocity over the wet surfaces. Beyond MRZ 1 there are only minor changes in the infiltration parameters with distance downslope.

Figure 7.32 compares the difference between modelled resistance and measured resistance (Figure 7.32a) and the unsaturated hydraulic conductivity (Figure 7.32b) measured at each

plot of the Del Prado hillslope. Figure 7.32a uses predictions from the individual regression equations (Table 6.3, model (d)), although Table 7.2 demonstrates that a similar pattern between plots is observed for each of the regression models. It appears as though the over-prediction is unrelated to the infiltration parameters. The MRZ 4 plot shows the least difference between modelled and measured values (the median error is −0.005) followed by MRZ 3 and MRZ 1. These three plots display the highest unsaturated hydraulic conductivity (and infiltration rate). The largest differences are found at the MRZ 2 and MRZ 5 plots which also display the lowest infiltration rates. This is the opposite relationship to that expected from hypothesis (a) (p.256).

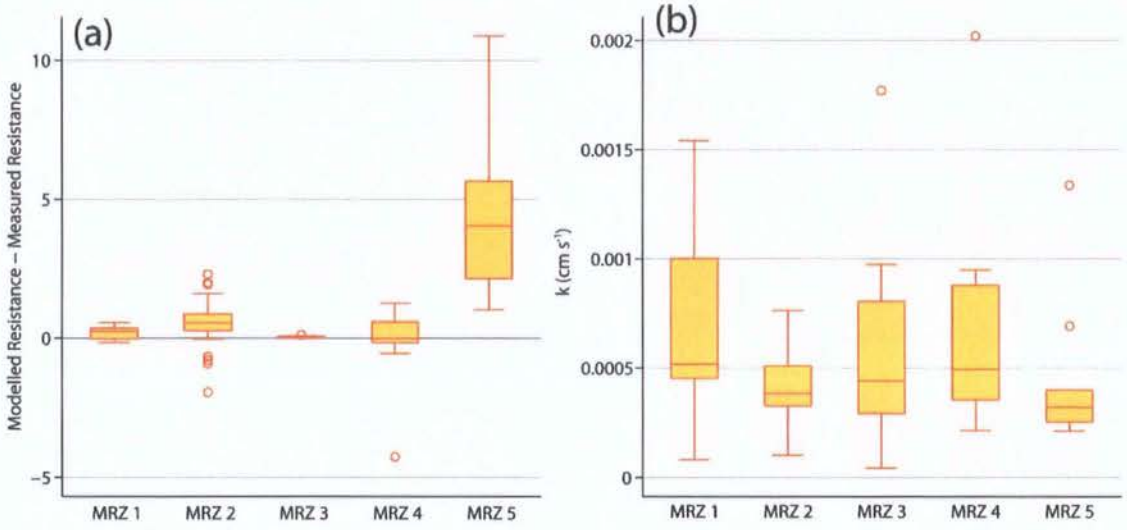

Figure 7.32. (a) Variation of the difference between modelled resistance (using the suite of equations in Table 6.3) and measured resistance and (b) unsaturated hydraulic conductivity k (cm s^{-1}) at each plot of the Del Prado hillslope.

7.4.3 Maximum Depressional Storage

The maximum depressional storage of each plot was calculated using the PCRaster GIS software (Van Deursen and Wesseling, 1992). A full discussion of this process was given by Smith (2005). The values calculated possibly represent a slight underestimate of maximum depressional storage as open boundaries allowed the water to drain freely off the edge of the surface. Given the reasonably large area under study (> 6 m^2 for all plots) compared with the area of those micro-watersheds in contact with open boundaries, this

would have only a small effect on the results. The estimated values are presented in Table 7.3 and Figure 7.33.

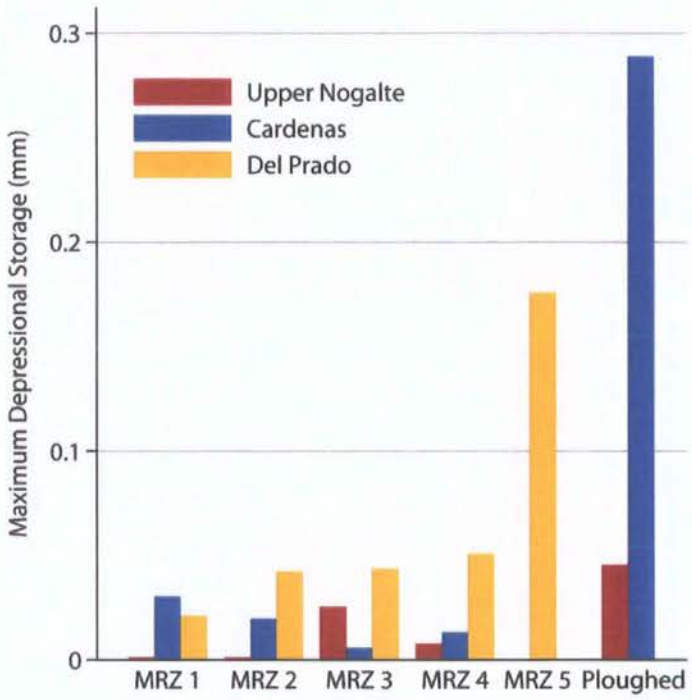

Figure 7.33. Maximum Depressional Storage (in mm) for each plot and site.

The estimates are much lower than values observed in other studies (which can reach 13 mm); this is because most studies calculate depressional storage by first removing the general plot slope (e.g. Kamphorst *et al.*, 2000). This practice has not been followed here as it leads to erroneous values especially on natural (unploughed) surfaces. Figure 7.33 shows that the Del Prado hillslope demonstrated the greatest depression storage on all plots apart from the MRZ 1 plot (where the Cardenas hillslope stored more water) and the Upper Nogalte showed the least storage (except for the MRZ 3 plot). The Del Prado and Upper Nogalte hillslopes appear to increase depressional storage with distance downslope. The reverse trend is found at the Cardenas hillslope. The ploughed plots store the most water at both the Upper Nogalte and Cardenas hillslopes. It should be noted that the ploughed plot used at the Upper Nogalte hillslope was an area of pre-May 2007 ploughing, whereas the ploughed surfaces at the Cardenas hillslope had been ploughed more recently.

Only one value of depression storage is available for each plot. As mentioned above, this may vary with both microtopography and slope angle. Smith (2005) suggests that an analysis of how maximum depressional storage changes with general slope at each MRZ would enable the microtopographic contribution to be kept reasonably constant, thereby isolating the effect of slope angle on depressional storage. The dataset of this study can be combined with that of Smith (2005) to provide an idea of what such an effect may be. Figure 7.34 demonstrates the effect of slope gradient on depressional storage for each plot type. Although insufficient data exist to make any firm conclusions, some interesting qualitative points arise.

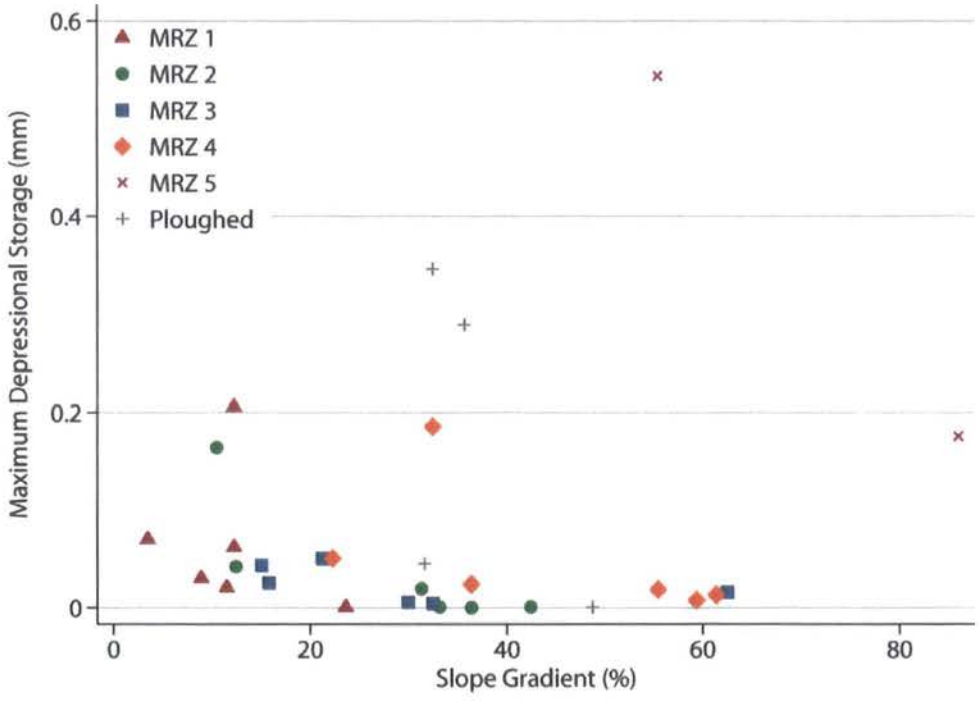

Figure 7.34. The influence of slope gradient on Maximum Depressional Storage (mm) for each plot-type.

Considered as a whole, this dataset potentially shows increasing depression storage with slope gradient. However, when the points are separated by plot-type it becomes apparent that depression storage decreases with slope for each MRZ. This illusion of increasing depression storage with slope demonstrates the importance of the microtopographic contribution. Figure 7.34 shows high depression storage across most values of slopes, but

each of these high values is located towards the lowest slopes found for each MRZ. Unfortunately, insufficient evidence exists to propose any relationships here, but this provides an interesting direction for future research.

Comparing the depression storage calculated at the Del Prado plots (Figure 7.33) with the difference between measured and modelled resistance (Figure 7.32a) shows some similarities. The gullied MRZ 5 plot demonstrated the highest maximum depressional storage (by some margin) and also considerably the highest degree of over-prediction by the resistance equations developed in Chapter 6. It may be hypothesised that satisfying the depressional store (or turbulence induced by this process) increased the effective resistance to flow of the first water wave and was responsible for the over-prediction of the later pulses. Although these results provide no direct evidence for this mechanism, they suggest that it might play an important role. However, the pattern is not consistent as MRZ 4 has the next largest depressional store and was the closest-fitting model.

These results are inconclusive; the over-prediction of the resistance equations of Chapter 6 could not be completely explained by either infiltration or depression storage. However, the filling of the depressional store may cause subsequent flows to relate to the surface roughness in a different manner (decreasing the development of three-dimensional flows and reducing the effect of pits). Although this dataset is of a limited size, the following section attempts to develop a second suite of resistance equations from the dye pulse flows. A comparison with those in Table 6.3 may provide some insight into the processes affecting resistance in established hydrological connections.

7.4.4 Resistance Equations for Established Hydrological Connections

A suite of resistance equations was developed from the dye pulse flow data using the same two-step method described in detail in Chapter 6. The equations are summarised in Table 7.4 (the individual MRZ regression model (d)) and Table 7.5 (the general model (a) and variable coefficients model (c)). These equations were developed from relatively few observations and should be treated with caution. Further measurements would be necessary before applying such equations to model overland flow resistance. Some differences

between Tables 6.3 and 7.4 will simply be a function of the particular dataset used to produce the equations. This cannot be avoided, but further testing may eventually show which features are reproducible over a wide variety of surfaces. The results presented here represent a first step towards an enhanced understanding of overland flows and offer an opportunity to examine which roughness measures are more relevant for established flow connections.

Plot	Roughness Equation			Predictors	R^2
GENERAL	$f = \frac{e^{6S+2\Lambda}}{27(\sigma_Z P_{dd})^{0.92}}$	S	+	Slope	0.49
		Λ	+	Inundation ratio	
		σ_Z	−	Elevation STDEV	
		P_{dd}	−	Pit density (downslope)	
MRZ 1	$f = \frac{e^{8.4S}\Lambda_\sigma^{1.17}}{2.3}$	S	+	Slope	0.53
		Λ_σ	+	Inundation ratio (STDEV)	
MRZ 2	$f = e^{55T_{3D}-0.18P_{dd}-2T_d-35}$	T_{3D}	+	3D Tortuosity (40 mm)	0.76
		P_{dd}	−	Pit density (downslope)	
		T_d	−	Downslope Tortuosity	
MRZ 3	$f = \frac{\Lambda_{Zd}^{0.93}}{40}$	Λ_{Zd}	+	Detrended Inundation ratio	0.94
MRZ 4	$f = \frac{e^{7.1S+D_{sk}}}{5.64\Lambda_\sigma^2}$	S	+	Slope	0.85
		D_{sk}	+	Depth skewness	
		Λ_σ	−	Inundation ratio (STDEV)	
MRZ 5	$f = \frac{e^{6S}\Lambda}{2(\sigma_Z P_{dd})^{1.3}}$	S	+	Slope	0.95
		Λ	+	Inundation ratio	
		σ	−	Elevation STDEV	
		P_{dd}	−	Pit density (downslope)	

Table 7.4. Summary of roughness-resistance relationships developed from dye pulse flow data. + and − indicate the direction of the relationship with resistance (measured by f). Compare Table 6.3.

The R^2 of the general model (0.49) was increased by including hillslope position (MRZ) as a dummy variable (R^2 = 0.61). Allowing the individual coefficients to vary (performing the regression separately by MRZ) increases the R^2 further to 0.69. Performing regressions individually (as seen in the MRZ equations of Table 7.4) produces an R^2 of 0.88. These

increases in model performance with increasing complexity are much larger than those seen in Chapter 6.

Including the nine variables found to be related to resistance at each MRZ into a general model (following the two-step approach of section 6.5.3) gives the equation

$$f = \frac{e^{7S - T_{3D} - 0.5T_d + 0.16D_{sk}} \Lambda^{0.8} \Lambda_{\sigma}^{0.4} \Lambda_{Zd}^{0.2}}{(\sigma_Z P_{dd})^{0.7}} \tag{7.2}$$

which has an R^2 of 0.57. Introducing dummy variables representing hillslope position into model 7.2 further increased the R^2 to 0.69 (using MRZ 1 as a reference, the constants added to model 7.2 were: −1.30 for MRZ 2; −1.07 for MRZ 3; −0.13 for MRZ 4 and −0.92 for MRZ 5). Finally, Table 7.5 displays the values of coefficients for each plot when the coefficient on each variable was allowed to alter according to plot-type (model (c) on p.196). This model gave an R^2 of 0.89. The relationships between each of these models and measured resistance (for the dye pulses only) are shown in Figure 7.35.

GENERAL	$\ln(f) =$	7.261	$S +$	−1.072	$T_{3D} +$	−0.498	$T_d +$	0.159	$D_{sk} +$
MRZ 1		10.515		21.47		15.029		−0.201	
MRZ 2		4.257		57.725		−1.059		−3.036	
MRZ 3		−5.108		−51.295		16.732		4.452	
MRZ 4		6.370		4.254		0.975		0.854	
MRZ 5		6.533		−0.364		0.317		−0.507	

G	0.791		0.415		0.204		−0.682		−0.030
1	0.440		−2.484		2.856		−3.581		47.969
2	−1.218	$\ln(\Lambda)$	−5.415	$\ln(\Lambda_\sigma)$	−0.004	$\ln(\Lambda_{Zd})$	−5.717	$\ln(\sigma_Z P_{dd})$	−62.058
3	−0.160	+	−4.055	+	10.497	+	−5.304	+	7.652
4	0.101		1.089		0.812		−0.803		−8.749
5	0.711		−0.144		−0.145		−1.249		−0.612

Table 7.5. Variation of the coefficients of each roughness measure related to flow resistance for the dataset as a whole (model 7.2) and at each Morphological Runoff Zone (MRZ) (model 7.3).

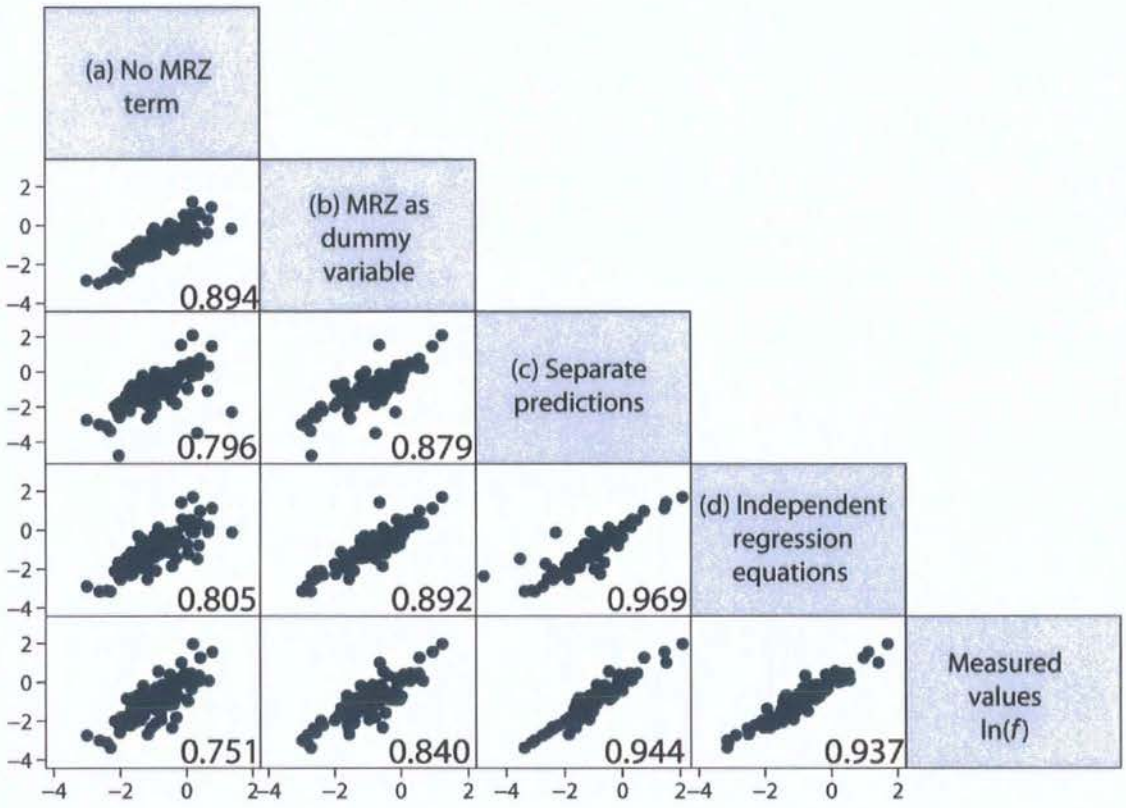

Figure 7.35. Scatter matrix demonstrating relationships between different methods of incorporating hillslope position into predictions of resistance to overland flows and the measured values (log scale). All roughness measures in Table 7.4 have been included in each prediction. Pearson's correlation coefficient is displayed in the lower right corner of each plot region.

The slope term remains a significant predictor (P>0.05) for the same reasons identified in Chapter 6. However, the pit density terms appeared to be much less important for predicting the resistance of established connections than those of the first water wave. Each MRZ equation of Table 6.3 contained a pit density term (which in all but one case, was cross-sectional pit density P_{dxc}); in Table 7.4 such a term is found only at the MRZ 5 plot and the general equation (incorporating all data-points). The downslope pit density is inversely related to resistance at these plots. Smith (2005) showed that downslope pit density was the most relevant measurement of roughness for predicting the depressional storage capacity of a rough soil surface. Once all the pits have been occupied with water, they will have less influence on any subsequent overland flow. The water stored in these

pits will provide lower resistance to subsequent overland flows which may explain this negative relationship at the MRZ 5 plot (which has the largest depression storage capacity; Figure 7.33). Where pits are occupied with water, flow vectors will be much less three-dimensional. This difference may reflect a change in the interaction of overland flow with roughness as a hydrological connection persists. Such dynamic relationships are extremely important for flood generation (Bracken and Croke, 2007) and are discussed further in section 8.4.

The inundation ratio was the key depth-varying term in many equations of Table 6.3. However, this is only a predictor of resistance at the MRZ 5 plot in Table 7.4. The related term Λ_σ (depth scaled by the standard deviation of elevations) of Smart *et al.* (2002) is related to f at the MRZ 1 and 4 plots (although with an opposite sign to the relationship). Similarly the detrended inundation ratio Λ_{Zd} (depth scaled by the mean elevation difference between a cell and its neighbours, following Ergenzinger (1992)) is positively related to resistance at the MRZ 3 plot as the only predictor. In the general model (7.2) each variant of the inundation ratio has a different exponent reflecting the variable influence on flow resistance. Table 7.5 shows that the importance of each term as a predictor of resistance varies with hillslope position. This demonstrates the difficulty of applying a single roughness measure to scale flow depth in resistance equations over a wide range of surfaces and explains the inclusion of all three terms in equation 7.2.

Figure 7.36 shows the predicted resistance using each model (a)–(d) against the measured resistance for both the dye pulse data (with which these equations were developed) and the original 'first wave' dataset. The models allowing less variation between plot-types predict the pulse-data least well but provide a much better prediction of the original first-wave dataset. Conversely, the approaches where coefficients or predictors included in the model can vary with each MRZ (models (c) and (d)) provide a much better prediction of the pulse dataset, but cannot predict the resistance of the first-wave dataset. Whereas the 'first wave' equations overpredicted the resistance of the pulse data, the pulse equations show a much more complicated relationship with the first-wave data (with a tendency towards underprediction). This restates the observation of Figure 7.27 that more specific models are less able to predict resistance in flow conditions different from those for which they were

developed. Model (d) appears to overpredict and underpredict the first-wave resistance measurements in equal value. Figure 7.37a–e examines this in greater detail by separating the predictions by Morphological Runoff Zone.

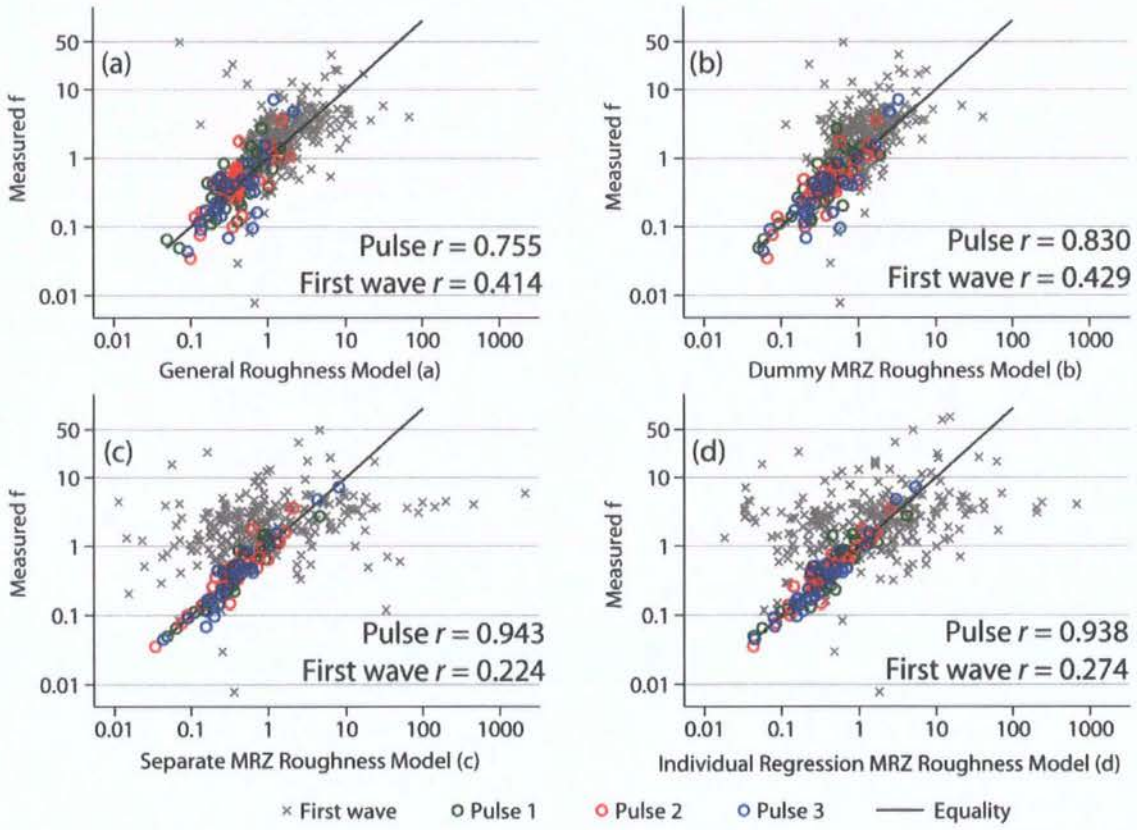

Figure 7.36. Roughness-resistance models developed from dye-pulse data (Tables 7.4 and 7.5) applied at the Del Prado hillslope. Grey crosses represent the original dataset presented in Chapter 6. Models (a)–(d) indicate the different representations of hillslope position in the model (as discussed on p.196). The Pearson correlation coefficient *r* shows the relationship between the predictions and the measured values for the both datasets.

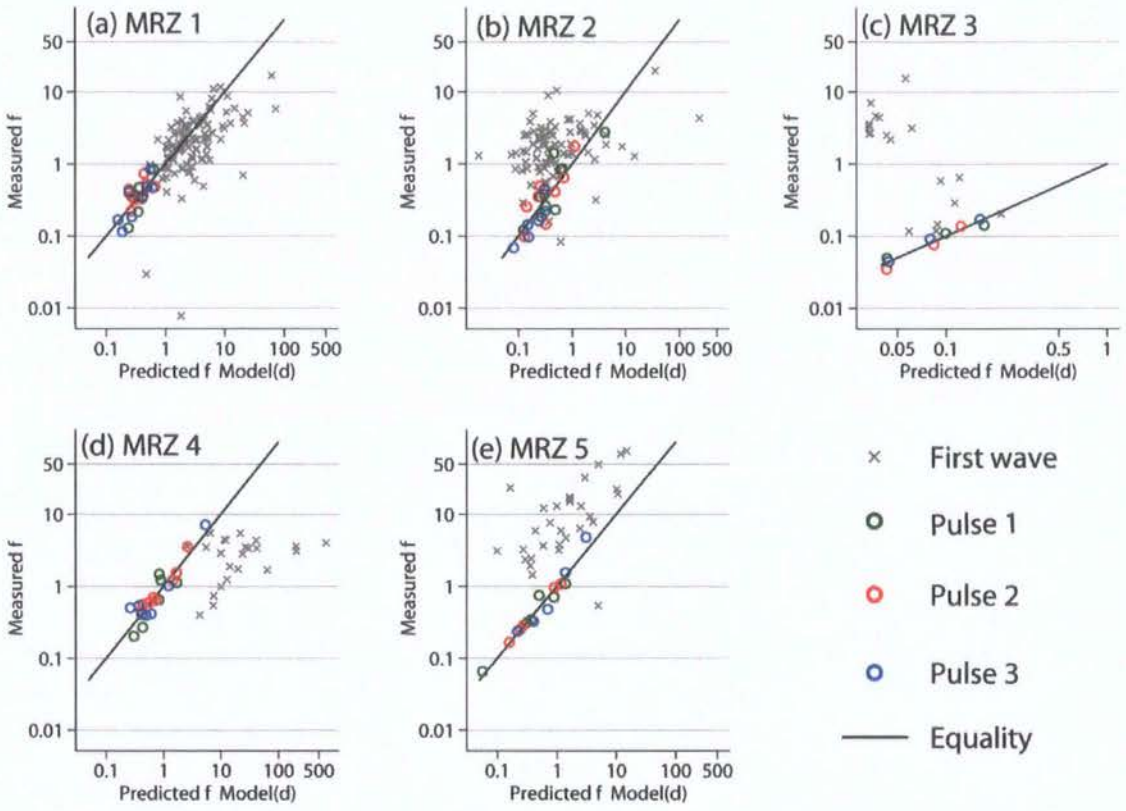

Figure 7.37. Roughness-resistance equations displayed in Table 7.4 applied at each plot of the Del Prado hillslope. Grey crosses represent the original dataset presented in Chapter 6.

Figure 7.37d shows that most of the overpredicted measurements occur at the MRZ 4 plot. An examination of the variables used in the MRZ 4 pulse resistance equation suggests that this over-prediction is caused by lower three-dimensional (or surface) standard deviation of elevations σ_Z measured on the first wave dataset (Figure 7.38). This is used to scale flow depth in the inundation ratio Λ_σ of Smart *et al.* (2002) and so is positively related to resistance in the prediction equation in Table 7.4. It could be suggested that the slight increase in depth for the later pulses inundated the rill walls to a greater degree. As all elevation values are lumped together to give σ_Z, the addition of these new high elevation points would increase σ_Z. A large increase in σ_Z was also observed at the MRZ 5 plot where the σ_Z term is negatively related to resistance and so this may be the cause of the under-prediction observed. Such a large increase in σ_Z for the dye pulses was not observed upslope of MRZ 3, presumably as there was less potential for progressive inundation. This

explains why the MRZ 1 equation, which contains the Λ_σ term as positively related to resistance, does not underpredict resistance (Figure 7.37a).

Similar effects of shifting roughness values were examined to explain differences between the first wave and dye pulse resistance predictions and measurements observed in section 7.4.1. However, none was observed.

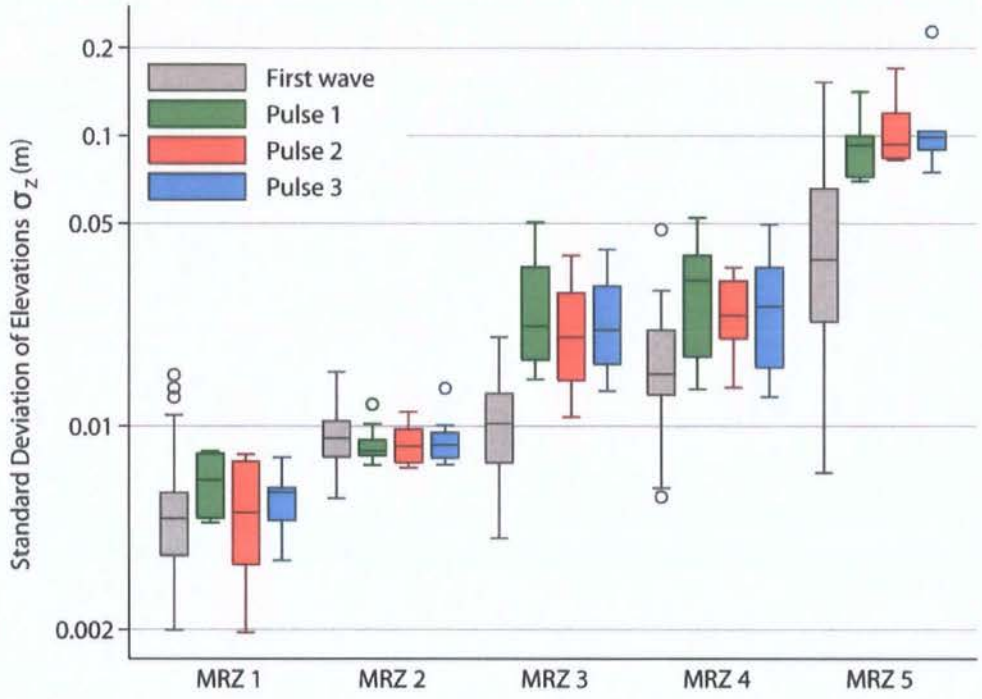

Figure 7.38. Variation of the three-dimensional (surface) standard deviation of elevations σ_z (in metres) between each plot on the Del Prado hillslope. Measurements are separated by the dye pulse from which they were measured.

In conclusion, the differences between resistance predictions for the initial 'first-wave' dataset and later dye pulses cannot be explained by variations in infiltration rates. Depression storage appears to exert some influence on this relationship (hypothesis (b) of p.256), but this influence cannot be separated from the more general effect of the effect of three-dimensional flow vectors on momentum transfer (c). The results of Table 7.4 suggest that the relationship between overland flow and surface roughness may be dynamic and shift with the establishment of flow connections. Finally, Figure 7.38 shows that the differences observed may partly be a consequence of changes in roughness measurements

with a small increase in depth (hypothesis (d) of p. 256). However, this was observed to occur in a single, isolated case.

7.5 Summary

This chapter has begun to consider the problem of flood generation at the hillslope scale. The Morphological Runoff Zone concept has been examined and the definition of each zone has been formalised into a method suitable for use with high-resolution topographic data at the hillslope scale (provided by a terrestrial laser scanner). These MRZs have been used to classify hillslope surfaces and upscale the plot investigations. The relationships between flow velocity and flow concentration have been examined alongside the influence of antecedent moisture conditions on runoff transfer. An investigation of the effect of soil wetness on flow velocity at the hillslope scale suggests a negligible influence on hillslope outflow and the development of connected flowpaths under the conditions simulated in these experiments.

However, once a flowpath has developed, the soil has become saturated and surface depressions filled, the results of section 7.4 suggest that the resistance to flow is decreased as overland flows interact with the soil surface in a different manner (as flow vectors become more parallel). The results emphasise the important distinction between flows establishing hydrological connections, and those travelling on previously established hydrological delivery pathways.

This chapter has been limited to an investigation of runoff routing over soil surfaces. It is well established that antecedent moisture conditions have a large effect on the generation of runoff at the source. Thus far, however, these two issues have been separated. Discussions of connectivity development and flow resistance have remained relatively independent. Chapter 8 combines these topics by demonstrating the incorporation of the resistance equations developed in Table 6.3 into a hillslope runoff model, thereby merging the two main threads of this thesis and highlighting them as crucial factors in any consideration of flood generation in semi-arid environments. Chapter 9 then concludes by summarising the main arguments of this thesis and identifying how the results can be used to advance our ability to predict and understand the dynamics of semi-arid flood events.

CHAPTER 8

TOWARDS A DYNAMIC REPRESENTATION OF HYDROLOGICAL CONNECTIVITY AT THE HILLSLOPE SCALE

8.1 Introduction

The impact of heterogeneities on hydrological and geomorphological processes can be assessed using the emerging conceptual framework of hydrological connectivity. This chapter examines the nature of hydrological connectivity and flood generation on semi-arid hillslopes and highlights research priorities for the development of a quantitative representation of this concept.

The results presented in Chapters 6 and 7 emphasised the temporal variability of overland flow resistance and velocity, examining the variation with both flow depth and antecedent conditions. For this to be usefully incorporated into a conceptual model of hillslope hydrology, the temporal structure of rainfall intensities should also be integrated into any analysis as these two factors interact with infiltration rates to determine rates of water supply and runoff transfer. The review in Chapter 3 suggested that the temporal structure of a rainstorm has an important effect on hillslope hydrographs. Thus, the main discussion of this chapter is preceded with an examination of rainfall characteristics and hydrographs recorded at the Rambla de Torrealvilla between 1997 and 2007 (section 8.2). Several rainstorm characteristics are investigated to explain the observed effect of time-varying rainfall intensity on the scale-dependency of runoff coefficients, selecting several key properties of rainstorms to examine further.

While much research has been directed towards understanding spatial and temporal variations of infiltration rates and runoff generation, this thesis argues that a similar degree of flexibility must be afforded to the representation of flow resistance in hydrological models if we are to quantify the effect of heterogeneities on nonlinear hillslope outflow. The results presented in Chapter 7 provided demonstration that the distribution of travel times and the arrival of runoff at key points in the flow network will have a large influence on flood magnitudes in environments where transmission losses are high. This is affected by interactions between the temporal structure of the rainfall event, the spatial structure of active runoff generating areas, distribution of flowpath lengths, integration of flowpaths and the routing velocity of overland flows.

The analysis of hillslope travel times of Chapter 7 was grounded in field observations of flow velocity during runoff simulations; it did not incorporate the resistance equations of Chapter 6 into velocity predictions. Moreover, the Instantaneous Unit Hydrograph approach ignores the variability of rainfall and changing hydraulic conditions on the soil surface as a storm event progresses. This chapter unites the two central threads of this thesis by demonstrating how the resistance equations of Table 6.3 can be applied to model hillslope runoff to understand the dynamic nature of connectivity development and runoff generation at sub-catchment scales.

Before the results of Chapter 6 can be implemented in a hydrological model, they must be presented in a form suitable for use in such models (which operate from a 'runoff depth' as given by equation 3.1; e.g. Kirkby *et al.*, 2002). This process is described in section 8.3 where depth-resistance relationships are developed for each plot of the Del Prado hillslope. These relationships are tested against an independent dataset obtained from the variable discharge experiments described in section 5.3.

Section 8.3 presents a formal and quantified approach to modelling the variation of flow resistance with available runoff depth as determined by infiltration. In turn, infiltration rate is affected by soil moisture distribution, as determined by both rainfall inputs and horizontal moisture transfers controlled by flow resistance. This interaction is responsible for the nonlinear runoff-response observed on natural semi-arid hillslopes, explaining not

just the peak runoff but also the total runoff amount (as a consequence of the limited 'travel opportunity time' in such areas; Aryal *et al.*, 2003). Thus, the framework presented in section 8.3 permits a quantitative understanding of this interaction. This is examined in section 8.4, which draws together the results of this thesis into a discussion of recent developments and important future research directions of semi-arid hydrology. The implications of the results for modelling hillslope hydrology are presented. It is suggested that efforts to model this interaction using the proposed conceptual framework of hillslope hydrological connectivity will improve our ability to predict the arrival time and size of initial flood waves and also flood volumes in arid and semi-arid catchments.

The method of modelling resistance implemented in this hydrological model is innovative and requires substantial development and further research before any firm conclusions can be made. An aim of this thesis is to provide an example of how recent advances in data collection methods offer an opportunity to reconsider how we conceptualise and measure overland flows over complex soil surfaces. While this first step has produced some interesting results, section 8.5 suggests how this approach can be taken further and highlights some important questions towards which future research should be directed. Finally, section 8.6 summarises the discussion of this chapter.

8.2 Rainfall Characteristics & Runoff Response

The conceptual framework of hydrological connectivity presented in Chapter 3 emphasised the importance of rainfall characteristics for flood generation and propagation in semi-arid environments. Although many authors have argued that the production of runoff is governed by a multitude of different storm characteristics (e.g. Costa, 1987; Yair and Raz-Yassif, 2004; section 3.2) the decision of which rainfall characteristics to examine should be grounded, where possible, on field data of rainfall-runoff response. Individual properties of rainstorms may be isolated as having a large effect on runoff response, providing a focus for future modelling investigations. A network of tipping bucket rain gauges is distributed across the Rambla Nogalte and Torrealvilla catchments (Figure 4.28). Figure 8.1 shows the location of the Del Prado hillslope with respect to the Torrealvilla rain gauge, Prado stage gauge and two crest-stage gauges. This section examines the relationship between the

temporal structure of rainfall events and runoff response at the Prado tributary of the Rambla de Torrealvilla.

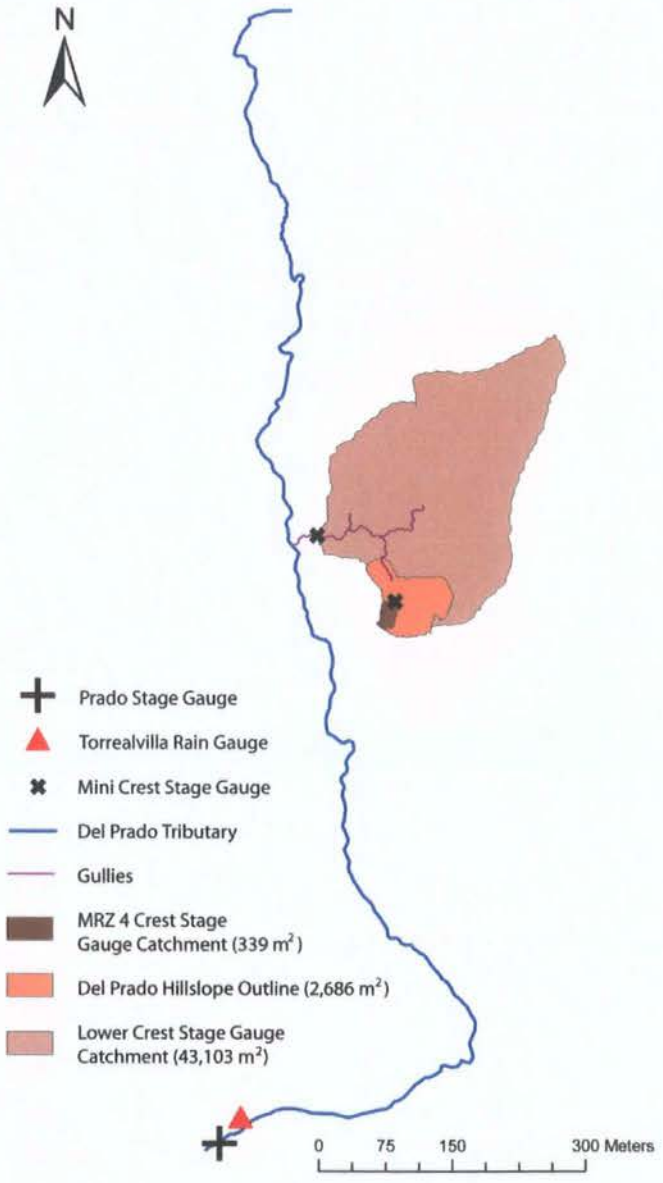

Figure 8.1. Location of the Del Prado hillslope with respect to the nearest rain gauge and stage gauge. The Prado tributary of the Rambla de Torrealvilla is also shown along with the gully system incised near the hillslope. The locations and catchments of two crest stage gauges are also shown.

A minimum flow stage of 20 mm was arbitrarily selected as the minimum threshold value for a runoff event. Table 8.1 displays the features of the rainstorms in this analysis. The

rainfall record was divided into spells defined as periods of rainfall without breaks greater than 12 h following Bracken *et al.* (2008) (see also Cox, 2007b). This criterion was selected to allow sufficient time for flow discontinuities to develop and the soil to dry out (see Bracken *et al.*, 2008 for a full discussion). This produced a dataset of 24 runoff events that could be linked to rainstorms recorded at the nearby rain gauge.

Spell	Date	Start Time	Duration (h)	Storm Total (mm)	Maximum Intensity (mm h^{-1})	Mean Intensity (mm h^{-1})	Peak Stage (m)
1	25-Apr-97	12:26	3.0	5.0	24.0	9.32	0.076
2	18-Jun-97	11:19	5.1	73.4	156.0	37.81	1.983
3	13-May-98	23:25	13.1	34.8	24.0	7.32	0.085
4	27-Sep-00	15:51	0.6	10.0	48.0	19.80	0.063
5	21-Oct-00	03:58	77.7	106.2	72.0	10.19	1.544
6	25-Oct-00	02:18	22.4	6.4	24.0	4.67	0.139
7	22-Sep-01	13:35	4.8	17.0	108.0	13.60	0.141
8	03-Mar-02	04:57	29.5	33.8	24.0	7.52	0.081
9	14-Nov-02	03:05	30.9	8.0	12.0	2.66	0.419
10	19-Nov-02	20:39	6.4	4.0	4.0	1.99	0.209
11	23-Nov-02	18:43	22.6	12.2	6.0	1.84	0.421
12	09-Dec-02	20:19	7.9	0.8	0.4	0.25	0.051
13	10-Jan-03	03:26	14.2	22.8	12.0	2.75	0.408
14	16-Oct-03	17:28	29.4	33.4	108.0	17.75	0.711
15	16-Nov-03	19:17	90.5	65.8	48.0	8.14	0.378
16	09-Dec-03	02:50	26.8	42.0	12.0	5.05	0.216
17	29-Feb-04	23:55	9.8	1.6	4.0	1.16	0.022
18	28-Mar-04	17:33	19.5	23.0	24.0	6.33	0.130
19	15-Apr-04	16:15	15.7	45.4	12.0	6.51	0.232
20	26-May-04	13:25	1.9	23	132	30.82	0.536
21	03-Feb-06	17:48	23.9	5.6	36.0	6.36	0.051
22	25-Jan-07	16:33	54.1	99.2	12.0	6.38	0.146
23	26-Mar-07	16:54	55.4	17.0	24.0	2.63	0.032
24	22-Aug-07	17:15	3.0	18.4	96.0	23.62	0.138

Table 8.1. Summary characteristics of the spells of rain recorded at the Prado rain gauge and stage gauge between March 1997 and November 2007.

Despite short gaps in both the rainfall and stage gauge records, the runoff events are well distributed over the 10 year period of instrumentation. The largest runoff events were recorded in June 1997 and October 2000, although other large events are known to have taken place in this time period (e.g. in September 1997; Bull *et al.*, 1999), but were during gaps in the record available for this analysis (where monitoring equipment was damaged).

Table 8.1 shows that a wide range of rainstorms and runoff events has been included in an attempt to understand the influence of storm characteristics on runoff generation. Figure 8.2 demonstrates the relationships between summary rainfall characteristics and runoff generation at the Prado tributary. Less conventional descriptions of rainstorms have also been included; the calculation of these has been informed by the connectivity framework outlined in Chapter 3. Correlation coefficients between rainfall characteristics and flow stage measured at the Prado are given in Table 8.2.

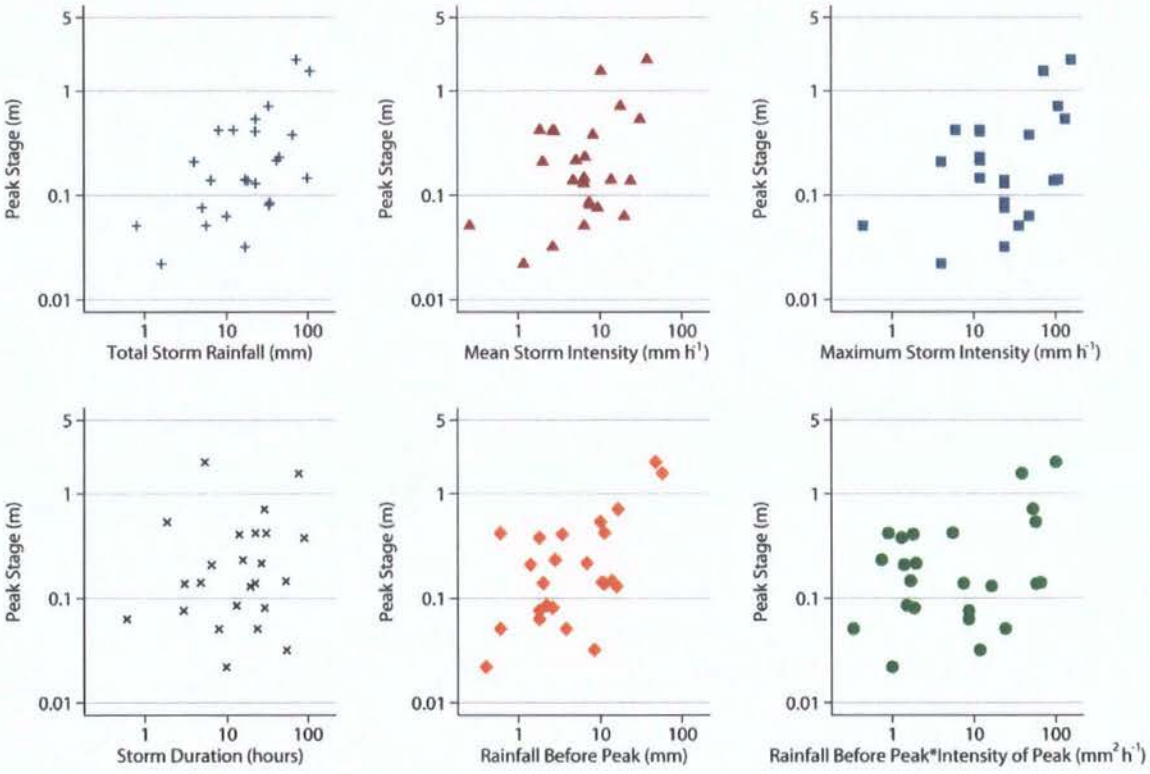

Figure 8.2. Relationships between flood generation and storm characteristics at the sub-catchment scale.

Total storm rainfall is well correlated with runoff generation; the largest flood peaks were produced from the largest total rainfalls and vice versa. Despite some scatter around the intermediate events, the relationship is significant at the 0.01 level. Both mean and maximum storm intensity are also significantly related to peak stage at the 0.01 level with a slightly stronger relationship evident between runoff and maximum intensity. Storm duration did not show a direct relationship with peak stage (although this will be influenced

by the selection of a 12 hour rain-free interval as the dividing criterion between spells). However, Figure 8.2 shows that two outliers are found where two of the largest runoff events were generated from relatively short-lived storms (of June 1997 and May 2004).

$n = 24$	Peak Stage
Total Storm Rainfall	0.61
Mean Storm Intensity	0.57
Maximum Storm Intensity	0.62
Storm Duration	0.20^{Δ}
Rainfall Before Peak Intensity	0.89
Rain Before Peak × Intensity of Peak	0.64
Duration Above 5 mm h^{-1}	0.33^{Δ}
Maximum Pulse Duration (5 mm h^{-1})	0.20^{Δ}
Duration Above 10 mm h^{-1}	0.56
Maximum Pulse Duration (10 mm h^{-1})	0.66
Duration Above 20 mm h^{-1}	0.90
Maximum Pulse Duration (20 mm h^{-1})	0.61

Table 8.2. Correlation between rainfall characteristics and peak stage at the Prado tributary. Note: All correlations are calculated on the raw scale and significant at the 0.01 level unless otherwise indicated Δ (where relationships are not significant).

The review in Chapter 3 suggested that flood generation is influenced by the relationship between infiltration rate and storm intensity. Whenever infiltration rate declines during the course of a rainstorm, the location of a high intensity burst or pulse of rain within the rainfall time series of a storm event will affect flood peaks. This can be assessed quantitatively as the depth of rainfall that has fallen before the intensity peak is reached. Figure 8.2 shows the relationship between this measure and flood stage which demonstrated the highest correlation of the measures in Figure 8.2. Again, the extreme values of the dataset fit more closely to the trend than the intermediate storms which display more scatter. Figure 8.2 also shows that adding an appreciation of the value of the peak intensity does not improve the relationship (the correlation coefficient drops substantially although the relationship remains significant at the 0.01 level). Figure 8.3 further examines the influence of intense pulses of rainfall on runoff generation.

The results presented above confirm the relationship between antecedent soil moisture conditions and runoff peaks at the Prado tributary. However, the review in Chapter 3 also emphasised the importance of connectivity development and runoff travel times for semi-arid flood generation. Although the reduced infiltration rate as the storm progresses increases the likelihood that any pulse of high-intensity rainfall will generate runoff, this intensity must be maintained for runoff to reach a flow concentration or channel. The intensity threshold and pulse duration required will vary between locations and throughout the course of a single event. Figure 8.3 attempts to identify important characteristics of intense pulses of rain within a storm for flood generation at the Prado tributary.

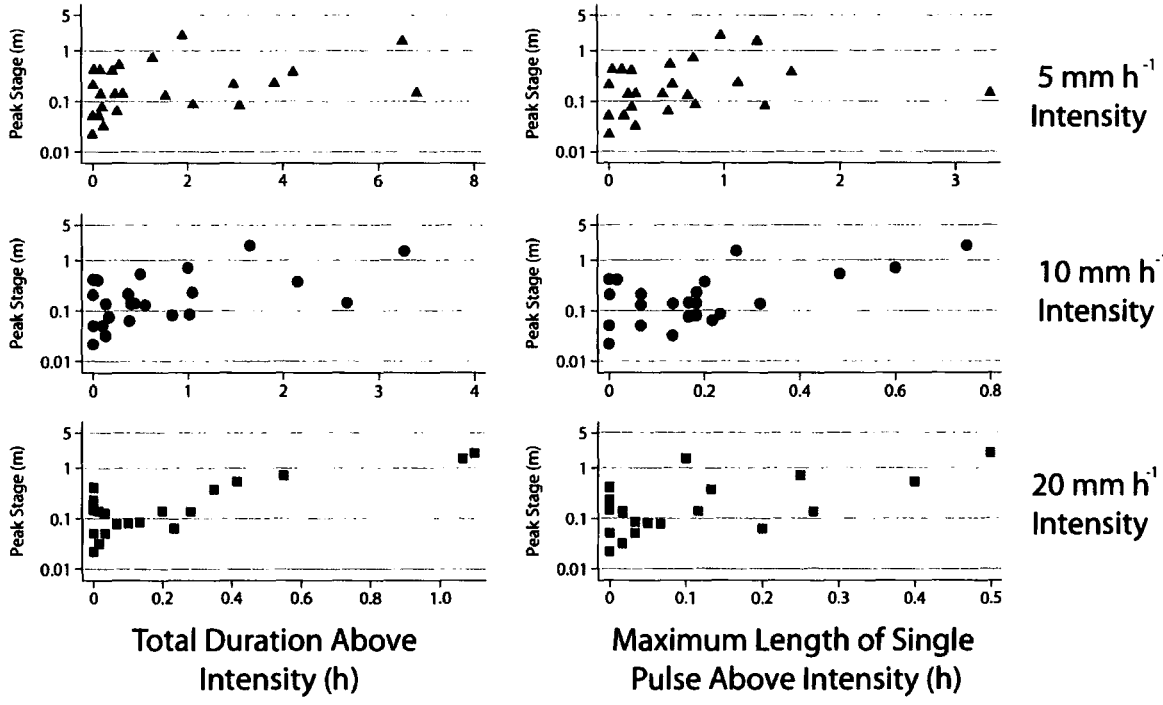

Figure 8.3. Relationships between flood generation and storm characteristics at the sub-catchment scale for three rainfall intensity thresholds.

Figure 8.3 shows the relationships between flow stage and total duration of time within each storm experiencing rainfall above an intensity threshold and also the maximum continuous duration of a single pulse above the intensity threshold. The relationships between these measures and peak stage are displayed for three thresholds (5, 10 and 20 mm h^{-1}). Table 8.2 presents the correlation coefficients for these relationships.

Both total duration above 5 mm h^{-1} and maximum pulse duration above 5 mm h^{-1} were uncorrelated with peak stage. This suggests that the Prado catchment has a higher runoff threshold. Indeed, at 10 and 20 mm h^{-1} the relationships are significant at the 0.01 level. The total duration above 20 mm h^{-1} was well correlated with peak stage (r = 0.90); this relationship appears to be especially significant for the largest runoff events. However, the maximum duration of a continuous pulse was better correlated with flood generation for the 10 mm h^{-1} threshold. This measure is complicated by the number of pulses experienced during the course of a storm event (a pulse is terminated even if the rain falls below the threshold for just one minute). This is evident in Figure 8.3 where outliers at the 10 and 20 mm h^{-1} thresholds experienced a short continuous pulse duration but a large number of pulses during the rainstorms. The three large flood events with lower pulse duration at the 20 mm h^{-1} intensity were much longer storms (>24 h, frontal-driven events) than the other four large flood events (0.6–5.3 h, most probably convective-driven events). Figure 8.3 shows that where individual spells of rain are distinguished by a 12 hour period of no rainfall (thereby permitting only limited drying out time during the course of each spell) the total time above the 20 mm h^{-1} intensity threshold is more significant than the length of individual pulses.

The stage gauge at the Prado tributary demonstrates the runoff response at the sub-catchment scale (>10 km^2). Field evidence suggests that the area close to the main Prado tributary contributes much of the runoff in the Rambla de Torrealvilla in large flood events (see Bull *et al.*, 1999). Two crest stage gauges shown in Figure 8.1 drain much smaller areas and can be used to assess whether the relationships identified above are relevant at the hillslope scale. These measurements only provide an approximate peak stage over a 6 month period; therefore only 5 measurements are available at the MRZ 4 gauge (located in the Del Prado MRZ 4 plot) and only a single flow depth was recorded at the lower gauge (at the bottom of the gully system) (Table 8.3). This single measure is displayed as an indication of the overall contribution of the area around the Del Prado hillslope to flow in the main channel.

Date	Start Time	Duration (h)	Storm Total (mm)	Maximum Intensity (mm h^{-1})	Mean Intensity (mm h^{-1})	Rain Before Peak Intensity (mm)	Peak Stage (m)
MRZ 4 Mini Crest Stage Gauge (339 m^2)							
01-Jul-02	18:32	10.3	56.0	96	18.49	39.06	0.100
15-Apr-04	16:15	15.7	45.4	12	6.51	4.92	0.075
04-Feb-06	17:48	23.9	5.6	36	6.36	5.55	0.095
27-Jan-07	16:33	54.1	99.2	12	6.38	59.76	0.060
22-Aug-07	17:15	3.0	18.4	96	23.62	1.31	0.036
Lower Crest Stage Gauge (43,103 m^2)							
26-Mar-07	16:54	55.4	17.0	24	2.63	5.59	0.750

Table 8.3. Summary characteristics of the spells of rain recorded at the Prado rain gauge and crest stage gauges.

At the MRZ 4 location, no relationship between mean or maximum intensity and runoff depth can be detected (from just 5 data points). However, the rainfall before peak intensity appeared to reflect the variation of runoff generation between the rainstorms. This rainstorm characteristic appears important at both hillslope and catchment scales. The total storm duration was also related to the peak stage recorded at this location (whereas the results at the Prado tributary suggested that this was unimportant at the small catchment scale). Figure 8.3 showed that increasing the intensity threshold appeared to provide a better representation of runoff response, but no such relationships could be distinguished from the 5 storm events recorded at the hillslope scale. Further research is necessary to present a full examination of this possible scale effect and requires the establishment of a larger number of flow depths monitoring sites over different hillslopes. In summary, the effect of storm duration may be important at the hillslope scale as flow connections gradually develop. Such an effect is less important at the small catchment scale where a greater range of travel times may be observed.

To conclude, it appears that the total duration above an intensity threshold of 20 mm h^{-1} provides a simpler and equally effective measure of relevant rainfall characteristics than identifying individual bursts of high intensity rainfall. The importance of the length of these pulses remains unclear. However, the location of high intensity rainfall within a rainfall

time series has an important effect on flood generation. A comparison of rainfall characteristics with flood magnitudes at the Prado tributary has shown that the measures incorporating the ratio between rainfall intensity and infiltration rate and the duration for which this ratio is above a certain threshold (as emphasised by the review of hydrological connectivity concepts) appear to best represent the processes responsible for flood generation. The discussion of section 8.4 provides an example of how these ideas can be used to inform a conceptual model of semi-arid hillslope hydrology from which important research questions can be identified.

8.3 Variation of Resistance with Flow Depth

Chapter 2 described traditional methods of modelling flow resistance. Approaches developed from pipe flows relate resistance to a property of the flow such as the Reynolds number (e.g. equations 2.7, 2.12 and 2.13) or a measure of surface roughness (e.g. the roughness height of equations 2.11, 2.22 and 2.23). A resistance equation that scales flow depth by such a roughness height (the inundation ratio of equation 2.21, for example) will predict a flow resistance that is depth-dependent. The resistance equations developed in Chapter 6 all predict f from two types of roughness measures: those dependent only on the microtopography of the soil surface f_A (initial resistance), and those that vary with flow depth f_B. This dichotomy follows the approach adopted by Scoging (1992) and permits the flow resistance to be predicted at any flow depth. Such depth-resistance relationships provide a crucial link in our understanding of dynamic connectivity. This section provides a detailed description of the development of depth-resistance relationships from the results of Chapter 6. Once established, the interaction between rainfall, infiltration, and runoff travel times at the hillslope scale can be examined. This opportunity is examined in detail in the discussion of section 8.4.

For each Morphological Runoff Zone (MRZ) the observed distribution of the constant 'initial resistance' term f_A was calculated (e.g. Figure 8.4c). The observed distribution of f_A is used here because combining the separate distributions of each of the roughness measures that contribute to f_A would produce misleading results as each measure is not necessarily independent. The final predicted resistance is the product of this f_A value and a

depth-dependent term f_B. In the equations of Tables 6.3 and 6.4 the depth-dependent term was a function of the inundation ratio, median depth or depth skewness. As a hydrological model will compute only a single flow depth for each cell, the variation of each of these terms with depth must be taken into account. The analysis of flow depth distributions described in section 5.4 showed that flow depths were not well described by a normal distribution and suggests that median depth provides a more suitable reference level than the mean. Each depth-dependent term was calculated for the range of flow depths from zero to the level where the soil surface was entirely submerged. While it is recognised that such progressive inundation will alter the roughness values measured for the constant term (as seen in Figure 7.38), this simplification can be justified as such variations appear minor compared with those of the depth-dependent terms.

The Darcy-Weisbach friction factor equation derived in section 6.3 indicates that the volumetric hydraulic radius R_v is more relevant than flow depth over surfaces of complex microtopography. Therefore, the equations of Table 6.3 were developed from a dataset that applied R_v in the calculation of f. To convert the predictions into a form that varies with median depth d_{50}, the variation of R_v with increasing water surface level was also examined (Figure 8.4a, p.286). At each level of flow depth the ratio between the depth-dependent term and R_v was calculated (Figure 8.4b). A natural or restricted cubic spline (a piecewise smooth function; see Harrell, 2001) was chosen to summarise the variation of this value with median depth. Although there was considerable scatter in this value, the restricted cubic spline is able to summarise the complex curve generated by the combined influence of a number of different variables (that each vary in a non-monotonic manner with increased inundation of roughness elements) in the depth-dependent term. A R^2 value is provided as an indicator of goodness of fit which was also confirmed by checking for any detectable patterns in smoothed residuals.

To obtain an estimate of the friction factor at any given depth, the constant term f_A (selected from the distribution of Figure 8.4c) is multiplied by the depth dependent term f_B and the ratio of the median depth to R_v (Figure 8.4b). This gives a distribution of predicted f that varies with depth (Figure 8.d) rather than R_v. To summarise, the predicted friction factor is calculated from

$$f = f_A f_B \frac{d_{50}}{R_v}. \tag{8.1}$$

For any simulated flows overtopping all surface roughness elements, the Keulegan equation (2.11) is then applied to model the declining f with the inundation ratio (as in Lawrence, 1997). This assigns an inundation ratio of 1 at the point where all roughness elements are overtopped and increases Λ with any further depth increase. Alternatively, a mixing model (e.g. equation 2.23) could be used to model the decline in f when all roughness elements are fully inundated.

This approach was used to model depth-resistance relationships at each plot of the Del Prado hillslope. This hillslope was chosen to demonstrate this approach as it remains undisturbed with no ploughed areas interrupting the natural grading between Morphological Runoff Zones. In this respect it is the most representative of other semi-arid hillslopes, especially considering the variability and degradation of ploughed surfaces with time discussed in section 3.3.3. The Del Prado hillslope also has the most complete record of results and is located within the sub-catchment analysed in section 8.2, a sub-catchment identified as an area of rapid runoff response by Bull *et al.* (1999). Note that Figure 6.1 shows that this hillslope was observed to have the lowest f values of the three hillslopes.

The generation of depth-resistance distribution curves for individual regression equations for each MRZ (described in Chapter 6) is described below (section 8.3.1). This represents the case where an empirical prediction of flow resistance was made selecting the predictors separately at each Morphological Runoff Zone. The analysis presented in Chapter 6 identified that this represented an end-member of a range of possible predictions and is demonstrated here as it allows for the largest variability between plot-types. Similar curves were developed for the other prediction methods. Section 8.3.2 compares the predictions of each of these methods against an independent dataset not used in the development of these roughness-resistance relationships (obtained from the variable discharge experiments of section 5.3).

8.3.1 Depth-Resistance Curves by Morphological Runoff Zone

Figure 8.4a shows that median depth increases more rapidly than the volumetric hydraulic radius at the MRZ 1 plot. The variation of f_B/R_v with median depth (Figure 8.4b) is summarised with a restricted cubic spline curve with an R^2 of 0.70. The distribution of f_A measured at the MRZ 1 plot is positively skewed (displayed using a kernel density function in Figure 8.4c); this distribution is then translated along the curve of Figure 8.4b with increasing depth (demonstrated by the summary percentiles in Figure 8.4d). The Darcy-Weisbach friction factor increases with depth at MRZ 1 until the point where all roughness elements are inundated (at a median depth of just 32 mm), beyond which it decreases according to equation 2.11.

There is a small reversal in the pattern with f decreasing with depth at a d_{50} of 15 mm. It is probable that this minor feature reflects the roughness dataset used to develop the curve of Figure 8.4b. Alternatively, it may be characteristic of areas of microtopography dominated by splash pedestals. Further research is necessary to confirm the validity of any such minor features observed in this section. In summary, predicted f values are relatively low at the MRZ 1 locations (mostly < 5).

Figure 8.5a–d shows the same relationships for the MRZ 2 plot at the Del Prado hillslope. The volumetric hydraulic radius increases more slowly with median depth at this plot, suggesting that submerged roughness elements have a greater influence on overland flows (as no flow concentrations have been incised). This is reflected in the greater f values predicted at this plot. The spline in Figure 8.5b provides a better summary of the variation of f_B/R_v with depth than at the MRZ 1 plot ($R^2 = 0.84$). The f_A values are positively skewed in a pattern similar to that observed at MRZ 1 (Figure 8.5c). Predicted f values initially increase with depth until the flow is just 2.3 mm deep. Beyond this level, a decrease in resistance with depth is observed. The transition between the empirically-derived relationship developed in this section and the Keulegan equation is very smooth.

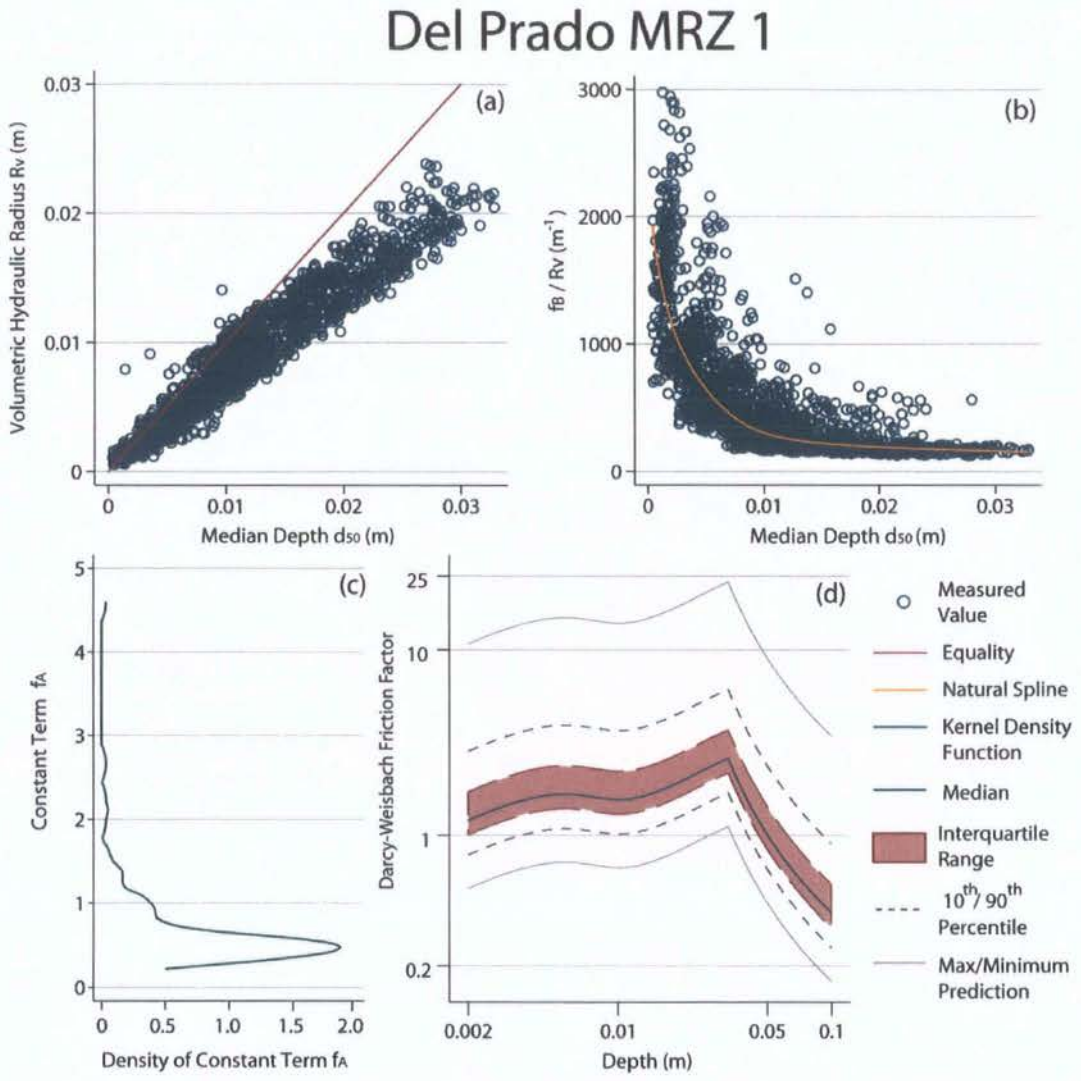

Figure 8.4. Variation of (a) volumetric hydraulic radius R_v and (b) the depth-dependent term f_B scaled by R_v with median depth at MRZ 1; (c) distribution of the constant roughness term f_A (Epanechnikov kernel density function, half-width 0.08); (d) variation of summary statistics of the distribution of calculated Darcy-Weisbach friction factor f with median depth at Del Prado MRZ 1.

Figure 8.6a shows that the increase in median depth is closer to that of R_v once flow concentrations develop at MRZ 3. This suggests that where the flow has concentrated, submerged roughness elements protrude less into the flow field (as the overland flow has eroded such large protrusions). The restricted cubic spline of f_B/R_v and depth has a lower R^2 of 0.62, although it appears to provide a reasonable summary of the dataset.

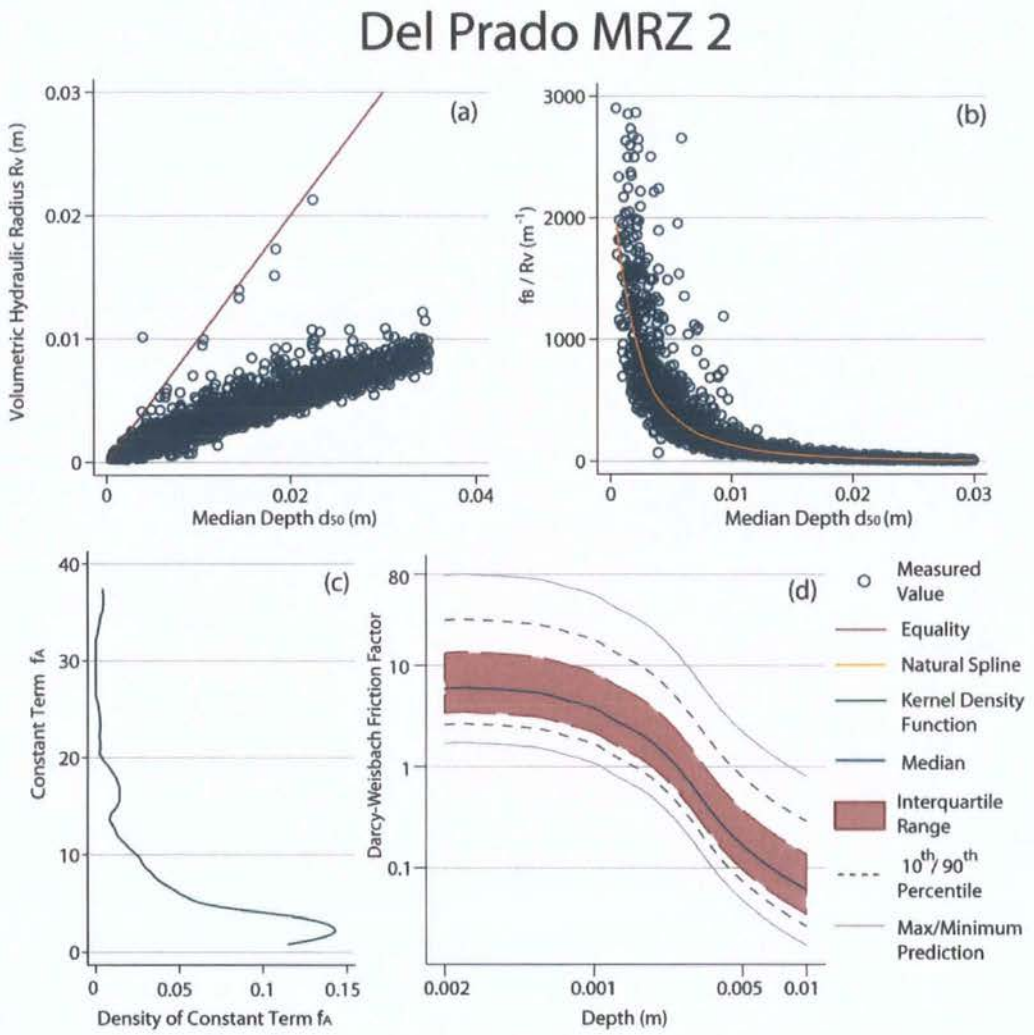

Figure 8.5. Variation of (a) volumetric hydraulic radius R_v and (b) the depth-dependent term f_B scaled by R_v with median depth at MRZ 2; (c) distribution of the constant roughness term f_A (Epanechnikov kernel density function, half-width 1.3); (d) variation of summary statistics of the distribution of calculated Darcy-Weisbach friction factor f with median depth at Del Prado MRZ 2.

The initial resistance remains positively skewed (Figure 8.6c) but less so than the two upslope plots. The predicted flow resistance is similar to that of MRZ 2 although it increases with depth until all roughness elements are submerged (Figure 8.6d); the increase is initially steep but becomes less pronounced beyond a depth of 4 mm. The increasing f with depth until complete submergence may be a consequence of expansion of the flow out of the hydraulically efficient flow concentration and on to the surrounding interrill surface.

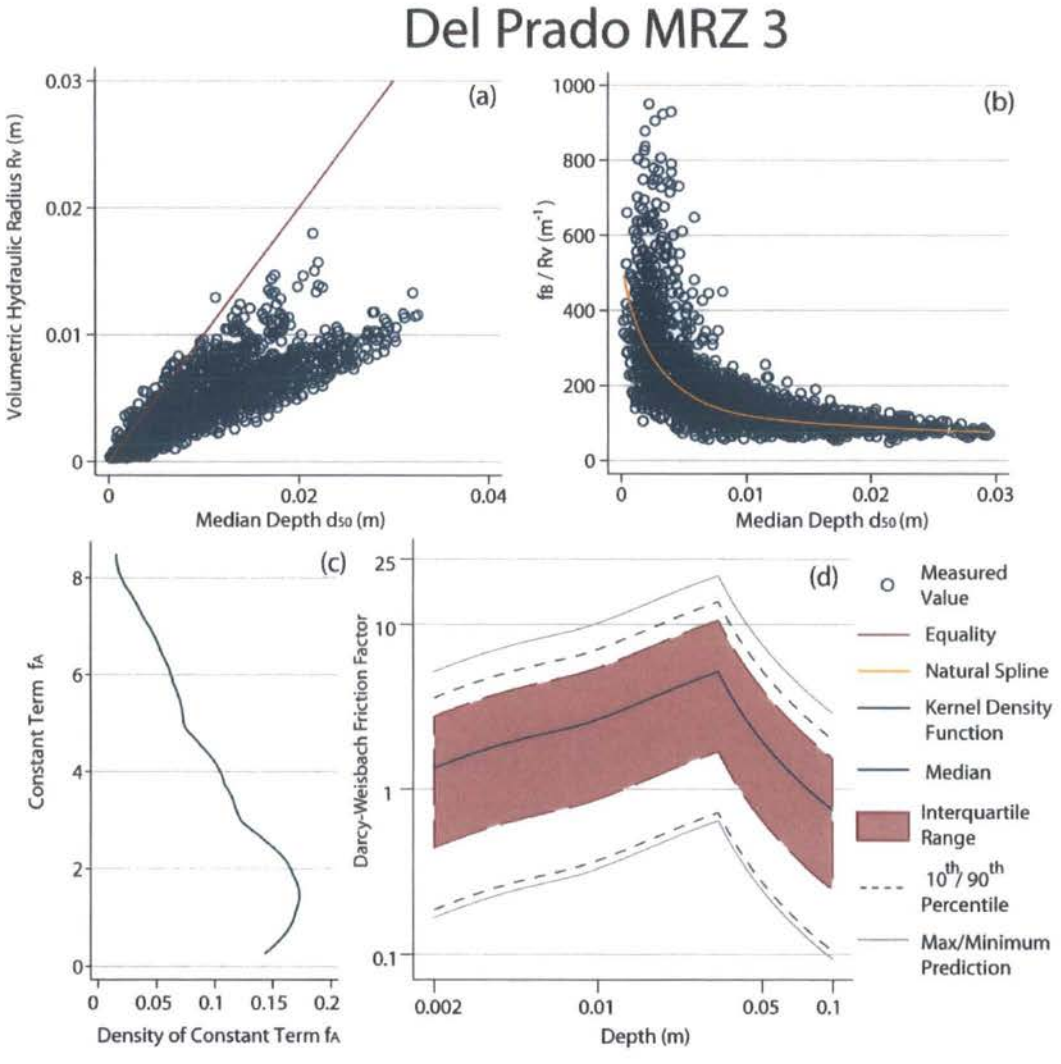

Figure 8.6. Variation of (a) volumetric hydraulic radius R_v and (b) the depth-dependent term f_B scaled by R_v with median depth at MRZ 3; (c) distribution of the constant roughness term f_A (Epanechnikov kernel density function, half-width 1.2); (d) variation of summary statistics of the distribution of calculated Darcy-Weisbach friction factor f with median depth at Del Prado MRZ 3.

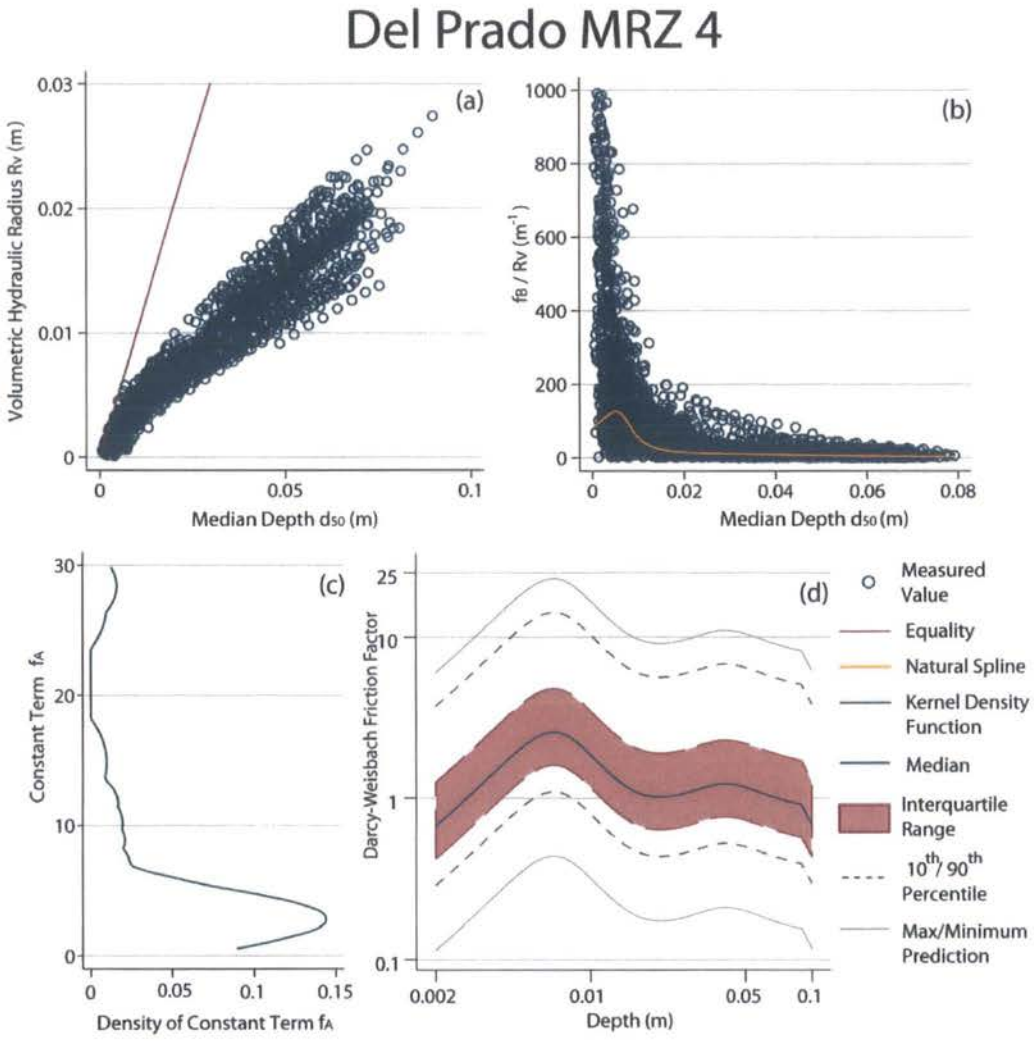

Figure 8.7. Variation of (a) volumetric hydraulic radius R_v and (b) the depth-dependent term f_B scaled by R_v with median depth at MRZ 4; (c) distribution of the constant roughness term f_A (Epanechnikov kernel density function, half-width 1.5); (d) variation of summary statistics of the distribution of calculated Darcy-Weisbach friction factor f with median depth at Del Prado MRZ 4.

At the Del Prado MRZ 4 plot, a consistent relationship between R_v and median depth can be seen (Figure 8.7a). This represents the dimensions and cross-sectional shape of the rill where R_v initially increases rapidly with d_{50} until a depth of 7 mm where roughness elements become submerged and disturb the flow. This may be reflected in the spike of predicted resistance at this depth seen in Figure 8.7d. The spline shown in Figure 8.7b

summarises the variation with an R^2 of 0.48, as a large degree of scatter was observed in the relationship between f_B / R_v and median depth. This is a consequence of the inclusion of the depth-skewness term D_{sk} in the resistance equation 6.17 which was quite variable between transects and produced some large positive residuals at shallow flows. The constant term f_A was positively skewed though a secondary peak can be observed in the kernel density function towards the maximum of observed values (Figure 8.7c).

The resultant resistance-depth relationship demonstrates a sharp increase in f to a depth of around 7 mm. This is followed by a steep decline beyond which resistance increases with depth for a second time (in the region of 30 mm to 50 mm) before finally declining with depth until maximum inundation where the resistance-depth function merges with the resistance predicted by the Keulegan equation. Given the large scatter observed in Figure 8.7b, it is possible that the finer structure of the resistance-depth relationship arises from an artefact of this methodology. The predicted resistance values are generally lower than those of the MRZ 3 plot.

Finally, Figures 8.8a–d demonstrate the development of a resistance-depth function for the MRZ 5 plot at the Del Prado hillslope. It should be noted that the relationship developed here has been derived from flow experiments with depths in the range of 15 mm. The large gully in the centre of this plot meant that very deep flows could be simulated; however, the procedure was limited to a maximum depth of 200 mm both for computational efficiency and to prevent the resistance equations from being applied even further beyond the conditions in which they were developed. The resistance predictions were extrapolated to 200 mm to allow the validation of predictions in section 8.3.2. The results presented for the MRZ 5 plot should therefore be treated with caution.

Such caution is also advised in the light of the low R^2 value of the natural spline in Figure 8.8b ($R^2 = 0.12$). The flow transects appeared to follow two different patterns; the summary curve represents a combination of both. The summary of depth-dependent terms at the rilled and gullied plots is less able to explain the full variability observed than elsewhere on the hillslope. This may reflect the recorded variability of f and V over these areas as

reported in Figure 7.11b. The variation of R_v with depth (Figure 8.8a) is similar to that seen at MRZ 4.

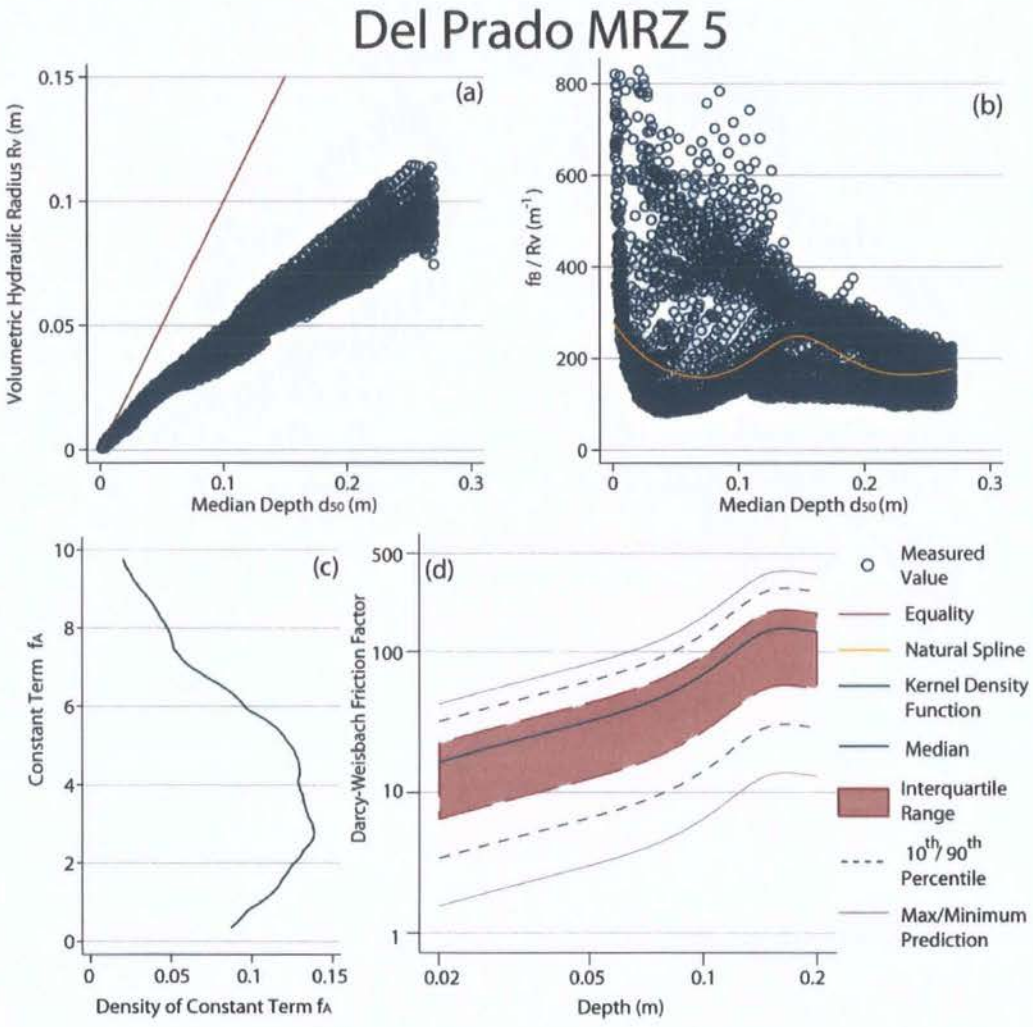

Figure 8.8. Variation of (a) volumetric hydraulic radius R_v and (b) the depth-dependent term f_B scaled by R_v with median depth at MRZ 5; (c) distribution of the constant roughness term f_A (Epanechnikov kernel density function, half-width 1.1); (d) variation of summary statistics of the distribution of calculated Darcy-Weisbach friction factor f with median depth at Del Prado MRZ 5.

The distribution of the initial resistance f_A is the least skewed distribution observed at any plot (although it remains positively skewed). When multiplied by the depth-dependent term to predict flow resistance, a large range of values are found. Note that Figure 8.8d shows

resistance against depth for a greater range of depths than in Figures 8.4–7. Predicted resistance is generally an order of magnitude larger in the gullies than elsewhere on the hillslope (as observed in Figure 6.2). The results of Section 7.4 demonstrated that this resistance decreases rapidly once a flow connection is established.

Figure 8.9a directly compares the median *f* values predicted for each plot-type. The gullied MRZ 5 areas demonstrate the greatest *f* at depths of greater than 9 mm. Though this graph extends to a maximum depth of 0.1 m it is unlikely that such depths will be either observed in the field or simulated by a hydrological model except possibly in flow concentrations during extreme runoff events (e.g. Table 4.1). Most depths simulated in the field experiments described in this thesis were <10 mm. In this region, MRZs 2 and 5 display the greatest flow resistance. Using this median resistance value (and the median slope of each plot) the variation of velocity with flow depth is predicted in Figure 8.9b.

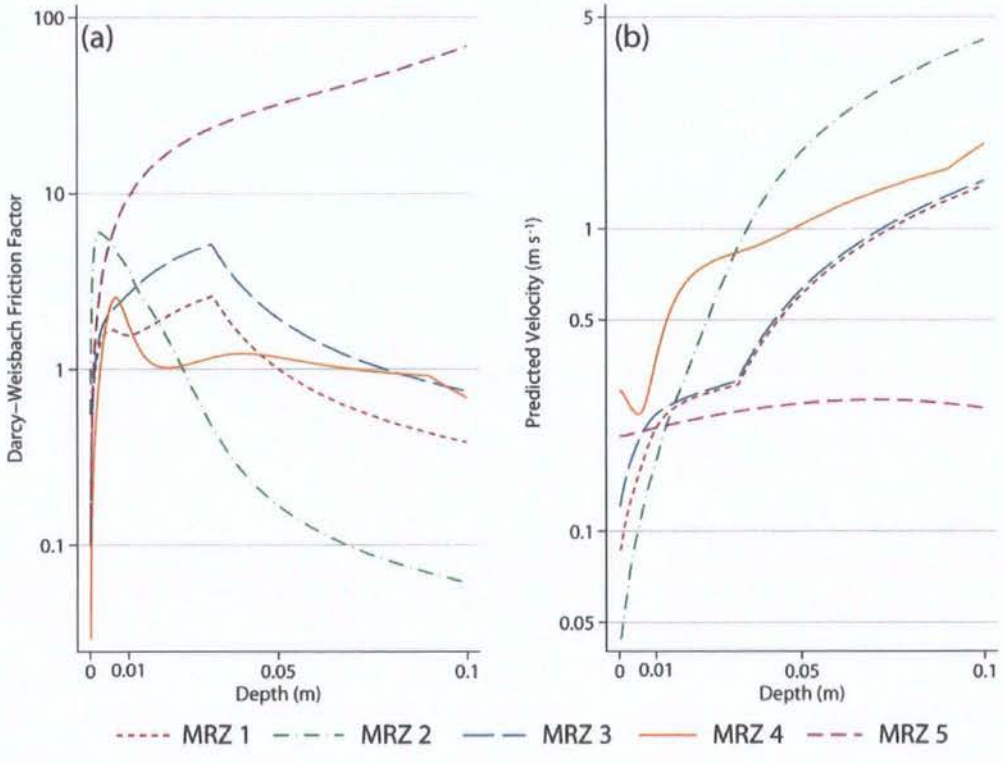

Figure 8.9. Modelled variation of (a) Darcy-Weisbach *f*; and (b) flow velocity with depth for each plot-type of the Del Prado hillslope. Median values of *f* and slope (for each MRZ) have been used in this example.

At depths of less than 10 mm, MRZs 3–5 demonstrate the fastest flow, although the rill flows are considerably the fastest. For deeper flows the gullied plot shows the slowest flow while at MRZ 2 velocity increases rapidly with flow depth. Despite the greater resistance of MRZ 3, the predicted velocity is similar to that of MRZ 1 due to the steeper slope at this part of the hillslope.

In summary, the resistance equations presented in Table 6.3 were developed from relationships between surface roughness, flow depth and flow resistance observed during flow simulation experiments over three semi-arid hillslopes. These empirical relationships include measures of the soil microtopography and flow depth terms. Dividing the equations into these two categories allows resistance to be calculated at any simulated flow depth. Figures 8.4–8.8 extrapolate these relationships beyond the range of flows from which they were developed; however, the modelled flow depths are unlikely to be much deeper than those simulated in the field experiments. During these experiments it was found that flow resistance demonstrated considerable spatial variability even over surfaces categorised as containing similar microtopography (especially in flow concentrations). Therefore, the approach described above provides a distribution of predicted resistance that varies with flow depth. This allows the spatial variability of resistance to be expressed but also, through the categorisation of the hillslope into five Morphological Runoff Zones, provides an indication of the spatial configuration and connectivity of areas of low and high resistance which, as Mueller *et al.* (2007) suggest, is of fundamental importance for modelling hydrological response (see sections 3.4 and 8.4).

8.3.2 Validation of Predictions

Section 8.3.1 described the calculation of resistance-depth distribution curves for each Morphological Runoff Zone using the regression equations developed for each plot-type separately (method (d) below). This represents the most complex model presented in Chapter 6 and was described in detail above as it allows for the most flexibility and variation between MRZs. To re-iterate the discussion of Chapter 6, predictions of resistance

were made using models with four degrees of flexibility for incorporating observed variation with hillslope position:

(a) predictions with no MRZ term included;

(b) predictions where intercept of the relationship can vary with hillslope location (MRZ term is incorporated as a dummy variable);

(c) predictions made separately at each MRZ (variable intercept and coefficients);

(d) independent regression equations developed for each MRZ (different predictors allowed).

Similar curves were developed using the predictions of each of these methods. In this section, the predictions are described and compared. Following section 6.5.3, each variable identified as a predictor of resistance at each plot (from Table 6.3) is included in models (a)–(c). Additionally, each prediction is tested against a small dataset of flow measurements obtained from the variable discharge experiments described in section 5.3. Only ten measurements were made at each plot (over two separate sections – one represented as open symbols in Figures 8.10–8.13; one as closed symbols) but they are spread over a wider range of depths than those simulated using the constant discharge trough (the data from which the resistance models were developed). An ability to predict resistance to flows slightly deeper than those for which the model was developed is an encouraging sign that the resistance models have identified functional relationships between surface roughness and flow resistance.

Figure 8.10 shows resistance predictions made with no Morphological Runoff Zone term included (model (a) above). The changing depth-dependent values were calculated from the dataset as a whole. All measured values are within the predicted range. A consequence of lumping together all hillslope positions is that a large range of predicted values exists at each depth (a variation of over two orders of magnitude). The measured values of most plot-types are distributed both sides of the median resistance prediction. The exception to this is MRZ 5 where all measured points are underpredicted (although they are still within the possible range of predictions). Only minor variation of predicted f with flow depth is observed when the results are averaged over the whole range of hillslope surfaces (although

a slight increase of resistance with depth can be detected). The large range of predicted values potentially limits the usefulness of predicting flow resistance in this way.

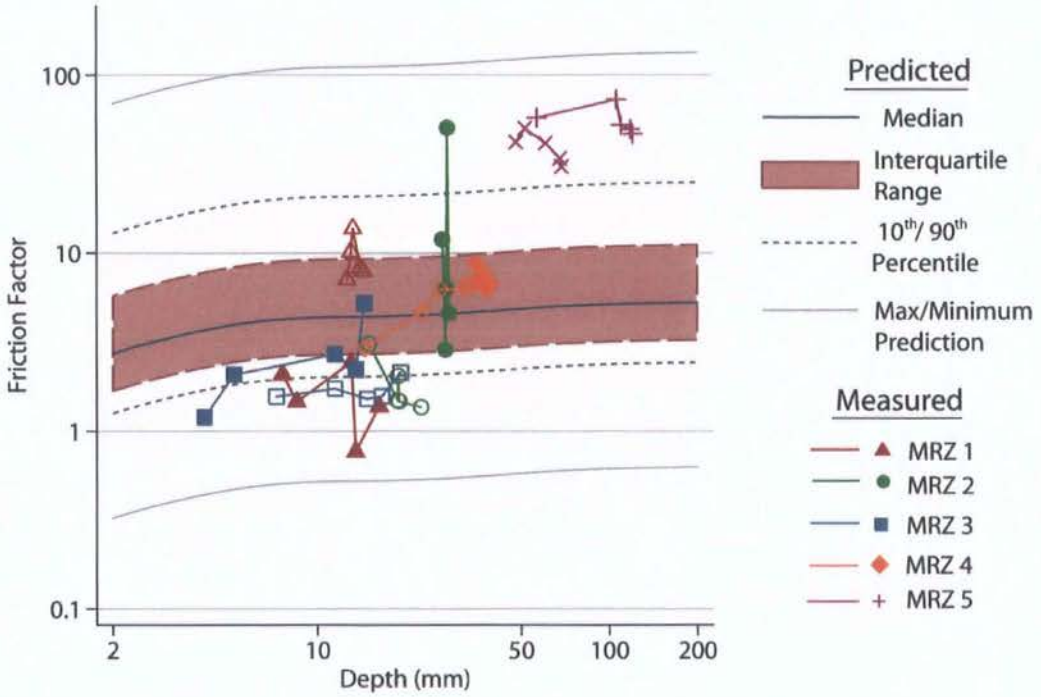

Figure 8.10. Comparison of measured flow resistance with that predicted from the general equation of Table 6.4 (the condition (a) where no MRZ term is included).

Representing hillslope position using a dummy variable produces similar results (Figure 8.11). Note that for ease of visualization, the measured values have been shifted towards the predictions by the offset of the dummy variable value (instead of the reverse) to enable the results to be shown on the same graph. An adjustment has been made for the underestimation of the MRZ 5 measurements (although they still lie around the 90th percentile of the predictions). The variation of predicted f with flow depth is even less than that of Figure 8.10 above, although a more pronounced increase in f can be seen for depths below 10 mm.

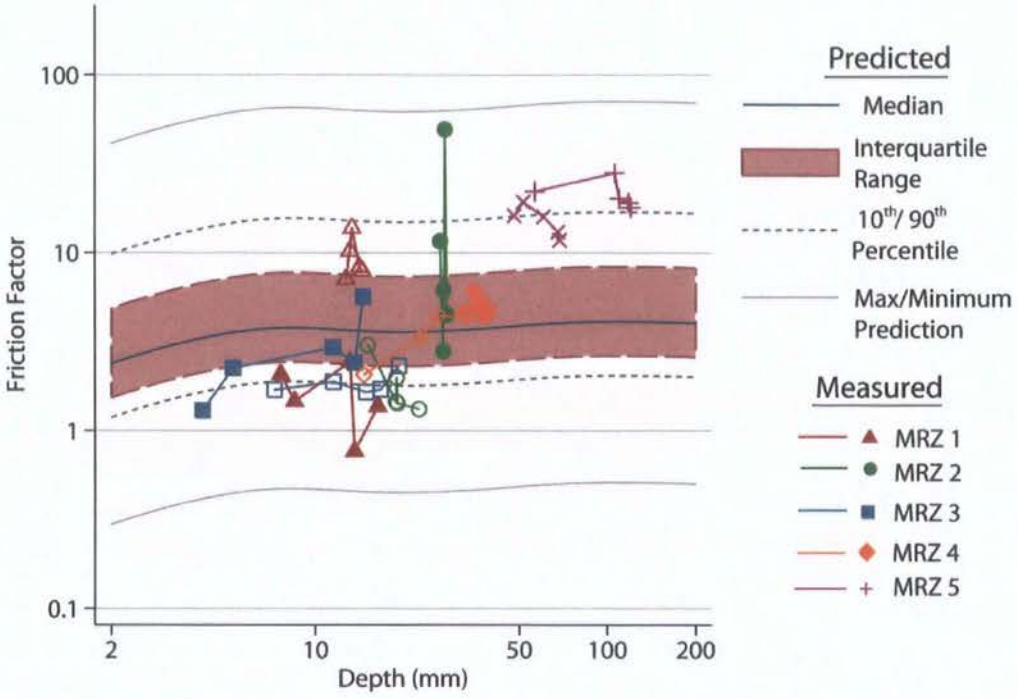

Figure 8.11. Comparison of measured flow resistance with that predicted in Chapter 6 (the condition (b) where the MRZ term is included as a dummy variable). To enable the results to be shown on a single graph, the measured values have been transformed rather than the predictions. The values were adjusted on a log-scale relative to the MRZ predictions with MRZ 2 (−0.027), MRZ 3 (+0.083), MRZ 4 (−0.350) and MRZ 5 (−0.957).

When flow resistance is calculated at each plot-type separately (model (c) above), the individual depth-resistance curves vary substantially between MRZs (Figure 8.12). This distinguishing feature is not apparent when predictions are made with no reference to hillslope position. At the MRZ 1 plot, the model predictions overestimate the resistance values of one section, yet the values of the second section lie very close to the median prediction. This emphasises the importance of including an appreciation of variability in resistance predictions as the measured values of the two sections vary substantially, despite being located close together.

Similarly, a wide range of measured values was observed in one section at the MRZ 2 plot (which demonstrated almost no increase in flow depth with an increase in discharge). These measured values span the range of predicted f values at this depth. Predicted and measured resistance values agree well at the MRZ 3 plot and nicely demonstrate the general trend of

increasing resistance with flow depth over this range (capturing the more pronounced increase at a depth of 20 mm (potentially a consequence of spilling out of the flow concentration).

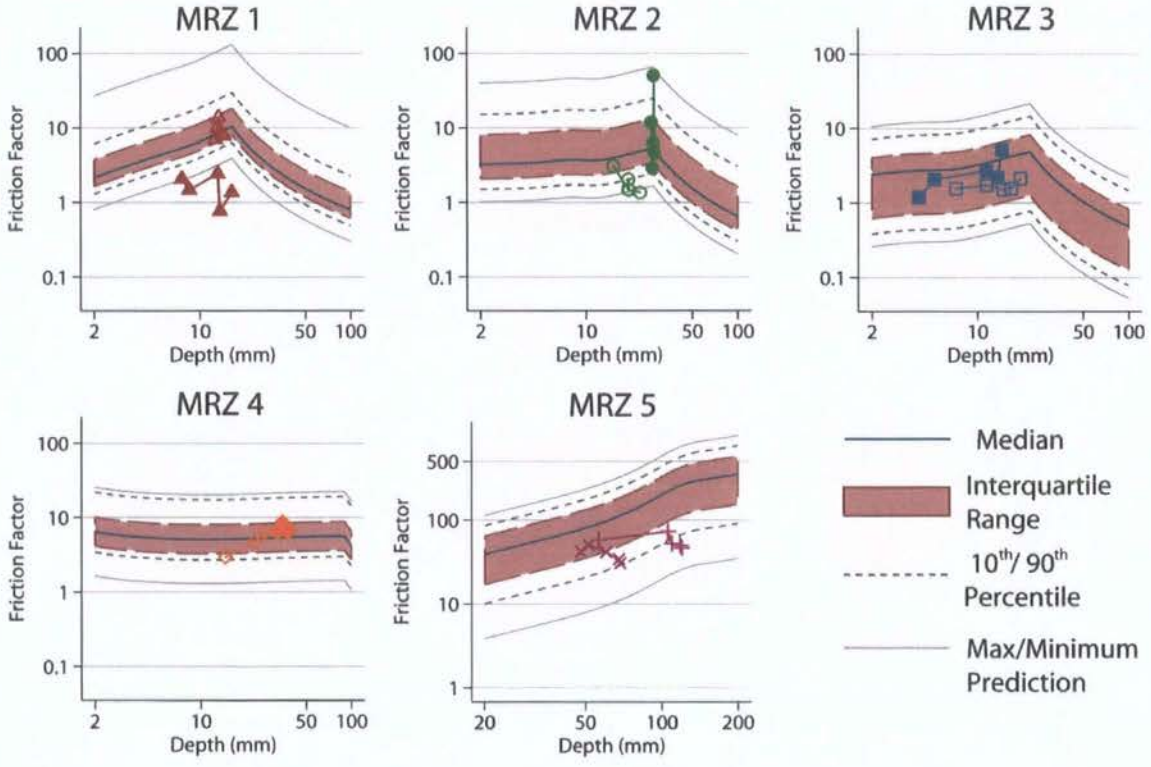

Figure 8.12. Comparison of measured flow resistance with that predicted from the equations of Table 6.4 (the condition (c) where the resistance predictions are made separately for each Morphological Runoff Zone).

The MRZ 4 plot shows almost no change in predicted resistance with flow depth. The predicted and measured values match up very closely, although one section showed an increase in resistance with depth at the lower discharge levels. Predicted resistance at the MRZ 5 plot is much higher than at the other hillslope locations (note the different scale of the MRZ 5 plot in Figure 8.12). Indeed, this appears to represent an overestimate of flow resistance, although the measured values are within the range predicted using this model. The MRZ 5 plot also shows a marked increase of resistance with depth.

The final method of predicting resistance (model (d) in the list above) is the individual regression equation approach where only significant predictors of resistance as identified for each plot-type (at the $P<0.05$ level) are included in the analysis. This corresponds to the curves described in section 8.2.1.

The predictions at the MRZ 1 plot agree more closely with the lower-resistance measurements (Figure 8.13). At the MRZ 2 plot, one transect is situated exactly on the median prediction and follows the same decrease with increasing flow depth. The other transect is less-well predicted and contains the only measurement lying outside the range of predictions using this model. The measured values from the MRZ 3 plot are also very close to the median resistance prediction and show the same increase of f with flow depth.

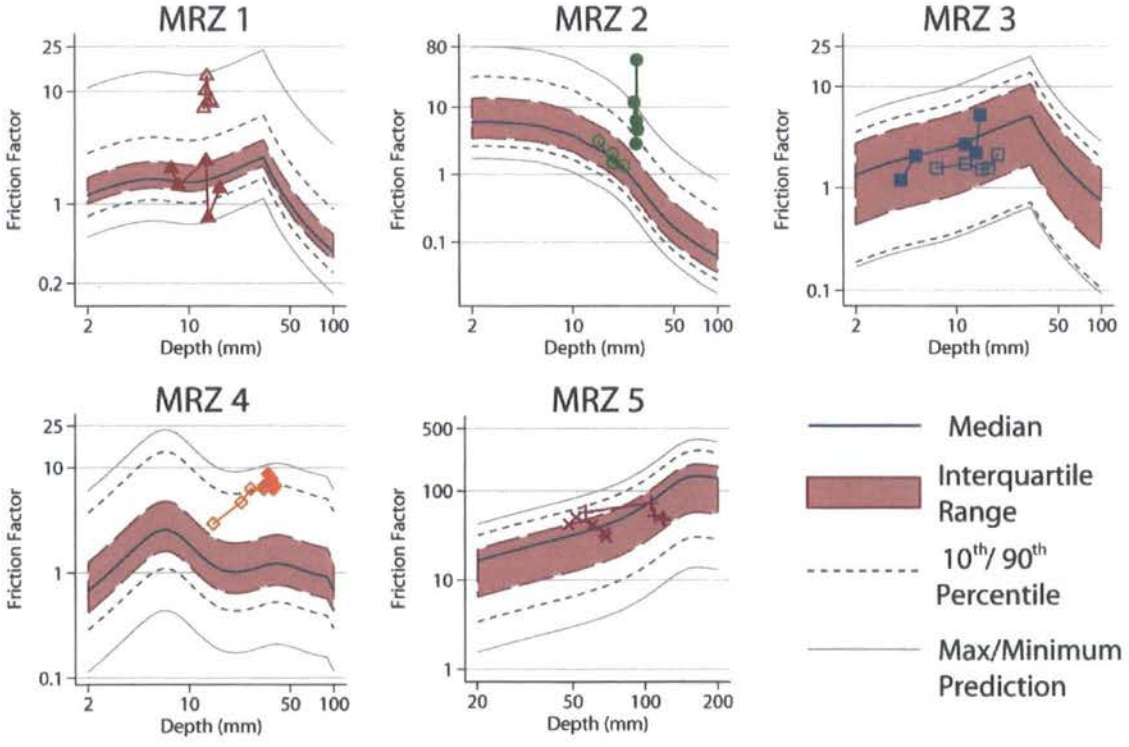

Figure 8.13. Comparison of measured flow resistance with that predicted from Table 6.3 (the condition (d) where the regression models are developed separately, using different predictors of resistance for each Morphological Runoff Zone).

Both sets of measurements from the MRZ 4 plot are rather poorly predicted by the regression model. The resistance is underestimated, but the measured points remain within

the range of predictions and observe the same pattern with increasing depth as the predicted values. Finally, the measured values at the MRZ 5 plot correspond closely to the median predicted values, although the increasing resistance with flow depth is not reproduced in the field measurements.

Although only a limited number of independent data points are available with which to validate the regression models presented in this thesis, they provide an indication that predictions are not dissimilar to measured values. The models were developed from measurements taken on hillslope surfaces with a wide range of soil types, yet they perform well when tested on just one of these hillslopes. Further development and testing of these curves over other semi-arid hillslopes is necessary; section 8.4 will argue that the inclusion of such curves in distributed models of hillslope hydrology represents an important research direction. Comparison of the different prediction curves shows the consequence of including hillslope location in estimates of flow resistance, as a great deal of variability exists between the different four regression methods. The distribution of resistance predictions covers a large range of values in some curves. This raises an important question of how much the observed variability should be reduced to an approximate value. The scatter in the measured values is testament to the requirement of a range of predictions, yet those models (e.g. Figure 8.10) which integrate all plot-types into a single curve have a large range of predicted f which may limit the effectiveness of making predictions in this way.

Comparing the performance of these models in predicting resistance is difficult where a distribution of values is predicted at each flow depth and only ten independent resistance measurements exist at each plot-type. Figure 8.14 summarises the distributions of the differences between measured and median predicted values at each Morphological Runoff Zone for each regression model. At the MRZ 1 plot the general equation provides the closest prediction of measured resistance. This model performs less well moving further downslope. At the MRZ 3 plot, the model predictions generally improve with increasing model complexity. However, this is not always the case as the independent regression equation model underpredicts resistance at MRZ 4 and the variable coefficient model overpredicts resistance at MRZ 5.

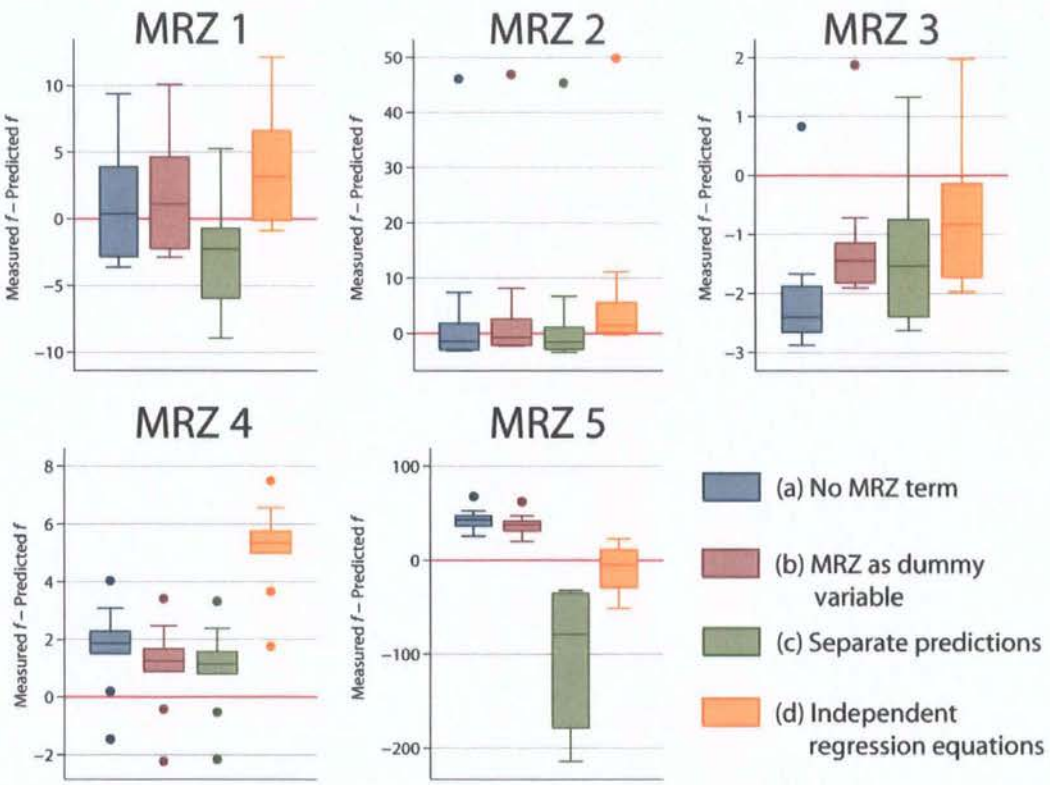

Figure 8.14. Distributions of prediction error (measured − predicted flow resistance) at each Morphological Runoff Zone (MRZ) for each of the four methods of representing hillslope position in predictions of flow resistance (increasing model complexity from (a)–(d)).

Although further validation is necessary before solid conclusions can be made, it appears from Figure 8.14 and Table 8.4 that including MRZ as a dummy variable (model (b) with a correction factor to adjust the predicted resistance for each MRZ) is able to predict the measured flow resistance most accurately. Only at the MRZ 3 plot was this model outperformed by both more complex models. As a percentage error, there is little difference between the dummy variable MRZ correction-factor model, and the most complex model (d). Although the errors reported in Table 8.4 appear large, they are calculated from the median prediction and do not represent the predicted variability around this median. These results should treated with caution, as Figure 6.23 shows that the predictions for the constant discharge trough were less well correlated with measured resistance than the more complex models. However, this indication that effect of hillslope position can be

incorporated into models of overland flow resistance without the need to incorporate much additional complexity is an interesting result worthy of further investigation.

	Median Absolute Difference				Median Percentage Difference			
Model	(a)	(b)	(c)	(d)	(a)	(b)	(c)	(d)
MRZ 1	3.27	3.15	3.75	3.18	74.1	68.7	96.9	78.0
MRZ 2	2.67	2.21	2.67	1.44	76.4	74.7	86.6	49.1
MRZ 3	2.40	1.72	1.53	1.02	130.4	77.8	91.2	53.4
MRZ 4	1.86	1.37	1.28	5.33	29.9	20.7	19.3	82.1
MRZ 5	42.95	37.48	79.16	14.33	89.2	77.8	212.4	35.2
Total	2.84	2.22	2.40	4.18	86.6	68.9	78.5	69.0

Table 8.4. Median absolute difference (measured f − predicted f) and median percentage difference (absolute difference as a percentage of measured f) of resistance predictions at each hillslope position (MRZ). Models represent the four degrees of complexity of incorporating hillslope position into predictions: (a) no MRZ term, (b) MRZ as dummy variable, (c) separate predictions, and (d) independent regression equations.

8.4 Synthesis: Flow Resistance & Dynamic Connectivity

This section synthesises and discusses the arguments and findings of this thesis by reviewing the development of equations for predicting flow resistance from surface roughness (section 8.4.1) and placing these results in the wider context of flood generation and runoff response of semi-arid areas (section 8.4.2). It is argued that the representation of flow resistance proposed here is a fundamental component of the study of semi-arid hydrology that is frequently neglected in hydrological models.

8.4.1 Predicting Flow Resistance

Flow resistance is often represented as a constant value in hydrological models and treated as a roughness parameter to be calibrated from field measurements. Several authors have long since concluded that such an approach is unsuitable to the study of fluvial systems where resistance can vary dynamically with flow stage (necessitating curves of resistance versus stage, e.g. Lane, 1951). Thus, flow resistance cannot be accurately represented by a single, constant value. Yet such a parameterisation is frequently applied to the study of

overland flows; this is most likely a consequence of the conceptualisation of resistance inherited from fluvial systems and pipe-flow experiments and the modelling of interrill flows as sheet flows (Hairsine and Rose, 1992). The majority of studies of hillslope hydrology have sought to describe resistance to overland flows over entire hillslope or even catchment surfaces with a single value (e.g. Morgan *et al.*, 1998; Takken *et al.*, 2005). More sophisticated approaches develop equations for resistance from measures incorporating some dependency on the flow itself, such as the Reynolds number or inundation ratio (e.g. Lawrence, 1997).

The analysis presented in Chapter 6 suggested that there is a need to move beyond such a basic conceptualisation of flow resistance, towards one that is befitting of the spatially and temporally variable nature of overland flow. The characteristics of overland flow share little in common with river flows, as the depth is very shallow in comparison with the size of surface roughness. Moreover, the submergence of complex microtopographic structures with increasing water depth means that progressive inundation of roughness elements will have a substantial influence on the hydraulics of overland flow. Given the observed variability of microtopography over hillslope surfaces, it might be expected that overland flow resistance will exhibit a larger degree of spatial variability.

The methodology developed in this thesis permitted high-resolution measurement of overland flow on natural soil surfaces. The variability of flow velocity over very fine scales of measurement was particularly apparent, especially within flow concentrations (section 5.2; Figure 7.18). At a broader scale, systematic changes in microtopography (described in Table 4.4) that either act to concentrate or divert runoff (section 7.3.1) contributed to an even larger range of measured flow velocities. Experiments with increasing discharges (section 5.3) demonstrated the complex relationship between flow depth and velocity that varies with microtopography.

These results can be attributed to spatially-variable flow resistance that changes with flow depth. An ability to predict this variability is of fundamental importance for hydrological and erosion models which Jetten *et al.* (1998) and Takken *et al.* (2005) have shown are very sensitive to hydraulic resistance parameters. Chapter 2 demonstrated that many hydraulic

principles that are applied uncritically to model overland flows rely on theories of fluid mechanics that have been transferred from an idealised situation to represent pipe flows, channel flows and more recently overland flows. The assumptions inherent in traditional resistance formulations were laid bare in Chapter 2. From this discussion, section 6.3 attempted to derive a method of representing flow resistance more suitable to complex topographies. The result was a modified version of the Darcy-Weisbach friction factor (equation 6.6) which allows some limiting assumptions to be relaxed and yet remains sufficiently simple to be employed in a field situation.

Examination of velocity profiles and empirical relationships in pipe and channel flows (e.g. Blasius, 1915; Prandtl, 1935; Keulegan, 1938; section 2.3) suggested that flow resistance could be predicted from the Reynolds number or inundation ratio (flow depth scaled by roughness height). Applying these equations to the field situation of shallow overland flows passing over complex partially-inundated topographies highlighted the inadequacy of these theories when employed in conditions well outside the range in which they were developed (section 6.2). A more theoretical analysis demonstrated that the meaning of roughness measures (such as 'roughness height' which implies either an equivalence between a soil surface and one which is uniformly coated with identical sand grains (Henderson, 1966) or the existence of an elevation above a reference level where the logarithmic vertical velocity profile is extrapolated to zero (Keulegan, 1938)) is subtly altered when applied to this situation.

A large variety of roughness measures was calculated to examine their relationship with flow resistance, developing a more suitable prediction of resistance whilst also using these relationships to infer the variation of overland flow processes over hillslope surfaces (section 6.5). Several roughness measurements were found to be related to flow resistance. These can be divided into two categories: constant measures representing simply the microtopography of the soil surface (initial roughness f_A), and measurements that are also a function of the flow depth (depth-dependent roughness f_B). The predictions developed in section 8.3 combined the observed distribution of initial roughness (e.g. Figure 8.4c) with a summarised curve of the variation of the depth-dependent terms with increasing water level (e.g. Figure 8.4b). This resulted in a distribution of resistance predictions which is

translated along a curve with increasing water depth (e.g. Figure 8.4d) that can be easily applied to distributed hydrological models.

Roughness-resistance relationships were observed to vary with hillslope position as a function of the systematic shifts in the organisation of surface features with distance downslope (representing the increasing dominance of runoff processes on surface morphology). This demonstrates the importance of classifying hillslope surfaces into areas of similar microtopography. Section 6.5.3 demonstrated that such a classification can be incorporated into flow resistance predictions in a number of ways, each of which offers a different degree of flexibility for incorporating the effects of hillslope position into resistance predictions (a basic validation of each of these models was presented in section 8.3.2).

It is recognised that the identification and measurement of surface roughness is extremely scale dependent and necessitates a distinction between roughness and topography. The value of roughness measurements depends on the resolution at which such measurements are made and has led some authors to divide roughness into separate scales (e.g. Robert, 1990; Clifford *et al.*, 1992; Lawless and Robert, 2001). Butler *et al.* (2001) were able to characterise roughness of a gravel-bed river in a scale-independent way using fractal analysis. However, there is some question as to the range of scales over which self-similar behaviour is observed on natural soil surfaces (e.g. Burrough, 1983; Bartoli *et al.*, 2005). Thus, for the majority of roughness measures, scale-dependency is unavoidable and requires that studies of roughness are consistent in their definition and clearly state their chosen scale and resolution. Roughness is, it has been argued, essentially that residual component of topography that must be dealt with implicitly at the chosen scale of enquiry (Lane, 2005). In this study, the resolution of roughness measurement was set at the maximum measurement resolution that could be achieved over all plot surfaces (2 mm). When transferring these results to the hillslope scale (discussed below) it is proposed that the spatial and temporal resolution employed in hydrological models should reflect the scale of roughness measurement. Section 4.3.5 explains that roughness measurements were calculated over the area that water was observed to travel during 1 s (this was extremely variable over each hillslope but was <0.2 m for the vast majority of measurements; Figure

5.4). Therefore, it is suggested that these results can be applied to a model of hillslope hydrology operating at a timestep of 1 s and with a grid size of 0.2 m (see section 8.4.2 below). This ensures a consistent and sensible distinction between roughness and topography. However, it is recognised that this scale dependence of roughness deserves a thorough investigation.

In summary, the methodology developed in this study has enabled the formulation of empirically-derived resistance predictions and demonstrated the apparent small-scale variability of overland flow resistance. This variability is incorporated into predictions as a distribution of values obtained for each flow depth. This is not a statistically-derived distribution but rather one that has been informed by field measurements of the distribution of 'initial roughness'. These predictions can also be made separately for areas demonstrating similar microtopographic structures (e.g. flow concentrations) which display characteristic resistance-stage curves. This approach is more complex than the usual treatment of flow resistance in hydrological models. However, the following section justifies this increased complexity and demonstrates how representing flow resistance in this way is of fundamental importance if we are to develop a full understanding of flood generation in semi-arid environments.

8.4.2 Flow Resistance and Runoff Generation

Understanding runoff generation at the hillslope scale requires an appreciation of the interactions between the temporal distribution of rainfall intensities, flowpath lengths, the spatial distribution of soil infiltration parameters and the routing velocity of overland flows (see Chapter 3 for a more detailed discussion). Over recent decades, numerous studies have focused on the importance of the spatial pattern of infiltration parameters and soil moisture on runoff generation (e.g. Morin and Benyamini, 1977; Sharma *et al.*, 1980; Yair *et al.*, 1980; Tricker, 1981; Scoging, 1982; Yair and Lavee, 1985; Berndtsson and Larson, 1987; Wilcox *et al.*, 1990; Yair, 1990; Casenave and Valentin, 1992; Bromley *et al.*, 1997; Solé-Benet *et al.*, 1997; Cantón *et al.*, 2002, 2004 amongst others) yet relatively little work has been directed towards the role of flow resistance in the development of connected flowpaths. Berndtsson and Larson (1987) noted that early rainfall-runoff models lumped

together infiltration characteristics of whole catchments into a single unit. In more recent hydrological models, infiltration is represented as being both spatially and temporally variable. This section argues that flow resistance must be parameterised in a similar manner if we are to develop a full understanding of the complex interactions observed between rainfall, infiltration and travel time distributions. This is crucial in semi-arid environments where overland flows provide a large contribution to flood hydrographs and are responsible for the redistribution of water soil and nutrients through a catchment (Brazier *et al.*, 2007).

The nature of an integrated hydrological system is such that when a water parcel travels further through the channel network, the likelihood of further transport is increased as the delivery pathway becomes stronger and the chance of contact with the soil is decreased (Figure 3.6b). Such positive feedback is less definite in semi-arid catchments where flows are intermittent and transmission losses high. Only during periods when abstractions from the rainfall total are negligible in comparison with rainfall depths can such positive feedback exist. Once a storm event crosses some threshold, the transmission of runoff through a catchment will increase in a nonlinear fashion. The identification of such a nebulous threshold and more importantly, the factors that determine its value remains a key unanswered question of semi-arid hydrology.

Analysis of a 10-year record from rain and stage gauges at the Prado sub-catchment (section 8.2) identified two characteristics of rainstorms that encourage flood generation: the rainfall depth falling before peak rain intensity is reached (Figure 8.2) and total storm duration above an intensity of 20 mm h^{-1} (Figure 8.3). The first factor reduces abstractions as the average infiltration rate will be lower when the intensity peak arrives whereas the second factor provides intense rainfall over a long duration of time, increasing the total rainfall available in that period. Both factors can be related to the 'travel opportunity time' (Aryal *et al.*, 2003) or the 'concentration time' (Yair and Raz-Yassif, 2004) as they reduce the ratio between abstractions and rainfall for a sufficient time to allow substantial flow connections to develop. Hence, flood generation is determined not by a runoff threshold alone, but also by the duration for which this threshold is exceeded.

This discussion essentially reduces to the notion that during any rainstorm there exists a window of opportunity for the transfer of runoff from active runoff generating areas to the channel (and beyond). Identifying the variable contributing area throughout a rainstorm requires an understanding of the extent to which connections can develop in this time, determined by routing velocities and flow resistance.

Despite the interactions described above, Wainwright and Parsons (2002) note that the nonlinear hydrological response of a hillslope or catchment and the scale-dependency of the runoff coefficient (decreasing with increasing catchment size or hillslope length; e.g. Yair and Kossovsky, 2002) have commonly been explained by the spatial variability of infiltration capacity (Sharma *et al.*, 1980; Wilcox *et al.*, 1997; Van Loon and Keesman, 2000; Van de Giesen *et al.*, 2000). Following the distinction of Ambroise (2004), 'variable active' areas generate runoff but may be disconnected from the stream network by an area of high infiltration capacity where run-on infiltration occurs (whereas 'variable contributing areas' are connected to the channel network). Consequently, much research has been directed towards developing our understanding of the spatial and temporal variation of infiltration characteristics.

The difficulty of characterising the spatial variability of infiltration has resulted in numerous attempts to classify surfaces demonstrating a similar hydrological response according to physical and chemical properties of the surface material (e.g. Solé-Benet *et al.*, 1997; Cantón *et al.*, 2002), topography (e.g. Moore *et al.*, 1988; Western *et al.*, 1999; Gomez-Plaza *et al.*, 2001), vegetation (e.g. Yair and Danin, 1980; Bromley *et al.*, 1997; Rodríguez-Iturbe *et al.*, 1999), land-use, or a combination of several such factors (e.g. Flügel, 1995; Bull *et al.*, 2003; Figure 3.2). In most hydrological models, infiltration rate is observed to decrease as a function of either time (e.g. Philip (1957); infiltration envelopes of Smith (1972) and Scoging and Thornes (1980)) or with soil moisture storage (e.g. Green and Ampt, 1911; Kirkby, 1975, 1985). Fitzjohn *et al.* (1998) and Michaelides and Wainwright (2002) have observed that this decrease in infiltration reduces the effect of its spatial variation on runoff coefficients as a storm progresses (Figure 3.4).

These studies have produced a complex representation of infiltration that is routinely applied in hydrological models and has vastly increased our understanding of the nonlinear threshold behaviour of flood generation. Infiltration parameters are both spatially and temporally variable and classified by observed surface properties. More recently, this has been combined with an examination of the effect of temporal variations of rainfall intensity on the scale dependency of runoff coefficients (e.g. Wainwright and Parsons, 2002; Kirkby *et al.*, 2005; Reaney *et al.*, 2007). Meanwhile, flow resistance is represented as a single constant value, lumping together entire hillslopes (e.g. Figure 8.15a; Morgan *et al.*, 1998). Michaelides and Wainwright (2002) and Wainwright and Parsons (2002) examined the effect of varying this resistance parameter (the latter study also simulated the effect of decreasing f as a simple function of flow depth), and found that higher friction factors increased run-on infiltration and decreased connectivity.

However, some investigations modelling the effect of spatial variability of infiltration fail even to pass comment on the resistance parameter used to route overland flows (e.g. Cantón *et al.*, 2002). Yair and Lavee (1985) noted that slopes dissected by rills and gullies were effective contributing areas, attributing this to the lower infiltration rate of these features compared with the surrounding interrill surfaces (the opposite pattern was observed in Figure 7.31), while paying little attention to the resultant effect of flow hydraulics. This highlights the current focus on infiltration characteristics, while the ability of microtopography to influence runoff production through the development of hillslope-scale emergent patterns and hydraulically efficient networks by concentrating or diverging runoff (Bergkamp, 1998; Roels, 1984) receives comparatively little attention.

Advances in modelling are likely to follow advances in measurement techniques (Beven, 2001). The flow experiments conducted in this study revealed a large variability of flow resistance over small areas. This may be expected where flows are extremely shallow and the soil microtopography is complex and heterogeneous. Michaelides and Wainwright (2002) found that increasing the spatial variability of resistance increased the variability of outflow. Adding this spatial variability produces an estimated distribution of flow resistance similar to that of Figure 8.15b where the resistance value is randomly sampled

from the distribution for each cell at a given flow depth. Further research is necessary to examine the spatial structure of such variability.

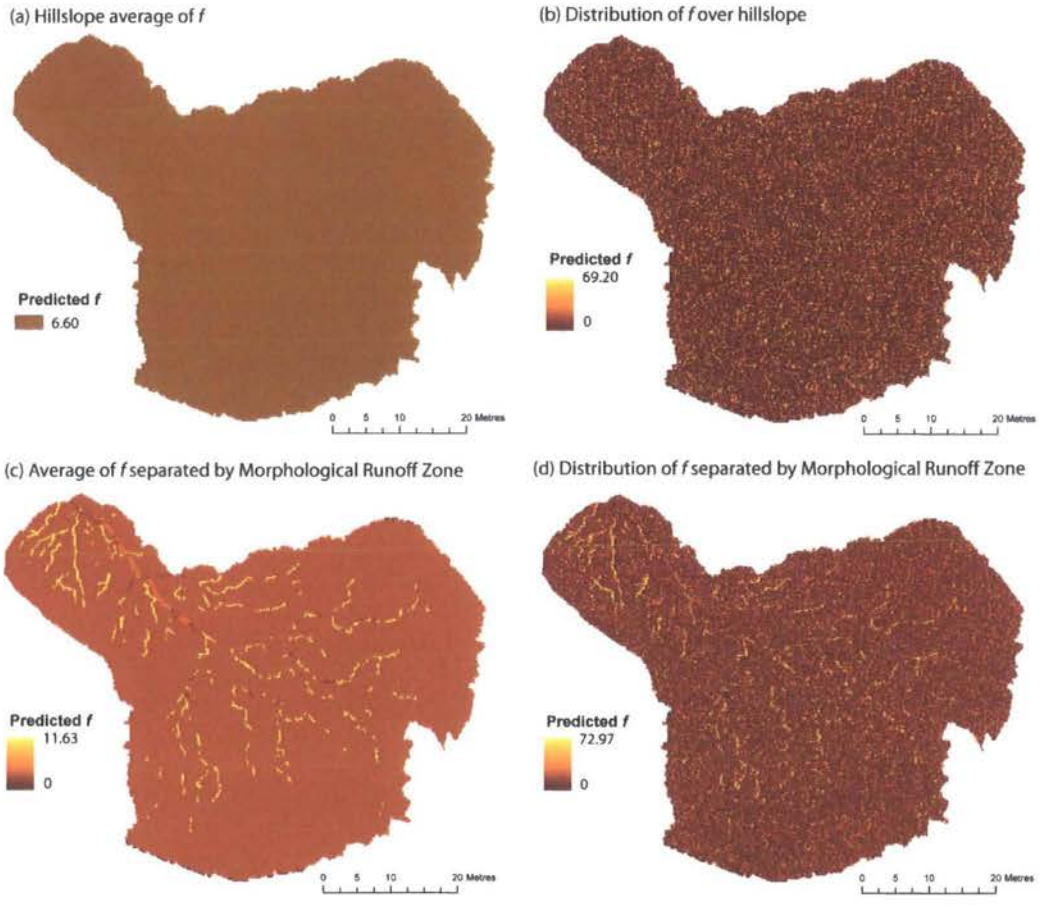

Figure 8.15. Spatial patterns of resistance predictions at the hillslope scale for the Del Prado hillslope (0.2 m DEM resolution) (a) using a single value for the entire hillslope; (b) introducing spatial variability into the prediction; (c) classifying flow resistance by mapped morphological features (Morphological Runoff Zones); (d) combining spatial variability with classification. Each prediction was made assuming a uniform flow depth of 2 mm.

Yet this approach misses a fundamentally important feature of hydrological connectivity – the interaction between *structural* connectivity (spatial patterns and the extent of physical connectedness of landscape elements) and *functional* connectivity (the linkage of landscape areas by a process) (Turnbull *et al.*, 2008; section 3.4). Articulating this in the context of overland flow resistance, spatial patterns of flow resistance determine overland flow velocities, which then influence flood generation through the development of connected

flows while also affecting future runoff transfer through the feedback between flow velocity and topographic form (i.e. high velocity flows eroding the soil surface). This defines what Bracken and Croke (2007) label 'dynamic connectivity' and is an emergent property of hillslopes (including both the variable hydrological connectivity throughout a storm event and also process-form interactions with implications for longer-term landscape development). This emergent interaction (also expressed as 'patterns, processes and functions' by many authors; e.g. Grayson *et al.*, 2002; Sivapalan, 2005; Schröder, 2006; McDonnell *et al.*, 2007) provides a coherent and reproducible pattern through which to engage in an analysis of hillslope hydrology, producing results of greater transferability and more general applicability than studies focused on small scale heterogeneities (McDonnell *et al.*, 2007).

The soil surface acts as the interface between the erosive forces of rainfall and runoff and the eroding soil itself. Throughout a rainfall event the morphology of the soil surface is continuously adjusting in response to these surface processes, and likewise, surface processes are influenced by surface topography. As a result of this dynamic connectivity, the soil surface bears the 'footprint' of the action of spatially varying processes (Huang and Bradford, 1993). Such process-form interactions were identified in section 5.5 where the relationship between flow velocity, surface roughness and erosion in rills and flow concentrations was examined (Figure 5.26). Similarly, the incision of concentrated flow pathways influences the distribution of flow depths (section 5.4) which has important consequences for the shear stress distribution and future erosion (e.g. Parsons and Wainwright, 2006).

Reproducible patterns of microtopography are observed over a wide range of semi-arid hillslopes. Here they have been classified into the Morphological Runoff Zones applied throughout this thesis (Table 4.4), although these patterns could equally be classified in any number of different ways. Chapter 7 demonstrated that these patterns can be easily mapped in the field and used to inform a thresholded index-based method of classifying hillslope surfaces. This structural connectivity is the result of previous functional connectivity and can be used to inform the examination of future flood generation by providing separate predictions of flow resistance for each structural unit (Figure 8.15c). This approach

provides a scaling tool to represent contiguous areas of low and high flow resistance across a hillslope and is analogous to the classification of surfaces of similar infiltration parameters discussed above. However, it is not suggested that surfaces should be classified in this way for modelling both flow resistance and infiltration capacity as it is unlikely that both processes are controlled by the same factors (and the results of section 7.4.2 indicated that the variation of infiltration between MRZs was negligible compared with the observed within-plot variability). The results of this thesis suggest that while soil-type and land-use affect infiltration rates, flow resistance is more influenced by the within-hillslope variation of microtopography. The prediction of flow resistance is thus classified into areas displaying the morphological indication of a similar set of surface processes (mostly through the degree of organisation of concentrated flow pathways; Figure 7.8). The distribution of these areas (Figures 7.4–7.6) has arisen from typical rainfall characteristics and also the hydrological properties of upslope areas (Yair and Raz-Yassif, 2004).

The results of section 6.2 suggest that this approach may overestimate structural connectivity by ignoring the substantial variability observed within each classification of microtopography (see Mueller *et al.*, 2007). Combining classification with spatial variability produces a more realistic picture of flow resistance at the hillslope scale (Figure 8.15d). Contiguous areas of high and low flow resistance can be observed, but these become less prominent as a consequence of the variation around the median value.

Figure 8.15a–d demonstrates each of these four approaches applied to predict flow resistance at the Del Prado hillslope (using the equations of Table 6.3 and the general equation of Table 6.4). Yet, as discussed in section 6.4, although flow resistance can be related to surface roughness, resistance is a property of the flow itself and does not exist independently of such flows. As a result, maps of flow resistance cannot be used to predict the velocity of overland flow as it will depend on the flow depth, much as infiltration rates are dependent on soil moisture. Indeed, Figures 8.15a–d assume a flow depth of 2 mm evenly spread over the hillslope surface. The predictions described in section 8.3 suggest that the resistance varies with flow depth.

This thesis developed an approach of predicting flow resistance from measures of surface roughness (or microtopography) and flow depths (or measures such as the volumetric hydraulic radius which represent the interaction between the two). When applied at the hillslope scale, the result is a spatial pattern of flow resistance values similar to that of Figure 8.15d, which varies with the predicted runoff depth of each cell. This approach gives models of hillslope hydrology the capacity to give flow resistance a similar treatment to infiltration rates (i.e. a distribution of values, organised by observed structural units that is dynamic and changes throughout a rainfall event). Whereas infiltration rate will vary with time or soil moisture storage, flow resistance relies on depth. As flow depth is necessary for the calculation of velocity in the Darcy-Weisbach equation, this depth-dependency requires no additional information. Infiltration equations typically vary as a simple function of time or soil storage; while similar relationships between flow resistance and flow depth can be identified, the typically complex and non-monotonic variation of surface roughness with increasing flow depth can produce rather more complex curves (e.g. Figure 8.4d). Section 7.4 suggested that resistance may also decrease as a function of time as it may initially represent an amalgamation of multiple processes (e.g. overcoming suction forces from infiltration or turbulence associated with the filling of surface depressions) which decrease even more dramatically (i.e. >80%) over a short period of time (i.e. within seconds) as a flow connection becomes more established. However, the intermittent nature of overland flow is such, that the establishment of such a steady and strong connection may be relatively rare.

Figure 8.16 demonstrates the variation of resistance with flow depth over the Del Prado hillslope. Whereas the example of Figure 8.15d assumed a uniform flow depth (2 mm), the maps of Figure 8.16 show the effect of a spatially-variable flow depth on resistance. This remains a simplification of the conceptual model outlined above, as the hillslope surface is assumed to generate runoff uniformly (thereby ignoring the spatial and temporal variability of infiltration and rainfall discussed above). The flow velocity maps demonstrate that with increasing water depth, areas of flow concentration produce faster flows relative to interrill areas, thereby promoting the hydrological connection of upslope areas to the main channel network.

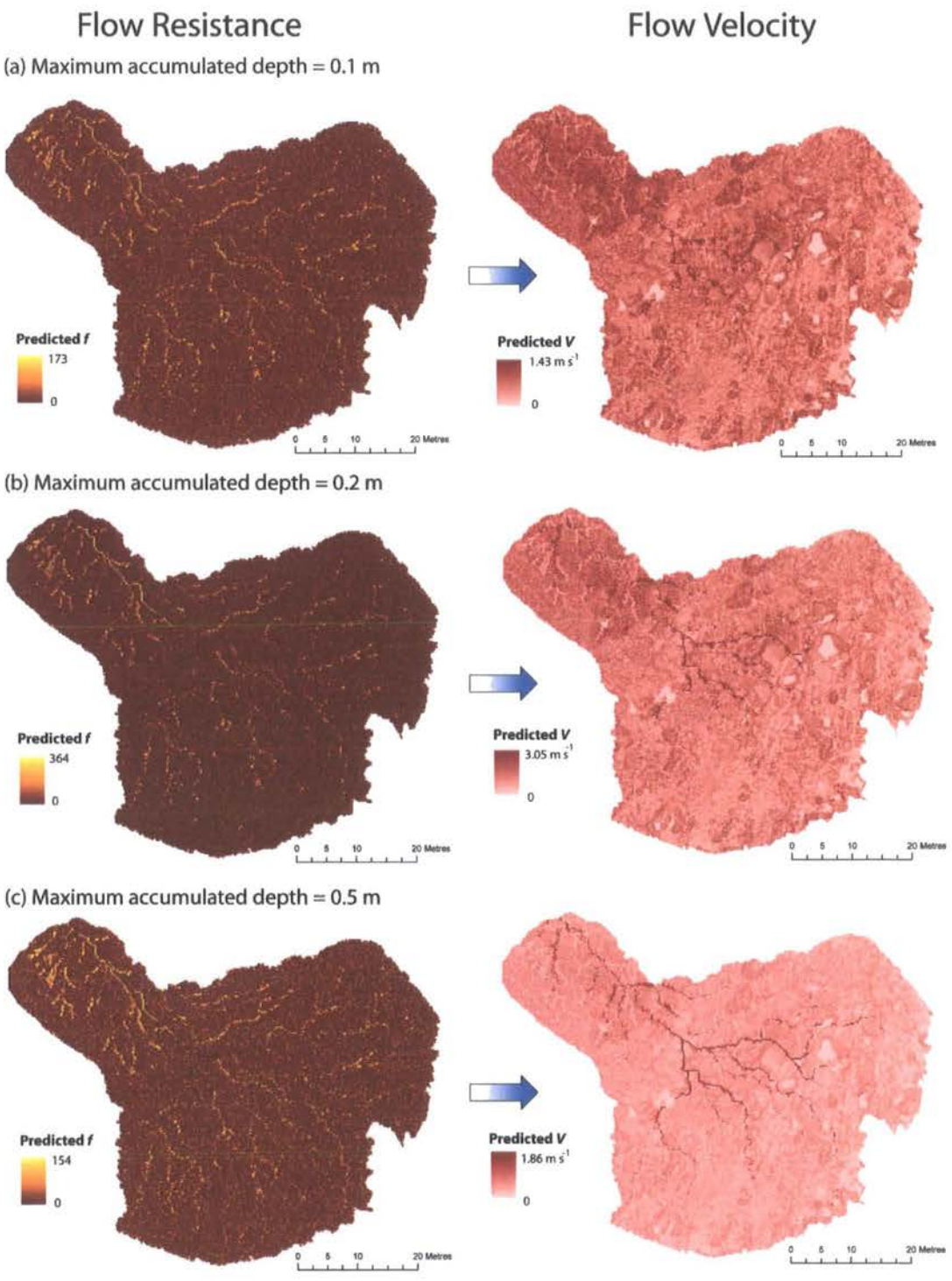

Figure 8.16. Predicted distribution of flow resistance and velocity at the Del Prado hillslope for three maximum flow depths. In this simplification, each cell is assumed to contribute an equal amount of runoff to the outlet.

Using velocity calculations derived from slope, flow depth and flow resistance offers the potential for a more sophisticated analysis of travel times than that of section 7.3.3. The resultant travel time distribution shows greater nonlinear threshold behaviour than Figure 7.24. The travel time distribution is similar to that of Figure 7.24d for the first 800 s, but Figure 8.17b predicts that some areas will remain isolated from the hillslope outlet for a much longer period of time. The map of Figure 8.17a highlights these areas, while also demonstrating the influence of flow concentrations and the accumulation of deeper flows on the travel time distribution. In Figure 8.17a the isolated areas are prevented from connecting with the hillslope outlet by areas of very low slopes. In reality, these areas will have a less prominent effect on the travel time distribution as water collects in depressions and overflows (as will be captured by any hydrological model using the water surface slope rather than the soil surface slope as approximated in this demonstration).

With increasing rainfall depth, the travel time distribution becomes more peaked and water is routed faster over the hillslope surface (Figure 8.17b). It is worth remembering that in the basic analysis of Figure 8.17 where rainfall is steady and no infiltration takes place, the variation of the flow resistance parameter with depth affects the peak stage and arrival of the flood wave. In a more realistic situation where runoff-producing rainfall is intermittent and variable, and runoff is generated at only a small portion of hillslope surfaces, flow resistance does not just determine the distribution of travel times, but plays a fundamental role in developing flow connections and will thus determine total runoff amounts.

That the effect of flow resistance is often ignored in studies of functional or dynamic connectivity (i.e. the development of continuous flowpaths) is a symptom of the paucity of quantitative analysis undertaken in such studies. When the connectivity framework is used to examine the hydrological system, soil moisture and runoff depth determine the driving forces towards establishing connections, and flow resistance acts to impede the development of a delivery pathway, yet the focus is entirely on the driving forces.

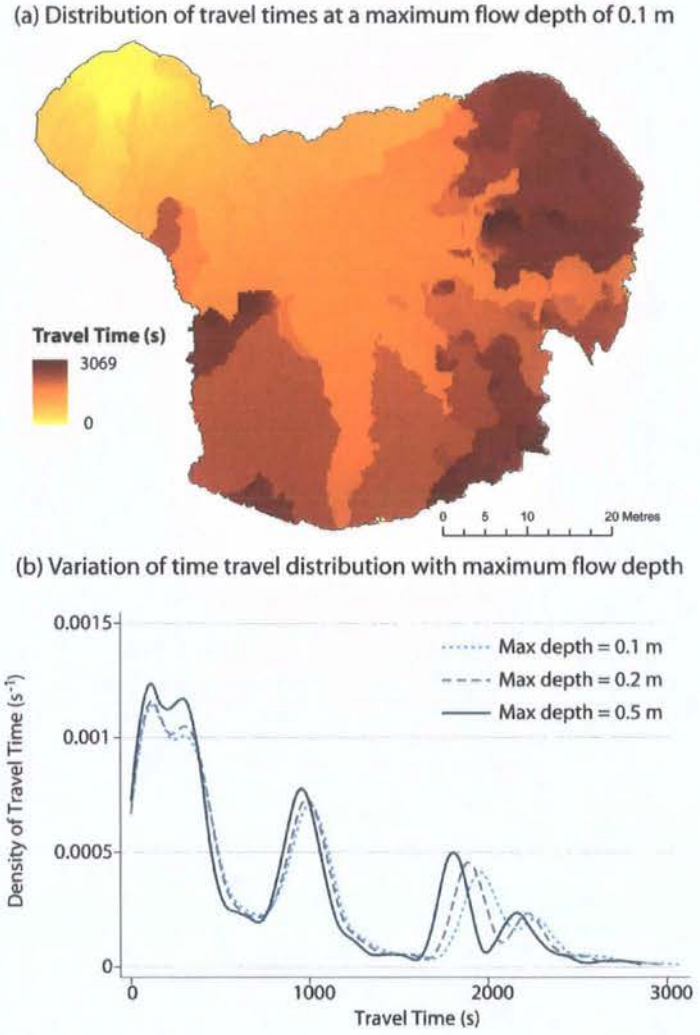

Figure 8.17. (a) Travel times calculated for the Del Prado hillslope using flow velocity predictions of Figure 8.16a and a maximum accumulated flow depth of 0.1 m; (b) kernel density estimates of the distribution of travel times for maximum accumulated flow depths of 0.1, 0.2 and 0.5 m (using the Epanechnikov kernel with half-width 65 s).

To conclude, the inclusion of resistance-depth relationships in hydrological models provides a critical linkage that permits the interaction between the spatial and temporal variation of both flow resistance and infiltration rates through the redistribution of soil moisture and runoff to determine the response of a hillslope or catchment to a particular storm event. This interaction is summarised in Figure 8.18. The approach developed in this thesis offers a framework for incorporating a dynamic and spatially variable flow resistance parameter into hydrological models alongside similarly dynamic and spatially variable

infiltration parameters. The discussion of Chapter 3 emphasised that it is the interaction between these two processes that determines the functional connectivity of a hillslope and the necessary storm properties for runoff to contribute to the outflow hydrograph (the 'travel opportunity time' of Aryal *et al.* (2003) or the 'concentration time' of Yair and Raz-Yassif (2004)).

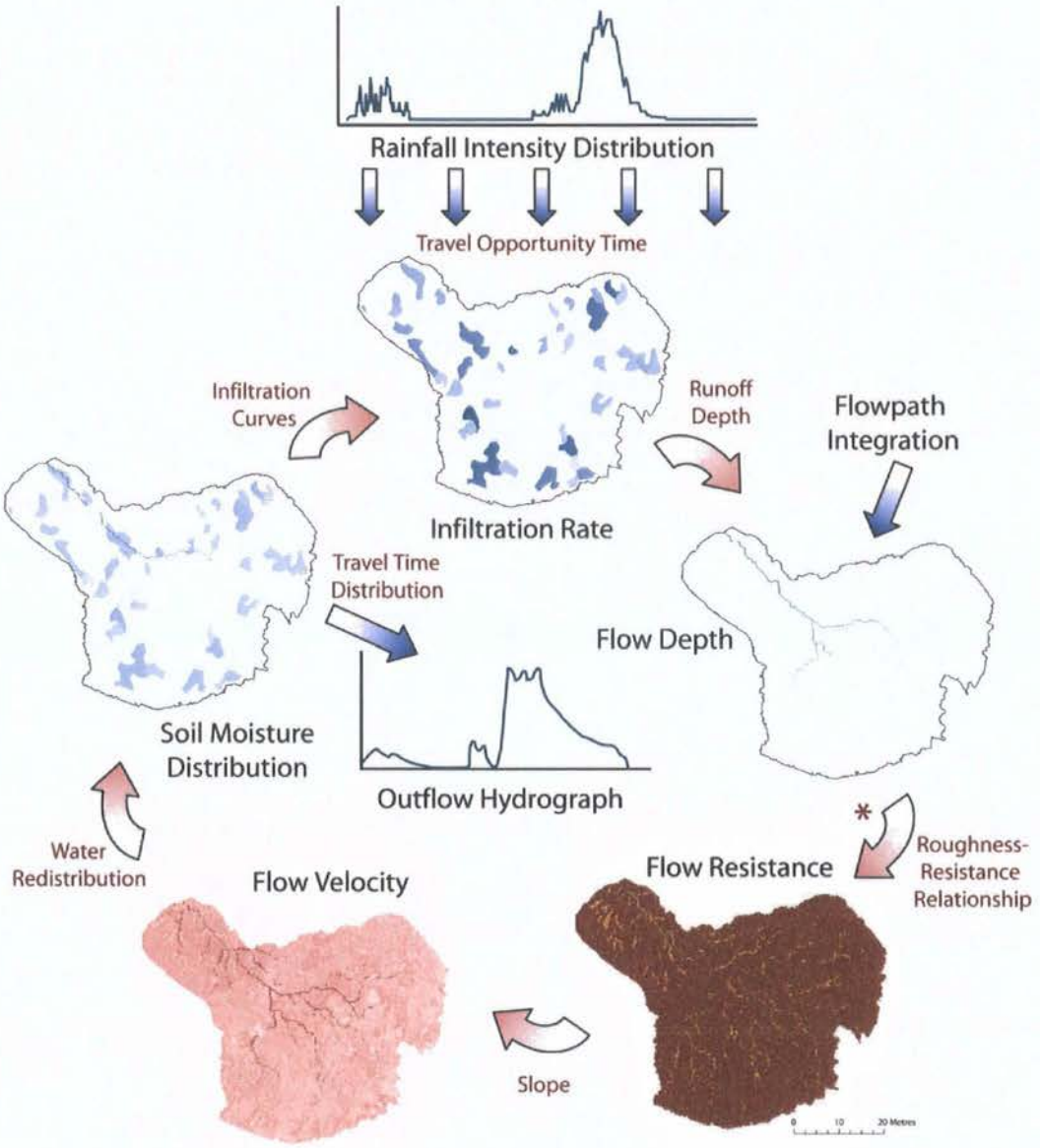

Figure 8.18. Summary of the conceptual model of dynamic hydrological connectivity over a semi-arid hillslope outlined in this section. Flow resistance and infiltration parameters interact through the redistribution of soil moisture and runoff to determine the runoff response to any given rainstorm. The feedback loop is completed by adding a representation of the changing flow resistance with depth (marked *).

8.5 Limitations & Opportunities for Further Research

This study pioneered a new method of measuring overland flows in the field. The application of terrestrial laser scanning technology towards developing our understanding of natural processes remains in its infancy. Increased accessibility of high-resolution elevation data presents considerable opportunities for enhancing our understanding of many areas of geomorphology (e.g. landslide and debris flow mechanisms, cliff and riverbank erosion). This new capability brings new challenges of calibration, data collection, processing and presentation. To date, attempts to apply terrestrial laser scanning techniques to solve geomorphological problems are relatively few and far between (with a few notable exceptions, e.g. Rosser *et al.*, 2005; Lim *et al.*, 2005; Rumsby *et al.*, 2008). Many researchers appear to collect laser-scanned digital elevation models simply for their aesthetic value, falling short of developing any general understanding of their subject. The methodology described here was a first attempt at applying this technology towards measuring and modelling overland flows over natural surfaces. As with any innovative technique, there exists considerable potential for this methodology to be developed further.

During the development of this project, there were a number of technical advances in terrestrial laser scanners. There is every reason to believe that such trends will continue to make such high resolution data both more accurate and more widely available. Applications of this technology represent an active research frontier where numerous advances are possible. This study pushed the resolution and precision of the current generation of laser scanners to their present limits. It was found (in the experiments of section 4.3.3.3) that the achievable precision at close-range was just within the necessary limits (approximately 2 mm) to capture the roughness of bare soil surfaces. The next generation of terrestrial laser scanners will inevitably push those limits even further and open up new opportunities to apply this general approach of measuring overland flows to a wider range of conditions.

This study employed simple criteria to reconstruct a water surface from elevation data provided by a terrestrial laser scanner and a flow extent derived from overhead imagery. This represents an area worthy of further development, employing more sophisticated

analysis to estimate the water surface elevation. The use of a constant discharge trough to supply overland flows to the plots could also be improved by replacing or combining the supply with rainfall simulation. However, this adds additional complications as the rainfall simulators and the rain itself would interfere with the overhead imagery capture techniques.

The results presented in this thesis were obtained from just three hillslopes. While there is some justification in suggesting that the downslope variation of microtopography over bare hillslopes might be reproduced on other semi-arid hillslopes, further work should be directed towards examining the validity of this assumption. More importantly, for this method to be advanced further and effectively applied to other locations, procedures must be automated to reduce the processing time required to generate flow measurements. Such opportunities do exist (discussed briefly in section 4.3.8) but were beyond the scope of this project. The methodology described in Chapter 4 was developed on a tight budget; investment in more sophisticated equipment would yield both more accurate and rapid data collection.

This study was restricted to the examination of bare soils; however, patches of vegetation are present on most semi-arid hillslopes. Their influence on runoff generation and connectivity development has recently been the focus of much research (e.g. Turnbull *et al.*, 2008; Mueller *et al.*, 2008). Integrating the results of this study with investigations of the influence of vegetation patches on runoff is essential if flood generation mechanisms are to be properly understood. Indeed, a greater understanding of this interaction may provide potential options for flood prevention strategies. Such integration represents a considerable challenge as distinguishing between soil surface roughness and the 'mobile' roughness of vegetation elements is subject to considerable error.

The assumption that the soil surface changed negligibly during the course of the runoff experiments was supported by field observations. However, another consideration for further research would be the establishment of monitoring plots where repeat surveys of the same area examine how the soil surface changes over time. This approach would feed into the connectivity development framework as the gradual establishment of concentrated flows after runoff events can be observed. This should be combined with a more

widespread application of the 'light-touch' monitoring methods of measuring maximum stage over a wider area (e.g. Bracken and Kirkby, 2005). This would address the paucity of data of runoff generation from real rainstorms. However, to some extent this data-gap is a result of the infrequent and often torrential nature of runoff in semi-arid environments. The field site selected for this research is the driest area of the western Mediterranean. Therefore, this methodology would be advanced more rapidly by choosing a less extreme location where more frequent runoff events produce more observations for analysis. The methodology can be later transferred back to drier areas once sufficient expertise and understanding has produced significant advances and developed a refined version of measurement techniques.

In more general terms, the study of semi-arid overland flows at the hillslope scale has much to offer the emerging framework of connectivity that is now an established concept in hydrology and ecology. Section 8.4 identified a key interaction between infiltration rates and overland flow resistance that may explain the nonlinear runoff response to rainfall events observed on semi-arid hillslopes. A research agenda focusing on connectivity development of such overland flows can augment recent conceptual advances being made in the study of subsurface flows. Ease of access and logistical advantages mean that semi-arid overland flows (where lateral subsurface flow is considered to be negligible) would be a convenient hydrological process with which to develop new theoretical constructs of connectivity (e.g. modelling flow connections using percolation theory; Lehmann *et al.*, 2007).

Finally, application of terrestrial laser scanning to the study overland flow hydraulics requires the distinction between roughness and topography to be re-examined. Overland flows are frequently very shallow and are of a similar scale as those microtopographic irregularities that are commonly labelled as simply 'roughness'. Naturally, such features can deviate, block or decelerate overland flows much more effectively than where such features are located on the bed or banks of much larger, deeper rivers. Despite this influence, it remains impractical to survey the microtopography of an entire hillslope or catchment. Therefore, the way in which this roughness is represented in hydrological models requires deeper consideration. Although this thesis has made some progress

towards identifying the relevant parameters of microtopography to apply to hillslope-scale analyses, there remains a large gap in our ability to effectively transfer plot-scale studies to the management scale.

8.6 Summary

The temporal variability of rainfall intensities determines the opportunity for runoff generation. At the Prado sub-catchment, the rainfall amount falling before peak intensity is reached and the duration for which intensity was above 20 mm h^{-1} were related to flood generation. Connectivity development at this location is therefore determined by a combination of the rainfall amount remaining once infiltration is satisfied and, crucially, the duration for which this rainfall-excess exists.

Spatially and temporally variable predictions of flow resistance permit a higher-level of analysis of hydrological connectivity development over semi-arid hillslopes. Depth-varying resistance predictions interact with soil moisture-dependent infiltration predictions to determine both the 'travel opportunity time' and the degree of connectivity that can be achieved during this time. Evidence of such functional connectivity is found in the morphological representations of runoff process observed over semi-arid hillslopes. In turn, this morphology development (or structural connectivity) determines future hydrological connectivity through the development of efficient flow pathways. A range of options exists to incorporate the effect of these morphological patterns into predictions of flow resistance.

In the conceptual model outlined in Figure 8.18, flow resistance represents a fundamentally important component of the connectivity framework that must be properly represented in hydrological models for a truly quantitative analysis of dynamic connectivity to be undertaken. The analysis presented in section 8.4 presented only an example of how this synthesis should be achieved. The next step is to examine the interaction of infiltration, resistance and rainfall intensities in a distributed, physically-based hillslope hydrological model. This represents a key research priority. Additionally, numerous opportunities exist to improve the field methodology developed in this thesis which may substantially enhance our understanding of semi-arid overland flows.

To conclude, Chapter 9 now reviews the key findings and results presented in this thesis in the context of the aims and objectives laid out in Chapter 1.

CHAPTER 9

CONCLUSIONS:
SUMMARY OF KEY FINDINGS

9.1 Introduction

The purpose of this concluding chapter is to summarise the findings and to emphasise the key results of this thesis. The summary (section 9.2) is structured around the original objectives identified in section 1.2. The key conclusions of this research are then related to the implications of the results for the management of flood hazard in semi-arid catchments and the wider research community (section 9.3).

9.2 Summary of Objectives

As stated in Chapter 1, the overall aim of this project is to provide a detailed examination of overland flow hydraulics, focusing on the influence of surface roughness and infiltration on flow resistance and hillslope-scale flood generation in semi-arid environments. This section examines the extent to which this research aim has been achieved and uses the individual objectives outlined in section 1.2 as a framework for a discussion of key findings.

9.2.1 Methodology Development

(1) To develop a methodology that allows the variables of overland flow to be precisely defined and measured in the field.

The methodology described in Chapter 4 offers a new perspective of runoff transfer on natural soil surfaces that can fill an important gap in our knowledge of overland flow processes (generating data such as that presented in Figure 9.1). Rapid-sequence overhead images were georeferenced over a high-resolution plot-scale Digital Elevation Model (obtained from a terrestrial laser scanner) onto which overland flows were simulated. Flow patterns and velocities were extracted and an understanding of the fine-scale variability of these can be gained from interrogation of the raw data.

Flow depths were not measured directly, but were estimated by making several assumptions about the nature of the water surface (section 4.3.5.2). The estimated water depths will not be as accurate as point measurements made during the experiments; a comparison of direct measures with estimates shows some scatter around the line of equality (Figure 4.23). However, the high-resolution and spatial distribution means that they present a complementary measure of depths. This comparison is also being made for optical remote mapping of rivers. Marcus and Fonstad (2008) suggest that true variability that is not captured by field measurements is often misidentified as error in the remote mapping technique, arguing that more robust assessments for validation and accuracy assessment are needed.

This methodology permits velocity and depth measurements to be taken at a high spatial resolution, thereby allowing hydraulic measurements to be examined alongside the finer structure of the soil surface topography. A distribution of depth measurements can be extracted from flow experiments revealing additional hydraulic information (e.g. the distribution of shear stress) that offers new insights into the process of overland flow. Indeed, the high-resolution of the dataset presented issues of terminology. Measures such as depth and velocity need to be more precisely defined before they can be extracted (e.g.

median depth and maximum velocity) especially over complex and partially-inundated soil surfaces (e.g. Smart *et al.*, 2002).

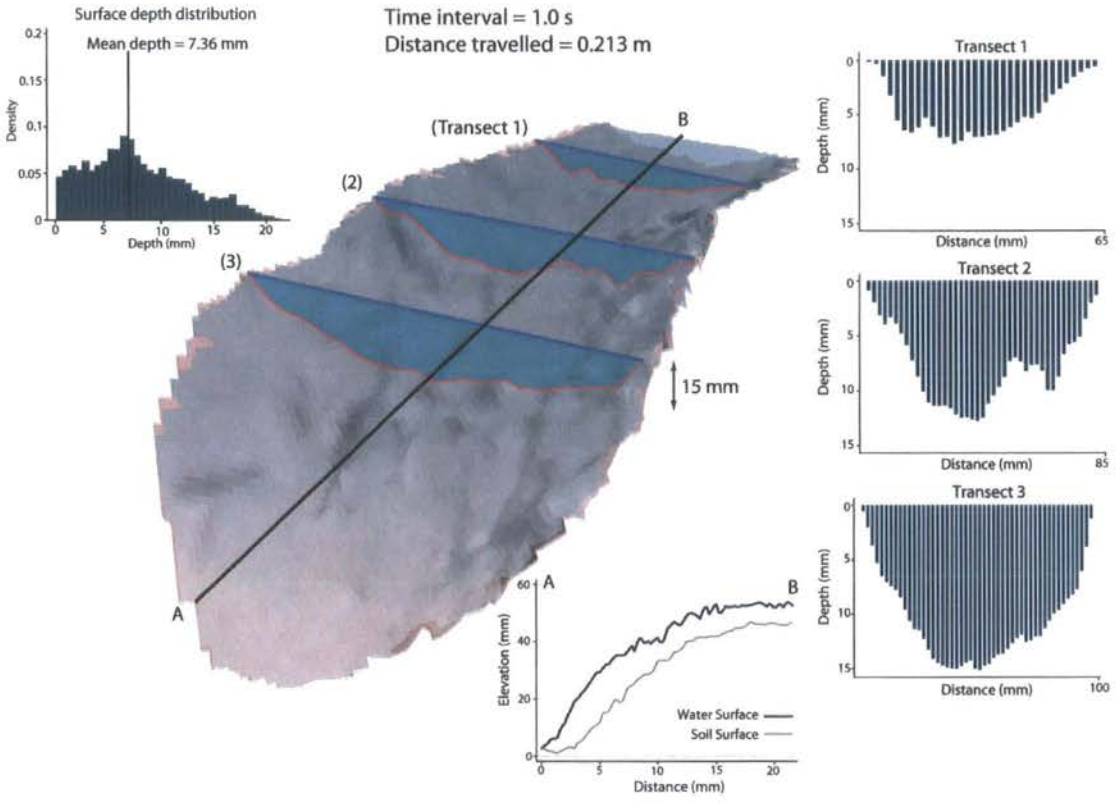

Figure 9.1. Example flow thread. The DEM has been cropped to just the surface over which water flowed during an interval of 1 s. The figure shows a soil surface with the calculated water surface overlain and depths on three example transects. The distribution of calculated depths for the surface as a whole is shown on the top-left, and longitudinal profiles of soil and water elevation are found at the bottom of the image (originally Figure 4.26).

Data collection in the field was relatively rapid. Crucially, the extraction of hydraulic variables takes place after the fieldwork has been completed when the user is able to deliberate on the measurements necessary and re-interrogate the dataset at any time. Additionally, the overhead image capture provides an ideal perspective for a user to observe the simulated overland flows. The image sequences can be easily imported into video editing software to create real-time footage. This provides a rich source of qualitative

information and can be studied to develop further hypotheses of the precise nature of overland flow processes.

There is much potential for further developing this methodology (discussed in section 8.5). Combining the runoff supply with rainfall simulation, collection of runoff at the bottom of the plot and monitoring the evolution of microtopography over several years would further develop our understanding of runoff production and transfer over semi-arid hillslopes.

9.2.2 Overland Flow Measurements

(2) To examine the variation of overland flows across and between hillslopes.

The dataset made available by this new methodology provided several interesting insights into the process of overland flow over natural soil surfaces in a semi-arid environment. The velocity and depth of simulated overland flows was observed to vary substantially within each hillslope. This was a consequence of the degree of flow concentration observed at each plot. Velocities greater than 0.2 m s^{-1} were rarely observed and were often much lower. Results suggest that flow velocity fluctuates markedly over the plot scale as a function of flow resistance and surface slope. The median flow depth showed a similar variation, although summarising overland flow depth with a single measure does not fully capture the nature of the water flow. This is problematic when assigning a Reynolds number as the use of a characteristic length in equation 2.1 requires the condition of geometric similarity to pipe-flows (Massey and Ward-Smith, 2001). The geometric complexity of the boundary between the soil surface and flowing water brings the validity of this assumption of geometric similarity into question and perhaps provides an explanation for the low Reynolds numbers recorded. The absence of rainfall impacts and the mechanism of water supply may have been more conducive to laminar flows than normal overland flow conditions; however, this does not fully explain the number of observed laminar flows, especially as observations during the experiments (and subsequent examination of overhead imagery) suggest that the flows were quite turbulent. In areas where flow concentrations had formed, the majority of flows were in the turbulent regime (Figure 5.5).

Although flow depth was only estimated, variation in the water surface topography over a cross-section is likely to be negligible compared with the soil surface microtopographic variation. Therefore, the methodology developed here can be considered to provide an estimate of the distribution of flow depths. Such a distribution of flow depths was recorded with each velocity measurement. This was observed to be positively skewed and was consistently modelled most accurately with a two-parameter gamma distribution (section 5.4). This finding is contrary to other studies of overland flow depth distributions, yet makes intuitive sense as the gamma distribution provides a more flexible form than most alternatives (see Table 5.3). The two parameters of this distribution (shape factor α and scale factor β, where the product $\alpha\beta$ equates to the mean depth d) varied independently with distance downslope. The scale parameter showed a positive relationship with discharge (and hence increased with degree of flow concentration), whereas the shape parameter varied inversely with the exponent of the depth-discharge relationship at each plot. It is hypothesised that the shape parameter decreases when an increase in water level inundates a large area of shallow flow alongside a smaller, deeper area (as experienced where a flow concentration cannot contain the imposed discharge and spreads over the surrounding area). This produces a depth distribution typical of those of a smaller gamma shape parameter. Modelling the extremely variable flow depth with a two-parameter gamma distribution captures both processes. An increased ability to model overland flow depth distributions will enhance our understanding of shear stress distributions on hillslope surfaces and will have important consequences for studies of sediment entrainment and the onset of rill erosion on such soil surfaces.

Examination of the hydraulic geometry of overland flows shows that variations within each hillslope were greater than differences between the three contrasting semi-arid hillslopes investigated in this study. As flow concentrations develop, the increase of flow width with discharge is reduced as efficient routing of flow increases depth and velocity more rapidly. Yet the increase in velocity with discharge of concentrated flows followed two different patterns: an upper limb of relatively high flow velocity where flow is supercritical ($Fr > 1$) and a lower limb where flow is subcritical ($Fr < 1$). This was demonstrated in Figure 5.8 and is reproduced below (Figure 9.2a) with concentrated flows separated by flow state.

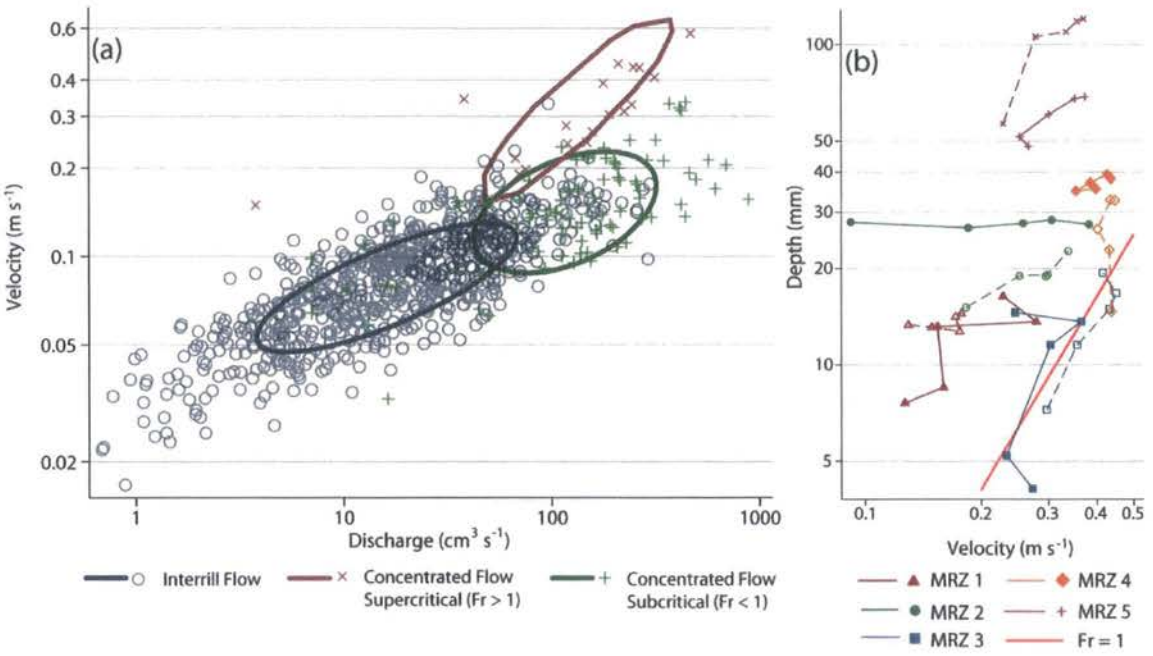

Figure 9.2. Downstream and at a point hydraulic geometry and the influence of flow state. (a) Polar smooths (see p.122) displaying the variation of velocity (m s^{-1}) with discharge (cm^3 s^{-1}) for interrill and concentrated flows (concentrated flows separated by flow state); (b) variation of depth (mm) and velocity (m s^{-1}) with increasing discharge for the Del Prado hillslope. The red line represents the relationship between depth and velocity where Fr = 1. Reproduced from Figure 5.18b.

At a point hydraulic geometry was investigated using a trough that was able to supply a variable discharge. In some flow concentrations decreasing velocity with increasing discharge was observed. Figure 9.2b (reproducing Figure 5.18b) shows that such velocity decreases were often a consequence of a transition from supercritical to subcritical flow (a hydraulic jump) and represent a switch from the upper limb of Figure 9.2a to the lower limb. These hydraulic jumps dissipate mechanical energy through turbulence and may erode the soil surface, thereby altering the roughness of the soil surfaces. This feedback between flow velocity and surface roughness has previously been proposed as a moderating influence on the effect of bed slope on flow velocity in eroding rills (e.g. Govers, 1992; Giménez *et al.*, 2004). Supercritical flow in eroding rills can only be maintained where surface roughness is below some threshold. When the soil becomes too rough, a hydraulic

jump is induced. Over time the resultant energy dissipation can erode the rill bed, thereby providing a feedback loop between surface roughness and overland flow. This study examined the relationship between hydraulic jumps and a variety of roughness measures to investigate the precise nature of this surface-flow interaction.

Several roughness measures demonstrated a relationship with the initiation of hydraulic jumps (e.g. Figure 9.3a). As proposed by Giménez *et al.* (2004), these relationships were only observed in flow concentrations. Where these roughness measures were greater than a particular threshold value, supercritical flow could not be maintained. Tortuosity (as measured by T_{3D}, T_p, T_r: the actual area or length of surfaces or profiles of surfaces normalised by the planar area or length) and protruding frontal area (F_T) appeared to trigger these hydraulic jumps (other roughness measures such as standard deviation of elevations showed no such relationship). Figures 9.3b and 9.3c show the variation of these roughness measures and the Froude number as flow moves down through a rill system where an increase in roughness is immediately followed by a decrease in the Froude number. In the at-a-point case, where progressive inundation incorporates such roughness elements into the flow, resistance increases and a hydraulic jump may be triggered. Where the soil is less erodible (observed at the Cardenas hillslope), supercritical flow does not develop, rill flow velocities are much slower (even where the slope is steeper) and the rill maintains a rougher bed.

These results show that overland flows on natural hillslope surfaces demonstrate much variability. They appear to confirm and expand upon existing theories of overland flows and provide a demonstration of how the interrogation of this new high-resolution dataset can advance our understanding of hillslope hydraulics.

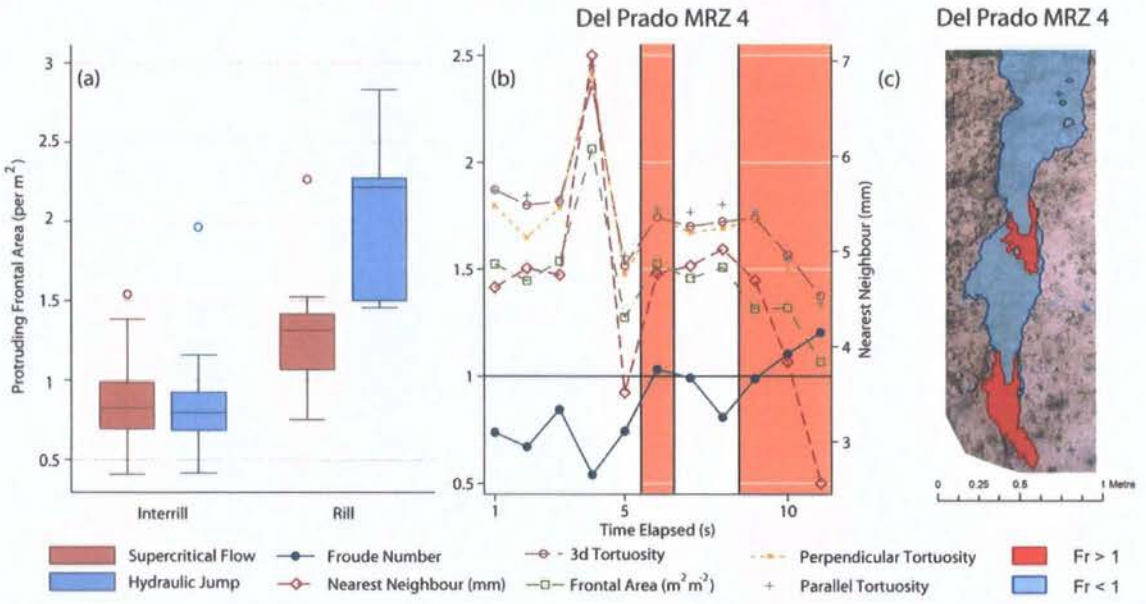

Figure 9.3. Demonstration of the initiation of hydraulic jumps by increased surface roughness: (a) comparison of the distributions of protruding frontal area (F_T) in areas where supercritical flow is maintained and where hydraulic jumps take place, separated for interrill and rill flows; (b) variation of Froude number and selected roughness measures along a rill at the Del Prado hillslope shown in (c). Reproduced from Figures 5.29, 5.31 and 5.32.

9.2.3 Parameterising Surface Roughness

(3) To identify which particular attributes of surface roughness or flow characteristics can be usefully parameterised for modelling the hydraulics of overland flow.

Roughness is a vague concept, and as such it can be made precise in a variety of ways. The definition of roughness may even extend beyond that of some measurable sub-grid scale property of a rough surface to become a calibration factor, implicitly representing those processes not directly included in any model including some fluid boundary (this will vary with the dimensionality of a model; see Lane and Ferguson, 2005; Morvan *et al.*, 2008). Limiting the definition of 'surface roughness' to a directly measurable variable, a great deal

of possibility remains. A brief examination of Appendix 1 reveals an example of the many possible parameterisations of surface roughness. Each offers a particular representation of a single perspective of surface roughness. A central argument of this thesis is that the selection of a roughness measure should be informed by the process for which it will be used.

Over each of the hillslopes investigated in this study, a wide variety of microtopographic forms were observed. It seems unlikely that the use of a 'roughness height' term ε, borrowed from studies of pipe flows and fluvial hydraulics, will accurately describe resistance to shallow overland flows moving over these surfaces. As this term is modified for use on complex soil surfaces (see section 6.2) its original meaning is altered. Where any structure or 'form roughness' exists (such as the development of concentrated flow pathways) this measure may become especially large and bear no resemblance to the original definition.

Indeed, this signifies a wider issue of the application of terminology developed for pipe flows and fluvial systems to studies of extremely shallow, partially-inundated overland flows. Recently, many authors (e.g. Smart *et al.* 2002; Ergenzinger, 1992) have identified the need to clarify or even alter some traditional measures (e.g. hydraulic radius) to more appropriate forms (e.g. volumetric hydraulic radius). Section 6.3 attempted to derive a more meaningful measure of flow resistance by reducing the restrictions introduced by several assumptions implicit in the traditional formulation of the Darcy-Weisbach friction factor. For example, flow depth is replaced by the volumetric hydraulic radius, while the uniform flow assumption is applied only over very small areas and the use of the energy gradient S_f (see equation 2.28) takes account for the observed variability of flow velocity. However, once the roughness-resistance relationships have been identified, the modelled results need to be translated into a form that can be applied to the type of data available to general models of hillslope hydrology (as described in section 8.2.1) which do not yet incorporate measures such as the volumetric hydraulic radius.

Conventional approaches, such as relating flow resistance to the Reynolds number or inundation ratio, performed relatively poorly. As described in Chapter 2, the most likely

reason is that these approaches were developed for a range of conditions very different from those found in overland flows (e.g. Figure 9.4, reproduced from Figure 6.6) and at a larger scale. Alternatively, the scatter may be partially a consequence of the methodology used to generate these data, as the flow simulation experiments did not accurately represent natural runoff events (resistance may have been increased at the side-edges of the wetted area). Amending conventional approaches to include slightly modified roughness parameterisations (e.g. replacing the roughness height ε in Figure 9.4 with the mean elevation difference between neighbouring cells in a grid Z_d) provided little improvement.

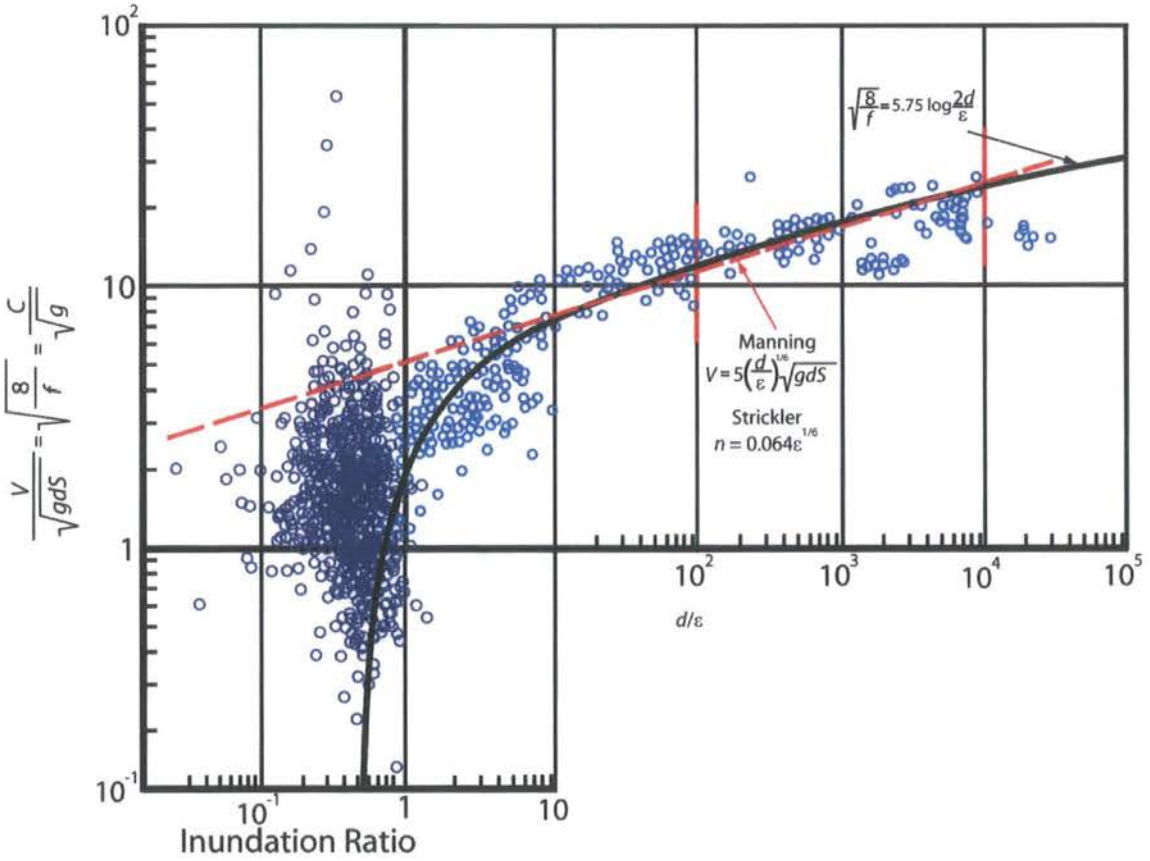

Figure 9.4. Resistance to flow as a function of the inundation ratio (y-axis is conveyance). Reproduced from Figure 6.6. This figure is a synthesis of the data collected in this study (in purple) and that of Julien (2002: p.93). Compare Figure 2.3.

Therefore, a regression methodology was applied to predict f from a number of different roughness measurements. Measures selected for analysis were limited to those that are

independent of the assumed overland flow (i.e. can be directly measured from the surface) or those that are scaled to a flow depth term. This excluded from analysis the Reynolds and Froude numbers, which require the calculation of flow velocity and produce spurious correlations with resistance. Despite the large number of roughness measures selected for investigation, a variety of different approaches (see Chapter 6) showed that the same 8 measures were regularly observed to describe overland flow resistance.

Rough surfaces create a variety of slopes at the sub-grid scale. This property of a surface is scale-dependent; in this study the length scale over which flow was observed to move during a 1 s interval was used. This sub-grid scale slope term S was positively related to flow resistance suggesting that locally increased slopes are less efficient at transmitting flows and counteracts the assumed influence of energy slope on velocity in the formulation of a resistance equation (agreeing with the observed slope-independence of rill flows demonstrated in section 5.5.1; Govers, 1992).

Depth-dependent roughness measures such as the inundation ratio Λ (= d/ε) were also related to resistance. Λ was positively related to f (the opposite direction to that relationship observed in open channels; Figure 9.4) which suggests that progressive inundation is an important consideration. Section 6.2 explains that in such situations, the Λ term is subtly different from the conventional form applied in fluvial hydraulics. Depth skewness was also found to be negatively related to resistance. As the observed skewness was always positive, this suggests that flow resistance was less where deep areas of concentrated flow exist. These terms demonstrate a non-monotonic variation with increasing flow depth. Their relationship with flow depth can be used to predict the variation of f with depth (as seen in the general curves of Figure 9.5).

The dimensionless product $\sigma_Z P_{dxc}$ (the standard deviation of surface elevations and the pit density measured in a cross-slope direction) combines a general roughness measure with a more specific measure. The increased roughness (defined generally with σ_Z) that manifested itself as flow concentrations (specifically, pits in the cross-slope direction) increased the conveyance of flow (thereby decreasing resistance). Finally, the protruding frontal area F_P was negatively related to resistance. This is the opposite of the hypothesised

relationship. However, this was only found at the upslope locations where such a frontal area may produce small concentrated threads in the interrill flow. This demonstrates the importance of including an appreciation of hillslope position in predictions of resistance.

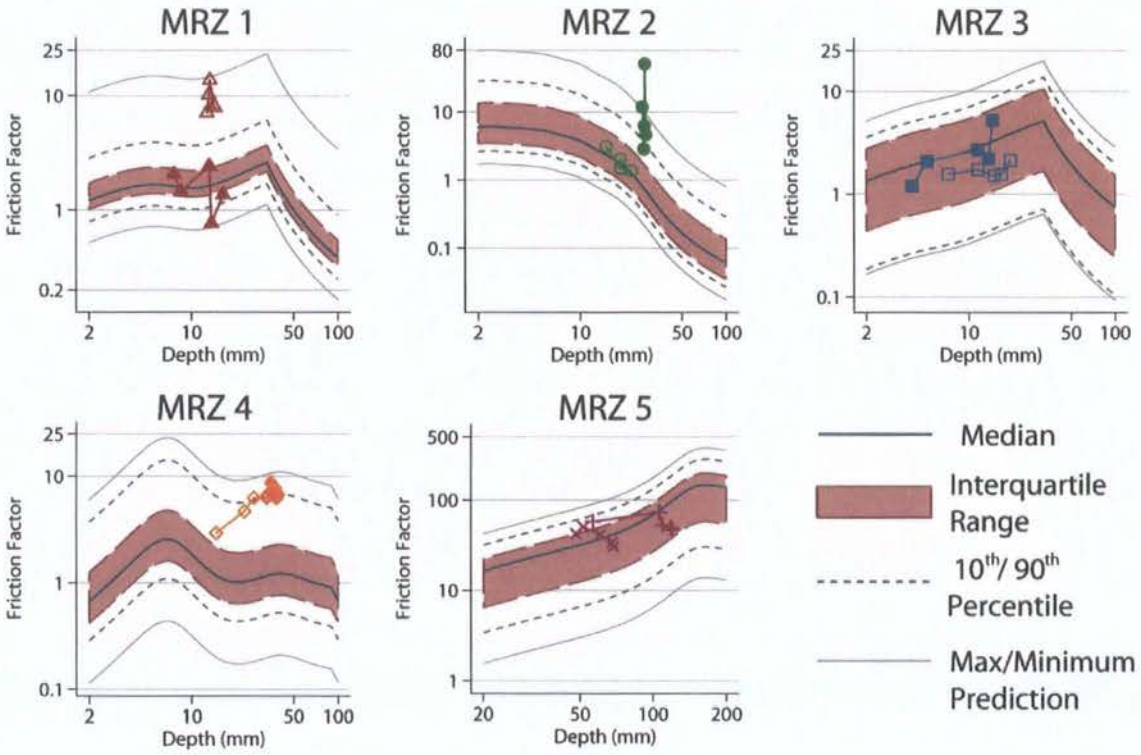

Figure 9.5. Variation of resistance predictions with hillslope position and flow depth. Measured flow resistance is compared with that predicted from Table 6.3. Originally Figure 8.13.

9.2.4 Within- and Between-Hillslope Variability

(4) To examine how hillslope location, soil type and land-use influence these roughness-resistance relationships.

Three hillslopes of different soil-type and hydrological response were examined over two semi-arid catchments in south-east Spain. Resistance to flow was generally highest at the crusted blue schist of the Cardenas hillslope and lowest at the marl Del Prado hillslope. Yet despite these observed differences, the roughness-resistance relationships developed in

Chapter 6 show little effect of soil type (e.g. Figure 6.9b). Examination of the residuals of the predictive equation where no hillslope position term has been included in the model (the general case in Table 6.4) shows that the residuals from the Upper Nogalte and Del Prado are almost identical, and those of the Cardenas hillslope are slightly less positive. However, this difference is minimal compared with the differences observed between hillslope positions (i.e. the position of the measurement within the hillslope).

Consistent variations of microtopography with increasing distance downslope can be observed over a variety of semi-arid hillslopes. These can be characterised using the Morphological Runoff Zone (MRZ) framework (Table 4.4; Bracken and Kirkby, 2005), although a variety of other possibilities exists. The transitions between MRZs were found to be related to the product of general slope and $\sqrt{\text{upslope area}}$ (section 7.2). From basic field maps, threshold values of this product can be estimated and the distribution of MRZs over a hillslope DEM can be predicted. This permits the results obtained for a single hillslope to be transferred to other slopes of that soil type. The methodology developed for objective (1) was applied to the entire range of MRZs observed at each hillslope, ensuring that the full range of observed surface features was included in this investigation.

Moving downstream through a flow network, the processes and surface topographic configurations contributing to flow resistance will change (Prestegaard, 1983; Bathurst, 1993). In Chapter 2 this idea was recast in the context of hillslope runoff and can be applied to the Morphological Runoff Zone framework. Several models to predict f from roughness were developed in Chapter 6. These offered a range of possibilities of incorporating the effect of hillslope position in the prediction, from developing separate regression equations with different variables for each MRZ, to predicting f for the dataset as a whole irrespective of hillslope position.

All models performed relatively well. However, examination of the regression equations when developed separately for each MRZ (Table 6.3) showed that different roughness-resistance relationships were observed at each hillslope position and that the large number of observations from the top of the hillslope (which covers the majority of the hillslope

area) dominates the general relationship. For example, Figure 6.12 showed the decreasing exponent and R^2 of the relationship between f and the Reynolds number with distance downslope. Also the inundation ratio was not related to resistance in areas where obvious organised flow structures were observed (see section 6.5.3).

Therefore, the most flexible model of individual regressions (Table 6.3) was used to identify the significant variables ($P<0.05$) at each MRZ. These were then included in the simpler models. Figure 9.6 (originally Figure 6.20) shows the correlations between the predictions of each model and the measured resistance values (log-scale). The greatest correspondence between predicted and observed values was found for the model where the coefficient of each of the roughness variables was allowed to change with each MRZ (although differences between all models were relatively minor).

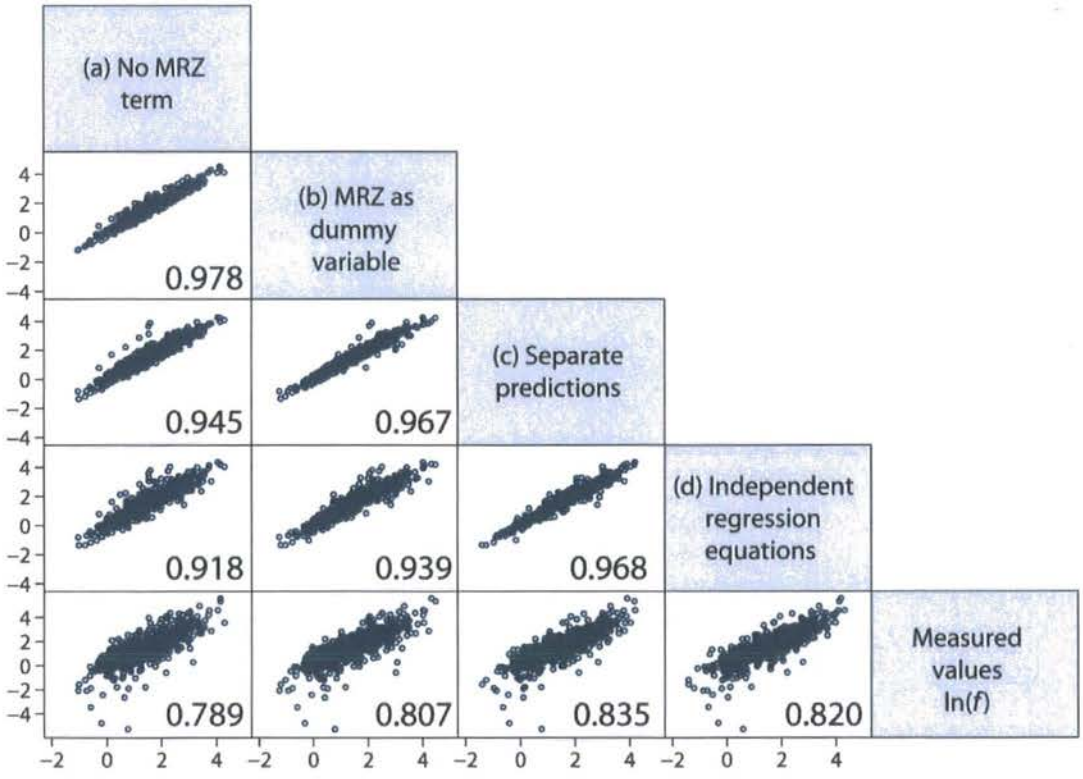

Figure 9.6. Scatter matrix demonstrating relationships between different methods of incorporating hillslope position into predictions of resistance to overland flows and the measured values (log scale). All roughness measures in Table 6.3 have been included in each prediction. Pearson's correlation coefficient is displayed in the lower right corner of each plot region. Originally Figure 6.20.

The predictions of each of these models were tested against a small independent dataset from the Del Prado hillslope in section 8.3.2. As demonstrated in Figure 9.5, the models predicted a distribution of resistance values, the location of which could vary with flow depth. Therefore measured values were tested against the median prediction. Measured resistance was best predicted by incorporating hillslope position as an additive term (or dummy variable) in the model and by developing separate equations for each Morphological Runoff Zone. The observed variation of measured resistance (e.g. Figure 9.5) demonstrates the importance of providing a distribution of predictions; however, this may result in a prohibitively large range of predictions for the more general models (e.g. Figure 8.10).

The influence of land-use was briefly examined as experiments on ploughed plots were conducted on two hillslopes. These areas demonstrated higher flow resistance than the surrounding natural surfaces. Roughness-resistance relationships for ploughed surfaces can be incorporated into models of hillslope hydrology using the same methodology described with respect to hillslope position. The resultant equation (6.15) differs from the conventional resistance equations, as the depth-dependency of resistance is captured by the depth skewness term. The conversion of mattoral to ploughed fields produces complex and temporary interactions with hillslope runoff through changes in flowpath lengths to the hillslope outlet (as can be seen in Figure 5.1). At the hillslope scale, the isochrones of Figure 7.25c demonstrate the much more tortuous flowpaths over ploughed surfaces and Figure 7.33 shows the greater depression storage of these surfaces (although the flow velocities were not much less, or greater than, at the upslope areas). While this is not a direct effect on flow resistance, it is an important influence on flood generation at the hillslope scale.

9.2.5 The Effect of Infiltration Rate

(5) To establish the effect of infiltration rate on the hydraulics of flow on hillslopes.

Infiltration rate was observed to be extremely variable, even within the plot scale. Figure 7.29 shows a large range of unsaturated hydraulic conductivity at each plot, although differences between the hillslopes can be distinguished with the marl of the Del Prado hillslope infiltrating the least, and the red schist of the Upper Nogalte hillslope infiltrating the most. Downslope trends are not consistent between hillslopes and are masked by within-plot variability. However, infiltration was consistently higher in flow concentrations than on the surrounding interrill areas, especially in soils of already high infiltration.

Antecedent moisture conditions showed no consistent effect on flow velocity and concentration. Flow experiments were repeated in dry conditions and after a 'wetting-up' event. While it might be expected that flow would be faster over a wetter soil (as infiltration rate is decreased) no such effect was consistently observed. From examination of the results presented in section 7.3.2, it could be tentatively hypothesised that antecedent soil moisture has the greatest effect on overland flow routing velocity at upslope areas where flow is more diffuse and is in greater contact with the soil (with a lower volumetric hydraulic radius). However, this effect was only observed at two of the three hillslopes examined.

Extrapolating these results up to the hillslope scale using the Morphological Runoff Zone framework, the effect of antecedent soil moisture on the distribution of travel times was examined. Few differences were observed; this was mainly a consequence of the inconsistent effect of soil wetness on flow velocity observed at the plot scale. At the Del Prado hillslope, the moist antecedent conditions produced an especially peaked distribution of travel times which, as Chapter 3 suggested, is more likely to produce flashy runoff. This represents a basic example of the interaction between flow velocity, patterns of rill

networks and flowpath length which will also interact with rainfall intensity (discussed in section 9.2.6).

Finally, section 7.4 demonstrated that flow resistance can vary over time, especially as a surface hydrological connection becomes established. The suggestion here is that since overland flows have been observed to be intermittent and variable in time and space (e.g. Emmett, 1970), several different and quite separate processes may be contributing to the overall measured flow resistance. Our ability to predict flow resistance is currently hampered by our limited quantitative understanding of processes contributing to resistance (Bathurst, 1993; section 2.5.1). The suction forces resulting from infiltration and turbulence from depression storage would reduce the velocity of an advancing flow connection. While these are conceptualised as distinct processes, they could contribute to the flow resistance as measured in this study. It was observed that once connections were well-established, resistance dropped by around 80% (although this value depends on the velocity coefficient used in measuring dye flows; p.251), yet comparison of infiltration rates and depression storage did not fully explain this. An alternative explanation is the turbulent and three-dimensional flow that exists as a hydrological connection is established over a surface. Such a hydrological connection becomes more efficient at transporting runoff once the connection is made. The initially higher resistance cannot be ignored, as the dynamic and intermittent nature of runoff generation inhibits the establishment of stable flow pathways for long periods (especially at upslope locations).

9.2.6 Synthesis: Conceptualising Dynamic Connectivity

(6) *To draw together this information within the framework of hydrological connectivity to develop an improved understanding of the role of topography, infiltration and the temporal structure of rainstorms for flood generation in semi-arid environments.*

While section 7.4.2 demonstrated the variability of observed infiltration rates, the role of infiltration on runoff generation has not been explicitly examined in this thesis. This is partially due to time constraints but also because of the wealth of literature that exists on

this subject (see section 8.4). It is recognised that this process is of fundamental importance for semi-arid hillslope hydrology as the spatial and temporal variability of surface infiltration rates plays a key role in the conceptual model initially outlined in Figure 3.1 and discussed further in section 8.4.

The concluding argument of this thesis is that flow resistance is the key to developing a more quantitative understanding of hydrological connectivity, particularly *dynamic* connectivity (where antecedent conditions and rainfall inputs produce nonlinear runoff responses; Bracken and Croke, 2007). This concept represents the establishment of functional hydrological connections as encouraged by runoff generation and inhibited by flow resistance. The spatial and temporal variation of both infiltration and flow resistance interact with each other and the temporal distribution of rainfall intensities through the redistribution of soil moisture and runoff to determine catchment outflow and the scale-dependency of runoff coefficients. This interaction is demonstrated for the Del Prado hillslope in Figure 9.7. Flow resistance varies with available runoff depth as determined by infiltration. In turn, infiltration rate is affected by soil moisture distribution, as determined by both rainfall inputs and horizontal moisture transfers as controlled by flow resistance. This interaction is responsible for the nonlinear runoff-response observed on natural semi-arid hillslopes, explaining not just the peak runoff but also the total runoff amount (as a consequence of the limited 'travel opportunity time' in such areas; Aryal *et al.*, 2003).

Much effort has been directed to understanding the spatial distribution and patterns of infiltration rates, yet the flow resistance element in this reciprocal partnership of runoff conveyance is frequently given only the most basic treatment (e.g. Figure 8.15a). The results of this study (objective (2) above) demonstrated the variability of flow velocity and resistance both over space and with increasing water depth. Classifying surfaces by microtopographic features accounts for part of this variability, but there remains a seemingly random component (the structure of which is worthy of further investigation) (see Dunne *et al.* (1991) and Phillips (1992) for a discussion of this with reference to infiltration rates). Crucially, resistance was observed to be depth-dependent as roughness elements are progressively inundated. This dependency provides the final connection to complete the loop in Figure 9.7.

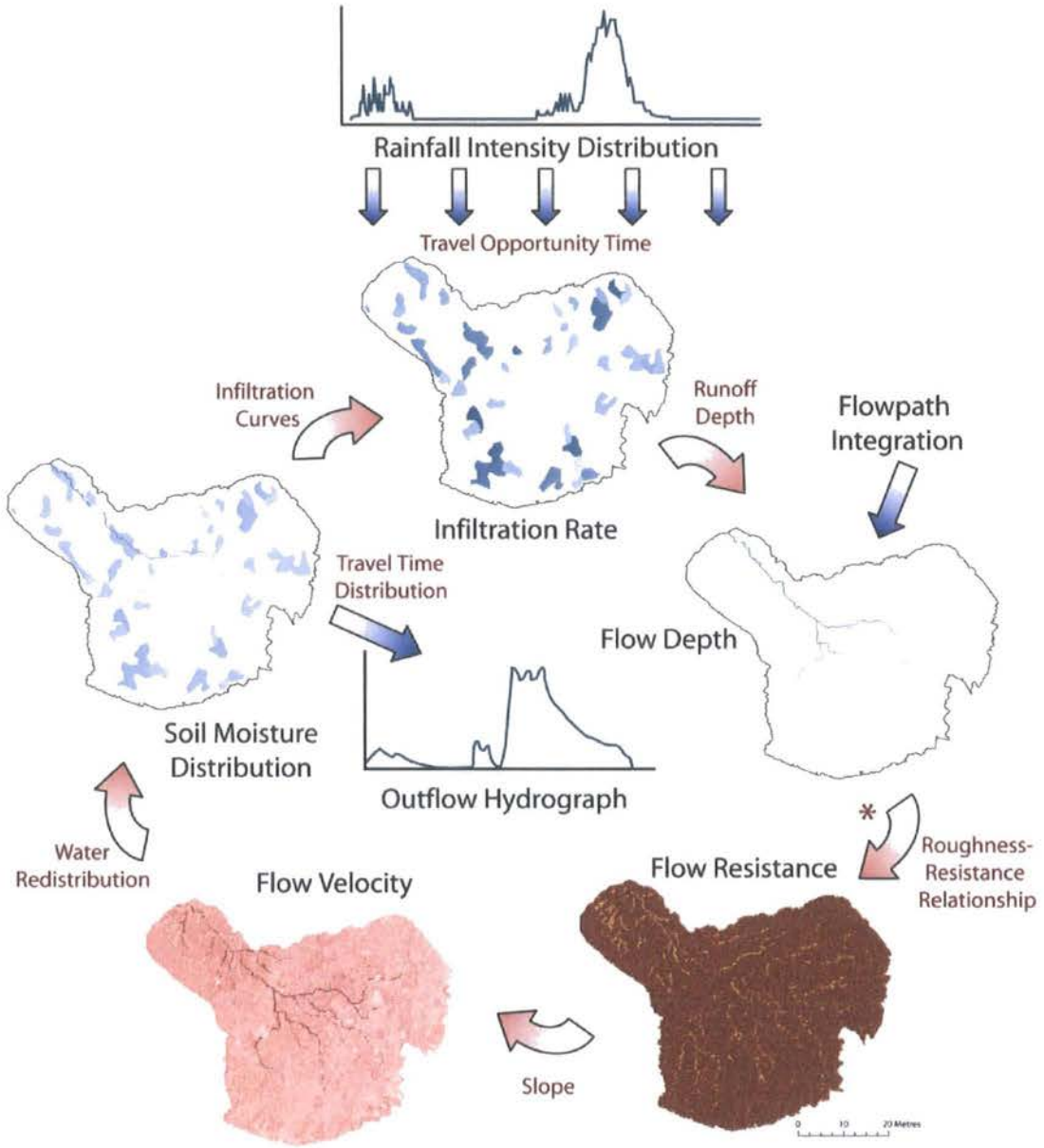

Figure 9.7. Summary of the conceptual model of dynamic hydrological connectivity over a semi-arid hillslope outlined in this section. Flow resistance and infiltration parameters interact through the redistribution of soil moisture and runoff to determine the runoff response to any given rainstorm. The feedback loop is completed by adding a representation of the changing flow resistance with depth (marked *).

Further examination of the variability of flow resistance and its full representation in distributed models of hillslope hydrology is essential to test this conceptual model of semi-arid flood generation. This will ultimately improve our ability to predict the arrival time and size of initial flood waves (e.g. Figure 1.2) and also total flood volumes in arid and semi-arid catchments.

9.3 Research Conclusions

Resistance to overland flows is much more complex than has been previously recognised. The application of theories originally developed in studies of pipe or fluvial hydraulics is inappropriate as a consequence of the more complex flow characteristics displayed by overland flows. On such complex soil surfaces, representing surface roughness with a single measure becomes a subjective process, as roughness can be characterised in a variety of ways. High-resolution field measurements enable the development of new equations to predict flow resistance from surface roughness more suited to the study of overland flows.

At the hillslope scale flow convergence encourages the development of emergent properties such as the incision of rills. These can be represented by a classification of hillslope surfaces into Morphological Runoff Zones that display characteristic microtopography. Such a classification is especially relevant in the prediction of flow resistance, as it might be expected that similar topographic forms demonstrate comparable resistance-depth relationships.

The observation that overland flow resistance varies both over space and with increasing flow depth has major implications for understanding semi-arid flood generation as it completes a crucial interaction between rainfall, infiltration and flow resistance that determines the development of connected flowpaths over a catchment area. This dynamic interaction provides a conceptual framework with which to explain the highly nonlinear hydrological response of semi-arid areas to runoff events. Further understanding of this interaction could have practical implications for catchment management, where key areas can be identified to prioritise land management decisions and focus efforts to artificially alter either infiltration rates or flow resistance. This is especially important in semi-arid

areas where overland flows control the redistribution of water, soil, nutrients and pollution through the landscape. In such nonlinear systems, small, carefully targeted changes can yield much larger results as the effects are propagated downstream. This reduces the reliance upon large and costly flood alleviation schemes targeted further downstream which only come into operation once floodwaters have reached a substantial velocity and eroding capacity with potentially devastating consequences.

REFERENCES

Aberle, J. and Smart, G.M. 2003. The influence of roughness structure on flow resistance on steep slopes. *Journal of Hydraulic Research* 41, 259–269.

Abrahams, A.D. 1984. Channel networks: a geomorphological perspective. *Water Resources Research* 20, 161–188.

Abrahams, A.D. 1998. Discussion: Macroscale surface roughness and frictional resistance in overland flow. *Earth Surface Processes and Landforms* 23, 857–859.

Abrahams, A.D. and Parsons, A.J. 1990. Determining the mean depth of overland flow in field studies of flow hydraulics. *Water Resources Research* 26, 501–503.

Abrahams, A.D. and Parsons, A.J. 1991. Resistance to overland flow on desert pavement and its implications for sediment transport modeling. *Water Resources Research* 27, 1827–1836.

Abrahams, A.D., Li, G. and Parsons, A.J. 1996. Rill hydraulics on a semi-arid hillslope, southern Arizona. *Earth Surface Processes and Landforms* 21, 35–47.

Abrahams, A.D., Parsons, A.J., and Hirsch, P. 1992. Field and laboratory studies of resistance to overland flow on semi-arid hillslopes, southern Arizona. In Parsons, A.J. and Abrahams, A.D. (eds.) *Overland Flow*, UCL Press, London, 1–24.

Abrahams, A. D., Parsons, A. J. and Luk, S.-H. 1986a. Resistance to overland flow on desert hillslopes. *Journal of Hydrology* 88, 343–363.

Abrahams, A.D., Parsons, A.J. and Luk, S.-H., 1986b. Field measurement of the velocity of overland flow using dye tracing. *Earth Surface Processes and Landforms* 11, 653–657.

Abrahams, A.D., Parsons, A.J. and Luk, S-H. 1989. Distribution of depth of overland flow on desert hillslopes and its implications for modelling soil erosion. *Journal of Hydrology* 106, 177–184.

Abrahams, A. D., Parsons, A. J. and Wainwright, J. 1994. Resistance to overland flow on semiarid grassland and shrubland hillslopes,Walnut Gulch, southern Arizona. *Journal of Hydrology* 156, 431–446.

Abrahams, A.D., Parsons, A.J. and Wainwright, J. 1995. Effects of vegetation change on interrill runoff and erosion, Walnut Gulch, southern Arizona. *Geomorphology* 13, 37–48.

Adrian, R.J. 1991. Particle-imaging techniques for experimental fluid mechanics. *Annual Review of Fluid Mechanics* 23, 261–304.

Allmaras, R., Burwell, R., Larson, W. and Holt, R. 1966. Total porosity and random roughness of the interrow zone as influenced by tillage. *United States Department of Agriculture Conservation Research Report* 7, 1-14.

Alonso-Sarría, F., López-Bermúdez, F. and Conesa-Garcia, C. 2002. Synoptic conditions producing extreme rainfall events along the Mediterranean coast of the Iberian Peninsula. In Bull, L.J. and Kirkby, M.J. (eds), *Dryland Rivers: Hydrology and Geomorphology of Semi-Arid Channels*, Wiley & Sons, Chichester, 351–370.

Ambroise, B. 2004. Variable 'active' versus 'contributing' areas or periods: a necessary distinction. *Hydrological Processes* 18, 1149–1155.

Aryal, S.K., Mein, R.G. and O'Loughlin, E.M. 2003. The concept of effective length in hillslopes: assessing the influence of climate and topography on the contributing area of catchments. *Hydrological Processes* 17, 131–151.

Baird, A.J., Thornes, J.B. and Watts, G.P. 1992. Extending overland-flow models to problems of slope evolution and the representation of complex slope-surface topographies. In Parsons, A.J. and Abrahams, A.D. (eds.) *Overland Flow*, UCL Press, London, 199–223.

Barnes, H.H. 1967. Roughness characteristics of natural channels. *USGS Water Supply Paper* 1849.

Bartoli, F., Genevois-Gomendy, V., Royer, J.J., Niquet, S., Viver, H. & Grayson, R. 2005. A multiscale study of silty soil structure. *European Journal of Soil Science* 56, 207–223.

Bates, P.D., Anderson, M.G., Baird, L., Walling, D.E. and Simm, D. 1992. Modelling flood plain flows using a two-dimensional finite element model. *Earth Surface Processes and Landforms* 17, 575–588.

Bathurst, J.C. 1993. Flow resistance through the channel network. In Beven, K. and Kirkby, M.J. (eds.) *Channel network hydrology*, John Wiley and Sons, Chichester, 69–98.

Bazin, H. 1897. Étude d'une nouvelle formule pour calculer le débit des canaux découverts [A new formula for the calculation of discharge in open channels]. *Annals des ponts et chaussées, Mémoire No.* 41, 14 (7), 20–70.

Becker, A. and Braun, P. 1999. Disaggregation, aggregation and spatial scaling in hydrological modelling. *Journal of Hydrology* 217, 239–252.

Benito, G., Rico, M., Sánchez-Moya, Y., Sopeña, A. and Thorndycraft, V.R. 2002. Magnitude and frequency of palaeofloods in the Upper Guadalentín Basin (SE-Spain) during the last 1000 years. EGS XXVII General Assembly, Nice, 21-26 April 2002, abstract #2345. Date Accessed 17/12/2007. http://adsabs.harvard.edu/cgi-bin/nph-bib_query?bibcode=2002EGSGA..27.2345B&db_key=PHY&data_type=HTML&format .

Bergkamp, G. 1998. A hierarchical view of the interactions of runoff and infiltration with vegetation and microtopography in semiarid shrublands. *Catena* 33, 201–220.

Bergkamp, G., Cammeraat, L.H., and Mertinez-Fernandez, J. 1996. Water movement and vegetation patterns on shrubland and an abandoned field in two desertification threatened areas in Spain. *Earth Surface Processes and Landforms* 21, 1073–1090.

Berk, R.A. 2004. *Regression Analysis: a constructive critique*. Sage, London.

Berndtsson, R. and Larson, M. 1987. Spatial variability of infiltration in a semi-arid environment. *Journal of Hydrology* 90, 117–133.

Bernoulli, D. 1738. *Hydrodynamica, Sive de Viribus et Motibus Fluidorum Commentarii*. Argentorati, Strasbourg.

Bethoux, J.P., Gentili, B., Morin, P., Nicolas, E., Pierre, C. and Ruiz-Pino, D. 1999. The Mediterranean Sea: a miniature ocean for climatic and environmental studies and a key for the functioning of the North Atlantic. *Progress in Oceanography* 44, 131–146.

Beven, K.J. 2001. *Rainfall-Runoff Modelling: The Primer*. John Wiley & Sons, Chichester.

Beven, K.J. and Kirkby, M.J. 1979. A physically based variable contributing area model of catchment hydrology. *Hydrological Sciences Bulletin* 24, 43–69.

Biron, P.M., Lane, S.N., Roy, A.G., Bradbrook, K.F. and Richards, K.S. 1998. Sensitivity of bed shear stress estimated from vertical velocity profiles: the problem of sampling resolution. *Earth Surface Processes and Landforms* 23, 133–139.

Bland, J. M. and D. G. Altman. 1986. Statistical methods for assessing agreement between two methods of clinical measurement. *Lancet I*, 307–310.

Blasius, H. 1913. Das Ähnlichkeitsgesetz bei Reibungsvorgängen in Flüssigkeiten, *Forschungs-Arbeit des Ingenieur-Wesens* 131.

Bochet, E., Rubio, J.L. and Poesen, J. 1998. Relative efficiency of three representative matorral species in reducing water erosion at the microscale in a semi-arid climate (Valencia, Spain). *Geomorphology* 23, 139–150.

Boehler, W. and Marbs, A. 2005. Investigating laser scanner accuracy. http://scanning.fh-mainz.de/scannertest/results300305.pdf Date Accessed 20/11/2007. Institute for Spatial Information and Surveying Technology, Mainz, Germany.

Boiffin, J. 1984. Structural degradation of the soil surface by the action of rainfall. [In French]. Ph.D. Dissertation. Paris Institut National d'Agronomie Paris-Grignon.

Bracken, L.J. and Croke, J. 2007. The concept of connectivity and its application in geomorphology. *Hydrological Processes* 21, 1749–1763.

Bracken, L.J. and Kirkby, M.J. 2005. Differences in hillslope runoff and sediment transport rates within two semi-arid catchments in southeast Spain. *Geomorphology* 68, 183–200.

Bracken, L.J., Cox, N.J. and Shannon, J. 2008. The relationship between rainfall inputs and flood generation in south-east Spain. *Hydrological Processes* 22, 683–696.

Brahms, A. 1754. Anfangsgründe der Deich- und Wasserbaukunst (Elements of Dam and Hydraulic Engineering), Aurich, Germany, vol I, p.105.

Bray, D.I. 1982. Flow resistance in gravel-bed rivers. In Hey, R.D., Bathurst, J.C. and Thorne, C.R. (eds). *Gravel-Bed Rivers*. Wiley, Chichester, 109–133.

Brazier, R.E., Parsons, A.J., Wainwright, J., Powell, D.M. and Schlesinger, W.H. 2007. Upscaling understanding of nitrogen dynamics associated with overland flow in a semi-arid environment. *Biogeochemistry* 82, 265–278.

Brierley, G., Fryirs, K. and Jain, V. 2006. Landscape connectivity: the geographic basis of geomorphic applications. *Area* 38, 165–174.

Bromley, J., Brouwer, J., Barker, A.P., Gaze, S.R. and Valentine, C. 1997. The role of surface water redistribution in an area of patterned vegetation in a semi-arid environment, south-west Niger. *Journal of Hydrology* 198, 1–29.

Brown, G.O. 2002. The history of the Darcy-Weisbach equation for pipe flow resistance. *Environmental and Water Resources History* 38(7), 34–43.

Bryan, R.B. and Yair, A. 1982. Perspectives on studies of badland geomorphology. In Bryan, R.B. and Yair, A. (eds.) *Badland Geomorphology and Piping*, Geobooks, Norwich, 1–12.

Bull, L.J. and Kirkby, M.J. 2002. Dryland river characteristics and concepts. In Bull, L.J. and Kirkby, M.J. (eds.) *Dryland Rivers: hydrology and geomorphology of semi-arid channels*. John Wiley & Sons, Chichester, 3–15.

Bull, L.J., Kirkby, M.J., Shannon, J. and Dunsford, H.D. 2003. Predicting Hydrologically Similar Surfaces (HYSS) in semi-arid environments. *Advances in Environmental Monitoring and Modelling* 1 (2), 1–26.

Bull, L.J., Kirkby, M.J., Shannon, J. and Hooke, J.M. 1999. The impact of rainstorms on floods in ephemeral channels in SE Spain. *Catena* 38, 191–209.

Bunte, K. and Poesen, J. 1994. Effects of rock fragment size and cover on overland flow hydraulics, local turbulence and sediment yield on an erodible surface. *Earth Surface Processes and Landforms* 19, 115–135.

Burrough, P.A. 1983. Multiscale sources of spatial variation in soil. I. The application of fractal concepts to nested levels of soil variation. *Journal of Soil Science* 34, 577–597.

Butler, J.B., Lane, S.N. and Chandler, J.H. 2001. Characterization of the structure of river-bed gravels using two-dimensional fractal analysis. *Mathematical Geology* 33, 301–330.

Cammeraat, E.L.H. 2004. Scale dependent thresholds in hydrological and erosion response of a semi-arid catchment in southeast Spain. *Agriculture, Ecosystems & Environment* 104, 317–332.

Cantón, Y., Domingo, F., Solé-Benet, A., and Puigdefábregas, J. 2002. Influence of soil-surface types on the overall runoff of the Tabernas badlands (south-east Spain); field data and model approaches. *Hydrological Processes* 16, 2621–2643.

Cantón, Y., Solé-Benet, A. and Domingo, F. 2004. Temporal and spatial patterns of soil moisture in semiarid badlands of SE Spain. *Journal of Hydrology* 285, 199–214.

Carsel, R.F. and Parish, R.S. 1988. Developing joint probability distributions of soil water retention characteristics. *Water Resources Research* 24, 755–769.

Casenave, A. and Valentin, C. 1992. A runoff capability classification system based on surface features criteria in semi-arid areas of West Africa. *Journal of Hydrology* 130, 231–249.

Chen, X., Ender, P., Mitchell, M. and Wells, C. 2003. *Regression with Stata*, from http://www.ats.ucla.edu/stat/stata/webbooks/reg/default.htm Date Accessed: 27/03/2008.

Chézy, A. de. 1775. Memoire sur la vitesse de l'eau conduite dans une régole. MS reprinted in *Annales des ponts et chaussées*, 60, 1921.

Chow, V.T. 1959. *Open-Channel Hydraulics*. McGraw-Hill, New York.

Cleveland, W. S. and R. McGill. 1984. The many faces of a scatterplot. *Journal of the American Statistical Association* 79, 809–822.

Clifford, N.J., Robert, A. and Richards, K.S. 1992. Estimation of flow resistance in gravel-bedded rivers; a physical explanation of the multiplier of roughness length. *Earth Surface Processes and Landforms* 17, 2, 111–126.

Colebrook, C.F. 1939. Turbulent flow in pipes with particular reference to the transition region between the smooth and rough pipe laws. *Proceedings of the Institution of Civil Engineers* 12, 393–422.

Colebrook, C.F. and White, C. M. 1937. Experiments with fluid-friction in roughened pipes. *Proceedings of the Royal Society of London A* 161, 367–381.

Connelly, J.S., Schultz, M.P. and Flack, K.A. 2006. Velocity-defect scaling for turbulent boundary layers with a range of relative roughness. *Experiments in Fluids* 40, 188–195.

Cook, R.D. 1977. Detection of influential observations in linear regression. *Technometrics* 19, 15–18.

Cooper, J.R., Tait, S.J. and Horoshenkov, K.V. 2006. Determining hydraulic resistance in gravel-bed rivers from the dynamics of their water surfaces. *Earth Surface Processes and Landforms* 31, 1839–48.

Corte-Real, J., Sorani, R. and Conte, M. 1998. Climate change. In Mairota, P., Thornes, J. and Geeson, N. (eds.) *Atlas of Mediterranean Environment in Europe: The desertification context*, Wiley, Chichester, 34–37.

Costa, J.E. 1987. A comparison of the largest rainfall-runoff floods in the United States and the People's Republic of China and the world. *Journal of Hydrology* 96, 101–115.

Cox, N.J. 1978. Hillslope profile analysis. *Area* 10, 131–133.

Cox, N.J. 1992. Precipitation statistics for geomorphologists: variations on a theme by Frank Ahnert. *Catena Supplement* 23, 189–212.

Cox, N.J. 2005. Speaking Stata: Smoothing in various directions. *The Stata Journal* 5, 574–593.

Cox, N.J. 2006. Assessing agreement of measurements and predictions in geomorphology. *Geomorphology* 72, 332–346.

Cox, N.J. 2007a. Kernel estimation as a basic tool for geomorphological data analysis. *Earth Surface Processes & Landforms* 32, 1902–1912.

Cox, N.J. 2007b. Identifying spells. *The Stata Journal* 7, 249–265.

Croke, J. and Mockler, S. 2001. Gully initiation and road-to-stream linkage in a forested catchment, south eastern Australia. *Earth Surface Processes & Landforms* 26, 205–217.

Crowe, P.R. 1933. The analysis of rainfall probability: a graphical method and its application to European data. *Scottish Geographical Magazine* 49, 73–91.

Currence, H.D. and Lovely, W.G. 1970. The analysis of soil surface roughness. *Transactions of the American Society of Agricultural Engineers* 13, 710–714.

D'Agostino, R.B., Balanger, A. and D'Agostino, Jr., R.B. 1990. A suggestion for using powerful and informative tests of normality. *American Statistician* 44, 316–321.

D'Odorico, P. and Rigon, R. 2003. Hillslope and channel contributions to the hydrologic response. *Water Resources Research* 39, 1113–1121.

Darboux, F., Davy, P., Gascuel-Odoux, C. and Huang, C. 2001. Evolution of soil surface roughness and flowpath connectivity in overland flow experiments. *Catena* 46, 125–139.

Darcy, H. 1857. *Recherches Expérimentales Relatives au Mouvement de L'Eau dans les Tuyaux* [Experimental Research Relating to the Movement of Water in Pipes]. 2 volumes, Paris: Mallet-Bachelier. 268 pages and atlas.

De Roo, A.P.J., Wesseling, C.G., Ritsema, C.J. 1996. LISEM: a single event physically based hydrological and soil erosion model for drainage basins: theory, input and output. *Hydrological Processes* 10, 1107–1117.

Dingman, S.L. and Sharma, K.P. 1997. Statistical development and validation of discharge equations for natural channels. *Journal of Hydrology* 199, 13–35.

Dooge, J. 1959. A general theory of the unit hydrograph. *Journal of Geophysical Research* 64, 241–256.

Dunkerley, D. 2001. Estimating the mean speed of laminar overland flow using dye injection - uncertainty on rough surfaces. *Earth Surface Processes and Landforms* 26, 363–374.

Dunkerley, D. 2002. Volumetric displacement of flow depth by obstacles, and the determination of friction factors in shallow overland flows. *Earth Surface Processes and Landforms* 27, 165–175.

Dunkerley, D. 2003. An optical tachometer for short-path measurement of flow speeds in shallow overland flows: improved alternative to dye timing. *Earth Surface Processes and Landforms* 28, 777–786.

Dunkerley, D. 2004. Flow threads in surface run-off: implications for the assessment of flow properties and friction coefficients in soil erosion and hydraulics investigations. *Earth Surface Processes & Landforms* 29, 1011–1026.

Dunne, T. and Dietrich, W. E. 1980. Experimental study of Horton overland flow on tropical hillslopes, 2. Hydraulic characteristics and hillslope hydrographs. *Zeitschrift für Geomorphologie, SupplementBand* 35, 60–80.

Dunne, T., Whipple, K.X. and Aubry, B.F. 1995. Microtopography of hillslopes and initiation of channels by Horton overland flow. In Costa, J.E., Miller, A.J., Potter, K.W. and Wilcock, P.R. (eds.), *Natural and anthropogenic influences in fluvial geomorphology: the Wolman Volume*, Geophysical Monograph 89, American Geophysical Union, Washington, DC, 27–44.

Dunne, T., Zhang, W. and Aubry, B.F. 1991. Effects of rainfall, vegetation and microtopography on infiltration and runoff. *Water Resources Research* 27, 2271–2285.

Emmett, W. W. 1970. *The hydraulics of overland flow on hillslopes*. U.S. Geological Survey Professional Paper 662–A, 68 pp.

Emmett, W.W. 1978. Overland flow. In Kirkby, M.J. (ed.) *Hillslope Hydrology*. John Wiley, Chichester, 145–176.

Engman, E.T. 1986. Roughness coefficients for routing surface runoff. *Journal of Irrigation and Drainage Engineering* 112, 39–53.

Ergenzinger, P. 1992. Riverbed adjustments in a step-pool system: Lainbach, Upper Bavaria. In Billi, P., Hey, R.D., Thorne, C.R. and Tacconi, P. (eds.) *Dynamics of Gravel-bed Rivers*, John Wiley & Sons, Chichester, 415–430.

Ferguson, R.I. 2007. Flow resistance equations for gravel- and boulder-bed streams. *Water Resources Research* 43, W05427, doi: 10.1029/2006WR005422.

Ferguson, R. I. and Ashworth, P. J. 1992. Spatial patterns of bedload transport and channel change in braided and near-braided rivers. In Billi, P., Hey, R. D., Thorne, C. R. and Tacconi, P. (eds). *Dynamics of gravel-bed rivers*. Wiley, Chichester, 477–496.

Ferro, V. and Baiamonte, G. 1994. Flow velocity profiles in gravel-bed rivers. *Journal of Hydraulic Engineering* 120, 1, 60–80.

Fischenich, C. 2000. Robert Manning (A Historical Perspective), *EMRRP Technical Notes Collection* (ERDC TN-EMRRP-SR-10), Vicksburg, MS. U.S. Army Engineer Research and Development Center, www.wes.army.mil/el/emrrp.

Fitzjohn, C., Ternan, J.L. and Williams, A.G. 1998. Soil moisture variability in a semi-arid gully catchment: implications for runoff and erosion control. *Catena* 32, 55–70.

Flügel, W.A., 1995. Delineating hydrological response units by geographical information system analyses for regional hydrological modelling using PRMS/MMS in the drainage basin of the river Brol, Germany. *Hydrological Processes* 9, 423–436.

Foster, G.R., Huggins, L.F. and Meyer, L.D. 1984. A laboratory study of rill hydraulics: I Velocity relationships. *Transactions of the American Society of Agricultural Engineers* 27, 790–796.

Foster, G.R. and Meyer, L.D. 1975. Mathematical simulation of upland erosion by fundamental erosion mechanics. In *Present and prospective technology for predicting sediment yields and sources*. United States Department of Agriculture, Agricultural Research Service, Paper S-40. Southern Region, New Orleans, LA, 190–207.

Freedman, D. 2005. *Statistical Models: Theory and Practice*. Cambridge, University Press.

Ganguillet, E. and Kutter, W.R. 1869. Versuch zur Aufstellung einer neuen allgemeinen Formel für die gleichförmige Bewegung das Wassers in Canälen und Flüssen [An investigation to establish a new general formula for uniform flow of water in canals and rivers]. *Zeitschrift des Österreichischen Ingenieur- und Architekten Vereines*, 21 (1), 6–25; 21 (2-3), 46–59.

Gauckler, P. 1868. Du mouvement de l'eau dans les conduites. *Annales des Ponts et Chaussées* 15, 229-281.

Gessler, J. 1990. Friction factor of armoured river beds. *Journal of Hydraulic Engineering* 116, 4, 531–543.

Gilley, J.E. and Finkner, S.C. 1991. Hydraulic roughness coefficients as affected by random roughness. *Transactions of the American Society of Agricultural Engineers* 34, 897–903.

Gilley, J.E., Flanagan, D., Kottwitz, E.R. and Weltz, M.A. 1992. Darcy-Weisbach roughness coefficients for overland flow. In Parsons, A.J. and Abrahams, A.D. (eds.) *Overland Flow*, UCL Press, London, 25–52.

Gilley, J.E., Kottwitz, E.R. and Simanton, J.R. 1990. Hydraulic characteristics of rills. *Transactions of the American Society of Agricultural Engineers* 33, 1900–1906.

Gilley, J.E. and Weltz, M.A. 1995. Hydraulics of overland flow. USDA-Water Erosion Prediction Project Hillslope Profile and Watershed Model Documentation NSERL Report #10, July 1995.

Giménez, R. and Govers, G. 2001. Interaction between bed roughness and flow hydraulics in eroding rills. *Water Resources Research* 37, 3, 791–799.

Giménez, R., Planchon, O., Silvera, N. and Govers, G. 2004. Longitudinal velocity patterns and bed morphology interaction in a rill. *Earth Surface Processes and Landforms* 29, 105–114.

Gómez, J.A. and Nearing, M.A. 2005. Runoff and sediment losses from rough and smooth soil surfaces in a laboratory experiment. *Catena* 59, 253–266.

Gomez-Plaza, A., Martínez-Mena, M., Albaladejo, J. and Castillo, V.M. 2001. Factors regulating spatial distribution of soil water content in small semi-arid catchments. *Journal of Hydrology* 253, 211–226.

Goodrich, D.C., Lane, L.J., Shillito, R.M., Miller, S.N., Syed, K.H. and Woolhiser, D.A. 1997. Linearity of basin response as a function of scale in a semiarid watershed. *Water Resources Research* 33, 2951–2965.

Gordon, N.D., McMahon, T.A. and Finlayson, B.L. 2004. *Stream Hydrology: An introduction for ecologists*. 2nd Edn. Wiley, Chichester.

Govers, G. 1992. Relationship between discharge, velocity and flow area for rills eroding loose, non-layered materials. *Earth Surface Processes and Landforms* 17, 515–528.

Govers, G., Takken, I. and Helming, K. 2000. Soil roughness and overland flow. *Agronomie* 20, 131–146.

Graf, W.H. 1998. *Fluvial Hydraulics*. John Wiley and Sons, Chichester.

Grant, G.E. 1997. Critical flow constrains flow hydraulics in mobile-bed streams: A new hypothesis. *Water Resources Research* 33, 2, 349–358.

Grayson, R.B., Blöschl, G., Western, A.W. and McMahon, T.A. 2002. Advances in the use of observed spatial patterns of catchment hydrological response. *Advances in Water Resources* 25, 1313–1334.

Green, W. and Ampt, G. 1911. Studies in soil physics. Part I. The flow of air and water through soils. *Journal of Agricultural Science* 4, 1–24.

Gumbel, E.J. 1958. *Statistics of Extremes*. Columbia University Press, New York.

Hagen, G.H.L. 1839. Ueber die Bewegung des Wassers in engen cylindrischen Rohren (Movement of water in a narrow cylindrical tube). *Annalen der Physik und Chemie (Leipzig)*, 46, 423–442.

Hagen, G.W. 1881. Neuere Beobachtung über die gleichförmige Bewegung des Wassers. *Zeitschrift für Bauwesen* 31, 221-223.

Hairsine, P.B. and Rose, C.W. 1992. Modeling water erosion due to overland flow using physical principles 1. Sheet flow. *Water Resources Research 28*, 237–243.

Hanke, K., Grussenmeyer, P., Grimm-Pitzinger, A. and Weinold, T. 2006. First experiences with the Trimble GX Scanner. ISPRS Communication V Symposium, Dresden, Sept. 25-27, Germany. *International Archives of Photogrammetry and Remote Sensing and Spatial Information Sciences*, Vol. XXXVI, Part 5, 6p.

Hansen, B. 2000. Estimation of surface runoff and water-covered area during filling of surface microrelief depressions. *Hydrological Processes* 14, 1235–1243.

Hansen, B., Schjønning, P. and Sibbesen, E. 1999. Roughness indices for estimation of depression storage capacity of tilled soil surfaces. *Soil & Tillage Research* 52, 103–111.

Harrell, F.E. 2001. *Regression Modeling Strategies*. Springer-Verlag, New York.

Hassan, M.A., Church, M. and Schick, A.P. 1991. Distance of movement of coarse particles in gravel bed streams. *Water Resources Research* 27,503–511.

Helming, K., Römkens, M.J.M. and Prasad, S.N. 1998. Surface roughness related processes of runoff and soil loss: a flume study. *Soil Science Society of America Journal* 62, 243–250.

Helsel, D.R. and Hirsch, R.M. 1992. *Statistical Methods in Water Resources*. Elsevier, Amsterdam.

Henderson, F.M. 1966. *Open Channel Flow*. Macmillan, New York.

Herschel, C. 1897. On the origin of the Chézy formula. *Journal of the Association of Engineering Societies*, 18, 363–369.

Hessel, R., Jetten, V. and Guanghui, Z. 2003. Estimating Manning's *n* for steep slopes. *Catena* 54, 77–91.

Hewlett, J.D. and Hibbert, A.R. 1967. Factors affecting the response of small watersheds to precipitation in humid areas. In Sopper, W.E. and Lull, H.W. (eds.) *Forest Hydrology*, Pergamon Press, New York, 275–290.

Hey, R.D. 1979. Flow resistance in gravel-bed rivers. *Journal of the Hydraulics Division, American Society of Civil Engineers* 105, 365–379.

Hey, R.D. and Thorne, C.R. 1984. Flow processes and river channel morphology. In: Burt, T.P. and Walling, D.E. (eds.) *Catchment experiments in fluvial geomorphology*, GeoBooks, Norwich, 489–514.

Hirsch, P. 1996. *Hydraulic Resistance to Overland Flow on Semiarid Hillslopes: A Physical Simulation*, unpublished Ph.D. dissertation, State University of New York at Buffalo, 154pp.

Holden, J., Kirkby, M.J., Lane, S.N., Milledge, D.G., Brookes, C.J., Holden, V. and McDonald, A. 2008. Overland flow velocity and roughness properties in peatlands. *Water Resources Research* 44, W06415, doi: 10.1029/2007WR006052.

Holland, K.T., Puleo, J.A. and Kooney, T.N. 2001. Quantification of swash flows using video-based particle image velocimetry. *Coastal Engineering* 44, 65–77.

Hooke, J.M. and Mant, J.M. 2000. Geomorphological impacts of a flood event on ephemeral channels in SE Spain. *Geomorphology* 34, 163–180.

Horton, R.E. 1945. Erosional development of streams and their drainage basins: hydrophysical approach to quantitative morphology. *Bulletin of the Geological Society of America* 56, 275–370.

Horton, R.E., Leach, H.R. and Van Vliet, R. 1934. Laminar sheet flow. *Transactions of the American Geophysical Union* 2, 393–404.

Hu, S. and Abrahams, A.D. 2006. Partitioning resistance to overland flow on rough mobile beds. *Earth Surface Processes and Landforms* 31, 1280–1291.

Huang, C. and Bradford, J.M. 1990. Portable laser scanner for measuring soil surface roughness. *Transactions of the American Society of Agricultural Engineers* 54, 1402–1406.

Huang, C. and Bradford, J.M. 1993. Applications of a laser scanner to quantify properties of soil crusts. In Poesen, J.W.A. and Nearing, M.A. (eds.) *Soil Surface Sealing and Crusting*, Catena Supplement 24, 129–139.

Huckleberry, G. 1994. Contrasting channel response to floods on the middle Gila River, Arizona. *Geology* 22, 1083–1086.

Jarrett, R.D. 1984. Hydraulics of high-gradient rivers. *Journal of Hydraulic Engineering* 110, 11, 1519–1539.

Jester, W. and Klik, A. 2005. Soil surface roughness measurement – methods, applicability, and surface representation. *Catena* 64, 174–192.

Jetten, V., De Roo, A. and Guérif, J. 1998. Sensitivity of the model LISEM to variables related to agriculture. In Boardman, J. and Favis-Mortlock, D. (eds.), *Modelling soil erosion by water*, NATO ASI Series, Springer, Berlin, 339–349.

Julien, P.Y. 2002. *River Mechanics*. Cambridge University Press, Cambridge.

Kamphorst, E.C., Jetten, V., Guérif, J., Pitkänen, J., Iversen, B.V., Douglas, J.T. and Paz, A. 2000. Predicting depressional storage from soil surface roughness. *Soil Science Society of America Journal* 64, 1749–1758.

Kármán, T. von. 1930. Mechanische Aehnlichkeit und Turbulenz. *Proceedings of the Third International Congress for Applied Mechanics*. Stockholm. Vol. 1, 85–92.

Kennedy, P. 1998. *A Guide to Econometrics* (4th ed.). Blackwell, Oxford.

Kersten, T., Sternberg, H., Mechelke, K. and Acevedo Prado, C., 2004. Terrestrial laser scanning system MENSI GS 100/GS 200 – accuracy tests, experiences and projects at the Hamburg University of Applied Sciences. *Panoramic Photogrammetry Workshop* 2004, University of Stuttgart, and ISPRS WG V/1. February 19 – 22.

http://www.commission5.isprs.org/wg1/workshop_pano/papers/PanoWS_Dresden2004_Kersten.pdf.

Kersten, T., Sternberg, H. and Mechelke, K., 2005. Investigations into the accuracy behaviour of the terrestrial laser scanning system MENSI GS 100. In Grün, A. and Kahmen, H. (eds.). *Proceedings of Optical 3-D Measurement Techniques VII*, Vienna, Austria, 122 – 131.

Keulegan, G.H. 1938. Laws of turbulent flow in open channels, paper RP1151. *Journal of Research, U.S. National Bureau of Standards* 21, 707–741.

King, H. W. 1918. *Handbook of hydraulics for the solution of hydraulic problems* (1st Edn.) McGraw-Hill, New York.

Kirkby, M.J. 1975. Hydrograph modelling strategies. In Peel, R., Chisholm, M. and Haggett, P. (eds.) *Processes in Physical and Human Geography*, Heinemann, London, 69–90.

Kirkby, M.J. 1985. Hillslope hydrology. In Anderson, M.G. and Burt, T.P. (eds.) *Hydrological Forecasting*, Wiley, Chichester, 3–37.

Kirkby, M.J. 1988. Hillslope runoff processes and models. *Journal of Hydrology* 100, 315–339.

Kirkby, M.J. 2001. Modelling the interactions between soil surface properties and water erosion. *Catena* 46, 89–102.

Kirkby, M.J., Bracken, L.J. and Reaney, S. 2002. The influence of land use, soils, and topography on the delivery of hillslope runoff to channels in SE Spain. *Earth Surface Processes and Landforms* 27, 1457–1473.

Kirkby, M.J., Bracken, L.J. and Shannon, J. 2005. The influence of rainfall distribution and morphological factors on runoff delivery from dryland catchments in SE Spain. *Catena* 62, 136–156.

Köppen, W. 1936. Das geographische System der Klimate. In Köppen, W. and Geiger, R. (eds.) *Handbuch der Klimatologie*, Vol 1, Part C, Gebrüder Borntraeger, Berlin, p46.

Kuhn, N. and Yair, A. 2004. Spatial distribution of surface conditions and runoff generation in small arid watersheds, Zin Valley Badlands, Israel. *Geomorphology* 57, 183–200.

Kuipers, H. 1957. A relief meter for soil cultivation studies. *Netherlands Journal of Agricultural Science* 5, 255–262.

Lamarre, H. and Roy, A.G. 2005. Reach scale variability of turbulent flow characteristics in a gravel-bed river. *Geomorphology* 68, 95–113.

Lane, E.W. 1951. Discussion on slope discharge formulae for alluvial streams and rivers, by E.C. Schnackenberg. *Proceedings of the New Zealand Institution of Engineers* 37, 435–438.

Lane, S.N. 2005. Roughness – time for a re-evaluation? *Earth Surface Processes and Landforms* 30, 251–253.

Lane, S.N. and Ferguson, R.I. 2005. Modelling reach-scale fluvial flows. In Bates, P.D., Lane, S.N. and Ferguson, R.I. (eds.) *Computational Fluid Dynamics: applications in environmental hydraulics*. John Wiley & Sons, Chichester, 217–269.

Lasanta, T., García-Ruiz, J.M., Pérez-Rontomé, C. and Sancho-Marcén, C. 2000. Runoff and sediment yield in a semi-arid environment: the effect of land management after farmland abandonment. *Catena* 38, 265–278.

Lawless, M. and Robert, A. 2001. Scales of boundary resistance in coarse-grained channels: turbulent velocity profiles and implications. *Geomorphology* 39, 221–238.

Lawrence, D.S.L. 1997. Macroscale surface roughness and frictional resistance in overland flow. *Earth Surface Processes and Landforms* 22, 365–382.

Lawrence, D.S.L. 1998. Reply: Macroscale surface roughness and frictional resistance in overland flow. *Earth Surface Processes & Landforms* 23, 861–863.

Lawrence, D.S.L. 2000. Hydraulic resistance in overland flow during partial and marginal surface inundation: Experimental observations and modelling. *Water Resources Research* 36 (8), 2381–2393.

Lee, A.J. and Ferguson, R.I. 2002. Velocity and flow resistance in step-pool streams. *Geomorphology* 46, 59–71.

Lehmann, E.L. 2008. On the history and use of some standard statistical models. In Nolan, D. and Speed, T. (eds.) *Probability and Statistics: Essays in Honor of David A. Freedman*, vol2, IMS Collections, Beachwood, Ohio, USA, 114–126.

Lehmann, P., Hinz, C., McGrath, G., Tromp-van Meervold, H.J. and McDonnell, J.J. 2007. Rainfall threshold for hillslope outflow: an emergent property of flow pathway connectivity. *Hydrology and Earth System Sciences* 11, 1047–1063.

Leopold, L.B. 1951. Rainfall frequency: an aspect of climatic variation. *Transactions of the American Geophysical Union* 32, 347–357.

Leopold, L.B., Bagnold, R.A., Wolman, M.G. and Brush, L.M. 1960. Flow resistance in sinuous or irregular channels. *United States Geological Survey Professional Paper* 282D, 111–134.

Leopold, L.B. and Miller, J.P. 1956. Ephemeral Streams – Hydraulic Factors and their Relation to the Drainage Net. *United States Geological Survey Professional Paper* 282A. US Geological Survey, Renton, VA, 37pp.

Leopold, L.B., Wolman, M.G. and Miller, J.P. 1964. *Fluvial processes in geomorphology*. Freeman, San Francisco.

Li, G. and Abrahams, A.D. 1997. Effect of saltating sediment load on the determination of the mean velocity of overland flow. *Water Resources Research* 33, 341–347.

Li, G., Abrahams, A.D. and Atkinson, J.F. 1996. Correction factors in the determination of mean velocity of overland flow. *Earth Surface Processes and Landforms* 21, 509–515.

Li, X.Y., González, A. and Solé-Benet, A. 2005. Laboratory methods for the estimation of infiltration rate of soil crusts in the Tabernas Desert badlands. *Catena* 60, 255–266.

Lichti, D.D. and Gordon, S.J., 2004. Error Propagation in Directly Georeferenced Terrestrial Laser Scanner Point Clouds for Cultural Heritage Recording. In Proceedings of FIG Working Week. Athens, Greece, May 22 – 27. Date Accessed 17/12/2007. URL: http://www.fig.net/pub/athens/papers/wsa2/WSA2_6_Lichti_Gordon.pdf

Lichti, D.D. and Harvey, B.R., 2002. The effects of reflecting surface material properties on time-of-flight laser scanner measurements. *Symposium on Geospatial Theory, Processing and Applications, Ottawa*. On CD-ROM. 9 pages.

Lichti, D.D. and Jamtsho, S. 2006. Angular resolution of terrestrial laser scanners. *The Photogrammetric Record* 21, 141–160.

Lim, M., Petley, D.N., Rosser, N.J., Allison, R.J., Long, A.J. and Pybus, D. 2005. Combined digital photogrammetry and time-of-flight laser scanning for monitoring cliff evolution. *Photogrammetric Record* 20(110), 109–129.

Limerinos, J.T. 1970. Determination of the Manning coefficient from measured bed roughness in natural channels. *US Geological Survey Water Supply Paper* 1898-B, USGS, Washington, DC.

Lin, L. I-K. 1989. A concordance correlation coefficient to evaluate reproducibility. *Biometrics* 45, 255–268.

Lin, L. I-K. 2000. A note on the concordance correlation coefficient. *Biometrics* 56, 324–325.

Linden, D.R. and Van Doren Jr., D.M. 1986. Parameters for characterising tillage-induced soil surface roughness. *Soil Science Society of America Journal* 50, 1560–1565.

López-Bermúdez, F. Conesa-García, C. and Alonso-Sarría, F. 2002. Floods: Magnitude and frequency in ephemeral channels of the Spanish Mediterranean region. In Bull, L.J. and

Kirkby, M.J. (eds.) *Dryland Rivers: hydrology and geomorphology of semi-arid channels.* John Wiley & Sons, Chichester, 329–350.

Ludwig, J.A., Boiffin, J., Chadoeuf, J. and Auzet, A.V. 1995. Hydrological structure and erosion damage by caused by concentrated flow in cultivated catchments. *Catena* 25, 227–252.

Mann, H. B., and D. R. Whitney. 1947. On a test whether one of two random variables is stochastically larger than the other. *Annals of Mathematical Statistics* 18, 50–60.

Manning, R. 1891. On the flow of water in open channels and pipes. *Transactions of the Institution of Civil Engineers of Ireland* 20, 161–207.

Marcus, W.A. and Fonstad, M.A. 2008. Optical remote mapping of rivers at sub-meter resolutions and watershed extents. *Earth Surface Processes & Landforms* 33, 4–24.

Marcus, W.A., Roberts, K., Harvey, L. and Tackman, G. 1992. An evaluation of methods for estimating Manning's *n* in small mountain streams. *Mountain Research and Development* 12, 227–239.

Markovic, R.D. 1965. Probability functions of best fit to distributions of annual precipitation and runoff, *Hydrology Paper* No.8, Colorado State University, Fort Collins, Colorado.

Martínez-Mena, M., Albaladejo, J. and Castillo, V.M. 1998. Factors influencing surface runoff generation in a Mediterranean semi-arid environment: Chicamo watershed, SE Spain. *Hydrological Processes* 12, 741–754.

Massey, B. and Ward-Smith, J. 2001. *Mechanics of Fluids* (7th Edition). Nelson Thornes, Cheltenham.

McDonnell, J.J. 2003. Where does water go when it rains? Moving beyond the variable source area concept of rainfall-runoff response. *Hydrological Processes* 17, 1869–1875.

McDonnell, J.J., Sivapalan, M., Vache, K., Dunn, S., Grant, G., Haggerty, R., Hinz, R., Hooper, J., Kirchner, J., Roderick, M.L., Selker, J. and Weiler, M. 2007. Moving beyond heterogeneity and process complexity: a new vision for watershed hydrology. *Water Resources Research* 43, doi:10.1029/2006WR005467.

Michaelides, K. and Wainwright, J. 2002. Modelling the effects of hillslope-channel coupling on catchment hydrological response. *Earth Surface Processes and Landforms* 27, 1441–1457.

Mikhailov, G.K. 1994. Hydrodynamics and hydraulics. In Grattan-Guinness, I. (ed.) Companion encyclopaedia of the history and philosophy of the mathematical sciences, vol. 2. Routledge, London, 1006–1022.

Millikan, C.M. 1938. A critical discussion of turbulent flows in channels and circular tubes. *Proceedings of the 5th International Congress on Applied Mechanics*. Cambridge, MA, 386–392.

Moody, L. F. 1944. Friction factors for pipe flow. *Transactions of the American Society of Mechanical Engineers* 66, 671–684.

Moore, I.D. and Foster, G.R. 1990. Hydraulics of overland flow. In Anderson, M.G. and Burt, T.P. (eds.) *Process Studies in Hillslope Hydrology*. John Wiley, Chichester, 215–253.

Moore, I.D. and Larson, C.L. 1979. Estimating micro-relief surface storage from point data. *Transactions of the American Society of Agricultural Engineers* 22, 1073–1077.

Moore, I.D., Burch, G.J. and Mackenzie, D.H. 1988. Topographic effects on the distribution of surface soil water and the location of ephemeral gullies. *American Society of Agricultural Engineers* 31, 1098–1107.

Morgan, R.P.C., Quinton, J.N., Smith, R.E., Govers, G., Poesen, J.W.A., Auerswald, K., Chisci, G., Torri, D. and Styczen, M.E. 1998. The European soil erosion model (EUROSEM): a dynamic approach for predicting sediment transport from fields and small catchments. *Earth Surface Processes and Landforms*, 23, 527–544.

Morin, J. and Benyamini, Y. 1977. Rainfall infiltration into bare soils. *Water Resources Research* 13, 813–817.

Morvan, H., Knight, D., Wright, N., Tang, X. and Crossley, A. 2008. The concept of roughness in fluvial hydraulics and its formulation in 1D, 2D and 3D numerical simulation models. *Journal of Hydraulic Research* 46, 2, 191–208.

Mueller, E.N., Wainwright, J. and Parsons, A. 2007. Impact of connectivity on the modeling of overland flow within semiarid shrubland environments. *Water Resources Research* 43, W09412, doi:10.1029/2006WR005006.

Mueller, E.N., Wainwright, J. and Parsons, A.J. 2008. Spatial variability of soil and nutrient characteristics of semi-arid grasslands and shrublands, Jornada Basin, New Mexico. *Ecohydrology* 1, 3–12.

Myers, T.G. 2002. Modeling laminar sheet flow over rough surfaces. *Water Resources Research* 38 (11), 1230–1242.

Nagihara, S., Mulligan, K.R. and Xiong, W., 2004. Use of a three-dimensional laser scanner to digitally capture the topography of sand dunes in high spatial resolution. *Earth Surface Processes and Landforms* 29, 391–398.

Nanson, G.C., Tooth, S. and Knighton, A.D. 2002. A global perspective on dryland rivers: perceptions, misconceptions and distinctions. In Bull, L.J. and Kirkby, M.J. (eds.) *Dryland*

Rivers: hydrology and geomorphology of semi-arid channels. John Wiley & Sons, Chichester, 17–54.

Nash, J. 1957. The form of the instantaneous unit hydrograph. *Bulletin of the International Association of Scientific Hydrology* 45, 114–121.

Nearing, M. A., Norton, L. D., Bulgakov, D. A., Larionov, G. A., West, L. T. and Dontsova, K. M. 1997. Hydraulics and erosion in eroding rills. *Water Resources Research* 33, 865–876.

Nearing, M.A., Simanton, J.R., Norton, L.D., Bulygin, S.J. and Stone, J. 1999. Soil erosion by surface water flow on a stony, semiarid hillslope. *Earth Surface Processes & Landforms* 24, 677–686.

Newton, I. 1687. *Philosophiae Naturalis Principia Mathematica.* Royal Society, London.

Nicolau, J.M., Solé-Benet, A., Puigdefábregas, J. and Gutiérrez, L. 1996. Effects of soil and vegetation on runoff along a catena in semi-arid Spain. *Geomorphology* 14, 297–309.

Nikuradse, J. 1933. Strömungsgesetze in rauhen Rohren. *Forschungs-Arbeit des Ingenieur-Wesens* 361.

Nowell, A.R.M. and Church, M. 1979. Turbulent flow in a depth-limited boundary layer. *Journal of Geophysical Research* 84, 4816–4824.

Oliver, M. and Webster, R. 1986. Semi-variograms for modelling the spatial pattern of landform and soil properties. *Earth Surface Processes and Landforms* 11, 491–504.

Onstad, C.A. 1984. Depressional storage on tilled soil surfaces. *Transactions of the American Society of Agricultural Engineers* 27, 729–732.

Palutikof, J.P., Conte, M., Mendes, J.C., Goodess, C.M. and Santo, F.E. 1996. Climate and climatic change. In Brandt, C.J. and Thornes, J.B. (eds.) 1996. *Mediterranean Desertification and Land Use.* John Wiley & Sons, Chichester, 43–86.

Parsons, A.J. and Wainwright, J. 2006. Depth distribution of interrill overland flow and the formation of rills. *Hydrological Processes* 20, 1511–1523.

Parsons, A.J., Abrahams, A.D. and Luk, S-H. 1990. Hydraulics of interrill overland flow on a semi-arid hillslope, southern Arizona. *Journal of Hydrology* 117, 255–273.

Parsons, A.J., Abrahams, A.D. and Wainwright, J. 1994. On determining resistance to interrill overland flow. *Water Resources Research* 30, 3515–3521.

Parsons, A.J., Abrahams, A.D. and Wainwright, J. 1996a. Responses of interrill runoff and erosion rates to vegetation change in southern Arizona. *Geomorphology* 14, 311–317.

Parsons, A.J., Wainwright, J. and Abrahams, A.D. 1996b. Runoff and erosion on semi-arid hillslopes. In Anderson, M.G. and Brooks, S.M. (eds.) *Advances in Hillslope Processes*, Volume 2, John Wiley & Sons, Chichester, 1061–1078.

Parsons, A.J., Wainwright, J., Abrahams, A.D. and Simanton, J.R. 1997. Distributed dynamic modelling of interrill overland flow. *Hydrological Processes* 11, 1833–1859.

Peebles, W.R., Smith, R.E. and Yakowitz, S.J. 1981. A leaky reservoir model for ephemeral channel flow recession. *Water Resources Research* 17, 628–636.

Phelps, H.O. 1975. Shallow laminar flows over rough granular surfaces. *Journal of the Hydraulics Division of the American Society of Civil Engineers* 101, 367–384.

Philip, J.R. 1957. The theory of infiltration. 1. The infiltration equation and its solution. *Soil Science*, 83, 345–357.

Phillips, J.D. 1992. Deterministic chaos in surface runoff. In Abrahams, A.D. and Parsons, A.J. (eds.) *Overland Flow*, UCL Press, London, 177–197.

Planchon, O., Silvera, N., Giménez, R., Favis-Mortlock, D., Wainwright, J., Lebissonnais, Y., and Govers, G. 2005. An automated salt-tracing gauge for flow-velocity measurement. *Earth Surface Processes and Landforms* 30, 833–844.

Poesen, J. and Hooke, J.M. 1997. Erosion, flooding and channel management in Mediterranean environments of southern Europe. *Progress in Physical Geography* 21, 157–199.

Prandtl, L. 1905. Über Flüssigkeitsbewegungen bei sehr kleiner Reibung. In Krazer, A. (ed.), *Verhandlungen des dritten internationalen Mathematiker-Kongresses in Heidelberg 1904*. Teubner, Leipzig, 484.

Prandtl, L. 1926. Über die ausgebildete Turbulenz. *Proceedings of the 2nd International Congress of Applied Mechanics*. Zürich, 62–74.

Prandtl, L. 1935. The mechanics of viscous fluids. In Durand, W.F. (ed.) *Aerodynamic Theory:A General Review of Progress*, vol. 3. Springer, Berlin, 34–208.

Prestegaard, K.L. 1983. Variables influencing water-surface slopes in gravel-bed streams at bankfull stage. *Geological Society of America Bulletin* 94, 673–678.

Prony, G.C.F.M.R. de, 1804. *Recherches Physico-mathématiques sur la Théorie des Eaux courants*. Paris: de l'Imprimerie Impériale.

Puigdefábregas, J., Del Barrio, G., Boer, M., Gutiérrez, L. and Solé, A. 1998. Differential responses of hillslope and channel elements to rainfall events in a semi-arid area. *Geomorphology* 23, 337–351.

Ramis, C. 1995. Las observaciones de la atmosfera fibre en Mallorca: una breve historia y algunos resultados. *Revista de Ciencia* 17, 41–58.

Rauws, G. 1988. Laboratory experiments on resistance to overland flow due to composite roughness. *Journal of Hydrology* 103, 37–52.

Reaney, S.M. 2008. The use of agent based modelling techniques in hydrology: determining the spatial and temporal origin of channel flow in semi-arid catchments. *Earth Surface Processes and Landforms* 33, 317–327.

Reaney, S.M., Bracken, L.J. and Kirkby, M.J. 2007. Use of the Connectivity of Runoff Model (CRUM) to investigate the influence of storm characteristics on runoff generation and connectivity in semi-arid areas. *Hydrological Processes* 21, 894–906.

Reshetyuk, Y. 2006. *Investigation and calibration of pulsed time-of-flight terrestrial laser scanners*. Licentiate thesis in Geodesy, Royal Institute of Technology, Department of Transport and Economics, Division of Geodesy, Stockholm.

Reynolds, O. 1883. An experimental investigation of the circumstances which determine whether the motion of water will be direct or sinuous, and the law of resistance in parallel channels. *Philosophical Transactions, Royal Society of London* 174, 935–982.

Richards, K.S. 1982. *Rivers: Form and Process in Alluvial Channels*. Methuen & Co. Ltd., London.

Robert, A. 1990. Boundary roughness in coarse-grained channels. *Progress in Physical Geography* 14, 42–70.

Robert, A. 2003. *River Processes: An introduction to fluvial dynamics*. London, Arnold.

Rodríguez-Iturbe, I. and Valdès, J. 1979. The geomorphic structure of hydrologic response. *Water Resources Research* 15, 1409–1420.

Rodríguez-Iturbe, I., D'Odorico, P., Porporato, A. and Ridolfi, L. 1999. On the spatial and temporal links between vegetation, climate and soil moisture. *Water Resources Research* 12, 3709–3722.

Roels, J. M. 1984. Flow resistance in concentrated overland flow on rough slope surfaces. *Earth Surface Processes and Landforms* 9, 541–551.

Romero, R., Ramis, C. and Alonso, S. 1997. Numerical simulation of an extreme rainfall event in Catalonia: Role of orography and evaporation from the sea. *Quarterly Journal of the Royal Meteorological Society* 123, 537–559.

Romero, R., Ramis, C. and Guijarro, J.A. 1999. Daily rainfall patterns in the Spanish Mediterranean area: an objective classification. *International Journal of Climatology* 19, 95–112.

Römkens, M. and Wang, J. 1986. Effects of tillage on surface roughness. *Transactions of the American Society of Agricultural Engineers* 29, 429–433.

Römkens, M. and Wang, J. 1987. Soil roughness changes from rainfall. *Transactions of the American Society of Agricultural Engineers* 30, 101–107.

Rosser, N.J., Petley, D.N., Lim, M., Dunning, S.A. and Allison, R.J. 2005. Terrestrial laser scanning for monitoring the process of hard rock coastal cliff erosion. *Quarterly Journal of Engineering Geology and Hydrogeology* 38, 363–375.

Rouse, H. 1943. Evaluation of boundary roughness. *Proceedings Second Hydraulics Conference*, University of Iowa Studies in Engineering, Bulletin No. 27.

Rouse, H. and Ince, S. 1957. *History of Hydraulics*. Iowa Institute of Hydraulic Research, Iowa.

Royston, P. and Cox, N.J. 2005. A multivariable scatterplot smoother. *The Stata Journal* 5, 405–412.

Rumsby, B.T., Brasington, J., Langham, J.A., McLelland, S.J., Middleton, R. and Rollinson, G. 2008. Monitoring and modelling particle and reach-scale morphological change in gravel-bed rivers: applications and challenges. *Geomorphology* 93, 40–54.

Saleh, A. 1993. Soil roughness measurement, chain method. *Journal of Soil and Water Conservation* 48, 527–592.

Savat, J. 1977. The hydraulics of sheet flow on a smooth surface and the effect of simulated rainfall. *Earth Surface Processes and Landforms* 2, 125–140.

Savat, J. 1980. Resistance to flow in rough supercritical sheet flow. *Earth Surface Processes and Landforms* 5, 103–122.

Schick, A.P. 1988. Hydrologic aspects of floods in extreme arid environments. In Baker, V.R., Kochel, R.C. and Patton, P.C. (eds.) *Flood Geomorphology*, Wiley, New York, 189–203.

Schröder, B. 2006. Pattern, process and function in landscape ecology and catchment hydrology – how can quantitative landscape ecology support predictions in ungauged basins? *Hydrology and Earth System Sciences* 10, 976–979.

Scoging, H.M. 1982. Spatial variations in infiltration, runoff and erosion on hillslopes in semi-arid Spain. In Bryan, R.B. and Yair, A. (eds.) *Badland Geomorphology and Piping*, Geobooks, Norwich, 89–112.

Scoging, H.M. 1992. Modelling overland-flow hydrology for dynamic hydraulics. In Parsons, A.J. and Abrahams, A.D. (eds.) *Overland Flow*, UCL Press, London, 89–103.

Scoging, H.M. and Thornes, J.B. 1980. Infiltration characteristics in a semi-arid environment. *Proceedings of the symposium on the hydrology of areas of low precipitation*, Canberra, December 1979, International Association of Scientific Hydrology Publication 128, 159–168.

Seibert J. and McDonnell J.J. 2002. On the dialog between experimentalist and modeller in catchment hydrology: use of soft data for multicriteria model calibration. *Water Resources Research* 38, doi:10.1029/2001WR000978.

Shannon, J. 2003. *Modelling transient flows in ephemeral channels*. Unpublished Ph.D. Thesis, King's College, University of London. 448pp.

Shannon, J., Richardson, R. and Thornes, J. 2002. Modelling event-based fluxes in ephemeral streams. In Bull, L.J. and Kirkby, M.J. (eds.) *Dryland Rivers: hydrology and geomorphology of semi-arid channels*. John Wiley & Sons, Chichester, 129–172.

Shapiro, A.H. 1961. *Shape and Flow: The fluid dynamics of drag*. Heinemann, London.

Shapiro, S.S. and Wilk, M.B. 1965. An analysis of variance test for normality. *Biometrika* 52, 591–599.

Sharma, K.D., Menenti, M., Huygen, J. and Fernandez, P.C. 1996. Distributed numerical rainfall-runoff modelling in an arid region using thematic mapper data and a geographical information system. *Hydrological Processes* 10, 1229–1242.

Sharma, M.L., Gander, G.A. and Hunt, C.G. 1980. Spatial variability of infiltration in a watershed. *Journal of Hydrology* 45, 101–122.

Sherman, L. 1932. Streamflow from rainfall by unit-graph method. *Engineering News Record* 108, 501–505.

Sidle, RC. 2006. Field observations and process understanding in hydrology: essential components in scaling. *Hydrological Processes* 20, 1439–1445.

Sidle, R.C., Noguchi, S., Tsuboyama, Y. and Laursen, K. 2001. A conceptual model of preferential flow systems in forested hillslopes: evidence of self-organisation. *Hydrological Processes* 15, 1675–1692.

Singh, V.P. 1996. *Kinematic Wave Modelling in Water Resources: Surface-water Hydrology*. John Wiley, New York.

Sivapalan, M. 2005. Pattern, process and function: elements of a unified theory of hydrology at the catchment scale. In Anderson, M.G. (ed.), *Encyclopedia of Hydrological Sciences*, Wiley, Chichester, 193–219.

Smart, G.M. 1999. Coefficient of friction for flow resistance in alluvial channels with granular beds. *Water Maritime and Energy, Proceedings of the Institute of Civil Engineers* 136, 4, 205–210.

Smart, G.M., Duncan, M.J. and Walsh, J.M. 2002. Relatively rough flow resistance equations. *Journal of Hydraulic Engineering* 128, 6, 568–578.

Smith, M.W. 2005. The influence of surface roughness on runoff generation and soil erosion in semi-arid environments. M.Sc. Thesis, Department of Geography, Durham University.

Smith, M.W., Cox, N.J. and Bracken, L.J. 2007. Applying flow resistance equations to overland flows. *Progress in Physical Geography* 31, 4, 363–387.

Smith, R.E. 1972. The infiltration envelope: results from a theoretical infiltrometer. *Journal of Hydrology* 17, 1–21.

Smith, T.R. and Bretherton, F.P. 1972. Stability and the conservation of mass in drainage basin evolution. *Water Resources Research* 8, 1506–1529.

Solé-Benet, A., Calvo, A., Cerdá, A., Lázaro, R., Pini, R. and Barbero, J. 1997. Influences of micro-relief patterns and plant cover on runoff related processes in badlands from Tabernas (SE Spain). *Catena* 31, 23–28.

Stark, C.P. 1991. An invasion percolation model of drainage network evolution. *Nature* 352, 423–425.

Stokes, G.G. 1851. On the effect of the internal friction of fluids on the motion of pendulums. *Transactions, Cambridge Philosophical Society* 9, 8–106.

Strahler, A.N., 1958, Dimensional analysis applied to fluvially eroded landforms, *Geological Society of America Bulletin* 69, 279–300.

Straub, L.G. 1939. Studies of the transition-region between laminar and turbulent flow in open channels. *Transactions of the American Geophysical Union* 20, 649–653.

Strickler, A. 1923. Beitraege zur Frage der Geschwindigheits-formel und der Rauhikeitszahlen für Strome Kanale und Geschlossene Leitungen. *Mitteilungen des Eidgenössischer Amtes für Wasserwirtschaft*, 16, Bern, Switzerland.

Takken, I. and Govers, G. 2000. Hydraulics of interrill overland flow on rough, bare soil surfaces. *Earth Surface Processes and Landforms* 25, 1387–1402.

Takken, I., Govers, G., Ciesiolka, C.A.A., Silburn, D.M., and Loch, R.J. 1998. Factors influencing the velocity-discharge relationship in rills. In Summer, W., Klaghofer, E. and Zhang, W. (eds.) *Modelling Soil Erosion, Sediment Transport and Closely Related*

Hydrological Processes, Proceedings of Symposium held at Vienna, July 1998, IAHS Publication. no. 249, 63–70.

Takken, I., Govers, G., Jetten, V., Nachtergaele, J., Steegen, A. and Poesen, J. 2005. The influence of both process descriptions and runoff patterns on predictions from a spatially distributed soil erosion model. *Earth Surface Processes and Landforms* 30, 213–229.

Tatard, L., Planchon, O., Wainwright, J., Nord, G., Favis-Mortlock, D., Silvera, N., Ribolzi, O., Esteves, M. and Huang, C.H. 2008. Measurement and modelling of high-resolution flow-velocity data under simulated rainfall on a low-slope sandy soil. *Journal of Hydrology* 348, 1–12.

Tetzlaff, D., McDonnell, J.J., Uhlenbrook, S., McGuire, K.J., Bogaart, P.W., Naef, F., Baird, A.J., Dunn, S.M. and Soulsby, C. 2008. Conceptualising catchment processes: simply too complex? *Hydrological Processes* 22, 1727–1730.

Tominaga, A. and Nezu, I. 1992. Velocity profiles in steep open-channel flows. *Journal of Hydraulic Engineering* 118, 1, 73–90.

Tooth, S. 2000. Process, form and change in dryland rivers: a review of recent research. *Earth Science Reviews* 51, 67–107.

Tricker, A. 1981. Spatial and temporal patterns of infiltration. *Journal of Hydrology* 49, 261–277.

Trimble Navigation Limited. 2005. Trimble GS Series 3D scanner Datasheet. Date Accessed 20/11/2007. http://trl.trimble.com/docushare/dsweb/Get/Document-217217/022543-119A_GSSeries_DS_0405_lr.pdf .

Tritton, D.J. 1988. *Physical fluid dynamics*. Clarendon Press, Oxford.

Tromp-van Meerveld, H.J. and McDonnell, J.J. 2006. Threshold relations in subsurface stormflow 2. The fill and spill hypothesis. *Water Resources Research*, 42, W02411, doi:10.1029/2004WR003800.

Tukey. J.W. 1977. *Exploratory Data Analysis*. Addison-Wesley, Reading, MA.

Turnbull, L., Wainwright, J. and Brazier, R.E. 2008. A conceptual framework for understanding semi-arid land degradation: ecohydrological interactions across multiple-space and time scales. *Ecohydrology* 1, 23–34.

UNEP. 1992. *World Atlas of Desertification*. Edward Arnold, Sevenoaks, UK.

Van Deursen, W.P.A. and Wesseling, C.G. 1992. *The PCRaster Package*. Department of Physical Geography, Utrecht University, the Netherlands.

Van de Giesen, N.C., Stomph, T.J. and de Ridder, N. 2000. Scale effects of Hortonian overland flow and rainfall-runoff dynamics in a West African catena landscape. *Hydrological Processes* 14, 165–175.

Van Loon, E.E. and Keesman, K.J. 2000. Identifying scale-dependent models: the case of overland flow at the hillslope scale. *Water Resources Research* 36, 243–254.

Wagener, T., Sivapalan, M., Troch, P., and Woods, R. 2007. Catchment classification and hydrologic similarity. *Geography Compass* 1/4, 901–931.

Wahl, K.L. 1994. Bias in regression estimates of Manning's *n*. In Cotroneo, G.V. and Rumer, R.R. (eds.) *Hydraulic Engineering '94*, Proceedings of the 1994 Conference of the Hydraulic Division, ASCE, New York, 727–731.

Wainwright, J. and Parsons, A.J. 2002. The effect of temporal variations in rainfall on scale dependency in runoff coefficients. *Water Resources Research* 38, 12, 1271–1280.

Webber, N.B. 1965. *Fluid Mechanics for Civil Engineers*. E. and F.N. Spon Ltd, London.

Weisbach, J., 1845. *Lehrbuch der Ingenieur- und Maschinen-Mechanik*. Vieweg und Sohn, Braunschweig, Germany.

Weisberg, S. 2005. *Applied Linear Regression* (3rd ed.). Wiley, Hoboken, New Jersey, USA.

Western, A.W., Blöschl, G. and Grayson, R.B. 2001. Towards capturing hydrologically significant connectivity in spatial patterns. *Water Resources Research* 37, 1, 83–97.

Western, A.W., Grayson, R.B., Blöschl, G., Willgoose, G.R. and McMahon, T.A. 1999. Observed spatial organisation of soil moisture and its relation to terrain indices. *Water Resources Research* 35, 797–810.

White, F.M. 2003. *Fluid Mechanics* (5th Edition). McGraw-Hill, New York.

Wiberg, P.L. and Smith, J.D. 1991. Velocity distribution and bed roughness in steep streams. *Water Resources Research* 32, 2897–909.

Wilcock, P. R. 1996. Estimating local shear stress from velocity observations. *Water Resources Research* 32, 3361–3366.

Wilcock, P.R., Barta, A.F., Shea, C.C., Kondolf, G.M., Matthews, W.V.G. and Pitlick, J. 1996. Observations of flow and sediment entrainment on a large gravel-bed river. *Water Resources Research* 32, 2897–2909.

Wilcox, B.P., Newman, B.D., Brandes, D., Davenport, D.W. and Reid, K. 1997. Runoff from a semiarid ponderosa pine hillslope in New Mexico. *Water Resources Research* 33, 2301–2314.

Wilcox, B.P., Rawls, W.J., Brakenseik, D.L. and Wight, J.R. 1990. Predicting runoff from rangeland catchments: a comparison of two models. *Water Resources Research* 26, 2401–2410.

Wilcoxon, F. 1945. Individual comparisons by ranking methods. *Biometrics* 1, 80–83.

Wohl, E. 2000. *Mountain Rivers*. Water Resources Monograph 14, American Geophysical Union, Washington, DC.

Wolman, M.G. 1955. The natural channel of Brandywine Creek, Pennsylvania. *U.S. Geological Survey Professional Paper* 271.

Wolman, M.G. and Gerson, R., 1978. Relative scales of time and effectiveness of climate in watershed geomorphology. *Earth Surface Processes & Landforms* 3, 189–208.

Yair, A. 1990. The role of topography and surface cover upon soil formation along hillslopes in arid climates. *Geomorphology* 3, 287–299.

Yair, A. and Danin, A. 1980. Spatial variation in vegetation as related to the soil moisture regime over an arid limestone hillside, northern Negev, Israel. *Oecologia* 47, 83–88.

Yair, A. and Kossovsky, A. 2002. Climate and surface properties: hydrological response of small arid and semi-arid watersheds. *Geomorphology* 42, 43–57.

Yair, A. and Lavee, H. 1985. Runoff generation in arid and semi-arid zones. In Anderson, M.G. and Burt, T.P. (eds.) *Hydrological Forecasting*, Wiley, Chichester, 183–220.

Yair, A. and Raz-Yassif, N. 2004. Hydrological processes in a small arid catchment: scale effects of rainfall and slope length. *Geomorphology* 61, 155–169.

Yair, A., Lavee, H., Bryan, R.B. and Adar, E. 1980. Runoff and erosion processes and rates in the Zin valley badlands, Northern Negev, Israel. *Earth Surface Processes* 5, 205–225.

Yen, B.-C. 1965. Discussion of 'Large-scale roughness in open-channel flow'. *Journal of the Hydraulics Division, Proceedings of the American Society of Civil Engineers* 97, 1367–1386.

Zhang, R. 1997. Determination of soil sorptivity and hydraulic conductivity from the disk infiltrometer. *Soil Science Society of America Journal* 61, 1024–1030.

Zobeck, T.M. and Onstad, C.A. 1987. Tillage and rainfall effects on random roughness: a review. *Soil & Tillage Research* 9, 1–20.

APPENDIX

GLOSSARY OF ROUGHNESS MEASURES

Soil surface roughness is defined in this thesis as either a property of the soil that exists independent of any overland flows, or such a property scaled to a measure of flow depth. From this imprecise definition, numerous roughness measures can be calculated. The calculation of any such measure in this thesis effectively represents an implicit hypothesis that the characterisation of roughness in that precise way will influence resistance to overland flows (at least in part).

The precise definition of each roughness measure examined in this thesis is given below. Some measures were extracted directly from the Digital Elevation Model (DEM) provided from the method described in Chapter 4 and summarise the entire surface over which the flow moved during each timestep. Other measures are split into orthogonal components (perpendicular and parallel) and are calculated from transects taken from the DEM.

d = **Mean flow depth** [L]
Mean water depth estimated for a DEM over which a thread of water has travelled during a single timestep.

d_{50} = **Median flow depth** [L]
Median water depth estimated for a DEM.

d_{sk} = **Depth skewness** [Dimensionless]

A measure of the asymmetry of the depth distribution estimated for a DEM. Skewness is defined as the standardised third moment about the mean. While this is a measure of the flow itself, it essentially summarises the distribution of elevations within the wetted area, taking into account variability in the elevation of the water surface.

F_P = **Frontal area per unit planar area 1–20** [Dimensionless]

Three-dimensional surface area directly opposing the flow calculated for the DEM as a whole (and normalised by total planar area). The numbers 1–20 represent grid sizes used to calculate both areas. Each number represents a multiple of the 2 mm grid-scale. This measure is an attempt to capture the area protruding into the flow contributing to total drag. However, any relationship will be complicated where roughness elements are so concentrated that slimming flow develops from wake interaction (Nowell and Church, 1979).

F_T = **Frontal area per unit surface area 1–20** [Dimensionless]

Three-dimensional surface area directly opposing the flow calculated for the DEM as a whole (and normalised by total 3d surface area). The numbers 1–20 represent grid sizes used to calculate both areas. Each number represents a multiple of the 2 mm grid-scale. This is similar to F_P above, though scaled to surface area (which may be more relevant over very rough surfaces).

P_d = **Parallel pit density** [L^{-1}]

Pit density measured using transects parallel to the flow direction (number of pits unit transect length). This is the mean value from each transect calculated on a DEM. A pit is defined as a point which is lower than both neighbours on a transect. The measure has been separated into orthogonal components as each component interacts with the flow in a very different manner. This measure is correlated with surface depression storage (Smith, 2005) and represents the trapping of water, reducing the ease with which water passes over the surface. However, once pits have been filled with water, subsequent flows may not interact with pits. Additionally, this measure allows no appreciation of the size of each pit.

P_{dmin} = **Minimum parallel pit density** [L^{-1}]

Pit density measured using transects parallel to the flow direction, as above. This is the minimum value from each transect calculated on a DEM and potentially represents the optimum flow pathway available to any overland flows.

P_{dmx} = **Maximum parallel pit density** [L^{-1}]

Pit density measured using transects parallel to the flow direction, as above. This is the maximum value from each transect calculated on a DEM.

P_{dxc} = **Perpendicular pit density** [L^{-1}]
Pit density of transects perpendicular to the flow direction (number of pits unit transect length). This is the mean value from each transect calculated on a DEM. In contrast to pits measured parallel to the flow direction, perpendicular pits represent flow concentrations and may have a very different relationship with flow resistance. However, this measure provides no indication of the size of any such concentrations.

R = **Perpendicular hydraulic radius** [L]
Mean hydraulic radius (cross-sectional area A /wetted perimeter P) as measured over transects perpendicular to the flow direction.

R_v = **Volumetric hydraulic radius** [L]
Volumetric hydraulic radius (water volume V_l / wetted surface area A_{3D}) as measured over the DEM as a whole (following Smart *et al.*, 2002). This presents a practical measure for overland flows over complex surfaces where both the water and soil surface are known (or estimated) and approximates to mean flow depth d where all roughness elements are inundated.

S = **Slope** [Dimensionless]
Soil surface slope (sine of the angle) as measured at the same scale as the roughness measurements. This is important as measured flow velocities varied substantially over ~1 second measurement timesteps. Such variability is often lost when measurements are aggregated up to larger scales. The slope of the microtopographic elements has been retained as a roughness measure. It has been measured at the length scale over which the overland flow travelled during an interval of approximately 1 second. Increasing the scale would decrease the observed variability and eventually approximate an average value.

T_{3D} = **3d tortuosity 1–20** [Dimensionless]
3d (or surface) tortuosity calculated for each DEM as a whole (3d surface area / 2d planar area). The numbers 1–20 represent grid sizes used to calculate both areas. Each number represents a multiple of the 2 mm grid-scale.

T_p = **Parallel tortuosity** [Dimensionless]
Mean value of the tortuosity of transects measured parallel to the flow direction (wetted perimeter P / flow length l). The tortuosity measures have been divided into orthogonal components for the reasons described for the pit density measures.

T_r = **Tortuosity ratio** [Dimensionless]
The ratio of T_p:T_{xc}. This represents the proportion of the total tortuosity that is represented as roughness in the flow direction opposing (rather than concentrating) flow.

T_{xc} = **Perpendicular tortuosity** [Dimensionless]
Mean value of the cross-sectional tortuosity measured on transects perpendicular to the flow direction (P/w). This equates to the 'wet tortuosity' of Takken and Govers (2000) without subtracting 1.

Z_d = **Mean surface elevation difference** [L]
Mean difference between the elevation of a point and its eight neighbouring cells averaged over the DEM. This is similar to the K3 parameter of Ergenzinger (1992) applied to a surface. This more effectively filters out large, structured roughness elements (such as rill walls) than the standard deviation σ_Z or roughness height ε measures as only the immediate neighbours of a point are used in the calculation.

Z_{NN} = **Nearest neighbour** [L]
Minimum elevation difference between each point and its neighbours, averaged over the DEM.

α = **Gamma alpha** [Dimensionless]
Shape factor of the observed distribution of depths as fitted to a two-parameter gamma distribution (see section 5.4).

β = **Gamma beta** [L]
Scale factor of the distribution of depths as fitted to a two-parameter gamma distribution (see section 5.4). The product $\alpha\beta$ gives the mean depth d.

ε = **Mean roughness height** [L]
Mean 'roughness height' as frequently used in classical hydraulics literature. This has been amended to incorporate the variable roughness heights and small grain sizes in comparison with form roughness (discussed in section 6.2). Treating each perpendicular transect separately, it is calculated as the median elevation minus the minimum elevation (the perpendicular transects have been used to remove any general slope effects that would influence transects parallel to the flow direction). The value given here is the mean value for the perpendicular transects of the DEM.

Λ = **Inundation ratio** [Dimensionless]
Ratio of thread median depth d_{50} to mean roughness height ε. This gives the inundation ratio used by Lawrence (1997).

Λ_σ = **Inundation ratio STDEV** [Dimensionless]
Ratio of thread median depth d_{50} to standard deviation of elevations σ_Z. This gives the inundation ratio used by Aberle and Smart (2003).

Λ_{Zd} = **Detrended inundation ratio** [Dimensionless]
Ratio of thread median depth d_{50} to thread mean elevation difference Z_d.

σ_Z = **3d standard deviation**[L]
Standard deviation of the elevation of all points of a Digital Elevation Model.

σ_{Zxc} = **Perpendicular standard deviation** [L]
Mean standard deviation of elevations of transects measured perpendicular to the flow direction. This is not calculated in the downslope direction as it will be highly dependent on slope.